[DR. BEVAN: PLEASE PRINT DOCUMENT ON LETTERHEAD PAPER]

Monday, December 31, 2018

To: U.S. Citizenship & Immigration Services

Re: I-140 Petition for Dr. Yuguang Yang

To Whom It May Concern:

I am writing on behalf of Dr. Yuguang Yang to give my strong support for his petition for permanent residency in the United States. Dr. Yang has made outstanding contributions in mathematical modeling, and I believe that his past achievements demonstrate that he will continue to make great strides in the future.

I am currently a Professor with the Department of Chemical Engineering at The Johns Hopkins University. I obtained my Ph.D. in Chemical Engineering from Carnegie Mellon University in 1999 and have since conducted research in complex fluid and material applications via sophisticated experimental and mathematical tools. For my work, I have received honors including American Chemical Society(ACS) Fellow (2016), Presidential Early Career Award for Scientists and Engineers (PECASE, 2005), and National Science Foundation CAREER Award (2004). I have also chaired the international ACS colloids conferences. With the above experiences, publication of over 90 refereed articles in conferences and journals, and service on over 25 program committees, I am considered an expert in colloidal physics, working on projects with funding coming from Department of Energy, National Science Foundation and the industry. Therefore, I am well qualified to judge Dr. Yang's significant contributions and their impacts.

I have known Dr. Yang since 2011 when he enrolled in the graduate program at the Johns Hopkins University. After joining our group for his Ph.D. research, Dr. Yang consistently distinguished himself by demonstrating outstanding capabilities in mathematical modeling and computer science skills. As a part of his Ph.D. research, Dr. Yang played the leading role in multiple projects in my group. I cannot imagine these projects being completed without Dr. Yang's work. He is, by far, one of the most creative and productive researchers that I have ever advised. Here, I list a series of projects Dr. Yang accomplished to illustrate his capabilities.

1) Optimal navigation of self-propelled colloidal particles

In this project, Dr. Yang was among the first in the world to develop general optimal path planning method for self-propelled particles based on a creative combination of methodologies from applied mathematics, computer science, and robotics. Self-propelled micro-sized colloidal particles have been widely believed to be the next-generation soft-robots to operate in complex microstructured environments (*e.g.*, porous media, tumor vasculature) to perform tasks such as oil recovery, environment remediation, drug delivery, and disease diagnosis etc. However, efficient navigation of self-propelled particle trajectories within micro-structured environments has not been sufficiently achieved due to the existence of obstacles and dead-ends, as in mazes, and the complex stochastic nature of the motion of self-propelled particle when near obstacles. Dr. Yang's method enables self-propelled particles to avoiding dead-end pathways (*e.g.*, like self-driving cars), efficiently navigate between start and end points by minimizing passage times, traversed distances, and consumption of scarce resources. For example, his algorithm enables a self-propelled particle to operate 80X faster than an uncontrolled robot in a 250 um

by 250 um maze transportation task. This optimal navigation performance is a superior advantage especially as the travel distance increases. These findings were published in the *ACS Nano* journal, which is a top journal in the field and has impact factor about 14.

2) Cargo capture and transport using micro-robot swarm

Based on his work of optimal navigation of single self-propelled particle as single robot, Dr. Yang then came up with a unique approach that involves employing multiple micro-robotics to cooperate on tasks beyond an individual robot's capacity, analogously to ants working altogether to carry over-sized food. This approach has significant robustness, flexibility, and error-tolerance compared to current cargo delivering micro-robotic systems. However, it also comes with the unprecedented challenges of simultaneously and efficiently controlling multiple stochastically moving particles to perform tasks. Dr. Yang creatively developed a multi-agent stochastic feedback control system, equipped with his own efficient control algorithm. It is notable that Dr. Yang successfully employed theory from Lie group, an extremely complicated mathematical theory, to derive an analytical solution for the individual robot dynamics and enable the implementation of the fast algorithm that is feasible in the real-world. Due to the novelty and implication of this work, he was offered a research internship in the Palo Alto Research Center (PARC), CA, to develop an algorithm for precise control assembly microchips, which is the key step towards an entirely new way to fabricate micro-electronic devices, as noted in MIT technology reviews. This project is funded by Defense Advanced Research Projects Agency, an agency of the United States Department of Defense.

3) Mathematically modelling of colloidal crystallization

Using an experimental model system, Dr. Yang contributed to the understanding of grain boundary formation in colloidal crystallization significantly. [Dr. Yang: Please provide 1-2 sentences describing the value of colloidal crystallization (e.g, Colloidal crystallization is a necessary step to achieve optimized XXXXX, etc.).] Dr. Yang developed a mathematical model describing the self-assembly dynamics by integrating a number of various tools from different fields. For example, Dr. Yang successfully used a cutting edge machine learning method to reduce the dimensionality of hundreds and thousands (which is impossible to model even in supercomputers and known as dimensionality curse) to less than 3. The resulting models reveal remarkable insights such as that equal sized domains at a maximum mis-orientation are prone to formation of grain boundary due to the lack the thermodynamic driving force. By quantifying such dynamics vs. compression (voltage), Dr. Yang revealed kinetic bottlenecks associated with slow grain boundary relaxation that can be used to guide the temporal assembly of defect-free single domain colloidal crystals. Taking this already significant achievement even further, Dr. Yang generalized his approach to a systematic model-construction methodology that can be used to understand other self-assembly systems. Dr. Yang's modeling framework sheds light on the underlying driving forces and dynamics governing self-assembly processes, and information about the existence of metastable states as well as the expected times for transitions between states. Self-assembly has been employed as a key approach to fabricate novel colloidal materials. Yet for a very long time, producing colloidal crystals via self-assembly has been employed mainly empirically, instead of in a rational and predictable manner, due to the lack of suitable mathematical model of colloidal crystallization process. Thus, Dr. Yang's model is the first to enable rational and predictable self-assembly for colloidal crystallization. These findings were published in *Scientific Reports* (an open-access journal in Nature Publishing Group) and the *Journal of Chemical Physics* (a top journal in the field).

4) Optimal feed-back control assembly of colloidal perfect crystals.

In a closely related project, Dr. Yang constructed a stochastic dynamic model that captures colloidal crystallization dynamics at different external driving force strengths. He then calculated a model-based control strategy and realized for the first time in the world a feed-back control assembly of defect-free colloidal crystals within minimum time. Dr. Yang's model ultimately serves as the road map to steer the self-assembly along different system states by switching between different external driving force strength. This achievement is of remarkable significance since this method is fundamental to the development of defect-free large scale manufacturing of meta-materials. The research has gathered the attention of researchers in their joint efforts to solve the large-scale metamaterial fabrication problem. Materials with perfectly ordered periodic micro-structures, known as "meta-materials", have unique electric, magnetic, and optical properties. The feedback control system Dr. Yang developed filled a critical gap, since no previously existing process was sufficiently controllable, scalable, and robust for high-throughput manufacturing. High-throughput manufacturing is necessary to enable meta-materials for commercial and military applications. The findings were published in journals and conference including *American Control Conference* (national control conference), *Journal of Process Control* (a top journal in process control), and *ACS Nano* (a top journal in material science).

5) Colloidal rod hydrodynamic interaction modeling

Dr. Yang also creatively developed constraint Stokesian dynamics, which enables not only the calculation of the transport coefficients in confined geometries, but also the direct simulation of colloidal rod-shape particles. Motion of micro- and nano-sized colloidal rod-shaped particles in interfacial and confined geometries are important in numerous dynamic processes involving, for example, biological macromolecules and drug particles transport within tissues, and novel constituent particle assembly in materials engineering, and nanoparticle fate within environmental porous media. However, many aspects of single rod dynamics near surfaces have remained unclear due to the intricate interplay of conservative colloidal forces (e.g., electrostatic, van der Waals, gravity), hydrodynamic drag (e.g., Stokes drag, lubrication), and Brownian motion. Dr. Yang's simulation model shed light on single rod motion under confinement, further paving the way for multiple colloidal rod assembly for anisotropic material engineering. To further verify his theoretical model, Dr. Yang worked with experimentalist Dr. Julie Bitter (currently works at National Institute of Standards and Technology) to construct easy-to-use, parametric, experimentally validated models to interpret and predict boundary effects on colloidal rod diffusion, which is of great use to practitioners in the long run. These findings were published in the *Journal of Chemical Physics* and *Langmuir* (both are top journals in the field).

6) Multi-scale reversible colloidal assembly

Dr. Yang developed a numerical model of local excluded volume affects to compute local depletion attraction in the presence of arbitrary geometries, which enables the design of colloidal based materials and devices. For metamaterials with constituent of colloidal particles, reversible colloidal assembly not only provides a promising method to fabricate large-area hierarchical structures in metamaterials, but also enables switching multi-scale structures between two or more configurations as a basis to develop reconfigurable metamaterial-based devices. Dr. Yang's computation method was applied to an experimental system (he collaborated with experimentalist Dr. Edward Tara, currently working at U.S. Army Research Laboratory) to create non-close-packed reconfigurable structures using tunable depletants. The re-configurability allows such systems to be used as static materials or programmable devices. These findings were published in *Scientific Reports* (an open-access journal in Nature Publishing Group) and *Journal of Colloid and Interface Science* (a prestigious journal in colloidal science).

Overall, Dr. Yang has consistently proven his advanced knowledge of mathematical modeling. As such modeling is the foundation of improved prediction capabilities in a number of areas ranging from transportation to medicine to finance to climatology, it is imperative that we retain not only scientists who are highly skilled in the theoretical and technical basis of mathematical modeling but also those who are experienced in tailoring models to fit the needs of different areas. Dr. Yang is one of these valuable scientists. Throughout his studies at Johns Hopkins University, he not only mastered various mathematical skills but also gained a deep understanding of the limitations of mathematical models and the need for supplemental solutions. He developed an impressive knowledge of cutting edge computational technology and demonstrated an exceptional ability in abstract and quantitative reasoning. Most significantly, he gained practical experience with real world complexities and challenges and excelled in using appropriate tools strategically while employing methodologies from different areas.

Given Dr. Yang's outstanding accomplishments, I believe he is a unique and important force in this research area and that it would hinder the maximization of mathematical modeling to improve predictive capabilities in a number of areas if he could not continue his research. He has deservedly established a very important niche in the research efforts in this area. For this reason, I heartily recommend Dr. Yang for permanent residency in the United States of America. His expertise and contributions in mathematical modeling make him an asset to any nation, and I have no doubt that he will continue to make substantial contributions in the future.

Sincerely,

Michael A. Bevan, Ph.D.
Professor
Whiting School of Engineering
The Johns Hopkins University
Office: (410) 516-7907
E-mail: mabevan@jhu.edu

MICHAEL A. BEVAN

Department of Chemical and Biomolecular Engineering
The Johns Hopkins University, Baltimore, MD 21218
voice: 410.516.7907, fax: 410.516.5510
mabevan@jhu.edu, www.jhu.edu/bevan

I. EDUCATION

1999 **Ph.D. Chemical Engineering**, Carnegie Mellon Univ., Pittsburgh, PA
1994 **B.S. Chemical Engineering**, high honors, Lehigh Univ., Bethlehem, PA
1994 **B.S. Chemistry**, high honors, Lehigh Univ., Bethlehem, PA

II. AWARDS & HONORS

2005 **PECASE,** National Science Foundation
2004 **CAREER**, National Science Foundation
2001 **Beckman Postdoctoral Fellowship**, Beckman Foundation
1998 **Henkel Doctoral Fellowship**, ACS Colloids & Surfaces Division

III. RESEARCH EXPERIENCE

01/08 - **Associate Professor**
Chemical & Biomolecular Engineering
Johns Hopkins University

03/07 - 12/07 **Associate Professor**
Chemical Engineering
Mechanical Engineering (joint appointment)
Texas A&M University

08/02 - 03/07 **Assistant Professor**
Chemical Engineering
Texas A&M University

09/01 - 08/02 **Postdoctoral Fellow**
Materials Science & Physics
Beckman Institute for Advanced Science & Technology
University of Illinois at Urbana-Champaign

08/99 - 08/01 **Postdoctoral Fellow**
Chemistry, Chemical Engineering, Mathematics
Particulate Fluids Processing Centre
University of Melbourne, Australia

01/95 - 08/99 **Graduate Research Assistant**
Chemical Engineering
Carnegie Mellon University

05/93 - 08/94 **Undergraduate Research Assistant**
Chemical Engineering, Lehigh University
Analytical Group, Rohm & Haas Company

05/89 - 05/90 **High School Research Assistant**
Chemistry
Franklin and Marshall College

IV. RESEARCH FUNDING

Current

1. Principal Investigator, “Colloidal Crystallization via Simultaneous Depletion and Electric Field Mediated Interactions” (CBET-1234981), NSF Particulate & Multiphase Processes, $300,000, 08/01/2012-07/31/2015.
2. Co- Principal Investigator (PI, Greg Huff, Texas A&M), “Material Systems for Reconfigurable Antennas in Superconfigurable Structures” Air Force Office of Scientific Research, Mechanics of Multifunctional Materials & Microsystems, $220,245 (total award $689,250), 01/01/2012-12/31/2014.
3. Principal Investigator, “Aperskin and Aperphores: Multifunctional (Thermal-Electromagnetic-Ballistic) Surfaces for Coordinated Counter-RCIED, Sensing, and Communications Applications” ONR Force Protection Thrust, Integration and Transition Division, $335,580 (total award $1,085,000), 01/01/2012-12/31/2014.
4. Principal Investigator, “Collaborative Research: CDI-Type II: First-Principles Based Control of Multi-Scale Meta-Material Assembly Processes” NSF Cyber-enabled Discovery and Innovation Type II (CMMI-1124648), $399,603 (total award $1,604,812), 09/01/2011-08/31/2015.
5. Co- Principal Investigator (PI, Howard Fairbrother, JHU), “Nanoparticle-Surface Interactions in Aqueous Environments”, NSF Environmental Chemical Sciences (CHE-1112335), $227,082, (total award $469,364), 06/15/2011-05/31/2014.
6. Principal Investigator, “Diffusing Probes of kT-scale Specific Protein-Protein & Protein-Carbohydrate Interactions”, NSF Interfacial Processes & Thermodynamics (CBET-1066254), $324,241, 06/01/2011-05/31/2014.
7. Principal Investigator, “Integrated Self & Directed Assembly of Multi-Component Colloidal Structures” (CBET-0932973), NSF Particulate & Multiphase Processes, $300,000, 08/01/2009-07/31/2013.

Completed

1. Principal Investigator, “CDI-Type I: Collaborative Research: Cyber Enabled Engineering of Particle Based Materials and Devices using Energy Landscapes” (CMMI-0835549), NSF Cyber-enabled Discovery and Innovation Type I (NSF07603), $294,065 (total award $544,647), 09/15/2008-09/14/2011 (no cost extension to 08/31/2012).
2. Principal Investigator, “Feedback Controlled Assembly of Colloidal Crystals”, National Institute of Standards and Technology, $15,580, 9/1/2010-11/30/2011.
3. Co- Principal Investigator (PI, Dimitris Lagoudas, Texas A&M), “Multi-scale Modeling and Characterization of Electromagnetically Tunable Colloidal-Based Materials”, Air Force Office of Scientific Research, Aerospace and Materials Sciences (AFOSR BAA 2007-6), $300,000, 07/01/2008-06/31/2011.
4. Principal Investigator, “Diffusing Probe Measurements of Specific Interactions between Surface Immobilized Biomacromolecules” (CBET-0755878), NSF Interfacial

Processes & Thermodynamics (NSF081414), $273,501, 06/01/2008-05/31/2011.

5. Principal Investigator, “CAREER: Direct Measurement and Manipulation of Colloidal Interactions and Dynamics in Template Directed Photonic Crystal Assembly” (CBET-0829353, previously CTS-0346473), NSF Particulate & Multiphase Processes (NSF NSF02111), $405,228, 02/15/2004-01/31/2009 (no cost extension to 01/31/2010).
6. Principal Investigator, “Diffusing Colloidal Probe Measurements of Protein and Synthetic Macromolecule Interactions” (CBET-0755878), NSF Interfacial Processes & Thermodynamics (NSF081414), $100,000, 08/01/2006-07/31/2008 (no cost extension to 07/31/2009).
7. Principal Investigator, “Diffusing Colloidal Probes of Protein-Protein Potentials of Mean Force on Arrays” (A1567), Robert A. Welch Foundation, $150,000, 06/01/2007-05/31/2010 (expired on 12/31/2007 with departure from Texas A&M University).
8. Principal Investigator, “Microfluidic Systems for Reconfigurable RF Surfaces and Systems”, Defense Advanced Research Projects Agency”, $300,000, 10/01/2006-09/30/2007.
9. Co-Principal Investigator (PI, Ali Beskok, Texas A&M), “Reversible Control of Anisotropic Electrical Conductivity Using Colloidal Microfluidic Networks”, Defense Advanced Research Projects Agency, $100,000, 03/01/2006-09/30/2006.
10. Principal Investigator, “Ensembles of Levitated Diffusing Colloids as Novel Biomolecular Probes” (A1567), Robert A. Welch Foundation, $150,000, 06/01/2004-05/31/2007.
11. Principal Investigator, “Mapping Potential Energy Landscapes using Diffusing Colloidal Probe Microscopy”, American Chemical Society Petroleum Research Fund, Type G, $35,000, 06/01/2004-05/31/2006.

V. RESEARCH PUBLICATIONS

Published & Submitted

1. Microfluidic-Enabled Reconfigurable Patch With Integrated Dielectric Spectrometer, Long, S.A.;, Dorsey, W.M.; Huff, G.H.; Brennan, N.; Rupp, B.; Bevan, M.A. *IEEE Trans. Antennas Propagation* submitted, 2013.
2. Self-Consistent Colloidal Energy and Diffusivity Landscapes in Macromolecular Solutions, Beltran-Villegas, D.J.; Edwards, T.D.; Bevan, M.A. *Phys. Rev. Lett.*, in revision, 2013.
3. Optimal Control of a Colloidal Self-Assembly Process, Xue, Y.; Beltran-Villegas, D.J.; Tang, X.; Bevan, M.A.; Grover, M.A. *IEEE Trans. Control Syst. Technol.* in revision, 2013.
4. Size Dependent Thermodynamics and Kinetics in Electric Field Mediated Colloidal Crystal Assembly, Edwards, T.D.; Beltran-Villegas, D.J.; Bevan, M.A. *Soft Matter,* accepted 2013.
5. Anomalous Silica Colloid Stability and Gel Layer Mediated Interactions, Bitter, J.; Duncan, G.; Beltran-Villegas, D.J.; Fairbrother, D.H.; Bevan, M.A. *Langmuir* accepted, 2013.
6. Diffusing Colloidal Probes of Protein-Carbohydrate Interactions, Eichmann, S.L.;

Meric, G.; Swavola, J.C.; Bevan, M.A. *Langmuir* Vol. 29, 2299–2310, 2013.

7. Colloidal Cluster Crystallization Dynamics, Beltran-Villegas, D.J.; Sehgal, R.M.; Maroudas, D.; Ford, D.M.; Bevan, M.A. *J. Chem. Phys.* Vol. 137, 134901, 2012.
8. Depletion Mediated Potentials and Phase Behavior for Micelles, Macromolecules, Nanoparticles, and Hydrogel Particles, Edwards, T.D.; Bevan, M.A. *Langmuir* Vol. 28, 13816-13823, 2012.
9. Multiple Electrokinetic Actuators for Feedback Control of Colloidal Crystal Size, Juarez, J.J.; Mathaib, P.P.; Liddle, J.A.; Bevan, M.A. *Lab Chip* Vol.12, 4063 - 4070, 2012.
10. Feedback Controlled Colloidal Self-Assembly, Juarez, J.J.; Bevan, M.A. *Adv. Funct. Mater.* Vol.22, 3833–3839, 2012.
11. Polymer Mediated Depletion Attraction & Interfacial Colloidal Phase Behavior, Iracki, T.D.; Bevan, M.A. *Macromolecules* Vol. 45, 585–594, 2012.
12. Electric Field Mediated Assembly of Three Dimensional Equilibrium Colloidal Crystals, Juarez, J.J.; Feicht, S.; Bevan, M.A. *Soft Matter* Vol. 8, 94-103, 2012.
13. Smoluchowski Model of Crystallization Dynamics of Small Colloidal Clusters, Beltran-Villegas, D.J.; Sehgal, R.M.; Maroudas, D.; Ford, D.M.; Bevan, M.A. *J. Chem. Phys.* Vol. 135, 154506, 2011.
14. kT-Scale Colloidal Interactions in High Frequency Inhomogeneous AC Electric Fields. II. Concentrated Ensembles, Juarez, J.J.; Liu, B.; Cui, J.; Bevan, M.A. *Langmuir* Vol. 27, 9219–9226, 2011.
15. kT-Scale Colloidal Interactions in High Frequency Inhomogeneous AC Electric Fields. I. Single Particles, Juarez, J.J.; Cui, J.; Liu, B.; Bevan, M.A. *Langmuir* Vol. 27, 9211–9218, 2011.
16. Imaging Carbon Nanotube Interactions, Diffusion, and Stability in Nanopores, Eichmann, S.L.; Smith, B.; Meric, G.; Fairbrother, D.H.; Bevan, M.A. *ACS Nano* Vol.5, 5909-5919, 2011.
17. Free Energy Landscapes for Colloidal Crystal Assembly, Beltran-Villegas, D.J.; Bevan, M.A. *Soft Matter* Vol. 7, 3280-3285, 2011.
18. Optical Microscopy Measurements of kT-Scale Colloidal Interactions, Bevan, M.A.; Eichmann, S.L. *Curr. Opin. Colloid Interface Sci.* 16, 149-157, 2011.
19. Concentrated Diffusing Colloidal Probes of Ca2+ Dependent Cadherin Interactions, Everett, W.N.; Beltran-Villegas, D.J.; Bevan, M.A. *Langmuir* 26, 18976–18984, 2010.
20. Charged Micelle Depletion Attraction and Interfacial Colloidal Phase Behavior, Iracki, T.D.; Beltran-Villegas, D.J.; Eichmann, S.L.; Bevan, M.A. *Langmuir* 26, 18710–18717, 2010.
21. Direct Measurements of Protein Stabilized Gold Nanoparticle Interactions, Eichmann, S.L.; Bevan, M.A. *Langmuir* 26, 14409–14413, 2010.
22. Confocal Laser Imaging & Annealing of Quantum Dot Coated Silica Colloidal Crystals, Beckham, R.E.; Bevan, M.A. *Langmuir* 26, 3779–3782, 2010.
23. Fokker-Planck Analysis of Separation Dependent Potentials and Diffusion Coefficients in Simulated Microscopy Experiments, Beltran-Villegas, D.J.; Sehgal,

R.M.; Maroudas, D.; Ford, D.M.; Bevan, M.A. *J. Chem. Phys.* 132, 044707, 2010.

24. Spatially Controlled Reversible Colloidal Self-Assembly, Fernandes, G.E.; Beltran, D.; Bevan, M.A. *J. Chem. Phys.* 131, 134705, 2009.
25. Electric Field Induced Colloidal Interactions & Microstructures, Juarez, J.J.; Bevan, M.A. *J. Chem. Phys.* 131, 134704, 2009.
26. Resonant Effects in Evanescent Wave Scattering of Polydisperse Colloids, Wu, H.; Shah, S.; Beckham, R.E.; Meissner, K.; Bevan, M. A. *Langmuir*, 24, 13790-13795, 2008.
27. Interfacial Colloidal Crystallization via Tunable Hydrogel Depletants, Fernandes, G.E.; Beltran, D.J.; Bevan, M.A. *Langmuir*, 24, 10776–10785, 2008.
28. Electrostatically Confined Nanoparticle Interactions and Dynamics, Eichmann, S.L.; Anekal, S.G.; Bevan, M.A. *Langmuir*, 24, 714 -721, 2008.
29. Closure-Based Density Functional Theory Applied to Interfacial Colloidal Fluids, Lu, M.; Bevan, M.A.; Ford, D.M. *Langmuir*, 23, 12481-12488, 2007.
30. Interfacial Colloidal Sedimentation Equilibrium. II. Closure Based Density Functional Theory, Lu, M.; Bevan, M.A.; Ford, D.M. *J. Chem. Phys.* 127, 164709, 2007.
31. Interfacial Colloidal Sedimentation Equilibrium. I. Intensity Based Confocal Microscopy, Beckham, R.E; Bevan, M.A. *J. Chem. Phys.* 127, 164708, 2007.
32. Evanescent Wave Excited Luminescence from Levitated Quantum Dot Modified Colloids, Everett, W.N.; Beckham, R.E; Meissner, K.E.; Bevan, M.A. *Langmuir* 23, 8950-8956, 2007.
33. Colloidal Microstructures, Transport, and Impedance Properties within Interfacial Microelectrodes, Bahukudumbi, P.; Everett, W.N.; Beskok, A.; Huff, G.H.; Ounaies, Z.; Lagoudas, D.; Bevan, M.A. *Appl. Phys. Lett.* 90, 224102, 2007.
34. Imaging Energy Landscapes with Concentrated Diffusing Colloidal Probes, Bahukudumbi, P.; Bevan, M.A. *J. Chem. Phys.* 126, 244702, 2007.
35. Equivalent Temperature and Specific Ion Effects in Macromolecule Coated Colloid Interactions, Fernandes, G.E.; Bevan, M.A. *Langmuir* 23, 1500-1506, 2007.
36. Diffusing Colloidal Probes of Protein and Synthetic Macromolecule Interactions, Everett, W.N.; Wu, H.; Anekal, S.G.; Bevan, M.A. *Biophys. J.* 92, 1005-1013, 2007.
37. Self-diffusion in Sub-Monolayer Colloidal Fluids Near a Wall, Anekal, S.G.; Bevan, M.A. *J. Chem. Phys.* 125, 034906, 2006.
38. Mapping Patterned Potential Energy Landscapes with Diffusing Colloidal Probes, Wu, H.; Everett, W.N.; Anekal, S.G.; Bevan, M.A. *Langmuir* 22, 6826-6836, 2006.
39. Dynamic Signature for the Equilibrium Percolation Threshold of Attractive Colloidal Fluids, Anekal, S.G.; Bahukudumbi, P.; Bevan, M.A. *Phys. Rev. E* 73, 020403, 2006.
40. Anomalous Potentials from Inverse Analyses of Interfacial Polydisperse Attractive Colloidal Fluids, Pangburn, T.O.; Bevan, M.A. *J. Chem. Phys.* 124, 054712, 2006.
41. Role of Polydispersity in Anomalous Interactions in Electrostatically Levitated Colloidal Ensembles, Pangburn, T.O.; Bevan, M.A. *J. Chem. Phys.* Vol. 123, 174904, 2005.
42. Measurement and Interpretation of Particle−Particle and Particle−Wall Interactions in

Levitated Colloidal Ensembles, Wu, H.; Pangburn, T.O.; Beckham, R.E; Bevan, M.A. *Langmuir* Vol. 21, No. 22, 9879-9888, 2005.

43. Inverse Density Functional Theory as an Interpretive Tool for Measuring Colloid-Surface Interactions in Dense Systems, Lu, M.; Bevan, M.A.; Ford, D.M. *J. Chem. Phys.* Vol. 122, 224710, 2005.
44. Direct Measurement of Single and Ensemble Average Particle-Surface Potential Energy Profiles, Wu, H.; Bevan, M.A. *Langmuir* Vol. 21, No. 4, 1244-1254, 2005.
45. Interpretation of Conservative Forces from Stokesian Dynamic Simulations of Interfacial and Confined Colloids, Anekal, S.G.; Bevan, M.A. *J. Chem. Phys.* Vol. 122, 034903, 2005.
46. Specific Ion-Dependent Attraction and Phase Behavior of Polymer-Coated Colloids, Hwang, K.; Wu, H.; Bevan, M.A. *Langmuir* Vol. 20, No. 26, 11393-11401, 2004.
47. Structural Evolution of Colloidal Crystals with Increasing Ionic Strength, Bevan, M.A.; Lewis, J.A.; Braun, P.V.; Wiltzius, P. *Langmuir* Vol. 20, No. 17, 7045-7052, 2004.
48. Comparison of Nanoparticle Size and Electrophoretic Mobility Measurements using a Carbon Nanotube-Based Coulter Counter, Dynamic Light Scattering, Transmission Electron Microscopy, and Phase Analysis Light Scattering, Ito, T.; Sun, L.; Bevan, M.A.; Crooks, R.M. *Langmuir* Vol. 20, No. 16, 6940-6945, 2004.
49. Calculation of van der Waals Forces with Diffuse Coatings: Applications to Roughness and Adsorbed Polymers, Dagastine, R.R.; Bevan, M.A.; White, L.R.; Prieve, D.C. *J. Adhesion* Vol. 80, 365-394, 2004.
50. Nanoparticle-Mediated Epitaxial Assembly of Colloidal Crystals on Patterned Substrates (cover story), Lee, W..; Chan, A.; Bevan, M.A.; Lewis, J.A.; Braun, P.V. *Langmuir* Vol. 20, No. 13, 5262-5270, 2004.
51. Solvent Quality Dependent Continuum van der Waals Attraction and Phase Behavior for Colloids Bearing Nonuniform Adsorbed Polymer Layers, Bevan, M.A.; Petris, S.N.; Chan, D.Y.C. *Langmuir* Vol. 18, No. 21, 7845-7852, 2002.
52. Light Scattering Characterization of Polystyrene Latex with and without Adsorbed Polymer, Min, G.; Bevan, M.A.; Prieve, D.C.; Patterson, G.D. *Colloids & Surfaces* Vol. 202, pgs. 9-21, 2002.
53. Solvent Quality dependent Interactions and Phase Behavior of Polystyrene Particles with Physisorbed PEO-PPO-PEO, Bevan, M.A. *Langmuir* 2002; Vol. 18, No. 5, 1474-1484, 2002.
54. Hydrodynamic and Electrokinetic Properties of Decane Droplets in Aqueous SDS Solutions, Nespolo, S.A., Bevan, M.A.; Grieser, F.; Chan, D.; Stevens, G; *Langmuir* Vol. 17, No. 23, pgs. 7210-7218, 2001.
55. Forces and Hydrodynamic Interactions between Polystyrene Surfaces with Adsorbed PEO-PPO-PEO, Bevan, M.A.; Prieve, D.C. *Langmuir* Vol. 16, No. 24, pgs. 9274-9281, 2000.
56. Aggregation Dynamics for Two Particles during Electrophoretic Deposition under Steady Fields, Guelcher, S.; Bevan, M.A.; Solomentsev, Y.; Anderson, J.L. *Langmuir* Vol. 16, No. 24, pgs. 9208-9216, 2000.
57. Hindered Diffusion of Colloidal Particles Very Near to a Wall: Revisited, Bevan, M.A.;

Prieve, D.C. *J. Chem. Phys.* Vol. 113, No. 3, pgs. 1228-1236, 2000.

58. Direct Measurement of Retarded van der Waals Attraction (cover story), Bevan, M.A.; Prieve, D.C. *Langmuir* Vol. 15, No. 23, pgs. 7925-7936, 1999.

Book Chapters

1. Effect of Physisorbed Polymers on the Interaction of Latex Particles and Their Dispersion Stability, Bevan, M.A.; Prieve, D.C. Polymers in Particulate Systems: Properties and Applications, *Surfactant Science Series,* Vol. 104, Marcel Dekker, New York, 2001.

To be Submitted

1. kT-scale Interactions between Supported Lipid Bilayer Modified Colloids and Surfaces, Everett, W.N.; Bevan, M.A. *Soft Matter* in preparation, 2013.
2. Effective Colloidal Potentials Mediated by Specific Biomacromolecular Interactions; Duncan, G.; Bevan, M.A. *Biophys. J.* in preparation, 2013.
3. Grain Boundary Migration and Diffusion in Small Colloidal Crystals, Edwards, T.D.; Yang. Y.; Beltran-Villegas, D.J.; Bevan, M.A. *Nature Mater.* in preparation, 2013.
4. Drug Particle Coatings Control Interactions and Transport near Mucus Boundaries; Swavola, J.C.; Beltran-Villegas, D.J.; Bevan, M.A. *Langmuir* in preparation, 2013.
5. Thermosensitive Colloidal Depletion Attraction and Crystallizaiton via Elastin-like Peptide Micelles, Hua, X.; Cui, H.; Bevan, M.A. *Adv. Mater.* in preparation, 2013.
6. Reversible Equilibrium Assembly of Nanoparticles at Drops and Fluid Interfaces, Hua, X.; Bevan, M.A.; Frechette, J. *Phys. Rev. Lett.* in preparation, 2013.
7. Lipid Bilayer Coated Colloid Stability: Chemical vs. Physically Anchored Polyethylene Oxide; Swavola, J.C.; Swavola, C.G.; Bevan, M.A. *Langmuir* in preparation, 2013.

VI. RESEARCH PRESENTATIONS

Invited

1. Colloidal Interactions, Dyanmics, and Assembly on Energy Landscapes, Chemical Engineering, Colorado School of Mines, 09.27.2013.
2. Feedback Controlled Colloidal Self-Assembly, Workshop on Programmable Functional Materials, University of Illinois at Urbana-Champaign, 05.23.2012.
3. Feedback Controlled Colloidal Self-Assembly, CECAM workshop on Emergent Dynamics in Driven Colloids, Lausanne, Switzerland, 04.27.2012.
4. Engineering Soft Matter: Colloidal Assembly on Energy Landscapes, Chemical Engineering, Purdue University, 03.06.2012.
5. Colloidal Interactions and Assembly on Energy Landscapes, Chemical Engineering, Penn State University, 10.06.2011.
6. Colloidal Interactions and Assembly on Energy Landscapes, Chemical Engineering, Virginia Tech University, 09.26.2011.
7. First Principles Control of Colloidal Meta-Materials Assembly, Nanofabrication Control Symposium, American Control Conference, San Francisco, CA, 06.30.2011.
8. Free Energy & & Diffusivity Landscapes for Colloidal Crystal Assembly, Mid-Atlantic

Soft Matter meeting, Univ. of Pennsylvania, Philadelphia, PA, 06.10.2011.

9. Free Energy Landscapes for Colloidal Crystal Assembly, Symposium in Honor of Dennis Prieve, 241st ACS National Meeting, Anaheim, CA, 03.29.2011.
10. Colloidal Interactions and Assembly on Energy Landscapes, Chemical Engineering, Carnegie Mellon University, 10.05.2010.
11. Colloids as Biomolecular Probes and in Reconfigurable Electromagnetic Materials, Applied Physics Lab, Aerospace and Materials Science Group, 07.08.2010.
12. Colloidal Interactions and Assembly on Energy Landscapes, Applied Physics Lab, Nanomaterials Symposium, 04.19.2010.
13. Colloidal Interactions and Assembly on Energy Landscapes, Chemical Engineering, University of Notre Dame, 02.01.2010.
14. Colloidal Interactions and Assembly on Energy Landscapes, 5th Sino-US Chemical Engineering Conference (Beijing, China), 10.13.2009.
15. Colloidal Interactions and Assembly on Energy Landscapes, Polymer Science, University of Massachusetts, 10.08.2009.
16. Colloidal Interactions and Assembly on Energy Landscapes, Physics, Johns Hopkins University, 09.16.2009.
17. Colloidal Interactions and Assembly on Energy Landscapes, Chemical Engineering, Lehigh University, 09.02.2009.
18. Colloidal Interactions and Assembly on Energy Landscapes, Self and Directed Colloidal Assembly Symposium, 238th ACS National Meeting, Washington, DC, 08.16.2009.
19. Colloidal Interactions and Assembly on Energy Landscapes, Chemical Engineering, City College of New York, 04.20.2009.
20. Colloidal Interactions and Assembly on Energy Landscapes, Chemical Engineering, University of Louisville, 04.17.2009.
21. Colloidal Interactions and Assembly on Energy Landscapes, Department of Geography and Environmental Engineering, Johns Hopkins University, 04.02.2009.
22. Self- & Directed- Assembly of Interfacial Colloidal Crystals, Physics, Georgetown University, 03.06.2009.
23. Colloidal Interactions and Assembly on Energy Landscapes, Chemical & Biomolecular Engineering, Rice University, 10.09.2008.
24. Colloidal Interactions and Assembly on Energy Landscapes, Chemical & Biomolecular Engineering, Tulane University, 09.19.2008.
25. Colloidal Interactions and Assembly on Energy Landscapes, Chemical & Biomolecular Engineering, Univ. of Pennsylvania, 09.10.2008.
26. Colloidal Interactions and Assembly on Energy Landscapes, 82nd ACS Colloid and Surface Science Symposium, North Carolina State Univ., 06.17.2008.
27. Colloidal Interactions and Assembly on Energy Landscapes, Chemistry, University of Maryland, Baltimore County, 04.15.2008.
28. Colloidal Interactions and Assembly on Energy Landscapes, National Institute of

Standards and Technology, Directed Assembly of Functional Materials and Devices, 03.19.2008.

29. Colloidal Interactions and Assembly on Energy Landscapes, Chemical & Biomolecular Engineering, University of Wisconsin, 12.04.2007.
30. Colloidal Interactions and Assembly on Energy Landscapes, Chemical & Biomolecular Engineering, University of Houston, 10.19.2007.
31. Colloidal Interactions and Assembly on Energy Landscapes, Chemical & Biomolecular Engineering, Johns Hopkins University, 10.12.2006.
32. Colloidal Interactions and Assembly on Energy Landscapes, Chemical Engineering, University of Massachusetts, 10.03.2006.
33. Diffusing Probe Measurements of Interactions, Dynamics, & Structure in Interfacial Colloidal & Macromolecular Systems, Chemical Engineering, Texas Tech University, 9.30.2005.
34. Diffusing Probe Measurements of Interactions, Dynamics, & Structure in Interfacial Colloidal & Macromolecular Systems, Sandia National Laboratory, 6.7.2005.
35. Self Assembly of Attractive Polymer Coated Colloids on Templates, Colloids Assembling Symposium, 229th ACS National Meeting, San Diego, CA, 3.17.2005
36. Measurement & Manipulation of Colloidal and Macromolecular Interactions, Dynamics, and Structures, Biomedical Engineering, Texas A&M University, College Station, TX, 10.2004.
37. Measurement & Manipulation of Colloidal and Macromolecular Interactions, Dynamics, and Structures, Material Science & Engineering, Georgia Tech, Atlanta, GA, 10.2004.
38. Measurement & Manipulation of Colloidal and Macromolecular Interactions, Dynamics, and Structures, Mechanical Engineering, Texas A&M University, College Station, TX, 9.2004.
39. Three Dimensional Interactions in Ensembles of Colloids Levitated above a Wall, AIChE 2003 National Meeting, San Francisco, CA, 11.18.2003.
40. Macroscopic Dispersion Properties from Microscopic Particle Interactions, Ceramic Seminar Series, Material Science & Engineering, Univ. of Illinois, Urbana, IL, 1.2002.
41. Particle Interactions and Stability in Polymerically Stabilized Dispersions, Johns Hopkins University, Baltimore, MD, 2.01.2001
42. Particle Interactions and Stability in Polymerically Stabilized Dispersions, Texas A&M University, College Station, TX, 2.19.2001.
43. Stability and Rheology of Polymerically Stabilized Dispersions as a Function of Solvent Quality, Max Planck Institute for Colloids and Interfaces, Potsdam, Germany, 10.20.2000.
44. Stability and Rheology of Polymerically Stabilized Dispersions as a Function of Solvent Quality, CNRS, Centre de Recherches Pétrographiques et Géochimiques, Nancy, France, 10.17.2000.
45. Stability and Rheology of Polymerically Stabilized Dispersions as a Function of Solvent Quality, Carnegie Mellon Univ., 10.09.2000.

46. Stability and Rheology of Polymerically Stabilized Dispersions as a Function of Solvent Quality, Princeton Univ., 10.02.2000.
47. Stability and Rheology of Polymerically Stabilized Dispersions as a Function of Solvent Quality, Univ. of Illinois, 9.26.2000.
48. Direct Measurement of Colloidal & Polymeric Interactions using TIRM, plenary lecture, 21st Australian Colloid and Surface Chemistry Student Conference, Univ. of Newcastle, Australia, 9.30.1999.
49. Direct Measurement of Colloidal & Polymeric Interactions using TIRM, Advanced Mineral Products Research Centre, Univ. of Melbourne, Australia, 8.15.1999.
50. Effect of Adsorbed Polymer on Colloidal Stability, Colloids, Polymers, and Surfaces Program, Carnegie Mellon Univ., 9.25.1997.

Conferences

1. Feedback Controlled Colloidal Crystal Assembly Via Electric Field and Depletion Mediated Interactions, AIChE 2012 National Meeting, Pittsburgh, PA, 11.01.2012.
2. Direct Measurement of Conservative and Dissipative Colloidal Forces in the Presence of Adsorbing and Nonadsorbing Polymer, AIChE 2012 National Meeting, Pittsburgh, PA, 11.01.2012.
3. Phase Behavior of Thermodynamically Small Assemblies of Colloidal Nanoparticles, AIChE 2012 National Meeting, Pittsburgh, PA, 10.30.2012.
4. Energy and Diffusivity Landscapes From Smoluchowski Analyses and Shape Matching of Colloidal Crystallization Dynamics, AIChE 2012 National Meeting, Pittsburgh, PA, 10.29.2012.
5. Effective Colloidal Potentials Mediated by Specific Biomacromolecular Interactions, 86th ACS Colloid and Surface Science Symposium, Johns Hopkins Univ., Baltimore, MD, 06.12.2012.
6. Conservative and dissipative forces between mucus and differently coated drug particles, 86th ACS Colloid and Surface Science Symposium, Johns Hopkins Univ., Baltimore, MD, 06.13.2012.
7. Direct measurements of non-DLVO forces between silica colloids and surfaces, 86th ACS Colloid and Surface Science Symposium, Johns Hopkins Univ., Baltimore, MD, 06.11.2012.
8. Feedback control of colloidal crystal size with electrokinetics, 86th ACS Colloid and Surface Science Symposium, Johns Hopkins Univ., Baltimore, MD, 06.11.2012.
9. Energy and Diffusivity Landscapes for Colloidal Crystal Assembly, 86th ACS Colloid and Surface Science Symposium, Johns Hopkins Univ., Baltimore, MD, 06.12.2012.
10. Feedback controlled colloidal crystal assembly via electric field and depletion mediated interactions, 86th ACS Colloid and Surface Science Symposium, Johns Hopkins Univ., Baltimore, MD, 06.13.2012.
11. Feedback Control of Electric Field Mediated Colloidal Assembly, AIChE 2011 National Meeting, Minneapolis, MN, 10.18.2011.
12. Complete Dynamic Description of Small Crystallizing Clusters, AIChE 2011 National Meeting, Minneapolis, MN, 10.19.2011.

13. Universal Colloidal Potentials and Phase Behavior in the Presence of Nonadsorbing Micelles, Nanoparticles, and Polymers, AIChE 2011 National Meeting, Minneapolis, MN, 10.20.2011.
14. A Modified AO Potential for Depletion Mediated Colloidal Crystallization in the presence of nonadsorbing Micelles, Nanoparticles, and Polymers, 85th ACS Colloid and Surface Science Symposium, McGill Univ., Canada, 06.20.2011.
15. A Fokker-Planck Model of Free Energy and Hydrodynamic Contributions to Microscopic Colloidal Dynamics in Colloidal Crystallization, 85th ACS Colloid and Surface Science Symposium, McGill Univ., Canada, 06.20.2011.
16. Electric Field Mediated Feedback Controlled Colloidal Crystal Assembly, 85th ACS Colloid and Surface Science Symposium, McGill Univ., Canada, 06.20.2011.
17. Constructing Free Energy Landscapes in Thermodynamically Small Colloidal Systems Using a Fokker-Planck Formalism, AIChE 2010 National Meeting, Salt Lake City, UT, 11.11.2010.
18. Diffusing Colloidal Probes of Protein-Carbohydrate Interactions, AIChE 2010 National Meeting, Salt Lake City, UT, 11.11.2010.
19. Concentrated Diffusing Colloidal Probes of Ca2+ Dependent Cadherin Interactions, AIChE 2010 National Meeting, Salt Lake City, UT, 11.10.2010.
20. Diffusing Colloidal Probes of Protein-Carbohydrate Interactions, 84th ACS Colloid and Surface Science Symposium, Univ. of Akron, Akron, OH, 06.22.2010.
21. Concentrated Diffusing Colloidal Probes of Ca2+ Dependent Cadherin Interactions, 84th ACS Colloid and Surface Science Symposium, Univ. of Akron, Akron, OH, 06.21.2010.
22. Constructing Free Energy Landscapes in Interfacial Colloidal Systems Using a Fokker-Planck Formalism, AIChE 2009 National Meeting, Nashville, KY, 11.12.2009.
23. Integrated Self & Directed Assembly of Interfacial Colloidal Crystals, AIChE 2009 National Meeting, Nashville, KY, 11.11.2009.
24. Diffusing Nanoparticle Measurements of Protein-Carbohydrate Interactions, AIChE 2009 National Meeting, Nashville, KY, 11.12.2009.
25. Diffusing Nanoparticle Measurements of Protein-Carbohydrate Interactions, 83rd ACS Colloid and Surface Science Symposium and International Association of Colloid & Interface Science meeting, New York, NY, 06.19.2009.
26. Electric Field and Depletion Attraction Mediated Colloidal Assembly, 83rd ACS Colloid and Surface Science Symposium and International Association of Colloid & Interface Science meeting, New York, NY, 06.19.2009.
27. Electric Field Induced Colloidal Interactions & Microstructures, 83rd ACS Colloid and Surface Science Symposium and International Association of Colloid & Interface Science meeting, New York, NY, 06.17.2009.
28. Diffusing Nanoparticle Measurements of Biomolecular Interactions, AIChE 2008 National Meeting, Philadelphia, PA, 11.21.2008.
29. Controlled Colloidal Assembly Via Navigation of Energy Landscapes, AIChE 2008 National Meeting, Philadelphia, PA, 11.19.2008.
30. Dielectrophoretic Assembly of Interfacial Colloidal Crystals, AIChE 2008 National

Meeting, Philadelphia, PA, 11.19.2008.

31. Nanoparticle Interactions in Slit Pores, 82nd ACS Colloid and Surface Science Symposium, North Carolina State Univ., 06.16.2008.
32. Confocal Microscopy Study of Electrostatic Colloidal Sediments, 8th International Electrokinetics Conference, Santa Fe, NM, 05.20.2008.
33. Equilibrium Crystallization of Attractive Colloids on Energetically Patterned Surfaces, AIChE 2007 National Meeting, Salt Lake City, UT, 11.08.2007
34. Interfacial Colloidal Sedimentation Equilibrium Microstructures, AIChE 2007 National Meeting, Salt Lake City, UT, 11.05.2007.
35. Interfacial Colloidal Sedimentation Equilibrium Microstructures, 81st ACS Colloid and Surface Science Symposium, Univ. of Delaware, 6.27.2007.
36. Diffusing Colloidal Probes of Calcium Mediated Cadherin Interactions, 81st ACS Colloid and Surface Science Symposium, Univ. of Delaware, 6.27.2007.
37. Imaging Energy Landscapes with Concentrated Diffusing Colloidal Probes, 81st ACS Colloid and Surface Science Symposium, Univ. of Delaware, 6.26.2007.
38. Colloidal Microfluidic Circuits for Reconfigurable RF Systems, DARPA Material Systems for Autonomous Structural Tailoring Meeting, San Diego, CA 3.23.2007.
39. Reversible Control of Anisotropic Electrical Conductivity Using Colloidal Microfluidic Networks, American Physical Society, Division of Fluid Dynamics, 11.21.2006.
40. Colloid-Surface Interactions from Optical Microscopy and Inverse Density Functional Theory, AIChE 2006 National Meeting, San Francisco, CA 11.14.2006.
41. Imaging Interfacial Energy Landscapes with Concentrated Diffusing Colloidal Probes, AIChE 2006 National Meeting, San Francisco, CA 11.14.2006.
42. Diffusing Colloidal Probe Measurements of Protein and Synthetic Macromolecule Interactions, AIChE 2006 National Meeting, San Francisco, CA 11.13.2006.
43. Engineering Colloidal Microfluidic Networks with Directed Assembly, Annual Technical Meeting of the Society of Engineering Science, Pennsylvania State Univ., 8.16.2006.
44. Dynamic Signature for Equilibrium Percolation in Bulk and Interfacial Colloidal Fluids, 80th ACS Colloid and Surface Science Symposium, University of Colorado, Boulder, CO, 6.18.2006.
45. Mapping Chemically Patterned Potential Energy Landscapes using Diffusing Colloidal Probes, 80th ACS Colloid and Surface Science Symposium, University of Colorado, Boulder, CO, 6.18.2006.
46. Direct Imaging of Interfacial Energy Landscapes with Concentrated Diffusing Colloidal Probes, 80th ACS Colloid and Surface Science Symposium, University of Colorado, Boulder, CO, 6.18.2006.
47. Diffusing Colloidal Probe Measurements of Protein and Synthetic Macromolecule Interactions, 80th ACS Colloid and Surface Science Symposium, University of Colorado, Boulder, CO, 6.18.2006.
48. Inverse Density Functional Theory as a Tool for Measuring Colloid-Surface Interactions, AIChE 2005 National Meeting, Cincinnati, OH, 10.30.2005.

49. Direct Measurement of Multi-dimensional and Multi-body Colloidal and Surface Interactions, AIChE 2005 National Meeting, Cincinnati, OH, 10.30.2005.
50. High School Science Teachers use Scientific Inquiry in Nanotechnology to Build Instructional Frameworks, AIChE 2005 National Meeting, Cincinnati, OH, 10.30.2005.
51. Dynamic Criterion for the Equilibrium Percolation Threshold of Weakly Attractive Colloids, AIChE 2005 National Meeting, Cincinnati, OH, 10.30.2005.
52. Mapping Potential Energy Landscapes on Patterned Surfaces Using Diffusing Colloidal Probe Microscopy, AIChE 2005 National Meeting, Cincinnati, OH, 10.30.2005.
53. Mapping Potential Energy Landscapes of Templated Substrates using Diffusing Colloidal Particles, American Physical Society, Division of Fluid Dynamics, 11.20.2005.
54. Self and Directed Assembly of Colloidal Particles on Patterned Electrode Surfaces, ASME IMECE Meeting, Orlando, FL 11.10.2005.
55. Measurement of Interactions in Interfacial Colloidal Ensembles using Diffusing Colloid Probe Microscopy, AIChE 2004 National Meeting, Austin, TX, 11.8.2004.
56. Stokesian Dynamics of Interfacial & Confined Colloids: Interplay of Forces, Hydrodynamics, & Brownian Motion, Austin, TX, 11.8.2004.
57. Multi-Dimensional Dynamic Imaging of Interfacial Colloidal Self Assembly, AIChE 2004 National Meeting, Austin, TX, 11.8.2004.
58. Specific Ion Effects in the Self Assembly of Attractive Polymer Coated Colloids on Templates, AIChE 2004 National Meeting, Austin, TX, 11.8.2004.
59. Specific Ion dependent Dispersion Forces and Phase Behavior of Polymer Coated Colloids, 78th ACS Colloid and Surface Science Symposium, Yale University, New Haven, CT, 6.21.2004.
60. Mapping Potential Energy Landscapes using Diffusing Colloidal Probe Microscopy, 78th ACS Colloid and Surface Science Symposium, Yale University, New Haven, CT, 6.21.2004.
61. Stokesian Dynamics Simulations of Colloids at Surfaces and in Confined Geometries, 78th ACS Colloid and Surface Science Symposium, Yale University, New Haven, CT, 6.21.2004.
62. Direct Observation of Adhesive Sphere Colloidal Crystal Assembly via Controlled Electrolyte Addition, 77th ACS Colloid and Surface Science Symposium, Georgia Institute of Technology, Atlanta, GA, 6.15.2003.
63. Direct Observation of Colloidal Crystal Structure with Changing Ionic Strength, 2002 Materials Research Society Fall Meeting, 12.2.2002.
64. Direct Observation of Wet and Dry Colloidal Crystals on Templated and Untemplated Surfaces, AIChE 2002 National Meeting, Indianapolis, IN, 11.7.2002.
65. Solvent Quality Dependent Continuum van der Waals Attraction and Phase Behavior for Colloids Bearing Nonuniform Adsorbed Polymer Layers, Chemistry at Interfaces Gordon Research Conference, Connecticut College, New London, CT, 7.8.2002.
66. Solvent Quality Dependent Continuum van der Waals Attraction and Phase Behavior for Colloids Bearing Nonuniform Adsorbed Polymer Layers, 76th ACS Colloid and

Surface Science Symposium, Univ. of Michigan, Ann Arbor, MI, 6.24.2002.

67. Calculation of van der Waals Forces at Rough Interfaces with Diffuse Polymer Coatings, AIChE 2001 National Meeting, Reno, NV, 11.6.2001.
68. Solvent Quality dependent Phase Behavior of Polystyrene Particles with Physisorbed Pluronic, AIChE 2001 National Meeting, Reno, NV 11.6.2001.
69. The Interpretation of Forces Involving Deformable Interfaces, 6th World Congress of Chemical Engineering, Univ. of Melbourne, Australia, 9.23.2001.
70. Hydrodynamics& Electrokinetics of Aqueous Decane/SDS Droplets, 75th ACS Colloid & Surface Science Symp., Carnegie Mellon Univ., Pittsburgh, PA, 6.10.2001.
71. Light Scattering and Electrophoresis of Aqueous Decane/SDS Droplets, Particles 2001 Meeting, Orlando, FL, 2.24.2001.
72. Rheology of an Aqueous Polymerically Stabilized Dispersion as a Function of Solvent Quality, 10th International Conference on Colloid and Interface Science, University of Bristol, United Kingdom, 7.28.2000.
73. Effect of Physisorbed Polymers on the Interaction of Latex Particles and Their Dispersion Stability, 10th International Conference on Colloid and Interface Science, Univ. of Bristol, United Kingdom, 7.23.2000.
74. Effect of Adsorbed Polymer on Colloidal Interactions, 73rd ACS Colloid and Surface Science Symposium, Massachusetts Institute of Technology, 6.13.1999.
75. Measurement of Retarded van der Waals Attraction: Effect of Adsorbed Polymer, AIChE 1998 Annual Meeting, Miami, FL, 11.17.1998.
76. Obtaining Hydrodynamic Separation with TIRM, 1998 CMU Symposium, 10.22.1998.
77. Direct Measurement of van der Waals Attraction with TIRM, poster, Gordon Conference, Chemistry at Interfaces, Meridan, NH, 7.19.1998.
78. Direct Measurement of van der Waals Attraction with TIRM, 72nd ACS Colloid and Surface Science Symposium, Pennsylvania State Univ., 7.23.1998.
79. Slow Flocculation of Sterically Stabilized Dispersions, 1997 CMU Symposium, 10.16.1997.
80. Reduction in van der Waals Forces by Adsorbed Polymer, 71st ACS Colloid and Surface Science Symposium, Univ. of Delaware, 6.30.1997.
81. Effect of Changing Solvent Quality on Steric Interactions, 1997 Pittsburgh Polymer Mini Symposium, Mellon Institute, 7.21.1997.
82. Effect of Changing Solvent Quality on Steric Interactions, 1996 CMU Symposium, 10.24.1996.

VIII. RESEARCH SUPERVISION

PhD (Current)

1. Annna Coughlin, Colloidal Crystallization via Simultaneous Depletion and Magnetic Field Mediated Interactions (PhD candidate, JHU, 2012-).
2. Xiaoqing Hua, Nanoparticle Interactions at Oil-Water and Liquid Crystal-Water Interfaces (PhD candidate, JHU, 2012-).

3. Yuguang Yang, First-Principles Based Control of Multi-Scale Meta-Material Assembly Processes (PhD candidate, JHU, 2011-).
4. Bradley Rupp, Multifunctional Particles, Surfaces, and Material Systems for Reconfigurable Antennas (PhD candidate, JHU, 2011-).
5. Julie Bitter, Nanoparticle-Surface Interactions in Aqueous Environments (PhD candidate in Chemistry, JHU, 2010-).
6. Gregg Duncan, Diffusing Colloidal Probes of Protein-Carbohydrate Interactions on Supported Lipid Bilayers (PhD candidate, JHU, 2009-).
7. Julia Swavola, Diffusing Colloidal Probes of Membrane Protein Interactions involved in Cell Sorting (PhD candidate, JHU, 2009-).

PhD (Completed)

1. Tara Edwards, 3D Interfacial Colloidal Crystal Assembly (PhD, JHU, 2007-2013). (current position: conducting job search)
2. Daniel Beltran, Self Assembly Dynamics in Inhomogeneous Colloidal Fluids and Crystals (PhD, JHU, 2006-2012). (current position: postdoc in Chem. Eng. at UMich)
3. Jaime J. Juarez, Electric Field Mediated Directed Colloidal Assembly (PhD, JHU, 2006-2011). (current position: postdoc in Mat. Sci. at UIUC)
4. Shannon L. Eichmann, Diffusing Nanoparticle Probes of Protein-Carbohydrate Interactions (PhD, JHU, 2004-2010) (postdoc in ChemBE at Rice University, current position: Saudi Aramco)
5. Richard E. Beckham, Direct Measurement and Manipulation of Interfacial Colloidal Crystallization (PhD, TAMU, 5/2008) (postdoc at Los Alamos Earth & Environmental Sciences, current position: Exxon)
6. Gregory E. Fernandes, Interfacial Colloidal Assembly via Attractive Interactions (MS, TAMU, 6/2004; PhD, TAMU, 8/2008) (current position: Milliken)
7. W. Neil Everett, Direct Measurement of Protein Interactions using Ensemble TIRM (PhD, TAMU, 8/2007) (postdoc in Biomed. Engr. at UT Austin, current position: cleannergylabs – Austin area nanotechnology start-up)
8. Mingqing Lu, Analysis of Interfacial Colloidal Fluids using Inverse Density Functional Theory (PhD, TAMU, 8/2007) (current position: Capital One)
9. Pradipkumar Bahukudumbi, Reversible Control of Anisotropic Electrical Conductivity Using Colloidal Microfluidic Networks (PhD, TAMU, 5/2007) (current position: Milliken)
10. Samartha G. Anekal, Stokesian Dynamics & Self Diffusion in Interfacial Colloidal Microstructural Transitions (PhD, TAMU, 5/2006) (postdoc in ChemBE at Univ. of Wisconsin, current position: Theranos, Inc. – Bay area health care start-up)
11. Hung-Jen Wu, Diffusing Colloidal Probe Microscopy on Physicochemically Patterned Surfaces (PhD, TAMU, 5/2006) (postdoc in Chemistry at Berkley, current position: Assitant Professor in Chemical Engineering at Texas A&M University)

MS (Completed)

1. Xiaoqing Hua, Preparation and Measurement of Temperature Dependent Elastin Peptide Depletants (MS, JHU, 12/2012) (current position: PhD candidate in Bevan

lab)

2. Gregory E. Fernandes, Interfacial Colloidal Assembly via Attractive Interactions (MS, TAMU, 6/2004; PhD, TAMU, 8/2008) (current position: Milliken)
3. Sumit Sharma, Physicochemical Patterning of Optically Transparent Substrates (MS, TAMU, 12/2004) (current position: Haliburton)

Postdoctoral (Completed)

1. Jingqin Cui, Integrated Self- & Directed- Interfacial Colloidal Assembly, JHU, 2008-2010.

Undergraduate (Current)

1. Paul Masih Das, Development of Non-Aqueous Dispersions for Antenna Applications, JHU, 2012-
2. Paul Park, Fabrication and Characterization of Bioconjugated Colloids, JHU, 2012-
3. Samantha Brandon, Direct Measurement of Nanoparticle-Cell Interactions, JHU, 2012-
4. Nicholas Liu, Light Scattering Characterization of Mucus, JHU, 2012-

Undergraduate (Completed)

1. Claudia Reyes, Drug Particle-Mucus Interactions with and without Mucolytic Agents, JHU, 2011-2012.
2. Skyler Stern, Feedback Controlled Colloidal Crystallization, JHU, 2011-2012.
3. Chao An Tien, Computer Simulations of Controlled Growth and Annealing of Sedimenting Depletion Crystals, JHU, 2009-2012.
4. Emilee Platz, Design of a Drug Delivery Particle to Cross Mucus Membrane, JHU, 2011.
5. Sandra Reyes, Engineering Microfabricated Electrodes For Measurement of Protein-Carbohydrate Interactions, JHU, 2011.
6. Sarah Feicht, Confocal Microscopy of 3D Electric Field Mediated Colloidal Crystal Assembly, JHU, 2009-2011.
7. Hsuan-Chin Wang, Preparation of Chemo-sensitive Hydrogel Colloids, JHU, 2009-2011.
8. Caitlin Schram, Preparation of Tunable Nonaqueous Depletion Crystals, JHU, 2009-2011.
9. Jason Liu, Diffusing Colloidal Probe Measurements of Folded and Unfolded Proteins, JHU, 2009-2011.
10. Gulsum Meric, TIRM measurements of Environmentally Aged Carbon Nanotubes, JHU, 2008-2010
11. Brian Liu, Single Dipolar Interactions in Inhomogeneous Electric Fields, JHU, 2008-2010
12. Juri Bassuner, Interactions of Protein & Carbohydrate Conjugated Nanoparticles, JHU (visiting from Univ. of Missouri), 2008.
13. Ai Nguyen, Preparation of PNIPAM and Fluorescent Latex Colloids, TAMU (visiting

from Tulane), 2007.

14. Luke Hunter, Monte Carlo and Brownian Dynamic Simulation Studies of Protein Mediated Colloidal Assembly on Patterns, TAMU, 2007 (now PhD student in Biophysics at Harvard).
15. Carlos Jaimes, Microparticle Transitions via Nanoparticle and Solvent Quality Mediated Depletion Interactions, TAMU (visiting from Universidad Autónoma de Bucaramanga, Colombia), 2007.
16. Daniel Beltran, Robust Inverse Analysis of Interfacial Colloidal Fluids, TAMU (visiting from Universidad de los Andes, Colombia), 2006.
17. Blake Bennett, Cell Migration and Diffusion on Peptide Patterned Surfaces, TAMU, 2006.
18. Christian Vogt, Site Directed Mutagenesis of E. coli Proteins for Attachment to Metal Nanoparticles and Surfaces, TAMU (visiting Molecular Biology Diploma Student from Univ. of Konstanz, Germany), 2005-2006.
19. Marshall Plunk, TIRM & Light Scattering Measurements of Protein Interactions, TAMU, 2005.
20. William Bryant, Thermodynamic and Mechanical Osmotic Pressure of Colloidal Dispersions, TAMU (visiting from Texas Southern University), 2004.
21. Tracie Book, Fluorescent Particle Assembly on Patterned Substrates, TAMU, 2004-2006.
22. Nicole Johnson, Synthesis of Non-Aqueous Fluorescent Silica Colloids, TAMU, 2003.
23. Ashley Hurley, Synthesis of Polymerically Stabilized Fluorescent Latex Colloids, TAMU, 2003.
24. Todd Pangburn, Inverse Monte Carlo Analyses of Quasi 2D Colloidal Fluids, TAMU, 2003-2005 (now PhD student in Chemical Engineering at University of Minnesota).

<u>High School Teachers (Completed)</u>

1. Marguerita Guerra, Nanotechnology in High School, 2005-2006.
2. Rachel Hensley, Nanotechnology in High School, 2005-2006.
3. Lana Hood, Nanotechnology in High School, 2005-2006.
4. Maria Magampon, Nanotechnology in High School, 2005-2006.
5. Patricia McMorris, Nanotechnology in High School, 2005-2006.
6. Natthu Parate, Nanotechnology in High School, 2005-2006.
7. Michael Parkhill, Nanotechnology in High School, 2005-2006.
8. Orlando Patricio, Nanotechnology in High School, 2005-2006.
9. Scott Travis, Nanotechnology in High School, 2005-2006.
10. Michael Turner, Nanotechnology in High School, 2005-2006.
11. Elbert Yeh, Nanotechnology in High School, 2005-2006.
12. Gloria Yoder, Nanotechnology in High School, 2005-2006.

High School Students (Completed)

1. Maryam Moaddel, Investigation of Brown Motion using Digital Video Microscopy and Toy Microscopes, 2007 (from College Station H.S., TX).

IX. TEACHING

Johns Hopkins University

1. Fall 2013, Physics and Chemistry of Nanomaterials (grad, 670.619).
2. Fall 2013, Thermodynamics I (ugrad, 540.203).
3. Spring 2013, Colloids & Nanoparticles (ugrad, 540.403), 14 students.
4. Spring 2013, Colloids & Nanoparticles (grad, 540.603), 9 students.
5. Fall 2012, Physics and Chemistry of Nanomaterials (grad, 670.619), 29 students. (with Chien, McCaffery, Searson, Wirtz)
6. Fall 2012, Thermodynamics I (ugrad, 540.203), 22 students.
7. Spring 2012, Colloids & Nanoparticles (ugrad, 540.403), 18 students.
8. Spring 2012, Colloids & Nanoparticles (grad, 540.603), 31 students.
9. Fall 2011, Thermodynamics I (ugrad, 540.203), 30 students.
10. Fall 2011, Physics and Chemistry of Nanomaterials (grad, 500.619), 20 students, (with Chien, McCaffery, Searson, Wirtz)
11. Spring 2011, Macromolecules at Interfaces (ugrad, 540.448), 7 students.
12. Fall 2010, Physics and Chemistry of Nanomaterials (grad, 500.619), 20 students, (with Chien, McCaffery, Searson, Wirtz)
13. Fall 2010, Thermodynamics I (ugrad, 540.203), 25 students.
14. Spring 2010, Special Topics in Colloid Science (ugrad, 540.448), 7 students.
15. Spring 2010, Thermodynamics I (ugrad, 540.203), 25 students.
16. Fall 2009, Physics and Chemistry of Nanomaterials (grad, 500.619), 20 students, (with Chien, McCaffery, Searson, Wirtz)
17. Fall 2009, Interfacial Science with Applications to Nanoscale Systems (ugrad, 540.415), 13 students.
18. Fall 2009, Interfacial Science with Applications to Nanoscale Systems (grad, 540.615), 32 students.
19. Fall 2008, Colloids & Nanoparticles (ugrad, 540.403), 3 students.
20. Fall 2008, Colloids & Nanoparticles (grad, 540.603), 7 students.

Texas A&M University

21. Fall 2007, Intro to Polymer Engr. (ugrad, CHEN451), 4 students.
22. Fall 2007, Intro to Polymer Engr. (grad, CHEN 641), 14 students.
23. Spring 2007, Colloidal & Interfac. Systems (grad, CHEN689), 10 students.
24. Fall 2006, Intro to Polymer Engr. (ugrad, CHEN451), 27 students.

25. Fall 2006, Intro to Polymer Engr. (grad, CHEN 641), 9 students.
26. Summer 2006, Nanotech. in H.S. Physics (grad, CHEN 685) 12 students.
27. Spring 2006, Thermodynamics I (ugrad, CHEN 205), 21 students.
28. Fall 2005, Intro to Polymer Engr. (ugrad, CHEN451), 30 students.
29. Fall 2005, Intro to Polymer Engr. (grad, CHEN 641), 4 students.
30. Summer 2005, Nanotech. in H.S. Physics (grad, CHEN 685) 13 students.
31. Spring 2005, Colloidal & Interfac. Systems (grad, CHEN689), 8 students.
32. Fall 2004, Intro to Polymer Engr. (ugrad, CHEN451), 19 students.
33. Fall 2004, Intro to Polymer Engr. (grad, CHEN 641), 5 students.
34. Spring 2004, Colloidal & Interfac. Systems (grad, CHEN689), 16 students.
35. Spring 2004, Departmental Seminar Series (grad, CHEN 681), 36 students.
36. Fall 2003, Intro to Polymer Engr. (ugrad, CHEN451), 24 students.
37. Fall 2003, Intro to Polymer Engr. (grad, CHEN 641), 9 students.
38. Fall 2003, Departmental Seminar Series (grad, CHEN 681), 40 students.
39. Fall 2002, Intro to Polymer Engr. (ugrad, CHEN451), 23 students.
40. Fall 2002, Intro to Polymer Engr. (grad, CHEN 641), 19 students.

New Courses Developed

1. Colloidal & Interfacial Systems (CHEN 689 at TAMU, 540.403/603 at JHU)

   Fundamental principles related to interactions, dynamics, and structure in colloidal and interfacial systems. Concepts include hydrodynamics, Brownian motion, diffusion, sedimentation, colloidal and surface forces, macromolecular forces, aggregation/deposition, and experimental methods. Modern topics related to colloids in nano-technology with recent literature references. This was a graduate course at TAMU and cross-listed for undergraduates and graduates at JHU. Students were from Aerospace, Biomedical, Chemical, and Mechanical Engineering at TAMU and from Biomedical, Chemical, Mechanical, and Materials Engineering at JHU.

2. Polymer Engineering (CHEN 451/641 at TAMU)

   Introduction to modern polymer engineering fundamentals including polymer structure, function, characterization, properties, solution behavior, and rheology. This was cross-listed for undergraduates and graduates at TAMU. Students were from Aerospace, Biomedical, Chemical, Mechanical, and Petroleum Engineering.

X. SERVICE

Department & Institution (Johns Hopkins University)

1. ChemBE, Director of Graduate Program, 2011-

   - assign TAs and PhD supervisors, advise students, organize annual graduate retreat, maintain graduate student handbook and policies

   - developed new policies for handling graduate student grievances

- developed and implemented annual reviews of graduate student progress

2. ChemBE, ABET committee, 2008-2011.

   - oversaw development of assesment tools and collection of data

   - authored ~350 page report resulting in acceditation from 2012-218

3. ChemBE, Faculty Search Committee, 2011, 2012, 2013.
4. ChemBE, Graduate Admissions Committee, 2008.
5. ChemBE, Undergraduate Academic Advisor, Class of 2012.
6. WSE Faculty IT Group, 2012-
7. IGERT, Physical and Biomolecular Foundations for Developing Nanoprobes for Biology, advisor (2 students), 2009-
8. INBT, industrial grants from C.P. Kelco (2009) and Martek (2011).
9. INBT, NanoBioTechnology REU site advisor, 2008.
10. Johns Hopkins University, Homewood Graduate Board, WSE representative 2010-2012.
11. Johns Hopkins University, Graduate Board Oral committees
12. Johns Hopkins University, defense committees

Department & Institution (Texas A&M University)

1. CHEN Computer Committee, 2003-2007.
2. CHEN Department Head Search Committee, 2006-2007.
3. CHEN Faculty Search Committee, 2003-2004.
4. CHEN Graduate Admissions Committee, 2005-2006.
5. CHEN Graduate Curriculum Committee (Chair), 2006-2007.
6. CHEN Lindsay Seminar Series Organizer, 2003-2004.
7. CHEN REU site advisor, 2006-2007.
8. CHEN Web Committee (Chair), 2003-2007.
9. Look College of Engineering, Faculty Advisory Committee, 2002-2003.
10. Look College of Engineering, Life Sciences Building Committee, 2004-2005.
11. Look College of Engineering, Material Science Curriculum Committee, 2006-2007.
12. Texas A&M University, Center for Integrated Microchemical Systems, 2002-2007.
13. Texas A&M University, Life Sciences Building Committee, 2006.
14. Texas A&M University, Materials Characterization Facility Committee, 2006-2007.
15. Texas A&M University, Material Science & Engineering Faculty, 2002-2007.
16. Texas A&M University, member of >60 PhD & MS committees in 10 departments (Aerospace, Biomedical, Chemical, Electrical, Industrial, Mechanical, and Petroleum Engineering, Chemistry, Physics, Education), 2002-2007.
17. Texas A&M University, Polymer Technology Center, 2002-2007.

Outreach Activities

1. Developed public presentations at the North Museum at Franklin & Marshall College (Lancaster, PA) and high school student presentations in the Bevan labs at JHU (part of NSF Portal to the Public at Franklin & Marshall College), 2008-
2. Developed three week (5 half days) summer course on authentic inquiry in nanotechnology for high school chemistry, physics, math teachers (part of NSF Center for Learning and Teaching in Texas A&M College of Education), 2005-2006.

Profession

1. ACS Conference Organizer (1 conference):

   86th ACS Colloids & Surface Science Symposium, Johns Hopkins University, Baltimore, MD, June 10-13, 2012. Meeting co-organizer with Joelle Frechette. Premier meeting in colloids and surfaces included 536 attendees, 464 oral presentations, 49 posters, 28 session organizers, 32 invited keynote speakers, 4 plenary lectures, 13 technical symposia, new Langmuir student awards, and participants from 186 institutions and 18 countries. Raised ~$60k from NSF, industry, and exhibitors.

2. ACS Colloids Division Summer Symposium Chair (2012-):

   Oversee the organization of largest ACS Division Summer meeting. Oversaw organization of meetings at University of California Riverside (2013), University of Pennsylvania (2014), Carnegie Mellon University (2015), Harvard University (2016)

3. ACS National Meeting Symposium Organizer (2 symposia):

   Colloidal Self & Directed Assembly, 2009 ACS National Fall Meeting, Washington, DC, 8.2009.

   Colloidal Assembly: Fundamentals, Approaches, Applications, 2005 ACS National Spring Meeting, San Diego, CA, 3.2005. ($12k raised for 10 invited speakers)

4. ACS Colloids Division Summer Session Organizer (2 sessions):

   General Papers in Colloidal Dispersions, 84th ACS Colloid and Surface Science Symposium, Univ. of Akron, Akron, OH, 6.2010.

   General Papers in Colloidal Dispersions, 82nd ACS Colloid and Surface Science Symposium, North Carolina State Univ., Raleigh, NC, 6.2008.

   General Papers in Colloidal Dispersions, 78th ACS Colloid and Surface Science Symposium, Yale Univ., New Haven, CT, 6.2004.

5. AIChE Session Organizer (3 sessions):

   Colloidal Dispersions, AIChE 2007 National Meeting, Salt Lake City, UT, 11.2007.

   Colloidal Dispersions, AIChE 2006 National Meeting, San Francisco, CA, 11.2006.

   Colloidal Dispersions, AIChE 2005 National Meeting, Cincinnati, OH, 10.2005.

6. Award Committees (2 committees):

   American Chemical Society Division of Colloid and Surface Science, LaMer Award Committee, chair 2009-2011. Members: Annelise Barron (Stanford, Bioengineering), John Crocker (Univ. of Penn, Chemical & Biomolecular Engineering), Christine Keating (Penn State, Chemistry), Ken Schweizer (Univ. of Illinois at Urbana-

Champaign, Mat. Sci. & Engr.), Darrell Velegol (Penn State, Chemical Engineering)

American Chemical Society Division of Colloid and Surface Science, LaMer Award Committee, member 2008.

7. Collaborators (9 senior personnel):

   Mark Dorsey (Naval Research Lab), David Ford (Chem. Eng., Univ. Mass Amherst), Joelle Frechette (ChemBE, Johns Hopkins Univ.), Martha Grover (Chem. Eng., Georgia Tech), Greg Huff (Elec. Eng., Texas A&M), Howard Fairbrother (Chemistry, Johns Hopkins Univ.), Dimitris Maroudas (Chem. Eng., Univ. Mass Amherst), Zoubeida Ounaies (Aero. Eng., Penn State), Benjamin Shapiro (Biomed. Eng., Univ. Maryland)

8. Journal Reviewer (34 journals):

   ACS Nano, Advanced Functional Materials, Advanced Materials, AIChE Journal, Analytical Chemistry, Applied Materials & Interfaces, Biomacromolecules, Biophysical Journal, Chemistry of Materials, ChemPhysChem, Colloids & Surfaces, Current Opinion in Colloid and Interface Science, Electrophoresis, Environmental Science & Technology, Experiments in Fluids, Langmuir, Industrial & Engineering Chemistry Research, Journal of the American Chemical Society, Journal of Chemical Physics, Journal of Colloid & Interface Science, Journal of Materials Chemistry, Journal of Material Science, Journal of Fluid Mechanics, Journal of Rheology, Journal of Physical Chemistry Letters, Nanoletters, Nanomedicine, Nature Communications, Nature Materials, Physica, PNAS, RSC Advances, Small, Soft Matter.

9. Member (4 societies):

   American Chemical Society (current), American Institute of Chemical Engineers (current), International Association of Colloidal and Interface Science (intermittent), Materials Research Society (intermittent).

10. Proposal Reviewer - Mail/Email (9 agencies):

    American Chemical Society Petroleum Research Fund, Canada Research Chairs, National Research Council, US Department of Energy, US Defense Threat Reduction Agency, Environmental Protection Agency, National Science Foundation, Netherlands Organisation for Scientific Research (NWO), US Department of Agriculture.

11. Proposal Reviewer - Panels (17 panels):

    Environmental Protection Agency, Nanotechnology Research Investigating Fate, Transport, Transformation, and Exposure of Engineered Nanomaterials, 12.2007.

    National Research Council, NRC Postdoctoral Research Applications, 5.2010.

    National Science Foundation, Chemical, Bioengineering, Environmental, and Transport Systems Division, Particulate and Multiphase Processes Program, 6.2004, 4.2005, 10.2005, 10.2006, 9.2009, 11.2010.

    National Science Foundation, Chemical, Bioengineering, Environmental, and Transport Systems Division, Interfacial, Transport, and Thermodynamics Program, 12.2006, 5.2007, 5.2008, 5.2010, 10.2012.

    National Science Foundation, Chemical, Bioengineering, Environmental, and Transport Systems Division, Fluids, 2.2008.

National Science Foundation, Civil, Mechanical and Manufacturing Innovation, Nanomanufacturing Program, 1.2012.

National Science Foundation, Division of Materials Research, Biomaterials Program, 2.2008.

National Science Foundation, Division of Materials Research, Reverse Site Visit Panel, MRSEC Program, 5.2008.

12. Advisory Boards:

Universidad de los Andes, Facultad de Ingenieria, Departmento de Ingerieria Quimica, 2010-

浙江大学
ZHEJIANG UNIVERSITY

Changyou Gao, Prof. Ph.D and Chair
Department of Polymer Science and Engineering,
Zhejiang University,
Hangzhou 310027, China
Tel/Fax: +86-571-87951108
Email: cygao@zju.edu.cn
Dec. 31, 2018

To Whom It May Concern:

It is my pleasure to recommend Dr. Yuguang Yang for U.S. permanent residency under National Interest Waiver (NIW) Petition. As I hope this letter conveys, Dr. Yang has unique scientific talents that have been well recognized by the international research community. By devising much-needed strategies for quantifying important phenomena in engineering, Dr. Yang has made critical contributions to his field.

To introduce myself, I am currently serving as a full professor as well as the Head of the Department of Polymer Science and Engineering at Zhejiang University, China. Since I got my Ph.D. in 1996, I have been focusing on material engineering for medical applications and cutting-edge technologies in material biocompatibility and tissue engineering. I have published extensively and am also the editor for a number of core journals in this field. Furthermore, over 50 patents based on my work have been granted.

In Dr. Yang's two-year experience in my lab, where I was his supervisor, Dr. Yang focused on novel methodologies to characterize and fabricate gradient biomaterials, which are a type of materials with a gradual change in physical and chemical properties. Fabricating gradient biomaterials to achieve the regulation of cell migration behaviors is of paramount importance in the field of tissue engineering. One ideal candidate for gradient biomaterial is polyelectrolyte multiplayer films because they have excellent biocompatibility and their chemical and physical properties can be conveniently altered. Dr. Yang successfully applied spectroscopic ellipsometry and quartz crystal microbalance to determine the thickness and the viscoelasticity of the films under salt solution treatment at different concentrations. He designed an approach that innovatively uses the key mathematical relationships among refraction angle, composition, thickness, and mechanical properties to correctly convert the measured refraction angle and vibration frequency to the film's thickness and viscoelasticity, which are considerably difficult to measure otherwise due to the film's nanometer thickness. These characterizations are a crucial part of a versatile and low-cost flow method to fabricate thin films with viscoelasticity gradient. These films now have diverse applications in biomaterials, medicine, and nanotechnology. The results were summarized in a paper published in *Langmuir* (2011).

After graduation, Dr. Yang pursued his Ph.D. at Johns Hopkins University. In one of his Ph.D. research accomplishments, he designed intelligent materials with periodic microstructures that can non-trivially interact with electromagnetic radiation and therefore possess critical properties for emerging applications, such as chemical sensors. There are two aspects of significance I want to highlight. First, the material he designed has excellent biocompatibility as he used the depletion interaction that is

derived from biological interactions. Second, this design is based on physical principles of depletion interaction and a solid mathematical model he developed, which enables more precise calculation of interaction strength as a function of external temperature stimulus than ever before. This work paves the way for designing robust, intelligent sensor materials and was published in *Scientific Reports* (2015). In another closely related paper, published in *Journal of Colloid and Interface Science* (2015), he generalized his mathematical modeling approach using advanced Monte Carlo method so that it can be used to compute and design depletion interaction for arbitrary geometries.

More recently, he investigated the optimal navigation of self-propelled nano-robots. This work can be viewed as a perfect example of transforming insights from fundamental science to groundbreaking applications. He studied these nano-robots' optimal navigation rules in complex microstructured environments. Contrary to the general approaches based on either intuitions or extensive empirical tests, Dr. Yang successfully constructed a dynamic model of self-propelled nano-robot in the presence of obstacles and then applied Markov decision method to find out the optimal navigation rules. The rules he devised can automatically seek the global shortest path and demonstrate superior performance in irregular maze-like settings, a common scenario for targeted drug delivery in tissues. Moreover, by exploring the model parameter space, he was able to identify the optimal choice of feedback control parameters and reveal the fundamental design limitations of self-propelled nano-robots. The results formed a paper published in *ACS Nano* (2018). I am highly intrigued by this work because nano-robots are poised to revolutionize various biomedical fields, such as targeted drug delivery, *in situ* sensing, and cancer cell isolation.

Dr. Yang's consistent record of past accomplishments indicates that he will likely continue to make positive impacts through mathematical modeling. He has repeatedly shown his exceptional aptitude for applying his mathematical modeling expertise to address questions that have challenged scientists and engineers for years. An average researcher could not have made the same contributions that Dr. Yang had made. Given the significant accomplishments, I have strong reasons to believe that his solid interdisciplinary background and strong quantitative skills will continue to impact various fields in both academia and industry. Therefore, I give my full support to Dr. Yang. Please do not hesitate to contact me at cygao@zju.edu.cn if I may be of further assistance.

Yours Sincerely,

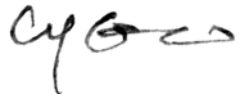

Changyou Gao

Changyou Gao Ph.D.

professor | Doctoral supervisor

Subject Materials Science and Engineering
Department Department of Polymer Science and Engineering
Position Director of Department of Polymer Science and Engineering

Phone +86-571-87951108 E-mail cygao@zju.edu.cn

Address Room 317, Polymer Building, Yuquan Campus of Zhejiang University

Research Polymer Materials

Biography | Courses | Student Supervising | Professional Achievements | Books and Book Chapters | Journal Articles/Re

Dr. Changyou Gao has published over 50 granted patents, 11 books/book chapters, and over 300 papers in pear-reviewed journals such as *Agnew. Chem.*, *Adv. Materials* and *Biomaterials* (WOS H-index 57, citations > 8000). He has delivered 75 invited/plenary lectures, and (co)organized 7 international conferences on biomaterials. He was awarded with the National Science Fund award for Distinguished Young Scholars of China in 2004, and was appointed as a Changjiang Scholar of the Ministry of Education in 2007. He was elected as a fellow of the American Institute for Medical and Biological Engineering (AIMBE) in 2017, and a fellow of the International Union of Societies of Biomaterials Science and Engineering in 2016. He was awarded twice for the 1st level award of Science and Technology of Zhejiang Province.

His research is focused on the development of biomaterials for tissue engineering, regenerative medicine, drug delivery and cellular interaction. In recent years he has been focusing on the gradient biomaterials and colloidal biomaterials for regulating cell migration and cellular uptake, and regenerative biomaterials for cartilage/subchondral bone regeneration. These leading works enabled him to be a PI for 4 key projects of Natural Science Foundation of China (NSFC) and 6 regular projects of NSFC, and 1 National Key Research and Development Program, and a co-PI of the National Major State Basic Research Program of China (973 program, 3 projects), and Frame Work Program 7 of European Commission (3 projects) and H2020. Among his (co)supervised 56 Ph.D and 39 Master students, 45 and 35 have obtained Ph.D and master degrees, respectively. Many of them take faculty positions, including 8 full Profs. and 17 assoc. Profs./AP inChina, 1 Prof. in Washinton Univ. at San Loius, 1 assoc. Prof in UT-Arlington, and 1 AP in Stanford Univ., respectively. He is serving as an executive member of Chinese Society for Biomaterials, and an editorial member of 8 international journals.

Education

1986.9-1996.7, Bachelor, Master and Ph.D. in Polymer Chemistry and Physics from Department of Chemistry, Jilin University,China.

Academic and Professional Career

1. 2017.8-present, Chair, Department of Polymer Science and Engineering, Zhejiang University
2. 2013.9-2017.8, Associate Chair, Department of Polymer Science and Engineering, Zhejiang University
3. 2013.4-2017.10, Director of Institute of Biomedical Macromolecules, Zhejiang University
4. 2001.12-present, Professor in Materials Science, and Polymer Chemistry and Physics at Department of Polymer Science and Engineering, Zhejiang University
5. 2009.3-2014.9, Deputy Director of Key Laboratory of Macromolecular Synthesis and Functionalization, Ministry of Education (Zhejiang University)
6. 1999.8-2004.11 (20 months in total), DAAD fellowship and visiting scholar at Max Planck Institute of Colloids and Interfaces,Germany
7. 1998.10.-2001.12, Associate professor in Materials Science at Department of Polymer Science and Engineering, Zhejiang University
8. 1996.9-1998.9, Postdoc in Materials Science at Department of Polymer Science and Engineering, Zhejiang University

Current grants

1. **European H2020 (co-PI): BIO**material **R**Isk **Ma**nagement (BIORIMA) (H2020 - 760928), 2017.11.1-2021.10.31. Matching funding from Chinese government, Phase 2.
2. **National Key Research and Development Program (PI)**: Surfaces/Interfaces of Biomaterials and Surface Modification, 2016.7-2020.12.
3. **NSFC key project (PI):** Gradient polymeric biomaterials with stimuli-response for regulating the migration of cells, 2015.1.1-2019.12.31.

Related People


QINFAXIA…
Materials Sc…


ZHUHANG
Materials Sc…


WANG XI…
Materials Sc…


WANLING…
Department …


Minmin Shi
Materials Sc…

Recent mainter
2018-09

Total visits

Changyou Gao Ph.D.

professor | Doctoral supervisor

Subject Materials Science and Engineering
Department Department of Polymer Science and Engineering
Position Director of Department of Polymer Science and Engineering

Phone +86-571-87951108 E-mail cygao@zju.edu.cn

Address Room 317, Polymer Building, Yuquan Campus of Zhejiang University

Research Polymer Materials

Biography | Courses | Student Supervising | Professional Achievements | Books and Book Chapters | Journal Articles/Re

1. **Fellow**, the American Institute for Medical and Biological Engineering (AIMBE) (2017)
2. **Fellow,** the International Union of Societies of Biomaterials Science and Engineering (2016)
3. **National Science Fund for Distinguished Young Scholars of China** (2004)
4. **Changjiang Scholar** nominated by the Ministry of Education ofChina(2007)
5. **The 1st level award** of Science and Technology of Zhejiang Province (1/9, 2008)
6. **The 1st level award** of Science and Technology of Zhejiang Province (4/12, 2011)
7. **The 2nd level award** of Science and Technology of Zhejiang Province (1/7, 2010)

Related People


QINFAXIA…
Materials Sc…


ZHUHANG
Materials Sc…


WANG XI…
Materials Sc…


WANLING…
Department …


Minmin Shi
Materials Sc…

Recent mainter
2018-09

Total visits

Changyou Gao Ph.D.

professor | Doctoral supervisor

Subject Materials Science and Engineering
Department Department of Polymer Science and Engineering
Position Director of Department of Polymer Science and Engineering

Phone +86-571-87951108 E-mail cygao@zju.edu.cn

Address Room 317, Polymer Building, Yuquan Campus of Zhejiang University

Research Polymer Materials

Biography | Courses | Student Supervising | Professional Achievements | Books and Book Chapters | Journal Articles/Re

1. **Changyou Gao.** Editor in chief, Polymeric Biomaterials for Tissue Regeneration: from Surface/Interface Design to 3D Constructs, Springer, ISBN 978-981-10-2292-0 ISBN 978-981-10-2293-7 (eBook), Springer Science+Business Media Singapore ,2016,10. DOI 10.1007/978-981-10-2293-7..
2. Weijun Tong, **Changyou Gao.** Assembly of multilayer microcapsules and their biomedical applications, in Layered Supramolecular Structures -- Interface and Biomedical Functions, edited by Jiacong Shen and Jijian Ji et al. Science Press, Beijing, 2016.5, ISBN978-7-03-047806-1.
3. Zhengwei Mao, **Changyou Gao.** Medication of the physicochemical properties of multilayers and their influence on cell functions, in Layered Supramolecular Structures -- Interface and Biomedical Functions, edited by Jiacong Shen and Jijian Ji et al. Science Press, Beijing, 2016.5, ISBN978-7-03-047806-1.
4. Bing Zhang, Xing Liu, Chunfen Zhang, Luyan Li, Lie Ma, **Changyou Gao.** Chapter 52, Bioengineering skin constructs, in Stem cell biology and tissue engineering in dental sciences, 703-717/900, edited by Ajaykumar Vishwakarma, Paul Sharpe, Songtao Shi, and Murugan Ramalingam, Elsevier, 2015. 2. ISBN 978-0-12-397157-9
5. Zhengwei Mao, Shan Yu, **Changyou Gao***. Chapter 5, Bioactive and Spatially Organized LbL Films, in Layer-by-Layer Films for Biomedical Applications, 79-102/545, edited by Catherine Picart, Frank Caruso, and Jean-Claude Voegel, Viely-VCH, Germany, 2015, 1. ISBN 978-3-527-33589-3.
6. Jie Zhou, Wenzhong Li, and **Changyou Gao***. Chapter 21, Functionalized Nanomaterials, in Regenerative Medicine-from Protocol to Patient, edited by Gustav Steinhoff, Springer Dordrecht Heidelberg London New York, ISBN 978-90-481-9074-4, 2011.3. P493-521
7. Weijun Tong, **Changyou Gao***. Responsive Polyelectrolyte Microcapsules, in Section 4 of Frontiers of Polymer Sciences (II), edited by Jianhua Dong, Science Press, Beijing, 2009.1, ISBN 978-7-03-023197-0.
8. **Changyou Gao.** Interaction between Materials and Hosts (Chapter 8), in Tissue Engineering, edited by Yilin Cao, Science Press, Beijing, 2008.1, ISBN 978-7-03-017724-7.
9. **Changyou Gao**, Lie Ma. Biomedical Polymeric Materials, Chemistry Industry Press, Beijing, 2006,6, ISBN 7-5025-8578-8.
10. **Changyou Gao.** Optical Functional Composite Materials, in Chinese Materials Engineering Handbook, Volume 10, edited by Xiaosu Yi e tal. Chemistry Industry Press, Beijing, 2006.3, ISBN 7-5025-7312-7.
11. **Changyou Gao.** Hollow Microcapsules (Chapter 2), in Layered Supramolecular Structures—-Assembly and Functions, edited by Jiacong Shen, Science Press, Beijing, 2004.2, ISBN 7-03-012081-7.

Related People


QINFAXIA…
Materials Sc…


ZHUHANG
Materials Sc…


WANG XI…
Materials Sc…


WANLING…
Department …


Minmin Shi
Materials Sc…

Recent mainter
2018-09

Total visits

Changyou Gao Ph.D.

professor | Doctoral supervisor

Subject Materials Science and Engineering
Department Department of Polymer Science and Engineering
Position Director of Department of Polymer Science and Engineering

Phone +86-571-87951108 E-mail cygao@zju.edu.cn

Address Room 317, Polymer Building, Yuquan Campus of Zhejiang University

Research Polymer Materials

tudent Supervising | Professional Achievements | Books and Book Chapters | Journal Articles/Reviews | Patents

Journal articles/reviews published in last 5 years:

2018

1. Sai Wu, Wang Du, Yiyuan Duan, Deteng Zhang, Yixiao Liu, Bingbing Wu, Xiaohui Zou, Hongwei Ouyang, **Changyou Gao***. Regulating the migration of smooth muscle cells by a vertically distributed poly (2-hydroxyethyl methacrylate) gradient on polymer brushes covalently immobilized with RGD peptides, *Acta Biomaterialia* **2018**, 75, 75–92.
2. Deteng Zhang, SaiWu, Jianyong Feng, Yiyuan Duan, Dongming Xing, **ChangyouGao***. Micropatterned biodegradable polyesters clicked with CQAASIKVAV promote cell alignment, directional migration, and neurite outgrowth, *Acta Biomaterialia* **2018**, 74, 143-155.
3. Haolan Zhang, Xiaowen Zheng, Wajiha Ahmed, Yuejun Yao, Jun Bai, Yicheng Chen, and **Changyou Gao***. Design and Applications of Cell-Selective Surfaces and Interfaces, *Biomacromolecules* **2018**, 19, 1746−1763.
4. Shan Yu, Xingang Zuo, Tao Shen, Yiyuan Duan, Zhengwei Mao*, **Changyou Gao***. A density gradient of VAPG peptides on a cell-resisting surface achieves selective adhesion and directional migration of smooth muscle cells over fibroblasts, *Acta Biomaterialia***2018**, 72: 70–81.
5. Tao Shen, Yuankun Dai, Xuguang Li, Sanzhong Xu, Zhongru Gou, and **Changyou Gao***. Regeneration of the Osteochondral Defect by a Wollastonite and Macroporous Fibrin Biphasic Scaffold, *ACS Biomater. Sci.Eng.* **2018**, 4, 1942-1953.
6. Yixian Zhang, Wang Du, Kathrin Smuda, Radostina Georgieva, Hans Bäumler*, and **Changyou Gao***. Inflammatory activation of human serum albumin- or ovalbumin-modified chitosan particles to macrophages and their immune response in human whole blood, *J. Mater. Chem. B*, **2018**, 6, 3096-3106.
7. Yuankun Dai, Tao Shen, Lie Ma*, Dongan Wang, **Changyou Gao***. Regeneration of osteochondral defects in vivo by a cell - free cylindrical poly(lactide - co - glycolide) scaffold with a radially oriented microstructure, *J Tissue Eng Regen Med*. **2018**;12:e1647–e1661.
8. Xinyi Chen, **Changyou Gao***. Influences of Surface Coating of PLGA Nanoparticles on Immune Activation of Macrophages, *Journal of Materials Chemistry B*, **2018**, 6, 2065 – 2077.
9. Deteng Zhang, Shengjun Xu, Sai Wu and **Changyou Gao***. Micropatterned poly(D,L-lactide-co-caprolactone) films entrapped with gelatin for promoting the alignment and directional migration of Schwann cells, *J. Mater. Chem. B*, **2018**, 6, 1226-1237.
10. Yuankun Dai, Xuguang Li, Ruihan Wu, Ying Jin, and **Changyou Gao***. Macrophages of Different Phenotypes Influence the Migration of BMSCs in PLGA Scaffolds with Different Pore Size, *Biotechnol. J.* **2018**, 13, 1700297
11. Haolan Zhang, Danyu Wang, Xue Lin, Nikolaos Politakos, Jimena S. Tuninetti, Sergio Enrique Moya*, **Changyou Gao***. Fabrication of UV responsive micelles-containing multilayers and their influence on cell adhesion, *Sci China Chem*, **2018**, 61(1): 54–63.
12. Huiying Li, Honghao Zheng, Yixian Zhang, Wenbo Zhang, Weijun Tong*, Changyou Gao*. Preparation of photo-responsive poly(ethylene glycol) microparticles and their influence on cell viability, *Journal of Colloid and Interface Science*, **2018**, 514, 182–189.
13. Xiaowen Zheng, Xin Pan, Qian Pang, Chong Shuai, Lie Ma*, Changyou Gao. Selective capture of mesenchymal stem cells over fibroblasts and immune cells on E7-modified collagen substrates under flow circumstances, *J. Mater. Chem. B*, **2018**, 6, 165-173.
14. Zheng Yuan, Shan Yu, Fangyi Cao, Zhengwei Mao*, **Changyou Gao** and Jun Ling*. Near-infrared light triggered photothermal and photodynamic therapy with an oxygen-shuttle endoperoxide of anthracene against tumor hypoxia, *Polym. Chem.*, **2018**, 9, 2124-2133.
15. Guocan Yu, Jie Yang, Xiao Fu, Zhantong Wang, Li Shao, Zhengwei Mao,* Yijing Liu, Zhen Yang, Fuwu Zhang, Wenpei Fan, Jibin Song, Zijian Zhou, **Changyou Gao**, Feihe Huang * and Xiaoyuan Chen *. A supramolecular hybrid material constructed from graphene oxide and a pillar[6]arene-based host–guest complex as an ultrasound and photoacoustic signal nanoamplifier, *Materials Horizon*, **2018**, **5**, 429-435.
16. Guocan Yu , Zhen Yang, Xiao Fu, Bryant C. Yung , Jie Yang, Zhengwei Mao*, Li Shao, Bin Hua, Yijing Liu, Fuwu Zhang, Quli Fan*, Sheng Wang, Orit Jacobson, Albert Jin, **Changyou Gao**, Xiaoying Tang, Feihe Huang* & Xiaoyuan Chen*. Polyrotaxane-based supramolecular theranostics, *Nature Communications*, **2018**, 9, article no. 766.
17. Cuixia Bi, Jin Chen, Ying Chen, Yahui Song, Anran Li, Shuzhou Li, Zhengwei Mao*, **Changyou Gao**, Dayang Wang, Helmuth Möhwald, and Haibing Xia*. Realizing a Record Photothermal Conversion Efficiency of Spiky Gold Nanoparticles in the Second Near-

Related People


QINFAXIA…
Materials Sc…


ZHUHANG
Materials Sc…


WANG XI…
Materials Sc…


WANLING…
Department …


Minmin Shi
Materials Sc…

Recent mainter
2018-09

Total visits

albumin/heparin nanoparticles for induced s o, *Acta Biomaterialia* **2018**, 72: 217–227.

2017

20. Huiying Li, Wenbo Zhang, Ning He, Weijun Tong,* and **Changyou Gao***. Phototriggered N2 Generating Submicron Particles for Selective Killing of Cancer Cells, *ACS Appl. Mater. Interfaces* **2017**, 9, 44369−44376

21. Xinyi Chen, **Changyou Gao***. Influences of size and surface coating of gold nanoparticles on inflammatory activation of macrophages, *Colloids and Surfaces B: Biointerfaces*, **2017**, 160: 372-380.

22. Huiying Li, Yu Xiong, Yixian Zhang, Weijun Tong, Radostina Georgieva, Hans Bäumler,* and **Changyou Gao***. Photo-Decomposable Sub-Micrometer Albumin Particles Cross-Linked by ortho-Nitrobenzyl Derivatives, *Macromol. Chem. Phys.* **2017**, 1700413

23. Wenbo Zhang, Huiying Li, Ying Qin and **Changyou Gao***. Self-assembled composite microparticles with surface protrudent porphyrin nanoparticles enhance cellular uptake and photodynamic therapy, *Materials Horizons*, **2017**, 4, 1135-1144.

24. Xiaofan Liu, Honghao Zheng, Guangyu Li, Huiying Li, Pan Zhang, Weijun Tong*, **Changyou Gao***. Fabrication of polyurethane microcapsules with different shapes and their influence on cellular internalization, *Colloids and Surfaces B: Biointerfaces*, **2017**, 158: 675–681.

25. Wenbo Zhang and **Changyou Gao***. Morphology transformation of self-assembled organic nanomaterials in aqueous solution induced by stimuli-triggered chemical structure changes, *J. Mater. Chem. A*, **2017**, 5, 16059–16104.

26. Dongming Xing, Lie Ma*, **Changyou Gao***. A bioactive hyaluronic acid–based hydrogel cross-linked by Diels–Alder reaction for promoting neurite outgrowth of PC12 cells, *Journal of Bioactive and Compatible Polymers*, **2017**, 32(4): 382–396.

27. Jianyong Feng, Deteng Zhang, Meifang Zhu* and **Changyou Gao** *. Poly(L-lactide) melt spun fiber-aligned scaffolds coated with collagen or chitosan for guiding the directional migration of osteoblasts in vitro, *J. Mater. Chem. B*, **2017**, 5, 5176-5188.

28. Su Liang, Shan Yu, Ning Zhou, Jun Deng, **Changyou Gao***. Controlling the selective and directional migration of hepatocytes by a complementary density gradient of glycosylated hyperbranched polymers and poly(ethylene glycol) molecules, *Acta Biomaterialia*, **2017**, 56, 161–170.

29. Xuguang Li, Yuankun Dai, Tao Shen and **Changyou Gao***. Induced migration of endothelial cells into 3D scaffolds by chemoattractants secreted by pro-inflammatory macrophages in situ, *Regenerative Biomaterials*, **2017**, 4(3): 139–148.

30. Tanchen Ren, Yelin Ni, Wang Du, Shan Yu, Zhengwei Mao, and **Changyou Gao***. Dual Responsive Surfaces Based on Host–Guest Interaction for Dynamic Mediation of Cell–Substrate, Interaction and Cell Migration, *Adv. Mater. Interfaces* **2017**, 4, 1500865

31. Jun Deng, Mengyun Yao, **Changyou Gao***. Cytotoxicity of gold nanoparticles with different structures and surface-anchored chiral polymers, *Acta Biomaterialia*, **2017**, 53, 610–618.

32. Yixian Zhang, Yiran Xu, Xiangyi Xi, Surakshya Shrestha, Pengfei Jiang, Wenjing Zhang and **Changyou Gao***. Amino acid-modified chitosan nanoparticles for Cu2+ chelation to suppress CuO nanoparticle cytotoxicity, *J. Mater. Chem. B*, **2017**, 5, 3521-3530.

33. Jun Deng, Honghao Zheng and **Changyou Gao***. Influence of protein adsorption on the cellular uptake of AuNPs conjugated with chiral oligomers, *Mater. Chem. Front.*, **2017**, 1, 542-549

34. Su Liang, Ning Zhou, Shan Yu, N. Polotakos, Jun Deng, Sergio Enrique Moya*, **Changyou Gao***. Buildup of hyperbranched polymer/alginate multilayers and their influence on protein adsorption and platelet adhesion, *Journal of Applied Polymer Science*, **2017**, 134(18), DOI: 10.1002/APP.44769

35. Huiying Li, Honghao Zheng, Weijun Tong*, **Changyou Gao***. Non-covalent assembly of poly(allylamine hydrochloride)/triethylamine microcapsules with ionic strength-responsiveness and auto-fluorescence, *Journal of Colloid and Interface Science* **2017**, 496:228–234.

36. Wenjing Zhang, Pengfei Jiang, Jin Chen, Chaonan Zhu, Zhengwei Mao*, **Changyou Gao***. Application of melatonin-loaded poly(N-isopropylacrylamide) hydrogel particles to reduce the toxicity of airborne pollutes to RAW264.7 cells, *Journal of Colloid and Interface Science* **2017**, 490: 181–189.

37. Hui Wang, Graeme George, Selena Bartlett, **Changyou Gao**, Nazrul Islam*. Nicotine hydrogen tartrate loaded chitosan nanoparticles: Formulation, characterization and in vitro delivery from dry powder inhaler formulation, *European Journal of Pharmaceutics and Biopharmaceutics* **2017**, 113: 118–131.

38. Qian Li, Dongming Xing, Lie Ma*, **Changyou Gao**. Synthesis of E7 peptide-modified biodegradable polyester with the improving affinity to mesenchymal stem cells, *Materials Science and Engineering C* **2017**, 73: 562–568.

39. Chen Zong, Meicong Wang, Fuchun Yang, Guojun Chen, Jiarong Chen, Zihua Tang, Quanwen Liu, **Changyou Gao**, Lie Ma* and Jinfu Wang*. A novel therapy strategy for bile duct repair using tissue engineering technique: PCL/PLGA bilayered scaffold with hMSCs, *J Tissue Eng Regen Med* **2017**; 11: 966–976.

40. Xiao-Yi Chen, San-Zhong Xu, Xuan-Wei Wang, Xian-Yan Yang, Liang Ma, Lei Zhang, Guo-Jing Yang, Fan Yang, Lin-Hong Wang, Xin-Li Zhang, Kang Ting, **Chang-You Gao**, Xiao-Zhou Mou*, Zhong-Ru Gou* and Hai Zou*. Systematic comparison of biologically active foreign ions-codoped calcium phosphate microparticles on osteogenic differentiation in rat osteoporotic and normal mesenchymal stem cells, *Oncotarget*, **2017**, 8 (22): 36578-36590.

41. Jiajun Xie, Changjun Wang, Qingyao Ning, Qi Gao, **Changyou Gao**, ,Zhongru Gou, Juan Ye*. A new strategy to sustained release of ocular drugs by one-step drug-loaded microcapsule manufacturing in hydrogel punctual plugs, *Graefes Arch Clin Exp Ophthalmol*, **2017**, 255: 2173–2184.

42. Qian Pang, Xiaowen Zheng, Yu Luo, Lie Ma* and **Changyou Gao**. A photo-cleavable polyprodrug-loaded wound dressing with UV-responsive antibacterial property, *J. Mater. Chem. B*, **2017**, 5, 8975-8982.

43. Guocan Yu, Mingming Zhang, Manik Lal Saha, Zhengwei Mao*, Jin Chen, Yong Yao, Zijian Zhou, Yijing Liu, Changyou Gao, Feihe Huang* Xiaoyuan Chen*, and Peter J. Stang*. Antitumor Activity of a Unique Polymer That Incorporates a Fluorescent Self-Assembled

2016

45. Yuankun Dai, Zhenzhen Gao, Lie Ma, [illegible] LGA Scaffolds with Radially Oriented Pores for In Situ Inductive Regeneration of Full Thickness Cartilage Defects, *Macromol. Biosci.* **2016**, 16, 1632-1642.

46. Jun Deng, Honghao Zheng, Xiaowen Zheng, Mengyun Yao, Zheng Li, and **Changyou Gao*.** Gold nanoparticles with surface-anchored chiral poly(acryloyl-L(D)-valine) induce differential response on mesenchymal stem cell osteogenesis, *Nano Research* **2016**, 9(12): 3683–3694.

47. Shan Yu, Ying Gao, Xu Mei, Tanchen Ren, Su Liang, Zhengwei Mao,* and **Changyou Gao*.** Preparation of an Arg-Glu-Asp-Val Peptide Density Gradient on Hyaluronic Acid-Coated Poly(ε-caprolactone) Film and Its Influence on the Selective Adhesion and Directional Migration of Endothelial Cells, *ACS Appl. Mater. Interfaces* **2016**, 8, 29280−29288.

48. Surakshya Shrestha, Zhengwei Mao,* Yuri Fedutik, and **Changyou Gao*.** Influence of titanium dioxide nanorods with different surface chemistry on the differentiation of rat bone marrow mesenchymal stem cells, *J. Mater. Chem. B*, **2016**, 4, 6955-6966.

49. Pengfei Jiang, Yixian Zhang, Chaonan Zhu, Wenjing Zhang, Zhengwei Mao*, **Changyou Gao*.** Fe3O4/BSA particles induce osteogenic differentiation of mesenchymal stem cells under static magnetic field, *Acta Biomaterialia* **2016**, 46:141-150.

50. Jun Deng, Sai Wu, Mengyun Yao, **Changyou Gao*.** Surface-anchored poly(acryloyl-L(D)-valine) with enhanced chirality-selective effect on cellular uptake of gold nanoparticles, *Scientific Reports* **2016**, 6, 31595. doi:10.1038/srep31595.

51. Su Liang, Shan Yu, **Changyou Gao*.** Preparation of complementary glycosylated hyperbranched polymer/poly(ethylene glycol) brushes and their selective interactions with hepatocytes, *Colloids and Surfaces B: Biointerfaces* **2016**, 145: 309–318.

52. Jun Deng, **Changyou Gao*.** Recent advances in interactions of designed nanoparticles and cells with respect to cellular uptake, intracellular fate, degradation and cytotoxicity, *Nanotechnology* **2016**, 27, 412002 (10pp). Oct.

53. Bin Hu, Jun Deng, Honghao Zheng, Shan Yu, **Changyou Gao*.** Synthesis of Chiral Oligomer-Grafted Biodegradable Polyurethanes and Their Chiral-Dependent Infl uence on Bone Marrow Stem Cell Behaviors, *Macromol. Rapid Commun.***2016**, 37, 1331−1336.

54. Yuankun Dai, Gang Liu, Lie Ma,* Dongan Wang and **Changyou Gao*.** Cell-free macro-porous fibrin scaffolds for in situ inductive regeneration of full-thickness cartilage defects, *J. Mater. Chem. B*, **2016**, 4, 4410-4419.

55. Kuihua Zhang, Honghao Zheng, Su Liang, **Changyou Gao*.** Aligned PLLA nanofibrous scaffolds coated with graphene oxide for promoting neural cell growth, *Acta Biomaterialia* **2016**, 37: 131–142.

56. Jun Deng, Zheng Li, Mengyun Yao, and **Changyou Gao*.** Influence of Albumin Configuration by the Chiral Polymer-Grafted Gold Nanoparticles, *Langmuir* **2016**, 32: 5608−5616.

57. Huiying Li, Wenbo Zhang, Weijun Tong,* and **Changyou Gao*.** Enhanced Cellular Uptake of Bowl-like Microcapsules,*ACS Appl. Mater. Interfaces* 2016, 8: 11210−11214.

58. Wenjing Zhang, Pengfei Jiang, Ying Chen, Peihua Luo, Guanqun Li, Botuo Zheng, Wei Chen, Zhengwei Mao*, and**Changyou Gao*.** Suppressing the cytotoxicity of CuO nanoparticles by uptake of curcumin/BSA particles, *Nanoscale*, 2016, 8: 9572-9582.

59. Kai Jin, Bo Li, Lixia Lou, Yufeng Xu, Xin Ye, Ke Yao, Juan Ye*, **Changyou Gao*.** In vivo vascularization of MSCloaded porous hydroxyapatite constructs coated with VEGFfunctionalized collagen/heparin multilayers, *Scientific Reports*, **2016**, 6:19871. DOI: 10.1038/srep19871.

60. Kai Jin, Xin Ye, Sha Li, Bo Li, Caiqiao Zhang, **Changyou Gao***, Juan Ye*. A biomimetic collagen/heparin multi-layered porous hydroxyapatite orbital implant for in vivo vascularization studies on the chicken chorioallantoic membrane, *Graefes Arch Clin Exp Ophthalmol,* **2016**, 254: 83–89.

61. Surakshya Shrestha, Pengfei Jiang, Marcelo Henrique Sousa, Paulo Cesar Morais, Zhengwei Mao*, **Changyou Gao*.** Citrate-capped iron oxide nanoparticles impair the osteogenic differentiation potential of rat mesenchymal stem cells, *J. Mater. Chem. B*, **2016**, 4, 245-256.

62. Huiying Li, Weijun Tong*, **Changyou Gao.** Photo-responsive polyethyleneimine microcapsules cross-linked by ortho-nitrobenzyl derivatives, *Journal of Colloid and Interface Science* **2016** 463: 22–28

63. Wei Yu, Wenbo Zhang, Ying Chen, Xiaoxue Song, Weijun Tong, Zhengwei Mao*, **Changyou Gao*.** Cellular uptake of poly(allylamine hydrochloride) microcapsules with different deformability and its influence on cell functions, *Journal of Colloid and Interface Science* **2016**, 465: 149–157.

64. Pan Zhang, Hui Yang, Guojun Wang, Weijun Tong*,* **Changyou Gao.** Polyamine/salt-assembled microspheres coated with hyaluronic acidfor targeting and pH sensing, *Colloids and Surfaces B: Biointerfaces*, **2016**, 142: 223–229.

65. Guangyu Li, Zhirui Dong, Yuting Zhu, Weijun Tong*, **Changyou Gao.** Dual-responsive colloidal microcapsules based on host-guest interaction on solid templates, *Journal of Colloid and Interface Science* **2016**, 475: 196–202.

66. Lijie Han, Ying Chen, Jie Niu, Lihua Peng, Zhengwei Mao* and **Changyou Gao.** Encapsulation of a photosensitizer into cell membrane capsules for photodynamic therapy, *RSC Adv.*, **2016**, 6: 37212–37220.

67. Jiajun Xie, XianyanYang, HuifengShao, JuanYe*, YongHe, Jianzhong Fu, **Changyou Gao**, ZhongruGou*. Simultaneous mechanical property and biodegradation improvement of wollastonite bioceramic through magnesium dilute doping, *Journal of the Mechanical Behavior of Biomedical Materials*, **2016**, 54: 60–71.

68. Feng Zhang, Xianyan Yang, Chen Zhuang, Lin Wang, Xin-Hua Gu,* Zheng Shen, Sanzhong Xu, **Changyou Gao** and Zhongru Gou*. Design and evaluation of multifunctional antibacterial ion-doped b-dicalcium silicate cements favorable for root canal sealing, *RSC Adv.*, **2016**, 6: 19707–19715.

Micelles and Their Influence on Cytoviab

71. Qi Gao, Bin Hu, Qingyao Ning, Chen Ye, Jiajun Xie, Juan Ye*, and **Changyou Gao***.A primary study of poly(propylene fumarate)–2-hydroxyethyl methacrylate copolymer scaffolds for tarsal plate repair and reconstruction in rabbit eyelids, *J. Mater. Chem. B,* **2015**, 3, 4052-4062.

72. Wenbo Zhang, Lingbo Xing, Haisheng Wang, Xiujun Liu, Yaqing Feng*, and **Changyou Gao***. Preparation of Novel Porphyrin Nanomaterials Based on the pH-Responsive Shape Evolution of Porphyrin Microspheres, *Langmuir*, **2015**, 31 (14), pp 4330–4340.

73. Jun Deng, Mingcong Sun, Shasha Wang, Lulu Han, Zhengwei Mao, Dan Li, Hong Chen, **Changyou Gao***. Adsorption of Fibronectin on Salt-EtchedPolyelectrolyte Multilayers and its Roles inMediating the Adhesion and Migration ofVascular Smooth Muscle Cells, *Macromolecular Bioscience*, **2015**, 15(2): 241-252.

74. Bin Hu, Chen Ye, **Changyou Gao***. Synthesis and characterization of biodegradable polyurethanes with unsaturated carbon bonds based on poly(propylene fumarate), *Journal of Applied Polymer Science*, **2015**, 132(24): 42065.

75. Pengfei Jiang, Dahai Yu, Wenjing Zhang, Zhengwei Mao* and **Changyou Gao.** Influence of bovine serum albumin coated poly(lactic-co-glycolic acid) particles on differentiation of mesenchymal stem cells, *RSC Adv.*, **2015**, 5, 40924-40931

76. Pengfei Jiang, Zhengwei Mao*, **Changyou Gao.** Combinational effect of matrix elasticity and alendronate density on differentiation of rat mesenchymal stem cells, *Acta Biomaterialia* **2015**, 19: 76–84.

77. Shan Yu, Zhengwei Mao*, **Changyou Gao.** Preparation of gelatin density gradient on poly(e-caprolactone) membrane and its influence on adhesion and migration of endothelial cells, *Journal of Colloid and Interface Science* **2015**, 451: 177–183.

78. Tanchen Ren, Shan Yu, Zhengwei Mao*, **Changyou Gao***. A complementary density gradient of zwitterionic polymer brushes and NCAM peptides for selectively controlling directional migration of Schwann cells, *Biomaterials* **2015**, 56: 58-67.

79. Sai Wu, Xuanyong Liu, **Changyou Gao***. Role of adsorbed proteins on hydroxyapatite-coated titanium in osteoblast adhesion and osteogenic differentiation, *Sci. Bull.* **2015**, 60(7): 691–700.

80. Mingcong Sun, Jun Deng, **Changyou Gao***. The correlation between fibronectin adsorption and attachment of vascular cells on heparinized polycaprolactone membrane, *Journal of Colloid and Interface Science* **2015**, 448: 231–237.

81. Jun Deng, Honghao Zheng, Sai Wu, Pan Zhang and **Changyou Gao***. Protein adsorption and cellular uptake of AuNPs capped with alkyl acids of different length, *RSC Adv.*, **2015**, 5, 22792-22801.

82. Tianxiang Wang, Haisheng Wang, Lingbo Xing, Wenbo Zhang, and **Changyou Gao***. Fabrication of Pyrene and Tetraphenylethylene Nanostructures by a Hydrolysis-Assisted Co-Assembly, *Chin. J. Chem.* **2015**, 33, 207-212.

83. Xiaofan Liu, Shupeng She, Weijun Tong* and **Changyou Gao.** Preparation of elastic polyurethane microcapsules using CaCO3 microparticles as templates for hydrophobic substances loading, *RSC Adv.*, **2015**, 5, 5775.

84. Qian Li, Lie Ma*, **Changyou Gao.** Biomaterials for in situ tissue regeneration: development and perspectives, *J. Mater. Chem. B*, **2015**, 3, 8921-8938.

85. Guocan Yu, Wei Yu, Zhengwei Mao, **Changyou Gao**, and Feihe Huang*. A Pillararene-Based Ternary Drug-Delivery System with Photocontrolled Anticancer Drug Release, *Small* **2015**, 11 (8): 919–925.

86. Huifeng Shao, Xianyan Yang, Yong He, Jianzhong Fu, Limin Liu, Liang Ma, Lei Zhang, Guojing Yang, **Changyou Gao** and Zhongru Gou. Bioactive glass-reinforced bioceramic ink writing scaffolds: sintering, microstructure and mechanical behavior,*Biofabrication* **2015**, 7: 035010.

2014

87. Haisheng Wang, Wei Yu, Wenbo Zhang, **Changyou Gao***. Decomposition and Transformation of Pyrene-Derivative Micelles at Intracellular Milieu and Their Influence on Cytoviability, *Macromol. Biosci.* **2014**, 14 (12): 1748–1754.

88. Meicong Wang, Lie Ma*, Bo Li, **Changyou Gao.** Modification of Polycaprolactone Microspheres-Aggregated Scaffolds with Galactosylated Chitosan for Modulating the Differentiation of Bone Mesenchymal Stem Cells, *Journal of Biomaterials and Tissue Engineering*, **2014**, 4 (8): 657-662.

89. Jun Deng, Tanchen Ren, Jiyu Zhu, Zhengwei Mao and **Changyou Gao***. Adsorption of plasma proteins and fibronectin on poly(hydroxylethyl methacrylate) brushes of different thickness and their relationship with adhesion and migration of vascular smooth muscle cells, *Regenerative Biomaterials*, **2014**, 1: 17–25.

90. Dongming Xing, Lie Ma,* **Changyou Gao***. Synthesis of Functionalized Poly(ester carbonate) with Laminin-Derived Peptide for Promoting Neurite Outgrowth of PC12 cells, *Macromol. Biosci.* **2014**, 14, 1429–1436.

91. Tanchen Ren, Shan Yu, Zhengwei Mao,* Sergio Enrique Moya, Lulu Han, and **Changyou Gao***. Complementary Density Gradient of Poly(hydroxyethyl methacrylate) and YIGSR Selectively Guides Migration of Endotheliocytes, *Biomacromolecules***2014**, 15, 2256−2264.

92. Bo Li, Feifei Li, Lie Ma,* Junzhou Yang, Chunfen Wang, Dongan Wang, and **Changyou Gao***. Poly(lactide-co-glycolide)/Fibrin Gel Construct as a 3D Model to Evaluate Gene Therapy of Cartilage in Vivo, *Mol. Pharmaceutics* **2014**, 11, 2062-2070.

93. Dongming Xing, Lie Ma*, **Changyou Gao***. Synthesis of poly(ester-carbonate) with a pendant acetylcholine analog for promoting neurite growth, *Acta Biomaterialia*, **2014**, 10: 4127-4135.

94. Dahai Yu, Yuying Zhang, Guangyang Zou, Xiaojing Cui, Zhengwei Mao*, **Changyou Gao***. Influence of surface coatings of poly(D,L-lactide-co-glycolide) particles on HepG2 cell behavior and particle fate, *Biointerphases*, **2014**, 9(3): 031015

95. Tanchen Ren, Zhengwei Mao,* Sergio Enrique Moya, and **Changyou Gao***. Immobilization of Enzymes on 2-Hydroxyethyl Methacrylate and Glycidyl Methacrylate Copolymer Brushes, *Chem. Asian J.* **2014**, 9, 2132-2139.

130.

98. Jindan Wu, Zhengwei Mao, Lulu Han, Hzhi Zhao, Jiabin Xi, **Changyou Gao***. A density gradient of basic fibroblast growth factor guides directional migration of vascular smooth muscle cells, *Colloids and Surfaces B: Biointerfaces*, **2014**, 117: 290-295.

99. Bo Li, Junzhou Yang, Lie Ma*, Feifei Li, Zhengyuan Tu, **Changyou Gao***. Influence of the Molecular Weight of Poly(Lactide-Co-Glycolide) on the *In Vivo* Cartilage Repair by a Construct of Poly(Lactide-Co-Glycolide)/Fibrin Gel/Mesenchymal Stem Cells/Transforming Growth Factor-β1, *Tissue Engineering Part A*, **2014**, 20(1-2): 1-11.

100. Bing Wang, Yuying Zhang, Zhengwei Mao*, Dahai Yu, and **Changyou Gao***. Toxicity of ZnO Nanoparticles to Macrophages Due to Cell Uptake and Intracellular Release of Zinc Ions, *Journal of Nanoscience and Nanotechnology*, **2014**, 14 (8): 5688-5696.

101. Rui Guo, Jianying Teng, Shaojun Xu, Lie Ma*, Aibin Huang, **Changyou Gao.** Comparison studies of the in vivo treatment of full-thickness excisional wounds and burns by an artificial bilayer dermal equivalent and J-1 acellular dermal matrix, *Wound Repair and Regeneration* **2014**, 22:390–398.

102. Xiangyan Zhou, Marco Dorn, Jürgen Vogt, Daniel Spemann, Wei Yu, Zhengwei Mao*, Irina Estrela-Lopis, Edwin Donath,**Changyou Gao.** A quantitative study of the intracellular concentration of graphene/noble metal nanoparticle composites and their cytotoxicity, *Nanoscale*, **2014**, 6(15): 8535-8542.

103. Wenjing Zhang, Zhengwei Mao*, **Changyou Gao.** Preparation of TAT peptide-modified poly(N-isopropylacrylamide) microgel particles and their cellular uptake, intracellular distribution, and influence on cytoviability in response to temperature change, *Journal of Colloid and Interface Science*, **2014**, 434: 122-129.

104. Lulu Han, Jindan Wu, Tanchen Ren, Zhengwei Mao*, Yang Guo and **Changyou Gao.** Polyelectrolyte Multilayer Patterns Created by Capillary Force and Their Impact on Cell Migration, *Chinese Journal of Chemistry*, **2014**, 32: 66-72

105. Feifei Li, Lie Ma*, Bo Li, **Changyou Gao.** Enhanced bioactivity of transform growth factor-β1 from sulfated chitosan microspheres for in vitro chondrogenesis of mesenchymal stem cells, *Pure and Applied Chemistry*, **2014**, 86 (12): 1885-1895.

106. Pan Zhang, Xiaoxue Song, Weijun Tong,* **Changyou Gao.** Nanoparticle/Polymer Assembled Microcapsules with pH Sensing Property, *Macromol. Biosci.* **2014**, 14, 1495–1504.

107. Chunfen Wang, Luyan Li, Lie Ma*, Bo Li and **Changyou Gao.** Biotin-triggered release and transfection of DNA complexes immobilized on a substrate via biotin-avidin interaction, *Journal of Bioactive and Compatible Polymers*, **2014**, 29(3): 221–234.

108. Chunfen Wang, Lie Ma* and **Changyou Gao.** Design of gene-activated matrix for the repair, of skin and cartilage,*Polymer Journal* **2014**, 46, 476–482.

109. Xiaoxue Song, Huanbin Li, Weijun Tong*, **Changyou Gao.** Fabrication of triple-labeled polyelectrolyte microcapsules for localized ratiometric pH sensing, *Journal of Colloids and Interfaces Science*, **2014**, 416: 252-257.

110. Mian Lin, Lei Zhang, Juncheng Wang, Xiaoyi Chen, Xianyan Yang, Wenguo Cui, Wen Zhang, Guojing Yang,* Min Liu, Yu Zhao, **Changyou Gao** and Zhongru Gou*. Novel highly bioactive and biodegradable gypsum/calcium silicate composite bone cements: from physicochemical characteristics to in vivo aspects, *J. Mater. Chem. B*, **2014**, 2, 2030–2038.

111. Xianyan Yang, Min Liu,* Yu Zhao, Hongyu Jia, Sanzhong Xu, Xigong Li, Xiaoyi Chen, Feng Zhang, **Changyou Gao** and Zhongru Gou*. Rational design and fabrication of a b-dicalcium silicate-based multifunctional cement with potential for root canal filling treatment, *J. Mater. Chem. B*, **2014**, 2, 3830–3838.

112. Lingzhi Lin, Lei Zhang, Juncheng Wang, Kailuo Xie, Xianyan Yang, Xiaoyi Chen, Guojing Yang*, **Changyou Gao**, Zhongru Gou*. Low-temperature sintering of 45S5 Bioglasss-based glass ceramics: Effect of biphasic mixing approach on the mechanical and biological properties, *Materials Letters* **2014**, 126 154-158.

113. Yvonne Peck, Ling Yen Ng, Jie Yi Lois Goh, **Changyou Gao**, and Dong-An Wang*. A Three-Dimensionally Engineered Biomimetic Cartilaginous Tissue Model for Osteoarthritic Drug Evaluation, *Mol. Pharmaceutics* **2014**, 11, 1997-2008.

114. Juan Ye*, Xin Shi, Xiaoyi Chen, Jiajun Xie, Changjun Wang, Ke Yao, **Changyou Gao** and Zhongru Gou*. Chitosan-modified, collagen-based biomimetic nanofibrous membranes as selective cell adhering wound dressings in the treatment of chemically burned corneas, *J. Mater. Chem. B*, **2014**, 2, 4226.

115. Jordi Llop, Irina Estrela-Lopis, Ronald F. Ziolo, Africa González, Jana Fleddermann, Marco Dorn, Vanessa Gomez Vallejo, Rosana Simon-Vazquez, Edwin Donath, Zwengei Mao, **Changyou Gao** and Sergio E. Moya. Uptake, Biological Fate, and Toxicity of Metal Oxide Nanoparticles, *Part. Part. Syst. Charact.* **2014**, 31: 24-35.

116. Liyue Liu, Chen Zong, Bo Li, Dan Shen, Zihua Tang, Jiarong Chen, Qiang Zheng, Xiangming Tong, Changyou Gao, and, Jinfu Wang*. The interaction between *β*1 integrins and ERK1/2 in osteogenic differentiation of human mesenchymal stem cells under fluid shear stress modelled by a perfusion system, *Journal of Tissue Engineering and Regenerative Medicine*, 2014, 8(2): 85-96.

117. Chen Zong, Xiaodan Qian, Zihua Tang, Qinghong Hu, Jiarong Chen, **Changyou Gao**, Ruikang Tang, Xiangmin Tong, Jinfu Wang*. Biocompatibility and Bone-Repairing Effects: Comparison Between Porous Poly-Lactic-Co-Glycolic Acid and Nano-Hydroxyapatite/Poly(lactic acid) Scaffolds, *Journal of Biomedical Nanotechnology*, **2014**, 10 (6): 1091-1104.

118. Y. Wang, X. Y. Zhou, Z. Chen, B. Cai, Z. Z. Ye, **C. Y. Gao**, J. Y. Huang*. Synthesis of cubic LiNbO3 nanoparticles and their application in vitro bioimaging, *Appl. Phys. A*, **2014**, 117:2121–2126.

2013

121. Jindan Wu, Zhengwei Mao*, Lulu [illegible] ional migration of vascular smooth muscle cells guided by synergetic surface gradient and chemical pattern of poly(ethylene glycol) brushes, *Journal of Bioactive and Compatible Polymers*, **2013**, 28(6): 605–620.

122. Shupeng She, Qinqin Li, Bowen Shan, Weijun Tong,* and **Changyou Gao***. Fabrication of Red-Blood-Cell-Like Polyelectrolyte Microcapsules and Their Deformation and Recovery Behavior Through a Microcapillary, *Adv. Mater.* **2013**, 25: 5814–5818.

123. DENG Jun, YU DaHai & **GAO ChangYou***. Biological identity of nanomaterials: Opportunities and challenges, *Science China Chemistry*, **2013**, 56(11): 1533–1541.

124. Bo Li, Junzhou Yang, Lie Ma, Feifei Li, Zhengyuan Tu, **Changyou Gao.** Fabrication of poly(lactide-co-glycolide) scaffold filled with fibrin gel, mesenchymal stem cells, and poly(ethylene oxide)-b-poly(L-lysine)/TGF-b1 plasmid DNA complexes for cartilage restoration in vivo, *J Biomed Mater Res Part A*, **2013**, 101A:3097–3108.

125. Meicong Wang, Lie Ma*, Dan Li, Pengfei Jiang, **Changyou Gao***. Preparation of polycaprolactone microspheres-aggregated scaffold with ultra big pores and fuzzy sphere surface by a one-step phase separation method, *J Biomed Mater Res Part A*, **2013**, 101A:3219–3227.

126. Jindan Wu, Zhengwei Mao, Yifeng Hong, Lulu Han, and **Changyou Gao***. Conjugation of Basic Fibroblast Growth Factor on a Heparin Gradient for Regulating the Migration of Different Types of Cells, *Bioconjugate Chem.* **2013**, 24, 1302-1313.

127. Jun Deng, Mingcong Sun, Jiyu Zhu and **Changyou Gao***. Molecular interactions of different size AuNP-COOH nanoparticles with human fibrinogen, ***Nanoscale***, 2013, 5 (17): 8130–8137.

128. Xing liu, Lie Ma*, **Changyou Gao***. RNAi functionalized scaffold for scarless skin regeneration, *Organogenesis*, **2013**, 9(2): 76-78.

129. Zhengwei Mao, Xiangyan Zhou, **Changyou Gao***. Influence of structure and properties of colloidal biomaterials on cellular uptake and cell functions, *Biomater. Sci.*, **2013**, 1 (9): 896-911.

130. Zhengwei Mao, Yuanhong Zhang, Huiying Li, Weijun Tong, **Changyou Gao***. Advanced Particulate Biomedical Materials and Their Interactions with Cells, *Progress in Chemistry*, **2013**, 25(7): 1061-1070.

131. Erjia Guan, Tianxiang Wang, Zhipeng Wang, **Changyou Gao***. Modulating the nanorods protrusion from poly(allylamine hydrochloride)-g-pyrene microcapsules by 1-pyrenesulfonic acid sodium salt, *Journal of Colloid and Interface Science*, **2013**, 405: 10–16.

132. Lulu Han, Zhengwei Mao*, Jindan Wu, Yang Guo, Tanchen Ren, **Changyou Gao***. Unidirectional migration of single smooth muscle cells under the synergetic effects of gradient swelling cue and parallel groove patterns, *Colloids and Surfaces B: Biointerfaces*, **2013**, 111: 1– 6.

133. Tanchen Ren, Zhengwei Mao,* Jian Guo, and **Changyou Gao***. Directional Migration of Vascular Smooth Muscle Cells Guided by a Molecule Weight Gradient of Poly(2-hydroxyethyl methacrylate) Brushes, *Langmuir*, **2013**, 29, 6386−6395.

134. Xiangyan Zhou, Bing Wang, Yiqi Chen, Zhengwei Mao*, **Changyou Gao.** Uptake of Cerium Oxide Nanoparticles and Their Influences on Functions of A549 Cells, *Journal of Nanoscience and Nanotechnology*, **2013**, 13 (1): 204-215.

135. Yang Zhu, Zhengwei Mao, **Changyou Gao***. Control over the Gradient Differentiation of Rat BMSCs on a PCL Membrane with Surface-Immobilized Alendronate Gradient, *Biomacromolecules*, **2013**, 14 (2): 342–349.

136. Yang Zhu, Zhengwei Mao, **Changyou Gao***. Aminolysis-based surface modification of polyesters for biomedical applications, *RSC Adv.*, **2013**, 3(8): 2509–2519.

137. Meicong Wang, Lie Ma*, Dan Li, **Changyou Gao***. Polycaprolactone scaffolds or anisotropic particles: The initial solution temperature dependence in a gelatin particle-leaching method, *Polymer*, **2013**, 54: 277-283.

138. Xing Liu, Lie Ma*, Jun Liang, Bing Zhang, Jianying Teng, **Changyou Gao***. RNAi functionalized collagen-chitosan/silicone membrane bilayer dermal equivalent for full-thickness skin regeneration with inhibited scarring,*Biomaterials*, 2013, 34: 2038-2048.

139. Lulu Han, Zhengwei Mao*, Jindan Wu, Yang Guo, Tanchen Ren, **Changyou Gao***. Directional cell migration through cellecell interaction on polyelectrolyte multilayers with swelling gradients, *Biomaterials*, 2013, 34: 975-984.

140. Guocan Yu, Jinying Li, Wei Yu, Chengyou Han, Zhengwei Mao, **Changyou Gao**, and Feihe Huang*. Carbon Nanotube/Biocompatible Bola-Amphiphile Supramolecular Biohybrid Materials: Preparation and Their Application in Bacterial Cell Agglutination, *Adv. Mater*. **2013**, 25, 6373–6379.

141. Guocan Yu, Yingjie Ma, Chengyou Han, Yong Yao, Guping Tang, Zhengwei Mao, **Changyou Gao**, and Feihe Huang*. A Sugar-Functionalized Amphiphilic Pillar[5]arene: Synthesis, Self Assembly in Water, and Application in Bacterial Cell Agglutination, *J. Am. Chem. Soc.* **2013**, 135, 10310-10313.

142. Xingang Wang, Chuangang You, Xinlei Hu, Yurong Zheng, Qiyin Li, Zhanzeng Feng, Huafeng Sun, **Changyou Gao**, Chunmao Han*. The roles of knitted mesh-reinforced collagen–chitosan hybrid scaffold in the one-step repair of full-thickness skin defects in rats, *Acta Biomaterialia*, **2013**, 9: 7822–7832.

143. Arun Ghosh, Lie Ma, **Changyou Gao.** Zeolite molecular sieve 5A acts as a reinforcing filler, altering the morphological, mechanical, and thermal properties of chitosan, *Journal of Materials Science*, **2013**, 48(11): 3926-3935.

144. Gabriela Romero, David J. Sanz, Yuan Qiu, Dahai Yu, Zhengwei Mao, **Changyou Gao**, Sergio E. Moya*. Lipid layer engineering of poly(lactide-co-glycolide) nanoparticles to control their uptake and intracellular co-localisation, *J. Mater. Chem. B*, **2013**, 1(17): 2252-2259.

612–620.

Changyou Gao Ph.D.

professor | Doctoral supervisor

Subject Materials Science and Engineering
Department Department of Polymer Science and Engineering
Position Director of Department of Polymer Science and Engineering

Phone +86-571-87951108 E-mail cygao@zju.edu.cn

Address Room 317, Polymer Building, Yuquan Campus of Zhejiang University

Research Polymer Materials

tudent Supervising | Professional Achievements | Books and Book Chapters | Journal Articles/Reviews | Patents

1. Zhengwei Mao, Lijie Han, **Changyou Gao.** A method to prepare cell membrane capsules containing chemotherapy drugs, Date of issue: 19 June 2018.
2. **Changyou Gao,** Jianyong Feng**.** A method to prepare cellulose acetate electrospun fibers with aligned structures and high adsorption property, Patent Number: ZL 201510717504.X, Date of issue: 27 April 2018.
3. **Changyou Gao,** Bin Hu. A method to synthesize unsaturated and biodegradable polyurethanes, Patent Number: ZL 201410667130.0, Date of issue: 13 June 2017.
4. **Changyou Gao**, Jianyong Feng. A method to prepare aligned polylactide scaff, Date of issue: 19 April 2017
5. **Changyou Gao,** Jianyong Feng. Random polylactide fiberous scaffolds fabricated by thermo-crosslinking, Patent Number: ZL 201510040458.4, Date of issue: 12 April 2017.
6. **Changyou Gao,** Jianyong Feng. Aligned polylactide fiberous scaffolds fabricated by thermo-crosslinking, Patent Number: ZL 201510041589.4, Date of issue: 17 August 2016.
7. **Changyou Gao,** Lie Ma, Dongming Xing. The acetyl choline functionalized biodegradable polyesters for nerve regeneration and their fabrication methods, Patent Number: ZL 201410274520.1, Date of issue: 21 October 2015.
8. Weijun Tong, Pan Zhang, **Changyou Gao**. A method to prepare sensors based on microcapseuls, Patentn Number: ZL 201310460418.9, Date of issue: 12 August 2015.
9. **Changyou Gao,** Wei Wang, Bo Li, Haiguang Zhao, Zhengwei Mao. A method to prepare a composite plasmid DNA/fibrinogen gel/polymer scaffolds, Patent Number: ZL 200910155117.6, Date of issue: 15 July 2015.
10. Lie Ma, Meicong Wang, Jie Dong, Qianqian Wang, **Changyou Gao**. The bile ducts with double composite layers and their preparation methods, Patent Number: ZL 201210121193.7, Date of issue: 24 December 2014.
11. Lie Ma, **Changyou Gao**, Yunyun Liu. A method to prepare collagen/chitosan scaffolds by a one-step freeze-drying, Patent Number: ZL 201210075386.3, Date of issue: 2 July 2014.
12. **Changyou Gao**, Weijun Tong, Yicao Song. Mediating the drug loading capacity into alginate microspheres by treatment with NaCl solution, Patent Number: ZL 201210115661.X, Date of issue: 29 May 2013.
13. **Changyou Gao**, Weijun Tong, Lili Xie**.** A method to prepare multifunctional nanocarriers, Patent Number: ZL 201210024989.0, Date of issue: 12 June 2013**.**
14. **Changyou Gao,** Yuan Qiu, Jichuan Zhang, Lihong Lao**.** A method to prepare galactose-modified chitosan/polyesters composite scaffolds, Patent Number: ZL 201010127810.5, Date of issue: 3 April 2013**.**
15. **Changyou Gao**, Lihong Lao, Yang Zhu, Yuan Qiu, Yuying Zhang**.** A method to prepare bioactive PLGA/collagen/HA composite fiberics for bone repair, Patent Number: ZL 201010125478.9, Date of issue: 27 Feb**.** 2013**.**
16. **Changyou Gao**, Dan Li, Weijun Tong, Wei Wang**.** A method to prepare polymers/inorganic particles composites for bone repair, Patent Number: ZL 201010125470.2, Date of issue: 28 Nov**.** 2012**.**
17. **Changyou Gao,** Lihong Lao, Yingjun Wang, Yang Zhu**.** A method to prepare PLGA Nanofibers/HA composite for bone repair, Patent Number: ZL 200910153388.8, Date of issue: 28 Nov**.** 2012**.**
18. **Changyou Gao,** Lulu Han, Jing Zhou, Xiao Gong**.** Micropatterning on polyelectrolyte multilayers, Patent Number: ZL 201010122919.X, Date of issue: 15 Oct**.** 2012**.**
19. **Changyou Gao**, Caiyu Peng, Yuying Zhang, Weijun Tong**.** A method to improve the hemocompatibility of microcapsules, Patent Number: ZL 201010127827.0, Date of issue: 25 Jan**.** 2012**.**
20. **Changyou Gao,** Yi Zhu, Weijun Tong**.** A method to prepare Con A and glycogen microcapsules, Patent Number: ZL 201010122924.0, Date of issue: 21 Dec**.** 2011**.**
21. **Changyou Gao,** Lie Ma, Haiguang Zhao, Jiacong Shen**.** Method for preparing hydroxyapatite modified collagen/chitosan composite scaffold**.** Patent Number: ZL 200710069734.5, Date of issue: 08 Dec 2010**.**
22. **Changyou Gao,** Lie Ma, Haiguang Zhao, Jiacong Shen**.** Method for preparing fibrin gel/ calcium-phosphorous nanoparticles composite scaffold**.** Patent Number: ZL 200710069109.0, Date of issue: 06 Oct 2010**.**

Related People


QINFAXIA…
Materials Sc…


ZHUHANG
Materials Sc…


WANG XI…
Materials Sc…


WANLING…
Department …


Minmin Shi
Materials Sc…

Recent mainter
2018-09

Total visits

cross-linking. Patent Number: ZL200710

26. **Changyou Gao,** Zhipeng Wang, Zhiqiang Feng. Method for preparing layer-by-layer assembled microcapsules based on host-guest interaction. Patent Number:ZL200710068262.1, Date of issue: 10 Jun 2009.
27. **Changyou Gao,** Feng Wang, Jun Feng, Weijun Tong. Method for preparing microcapsules by using doped porous calcium carbonate as templates. Patent Number: ZL200610052940.0, Date of issue: 06 May 2009.
28. **Changyou Gao,** Huaping Tan, Lihong Lao. Method for preparing the polymer materials with gradient distributed biomacromolecules on their surfaces. Patent Number:ZL200710067682.8, Date of issue: 08 Apr 2009.
29. **Changyou Gao,** Bo Chen, Hui Liu, Jiacong Shen. Preparation method of bio-adhesive chitosan microparticles for embedding and delivery active drugs. Patent Number: ZL 200610049872.2, Date of issue: 21 Jan 2009.
30. **Changyou Gao,** Yi Hong, Jiacong Shen. Method for preparing injectable polylatic acid micro-carrier/chitosan hydrogel composite scaffold. Patent Number: ZL 200510061868.3, Date of issue: 12 Nov 2008.
31. **Changyou Gao,** Yi Hong, Jiacong Shen. A method for preparing polylactic acid porous microspheres. Patent Number: ZL 200410052981.0, Date of issue: 21 May 2008.
32. **Changyou Gao,** Xuegui Zhan, Tao He, Yuegang Shao. Wear-resistant transparent organic silicon paint for surface reinforcement of optical plastic. Patent Number: ZL 200610050422.5, Date of issue: 19 Mar 2008.
33. **Changyou Gao,** Bingbing Jiang, Jiacong Shen. An injection of water-soluble drug encapsulated in degradable polymer microcapsule and its preparation method. Patent Number: ZL 200510060925.6, Date of issue: 30 Jan 2008.
34. **Changyou Gao,** Bingbing Jiang, Jiacong Shen. An injection of oil-soluble drug encapsulated in degradable polymer microcapsule and its preparation method. Patent Number: ZL 200510060926.0, Date of issue: 02 Jan 2008.
35. **Changyou Gao,** Qinghe Zhao, Shuang Zhang, Jiacong Shen. Preparation process of microcapsules loaded with anticancer drugs. Patent Number: ZL 200510061354.8, Date of issue: 14 Nov 2007.
36. **Changyou Gao,** Bingbing Jiang, Ling Hu, Jiacong Shen. Water-dispersive nano-size ibuprofen injection and its preparation method. Patent Number: ZL 200510060924.1, Date of issue: 14 Nov 2007.
37. **Changyou Gao,** Zhiqiang Feng, Zhipeng Wang, Jiacong Shen. Covalent layer-by-layer self-assembly method for constructing polymer thin films on planar substrates. Patent Number: ZL 200510061357.1, Date of issue: 15 Aug 2007.
38. **Changyou Gao,** Zhiqiang Feng, Zhipeng Wang, Jiacong Shen. A method for preparing hollow microcapsules. Patent Number: ZL 200510061356.7, Date of issue: 15 Aug 2007.
39. **Changyou Gao,** Zhiqiang Feng, Zhipeng Wang, Jiacong Shen. Method for preparing micocapsules based on covalent layer-by-layer assembly. Patent Number: ZL 200510061355.2, Date of issue: 15 Aug 2007.
40. **Changyou Gao,** Yi Hong, Jiacong Shen. Method for preparing injectable chitosan hydrogel for tissue engineering. Patent Number: ZL 200510061869.8, Date of issue: 08 Aug 2008.
41. **Changyou Gao,** Yabin Zhu, Xingyu Liu, Jiacong Shen. Method of modifying polyester material into biological material with cell compatible surface. Patent Number: ZL 02112170.2, Date of issue: 15 Aug 2007.
42. **Changyou Gao,** Lie Ma, Yanchao Shi, Jiacong Shen, Chunmao Han. Collagen-chitosan and silicon rubber bilayer skin regeneration scaffold and its preparation method. Patent Number: ZL 200510061872.X, Date of issue: 06 Jun 2007.
43. **Changyou Gao,** Yihong Gong, Lijuan He, Zuwei Ma, Jiacong Shen. Method for filling hydrogel into porous tissue engineering scaffolds. Patent Number: ZL 200410052984.4, Date of issue: 09 May 2007.
44. **Changyou Gao,** Lie Ma, Jie Zhou, Zhengwei Mao, Jiacong Shen. Method for immobilizing biological active factors on tissue engineering materials by layer-by-layer self-assembly. Patent Number: ZL 03150628.3, Date of issue: 28 Dec 2005.
45. **Changyou Gao,** Zuwei Ma, Yihong Gong, Jiacong Shen. Method of preparing porous polymer scaffolds by the combination of thermal induced phase separation and paraffin spheres porogen-leaching. Patent Number: ZL 03116446.3, Date of issue: 09 Nov 2005.
46. **Changyou Gao,** Zuwei Ma, Yihong Gong, Jiacong Shen. Method for introducing cell growth factors to the surfaces of polymer biomaterials. Patent Number: ZL 03117084.6, Date of issue: 31 Aug 2005.
47. **Changyou Gao,** Lie Ma, Zhengwei Mao, Jiacong Shen. Method of regulating degradation rate of porous collagen-based scaffold with amino acids. Patent Number: ZL 03117083.8, Date of issue: 17 Aug 2005.
48. **Changyou Gao,** Jie Feng, Jiacong Shen. Method for fixing biomacromolecule patterns on active polymer surfaces by micro-transfer technology. Patent Number: ZL 02160335.9, Date of issue: 27 Jul 2005.
49. **Changyou Gao,** Jie Feng, Bo Wang, Jiacong Shen. Method for fixing biomacromolecules on co-patterns on inorganic silicone material surface. Patent Number: ZL 02160334.0, Date of issue: 24 Aug 2005.
50. **Changyou Gao,**Zuwei Ma, Yihong Gong, Jiacong Shen. Method for preparing stable biomacromolecules coatings on surface of polymeric biomaterials. Patent Number: ZL 03116450.1, Date of issue: 15 Jun 2005.
51. **Changyou Gao,** Yabin Zhu, Xingyu Liu, Jiacong Shen. Ammonolysis process for preparing polyester biomaterials with free amino groups on their surfaces. Patent Number: ZL 02112169.9, Date of issue:2005.3.23
52. **Changyou Gao,** Yabin Zhu, Jiacong Shen. Method of using electrostatic layer-by-layer self-assembly to modify polyester material as biomaterial with cell compatible surface. Patent Number: ZL 02112499.X, Date of issue: 16 Mar 2005.
53. **Changyou Gao,** Bingbing Jiang, Jiacong Shen, Fuyu Sun, Xiaoguang Li. Water dispersive nano-size bone morphogenetic protein injection and its preparation process. Patent Number: ZL 02137395.7, Date of issue: 24 Nov 2004.
54. **Changyou Gao,** Yihong Gong, Zuwei Ma, Jiacong Shen. Polylactic acid porous scaffold for tissue engineering and its preparation method, Patent Number: ZL 02112497.3, Date of issue: 24 Nov 2004.

immobilizing process for cell compatible 2004.

6032.4, Date of issue: 01 Sep

[DR. WU: PLEASE PRINT DOCUMENT ON LETTERHEAD PAPER]

12/31/18

Department of Homeland Security
U.S. Citizenship and Immigration Services

Re: Yuguang Yang, PhD

Dear U.S. Citizenship and Immigration Services:

I am pleased to offer my recommendation of Dr. Yuguang Yang for his U.S. immigration petition for U.S. permanent residency.

I am Dr. Yang's supervisor at Wells Fargo, and as such, I am very familiar with his outstanding contributions at the company. With over 20 years of quantitative research experience, I am currently serving as Director of XVA quant team at Wells Fargo Securities department, which consists of a group of PhD quantitative associates to perform the enterprise level counterparty risk analysis practice. Prior to joining Wells Fargo in 2007, I served briefly as principal scientist at ID Analytics, a start-up that specializes in consumer identity risk and creditworthiness. Previously, I also worked as Vice President at Morgan Stanley as well as JPMorgan Chase. Like Dr. Yang, I come from a non-financial background - I got my PhD in physics from the University of Idaho in 1995 and later translated my mathematical and analytical skills acquired from the field of physics to finance and other applicable areas. As stated above, I have extensive experiences both in both the banking/financial industry and in various start-ups and tech-heavy companies.

Wells Fargo hired Dr. Yang based on his excellent PhD academic achievements and superior skill set in quantitative modeling and computation technologies. His performance has already exceeded our expectations. In the past one year and a half, he has demonstrated his capabilities and made exceptional contributions to our financial risk management platform. Dr. Yang has converted his superb capabilities in engineering-focused mathematical modeling and computer programming into exceptional quantitative modeling and analysis skills that are crucial for our line of work.

At Wells Fargo, Dr. Yang has utilized his skill sets and significantly contributed to the pricing and risk management modeling of a broad set of financial products as well as the effective implementation of enterprise risk management approach to modeling, monitoring and mitigating risks faced by the bank. For example, he has investigated and improved the stability, efficiency, and accuracy of many of our existing pricing models, such as the interest rate Hull-White model and counterparty credit valuation adjustment model, etc. Moreover, he has constructed several new pricing models such as total return swap model and auto-callable bond model. Finally, he has successfully completed several monitoring and validating projects related to enterprise risk management.

One impressive project Dr. Yang accomplished is the risk analytics for auto-callable investment products. An auto-callable product is a type of financial product offered by the bank to investors the opportunity for higher coupon rates by linking the coupon rate to the performance of a stock index. A large part of managing the risk of this product is required to estimate the probability of the stock price hitting different levels at different future times. Dr. Yang used a Monte Carlo simulation method to draw key findings that most of hitting events occur at the first two future

callable dates. Using this critical finding, Dr. Yang further developed an analytical formula to derive the stock price distributions after stocks hitting triggered level and being called. All these combined finally enables the design of an approximate portfolio consisting of simple products which share similar risk characteristics of this complicated product. Managing the risk of this simple portfolio is considerably easier than with the original complicated products.

Dr. Yang also contributed significantly to developing a risk management strategy for total return swaps. A total return swap is a common financial instrument exchange high-risk Treasury bonds' returns (coupons and capital gains) with a relatively low-risk cash flow. We used to only consider the market risk associated with the total return swap, which is insufficient as counterparty default risk is not properly addressed. Calculating counterparty default risk is considerable challenging since it requires characterizing its risk profile, stemming from interact rate fluctuations, along with its long life of 30 years. Dr. Yang innovatively conducted statistical regression analysis to identify the high correlation nature between treasure bond price and a common market index. He then subsequently applied a critical mathematical theorem to justify that the complicated dynamics of Treasury bond price dynamics can be approximated by a linear transformation of the market index dynamics. This key finding not only enables us to develop a simple linear factor process to model its interest rate risk characteristics, therefore obtaining the fair value with credit risk considered, but also provides a trading strategy to hedge and mitigate the risk. Wells Fargo is providing total return swaps to customers for them to achieve risk exposure adjustment and diversification. Therefore, understanding the various risks associated with total return swaps and designing effective strategies to properly control the risk is critical to the risk management of the bank. The strategy is in production, meaning it is a standard tool used by our portfolio managers in their assessments of funds available on the national stock market.

Additionally, Dr. Yang is the major contributor to interest rate product credit risk valuation methodology by validating and enhancing the existing theory and computation implementation. Interest rate product (bonds, loans, swaps) usually entails significant market risk and credit risk because of their long life span (> 10 Year), large notional amount (usually > 1 million USD), and the credit quality of the counterparty. Interest rate modeling is inherently more challenging than stocks, currency, and commodity due to its term structure characteristics. Thanks to his solid theory background in stochastic process modeling and extensive experience in computation library development in his PhD program, Dr. Yang can quickly fix bugs and extend additional functionality of existing computation tools. For example, after he detected a pricing bug in interest rate cap counterparty credit valuation pricing, he promptly studied various financial literature and fixed the bug in the complicated Hull-White interest rate simulation tree implementation. He also quickly extended a Monte Carlo simulation approach from multiple-currency swaps to single-currency non-USD swaps, which can be used to reveal trajectory-based pricing details unavailable in the limited Hull-White tree pricing approach. In addition, Dr. Yang implemented the *haircut* adjustment to capture the market risk of collateral value when calculating the counterparty risk valuation for a broad range of collateralized trades in Wells Fargo. This enhancement is critical since it affects around 10% counterparty risk valuation calculation for collateralized trades. All these improvements and enhancements to the library mentioned above are now in production and used by the bank on a national basis.

Finally, Dr. Yang is also actively involved in various projects that enhance Wells Fargo enterprise risk management framework. Enterprise risk management addresses risks stemming from cross-asset market risk and counterparty credit and presents more quantitative modeling challenges compared to traditional risk management. In the General Wrong Way Risk Monitoring project, a particularly impressive research project, Dr. Yang examined the

correlation between counterparties' credit quality and market movements (i.e., fluctuation of stock price, interest rate, and commodity prices such as oil, medal, natural gas prices and etc.) and improved the estimation of counterparty risk exposure faced by Wells Fargo. The financial crisis in 2008, for example, is largely due to the oversight of correlation between companies' default behavior and the overall market risks. To achieve accurate, robust detection of such correlation, Dr. Yang employed advanced, robust statistical and probability tools to screen the observed market data in different asset classes including, interest rate, commodity, foreign exchange, and equity. In addition, he also automated the process with computer programs thanks to his programming proficiency. The monitoring project is performed on the quarterly basis in the production system to enhance the risk management of Wells Fargo. Dr. Yang has also significantly contributed to the Comprehensive Capital Analysis and Review (CCAR) validation project. CCAR is required by Federal Reserve to evaluate the capital planning processes and capital adequacy of the largest US-based banks. Dr. Yang performed extensive quantitative tests to ensure the accuracy of the CCAR calculation by the production system. The validated CCAR results are used by senior management in Wells Fargo to ensure effective risk management, gauge the financial health of Wells Fargo, and meet the requirement from Federal Reserve.

In summary, Dr. Yang has made significant contributions in quantitative analysis that have been implemented at Wells Fargo. Dr. Yang's modeling and analyses have ensured Wells Fargo's methodologies and frameworks remain at the cutting-edge of the industry. Considering the immense value of his work to risk management and financial system stability, it would be in the interest of the financial services industry and national economy if Dr. Yang's work continues. I strongly vouch for his scientific abilities.

Sincerely,

Guowei Wu
Director
Wells Fargo

Guowei Wu • 1st

Fixed Income Quant

Charlotte, North Carolina Area

Message More...

Wells Fargo Securities

University of Idaho

See contact info

See connections (149)

Highlights

8 Mutual Connections
You and Guowei both know Cristian Homescu, Jian-Huang She, and 6 others

Guowei can introduce you to 2 people at Morgan Stanley
Guowei worked at Morgan Stanley

Get introduced

Show more

Experience

Fixed Income Quant
Wells Fargo Securities
Jul 2007 – Present · 11 yrs 6 mos

Principal Scientist
ID Analytics
Oct 2005 – Jul 2007 · 1 yr 10 mos

VP
Morgan Stanley
Jul 2004 – Oct 2005 · 1 yr 4 mos

VP
JPMorgan Chase
Jul 1999 – Jul 2004 · 5 yrs 1 mo

Senior Scientist
Center for Adaptive Systems Applications (CASA)
1996 – 1999 · 3 yrs

People Also Viewed

Huang Hongwei
Vice President at Wells Fargo

Robert Wilson • 3rd
"That Guy" behind the Kaua'i ba action apparel brand Edikt.

John Campbell • 3rd
Senior Product Technologist at B America

Sridhar Narhari • 3rd
Market Risk Tech - Wells Fargo

Khiem Ngo • 2nd
Wells Fargo Securities

Jessica Yang • 2nd
Software Engineer III at Walmart

Jennifer O'Gara • 3rd
C-Suite Search Executive at Que Groups LLC

Dr Nousheen Thakur • 3rd
life enrichment Director , Admiss and Marketing Director, Alternat Assisted living Manager at Golde

JEREMY KANE • 3rd
WOODWORKER/ ARTIST/ ENGIN DRAFTER/ TEXTILE DESIGNER/ WEAVER/ SKATE-SNOW ADVOC CANNABIS ACTIVIST

Emily Shung • 3rd
Software Engineer at Abalta Technologies

University of Idaho
Ph.D., Physics
1991 – 1995

Skills & Endorsements

Analytics · 7

Endorsed by **2 of Guowei's colleagues at Wells Fargo**

Risk Management · 5

Endorsed by **Margaret Trench, who is highly skilled at this**

Endorsed by **2 of Guowei's colleagues at ID Analytics, a Symantec company**

Credit Risk · 4

Endorsed by **Cristian Homescu (mutual connection)**

Show more

Accomplishments

1 **Honor & Award**
Patents:

Interests

Wells Fargo
719,026 followers

University of Idaho
60,439 followers

ID Analytics, a Symantec company
3,175 followers

SIBANI LISA BISWAL, PH.D.

PROFESSIONAL PREPARATION

Institution	Major	Degree	Year
California Institute of Technology	Chemical Engineering	BS 1999	1999
Stanford University *Advisor: Prof. Alice Gast*	Chemical Engineering	PhD	2004
UC Berkeley *Advisor: Prof. Arun Majumdar*	Mechanical Engineering	Postdoc	2004-2006

APPOINTMENTS

2013 - present Associate Professor, Chemical and Biomolecular Engineering, Rice University, Houston, TX
2014 – present Associate Professor, Materials Science and Nanoengineering, Rice University, Houston, TX
2006-2013 Assistant Professor, Chemical and Biomolecular Engineering, Rice University, Houston, TX

PRODUCTS (80+ peer-reviewed publications)

Five Recent Products Related to Soft Matter Engineering

1. Vecchiolla, D., Giri, V., Biswal, S.L. Bubble–bubble pinch-off in symmetric and asymmetric microfluidic expansion channels for ordered foam generation. *Soft Matter*, 2018, Advance Article: DOI: 10.1039/C8SM01285G. *Featured on Front Cover Jan 2019*
2. Zhao, J., Du., D., and Biswal, S.L. Nonlinear Multimode Buckling Dynamics Examined with Semiflexible Magnetic Filaments. *Physical Review E* 98, 012602-1-11, 2018.
3. Du, D., Hilou, E., and Biswal, S. L. Reconfigurable paramagnetic microswimmers: Brownian motion affects non-reciprocal actuation. *Soft Matter*, 14, 3463-3470, 2018.
4. Hilou, E., Du, D., Kuei, S., and Biswal, S. L. Interfacial energetics of two-dimensional colloidal clusters generated with a tunable anharmonic interaction potential. *Physical Review Materials*, 2(2), 025602, 2018.
5. Kuei, S., Garza, B., Biswal, S.L. From Strings to Coils: Rotational Dynamics of DNA-Linked Colloidal Chains. *Physical Review Fluids*, 2(10), 104102, 2017.

Five Other Significant Products

1. Du, D., Doxastakis, M., Hilou, E., and Biswal, S.L. Two-Dimensional Melting of Paramagnetic Colloids with Long-Range Attractive Interactions. *Soft Matter*, 13 (8), 1548-1553, 2017. *featured on back cover of journal
2. Wang, Q., Puerto, M.C., Warudkar, S., Buehler, J. Biswal, S.L., Recyclable amine-functionalized magnetic nanoparticles for efficient demulsification of crude oil-in-water emulsions. *Environmental Science: Water Research & Technology* 4, 1553-1563, 2018.
3. Xiao, S., Zeng, Y., Vavra, E.D., He, P., Puerto, M., Hirasaki, G.J. and Biswal, S.L. Destabilization, Propagation, and Generation of Surfactant-Stabilized Foam during Crude Oil Displacement in Heterogeneous Model Porous Media. *Langmuir*, 34(3), 739–749, 2017. *Featured on the front cover
4. Lin, Y., He, P., Tavakkoli, M., Mathew, N.T., Fatt, Y.Y., Chai, J.C., Goharzadeh, A., Vargas, F., Biswal, S.L. Characterizing Asphaltene Deposition in the Presence of Chemical Dispersants in Porous Media Micromodels. *Energy & Fuels*, 31(11), 11660-11668, 2017.
5. Conn, C.A., Ma, K., Hirasaki, G.J. and Biswal, S.L. Visualizing oil displacement with foam in a microfluidic device with permeability contrast. Lab on a Chip, 14(20), 3968-3977, 2014. *Lab on a Chip 2014 HOT Article

SYNERGISTIC ACTIVITES

Proposal Reviewer: National Science Foundation (CBET, DMR, MRSEC); Army Research Office, Defense Threat Reduction Agency, ARPA-E, NASA, American Chemical Society Petroleum Research Fund, European Research Council, Austrian Science Fund

Journal Reviewer: **AAAS** (Science, Science Advances), **ACS** (Analytical Chemistry, Langmuir, Nanoletters, ACS Nano, Applied Materials & Interfaces, Energy & Fuels, J Phys Chem, Chem of Materials), **Elsevier** (J Colloid and Interface Science, Colloid and Surfaces A, Advances in Colloid and Interface Science, Fuel, J. Magnetism & Magnetic Materials, Reactive & Functional Polymers, Electrochimica Acta, J. Power Sources, J. Petrol Science & Engineering), **Nature Publishing Group** (Nature, Nature Communications, Nature Chemistry, Nature Materials, Scientific Reports), **RSC** (Soft Matter, Lab on a Chip, RSC Advances, Energy & Environmental Science, PCCP, Nanoscale), **Springer** (Transport in Porous Media), **Wiley** (Advanced Materials, Small), Biointerphases, Society of Petroleum Engineers, Europhysics Letters

Editorial Board: Journal of Colloid and Interface Science Scientific Advisory Board

Conference Organization:

1. 2020 Organizer for 94th ACS Colloid and Surface Science Symposium at Rice U.
2. 2020 Vice Chair of Gordon Research Conference on Colloidal, Macromolecular and Polyelectrolyte Solutions
3. 2019 Technical Chair for Society of Rheology Annual Meeting, Raleigh, NC
4. 2018 Local Organizing Committee for Society of Rheology Annual Meeting, Houston, TX
5. 2017 Programming Chair for Area 1J Fluid Mechanics of American Institute of Chemical Engineers Fall National Meeting, Minnesota, MN.
6. Session Chair: ACS CSSS (2017 for Directed Colloidal Assembly), AICHE (1C, 2008-2010 for Colloidal Assembly, 1J, 2011-2012 for Complex Fluids), MRS (S2017 Energy Storage), ACS National Meeting (S2012 Colloidal Assembly)

- University Service: Chair – Rice University Shared Equipment Authority (SEA): 2016-present. The SEA at Rice governs the administrations of shared instruments for the university. I chair a 12-member faculty board that oversees a group of 13 staff scientists and over 100 shared instruments. I helped lead a proposal for Rice to build a new $20 million cleanroom that will be completed in Dec 2018. Mentor – Rice University Triad Junior Faculty Mentoring Program: 2014-present. This program pairs tenured faculty with two untenured faculty from other departments to provide mentorship for junior faculty.
  Molecular Nanotechnology Faculty Search: 2016-present.

- Graduate Research: Mentored 7 Postdocs previously, and 2 currently. Primary advisor for 12 completed PhDs and current 16 PhD students in progress. Mentored 70 undergrad students.

Awards

2018 *Best Applied Paper* – South Texas Section American Institute of Chemical Engineers (STS-AICHE)
2017 Rice University Chemical Engineering Alumni Professional Progress Award
2015 Rice University George R. Brown Award for Superior Teaching; *based on votes from recent alumni*
2015 2015 Energy R&D Summit; Abu Dhabi International Research and Development Conference (ARDAC) Innovation Award
2014 *Best Fundamental Paper* – South Texas Section American Institute of Chemical Engineers (STS-AICHE)
2013 *Best Applied Paper* – South Texas Section American Institute of Chemical Engineers (STS-AICHE)
2012 Rice University Graduate Student Association (GSA) *Faculty Teaching and Mentoring Award*
2010 Donald J. Nash Award AAA-SWARM Annual Meeting
2010 Institute of Bioscience and Bioengineering Medical Innovation Award
2009 *Hamill Research Innovation Award*
2009 National Science Foundation *CAREER Award*
2007 Office of Naval Research (*ONR-YIP*) Young Investigator Award
2006 Lab Automation Innovator Award, Palm Springs, CA.

Sibani Lisa Biswal, Ph.D.
Associate Professor
Chemical and Biomolecular Engineering and
Material Science & Nanoengineering

December 21, 2018

Department of Homeland Security
United States Citizenship and Immigration Services
Re: Independent Recommendation Letter for Dr. Yuguang Yang

Dear Adjudicating Officer:

I am writing this recommendation letter in support of Dr. Yuguang Yang's petition for U.S. permanent residency. In my independent expert opinion, Dr. Yang has distinguished himself by his notable expertise and valuable findings regarding colloidal crystal formation. His past contributions give me reasons to believe that his career will continue to flourish.

I am currently an Associate Professor at the Department of Chemical and Biomolecular Engineering with a joint appointment in the Department of Material Science and Nanoengineering at Rice University in Houston, TX. I graduated with BS degree in Chemical Engineering from Caltech in 1999 and a Ph.D. in Chemical Engineering from Stanford University in 2004, followed by Postdoctoral position at the University of California, Berkeley. My research is centered on the use of chemical, biological, and engineering approaches to characterize and understand soft materials like colloids, polymers, lipids, and surfactants, and this research earned me a National Science Foundation CAREER Award in 2009 and an Office of Navel Research Young Investigator Award in 2007. I am the author of numerous book chapters and articles published in peer-reviewed journals and conference proceedings. Additionally, my research has resulted in a number of patents pertaining to colloidal materials and biosensing applications.

One of my research focuses is soft matter engineering, a field closely related to Dr. Yang's. I know first-hand how valuable Dr. Yang's work is because I have cited his publication: "Colloidal Crystal Grain Boundary Formation and Motion," Scientific Reports—in my own research paper. In this paper, Dr. Yang studied a classical 2D colloidal crystallization experimental system and developed mathematical modeling of the colloidal cluster crystallization process.

Let me provide some background to Dr. Yang's research. Colloidal cluster crystallization is a process in which multiple colloidal particles (usually over hundreds) organize into an ordered lattice structure due to the interactions among colloidal particles. In order to make progress in the development of advanced materials, it is necessary to refine our ability to assemble colloidal components into highly ordered configurations. Unfortunately, there is very little quantitative research regarding the dynamics of stochastic grain boundary (one major type of defect) formation and motion, and this lack of knowledge prevents us from developing efficient and robust approaches to the fabrication of large-scale defect-free colloidal materials for emerging applications.

To bridge the gap between experiment and theory, Dr. Yang first constructed a particle scale simulation model that simulates the real experimental system accurately. This is already remarkable considering the complicated interactions among particles in the experiment system. Based on a sufficiently large data sample generated by the particle simulation model, he then successfully applied a cutting-edge nonlinear machine learning algorithm to reduce the dimensionality of the original system from over 400 to the two

E-mail biswal@rice.edu Office 713-348-6055 Fax 713-348-5478 Rice University CHBE-MS 362
6100 Main St. Houston, TX 77005 www.ruf.rice.edu/~biswalab

most significant dimensions. These two-dimensional coordinates capture the most important collective motions, condensation and global ordering, of all particles. Using a sophisticated state-dependent Smoluchowski model, Dr. Yang constructed a two-dimensional free energy landscape that fully explains the key aspects of the colloidal crystallization process.

Since the mathematical kinetic model Dr. Yang constructed quantifies the crystallization process in terms of structure characterization and expected time needed for structure transitions, it offers critical insight into how individual components interact with each other, rearrange themselves, and form the final structures. This is the first quantitative evidence, from the principles of thermodynamics, showing that the discoordination between condensation and global ordering processes can cause severe grain boundary defects to form. Dr. Yang's study also quantitatively showed that, on the other hand, good coordination of condensation and global ordering processes can result in the fast formation of perfect colloidal crystals. In our paper, we cited his findings to explain why topological defects can dramatically slow down the colloidal cluster crystallization process, thus motivating our novel method to repair topological defects in colloidal crystals.

I am also familiar with another one of Dr. Yang's publications: "Optimal Feedback Controlled Assembly of Perfect Crystals," in the journal ACS Nano. In this paper, Dr. Yang reported a model-based optimal control strategy to produce perfect colloidal crystals. He constructed an external compression level parameterized dynamical model that universally quantifies the distinct crystallization dynamics at different compression levels via calculated precise probability of forming various intermediate states that lead to perfect crystals vs. defected structures. He further leveraged this critical quantitative information via a feedback control system consisting of a sensor, a controller, and an actuator, with the controller implementing an optimal strategic control of the external compression to achieve fast formation of perfect colloidal crystals. Dr. Yang innovatively used the Markov decision framework built upon the parameterized model to produce the best choice of compression level at each stage of the crystallization process. Dr. Yang thus designed a control strategy that optimally steers the system to a perfect colloidal crystal state by avoiding various system states conducive to the formation of defects and ramping up the driving force at rate-limiting stages. His optimal feedback method achieves nearly 100% success rate in producing perfect crystals vs. 60% success rate using uncontrolled assembly method. These results are significant because they are based on an integration of experimental observation, mathematical model, and optimization theory that has not been executed before in determining the best way to fabricate colloidal crystals. Such integration is the first major step towards fabricating large-scale defect-free colloidal materials via an efficient, robust, and rationally designed approach. Moreover, Dr. Yang's feedback control approach overcomes the inherent weaknesses, such as inefficiency and non-robustness, in various traditional material fabrication methods, thus providing inspiration to the development of novel soft matter engineering methods.

There is no question that the field will continue to benefit from Dr. Yang's sustained efforts and ability to outperform other experienced and skilled researchers similarly employed. Dr. Yang has thrived in soft matter engineering because he has the necessary knowledge and experience, but more importantly, he has the ability to apply his skills and knowledge in original and imaginative ways to solve problems. Thus, I happily validate Dr. Yang's academic/scientific credentials.

Sincerely,

E-mail biswal@rice.edu Office 713-348-6055 Fax 713-348-5478 Rice University CHBE-MS 362
6100 Main St. Houston, TX 77005 www.ruf.rice.edu/~biswalab

Wei Gao

Contact Information

139 Keck Laboratory, MC 138-78
California Institute of Technology
Pasadena, CA, 91125

Tel: (626) 395-2958
Email: weigao@caltech.edu
Webpage: www.gao.caltech.edu

Professional Experience

08/2017 –	Assistant Professor of Medical Engineering Division of Engineering and Applied Science California Institute of Technology	Pasadena, CA, USA

Education

07/2014 – 06/2017	Postdoctoral Fellow in Electrical Engineering & Computer Sciences University of California, Berkeley Advisor: Professor Ali Javey	Berkeley, CA, USA
09/2009 – 06/2014	Ph.D. in Chemical Engineering University of California, San Diego Advisor: Professor Joseph Wang	La Jolla, CA, USA
09/2007 – 07/2009	M.S. in Precision Instrument Tsinghua University	Beijing, China
09/2003 – 07/2007	B.S. in Mechanical Engineering Huazhong University of Science & Technology	Wuhan, Hubei, China

Research Interests

Wearable Devices, Biosensors, Flexible Electronics, Micro/Nanorobotics, Micro/Nanomachines, Nanomotors, Nanomaterials, Nanomedicine, BioMEMS, Electrochemistry.

Awards & Honors

06/2018	McKenna Family Innovation Award
06/2018	Interstellar Initiative by the New York Academy of Sciences (Outstanding Team Presentation Award)
02/2018	Sensors Young Investigator Award
03/2017	ACS Nano Junior Fellow
08/2016	MIT Technology Review Top 35 Innovators Under 35 (TR35, Global List)
08/2015	ACS Young Investigator Award (Division of Inorganic Chemistry)
04/2014	MRS Graduate Student Award
11/2013	AICHE Bionanotechnology Graduate Student Award (1st place).
04/2013	MRS Graduate Student Award
02/2013	Chinese Government Award for Outstanding Students Abroad
07/2012	HHMI International Student Research Fellowship (2012-2014)
09/2009	Jacobs Fellowship, University of California, San Diego (2009-2010)
10/2008	Comprehensive Outstanding Scholarship, Tsinghua University
06/2007	Outstanding Graduate Award, Huazhong University of Science & Technology
09/2005	Academic Excellence Award, Huazhong University of Science & Technology

Publications **(80 papers, >7500 citations, h-index 47, Google Scholar - 12/2018).**

1. Y. Yang, W. Gao*, "Wearable pH sensing beyond the Nernst limit", *Nature Electronics*, 2018, 1, 580-581.

2. Yiran Yang, W. Gao*, "Wearable and Flexible Electronics for Continuous Molecular Monitoring", *Chemical Society Review*, 2018, 10.1039/c7cs00730b.
   Featured on Journal Front Cover.
3. Y. Zhong, X. Tang, J. Li, Q. Lan, L. Min, C. Ren, X. Hu, R. M. Torrente-Rodríguez, W. Gao*, Z. Yang, Nanozyme Tags Enabled Chemiluminescence Imaging Immunoassay for Multiplexed Cytokine Monitoring. *Chemical Communications*, 2018, 10.1039/C8CC07779G.
4. L.-C. Tai,§ W. Gao,§ M. Chao, M. Bariya, Q. P. Ngo, Z. Shahpar, H. Y. Y. Nyein, H. Park, J. Sun, Y. Jung, E. Wu, H. M. Fahad, D.-H. Lien, H. Ota, G. Cho, and A. Javey, "Methylxanthine drug monitoring with wearable sweat sensors", *Advanced Materials*, 2018, 1707442. *[§] Equal contribution*.
5. W. Gao, G. A. Brooks, D. C. Klonoff, "Wearable Physiological Systems and Technologies for Metabolic Monitoring", *Journal of Applied Physiology*, 2018, 124, 548-556.
6. H. Wu, W. Gao*, Z. Yin, "Materials, Devices and Systems of Soft Bioelectronics for Precision Therapy", *Advanced Healthcare Materials*, 2017, 6, 1700017.
   Highlighted in Advanced Science News, featured on Journal Cover.
7. S. Emaminejad,§ W. Gao,§ E. Wu, Z. Davies, H. Y. Y. Nyein, S. Challa, S. Ryan, H. M. Fahad, K. Chen, Z. Shahpar, S. Talebi, C. Milla, A. Javey, R. W. Davis, "Autonomous Sweat Extraction and Analysis Using a Fully-Integrated Wearable Platform", *Proceedings of the National Academy of Sciences*, 2017, 114, 4624.
   Highlighted in NBC News, Reuters and Daily Mail.
8. T. Xu,§ W. Gao,§ L.-P. Xu, S. Wang, X. Zhang, "Fuel-Free Synthetic Micro/Nanomachines", *Advanced Materials* 2017, 29, 1603250.
   Highlighted in Advanced Science News, featured on Journal Frontispiece.
9. W. Gao,§ S. Emaminejad,§ H. Y. Y. Nyein, S. Challa, K. Chen, A. Peck, H. Fahad, H. Ota, S. Hiroshi, D. Kiriya, D. H. Lien, G. A. Brooks, R. W. Davis, A. Javey, "Fully-Integrated Wearable Sensor Arrays for Multiplexed In-Situ Perspiration Analysis", *Nature*, 2016, 529, 509-514.
   Selected by Nature Publisher Group as 'Hot Topics' (one paper per week from all NPG journals).
   Highlighted in Nature, Science, The Wall Street Journal, New York Times, Time, Daily Mail, Yahoo!, The Times, LA Times, Newsweek, Forbes, Scientific American, IEEE Spectrum, MIT Technology Review, Chemical & Engineering News, VOA News, Fox News, Wired, Popular Science, Chemistry World, Science News, New Scientist, ScienceDaily, UC Berkeley News etc.
10. W. Gao, H. Y. Y. Nyein, Z. Shahpar, L.-C. Tai, E. Wu, M. Bariya, H. Ota, H. M. Fahad, K. Chen and A. Javey, "Wearable Sweat Biosensors", *IEEE IEDM*, 2016, pp. 6.6.1-6.6.4. (Invited article)
11. W. Gao,§ H. Y. Y. Nyein,§ Z. Shahpar, H. M. Fahad, K. Chen, S. Emaminejad, Y. Gao, L.-C. Tai, H. Ota, E. Wu, J. Bullock, Y. Zeng, D.-H. Lien, A. Javey, "Wearable Microsensor Array for Multiplexed Heavy Metal Monitoring of Body Fluids", *ACS Sensors*, 2016, 1, 866.
    Selected as ACS Editors' Choice (one paper per day from all ACS publications).
    Featured on Journal Cover.
12. H. Y. Y. Nyein,§ W. Gao,§ Z. Shahpar, S. Emaminejad, K. Chen, H. M. Fahad, L.-C. Tai, H. Ota, Y. Gao, A. Javey, "A Wearable Electrochemical Platform for Non-Invasive Monitoring of Ca^{2+} and pH", *ACS Nano*, 2016, *10*, 7216.
13. W. Gao,§ R. Dong,§ S. Thamphiwatana,§ J. Li, W. Gao, L. Zhang and J. Wang, "Artificial Micromotors in the Mouse's Stomach: A Step Towards In Vivo Use of Synthetic Motors", *ACS Nano*, 2015, 9, 117.
    Selected as ACS Editors' Choice (one paper per day from all ACS publications). Highlighted in Nature, Fox News, BBC News, Daily Mail, Scientific American, Yahoo, Popular Science, New Scientist, Chemical & Engineering News, Science Daily etc.
14. Z. Wu§, T. Li§, W. Gao§, T. Xu, B. Jurado-Sánchez, J. Li, W. Gao, Q. He, L. Zhang*, and J. Wang*, "RBC Membrane-Coated Biomimetic Motors for Effective Biodetoxification", *Advanced Functional Materials,* 2015*, 25*, 3881. *[§] These authors contribute equally*.
15. W. Gao, X. Feng, A. Pei, C. R Kane, R. Tam, C. Hennessy, J. Wang, "Bio-Inspired Helical Microswimmer based on Vascular Plant", *Nano Letters,* 2014, 14, 305.

Highlighted in PhysOrg, ScienceDaily, Nanowerk, Gizmodo, Gizmag, la Repubblica (Italy) etc.

16. J. Li,[§] W. Gao,[§] R. Dong, A. Pei, S. Sattayasamitsathit, J. Wang, "Nanomotor Lithography", *Nature Communications*, 2014, 5, 5026. *[§] These authors contribute equally*.
    Highlighted in Nanowerk, ScienceDaily etc.
17. W. Gao, A. Pei, R. Dong, J. Wang, "Catalytic Iridium-Based Janus Micromotors Powered by Ultralow Levels of Chemical Fuels", *Journal of the American Chemical Society*, 2014, 136, 2276.
18. W. Gao, J. Wang, "Synthetic Micro/Nanomotors in Drug Delivery", *Nanoscale*, 2014, 6, 10486.
19. W. Gao, J. Wang, "The Environmental Impact of Micro/Nanomachines: A Review", *ACS Nano*, 2014, 8, 3170.
    Highlighted in Nanowerk.
20. W. Gao, S. Sattayasamitsathit, J. Orozco, J. Wang, "Efficient Bubble Propulsion of Polymer-Based Microengines in Real-Life Environments", *Nanoscale*, 2013, 5, 8909. *'HOT' article.*
21. W. Gao[§], X. Feng[§], A. Pei[§], Y. Gu, J. Li, J. Wang, "Seawater-Driven Magnesium based Janus Micromotors for Environmental Remediation", *Nanoscale*, 2013, 5, 4696.
    'HOT' article. Highlighted in Chemistry World.
22. W. Gao, A. Pei, X. Feng, C. Hennessy, J. Wang, "Organized Self-Assembly of Janus Micromotors with Hydrophobic Hemispheres", *Journal of the American Chemical Society*, 2013, 135, 998.
23. W. Gao[§], M. D'Agostin[§], V. Garcia Gradilla[§], J. Orozco, J. Wang, "Multi-Fuel Driven Janus Micromotors"*, Small,* 2013, 9, 467.
    "*VIP" (Very Important Paper) by Wiley*. *Highlighted in Materials Views*.
24. W. Gao, A. Pei, J. Wang, "Water-Driven Micromotors", *ACS Nano*, 2012, 6, 8432.
    Highlighted in Nanowerk, IEEE Spectrum, and Chemical & Engineering News etc.
25. W. Gao, S. Sattayasamitsathit, A. Uygun, A. Pei, A. Ponedal, J. Wang, "Polymer-based Tubular Microbots: Role of Composition and Preparation", *Nanoscale*, 2012, 4, 2447.
26. W. Gao, A. Uygun, J. Wang, "Hydrogen-Bubble Propelled Zinc-based Microrockets in Strongly Acidic Media", *Journal of the American Chemical Society*, 2011, 134, 897.
    Highlighted in The Economist, *Chemical & Engineering News*, *Popular Science*, *Discovery News*, *ScienceDaily*, *American Scientist, New Scientist*, *The Scientist etc*.
27. W. Gao, S. Sattayasamitsathit, J. Wang, "Catalytically-Propelled Micro/Nanomotors: How Fast Can They Move?", *The Chemical Record*, 2012, 12, 224.
28. W. Gao[§], D. Kagan[§], O. S. Pak, C. Clawson, S. Campuzano, E. Chuluun-Erdene, E. Shipton, E. E. Fullerton, L. Zhang, E. Lauga, J. Wang, "Cargo-Towing Fuel-Free Magnetic Nanoswimmers for Targeted Drug Delivery", *Small*, 2012, 8, 460.
    "VIP" (Very Important Paper) by Wiley. Highlighted in Chemistry Views.
29. W. Gao, S. Sattayasamitsathit, J. Orozco, J. Wang, "Highly Efficient Catalytic Microengines: Template Electro-synthesis of Polyaniline-Platinum Microtubes", *Journal of the American Chemical Society*, 2011, 133, 11862.
    Highlighted in Materials Views.
30. W. Gao, K. M. Manesh, J. Hua, S. Sattayasamitsathit, J. Wang, "Hybrid Nanomotor: A Catalytically/ Magnetically Powered Adaptive Nanowire Swimmer", *Small*, 2011, 7, 2047.
    "VIP" (Very Important Paper) by Wiley. Highlighted in Materials Views.
31. O. S. Pak[§], W. Gao[§], J. Wang, E. Lauga. "High-Speed Propulsion of Flexible Nanowire Motors: Theory and Experiments", *Soft Matter*, 2011, 7, 8169.
    Highlighted in Chemistry World.
32. W. Gao, S. Sattayasamitsathit, K. M. Manesh, D. Weihs, J. Wang, "Magnetically-Powered Flexible Metal Nanowire Motors", *Journal of the American Chemical Society*, 2010, 132, 14403.
    Highlighted in Science, 2010, 330, 296-297.
33. X. He, T. Xu, W. Gao, L.-P. Xu, T. Pan, X. Zhang, "Flexible Superwettable Tapes for On-Site Detection of Heavy Metals", *Analytical Chemistry*, 2018, 10.1021/acs.analchem.8b04536.

34. R. Dong, Y. Cai, Y. Yang, W. Gao, B. Ren, “Photocatalytic Micro-/Nanomotors: From Construction to Applications”, *Accounts of Chemical Research*, 2018, 51, 1940-1947.
35. M. Bariya, Z. Shahpar, H. Park, J. Sun, Y. Jung, W. Gao, H. Y. Y. Nyein, T. S. Liaw, L.-C. Tai, Q. P. Ngo, M. Chao, Y. Zhao, M. Hettick, G. Cho, and A. Javey, Roll-to-Roll Gravure Printed Electrochemical Sensors for Wearable and Medical Devices. *ACS Nano*, 2018, 12, 6978-6987.
36. H. Y. Y. Nyein, L.-C. Tai, Q. P. Ngo, M. Chao, G. Zhang, W. Gao, M. Bariya, J. Bullock, H. Kim, H. M. Fahad, A. Javey, “A Wearable Microfluidic Sensing Patch for Dynamic Sweat Secretion Analysis”, *ACS Sensors*, 2018, 3, 944.
37. T. Xu, Y. Song, W. Gao, T. Wu, L.-P. Xu, X. Zhang, and S. Wang, "Superwettable Electrochemical Biosensor toward Detection of Cancer Biomarkers", *ACS Sensors*, 2018, 3, 72-78.
38. H. Wang, Y. Liang, W. Gao, R. Dong, and C. Wang, “An Emulsion-Hydrogel Soft Motor Actuated by Thermal Stimulation”, *ACS Applied Materials & Interfaces*, 2017, 9, 43211.
39. B. E.-F. de Ávila, P. Angsantikul, J. Li, W. Gao, L. Zhang, and J. Wang, "Micromotors Go In Vivo: from Test Tubes to Live Animals", *Advanced Functional Materials*, 2018, 28, 1705640.
40. Y. Gao, H. Ota, E. W. Schaler, K. Chen, A. Zhao, W. Gao, H. M. Fahad, Y. Leng, A. Zheng, F. Xiong, C. Zhang, L. Tai, P. Zhao, R. S. Fearing, A. Javey, "Wearable Microfluidic Diaphragm Pressure Sensor for Health and Tactile Touch Monitoring", *Advanced Materials*, 2017, 29, 1701985.
    Featured on Journal Cover.
41. H. Ota, M. Chao, Y. Gao, E. Wu, L.-C. Tai, K. Chen, Y. Matsuoka, K. Iwai, H. M. Fahad, W. Gao, H. Y. Y. Nyein, L. Lin, A. Javey. "3D Printed Earable Smart Devices for Real-time Detection of Core Body Temperature", *ACS Sensors*, 2017, 2, 990.
    Selected as ACS Editors' Choice (one paper per day from all ACS publications).
    Highlighted in IEEE Spectrum.
42. H. M. Fahad, H. Shiraki, M. Amani, C. Zhang, V. S. Hebbar, W. Gao, H. Ota, M. Hettick, D. Kiriya, Y.-Z. Chen, Y.-L. Chueh and A. Javey, "Room temperature multiplexed gas sensing using chemical-sensitive 3.5-nm-thin silicon transistors", *Science Advances*, 2017, 3, e1602557.
    Highlighted in Nature Nanotechnology, IEEE Spectrum.
43. J. Li, B. Esteban-Fernandez de Avila, W. Gao, L. Zhang, J. Wang, "Micro/nanorobots for biomedicine: delivery, surgery, sensing and detoxification", *Science Robotics*, 2017, 2, eaam6431.
    Highlighted in IEEE Spectrum.
44. Q. Zhang, R. Dong, Y. Wu, W. Gao, Z. He, and B. Ren, “Light-Driven Au-WO3@C Janus Micromotors for Rapid Photodegradation of Dye Pollutants”, *ACS Applied Materials & Interfaces*, 2017, 9, 4674.
45. R. Dong, Y. Hu, Y. Wu, W. Gao, B. Ren, Q. Wang, Y. Cai, "Visible Light-Driven BiOI-Based Janus Micromotor in Pure Water", *Journal of the American Chemical Society*, 2017, 139, 1722-1725.
46. D. Kiriya, P. Lobaccaro, H. Y. Y. Nyein, P. Taheri, M. Hettick, H. Shiraki, C. M. Sutter-Fella, P. Zhao, W. Gao, R. Maboudian, Joel W. Ager, A. Javey, “General Thermal Texturization Process of MoS_2 for Efficient Electrocatalytic Hydrogen Evolution Reaction”, *Nano Letters*, 2016, 16, 4047.
47. K. Chen, W. Gao, S. Emaminejad, D. Kiriya, H. Ota, H. Y. Nyein, A. Javey, “Printed Carbon Nanotube-Based Flexible Electronics and Systems”, *Advanced Materials*, 2016, 28, 4397.
    Featured on Journal Frontispiece.
48. H. Ota, S. Emaminejad, Y. Gao, A. Zhao, E. Wu, S. Challa, K. Chen, H. M. Fahad, A. K. Jha, D. Kiriya, W. Gao, H. Shiraki, K. Morioka, A. R. Ferguson, K. E. Healy, R. W. Davis, A. Javey, “Application of 3D Printing for Smart Objects with Embedded Electronic Sensors and Systems”, *Advanced Materials Technologies*, 2016, 1, 1600013.
    Featured on Journal Cover.
49. R. Dong, Q. Zhang, W. Gao, A. Pei, B. Ren, “Highly Efficient Light-driven TiO2-Au Janus Micromotors”, *ACS Nano*, 2016, 10, 839.
50. Z. Wu, T. Si, W. Gao, Y. Wu, J. Wang, Q. He, “Superfast Near-Infrared Light-Driven Polymer Multilayer Rockets”, *Small*, 2016, 12, 577.
    Featured on Journal Cover.

51. R. Dong, J. Li, I. Rozen, B. Ezhilan, T. Xu, C. Christianson, W. Gao, D. Saintillan, B. Ren, J. Wang, "Vapor-Driven Propulsion of Catalytic Micromotors", *Scientific Reports,* 2015, 5, 13226.
52. W. Zhu, J. Li, Y. J. Leong, I. Rozen, X. Qu, R. Dong, Z. Wu, W. Gao, P. H. Chung, J. Wang, and Shaochen Chen*, "3D-Printed Artificial Micro-Fish", *Advanced Materials*, 2015, 27, 4411.
Featured on Journal Cover. Highlighted in The Washington Post, Forbes, Fortune, Discovery News, Wired, BBC Focus, Popular Science, Science Daily etc.
53. S. Cinti, G. Valdés-Ramírez, W. Gao, J. Li, G. Palleschi, J. Wang, "Microengine-Assisted Electrochemical Measurements at Printable Sensor Strips", *Chemical Communications*, 2015, 51, 8668.
54. T. Xu, F. Soto, W. Gao, R. Dong, V. Garcia-Gradilla, E. Magana, X. Zhang, J. Wang, "Reversible Swarming and Separation of Self-propelled Chemically-Powered Nanomotors under Acoustic Fields", *Journal of the American Chemical Society*, 2015, 37, 2163.
55. B. Ezhilan, W. Gao, A. Pei, I. Rozen, R. Dong, B. Jurado-Sanchez, J. Wang, D. Saintillan, "Motion-based Threat Detection using Microparticles: Experiments and Numerical Simulations", *Nanoscale*, 2015, 7, 7833.
56. B. Jurado-Sánchez, S. Sattayasamitsathit, W. Gao, L. Santos, Y. Fedorak, V. V. Singh, J. Orozco, M. Galarnyk, J. Wang, "Self-Propelled Activated-Carbon Janus Micromotors for Efficient Water Purification", *Small,* 2015, 11, 499.
57. Z. Wu, T. Li, J. Li, W. Gao, T. Xu, C. Christianson, W. Gao, M. Galarnyk, Q. He, L. Zhang, J. Wang, "Turning Erythrocytes to Functional Micromotors", *ACS Nano*, 2014, 8, 12041.
58. J. Li, V. V. Singh, S. Sattayasamitsathit, J. Orozco, K. Kaufmann, R. Dong, W. Gao, B. Jurado-Sanchez, Y. Fedorak, J. Wang, "Water-Driven Micromotors for Rapid Photocatalytic Degradation of Biological and Chemical Warfare Agents", *ACS Nano*, 2014, 8, 11118.
Highlighted in BBC News, ScienceDaily, Nanowerk etc.
59. T. Xu, F. Soto, W. Gao, V. Garcia-Gradilla, J. Li, X. Zhang, J. Wang, "Ultrasound-Modulated Bubble Propulsion of Chemically-Powered Microengines", *Journal of the American Chemical Society*, 2014, 136, 8552.
60. J. Orozco, B. Jurado-Sánchez, G. Wagner, W. Gao, R. Vazquez-Duhalt, S. Sattayasamitsathit, M. Galarnyk, A. Cortés, D. Saintillan, J. Wang, "Bubble-Propelled Micromotors for Enhanced Transport of Passive Tracers", *Langmuir*, 2014, 30, 5082.
61. S. Sattayasamitsathit, H. Kou, W. Gao, W. Thavarajah, K. Kaufmann, L. Zhang, J Wang, "Fully-Loaded Micromotors for Combinatorial Delivery and Autonomous Release of Cargoes", *Small,* 2014, 10, 2830.
62. J. Li, S. Sattayasamitsathit, R. Dong, W. Gao, R. Tam, X. Feng, S. Ai, J. Wang, "Template Electrosynthesis of Tailored-Made Helical Nanoswimmers", *Nanoscale*, 2014, 6, 9415-9420. *'HOT' article.*
63. E. S. Olson, J. Orozco, Z. Wu, C. D. Malone, B. Ha Yi, W. Gao, M. Eghtedari, J. Wang, R. F. Mattrey, "Toward *In Vivo* Detection of Hydrogen Peroxide with Ultrasound Molecular Imaging", *Biomaterials*, 2013, 34, 8918.
64. V. Garcia-Gradilla, J. Orozco, S. Sattayasamitsathit, F. Soto, F. Kuralay, A. Pourazary, A. Katzenberg, W. Gao, Y. Shen, J. Wang, "Functionalized Ultrasound-Propelled Magnetically-Guided Nanomotors: Towards Practical Biomedical Applications", *ACS Nano*, 2013, 7, 9232.
Highlighted in ACS Nano, The Guardian (UK).
65. J. Li, J. Zhang, W. Gao, G. Huang, Z. Di, R. Liu, J. Wang, Y. Mei, "Dry-Released Nanotubes and Nanoengines by Particle-Assisted Rolling", *Advanced Materials*, 2013, 25, 3715.
66. Y. Gu, S. Sattayasamitsathit, K. Kaufmann, R. Vazquez-Duhalt, W. Gao, J. Wang, "Self-Propelled Chemically-Powered Plant-Tissue Biomotors", *Chemical Communications,* 2013, 49, 7307.
Highlighted in Chemistry World.
67. J. Orozco, A. Cortés, G. Cheng, S. Sattayasamitsathit, W. Gao, X. Feng, Y. Shen, J. Wang, "Molecularly Imprinted Polymer-Based Catalytic Micromotors for Selective Protein Transport", *Journal of the American Chemical Society*, 2013, 135, 5336.
68. J. Orozco, V. García-Gradilla, M. D'Agostino, W. Gao, A. Cortés, J. Wang, "Artificial Enzyme-Powered Microfish for Water-Quality Testing", *ACS Nano*, 2013, 7, 818.
Highlighted in Nanowerk.

69. K. M. Manesh, S. Campuzano, W. Gao, M. J. Lobo-Castañón, I. Shitanda, K. Kiantaj, J. Wang, "Nanomotor-Based Biocatalytic Patterning of Helical Metal Microstructures", *Nanoscale*, 2013, 5, 1310.
70. M. García, J. Orozco, M. Guix, W. Gao, S. Sattayasamitsathit, A. Escarpa, A. Merkoci, J. Wang, "Micromotor-based Lab-on-Chip Immunoassay", *Nanoscale*, 2013, 5, 1325.
    'HOT' article. Highlighted in RSC Blog.
71. F. Kuralay, S. Sattayasamitsathit, W. Gao, A. Uygun, A. Katzenberg, J. Wang, "Self-Propelled Carbohydrate-Sensitive Microtransporters with 'Built-In' Boronic-Acid Recognition for Isolating Sugars and Cells", *Journal of the American Chemical Society*, 2012, 134, 15217.
72. J. Wang, W. Gao, "Nano/Microscale Motors: Biomedical Opportunities and Challenges", *ACS Nano*, 2012, 6, 5745.
    Highlighted in Nanowerk.
73. M. Guix, J. Orozco, M. Garcia, W. Gao, S. Sattayasamitsathit, A. Merkoci, A. Escarpa, J. Wang, "Superhydrophobic Alkanethiol-Coated Microsubmarines for Effective Removal of Oil", *ACS Nano*, 2012, 6, 4445.
    Highlighted in Chemical & Engineering News, *BBC News*, *The Engineer*, *Wired*, *Popular Science* and *Discovery News* etc.
74. S. Sattayasamitsathit, A. M. O'Mahony, X. Xiao, S. M. Brozik, C. M. Washburn, D. R. Wheeler, W. Gao, S. Minteer, J. Cha, D. B. Burckel, R. Polsky, J. Wang, "Highly Ordered Tailored Three-Dimensional Hierarchical Nano/Microporous Gold-Carbon Architectures", *Journal of Materials Chemistry*, 2012, 22, 11950.
75. S. Campuzano, J. Orozco, D. Kagan, M. Guix, W. Gao, S. Sattayasamitsathit, J. C. Claussen, A. Merkoçi, J. Wang, "Bacterial Isolation by Lectin-Modified Microengines", *Nano Letters*, 2012, 12, 396.
    Highlighted in Nanowerk.
76. J. Orozco, S. Campuzano, D. Kagan, M. Zhou, W. Gao, J. Wang, "Dynamic Isolation and Unloading of Target Proteins by Aptamer-Modified Microtransporters", *Analytical Chemistry*, 2011, 83, 7962.
77. S. Sattayasamitsathit, W. Gao, P. Calvo-Marzal, K. M. Manesh, J. Wang, "Simplified Cost-Effective Preparation of High Performance Pt-Ag Nanowire Motors", *ChemPhysChem*, 2010, 11, 2802.
78. Y. Dong, W. Gao, Q. Zhou, Y. Zheng, Z. You, "Characterization of the Gas Sensors based on Polymer-Coated Resonant Microcantilevers for the Detection of Volatile Organic Compounds", *Analytica Chimica Acta*, 2010, 671, 85.
79. Y. Dong, W. Gao, Y. Zheng, Z. You, "Electrothermal Driving Microcantilever Resonator as a Platform for Chemical Gas Sensing", *Tsinghua Science and Technology*, 2010, 15, 481.
80. Y. Dong, W. Gao, Z. You, "Direct Bonding SOI Wafer Based Cantilever Resonator for Trace Gas Sensor Application", *IEEE NEMS*, 2009, 134.

Patents

1. "Autonomous Sweat Extraction and Analysis Using a Fully-Integrated Wearable Platform", S. Emaminejad, C. Milla, W. Gao, A. Javey, R. W. Davis, 2016, US Patent App. 15/700,119.
2. "Wearable Sensor Arrays for In-Situ Body Fluid Analysis", W. Gao, S. Emaminejad, R. W. Davis, A. Javey, 2015, PCT/US2016/053988.
3. "Nanomotor Photolithography", J. Wang, J. Li, W. Gao, 2014, patent filed.
4. "Method and System for In Vivo Hydrogen Peroxide Detection with Ultrasound", R. F. Mattrey, Z. Wu, E. S. Olsen, J. Wang, W. Gao, US 9,713,459.
5. "Membrane Template Synthesis of Microtube Engines", J. Wang, W. Gao, S. Sattayasamitsathit, US 9,982,356.
6. "Electronic Nose Used for Food Safety Monitoring", Y. Dong, Z. You, W. Gao, Y. Zheng, CN 101788440.

Professional Activities

- Member of *Sigma Xi, ACS, MRS, AICHE, NYAS and IEEE.*
- Member of Editorial Board of International Journals including *Micromachines, Sensors.*

- Proposal Reviewer for *U. S. Air Force Office of Scientific Research, U.S. National Institute of Standards and Technology (NIST), European Research Council, Ontario Research Fund, AAAS/MTI, The Netherlands Organisation for Scientific Research.*
- Independent Reviewer of over 65 International Journals, including:
  Science, Nature Biotechnology, Nature Electronics, Nature Communications, Science Translational Medicine, Science Advances, Science Robotics, Proceedings of the National Academy of Sciences, Journal of the American Chemical Society, Angewandte Chemie, Accounts of Chemical Research, Nano Letters, ACS Nano, Advanced Materials, Advanced Functional Materials, Advanced Healthcare Materials, Advanced Science, Advanced Biosystems, Microsystems & Nanoengineering, Energy & Environmental Science, Nano Energy, Small, Chemistry - A European Journal, Scientific Reports, Analytical Chemistry, ACS Applied Materials & Interfaces, ACS Sensors, Langmuir, ACS Biomaterials Science & Engineering, Chemical Science, ChemSusChem, ChemCatChem, ChemElectroChem, The Chemical Record, Chemical Communications, Nanoscale, Journal of Materials Chemistry A, B, C, Lab on a Chip, Soft Matter, Analyst, RSC Advances, Physical Chemistry Chemical Physics, New Journal of Chemistry, Advanced Drug Delivery Reviews, Sensors and Actuators B: Chemical, Talanta, Electroanalysis, ChemistrySelect, Materials Science & Engineering - R: Reports, Journal of Physics and Chemistry of Solids, Applied Physics Letters, Journal of Applied Physics, AIP Advances, Applied Materials Today, Sensors, IEEE Sensors, IEEE Transactions on Electron Devices, IEEE Transactions on NanoBioscience, IEEE Transactions on Biomedical Engineering, The Robotics and Biomimetics, Journal of Fluids and Structures, The Journal of The Electrochemical Society, ECS Journal of Solid State Science and Technology, Review of Scientific Instruments.

Caltech Division of Engineering and Applied Science

Wei Gao, Ph.D.
1200 E. California Blvd., MC 138-78
Pasadena, CA 91125
(626) 395-2958
weigao@caltech.edu

Monday, December 17, 2018

To: U.S. Citizenship & Immigration Services

Re: Recommendation Letter for Dr. Yuguang Yang

Dear Immigration Officer:

It is my pleasure to provide this recommendation letter for Dr. Yuguang Yang. Dr. Yang is a leading scientist in colloidal science, especially with his application of mathematical modeling. His analytical abilities, particularly in constraint Stokesian dynamics and Markov decision process, have clearly benefited biomedical technology research. I have learned of his work through his publications.

As you can see from my academic credentials summarized below, my research interest is closely related to Dr. Yang's fields, and thus I believe I am very well placed to evaluate the qualifications of Dr. Yang's work. Currently, I am serving as an Assistant Professor in the Department of Medical Engineering at the California Institute of Technology, one of the best scientific research universities in the world. I obtained my Ph.D. degree from the University of California, San Diego and served as a Postdoctoral Fellow at the University of California, Berkeley. My group at Caltech is a highly interdisciplinary research team devoted to developing versatile bioelectronic devices for fundamental and applied biomedical studies, including wearable/portable biosensors that perform real-time health monitoring and clinical assessment, and medical micro/nanorobots that offer the therapeutic capability of rapid drug delivery and precision surgery. I have published more than 70 papers on top journals, including *Nature*, *Nature Electronics*, *Nature Communications*, *Science Robotics*, *Science Advancement*, *ACS Nano*, *Chemical Society Reviews*, etc., with more than 7,000 citations. I have also received a series of awards, including McKenna Family Innovation Award, MIT Technology Review Top 35 Innovators Under 35, Sensors Young Investigator Award and ACS Nano Junior Fellow.

Dr. Yang has done cutting-edge work in optimizing the control of micro-robots for drug delivery and precision surgery through single rod dynamics modeling near solid-liquid interfaces and under confined geometries, such as those encountered in blood vessels. The accurate modeling of micro-sized colloidal rod motion near-interfacial and confined geometries is crucial in applications such as drug delivery and precision surgery, where the position of rod-shaped micro-robot needs to be precisely controlled. However, since the movement of micro-sized rods is driven by multiple forces including the interaction of gravity, hydrodynamic drag, etc., many aspects of the movement are challenging to comprehend. Dr. Yang built a sophisticated constraint Stokesian dynamics model that is capable of calculating rod diffusion parameters and, more importantly, directly simulates rod-shaped particles in biologically relevant settings. Impressively, his model prediction results were directly verified by experiments. Moreover, his model reveals the unusual correlations of motion modes due to hydrodynamic interaction when rod-shaped particles translate and rotate near flat surfaces. Dr. Yang's model provides simulations that inform the development of effective guidelines for the design of precise control features in micro-robots.

Dr. Yang has also propelled the optimization of the navigation of self-propelled particles, also known as micro-robots, for drug delivery and precision surgery. One main obstacle in this is

efficient navigation within micro-structured environments. Dr. Yang unprecedently provided a solution to this problem. This outstanding work started with Dr. Yang's realistic model of micro-robot's motion and its interaction with the obstacles, which is grounded on his fundamental understanding of colloidal particle physics. The most creative and impressive part is his use of a Markov decision framework to produce the optimal navigation strategy that specifies the strength of the propulsion necessary given the robot's position information. Different from traditional robot science, Dr. Yang's model takes into account the stochastic nature of the micro-robotics. In the various testing cases of this optimal navigation strategy, the benefit and efficiency brought by his model are remarkable. On a millimeter length scale, his method enables the micro-robot to realize a completion of maze transportation task several orders of magnitude faster than an uncontrolled one by designing a navigation path that minimizes passage time and traveled distance. He captured the critical principles in optimal navigation in order to provide rule-of-thumb actions in complicated scenarios that are not easy to model. Using the scaling analysis, he identified the control update time and maximum allowable speed as two extrinsic control parameters affecting the performance. These two parameters have an optimal ratio and any deviation from this optimal ratio can deteriorate the performance. Dr. Yang's navigation solution is sufficiently generalized to be compatible with a broad range of micro-robot designs. As such, Dr. Yang's findings lay a critical foundation for the cutting-edge development of efficient and intelligent micro-robots.

Without any doubt, Dr. Yang's contributions have impacted our ability to optimize micro-robot technology. He is a distinct talent who will undoubtedly continue to benefit the research community and related industries. While Dr. Yang's education and training equipped him with knowledge and skills related to his projects, it is his creative and probing intelligence that have allowed him to have such a dramatic impact, evidenced in his publications. Dr. Yang has proven his ability to generate high quality, provocative contributions that aid scientific development and advance our abilities in technology. Top-notch researchers such as Dr. Yang are critical for the U.S. to maintain its leadership role in science and technology. If you need further assistance in this matter, please feel free to contact me.

Sincerely,

Wei Gao, Ph.D.
Assistant Professor of Medical Engineering
Division of Engineering and Applied Science
California Institute of Technology, Pasadena, CA
Phone: (626) 395-2958 (office)
Email: weigao@caltech.edu
Webpage: www.gao.caltech.edu

Yuguang Yang

(+1) 4102946268 | yangyutu123@gmail.com | Charlotte, NC | Github: https://github.com/yangyutu

EDUCATION

- **Master**, **Computer Science**, **GPA 3.95**, Johns Hopkins University (JHU), 2016.
- **PhD**, **Chemical Engineering**, **GPA 4.0**, JHU, 2011.9-2017.2.

Thesis: Stochastic Modeling and Optimal Control for Colloidal Organization, Navigation, and Machine (Advisor: *Michael Bevan*)

- **BE, Polymer Engineering**, **GPA 4.0**, Zhejiang University (ZJU), 2011.

WORK EXPERIENCE

Part-time Researcher, Tsinghua University, China (2018. 7 – present)

- Investigate collective oscillatory dynamics in chiral self-propelled rod system.
- Design optimal feedback control strategy for L-shaped self-propelled rod swarms.

Quantitative Associate, Wells Fargo Securities, Charlotte, NC (2017. 7 – present)

- Construct and calibrate pricing and risk analytics models for financial derivatives.
- Develop production computation code for pricing and risk analytics.

Research Intern, PARC (Palo Alto Research Center), Palo Alto, CA (2016. 10 – 2016.12)

- Constructed and calibrated mathematical models for Brownian chiplet particles.
- Developed online large-scale multi-agent optimal constrained stochastic control algorithms in C++.

Software Engineer (C++) Intern, Vectorworks, MD (2015.6 – 2015.8)

Teaching Assistant of Applied Physical Chemistry, JHU, MD (2013.9-2013.12, 2012.9-2012.12)

ACADEMIC RESEARCH

- Development of high-performance Monte Carlo and stochastic differential equation simulators for high-dimensional coupled Brownian systems.
- Low-Reynold number hydrodynamics and simulation algorithm for colloidal rod system.
- Low-dimensional model construction and calibration for high-dimensional stochastic systems.
- Optimal control in complex stochastic systems *via* Markov decision framework and reinforcement learning.
- Dimensional reducation and parameter estimation in high-dimensional state-space models.

SELECTED MATH COMPETITIONS AND PRIZES

2010 **Outstanding Winner (top 3 among 2254 teams)** in Mathematical Contest in Modeling, USA
2009 **First Class Prize** in Undergraduate Mathematical Contest in Modeling, China
2009 **First Class Prize** in Mathematical Contest in Modeling of ZJU, China
2008 **First Class Prize** in Advanced Mathematics Contest, Zhejiang Province, China

SELECTED PUBLICATIONS (* denotes equal contribution)

- Optimal Navigation of Self-Propelled Colloids
  Y. Yang, M.A. Bevan
  ACS Nano 12 (11), 10712-10724 (2018)
- Energy Landscapes for Ellipsoids In Non-Uniform AC Electric Fields
  I. Torres-Díaz, B. Rupp, Y. Yang, M.A. Bevan
  Soft Matter 14 (6), 934-944, (2018)
- Interfacial and Confined Colloidal Rod Diffusion
  J.L. Bitter, Y. Yang, G. Duncan, H. Fairbrother, M.A. Bevan
  Langmuir 33 (36), 9034-9042 (2017)
- Chemical Antagonism Between Photodynamic Agents and Chemotherapeutics: Mechanism and Avoidance
  Q. Meng, J. Meng, W. Ran, J. Su, Y. Yang, P Zhang, Y Li

Chemical Communications 53 (92), 12438-12441, 2017

- Interfacial Colloidal Rod Dynamics: Coefficients, Simulations, and Analysis.
  Y. Yang, M.A. Bevan. 147 (5), 054902,
  Journal of Chemical Physics 147 (5), 054902, (2017)
- An M-Estimator for Reduced-Rank System Identification.
  S. Chen, K. Liu, Y. Yang, Y. Xu, S. Lee, M. Lindquist, B.S. Caffo, J.T. Vogelstein.
  Pattern Recognition Letters 86, 76-81, (2017)
- Dynamic Colloidal Assembly Pathways via Low Dimensional Models.
  Y. Yang, R. Thyagarajan, D.M. Ford, M.A. Bevan.
  The Journal of Chemical Physics 144 (20), 204904 (2016)
- Optimal Feedback Controlled Assembly of Perfect Crystals.
  X Tang*, B Rupp*, Y. Yang*, T.D. Edwards, M.A. Grover, M.A. Bevan.
  ACS Nano 10 (7), 6791-6798, (2016)
- Modeling Depletion Mediated Colloidal Assembly on Topographical Patterns.
  Y. Yang, T.D. Edwards, M.A. Bevan.
  Journal of colloid and interface science 449, 270-278 (2015)
- Reconfigurable Multi-Scale Colloidal Assembly on Excluded Volume Patterns.
  T.D. Edwards, Y. Yang, W.N. Everett, MA Bevan.
  Scientific reports 5, 13612 (2015)
- Controlling Assembly of Colloidal Particles into Structured Objects: Basic Strategy and A Case Study
  MA Bevan, DM Ford, MA Grover, B Shapiro, D Maroudas, Y. Yang, et al.
  Journal of Process Control 27, 64-75**,** (2015)
- Colloidal Crystal Grain Boundary Formation and Motion.
  T.D. Edwards*, Y. Yang*, D.J. Beltran-Villegas, M.A Bevan.
  Scientific reports 4, 6132 (2014)
- Grain Boundary Control in Colloidal Self-Assembly with Dynamic Programming.
  X Tang, Y. Yang, MA Bevan, MA Grover.
  American Control Conference, Portland, OR, 1120-1125, (2014)
- Modulating the Structure and Properties of Poly (sodium 4-styrenesulfonate)/Poly (diallyldimethylammonium chloride) Multilayers with Concentrated Salt Solutions.
  L. Han, Z, Mao, H. Wuliyasu, J. Wu, X. Gong, Y. Yang, C. Gao.
  Langmuir 28 (1), 193-199 (2011)

CONFERENCE TALK

- Hierarchical Assembly of Anisotropic Particles in AC Electric Fields.
  I. Torres Diaz, B. Rupp, X. Hua, Y. Yang, M.A. Bevan
  American Physical Society (APS) March Meeting, Baltimore, 2016
- Optimal Navigation of Self-Propelled Colloids in Microstructured Mazes.
  Y. Yang, M.A. Bevan
  American Physical Society (APS) March Meeting, Baltimore, 2016

- Optimal Navigation of Self-propelled Colloidal Rods in Mazes.
  Y. Yang, M.A. Bevan.
  American Chemical Society (ACS) colloids symposium, Boston, 2016
- Self-Propelled Colloids Navigating Mazes & Organizing into Machines.
  M.A. Bevan, Y. Yang,
  Gordon Conference, 2016
- Constraint Stokesian Dynamics Simulation for Single Rod.
  Y. Yang, M.A. Bevan.
  The Mid-Atlantic Soft Matter Workshop at University of Delaware, 2015
- Continuous Growth of Defect-Free Colloidal Crystals via Feedback Control
  Y. Yang, M.A. Bevan.
  American Chemical Society (ACS) colloids symposium, Philadelphia, 2014
- Grain Boundary Formation and Motion in Colloidal Crystals
  Y. Yang, T.D. Edwards, M.A. Bevan.
  American Chemical Society (ACS) colloids symposium, Philadelphia, 2014
- Measuring Noisy Colloidal Dynamics using a Hidden Markov Model Analysis.
  Y. Yang, M.A. Bevan.
  The Mid-Atlantic Soft Matter Workshop at University of Delaware, 2014

The Johns Hopkins University

Upon the recommendation of the Faculty of

The G. W. C. Whiting School of Engineering

has conferred upon

Yuguang Yang

the degree of

Doctor of Philosophy

Chemical and Biomolecular Engineering

with all the rights, honors and privileges appertaining thereto.

Given under the seal of the University at Baltimore, Maryland

on May twenty-fourth, two thousand and seventeen.

THE JOHNS HOPKINS UNIVERSITY · BALTIMORE · 1876 · VERITAS VOS LIBERABIT

Benjamin T. Rome Dean for the School of Engineering

President

Chair of the Board of Trustees

The Johns Hopkins University

Upon the recommendation of the Faculty of

The G. W. C. Whiting School of Engineering

has conferred upon

Yuguang Yang

the degree of

Master of Science in Engineering

Computer Science

with all the rights, honors and privileges appertaining thereto.
Given under the seal of the University at Baltimore, Maryland
on May eighteenth, two thousand and sixteen.

THE JOHNS HOPKINS UNIVERSITY · VERITAS VOS LIBERABIT · 1876 · BALTIMORE

Benjamin T. Rome Dean for the School of Engineering

President

Chair of the Board of Trustees

SCIENTIFIC REPORTS

OPEN

SUBJECT AREAS:
CHEMICAL ENGINEERING
SELF-ASSEMBLY

Received
28 April 2014

Accepted
22 July 2014

Published
20 August 2014

Correspondence and requests for materials should be addressed to M.A.B. (mabevan@jhu.edu)

* These authors contributed equally to this work.

Colloidal crystal grain boundary formation and motion

Tara D. Edwards*, Yuguang Yang*, Daniel J. Beltran-Villegas & Michael A. Bevan

Chemical & Biomolecular Engineering, Johns Hopkins University, Baltimore, MD 21218.

The ability to assemble nano- and micro- sized colloidal components into highly ordered configurations is often cited as the basis for developing advanced materials. However, the dynamics of stochastic grain boundary formation and motion have not been quantified, which limits the ability to control and anneal polycrystallinity in colloidal based materials. Here we use optical microscopy, Brownian Dynamic simulations, and a new dynamic analysis to study grain boundary motion in quasi-2D colloidal bicrystals formed within inhomogeneous AC electric fields. We introduce "low-dimensional" models using reaction coordinates for condensation and global order that capture first passage times between critical configurations at each applied voltage. The resulting models reveal that equal sized domains at a maximum misorientation angle show relaxation dominated by friction limited grain boundary diffusion; and in contrast, asymmetrically sized domains with less misorientation display much faster grain boundary migration due to significant thermodynamic driving forces. By quantifying such dynamics vs. compression (voltage), kinetic bottlenecks associated with slow grain boundary relaxation are understood, which can be used to guide the temporal assembly of defect-free single domain colloidal crystals.

Photonic and meta- materials provide examples where ordered particles on length scales comparable to electromagnetic wavelengths produce exotic emergent properties[1]. Colloidal crystallization provides a potential route to self-assemble such materials *via* processes amenable to scalable manufacturing; however, robust schemes have yet to be identified to obtain the necessary low defect densities. From a broader perspective, obtaining perfect crystals on any length scale remains more art than science (*e.g.*, atoms, molecules, macromolecules)[2,3]. To design robust crystal growth, recrystallization, and annealing schemes to minimize defects, it is necessary to know the basic mechanisms of defect formation and motion.

Although three-dimensional configurations of complex particles are the ultimate goal of self-assembly schemes[4,5], here we investigate a relatively simple problem that is still not well understood: how grain boundaries form and move during quasi two-dimensional (2D) crystallization of spherical colloids. Quasi-2D colloidal crystals have been used in studies of melting[6], nucleation[7], point defect diffusion[8], and grain boundary fluctuations[9]. Other relevant studies include 2D analyses of colloidal crystals to investigate impurity mediated growth[10], particle motion within grain boundaries[11], and grain boundary pre-melting[12]. Despite these extensive studies, fundamental understanding of grain boundary formation and motion remains rudimentary[13] in all but the most model simulation studies[14]. 2D crystals are also of interest based on their relevance to thin films[15], bubble rafts[16], and graphene[17]. Understanding how grain boundary motion enables relaxation of multi-domain crystals into defect-free crystals is therefore scientifically and technologically interesting.

Results

In this work, we employ real-time microscopy to observe grain boundary formation and motion in a quasi-2D colloidal crystal containing ~200 colloidal particles (Fig. 1a, Supplementary Videos 1–4). Aqueous ~3 micron SiO_2 charged colloids crystallize in a quadrupole electrode in MHz AC electric fields (see Methods, Supplementary Information)[18], where field-mediated compression of induced dipoles is balanced by the quasi-2D colloid osmotic pressure (*i.e.*, effective hard disk). The electric field amplitude (*i.e.*, applied voltage) is effectively a surrogate for pressure and hence acts as a global thermodynamic variable that determines the relative free energy of all particle configurations for fixed voltage, number, and temperature. In the following, we report non-dimensional voltages, where $V^* = 1$ is the voltage required for N particles to produce a hexagonal close packed crystal with hexagonal morphology (as demonstrated in previous work with agreement between microscopy experiments, MC simulations, and perturbation theory[19], see Supplemental Information for additional details).

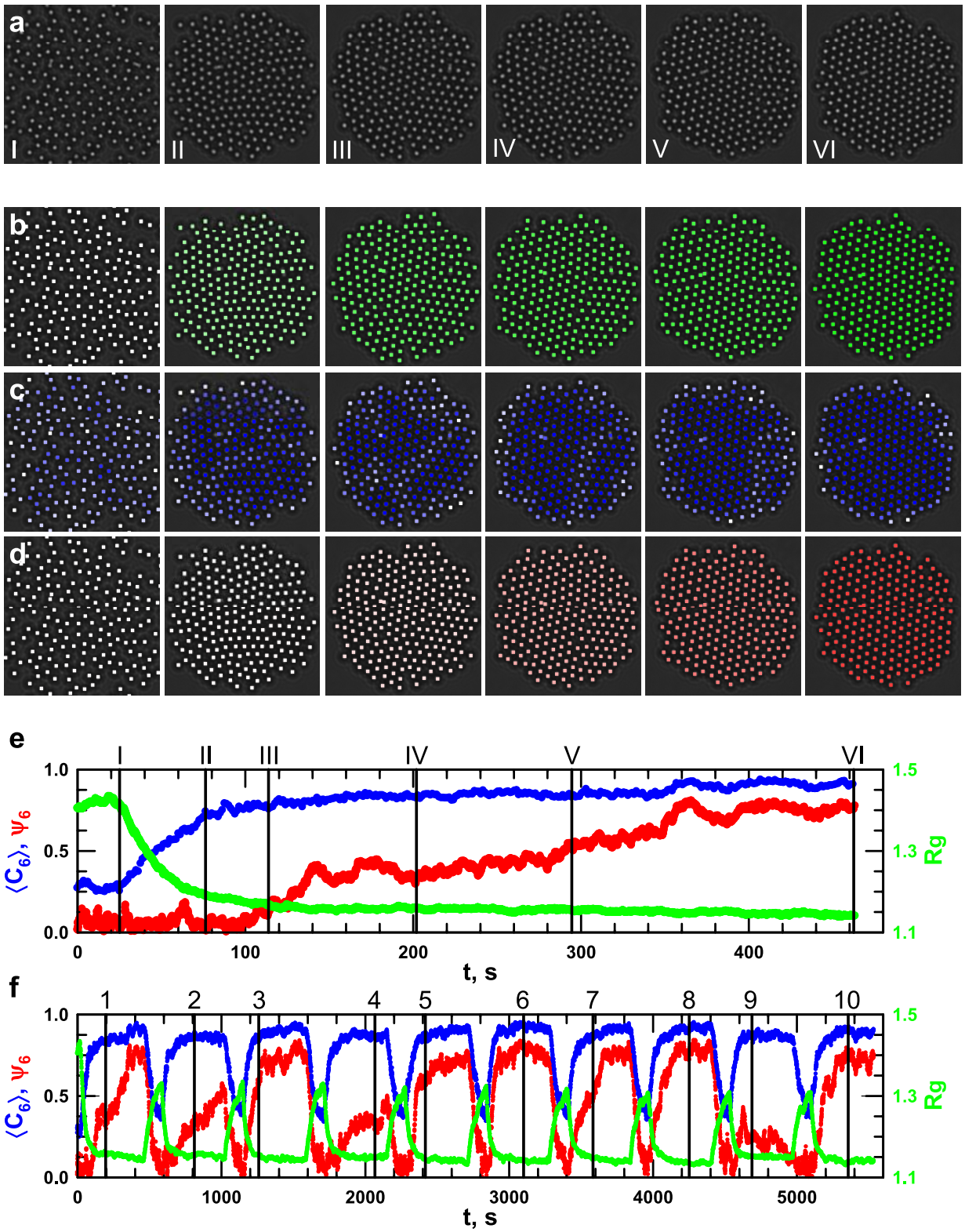

Figure 1 | Reaction coordinates for grain boundary formation and motion can be computed from image analysis of optical microscopy images of electric field mediated colloidal crystallization. (a) Raw images show representative configurations of 210 ~ 3 μm silica colloids in fluid, bicrystal, and single crystal configurations observed over ~7.5 min following a quench (step voltage change) to $V^* = 0.57$ (see main text and Supplementary Methods for definition). Snapshot times are shown by solid black lines in Fig. 1e. Computed reaction coordinates shown by colored particle centers on 8-bit intensity scale for the (b) radius of gyration, R_g, (c) local hexagonal order, $\langle C_6 \rangle$, (d) global hexagonal order, ψ_6, and time dependent traces for (e) a single voltage quench and (f) ten consecutive cycles (numbered vertical black lines indicate representative images included in Supplementary Fig. 2).

Our previous characterization of electric field mediated colloidal interactions and assembly has yielded kT-scale potentials[20,21], feedback control over system size[18], and conditions to crystallize N particles[19]. Based on these findings, we set $N = 210$ in Fig. 1, which routinely forms bicrystals (*i.e.*, 1 grain boundary between 2 domains) in contrast to single domains in smaller systems and >2 domains in

larger systems. As shown in Fig. 1, step-quenches to $V^* = 0.57$ cause an initially dilute fluid phase to first rapidly condense, then form grain boundaries *via* coalescence of local domains, and finally display grain boundary motion as bicrystals relax to single crystals. Reversibility allows repeated quenches between fluid and crystal states to probe the stochastic dynamics of grain boundary formation, diffusion (*i.e.*, random motion), and migration (*i.e.*, drift). We first focus on the $V^* = 0.57$ case, but later investigate step-changes to both lower and higher values of V^*.

To interpret and model these measurements, we aim to develop a "low-dimensional model" that quantitatively captures the observed dynamics using "reaction coordinates"[22] (rather than enumerating all $2N$ translational degrees of freedom)[23,24]. The use of the term "low-dimensional" here does not refer to the Euclidian spatial dimension (*i.e.*, x and y particle center coordinates), which is effectively quasi-two dimensional, but rather, "dimensionality" refers to the number of reaction coordinates necessary to capture the stochastic dynamics of grain boundary formation. It is "low dimensional" because we expect the number of reaction coordinates to be considerably less than the $2 \times (N = 210) = 420$ dimensions that would be necessary to uniquely specify all possible two-dimensional configurations of 210 particles. Although the term "low-dimensional" may be unfamiliar to some readers, other synonymous terms such as "coarse-grained models" could also be confusing based on an unfortunate overlap of terms relevant to the application of interest in this work.

Candidate reaction coordinates are computed from particle centers and used to color code images (Figs. 1b–f) including: the radius of gyration, R_g[18], to capture condensation from fluid to crystal states, average local hexagonal order, $\langle C_6 \rangle$[25], to capture the onset of crystallization, and global hexagonal order, ψ_6[26], to capture the degree of polycrystallinity. R_g and $\langle C_6 \rangle$ are normalized by their N particle single crystal values (see Supplementary Methods), so that $\langle C_6 \rangle$ goes from 0–1 for fluids to complete locally ordered states, and R_g decreases from arbitrarily high numbers to 1 for complete condensation[19]. ψ_6 is 0 for fluids and 1 for single-domain crystals like $\langle C_6 \rangle$, but in contrast, depends strongly on relative domain size and misorientation (*e.g.*, $\psi_6 = 0$ for bicrystals of identically sized 111 domains with 30° misorientation).

The reaction coordinates trajectories following a single voltage quench (Fig. 1e) show initially decreasing R_g and increasing $\langle C_6 \rangle$ occur in unison (*i.e.*, $R_g^{-1} \approx \langle C_6 \rangle$), which demonstrates a close coupling between condensation and local ordering. As R_g and $\langle C_6 \rangle$ plateau, indicating an overall condensed configuration with all particles contained in locally crystalline domains, $\psi_6 \approx 0$, indicating a bicrystal. For $t > 100$ s, R_g and $\langle C_6 \rangle$ remain essentially unchanged while ψ_6 rises from 0 to ~0.8, which clearly corresponds to grain boundary motion from the bicrystal interior to the periphery where it vanishes (Fig. 1d, Supplementary Video 1).

Ten successive voltage quenches from initial fluid states (Fig. 1f) demonstrate the stochastic nature of the grain boundary dynamics, which is expected from the underlying probabilistic colloidal motion. While R_g and $\langle C_6 \rangle$ reveal condensation and local order emerge in a similar manner for each cycle, the ψ_6 trajectories can be categorized into several cases: (1) ψ_6 tracks $\langle C_6 \rangle$ indicating the simultaneous emergence of local and global order, (2) ψ_6 becomes localized at intermediate values for varying time periods before again increasing, (3) ψ_6 becomes arrested for the duration of the observation time, and (4) in one case, ψ_6 initially increases but then vanishes. The stochastic nature of the observed grain boundary dynamics apparent in an ensemble of trajectories is an important aspect to capture in a quantitative model.

To develop a low-dimensional model of grain boundary formation and motion, it is necessary to determine the number and type of reaction coordinates. For example, it could be speculated that ψ_6 is all that is required to track grain boundaries since it visually tracks polycrystallinity in Fig. 1. However, simply tracking ψ_6 does not capture how parallel processes of local condensation and crystallization determine the formation and motion of grains of different sizes, shapes, and orientations, which ultimately determine the mechanisms of polycrystals relaxing to single crystals. In addition, ψ_6 does not uniquely identify some configurations; for example, fluid configurations and maximally misaligned bicrystals both have $\psi_6 = 0$.

To illustrate how reaction coordinate pairs capture additional information, experimental configurations are colored using two coordinates (Figs. 2a, b) and 2D trajectories of (ψ_6, $\langle C_6 \rangle$) (Fig. 2c) or (ψ_6, R_g) (Fig. 2d) vs. time, where time is indicated by a 256-color scale. We do not plot (R_g, $\langle C_6 \rangle$) since these coordinates are highly correlated in Fig. 1, although such a pair could be useful to distinguish condensed amorphous microstructures (*i.e.*, glasses/gels). Such 2D plots immediately address one issue; plotting ψ_6 against either R_g or $\langle C_6 \rangle$ distinguishes fluid and bicrystal configurations (*e.g.*, high R_g, low ψ_6 vs. low R_g, low ψ_6). These trajectories also show how local ordering (*i.e.*, increasing $\langle C_6 \rangle$) and condensation (*i.e.*, decreasing R_g) influence the emergence of polycrystallinity and subsequent grain boundary motion. Trajectories starting at lower ψ_6 tend to become localized at lower ψ_6 after condensation, whereas trajectories with initially higher ψ_6 tend to rapidly form single crystals.

Although tools exist to identify the minimum dimensionality (*i.e.*, number of reaction coordinates) from observed dynamics (*e.g.*, diffusion mapping[27–29]), such methods are not currently able to predict physically meaningful reaction coordinates[22]. Ultimately, the number and types of reaction coordinates can be determined empirically by finding what is necessary to produce a quantitative stochastic dynamic model. Because the measured trajectories display both drift and diffusion along reaction coordinates, which appear to be mediated by free energy gradients (*i.e.*, driving forces) and fluctuations/friction (*i.e.*, randomness/resistance), it is assumed that such processes can be captured by a low-dimensional Smoluchowski equation given by[30],

$$\frac{\partial p(\mathbf{x},t)}{\partial t} = \nabla \cdot \mathbf{D}(\mathbf{x}) \cdot \left[\nabla + \frac{1}{k_B T} \nabla W(\mathbf{x}) \right] p(\mathbf{x},t) \qquad (1)$$

where $p(\mathbf{x}, t)$ is the probability density of finding the system at coordinate $\mathbf{x}$ at time, t, $W(\mathbf{x})$ is the free energy landscape, kT is thermal energy, and $\mathbf{D}(\mathbf{x})$ is the diffusivity landscape, which can be related in the usual way to mobility, $\mathbf{m}(\mathbf{x})$, and friction, $\boldsymbol{\zeta}(\mathbf{x})$, landscapes as $\mathbf{D}(\mathbf{x}) = \mathbf{m}(\mathbf{x})kT = \boldsymbol{\zeta}(\mathbf{x})^{-1}kT$. The variable $\mathbf{x}$ is a vector of reaction coordinates where the number of coordinates is the model "dimension." The Smoluchowski equation is a special case of the Fokker-Planck equation that also satisfies the fluctuation-dissipation theorem and leads to Boltzmann sampling at equilibrium (*i.e.*, $p(\mathbf{x}) = \exp[-W(\mathbf{x})/kT]$)[23,30]. In more descriptive terms, $W(\mathbf{x})$ is the free energy change associated with moving from one particle configuration to another (or one reaction coordinate to another; (*e.g.*, $\mathbf{x_1} = (\psi_{6,1}, R_{g,1})$ to $\mathbf{x_2} = (\psi_{6,2}, R_{g,2})$), and $\mathbf{D}(\mathbf{x})$ captures the associated configuration dependent changes in diffusion and friction (*i.e.*, fluctuations and dissipation).

To obtain $W(\mathbf{x})$ and $\mathbf{D}(\mathbf{x})$ in Eq. (1) from trajectories like those in Figs. 1 and 2, we analyzed Brownian Dynamic (BD) simulations that were matched to experiments (by capturing all equilibrium and dynamic properties of the quadrupole experiment on the particle scale[19–21], see Supplementary Methods). This approach was used because statistics on the particle scale are easily obtained to match experiments and simulations, but BD simulations are better suited to generating large numbers of grain boundary trajectories (*e.g.*, each experimental grain boundary trajectory in Fig. 1 is acquired for ~10 min.).

To provide more details of the matching process, inverse Monte Carlo was used to obtain interaction potentials that capture all equilibrium properties (*i.e.*, radial distribution functions), which were then employed in BD simulations that captured all dynamic properties (*i.e.*, particle scale diffusion, reaction coordinate trajectories). It

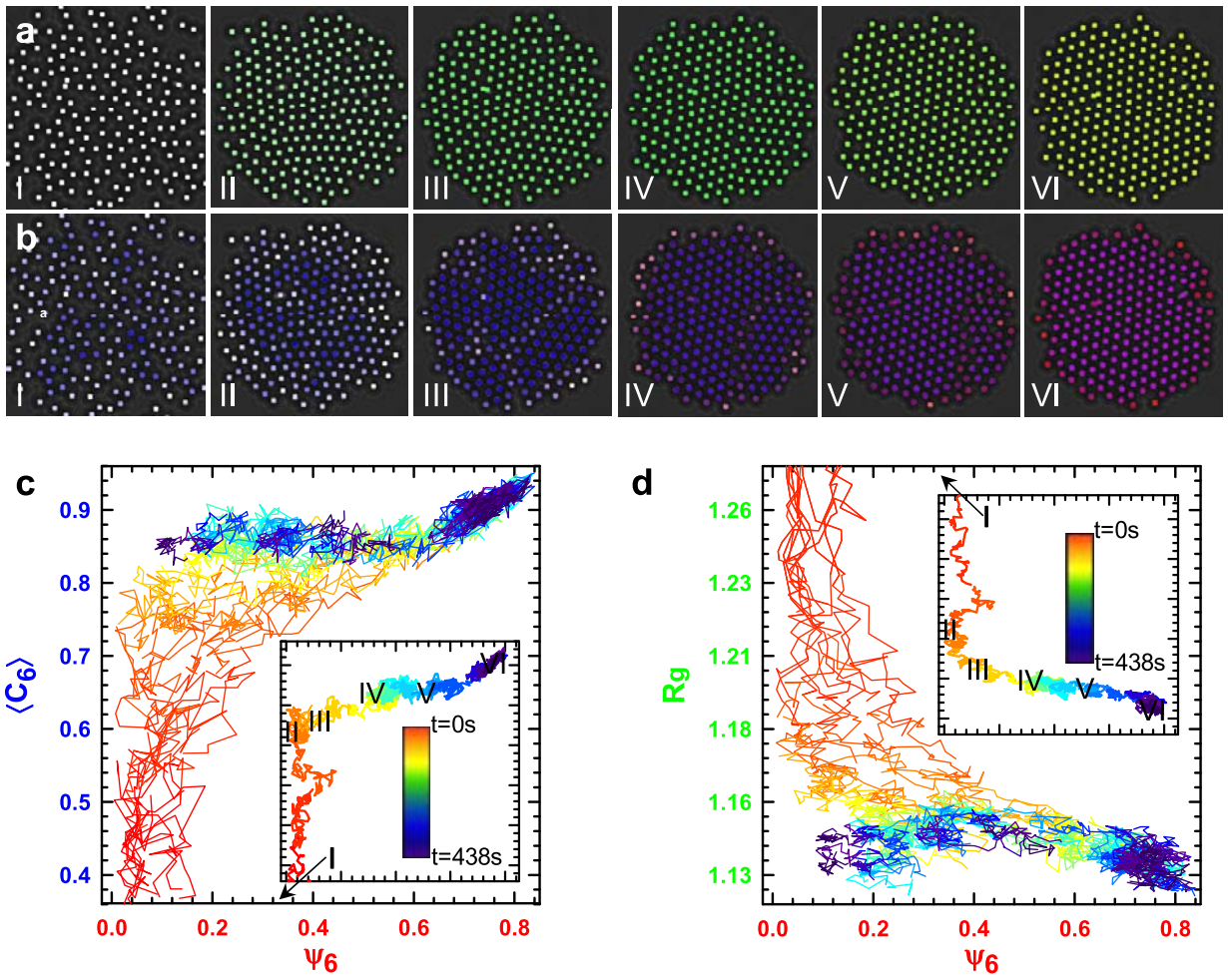

Figure 2 | "Two dimensional" trajectories (*i.e.*, two reaction coordinates) capture coalescence of local domains during fast condensation processes to produce bicrystals that relax to single crystals via grain boundary motion over a broad range of timescales. Microscopy images from Figs. 1a with particle centers colored using RGB (Red/Green/Blue) mixing rules for colors represented by two reaction coordinates including (a) ψ_6 and C_6 and (b) ψ_6 and R_g to visualize how global order emerges from local order and during condensation. Ten trajectories following quenches to $V^* = 0.57$ with time represented by a 256-color scale (inset scale bar) for (c) (ψ_6, $\langle C_6 \rangle$) and (d) (ψ_6, R_g) reaction coordinate pairs with inset plots of single trajectories from Fig. 1e.

is important to note that it was necessary to include concentration dependent, but not configuration dependent, hydrodynamic interactions in the BD simulations to produce agreement with experiments. In particular, Stokesian Dynamic simulations[31] were used to show that approximate local, concentration dependent hydrodynamic interactions were sufficient to match experiments without the need to consider multi-body, configuration dependent hydrodynamic interactions. This finding indicates local microstructure or morphology do not obviously influence the hydrodynamic interactions involved in the colloidal crystal grain boundary dynamics observed in our work.

Statistical methods reported in the literature[23], and further developed by us for application to colloidal assembly[32], were used to analyze large numbers of BD simulated trajectories to construct $W(\mathbf{x})$ and $\mathbf{D}(\mathbf{x})$ (see more details in Supplementary Methods and our previous work[29,32]). In brief, the displacement and mean squared displacement of reaction coordinate vs. time trajectories can be used to measure drift and diffusion at each value of $\mathbf{x}$, which ultimately yield $W(\mathbf{x})$ and $\mathbf{D}(\mathbf{x})$.To assess the quantitative accuracy of candidate low-dimensional dynamic models, we compared first passage time distributions for ensembles of trajectories between different starting and ending states from particle-scale BD simulations and low-dimensional Langevin dynamic (LDLD) simulations. The LDLD simulations are based on a Langevin equation given as,

$$\mathbf{x}(t+\Delta t) = \mathbf{x}(t) - \mathbf{D}[\mathbf{x}(t)]\cdot(kT)^{-1}\nabla W[\mathbf{x}(t)]\Delta t + \nabla\cdot\mathbf{D}[\mathbf{x}(t)] + [2\mathbf{D}[\mathbf{x}(t)]\Delta t]^{1/2}\Gamma(t) \quad (2)$$

where the coefficients are the same as in Eq. (1), Δt is the integration time step, and $\Gamma(t)$ is a noise variable. A successful LDLD model will accurately reproduce first passage time distributions obtained from high $2N$-dimensional particle-scale BD simulations, and hence the experimental trajectories that were quantitatively matched to the BD simulations.

The only quantitatively accurate model to emerge from candidate 1D and 2D models was one based on (ψ_6, R_g) (so higher dimensional models were not considered). Fig. 3a shows the $W(\mathbf{x})$ that quantifies the relative free energy of every configuration and the free energy gradients that drive motion. The global free energy minimum at $\mathbf{x} = (\psi_6, R_g) \approx (0.8, 1.14)$ indicates a single domain crystal (with a thin fluid envelope at its periphery) is the thermodynamically favored configuration (image VI in Fig. 3c).

The diffusivity landscape, $\mathbf{D}(\mathbf{x})$, in Eqs. (1) and (2) is a 2×2 tensor; it has diagonal components that capture how friction/mobil-

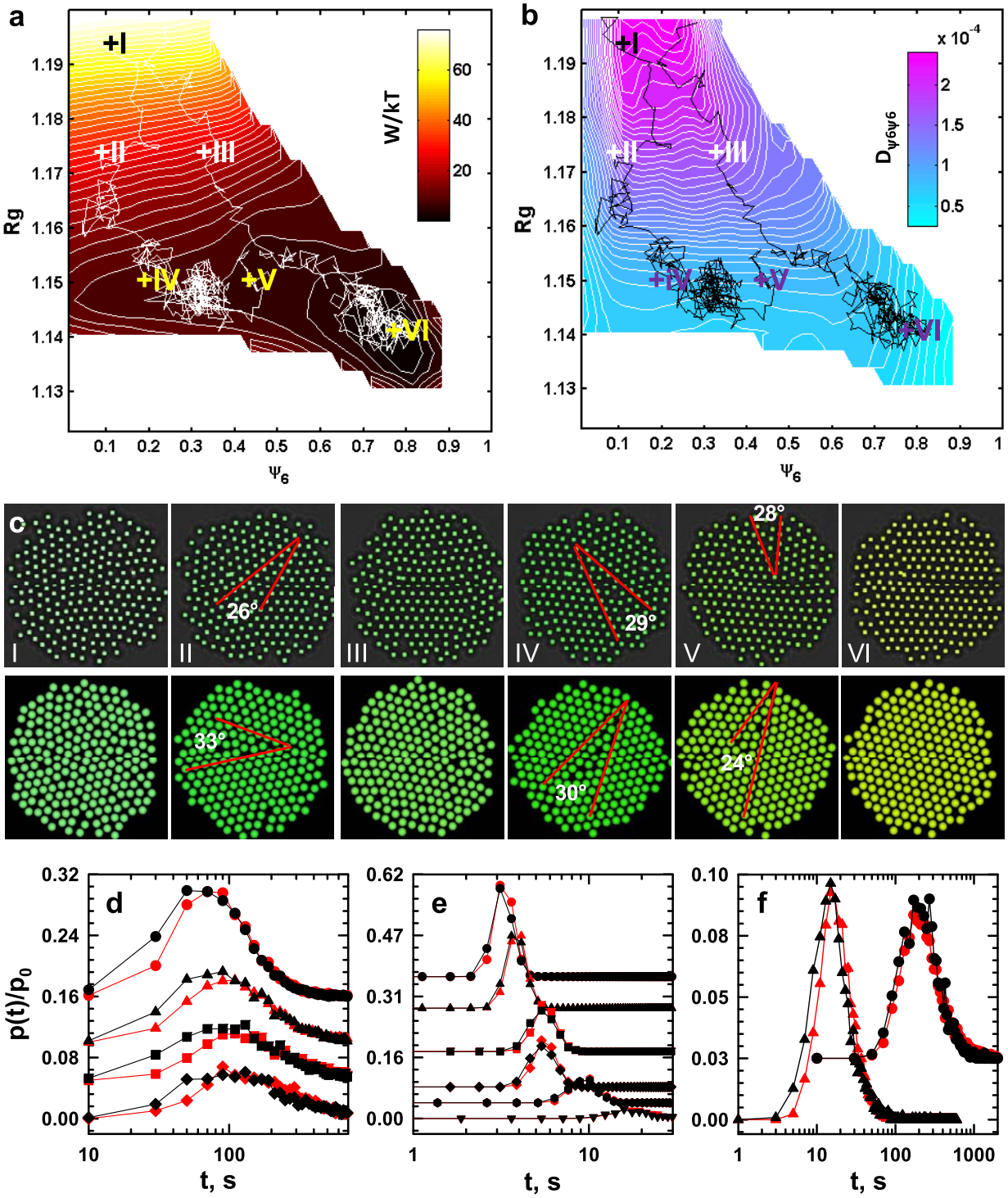

Figure 3 | Free energy and friction landscapes obtained by fitting trajectories to Smoluchowski equation (equation 1) that quantitatively capture grain boundary diffusion and migration vs. relative domain sizes and misorientation angles. (a) $W(\psi_6, R_g)/kT$ with inset scale bar and two trajectories obtained from the experiments in Figs. 1 and 2. (b) $D_{\psi 6\psi 6}/(kT{\cdot}s)$ with inset scale bar with the same trajectories as in (a). (c) Representative configurations from microscopy images and simulated renderings for coordinates marked along trajectories in (a) and (b). Labeled misorientation angles shown by red lines and particle centers are colored according to the RGB composite convention in Fig. 2. First passage time distributions for BD (red) and LDLD (black) trajectories projected onto (d) the ψ_6-axis between 0.47–0.66 (●,●), 0.38–0.56 (▲,▲), 0.28–0.47 (■,■), 0.19–0.38 (◆,◆) and (e) R_g-axis between 1.27–1.25 (●,●),1.25–1.23(▲,▲), 1.23–1.21 (■,■), 1.21–1.19 (◆,◆), 1.21–1.19 (⬢,⬢), 1.19–1.17 (▼,▼), and (f) for trajectories between a sink at (ψ_6 = 0.8 R_g = 1.14) (*i.e.*, global minimum) and sources at (ψ_6 = 0.38 R_g = 1.15) (●,●) and (ψ_6 = 0.65 R_g = 1.16) (▲,▲).

ity in each reaction coordinate mediate drift due to free energy gradients in the same coordinate ($D_{\psi 6\psi 6}$, D_{RgRg}), and cross-terms that capture how friction/mobility mediate drift due to free energy gradients in orthogonal coordinates ($D_{\psi 6Rg}$, $D_{Rg\psi 6}$). Fig. 3b shows $D_{\psi 6\psi 6}/kT$, which captures how friction mediates drift and diffusion in ψ_6 due to free energy gradients in ψ_6. The other components of $\mathbf{D}(\mathbf{x})$ are reported in Supplementary Fig. 5. D_{RgRg} shares similar features with $D_{\psi 6\psi 6}$. The cross-terms ($D_{\psi 6Rg}$, $D_{Rg\psi 6}$) indicate a weak

coupling between driving forces and drift/diffusion (*i.e.*, friction increases as free energy increases) along orthogonal coordinates for $\psi_6 \gtrsim 0.5$, although this is relatively minor compared to the diagonal terms.

Representative configurations (Fig. 3c) and first passage time distributions (Fig. 3d–f) show the resulting low dimensional ψ_6, R_g model quantitatively captures the measured grain boundary dynamics. The agreement between the BD and LDLD simulations is excellent (Fig. 3d–f), demonstrating that Eqs. (1) and (2) with the $W(\psi_6, R_g)$ and $\mathbf{D}(\psi_6, R_g)$ in Fig. 3 provide accurate low dimensional dynamic models of the experiments in Figs. 1 and 2.

Discussion

To aid discussion of how features on $W(\psi_6, R_g)$ and $\mathbf{D}(\psi_6, R_g)$ are connected to microscopic mechanisms, two limiting trajectories are shown on these landscapes; one where a grain boundary forms between two domains and does not move out of the crystal on the ~10 min observation time [trajectory 1 (T1): I–II–IV–V], and one where two domains form but the grain boundary quickly moves to the crystal periphery in <1 min to produce a single domain crystal [trajectory (T2): I–III–VI]. Both trajectories are consistent with expectations by showing drift (*i.e.*, migration) along free energy gradients and superimposed stochastic motion (*i.e.*, diffusion) that is most evident where free energy gradients are minimal. The dramatic difference between these two trajectories is most evident as they approach the global minimum (Fig. 3f) (as quantified between "sources" at III and IV and a "sink" at VI). An order of magnitude difference is observed in the most probable first passage times with ~20 s for III–VI and ~200 s for IV–VI; the latter distribution also shows a much longer asymmetric tail with some trajectories taking >1,000 s to traverse the $W(\psi_6, R_g)$ plateau at low R_g.

The T1 trajectory corresponds to rapid condensation along a steep free energy gradient where two locally ordered domains coalesce into a bicrystal with a near maximum 30° misorientation angle. At point IV on T1, the grain boundary randomly diffuses on a free energy plateau with a minimal free-energy gradient (*i.e.*, driving force) to drive migration of the grain boundary to the crystal edge; the trajectory is localized between IV–V for ~10 min. In addition to vanishing free energy gradients, the friction in the vicinity of IV–V is increased ~6× compared to uncondensed states. Multi-body hydrodynamic interactions (*i.e.*, near-field lubrication and far-field flow within the particle structure[33]) increase particle-scale friction during condensation, which is consistent with the increased friction for trajectories at low R_g on $\mathbf{D}(\psi_6, R_g)$ (Fig. 3b). Although first passage times vary linearly with frictional changes compared to an exponential dependence for free energy changes[34,35], diffusion mediated by friction is the rate determining process in the presence of vanishing free energy gradients (plateau of Fig. 3a).

In contrast to T1, the T2 trajectory is initiated with higher global order before moving down the free energy gradient and rapidly continuing towards the global free energy minimum single crystal. Although T2 passes close to T1, low friction at high R_g allows sufficient diffusion towards higher ψ_6, As a result, T2 bypasses the free energy plateau region at low R_g to avoid slow diffusion like T1, and instead shows much faster grain boundary migration. Friction uniformly increases with decreasing R_g (due to hydrodynamic interactions), and has almost no dependence on ψ_6, so there is no path of least resistance on $\mathbf{D}(\psi_6, R_g)$. In short, the fastest trajectories are ones that bypass the free energy plateau region.

The microscopic mechanisms associated with these different trajectories can be understood from the images/renderings (Fig 3c) and the physical meaning of the reaction coordinates. R_g clearly captures condensation as shown by large free-energy gradients on $W(\psi_6, R_g)$ and increasing resistance to configurational changes on $\mathbf{D}(\psi_6, Rg)$ as the result of multi-body hydrodynamic interactions. At this point, we can speculate why $\langle C_6 \rangle$ was not part of a successful dynamic model; it is an indirect measure of condensation, and thus not as good as R_g, and it is the emergence of global order, captured by ψ_6, that is most important to track grain boundaries.

The ψ_6 dependence of $W(\psi_6, R_g)$ indicates that domains coalescing with minimal misorientation produce higher global order from the outset, which also translates to faster grain boundary migration (*via* free-energy gradients) from the crystal interior to the periphery. Practically, low misorientation angles produce smaller energy barriers to particle-scale motion (in full $2N$-dimensional particle-scale space) within (*e.g.*, string-like motion) and across (*e.g.*, cooperative motion) grain boundaries[36]. In contrast, domains that coalesce near the maximum 30° misorientation display low initial global order that translates into slow grain boundary diffusion on a $W(\psi_6, R_g)$ plateau. Such bicrystals represent an unstable equilibrium where the energy (*e.g.*, energy/atom, interfacial energies)[15] of the two sides balance, however, the lower free energy state single crystal (~10 kT) is achieved by fluctuations that eventually allow one grain to increase at the expense of the other grain decreasing.

Because ψ_6 does not resolve different combinations of domain size and misorientation, but accurately captures the dynamics, it appears that all such configurations relax in an indistinguishable manner. In particular, greater misorientations between dissimilar sized grains produces relaxation rates equivalent to cases where domains have less misorientation but are of similar size. This finding shows how using ψ_6 as a reaction coordinate indicates an aspect of grain boundary motion that would not be easily discovered from tracking particle-scale motion alone. Because grain boundary motion involves many particles rearranging in a cooperative fashion based on relative domain sizes and orientations, it is useful to have a global parameter that captures configurational changes of the entire particle ensemble, and therefore naturally captures cooperative phenomena. Although ψ_6 should be a good reaction coordinate to monitor relaxation of bicrystals of any size (*i.e.*, distinguish two-domain from single-domain crystals), it may be unsuitable for many-domain crystals because it would remain near zero and miss most of the structure evolution until only a few domains remained. In many-domain crystals, it might be more appropriate to capture the evolution of polycrystallinity using a different reaction coordinate, like average domain size or average misorientation angle across grain boundaries.

The approaches used to measure and model grain boundary motion for $V^* = 0.57$ in Figs. 1–3 can be applied at other V^*. Using the same BD simulations and non-equilibrium analyses, $W(\psi_6, R_g)$ were constructed in the range $V^* = 0.31$–0.69 (Fig. 4a–d) along with representative trajectories and global minimum configurations. At the lowest V^*, particles are weakly confined in concentrated fluid configurations without crystal grains or boundaries, which produces a relatively featureless $W(\psi_6, R_g)$. At the highest V^*, $W(\psi_6, R_g)$ is qualitatively similar to Fig. 3a, but the plateau stretches from very low to high ψ_6 with an even shallower gradient and deeper global minimum at $\psi_6 \rightarrow 1$. At intermediate V^*, the $W(\psi_6, R_g)$ show a continuously shifting global minimum towards lower R_g and higher ψ_6 and a stretching plateau corresponding to slower grain boundary migration. $\mathbf{D}(\mathbf{x})$ vs. V^* are not reported here, but the general trend with increasing voltage is a decreasing magnitude (*i.e.*, decreasing mobility, increasing friction), which is consistent with more condensed configurations hindering particle motion and hence motion along both reaction coordinates. In short, with increasing compression, once grain boundaries form, they experience slower migration and diffusion, and the single perfect crystal clearly emerges as the global free energy minimum configuration.

The results show voltage cannot simply be increased to increase order, since in general this produces increasingly arrested polycrystalline states. It is interesting to consider how grain boundary formation and motion might be manipulated by "switching" between $W(\psi_6, R_g)$ at different V^*. If V^* is increased very slowly, it would be possible to remain in the global free energy minimum configuration

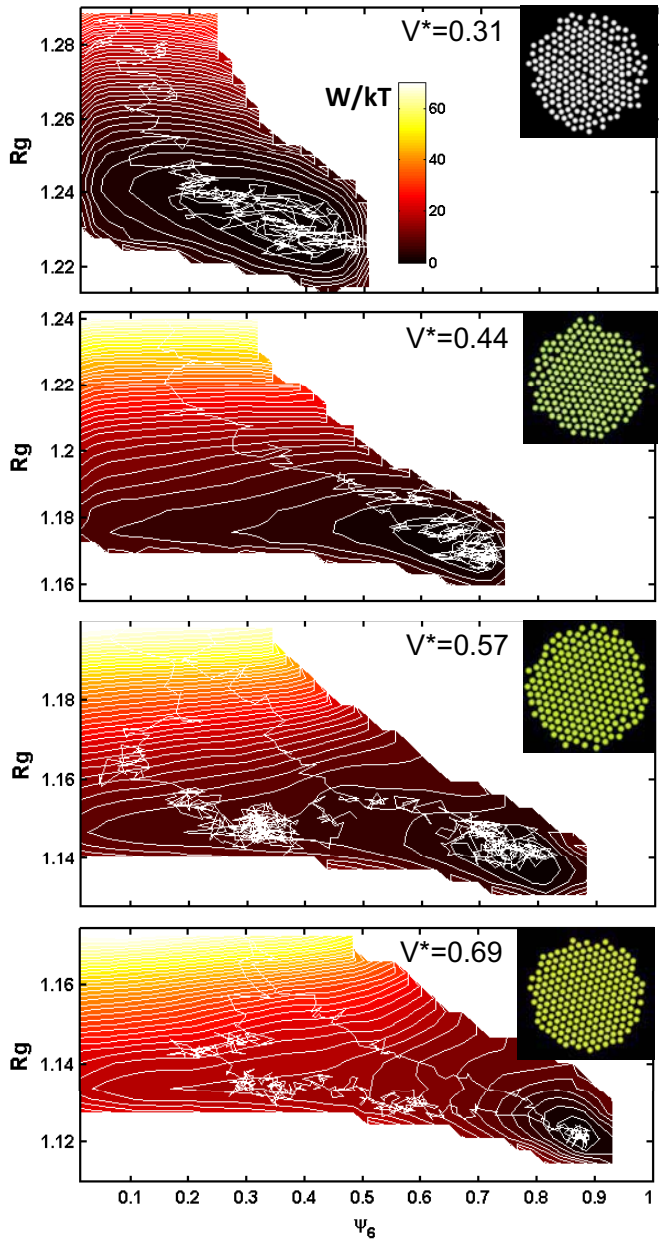

Figure 4 | Free energy landscapes based on ψ_6, R_g reaction coordinate pair capture dynamics at all V* to provide quantitative models of grain boundary formation and motion. $W(\psi_6, R_g)/kT$ at (a) $V^* = 0.31$, (b) $V^* = 0.44$, (c) $V^* = 0.57$, and (d) $V^* = 0.69$ with inset renderings of global minimum configuration and representative trajectories from BD simulations that were matched to the experiments (see Supplementary Methods). The free energy scale is indicated by the inset in (a).

at all voltages; this is the thermodynamic equilibrium limit and a known strategy to make single crystals. However, faster schemes are generally desirable. The optimal control policy[37] to achieve a single perfect crystal in minimal time could employ the quantitative non-equilibrium dynamic models in Eqs. (1) and (2) to switch between $W(\psi_6, R_g)$ at different V^* in an automated, informed manner using feedback control[38]. In particular, monitoring reaction coordinates in real-time could identify slowly relaxing polycrystalline configurations (*i.e.*, due to vanishing free-energy gradients and high friction), and then V^* could be tuned to "land" on another $W(\psi_6, R_g)$ at the same coordinates where faster relaxation occurs.

In summary, we report agreement between optical microscopy measurements, Brownian Dynamic simulations, and low-dimensional models of stochastic grain boundary formation and motion in quasi-2D colloidal bicrystals. Our results show that two reaction coordinates, one for condensation and one for global order, are sufficient to quantitatively capture first passage times between critical configurations at each applied voltage. Free energy and diffusivity landscapes show that the relative misorientation angles and domain sizes formed during condensation determine the subsequent grain boundary motion. Bicrystals with similar sized domains and a near 30° maximum misorientation angle relax *via* slow grain boundary diffusion mediated by high friction and vanishing free energy gradients, whereas bicrystals with asymmetrically sized and/or less misoriented domains relax *via* much faster grain boundary migration due to greater thermodynamic driving forces. By quantifying such dynamics as a function of voltage, ongoing work is developing optimal control algorithms to dynamically tune voltages to avoid kinetic bottlenecks associated with slow grain boundary dynamics.

Future work will extend the modeling approaches developed in this work to understand other mechanisms and defect types involved in colloidal crystal formation/relaxation (*e.g.*, nucleation, growth, point defects, multiple domains, etc.), which will require identification of the minimal number and type of order parameters to accurately capture relevant dynamic processes. Additionally, the role of multi-body, configuration dependent hydrodynamic interactions on diffusivity (friction) landscapes will be explored in attractive particle systems, where changes in near-field interactions during clustering[39] and percolation[40] have previously been shown to have non-trivial dynamic signatures.

Methods

Coplanar gold thin film quadrupole electrodes were patterned on glass microscope coverslips by spin coating photoresist and physical vapor deposition of a 15 nm chromium layer and a 35 nm gold layer. Nominal 3.13 μm diameter SiO_2 colloids with ~50 mV zeta potentials were fractionated in DI water and centrifuged/redispersed five times in 0.1 mM NaOH. PDMS o-rings were coated with vacuum grease and sealed between a coverslip with the patterned quadrupole electrode before it was connected in series with a function generator. Microscopy was performed on an inverted optical microscope with a 63× objective and a 12-bit CCD camera that captured 336 pixel × 256 pixel (81 μm × 62 μm) digital images at rate of 8 frames/s. Video capture and image manipulation were performed using algorithms in MATLAB.

BD simulations in the canonical ensemble were performed for 210 colloidal particles at constant voltage using numerical methods described in previous papers[31,32,40–42]. A 0.1 ms time step was used for at least 2×10^7 steps, and reaction coordinates were stored every 1250 steps for subsequent analysis. Particles in simulations were confined within 2D planes. Inverse Monte Carlo methods (including image resolution limiting effects)[43–45] were used to match measured and simulated radial distribution functions to determine parameters in interactions potentials. The diffusivity was matched by comparing measured and simulated mean square displacements. Parameters used in the BD simulations are reported in the Supplementary Information.

1. Arpin, K. A. *et al.* Multidimensional Architectures for Functional Optical Devices. *Adv. Mater.* **22**, 1084–1101, doi:10.1002/adma.200904096 (2010).
2. Hulliger, J. Chemistry and Crystal Growth. *Angew. Chem. Int. Ed.* **33**, 143–162, doi:10.1002/anie.199401431 (1994).
3. Hammadi, Z. & Veesler, S. New approaches on crystallization under electric fields. *Prog. Biophys. Mol. Biol.* **101**, 38–44, doi:10.1016/j.pbiomolbio.2009.12.005 (2009).
4. Glotzer, S. C. & Solomon, M. J. Anisotropy of building blocks and their assembly into complex structures. *Nat Mater* **6**, 557–562 (2007).
5. Damasceno, P. F., Engel, M. & Glotzer, S. C. Predictive Self-Assembly of Polyhedra into Complex Structures. *Science* **337**, 453–457, doi:10.1126/science.1220869 (2012).
6. Zahn, K., Lenke, R. & Maret, G. Two-Stage Melting of Paramagnetic Colloidal Crystals in Two Dimensions. *Phys. Rev. Lett.* **82**, 2721–2724, doi:10.1103/PhysRevLett.82.2721 (1999).
7. Savage, J. R., Blair, D. W., Levine, A. J., Guyer, R. A. & Dinsmore, A. D. Imaging the Sublimation Dynamics of Colloidal Crystallites. *Science* **314**, 795–798 (2006).
8. Pertsinidis, A. & Ling, X. S. Diffusion of point defects in two-dimensional colloidal crystals. *Nature* **413**, 147–150, doi:10.1038/35093077 (2001).
9. Skinner, T. O. E., Aarts, D. G. A. L. & Dullens, R. P. A. Grain-Boundary Fluctuations in Two-Dimensional Colloidal Crystals. *Phys. Rev. Lett.* **105**, 168301, doi:10.1103/PhysRevLett.105.168301 (2010).

10. de Villeneuve, V. W. A. *et al.* Colloidal Hard-Sphere Crystal Growth Frustrated by Large Spherical Impurities. *Science* **309**, 1231–1233, doi:10.1126/science.1113207 (2005).
11. Nagamanasa, K. H., Gokhale, S., Ganapathy, R. & Sood, A. K. Confined glassy dynamics at grain boundaries in colloidal crystals. *PNAS* **108**, 11323–11326, doi:10.1073/pnas.1101858108 (2011).
12. Alsayed, A. M., Islam, M. F., Zhang, J., Collings, P. J. & Yodh, A. G. Premelting at Defects Within Bulk Colloidal Crystals. *Science* **309**, 1207–1210 (2005).
13. Gokhale, S., Nagamanasa, K. H., Ganapathy, R. & Sood, A. K. Grain growth and grain boundary dynamics in colloidal polycrystals. *Soft Matter* **9**, 6634–6644, doi:10.1039/c3sm50401h (2013).
14. Janssens, K. G. F. *et al.* Computing the mobility of grain boundaries. *Nat Mater* **5**, 124–127 (2006).
15. Thompson, C. V. Structure Evolution During Processing of Polycrystalline Films. *Annu. Rev. Mater. Sci.* **30**, 159–190, doi:10.1146/annurev.matsci.30.1.159 (2000).
16. Bragg, L. & Nye, J. F. A Dynamical Model of a Crystal Structure. *Proc. R. Soc. A* **190**, 474–481, doi:10.1098/rspa.1947.0089 (1947).
17. Kurasch, S. *et al.* Atom-by-Atom Observation of Grain Boundary Migration in Graphene. *Nano Letters* **12**, 3168–3173, doi:10.1021/nl301141g (2012).
18. Juarez, J. J., Mathai, P. P., Liddle, J. A. & Bevan, M. A. Multiple electrokinetic actuators for feedback control of colloidal crystal size. *Lab on a Chip* **12**, 4063–4070 (2012).
19. Edwards, T. D., Beltran-Villegas, D. J. & Bevan, M. A. Size dependent thermodynamics and kinetics in electric field mediated colloidal crystal assembly. *Soft Matter* **9**, 9208–9218, doi:10.1039/c3sm50809a (2013).
20. Juarez, J. J., Cui, J.-Q., Liu, B. G. & Bevan, M. A. kT-Scale Colloidal Interactions in High Frequency Inhomogeneous AC Electric Fields. I. Single Particles. *Langmuir* **27**, 9211–9218, doi:10.1021/la201478y (2011).
21. Juarez, J. J., Liu, B. G., Cui, J.-Q. & Bevan, M. A. kT-Scale Colloidal Interactions in High-Frequency Inhomogeneous AC Electric Fields. II. Concentrated Ensembles. *Langmuir* **27**, 9219–9226, doi:10.1021/la2014804 (2011).
22. Rohrdanz, M. A., Zheng, W. & Clementi, C. Discovering Mountain Passes via Torchlight: Methods for the Definition of Reaction Coordinates and Pathways in Complex Macromolecular Reactions. *Ann. Rev. Phys. Chem.* **64**, 295–316, doi:10.1146/annurev-physchem-040412-110006 (2013).
23. Kopelevich, D. I., Panagiotopoulos, A. Z. & Kevrekidis, I. G. Coarse-grained kinetic computations for rare events: Application to micelle formation. *J. Chem. Phys.* **122**, 044908 (2005).
24. Hummer, G. Position-dependent diffusion coefficients and free energies from Bayesian analysis of equilibrium and replica molecular dynamics simulations. *New J. Phys.* **7**, 34, doi:10.1088/1367-2630/7/1/034 (2005).
25. Fernandes, G. E., Beltran-Villegas, D. J. & Bevan, M. A. Interfacial Colloidal Crystallization via Tunable Hydrogel Depletants. *Langmuir* **24**, 10776–10785, doi:10.1021/la802025d (2008).
26. Nelson, D. R. & Halperin, B. I. Dislocation-mediated melting in two dimensions. *Phys. Rev. B*, 2457–2484, doi:10.1103/PhysRevB.19.2457 (1979).
27. Coifman, R. R., Kevrekidis, I. G., Lafon, S., Maggioni, M. & Nadler, B. Diffusion Maps, Reduction Coordinates, and Low Dimensional Representation of Stochastic Systems. *Multiscale Model. Simul.* **7**, 842–864, doi:10.1137/070696325 (2008).
28. Ferguson, A. L., Panagiotopoulos, A. Z., Debenedetti, P. G. & Kevrekidis, I. G. Systematic determination of order parameters for chain dynamics using diffusion maps. *PNAS* **107**, 13597–13602, doi:10.1073/pnas.1003293107 (2010).
29. Beltran-Villegas, D. J., Sehgal, R. M., Maroudas, D., Ford, D. M. & Bevan, M. A. Colloidal cluster crystallization dynamics. *J. Chem. Phys.* **137**, 134901, doi:10.1063/1.4754870 (2012).
30. Risken, H. *The Fokker-Planck Equation: Methods of Solution and Applications.* Second edn, Vol. 18 (Springer, 1996).
31. Anekal, S. & Bevan, M. A. Self diffusion in sub-monolayer colloidal fluids near a wall. *J. Chem. Phys.* **125**, 034906, doi:10.1063/1.2211616 (2006).
32. Beltran-Villegas, D. J., Sehgal, R. M., Maroudas, D., Ford, D. M. & Bevan, M. A. A Smoluchowski model of crystallization dynamics of small colloidal clusters. *J. Chem. Phys.* **135**, 154506, doi:10.1063/1.3652967 (2011).
33. Brady, J. F. The Long-Time Self-Diffusivity in Concentrated Colloidal Dispersions. *J. Fluid Mech.* **272**, 109–133, doi:10.1017/S0022112094004404 (1994).
34. Hanggi, P. & Talkner, P. Reaction-rate theory: fifty years after Kramers. *Rev. Mod. Phys.* **62**, 251–341, doi:10.1103/RevModPhys.62.251 (1990).
35. Zwanzig, R. Diffusion in a rough potential. *PNAS* **85**, 2029–2030, doi:10.1073/pnas.85.7.2029 (1988).
36. Zhang, H., Srolovitz, D. J., Douglas, J. F. & Warren, J. A. Characterization of atomic motion governing grain boundary migration. *Phys. Rev. B* **74**, 115404, doi:10.1103/PhysRevB.74.115404 (2006).
37. Xue, Y., Beltran-Villegas, D. J., Tang, X., Bevan, M. A. & Grover, M. A. Optimal Design of a Colloidal Self-Assembly Process. *IEEE Trans. Control Sys. Tech.* **PP**, 1–1, doi:10.1109/tcst.2013.2296700 (2014).
38. Juarez, J. J. & Bevan, M. A. Feedback Controlled Colloidal Self-Assembly. *Adv. Funct. Mater.* **22**, 3833–3839, doi:10.1002/adfm.201200400 (2012).
39. Tanaka, H. & Araki, T. Simulation Method of Colloidal Suspensions with Hydrodynamic Interactions: Fluid Particle Dynamics. *Physical Review Letters* **85**, 1338–1341 (2000).
40. Anekal, S. G., Bahukudumbi, P. & Bevan, M. A. Dynamic signature for the equilibrium percolation threshold of attractive colloidal fluids. *Phys. Rev. E* **73**, 020403, doi:10.1103/PhysRevE.73.020403 (2006).
41. Anekal, S. & Bevan, M. A. Interpretation of Conservative Forces from Stokesian Dynamic Simulations of Interfacial and Confined Colloids. *J. Chem. Phys.* **122**, 034903, doi:10.1063/1.1830012 (2005).
42. Beltran-Villegas, D. J., Sehgal, R. M., Maroudas, D., Ford, D. M. & Bevan, M. A. Fokker–Planck Analysis of Separation Dependent Potentials and Diffusion Coefficients in Simulated Microscopy Experiments. *J. Chem. Phys.* **132**, 044707, doi:10.1063/1.3299731 (2010).
43. Wu, H.-J., Pangburn, T. O., Beckham, R. E. & Bevan, M. A. Measurement and Interpretation of Particle-Particle and Particle-Wall Interactions in Levitated Colloidal Ensembles. *Langmuir* **21**, 9879–9888, doi:10.1021/la050671g (2005).
44. Pangburn, T. O. & Bevan, M. A. Role of polydispersity in anomalous interactions in electrostatically levitated colloidal systems. *J. Chem. Phys.* **123**, 174904, doi:10.1063/1.2074887 (2005).
45. Pangburn, T. O. & Bevan, M. A. Anomalous potentials from inverse analyses of interfacial polydisperse attractive colloidal fluids. *J. Chem. Phys.* **124**, 054712, doi:10.1063/1.2162536 (2006).

Acknowledgments

We acknowledge financial support provided by AFOSR (FA9550-12-1-0090), NSF Cyber Enabled Discovery and Innovation grants (CMMI-0835549, CMMI-1124648), NSF unsolicited grants (CBET-0932973, CBET-1234981), and ONR (N000141210134).

Author contributions

T.E. and M.B. designed the experiments and their analysis. T.E. performed and analyzed the experiments. Y.Y., D.B. and M.B. designed the simulations and their analysis. Y.Y. performed and analyzed the simulations. T.E., Y.Y. and M.B. interpreted the data and wrote the manuscript.

Additional information

Supplementary information accompanies this paper at http://www.nature.com/scientificreports

Competing financial interests: The authors declare no competing financial interests.

How to cite this article: Edwards, T.D., Yang, Y., Beltran-Villegas, D.J. & Bevan, M.A. Colloidal crystal grain boundary formation and motion. *Sci. Rep.* **4**, 6132; DOI:10.1038/srep06132 (2014).

Dynamic colloidal assembly pathways via low dimensional models

Yuguang Yang, Raghuram Thyagarajan, David M. Ford, and Michael A. Bevan

Citation: The Journal of Chemical Physics **144**, 204904 (2016); doi: 10.1063/1.4951698
View online: https://doi.org/10.1063/1.4951698
View Table of Contents: http://aip.scitation.org/toc/jcp/144/20
Published by the American Institute of Physics

Dynamic colloidal assembly pathways via low dimensional models

Yuguang Yang,[1] Raghuram Thyagarajan,[2] David M. Ford,[2] and Michael A. Bevan[1,a)]
[1]*Chemical and Biomolecular Engineering, Johns Hopkins University, Baltimore, Maryland 21218, USA*
[2]*Chemical Engineering, University of Massachusetts, Amherst, Massachusetts 01003, USA*

(Received 3 February 2016; accepted 10 May 2016; published online 31 May 2016)

Here we construct a low-dimensional Smoluchowski model for electric field mediated colloidal crystallization using Brownian dynamic simulations, which were previously matched to experiments. Diffusion mapping is used to infer dimensionality and confirm the use of two order parameters, one for degree of condensation and one for global crystallinity. Free energy and diffusivity landscapes are obtained as the coefficients of a low-dimensional Smoluchowski equation to capture the thermodynamics and kinetics of microstructure evolution. The resulting low-dimensional model quantitatively captures the dynamics of different assembly pathways between fluid, polycrystal, and single crystals states, in agreement with the full N-dimensional data as characterized by first passage time distributions. Numerical solution of the low-dimensional Smoluchowski equation reveals statistical properties of the dynamic evolution of states vs. applied field amplitude and system size. The low-dimensional Smoluchowski equation and associated landscapes calculated here can serve as models for predictive control of electric field mediated assembly of colloidal ensembles into two-dimensional crystalline objects. *Published by AIP Publishing.* [http://dx.doi.org/10.1063/1.4951698]

INTRODUCTION

Self-assembly refers to dynamical processes where predefined components spontaneously organize into ordered structures. Self-assembly is considered as a key bottom-up approach to fabricate novel micro- and nano-scale materials.[1–3] Modeling studies of self-assembly generally focus on predicting the resulting equilibrium or steady-state structures as a function of particle interactions, particle shapes, temperature, and concentration.[4,5] Such equilibrium information is important for yielding design rules for building blocks capable of assembling into complex structures. However, the existence of metastable states, kinetic bottlenecks, and competing pathways during dynamical assembly processes can prevent self-assembling systems from reaching thermodynamically stable states on experimentally accessible time scales.[6,7]

In addition to understanding the thermodynamics of self-assembly, it is beneficial to uncover the underlying driving forces and dynamics governing self-assembly processes. In general, dynamic models should contain information about the existence of metastable states as well as the expected times for transitions between states. Ideally, construction of such dynamic models at different thermodynamic conditions can enable the rational design of optimal kinetic pathways to achieve desired states by performing state-dependent temporal actuation of the system.[8–10] The evolution of stochastic dynamical self-assembling systems can be formulated using, for example, a master equation,[11] Fokker Planck equation,[12] or Smoluchowski equation (SE).[13]

The Smoluchowski equation (SE) is suitable to describe Markovian stochastic processes for thermally equilibrated systems. The SE contains thermodynamic and kinetic information in its coefficients and has been applied to complex systems involving protein folding,[14] colloidal assembly,[15] and micellization.[13] In such complex systems, the SE is usually not parameterized by $3N$ particle coordinates, but instead by low-dimensional coordinates capturing the collective behavior of the system. The procedure to obtain a suitable SE can be briefly described as follows: (1) identifying the dimensionality of the dynamics (*i.e.*, number of slow modes of collective motion) via trajectory analysis (*e.g.*, principal component analysis,[16] diffusion mapping[17,18]), (2) finding a suitable set of coordinates, which are often scalar functions of the $3N$ particle coordinates, to capture the slow modes (usually heuristically chosen based on coarse grained physics), and (3) obtaining coefficients for the SE in the low dimensional coordinates via fitting schemes (e.g., local linear fitting,[19] global Bayesian inference[20]). The SE coefficients include the free energy landscape, W, which reflects free energy differences between different configurations, and the diffusivity landscape (DL), D, which captures the mobility of trajectories in configuration space. The SE solution describes the probability distribution of states as a function of time, thus providing a dynamic statistical model for assembly processes. We have previously applied these tools to develop dynamic models of depletion attraction mediated colloidal cluster crystallization,[15,20] which we applied in subsequent studies focused on optimal control of such systems.[9,10]

In this work, we present a systematic framework for building a low-dimensional model to capture the assembly of finite sized quasi-2D colloidal crystals using Brownian Dynamic (BD) simulations matched to our previous experiments.[21] The experiment involves using an electric field

a)Author to whom correspondence should be addressed. Electronic mail: mabevan@jhu.edu

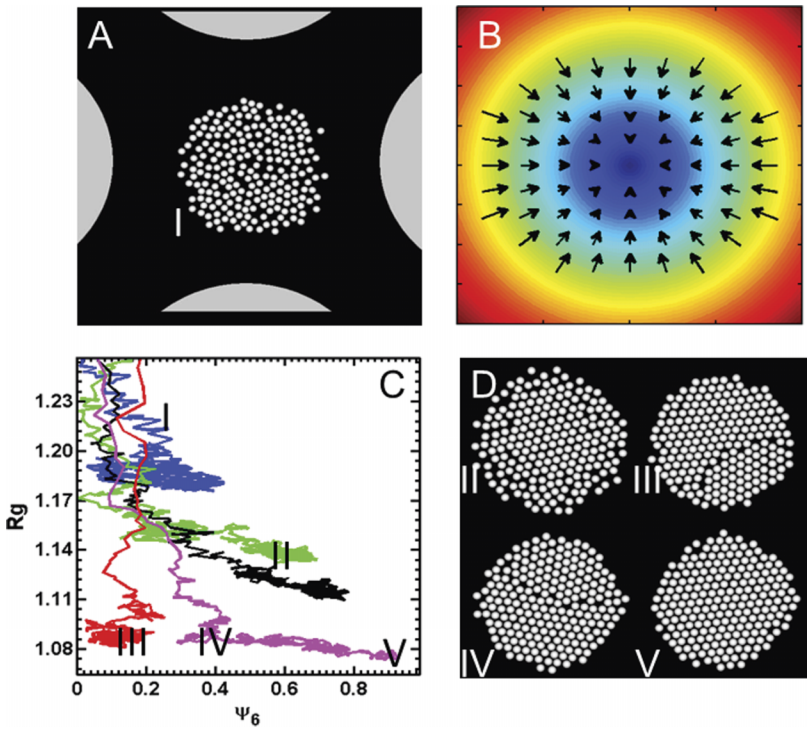

FIG. 1. (a) Top view of simulated experiment of quasi-2D configuration of $N = 210$ colloidal particles ($2a = 3$ μm) compressed within a quadrupolar electrode (with electrode gap of $d_g = 100$ μm). (b) Electric field magnitude contour plot within quadrupole electrode center (Eq. (5)) with arrows indicating relative magnitude and direction of force due to dipole-field interactions (Eqs. (2) and (7)) that concentrates particles in quadrupole center. (c) Typical colloidal assembly trajectories in the order parameter pair (ψ_6, R_g) for a system size of $N = 210$ at voltages of (see definition of nondimensional V^* in Eq. (21) where $V^* = 1$ corresponds to thermodynamic condition for perfect crystal as free energy minimum configuration[21]): $V^* = 0.42$ (blue), $V^* = 0.5$ (green), $V^* = 0.57$ (black), $V^* = 0.80$ (pink), and $V^* = 0.80$ (red). Representative states in part (c) are marked as (rendered in part (d) with exceptions noted): I (initial fluid state, part (a)), II (crystal configuration coexisting with peripheral fluid particles), III (low order bicrystal), IV (higher order bicrystal), and V (single crystal with a few particles still experiencing thermal motion at crystal periphery).

to compress colloids in the center of a quadrupole (Fig. 1). This simple assembly problem demonstrates the basic features of competing pathways, metastable states, and relaxation from metastable state, and we have quantified the interaction potentials,[22–24] system size dependent thermodynamics and kinetics,[21] and grain boundary formation.[7] As such, it serves as a well characterized and understood test case for a general low-dimensional modeling method. From an application standpoint, it is interesting in its own right for reconfigurable colloidal materials and devices,[25,26] which we have demonstrated in circuit elements,[27] feedback controlled colloidal crystal assembly,[8,28] and in the formation of three dimensional crystals.[29] Assembly trajectories in candidate order parameters (Fig. 1(c)) help to show the general approach investigated in this work, where parameters that quantify condensation and order together capture the relevant states and dynamics as particles move from fluid to polycrystal to single crystal states (Fig. 1(d)). Our results demonstrate the ability to fit a low-dimensional SE to a large number of BD simulations to obtain the W and D coefficients, which we relate to physical states and dynamic processes associated with colloidal crystal assembly vs. applied field amplitude and system size (number of particles). Our modeling efforts in this work include dimensionality reduction, order parameter estimation, model validation, and physical interpretation of the dynamic model.

THEORY

Interaction potentials

In this paper, we model electric field mediated quasi-2D colloidal assembly in a quadrupole electrode using previously measured potentials.[22–24] In brief, colloidal particles interact via electrostatic double layer repulsion, dipole-field potentials, and dipole-dipole potentials. The electrostatic repulsion between particle i and j is given as[30]

$$u_{e,i,j}^{pp}(r_{ij}) = B^{pp}\exp\left[-\kappa\left(r_{ij} - 2a\right)\right], \tag{1}$$

where r_{ij} is center-to-center distance between particles, a is particle radius, and B^{pp} is the pre-factor for pair electrostatic repulsion between colloidal particles.[30] The dipole-field potential for particle i in a spatially varying electric field is given as[23]

$$u_{de,i}^{pf}(\mathbf{r}) = -2kT\lambda f_{cm}^{-1}[E(\mathbf{r}_i)/E_0]^2,$$
$$\lambda = \frac{\pi\varepsilon_m a^3(f_{cm}E_0)^2}{kT}, \tag{2}$$

where $\mathbf{r}_i$ is the position of particle i, k is Boltzmann's constant, T is temperature, f_{cm} is the Clausius-Mossotti factor, λ is a non-dimensional amplitude, ε_m is the medium dielectric constant, $E(\mathbf{r}_i)$ is the local electric field peak magnitude at the particle position, and E_0 is given by

$$E_0 = 8^{-0.5}\left(V_{pp}/d_g\right), \tag{3}$$

where V_{pp} is the peak-to-peak voltage and d_g is the electrode gap. The dipole-dipole interaction potential between particles i and j is given by[24]

$$u_{dd,i,j}^{pp}(\mathbf{r}_{ij}) = -kT\lambda P_2(\cos\theta_{ij})\left(2a/r_{ij}\right)^3[E(\mathbf{r}_i)/E_0]^2, \tag{4}$$

where $P_2(\cos\theta_{ij})$ is the second Legendre polynomial and θ_{ij} is the angle between the line connecting particle centers and the electric field line direction. The electric field in the quadrupole center is approximated as[8,28,29]

$$\left|\frac{E(\mathbf{r}_i)}{E_0}\right| = \frac{4r}{d_g}, \tag{5}$$

where $r = (x^2 + y^2)^{0.5}$, and x and y are Cartesian coordinates with origin at the quadrupole center.

Colloidal particle dynamics

Particle dynamics in quasi-2D configurations near a planar surface are modelled using previously reported methods[31] with several modifications. The equation of motion for Brownian particles is given as[32]

$$\mathbf{r}(t+\Delta t) = \mathbf{r}(t) + \frac{\mathbf{D}^P}{kT}(\mathbf{F}^P + \mathbf{F}^B)\Delta t + \nabla \cdot \mathbf{D}^P \Delta t,$$
$$\langle \mathbf{F}^B \rangle = 0, \qquad \langle \mathbf{F}^B(t_1)(\mathbf{F}^B(t_2))^T \rangle = 2(kT)^2 (\mathbf{D}^P)^{-1} \delta(t_1 - t_2), \tag{6}$$

where $\mathbf{r}$ is the $2N$ dimensional position vector, $\mathbf{F}^B$ is the Brownian force vector, and $\mathbf{F}^P$ is the total conservative force vector and the superscript T denotes transpose. The components of $\mathbf{F}^P$ describing the conservative force acting on particle i are given as

$$\mathbf{F}_i^P = -\nabla_{\mathbf{r}_i}\left[u_{de,i}^{pf} + \sum_{j\neq i}\left(u_{e,i,j}^{pp} + u_{dd,i,j}^{pp}\right)\right] \tag{7}$$

and $\mathbf{D}^P$ is the diffusivity tensor, related to grand resistance tensor $\mathbf{R}^P$ via Stokes-Einstein relation $\mathbf{D}^P = kT(\mathbf{R}^P)^{-1}$, where $\mathbf{R}^P$ is given by[33]

$$\mathbf{R}^P = (\mathbf{M}^\infty)^{-1} + \mathbf{R}_{2B} - \mathbf{R}_{2B}^\infty, \tag{8}$$

which includes pair-wise lubrication interactions, $\mathbf{R}_{2B}$, and many-bodied far-field interactions, $(\mathbf{M}^\infty)^{-1} - \mathbf{R}_{2B}^\infty$, above a no-slip plane.[34,35]

Diffusion mapping

From a set of particle configurations (*i.e.*, snapshots), we compute a Markov probability matrix, $\mathbf{M}$, whose elements $\mathbf{M}_{ij}$ are a measure of the probability of hopping between the snapshots i and j. We denote each snapshot as a set X composed of the coordinate vectors of all particles (*i.e.*, $X = (\mathbf{r}_1, \mathbf{r}_2, \ldots, \mathbf{r}_N)$). To construct $\mathbf{M}$, a measure of the distance between snapshots is required that resides in a $2N$ dimensional space. First, it is necessary to calculate a distance matrix, $\mathbf{\Delta}$, whose elements $\mathbf{\Delta}_{ij}$ are the distance metric between two snapshots X_i and X_j. In this work, the distance metric is a weighted combination of the Hausdorff distance matrix, $\mathbf{H}$,[20] and a local orientation distance matrix, $\mathbf{O}$, given as

$$\begin{aligned}
\Delta_{ij} &= \left[\left(\mathbf{H}_{ij}/\|\mathbf{H}\|_F\right)^2 + \left(\mathbf{O}_{ij}/\|\mathbf{O}\|_F\right)^2\right]^{0.5},\\
\mathbf{H}_{ij} &= \max_{\mathbf{r}_m \in X_i}\min_{\mathbf{r}_n \in X_j}\|\mathbf{r}_m - \mathbf{r}_n\|_2,\\
\mathbf{O}_{ij} &= \min_{\theta_t}\left\|h_i(\theta) - h_j(\theta + \theta_t)\right\|_2,
\end{aligned} \tag{9}$$

where $\|\cdot\|_F$ denotes the Frobenius norm, and $h_i(\theta)$ is the normalized bonding angle histogram for snapshot i, where θ_t is the offset in order to achieve the global optimal alignment. The geometric average of H and O is motivated by considering the norm of a two-component vector. Hausdorff distance is the greatest of all distances from a particle in one snapshot to the closest particle in another snapshot and has been used previously in systems of unlabeled particles.[18,20] The bonding angle is the angle of the vector $(\mathbf{r}_i - \mathbf{r}_j)$ joining neighboring particles i, j with respect to the x-axis. We then define the kernel matrix using $\mathbf{K}_{ij} = \exp(-\mathbf{\Delta}_{ij}{}^2/2\varepsilon^2)$, with ε being the parameter that sets the correlation length in the system. The parameter ε is chosen using a technique outlined elsewhere.[36,37] Each row of the kernel matrix $\mathbf{K}$ is normalized to obtain $\mathbf{M}$ as

$$\mathbf{M}_{ij} = \frac{\mathbf{K}_{ij}}{\sum_j \mathbf{K}_{ij}}, \tag{10}$$

where the solution of the right eigenvalue problem,

$$\mathbf{M}\nu = \lambda\nu, \tag{11}$$

produces an eigenvalue spectrum, λ_n, and corresponding set of eigenvectors, ν. The eigenvalue spectrum provides insight into the number of dimensions required to describe the process dynamics. The corresponding eigenvectors provide a low dimensional embedding of the $2N$ dimensional configurations in the data set. In this work, the eigenvectors are not used directly as order parameters but are correlated against candidate coarse variables to identify a suitable set of order parameters.

Order parameters

Following procedures similar to our previous study,[20] here we define two order parameters, R_g and ψ_6, as order parameters ultimately to be employed in a low-dimensional dynamic model (in the section titled "Results and Discussion," we provide justification for their use based on diffusion mapping). The degree of condensation of colloidal particles is captured using the radius of gyration, R_g, which is given as

$$R_g = 0.5N^{-1}\left[\sum\left\|\mathbf{r}_i - \mathbf{r}_j\right\|_2^2\right]^{0.5}/R_{g,HEX} \tag{12}$$

which is a measure of the root mean square distance between particles within an ensemble normalized by a factor $R_{g,\mathrm{HEX}}$. This factor is the radius of gyration for 2D HCP (hexagonal closed packing) particles within regular polygon morphologies given by[8]

$$R_{g,HEX} = 5^{0.5}3^{-1}aN^{0.5}, \tag{13}$$

where a is the particle radius and N is the particle number in the system. The degree of global orientational order in particle configurations was obtained from particle coordinates using[38]

$$\psi_{6,j} = \frac{1}{N_{C,j}}\sum_{k=1}^{N_{C,j}} e^{i6\theta_{jk}}, \tag{14}$$

$$\psi_6 = \frac{1}{N}\left|\sum_j^N \psi_{6,j}\right|, \tag{15}$$

where $\psi_{6,j}$ is the local six-fold bond orientation order parameter of particle j, $N_{C,j}$ is the number of neighbors within the first $g(r)$ peak (coordination radius) of particle j, θ_{jk} is the angle between particle j and each neighboring particle with an arbitrary reference direction, and ψ_6 is the global bond orientation order determined by averaging over all particles, which produces values between 0 for disordered fluids and perfect bicrystals (*i.e.*, crystal with equal sized domains misoriented by 30°) and 1 for defect-free, single domain hexagonal packed lattices.

Low-dimensional Smoluchowski and Langevin equations

Colloidal assembly trajectories are modeled using a low-dimensional Smoluchowski Equation (SE) parameterized by order parameter coordinates given as[7,15,20]

$$\frac{\partial p(\mathbf{x},t)}{\partial t} = \nabla \cdot \mathbf{D}(\mathbf{x}) \cdot \left[(kT)^{-1}\nabla W(\mathbf{x}) + \nabla\right] p(\mathbf{x},t), \tag{16}$$

where $p(\mathbf{x},t|\,\mathbf{x}_0,0)$ is the probability density for system to be at a state characterized by the coordinate $\mathbf{x} = (\psi_6, R_g)$ at time t given that the system starts at $\mathbf{x}_0$ at $t = 0$. The coefficient, $\mathbf{D}(\mathbf{x})$, which is a symmetric tensor, is the diffusivity landscape (DL) consisting of two diagonal terms $D_{\psi 6\psi 6}$, D_{RgRg}, and two off-diagonal terms $D_{\psi 6 Rg}$ and $D_{Rg\psi 6}$. The coefficient $W(\mathbf{x})$ is the free energy landscape (W), which captures the free energy of every configuration based on its coordinate $\mathbf{x} = (\psi_6, R_g)$. The SE describes the probability density evolution in the order parameter space, given the initial probability distribution. The evolution is determined by the right hand side propagator, which contains $\mathbf{D}(\mathbf{x})$ and $W(\mathbf{x})$ that dictate the kinetic and thermodynamic aspects of the system. Our assumption implies that the stationary distribution from Eq. (16) is the thermodynamic equilibrium probability distribution $p(\mathbf{x}) = \exp[-W(\mathbf{x})/kT]$, which can be obtained by setting the right-hand-side to be zero.

The coefficients $\mathbf{D}(\mathbf{x})$ and $W(\mathbf{x})$ in Eq. (16) can be extracted from assembly trajectories using a linear fitting procedure.[7,15,20] In brief, the initial slope of the mean displacement vs. time and mean displacement variance vs. time (*i.e.*, mean squared displacement, covariance matrix) at each local coordinate can be used to evaluate drift, $\mathbf{v}(\mathbf{x})$, and diffusivity tensor, $\mathbf{D}(\mathbf{x})$, as

$$\begin{aligned}\mathbf{v}_i(\mathbf{x}) &= \frac{\partial \mu_i}{\partial \Delta t} = \lim_{\Delta t\to 0}\frac{1}{\Delta t}\left\langle(\boldsymbol{\chi}(t+\Delta t) - \boldsymbol{\chi}(t))_i\right\rangle_{\boldsymbol{\chi}(t)=\mathbf{x}},\\ \mathbf{D}_{ij}(\mathbf{x}) &= \frac{1}{2}\frac{\partial \sigma_{ij}^2}{\partial \Delta t}\\ &= \lim_{\Delta t\to 0}\frac{1}{2\Delta t}\left\langle(\boldsymbol{\chi}(t+\Delta t) - \boldsymbol{\chi}(t))_i(\boldsymbol{\chi}(t+\Delta t) - \boldsymbol{\chi}(t))_j\right\rangle_{\boldsymbol{\chi}(t)=\mathbf{x}},\end{aligned} \tag{17}$$

where $\boldsymbol{\chi}$ is the instantaneous order parameter coordinate $\mathbf{x}$, and the bracket indicates the average of all trajectories sampling each coordinate. The free energy landscape, $W(\mathbf{x})$, is related to the drift as (by expanding the derivative of Eq. (16) and comparing with the Fokker-Planck equation[12])

$$-\frac{\mathbf{D}}{kT}\cdot\nabla W + \nabla\cdot\mathbf{D} = \mathbf{v}, \tag{18}$$

where the first term on the left has the typical form of mobility coefficient multiplied by the gradient of the energy, and the second term is the noise-induced drift.[12,39] This expression can be integrated to obtain

$$W(\mathbf{x}_2) - W(\mathbf{x}_1) = -kT\int_{\mathbf{x}_1}^{\mathbf{x}_2}(\mathbf{D})^{-1}\cdot(\mathbf{v} - \nabla\cdot\mathbf{D}). \tag{19}$$

The coefficients $\mathbf{D}(\mathbf{x})$ and $W(\mathbf{x})$ can also be used to produce a low dimensional Langevin dynamic (LDLD) equation given by

$$\mathbf{x}(t+\Delta t) = \mathbf{x}(t) - \frac{\mathbf{D}}{kT}\cdot\nabla W\Delta t + \nabla\cdot\mathbf{D}\Delta t + \sqrt{2\mathbf{D}\Delta t}\cdot\boldsymbol{\zeta}, \tag{20}$$

where $\boldsymbol{\zeta}$ is a vector of Gaussian random numbers with zero mean and unity variance based on the Ito convention.[40] The LDLD equation can be used to directly generate trajectories in the low-dimensional order parameter space.

METHODS

Brownian and Langevin dynamic simulations

Particle scale dynamics were simulated in the canonical ensemble using Brownian Dynamics (BD) via Eq. (6). In particular, ~2000-4000 BD simulations were performed for different system sizes (N = 110, 210, 300), different applied electric fields, and from many different initial configurations spanning dilute fluid to crystalline states. The initial configurations used to launch simulations were chosen adaptively to ensure that every point in the order parameter space has ~200 samplings to reduce variance in subsequent analyses. This single large set of BD simulations was used for extracting SE coefficients (Figs. 3, 4, and 7) and first passage time characterization (Fig. 5). Simulation parameters are reported in Table I. The electric field in each simulation is computed via Eq. (3) using voltages normalized as

$$V^* = V_{pp}/V_{xtal}, \tag{21}$$

$$\begin{aligned}V_{xtal} &= a_0 N^{-b_0},\\ a_0 &= 7.15 + 4.10\cdot 10^{-3}\kappa^{-1},\\ b_0 &= 0.219 + 4.24\cdot 10^{-4}\kappa^{-1},\end{aligned} \tag{22}$$

where V_{pp} is the peak-to-peak applied voltage, and V_{xtal} is the lowest voltage to crystalize all particles based on system size and Debye length, κ^{-1}, as reported in our previous work.[21] For each simulation, a 0.1 ms integration time step was used for at least 1.5×10^7 steps (so that each simulation reaches equilibrium). Particle coordinates were stored every 125 ms for calculation of ψ_6 and R_g. Particles in BD simulations were fixed within a 2D plane. To reduce computational cost in the BD simulations, hydrodynamic interactions were approximated by the diagonal elements of $\mathbf{D}^P$ computed using Eq. (8), which were parameterized in a look-up table vs. the configuration R_g and the distance of particle i to the configuration center of mass (see previous work for details[7]). Low Dimensional Langevin Dynamics (LDLD) for the first passage time characterization (Fig. 5) were simulated via the equation of motion in Eq. (20) using the $W(\mathbf{x})$ and $\mathbf{D}(\mathbf{x})$ obtained from Eqs. (17) and (19) using an integration time step of Δt = 0.125 s.

Diffusion mapping

For the diffusion mapping analysis, a large number of configurations (snapshots) were generated using BD simulations for a system size of N = 210 with V^* = 0.80. The data set contained ~8000 configurations covering all of configuration space including fluid, polycrystalline, and crystalline states. Each configuration snapshot in the data set was processed to remove the translational degrees of freedom by setting the configuration origin as the center-of-mass as

TABLE I. Parameters for simulations of colloidal particles in a quadrupole electrode.

Variable	Value
N[a]	110, 210, 300
a (nm)[b]	1400
κ^{-1} (nm)[c]	10
B^{pp} (kT)[d]	3206
f_{cm}[e]	−0.4667
$\varepsilon_m/\varepsilon_0$[f]	78
d_g (μm)[g]	100
T (°C)[h]	20
$R_{g,HEX}$ (nm)[i]	15 122 ($N = 210$); 10 944 ($N = 110$); 18 074 ($N = 300$)
V_{xtal} (V)[j]	1.89 ($N = 210$); 2.71 ($N = 110$); 1.43 ($N = 300$)
V (V)[k]	0.8, 0.94, 1.07, 1.51 ($N = 210$); 2.3 ($N = 110$); 1.07 ($N = 300$)
V^* (V)[l]	(0.42, 0.5, 0.57, 0.80) ($N = 210$); 0.85 ($N = 110$); 0.75 ($N = 300$)
λ[m]	2.5, 3.5, 4.5, 9 ($N = 210$); 21 ($N = 110$); 4.5 ($N = 300$)

[a]Number of particles.
[b]Particle size.
[c]Debye screening length.
[d]Electrostatic potential pre-factor.
[e]Clausius-Mossotti factor for 1 MHz AC field.
[f]Medium permittivity.
[g]Electrode spacing.
[h]Temperature.
[i]Radius of gyration for 2D HCP particles within regular hexagon morphologies.
[j]Lowest voltage to crystallize system.
[k]Applied voltage.
[l]Normalized voltage.
[m]Non-dimensional field strength.

$$\mathbf{r}'_i = \mathbf{r}_i - \bar{\mathbf{r}}, \qquad \bar{\mathbf{r}} = \frac{1}{N}\sum_{i=1}^{N}\mathbf{r}_i, \qquad i = 1,2,\ldots,N, \tag{23}$$

where the translated coordinates form a data matrix, $X = [\mathbf{r}'_1, \mathbf{r}'_2, \ldots, \mathbf{r}'_N]$, which can be used to find the eigenvector $\mathbf{n}_1$ of matrix with the largest magnitude XX^T as principle angle with the x-axis as $\theta = \cos^{-1}(\mathbf{n}_1 \cdot \mathbf{e}_1)$. This angle is used to remove rotational degrees of freedom using a rotational transformation given as

$$\mathbf{r}''_i = \begin{pmatrix} \cos(\theta) & \sin(\theta) \\ -\sin(\theta) & \cos(\theta) \end{pmatrix} \mathbf{r}'_i, \tag{24}$$

where the position vectors $\mathbf{r}''$ is used as the input to the diffusion mapping analysis, so as to not include dynamics in these additional degrees of freedom, but instead capture microstructural dynamic processes. The bonding angle histogram is discretized into 128 bins from $-\pi$ to π.

Smoluchowski equation solution

The coefficients $\mathbf{D}(\mathbf{x})$ and $W(\mathbf{x})$ in Eq. (16) can be extracted from assembly trajectories using the linear fitting procedure[7,15,20] described in Eqs. (17)-(19). In this work, R_g and ψ_6 coordinates are discretized with a resolution of 0.0032 and 0.025. After the coefficients are obtained, the resulting SE (Eq. (16)) can be numerically solved to obtain the probability evolution $p(\mathbf{x}, \Delta t \,|\, \mathbf{x}_0, 0)$ at different observation times, Δt, for given initial conditions. In this work, the SE is solved using explicit upwind differentiation for parabolic partial differential equations with zero-flux boundary conditions.[41] The discrete version of Eq. (16) is given as

$$\begin{aligned} p^{n+1}_{i,j} - p^n_{i,j} \approx & \frac{D^{\psi_6}_{i+1,j}p^n_{i+1,j} - 2D^{\psi_6}_{i,j}p^n_{i,j} + D^{\psi_6}_{i-1,j}p^n_{i-1,j}}{(\Delta\psi_6)^2}\Delta t + \frac{D^{R_g}_{i,j+1}p^n_{i,j+1} - 2D^{R_g}_{i,j+1}p^n_{i,j+1} + D^{R_g}_{i,j-1}p^n_{i,j-1}}{(\Delta R_g)^2}\Delta t \\ & + \frac{\mathbf{max}(v^{\psi_6}_{i-1,j}p^n_{i-1,j}, 0) + \mathbf{min}(v^{\psi_6}_{i+1,j}p^n_{i+1,j}, 0) - v^{\psi_6}_{i,j}p^n_{i,j}}{\Delta\psi_6}\Delta t \\ & + \frac{\mathbf{max}(v^{R_g}_{i,j-1}p^n_{i,j-1}, 0) + \mathbf{min}(v^{R_g}_{i,j+1}p^n_{i,j+1}, 0) - v^{R_g}_{i,j}p^n_{i,j}}{\Delta R_g}\Delta t, \end{aligned} \tag{25}$$

where the subscripts indicate order parameter grid points, the superscript, n, on p denotes the time step, the superscript order parameter on v denotes the drift component from Eq. (17), and the superscripts in D denotes the diagonal components in $\mathbf{D}$ from Eq. (17). The off-diagonal components of $\mathbf{D}$ are ignored in this work for simplicity and because they are relatively

small compared to the diagonal terms. One constraint on the set of equations given by Eq. (25) is that the sum of the right-hand-side of all equations must be zero via the conservation of probability. Eq. (25) is discretized with a resolution of $\Delta\psi_6 = 0.032$, $\Delta R_g = 0.0025$, and $\Delta t = 0.01$ s.

First passage time distributions (FPTDs)

To verify the extracted coefficients in Eq. (17), we compare BD (Eq. (6)) and LDLD (Eq. (20)) simulations based on first passage time distributions between different states. These different states are chosen to capture the condensation process (fluid to polycrystal), grain boundary migration process (polycrystal to single domain crystal), as well as the combination of the two (fluid to single domain crystal). The first passage time distributions are constructed by counting the first arrival time to specified ending states of trajectories starting from the same initial state. The same BD trajectory data used to obtain the SE coefficients were used to construct first passage time distributions. For LDLD simulation results, statistics were first collected from 4000 trajectories initiated in fluid and polycrystalline states (from 40 grid points with 100 different random number generator seeds). After initial sampling, another 4000 simulations were performed for states with insufficient sampling. These 8000 dynamic trajectories in low dimensional space via LDLD were used to construct first passage time distributions between different states.

RESULTS AND DISCUSSION

Dimensionality from diffusion mapping

The first step towards building a low dimensional Smoluchowski model is to identify the number and the appropriate choice of order parameters. To this end, we have used a machine learning technique, called diffusion mapping, which identifies the intrinsic manifold of a large data set and provides a suitable low dimensional representation.[18] We have applied the diffusion maps technique to smaller systems in our earlier work to build low dimensional models.[20] In the current implementation of diffusion mapping, we use a new composite distance metric (**Δ**) based in complementary metrics for both condensation (**H**) and ordering (**O**) processes important to colloidal crystallization. We apply the analysis to simulation data that were previously matched to experiments, which enables high spatial and temporal resolution and statistical sampling to avoid some issues[42,43] when working directly with experimental microscopy data (which can be overcome when treated carefully[44]).

Fig. 2 shows results of a diffusion mapping[45] analysis of a large number of Brownian Dynamic (BD) simulations

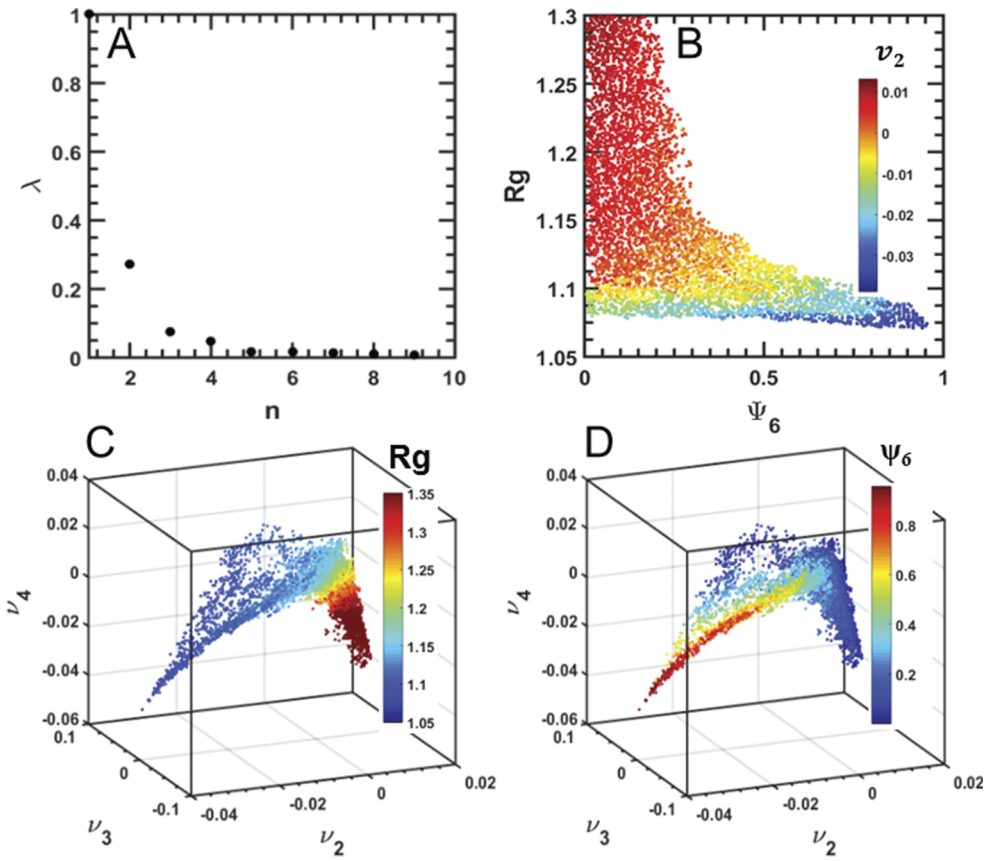

FIG. 2. (a) Eigenvalue spectrum obtained from diffusion mapping (Eqs. (9)-(11)) the process of electric field mediated colloidal assembly in a quadrupole electrode (see Fig. 1) for a system size of $N = 210$ and a non-dimensional applied voltage of $V^* = 0.8$. (b) Plot of ~8000 configurations sampled in BD simulations plotted in (ψ_6, R_g) space and colored by values of first non-trivial eigenvector, ν_2, shows good sampling of final order parameters. Bottom two plots show points indicating values of the top three non-trivial eigenvector coordinates (ν_2, ν_3, ν_4) for the same ~8000 configurations shown in (b) but now colored by their values of (c) the order parameter R_g (Eq. (12)) and (d) the order parameter ψ_6 (Eq. (15)).

of the assembly of $N = 210$ particles into quasi-2D colloidal crystals in a quadrupolar electric field. The BD simulations were matched to experiments in previous work.[7,22–24] Fig. 2(a) shows the eigenvalue spectrum obtained from the diffusion mapping analysis. A large spectral gap after the first non-trivial eigenvalue, λ_2, and smaller gaps after the third and fourth eigenvalues, λ_3 and λ_4, suggest a one-dimensional nature to the data but two additional dimensions need to be considered. When plotting the data in the space of the first three eigenvectors (ν_2, ν_3, and ν_4) (Figs. 2(c) and 2(d)), the data points are seen to lie on a 2D surface in the 3D space, indicating that the dynamical system is effectively two-dimensional and described primarily by the coordinates ν_2 and ν_3. The ν_4 values are highly correlated with the values of ν_2; such dependencies indicate multiple eigenvectors characterizing the same dynamic pathway.[37]

We also studied how the eigenvectors correlate with physically meaningful candidate order parameters[7,9,15,20,21,46–48] by coloring the data in Fig. 2. Although eigenvectors from diffusion mapping can be used directly as order parameters[49] or for high-throughput screening of candidate order parameters,[50,51] such methods are computationally expensive and were not explored in this work. Fig. 2(c) shows the data colored by values of R_g. R_g is highly correlated with ν_2, as indicated by the continuous spectrum of color vs. that coordinate. Fig. 2(d) shows the data colored by values of ψ_6. It is found that ψ_6 is highly correlated with a combination of ν_2 and ν_3. The data points plotted in (ψ_6, R_g) space in Fig. 2(b) show that the data span the regions of interest in the configuration space (based on the candidate order parameters) and are well correlated with the top non-trivial eigenvector, ν_2. Therefore, it appears that R_g and ψ_6 are able to parameterize data embedded in the 2 significant coordinates identified by the diffusion mapping analysis. We will use these variables to build a low dimensional model of quasi-2D colloidal crystallization in electric fields.

Smoluchowski analysis of assembly trajectories

Fig. 3 shows examples of dynamic quantities obtained by analyzing a large set of ψ_6, R_g coordinates generated from BD simulated trajectories. Results in Fig. 3 are for $N = 210$ particles with the following combinations of starting coordinates and applied non-dimensional voltages: $(\psi_6, R_g) = (0.138, 1.15)$, $V^* = 0.80$ (example of fluid condensation); $(\psi_6, R_g) = (0.3875, 1.146)$, $V^* = 0.57$ (example of grain boundary motion); and $(\psi_6, R_g) = (0.7125, 1.125)$, $V^* = 0.5$ (example of melting). Figs. 3(a) and 3(b) show the ensemble average of displacement vs. time for each starting coordinate. Positive slopes indicate the existence of driving force to increase ψ_6 (*i.e.*, ordering) or R_g (*i.e.*, expansion), whereas negative slopes indicate driving forces to decrease these quantities. The steepness of the slope characterizes the magnitude of the driving force (*i.e.*, Eqs. (17)-(19)). The slopes of each curve are qualitatively consistent with expectations for condensation ($\Delta\psi_6 \uparrow, \Delta R_g \downarrow$) and melting ($\Delta\psi_6 \downarrow, \Delta R_g \uparrow$), and the shallow slope associated with grain boundary motion shows the weak driving force for this process.

Figs. 3(c)-3(f) show the ensemble average of the four components in covariance matrix as a function of time for the same initial coordinates and applied voltage as in Figs. 3(a) and 3(b). As shown in the section titled "Theory" (Eq. (17)),

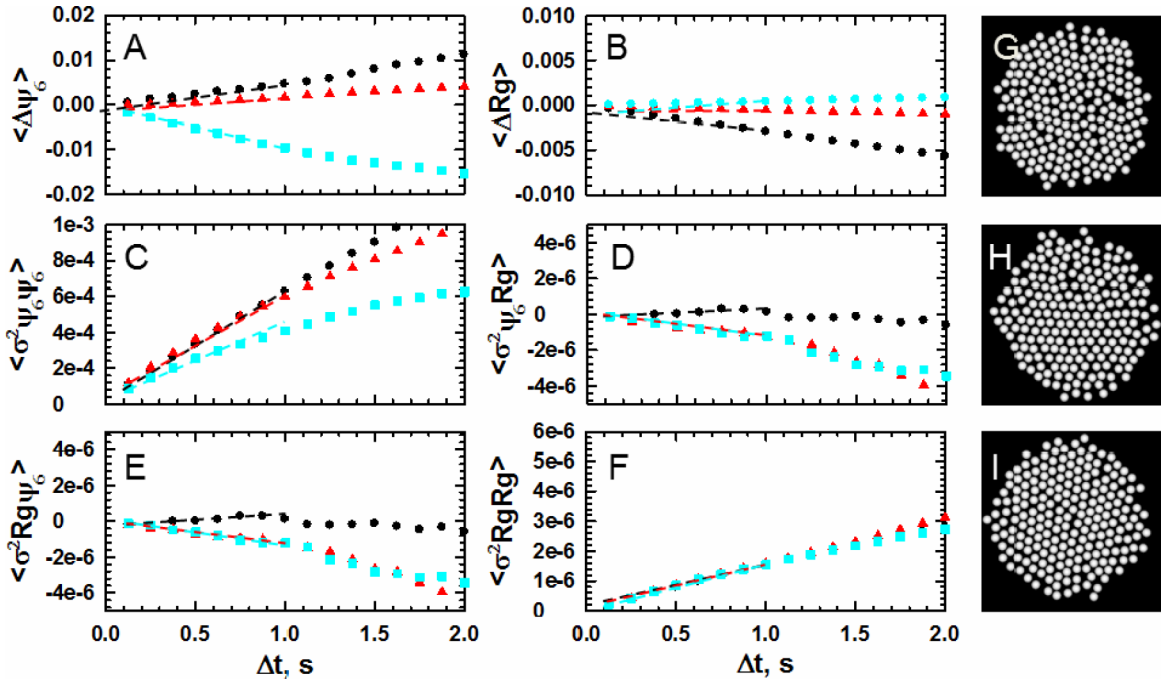

FIG. 3. Representative local order parameter trajectories used to obtain Smoluchowski equation coefficients. Results are shown for a system size of $N = 210$. Plots show ensemble average: displacement vs. time for (a) ψ_6 and (b) R_g; displacement variance vs. time in (c) and (f); displacement covariance in (d) and (e). Representative data are shown for several different combinations of starting configurations and applied voltages including: (g) (black circles) $(\psi_6, R_g) = (0.1375, 1.146) V^* = 0.80$; (h) (red triangles) $(\psi_6, R_g) = (0.3875, 1.146) V^* = 0.57$; (i) (cyan squares) $(\psi_6, R_g) = (0.7125, 1.125) V^* = 0.50$. Linear fits to the initial slopes (illustrated by dashed lines) of the data in each plot are used in Eqs. (17)-(19) to obtain $\mathbf{D}(\mathbf{x})$ and $W(\mathbf{x})$ in Figs. 4 and 7.

the initial slopes are proportional to the magnitude of the four components of the diffusivity tensor of the low-dimensional Smoluchowski equation (Eq. (16)). The cross terms in the diffusivities tensor reflect the coupling between both drift and diffusion along the ψ_6 and R_g coordinates. Deviations of slopes at longer times from the initial short time slopes indicate effects of drift due to the underlying landscape (that can either produce migration or localization of trajectories). Most of the fitted initial slopes via Eq. (17) have relative uncertainties (i.e., the standard value of the fitted value divided by the value itself) on the order of ∼2% or smaller, which cause the resulting free energy landscape via Eq. (19) and propagation of error to have relative uncertainties of ∼4%.

Field dependent landscapes (for fixed system size)

By performing the analysis illustrated in Fig. 3 at many grid points in the order parameter space, it is possible to construct coordinate dependent W and $\mathbf{D}$ (*i.e.*, "landscapes") for fixed thermodynamic conditions. For the example in the present study, the voltage, V, determines the magnitude of the electric field compressing induced dipoles, and therefore acts as a global thermodynamic variable. As such, for each V^*, the relative free energy and diffusivity of each configuration can be determined to construct W and $\mathbf{D}$ for all possible configurations. Fig. 4 shows the landscapes of W and $\mathbf{D}$ for several values of increasing V^* for a system size of $N = 210$.

At the lowest voltage, $V^* = 0.42$ (Fig. 4(a)), the global minimum of W is located at ψ_6, $R_g \approx 0.25, 1.18$; the structure is a dense fluid consisting of several small ordered clusters (rendering I) but lacks global orientational order due to minimal coalescence in the presence of weak compression of dipoles. Fig. 4(a) shows a single example trajectory plotted on W, which illustrates compression of an expanded fluid configuration (*i.e.,* low ψ_6, high R_g) towards the global minimum with a relatively small free energy change (∼15 kT) where it then diffuses locally.

The four diffusivity components are shown in middle column of Fig. 4(a). The $\mathbf{D}_{\psi 6 \psi 6}$ component (upper left) has relatively larger values in the vicinity of $\psi_6 \approx 0.2$-0.3, which is consistent with grain boundary motion in polycrystalline structures that produces larger fluctuations in ψ_6. $\mathbf{D}_{\psi 6 \psi 6}$ decreases only slightly as R_g decreases due to hydrodynamic hindrance in compact configurations. Large regions of the diffusivity landscape cross-terms, $\mathbf{D}_{\psi 6 R g}$ and $\mathbf{D}_{R g \psi 6}$, have values near zero, except for slightly negative values encountered in the vicinity of ψ_6, $R_g \approx (0.4, 1.18)$. These negative values in the cross-terms indicate a weak correlation between decreasing R_g and increasing ψ_6, which is consistent with condensation being correlated with ordering. Given the different relative magnitudes of ψ_6 and R_g, the relative importance of the cross terms can also be interpreted using a correlation coefficients defined as $\rho = \mathbf{D}_{\psi 6 R g}/(\mathbf{D}_{\psi 6 \psi 6}\mathbf{D}_{R g R g})^{0.5}$. In all cases, this correlation coefficients is less than 5%, suggesting very little correlation between R_g and ψ_6 such that the cross terms are negligible. This finding is supported by comparing BD and LDLD simulations with and without the cross terms, which are quantitatively indistinguishable.

As V^* increases to 0.5, the global minimum in W (Fig. 4(b)) shifts to ψ_6, $R_g \approx (0.6, 1.14)$, indicating both increased condensation and global ordering compared to $V^* = 0.42$. The equilibrium structure (rendering III) is characterized has a single central hexagonal close packed core with small number of peripheral fluid-like particles. While the free energy gradient in the R_g coordinate increases when increasing V^* from 0.42 to 0.5, the free energy gradient in the ψ_6 direction is shallow. For example, bi-domain crystals formed in the vicinity of $R_g \approx$ 1.14-1.16, $\psi_6 \approx$ 0-0.3 (*i.e.*, low ψ_6, low R_g) (rendering II) have misorientation angles close to 30°, which are metastable structures with minimal driving force for grain boundary migration. As for the diffusivity landscape at $V^* = 0.5$, $\mathbf{D}_{\psi 6 \psi 6}$ and $\mathbf{D}_{R g R g}$ decrease as R_g become smaller, which is due to the increased hindrance at denser configuration slows down the particle arrangement behavior. At $V^* = 0.57$ (Fig. 4(c)), the global minimum in W now shifts to ψ_6, $R_g \approx (0.6, 1.14)$, with more ordered and condensed equilibrium structure (rendering VI). The diffusivity landscape components share similar features with the other voltages. At this voltage, the free energy plateau region on W (with a minimal free energy gradient) shifts and stretches to coordinates in the range around $R_g \approx$ 1.12-1.13, $\psi_6 \approx$ 0-0.5.

Field dependent assembly pathways

On the landscapes in Fig. 4(c), there are two typical assembly kinetic pathways, as exemplified by the trajectories T1 and T2 plotted on W. The T1 trajectory corresponds to rapid condensation along a steep free energy gradient where two locally ordered domains coalesce into a bi-crystal with a near maximum 30° misorientation angle. From V to VI, the bi-crystal relaxes into a single domain as one grain grows at the expense of the other.

In contrast to T1, the T2 trajectory develops higher global order via initial stochastic motion before it moves down the free energy gradient and is rapidly funneled towards the global free energy minimum. The intermediate microstructure (rendering IV) is typically characterized by domains with similar orientation (*i.e.*, small misorientation angle). Domains with small misorientation angles easily relax during coalescence and condensation, which is consistent with a smaller free energy barrier to grain boundary motion. As a result, T2 is able to bypass the free energy plateau at low R_g to avoid the slow diffusion process encountered in the T1 trajectory, which results in much faster equilibration in the global free energy minimum single crystal. For all voltages, all diffusivity components uniformly decreases with decreasing R_g, so that paths T1 and T2 do not experience significantly different levels of friction as part of determining the total time to produce single perfect crystals.

Assembly pathway times

The low dimensional models based on the landscapes shown in Fig. 4 not only provide qualitative information about the assembly process but also quantitatively capture assembly dynamics. By evaluating statistical properties of trajectories from the full N-dimensional BD simulations

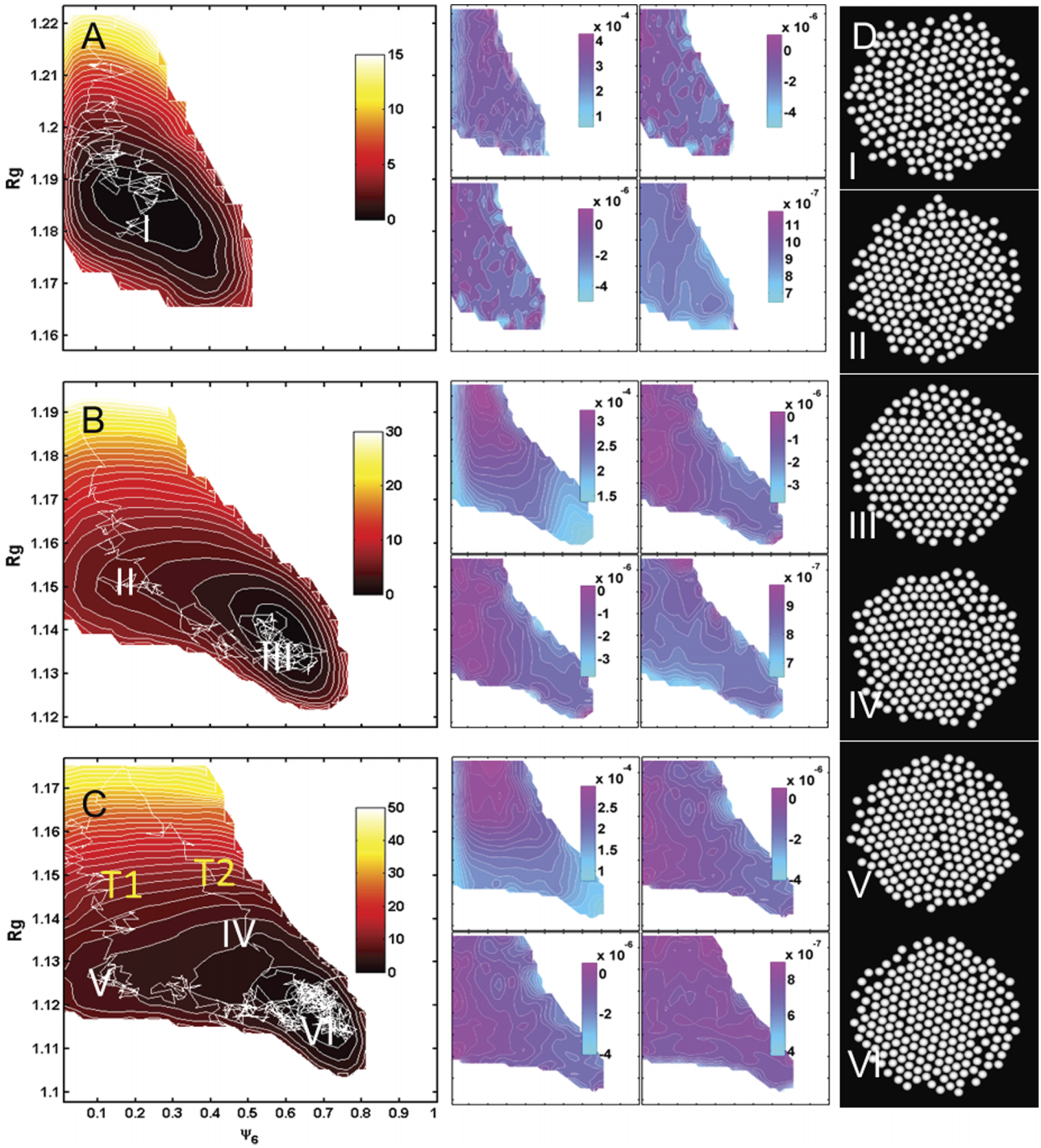

FIG. 4. Free energy and diffusivity landscapes obtained by fitting trajectories to Smoluchowski equation to BD trajectories for $N = 210$ and applied voltages of (top-to-bottom): (a) $V^* = 0.42$, (b) $V^* = 0.50$, (c) $V^* = 0.57$. Plots show (left) free energy landscapes, $W(\psi_6, R_g)/kT$ (Eq. (19)), with trajectories, marked coordinates of interest, and inset scale bars, and (middle) four components of diffusivity tensor, $\mathbf{D}/(kT \cdot s)$ (Eq. (17)), with inset scale bar and same axes as W plots (left-to-right, top-to-bottom): $\mathbf{D}_{\psi 6 \psi 6}$, $\mathbf{D}_{\psi 6 R g}$, $\mathbf{D}_{R g \psi 6}$, and $\mathbf{D}_{R g R g}$. T1 and T2 in the left most column of part (c) denote two representative trajectories following different pathways. (d) Renderings in column on far right show representative configurations for coordinates marked on W plots.

and low-dimensional Langevin dynamic (LDLD) simulations, such as the first passage times for transitions from one state to another state, it is possible to evaluate the accuracy of the LDLD model.[7,20] Fig. 5 compares first passage time distributions from BD and LDLD simulations at $V^* = 0.57$ for $N = 210$. First passage time distributions show histograms of the times it takes to pass for the first time between initial states end states characterized by (ψ_6, R_g) coordinates on the W. The first passage time is a distribution due to the stochastic nature of the assembly dynamics.

As depicted in Fig. 5(a), we simplify the presentation of first passage time distributions by comparing assembly processes characterized by either (1) condensation along the steep W gradient parallel to the R_g axis (plotted in Fig. 5(b)) or (2) grain boundary relaxation along the W plateau parallel to the ψ_6 axis (plotted in Fig. 5(c)). For

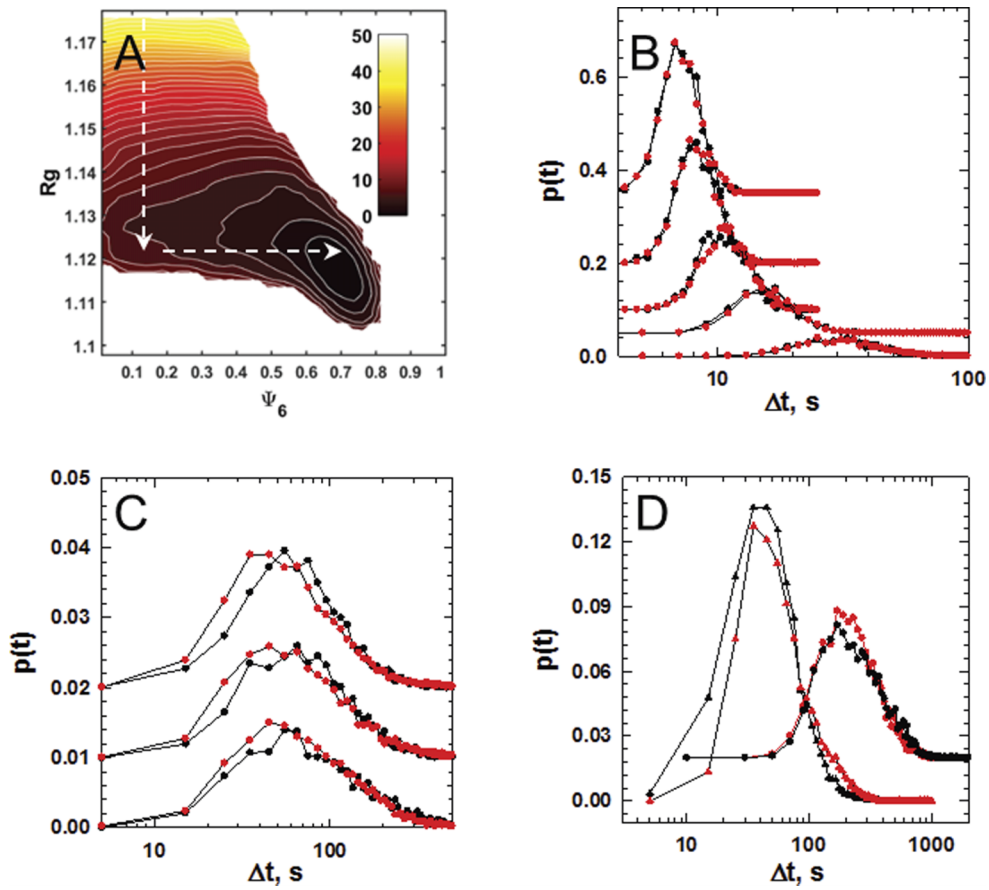

FIG. 5. First passage time distributions (FPTDs) for BD (black) and LDLD (red) trajectories during processes of condensation and grain boundary migration for system size of $N = 210$ at applied voltage of $V^* = 0.57$. (a) Schematics for the process of condensation (vertical arrow along the steep W gradient at R_g direction) and the process of grain boundary migration (horizontal arrow along the W plateau at ψ_6 direction). (b) FPTD during the condensation process measured from trajectories from starting points to end points on the R_g-axis between (top to bottom): (1.24, 1.22), (1.22, 1.20), (1.20, 1.18), (1.18, 1.16), and (1.16, 1.14). (c) FPTD during grain boundary migration process measured by tracking trajectories from starting points to end points on the ψ_6-axis between (top to bottom): (0.4, 0.6), (0.3, 0.5), and (0.2, 0.4). (d) FPTD corresponding to T1 and T2 in Fig. 4(c) between a sink at ($\psi_6 = 0.7$ $R_g = 1.18$) (*i.e.*, global minimum) and sources at ($\psi_6 = 0.15$ $R_g = 1.13$) (circles) and ($\psi_6 = 0.5$ $R_g = 1.14$) (triangles).

predominantly condensation processes, Fig. 5(b) shows a set of first passage time distributions for assembly trajectories between initial and final R_g coordinates specified in the figure caption. These distributions are obtained by averaging over all ψ_6 coordinates sampled during condensation. In the case of trajectories dominated by grain boundary relaxation, Fig. 5(c) shows first passage time distributions for trajectories between initial and final ψ_6 coordinates, which are averaged over all R_g coordinates. It is interesting to note the order of magnitude greater first passage time for grain boundary motion compared to condensation. Good agreement between N-dimensional BD simulations and the LDLD simulations is observed, indicating the accuracy of the W and **D** from the Smoluchowski analysis.

Although the first passage time distributions projected onto the R_g and ψ_6 axes show the full N-dimensional BD and LDLD models agree quantitatively, they do not tell the whole story in terms of the assembly dynamics. It is still essential to use the two dimensions to characterize first passage times for different assembly pathways. For example, Fig. 5(d) shows first passage time distributions roughly corresponding to trajectories T1 and T2 in Fig. 4(c) (*i.e.*, one starts at ($\psi_6 = 0.38$ $R_g = 1.15$) and the other one starts at ($\psi_6 = 0.65$ $R_g = 1.16$); both terminate at the global minimum). The fast T2 trajectory makes it to the global free energy minimum single crystal nearly two orders of magnitude faster than the slow T2 trajectory that is detained on the free energy plateau corresponding to grain boundary diffusion. This large difference in first passage times is not captured by projecting the 2D trajectories either onto the ψ_6 or R_g axes as shown by the first passage times in Figs. 5(b) and 5(c).

After showing the accuracy of the LDLD model via first passage time distributions, it is possible to more completely explore the dynamic evolution of the system using the low dimensional W and **D** in Fig. 4 to numerically solve the SE (Eq. (16)). This provides more complete information on the time evolution of states during stochastic assembly processes (e.g., compared to first passage times alone). Fig. 6 shows the solution of SE (*i.e.*, $p(\mathbf{x},t)$) for $N = 210$ at different voltages and observation times, Δt, with given initial conditions, $p(\mathbf{x},0) = \delta(\mathbf{x} - \mathbf{x}_0)$, $\mathbf{x}_0 = (0.025, 1.22)$, which corresponds to a starting fluid configuration.

At the lowest V^*, Figs. 6(a) and 6(b) show that the evolution of $p(\mathbf{x},\Delta t)$ is characterized by slow drift and diffusion of the initial delta function towards the new equilibrium state, which is a broader distribution of

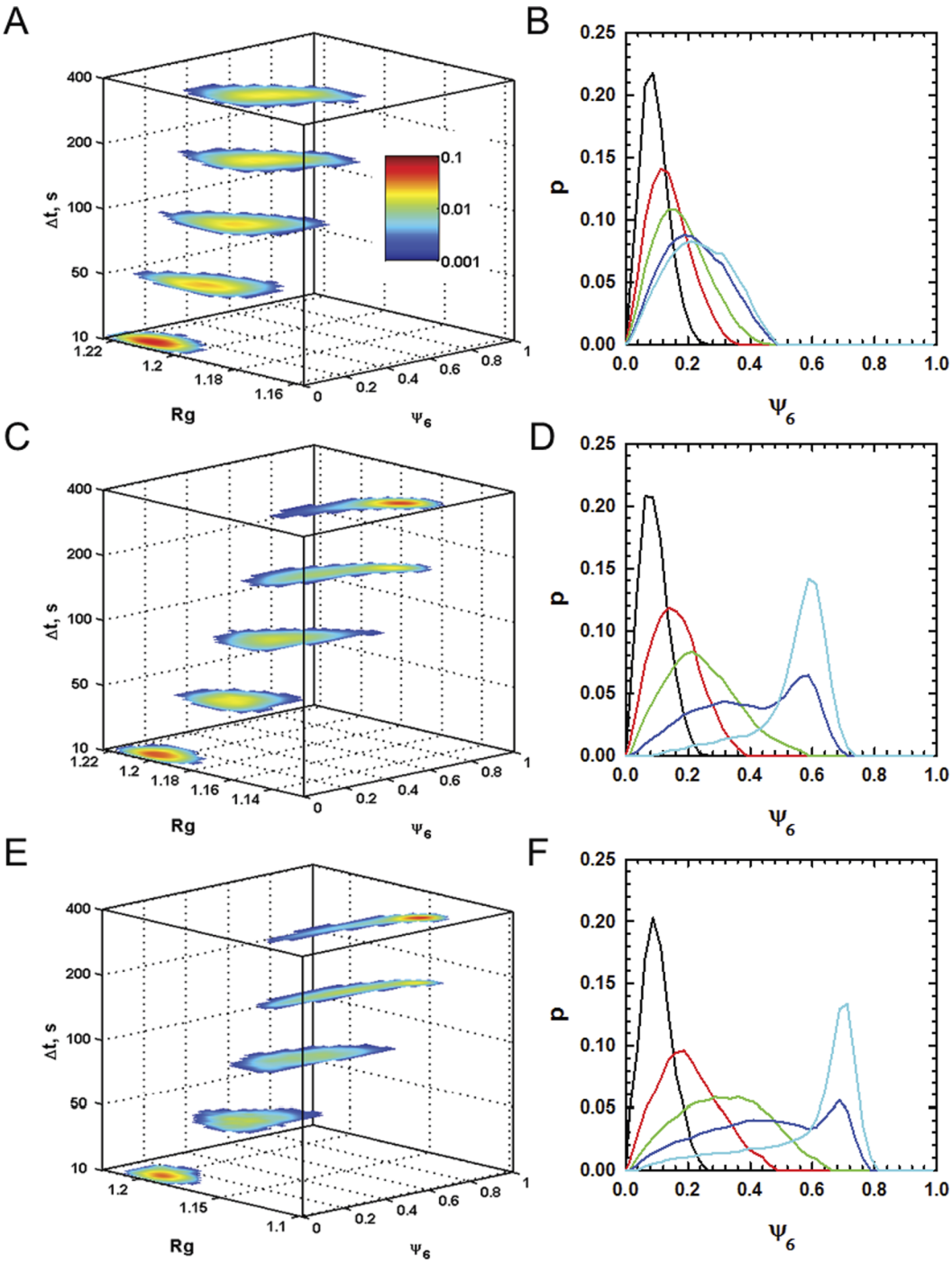

FIG. 6. Numerical solution of Smoluchowski equation to compute $p(\mathbf{x}, t)$ at observation times of $\Delta t = 10$ s, 50 s, 100 s, 200 s, and 400 s for a system size of $N = 210$ at applied voltages of: ((a) and (b)) $V^* = 0.42$, ((c) and (d)) $V^* = 0.50$, and ((e) and (f)) $V^* = 0.57$. The initial condition in all cases is $p(\mathbf{x}, 0) = \delta(\mathbf{x} - \mathbf{x}_0)$ where $\mathbf{x}_0 = (\psi_{60}, R_{g0}) = (0.025, 1.22)$. The left hand plots are two dimensional contour plots of probability density with an inset scale bar in part (a). The right hand plots are one dimensional projections of the two dimensional probability density onto the ψ_6 coordinate for: $\Delta t = 10$ s (black), 50 s (red), 100 s (green), 200 s (blue), and 400 s (cyan).

configurations centered on a more condensed fluid state. Convergence to the equilibrium Boltzmann distribution is observed to occur within ~200 s (most easily seen from blue and cyan curves in Fig. 6(b)). At the intermediate V^*, Figs. 6(c) and 6(d) show how $p(\mathbf{x}, \Delta t)$ more rapidly drifts towards more condensed and ordered states before a new most probable loosely packed crystal state emerges between 100 and 200 s and the equilibrium distribution is reached within ~400 s. At the highest V^*, which corresponds to conditions when a single crystal is expected as the global free energy minimum configuration, Figs. 6(e) and 6(f) show how $p(\mathbf{x}, \Delta t)$ drifts even more rapidly toward evolving ordered configurations that once again reach the equilibrium distribution in ~400 s. The results in Fig. 6 show how the low dimensional model captures the stochastic evolution of the probability density of states at different thermodynamic conditions, which captures all dynamic information necessary to design, control, and optimize colloidal assembly schemes in this system.

System size dependent assembly pathways

Because the results in Figs. 1-6 are for a single system size of $N = 210$, we now explore different systems sizes and voltages to see how the low dimensional model and assembly behavior changes. Fig. 7 shows W and $\mathbf{D}$ for $N = 110$, 210, and 300 at voltages that produce equilibrium structures of comparable global order and degree of condensation (*i.e.*, similar equilibrium ψ_6 and R_g; see Fig. 7 caption for details). All W and $\mathbf{D}$ share similar qualitative features (*e.g.*, a steep free energy gradient followed by a plateau) and corresponding microstructures at the plateau region (*i.e.*, bicrystals at low ψ_6 and single crystals at high ψ_6) marked on the landscapes and shown in the right column of Fig. 7. Quantitative differences with increasing system size include a shift of the global minimum on each W towards somewhat higher R_g and lower ψ_6, which is due to the smaller number of particles packing more densely and being more easily ordered. Increasing system size also produces a systematic decrease in the diagonal terms of $\mathbf{D}$ (*i.e.*, $\mathbf{D}_{\psi 6 \psi 6}$, $\mathbf{D}_{\mathrm{RgRg}}$), which is most likely due to

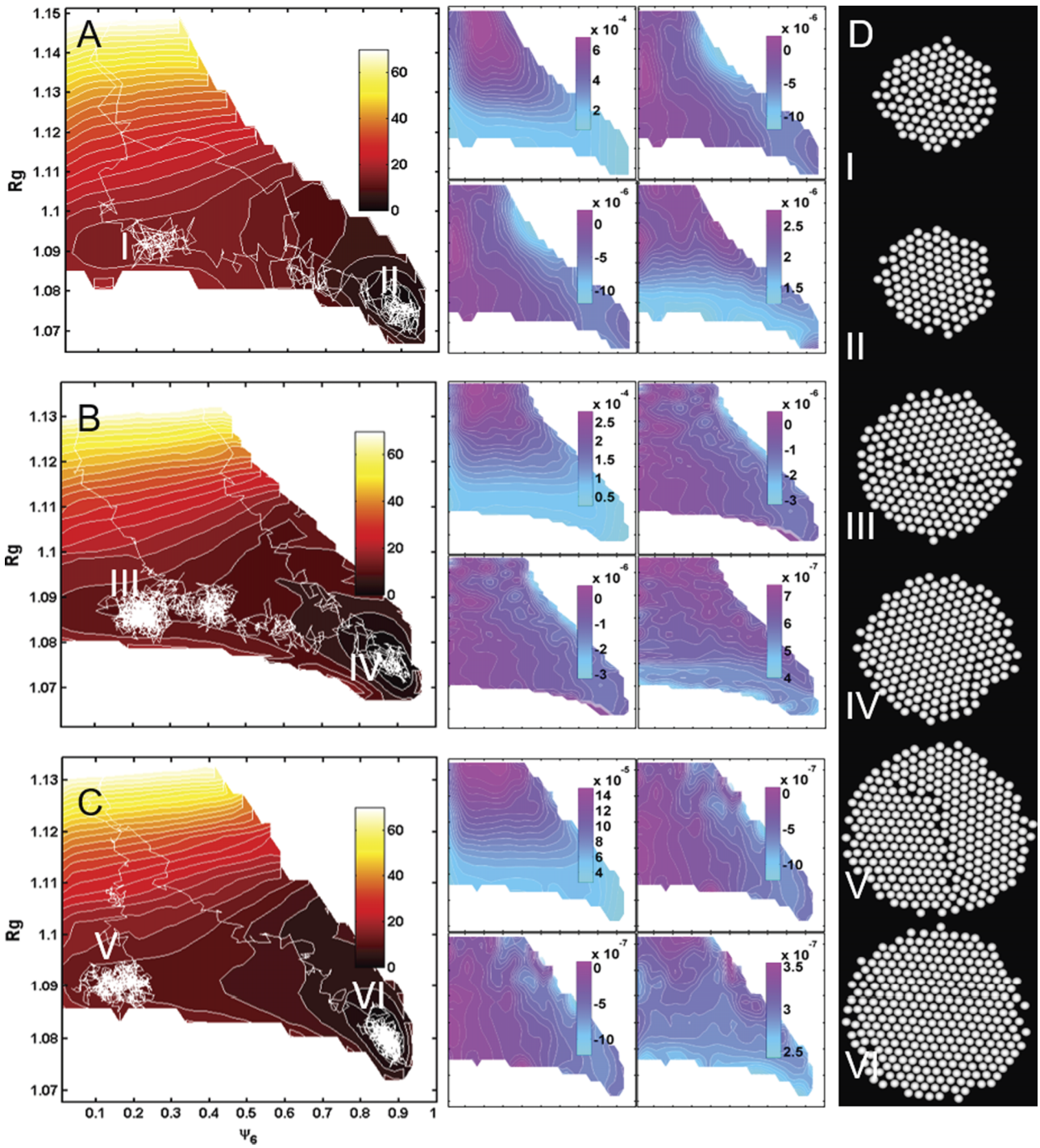

FIG. 7. Free energy and diffusivity landscapes with same formatting and procedure to obtain plots in Fig. 4 (see Fig. 4 caption), except results are now shown for different systems sizes (and applied voltages) of (top-to-bottom): (a) $N = 110$ (at $V^* = 0.85$), (b) $N = 210$ (at $V^* = 0.80$), and (c) $N = 300$ (at $V^* = 0.75$). (d) Renderings in column on far right show representative configurations for coordinates marked on W plots.

increasing hydrodynamics hindrance and associated resistance to rearrangement with increasing crowding.

Using the W and $\mathbf{D}$ from Fig. 7, quantitative differences in the assembly kinetics can be examined by numerically solving the SEs for the three system sizes in Fig. 8 (using the same procedure and formatting as Fig. 6). Fig. 8 shows the solution of SE from initial conditions of $p(\mathbf{x},0) = \delta(\mathbf{x} - \mathbf{x}_0)$, $\mathbf{x}_0 = (0.025, 1.18)$ for $N = 110$, 210, and 300 for $\Delta t = 10$ s, 50 s, 100 s, 200 s, and 300 s. Within the first ~100 s, the distributions in all cases show rapid condensation along the R_g direction (*i.e.,* R_g decreases) towards the W plateau near $R_g \approx 1.09$ with $p(\mathbf{x},t)$ spanning all ψ_6 coordinates. At longer times, the probability density is depleted at the low ψ_6 region and simultaneously accumulates towards the high ψ_6 region.

The general trend in these data vs. system size is that smaller systems more rapidly approach the global free energy minimum ordered state compared to larger systems sizes. Specifically, for the $N = 110$ system at $\Delta t = 100$ s, around half of all trajectories have already reached the general vicinity

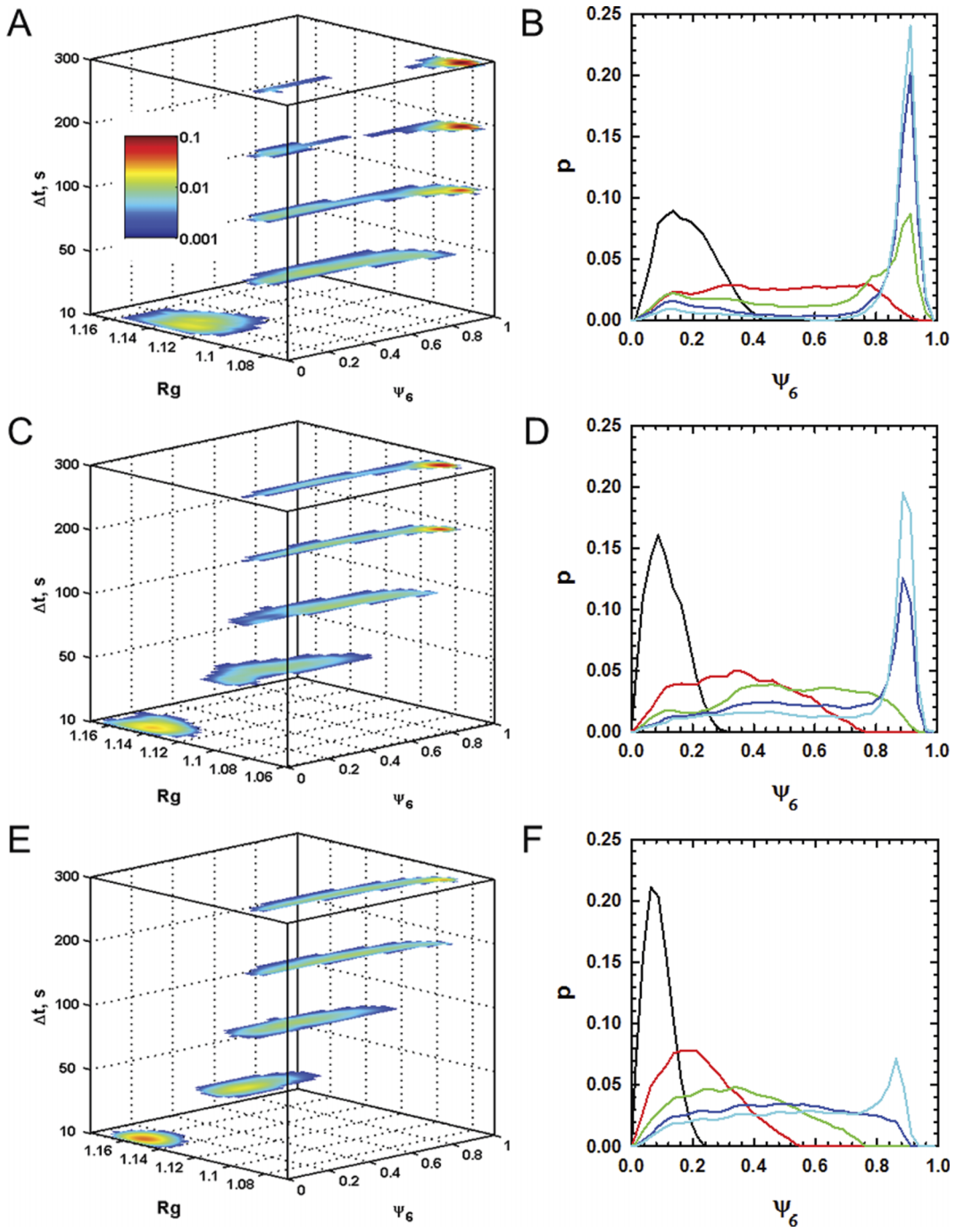

FIG. 8. Numerical solution of Smoluchowski equation to compute $p(\mathbf{x},t)$ at observations times of $\Delta t = 10$ s, 50 s, 100 s, 200 s, and 300 s for different systems sizes (and applied voltages) of (top-to-bottom): ((a) and (b)) $N = 110$ (at $V^* = 0.85$), ((c) and (d)) $N = 210$ (at $V^* = 0.80$), and ((d) and (e)) $N = 300$ (at $V^* = 0.75$). The initial condition in all cases is $p(\mathbf{x},0) = \delta(\mathbf{x} - \mathbf{x}_0)$ where $\mathbf{x}_0 = (\psi_{60}, R_{g0}) = (0.025, 1.18)$. The left hand plots are two dimensional contour plots of probability density with an inset scale bar in part (a). The right hand plots are one dimensional projections of the two dimensional probability density onto the ψ_6 coordinate for $\Delta t = 10$ s (black), 50 s (red), 100 s (green), 200 s (blue), and 300 s (cyan).

of equilibrium (i.e., area under the curve at high ψ_6) whereas the rest are trapped in the plateau regions of the Ws shown in Fig. 7. From $\Delta t > 100$ s, most trajectories relax towards the equilibrium ordered state except for a small persistent portion in the vicinity of $\psi_6 \approx 0.1$. The microstructures in the region of low R_g and $\psi_6 \approx 0.1$ correspond to nearly perfect bi-crystals, which are metastable with essentially no free energy gradient to drive relaxation (which only occurs when stochastic fluctuations initiate an imbalance that causes one domain to grow at the expense of the other[7]).

With increasing system size, and particularly for the largest system here of $N = 300$, at $\Delta t = 100$-200 s, nearly all the trajectories are trapped on the W plateau, and their subsequent relaxation towards the perfect crystal state are significantly slowed compared to the $N = 110$ system. This slowing down with increasing system size can be attributed to the differences in the absolute values of the diffusivity landscapes in the region of configuration space corresponding to polycrystal relaxation towards single crystals states. Because all system sizes have plateaus on W in this region, there is little to no thermodynamic driving force all cases, so the kinetics is governed by diffusion and resistance in the ψ_6 direction. The relatively larger diffusivities in the ψ_6 coordinate for smaller systems allow trajectories to "fluctuate" more as part of relaxing towards the single crystal in the global free energy well. This system size dependent behavior has been observed in our previous experiments,[21] which indicates the validity of the low dimensional models developed in this work. Extension of the approach here to even larger system sizes could slow dynamics to the point that assumptions underlying the analysis and interpretation in the present study (*i.e.*, ergodicity, detailed balance, thermodynamic equilibrium) could be called into question. There are no signatures of non-Markovian behavior to indicate any issues with the validity of these assumptions in the present work (all properties are independent of path and initial conditions in order parameter space).

CONCLUSIONS

We reported the development of a low-dimensional Smoluchowski equation to quantify the thermodynamics and kinetics of colloidal crystal assembly in electric fields. The dimensionality and order parameter choice was supported by a diffusion mapping analysis. Order parameters describing global order, ψ_6, and degree of condensation, R_g, were found to yield a low-dimensional model that quantitatively captured assembly dynamics as determined by first passage times in agreement with N-dimensional dynamic data. The free energy and diffusivity landscapes from the Smoluchowski model revealed two types of kinetic pathways; one where condensation and global order emerge simultaneously to rapidly yield single domain crystals, and another one where fast condensation with local ordering, but not global ordering, results in polycrystal formation. Numerical solution of the low-dimensional Smoluchowski equation shows the temporal evolution of the probability of states for different voltages and system sizes, which quantifies how these two variables determine the evolution of order in electric field mediated quasi-2D crystallization. Ultimately, the low dimensional model quantitatively captures slow grain boundary dynamics in the presence of vanishing free energy gradients, where friction associated with configurational rearrangements determines the relaxation rate for polycrystals to form single crystals via grain boundary motion. These low-dimensional models are currently being used to design optimal control policies for closed loop and open loop control of colloidal assembly processes designed to form single crystal structures.

ACKNOWLEDGMENTS

M.A.B. and D.M.F. acknowledge financial support by the National Science Foundation through Cyber Enabled Discovery and Innovation Grant (Nos. CMMI-1124648 and CMMI-1125188).

[1]S. C. Glotzer and M. J. Solomon, Nat. Mater. **6**(7), 557–562 (2007).
[2]M. Grzelczak, J. Vermant, E. M. Furst, and L. M. Liz-Marzán, ACS Nano **4**(7), 3591–3605 (2010).
[3]O. D. Velev and S. Gupta, Adv. Mater. **21**(19), 1897–1905 (2009).
[4]P. F. Damasceno, M. Engel, and S. C. Glotzer, Science **337**(6093), 453–457 (2012).
[5]J. A. Millan, D. Ortiz, G. van Anders, and S. C. Glotzer, ACS Nano **8**(3), 2918–2928 (2014).
[6]P. F. Damasceno, M. Engel, and S. C. Glotzer, ACS Nano **6**(1), 609–614 (2011).
[7]T. D. Edwards, Y. Yang, D. J. Beltran-Villegas, and M. A. Bevan, Sci. Rep. **4**, 6132 (2014).
[8]J. J. Juarez and M. A. Bevan, Adv. Funct. Mater. **22**(18), 3833–3839 (2012).
[9]Y. Xue, D. J. Beltran-Villegas, X. Tang, M. A. Bevan, and M. A. Grover, IEEE Trans. Control Syst. Technol. **22**, 1956 (2014).
[10]M. A. Bevan, D. M. Ford, M. A. Grover, B. Shapiro, D. Maroudas, Y. Yang, R. Thyagarajan, X. Tang, and R. M. Sehgal, J. Process Control **27**, 64–75 (2015).
[11]S. Sriraman, I. G. Kevrekidis, and G. Hummer, J. Phys. Chem. B **109**(14), 6479–6484 (2005).
[12]H. Risken and T. Frank, *The Fokker-Planck Equation: Methods of Solution and Applications* (Springer, 1996).
[13]D. I. Kopelevich, A. Z. Panagiotopoulos, and I. G. Kevrekidis, J. Chem. Phys. **122**, 044908 (2005).
[14]R. B. Best and G. Hummer, Phys. Rev. Lett. **96**(22), 228104 (2006).
[15]D. J. Beltran-Villegas, R. M. Sehgal, D. Maroudas, D. M. Ford, and M. A. Bevan, J. Chem. Phys. **135**(15), 154506 (2011).
[16]I. T. Jolliffe, *Principal Component Analysis* (Springer, 2002).
[17]A. L. Ferguson, A. Z. Panagiotopoulos, I. G. Kevrekidis, and P. G. Debenedetti, Chem. Phys. Lett. **509**(1-3), 1–11 (2011).
[18]R. Coifman, I. Kevrekidis, S. Lafon, M. Maggioni, and B. Nadler, Multiscale Model. Simul. **7**(2), 842–864 (2008).
[19]D. J. Beltran-Villegas, R. M. Sehgal, D. Maroudas, D. M. Ford, and M. A. Bevan, J. Chem. Phys. **132**(4), 044707 (2010).
[20]D. J. Beltran-Villegas, R. M. Sehgal, D. Maroudas, D. M. Ford, and M. A. Bevan, J. Chem. Phys. **137**(13), 134901 (2012).
[21]T. D. Edwards, D. J. Beltran-Villegas, and M. A. Bevan, Soft Matter **9**(38), 9208–9218 (2013).
[22]J. J. Juarez and M. A. Bevan, J. Chem. Phys. **131**, 134704 (2009).
[23]J. J. Juarez, J.-Q. Cui, B. G. Liu, and M. A. Bevan, Langmuir **27**(15), 9211–9218 (2011).
[24]J. J. Juarez, B. G. Liu, J.-Q. Cui, and M. A. Bevan, Langmuir **27**(15), 9219–9226 (2011).
[25]S. K. Smoukov, S. Gangwal, M. Marquez, and O. D. Velev, Soft Matter **5**(6), 1285–1292 (2009).
[26]N. I. Zheludev and Y. S. Kivshar, Nature Mater. **11**(11), 917–924 (2012).
[27]P. Bahukudumbi, W. N. Everett, A. Beskok, G. H. Huff, D. Lagoudas, Z. Ounaies, and M. A. Bevan, Appl. Phys. Lett. **90**, 224102 (2007).
[28]J. J. Juarez, P. P. Mathai, J. A. Liddle, and M. A. Bevan, Lab Chip **12**(20), 4063–4070 (2012).
[29]J. J. Juarez, S. E. Feicht, and M. A. Bevan, Soft Matter **8**(1), 94–103 (2012).

[30]G. M. Bell, S. Levine, and L. N. McCartney, J. Colloid Interface Sci. **33**(3), 335–359 (1970).
[31]S. Anekal and M. A. Bevan, J. Chem. Phys. **125**, 034906 (2006).
[32]D. L. Ermak and J. A. McCammon, J. Chem. Phys. **69**(4), 1352–1360 (1978).
[33]J. F. Brady and G. Bossis, Annu. Rev. Fluid Mech. **20**, 111–157 (1988).
[34]D. J. Jeffrey and Y. Onishi, J. Fluid Mech. **139**, 261–290 (1984).
[35]J. W. Swan and J. F. Brady, Phys. Fluids **19**(11), 113306 (2007).
[36]R. R. Coifman, Y. Shkolnisky, F. J. Sigworth, and A. Singer, IEEE Trans. Image Process. **17**(10), 1891–1899 (2008).
[37]A. L. Ferguson, A. Z. Panagiotopoulos, P. G. Debenedetti, and I. G. Kevrekidis, Proc. Natl. Acad. Sci. U. S. A. **107**(31), 13597–13602 (2010).
[38]B. I. Halperin and D. R. Nelson, Phys. Rev. Lett. **41**(2), 121–124 (1978).
[39]A. W. C. Lau and T. C. Lubensky, Phys. Rev. E **76**(1), 011123 (2007).
[40]C. W. Gardiner, *Handbook of Stochastic Methods for Physics, Chemistry, and the Natural Sciences*, 2nd ed. (Springer, Berlin, 2009).
[41]J. A. Trangenstein, *Numerical Solution of Hyperbolic Partial Differential Equations* (Cambridge University Press, 2009).
[42]J. Baumgartl and C. Bechinger, Europhys. Lett. **71**, 487–493 (2005).
[43]T. O. Pangburn and M. A. Bevan, J. Chem. Phys. **123**, 174904 (2005).
[44]D. J. Beltran-Villegas, T. D. Edwards, and M. A. Bevan, Langmuir **29**(40), 12337–12341 (2013).
[45]R. A. Mansbach and A. L. Ferguson, J. Chem. Phys. **142**(10), 105101 (2015).
[46]D. J. Beltran-Villegas and M. A. Bevan, Soft Matter **7**(7), 3280–3285 (2011).
[47]G. E. Fernandes, D. J. Beltran-Villegas, and M. A. Bevan, J. Chem. Phys. **131**, 134705 (2009).
[48]G. E. Fernandes, D. J. Beltran-Villegas, and M. A. Bevan, Langmuir **24**, 10776–10785 (2008).
[49]C. R. Laing, T. A. Frewen, and I. G. Kevrekidis, Nonlinearity **20**(9), 2127 (2007).
[50]B. Peters and B. L. Trout, J. Chem. Phys. **125**(5), 054108 (2006).
[51]A. Ma and A. R. Dinner, J. Phys. Chem. B **109**(14), 6769–6779 (2005).

Interfacial colloidal rod dynamics: Coefficients, simulations, and analysis

Yuguang Yang, and Michael A. Bevan

Citation: The Journal of Chemical Physics **147**, 054902 (2017); doi: 10.1063/1.4995949
View online: https://doi.org/10.1063/1.4995949
View Table of Contents: http://aip.scitation.org/toc/jcp/147/5
Published by the American Institute of Physics

Interfacial colloidal rod dynamics: Coefficients, simulations, and analysis

Yuguang Yang and Michael A. Bevan[a)]
Chemical and Biomolecular Engineering, Johns Hopkins University, Baltimore, Maryland 21218, USA

(Received 21 May 2017; accepted 13 July 2017; published online 1 August 2017)

Colloidal rod diffusion near a wall is modeled and simulated based on a constrained Stokesian dynamic model of chains-of-spheres. By modeling colloidal rods as chains-of-spheres, complete diffusion tensors are computed for colloidal rods in bulk media and near interfaces, including hydrodynamic interactions, translation-rotation coupling, and all diffusion modes in the particle and lab frames. Simulated trajectories based on the chain-of-spheres diffusion tensor are quantified in terms of typical experimental quantities such as mean squared positional and angular displacements as well as autocorrelation functions. Theoretical expressions are reported to predict measured average diffusivities as well as the crossover from short-time anisotropic translational diffusion along the rod's major axis to isotropic diffusion. Diffusion modes are quantified in terms of closed form empirical fits to model results to aid their use in interpretation and prediction of experiments involving colloidal rod diffusion in interfacial and confined systems. *Published by AIP Publishing.* [http://dx.doi.org/10.1063/1.4995949]

I. INTRODUCTION

Micro- and nano-sized colloidal rod-shaped particles are important in numerous dynamic processes involving, for example, biological macromolecules and micro-organisms[1] and novel building blocks in materials engineering.[2,3] Rod-shaped colloidal particles experience Brownian translation and rotation that are important to dynamic processes including their transport and self-assembly. Colloidal rod collective dynamics are important to many phenomena such as phase transitions,[4] packing,[5] aggregation,[6] and assembly.[7] However, all aspects of single rod dynamics near surfaces are still not understood in terms of comprehensive models, which is important to problems involving transport in natural and biological porous media as well as rod assembly dynamics on substrates. Spherical colloidal particle motion near a wall has been accurately quantified in theory,[8] simulations,[9–11] and experiments,[12–15] but for colloidal rods near a wall, the interplay of conservative (e.g., electrostatic) and non-conservative (i.e., hydrodynamic) forces in dynamics processes is significantly more complex.

Historically, some of the earliest relevant models for bulk rod diffusion were for cylinders[16] and from slender-body theory for large aspect ratio particles.[17] A method for treating rod shaped particles as collections of many small spheres more accurately accounted for end-effects for shorter aspect ratios, which have been corroborated in experiments.[18] Other approaches such as boundary element[19] and path integral[20] methods have produced increasingly accurate bulk rod transport properties. In addition to translational and rotational diffusion, rod particles have also been shown to exhibit a transition between short-time anisotropic translational diffusion along the particle long-axis and long-time isotropic translation diffusion, which occurs after rotational diffusion that allows sampling of all translational modes. This effect is understood in two-dimensional (2D) systems[21] but has not been studied for three-dimensional (3D) rod diffusion in bulk media or near walls.

For rods near a no-slip planar wall surface, the rod's translational and rotational diffusivities depend on aspect ratio, orientation, and separation relative to the wall. Models that capture some aspects of rod motion near surfaces include infinitely long cylinders adjacent to walls,[22] slender-body theory for rods parallel or perpendicular to walls for separations comparable to the rod length,[23] chains-of-spheres for single aspect ratios vs. elevation and orientation using stochastic rotation dynamics,[24] multipole expansion of Green's function for axisymmetric particles near walls,[25] and finite element simulations of spheroid shaped particles near boundaries.[26] These previous studies have limitations either in terms of accurately capturing hydrodynamic interactions important to rod translation and rotation near surfaces or in terms of probing a broad range of rod separations, orientations, and aspect ratios. In short, to the best of our knowledge, a comprehensive model is not available to quantify for rods near walls how all the components of the diffusivity tensor, $\mathbf{D}$ (and the resistance tensor, $\mathbf{R}$, via $\mathbf{D} = kT\mathbf{R}^{-1}$), depend on all possible rod configurations and aspect ratios. By obtaining such a model, it will be possible to accurately simulate and analyze rods near surfaces in terms of translational and rotational diffusivities as well as translational and rotational velocities due to external forces and torques.

One approach to compute $\mathbf{D}$ is Stokesian dynamics,[27] which is the method employed in this work. Although Stokesian dynamics is often applied to problems in suspension rheology, it has been used successfully in bulk chain-of-sphere models to produce agreement with slender body theory,[28] as

a) Author to whom correspondence should be addressed: mabevan@jhu.edu

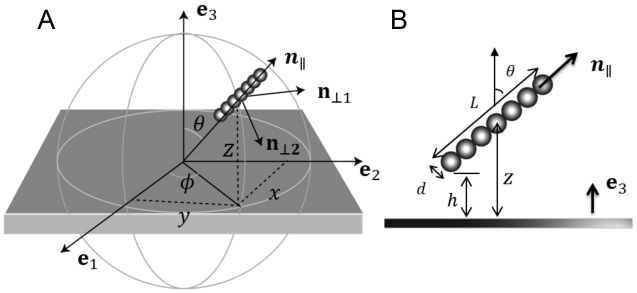

FIG. 1. Schematics of "chain-of-spheres" colloidal rod above the wall. (a) 3D view and (b) side view looking along $\mathbf{n}_{\perp 1}$. In both schematics, $\mathbf{e}_1$, $\mathbf{e}_2$, and $\mathbf{e}_3$ are unit vectors in a Cartesian coordinate lab frame, and $\mathbf{n}_\parallel$, $\mathbf{n}_{\perp 1}$, and $\mathbf{n}_{\perp 2}$ are unit vectors in spherical coordinates in the particle frame with origin located at the rod center of mass.

well as spherical particles near surfaces[9,29] and in confinement.[10] In this work, we implement a Constrained Stokesian Dynamics (CSD) method to compute **D** using a constraint strategy[30] to maintain a rigid linear chain-of-spheres as they interact with a wall. The CSD approach allows accurate modeling of chains-of-spheres to include both non-conservative hydrodynamic forces and conservative forces such as electrostatic and gravitational interactions.

In this work, we compute diffusivities for colloidal rods by modeling them as rigid chains-of-spheres in bulk media and near walls (Fig. 1) vs. aspect ratio, separation, and orientation. The theory, results, and their discussion are based on the systematic approach to compute diffusion coefficients, use these to perform dynamic simulations, and obtain diffusivities by analyzing trajectories (as they would be in experiments). In more detail, the paper is organized as follows. Translational and rotational components of **D** are calculated using CSD for chain-of-sphere rods in bulk media for aspect ratios of $p = 2$-30. This approach is extended to chain-of-sphere rods near walls where separation dependent components of **D** are calculated for parallel, perpendicular, and oblique orientations including translation, rotation, and translation-rotation cross terms. Dynamic simulations using the calculated **D** are analyzed using mean squared positional and angular displacements and autocorrelation functions. These results are used to show how experimentally measured diffusivities can be quantitatively connected to components of **D** and the conservative forces acting on rods near surfaces. Finally, the crossover from anisotropic to isotropic diffusion in bulk media and near walls is quantified from measured trajectories and shown to agree with theoretical predictions developed in this paper.

II. THEORY

A. Resistance, mobility, and diffusion coefficients

1. Coordinate systems

The following analysis uses two coordinate frames: a lab frame and a particle frame. As illustrated in Fig. 1, the lab frame is a right-hand Cartesian coordinate system with basis vectors $\mathbf{e}_1 = (1,0,0)$, $\mathbf{e}_2 = (0,1,0)$, and $\mathbf{e}_3 = (0,0,1)$. The particle frame is a right-hand Cartesian coordinate system with the origin at the rod center of mass with axis directions relative to the rod long axis; specifically, $\mathbf{n}_{||}$ is the unit vector parallel to the rod long axis, $\mathbf{n}_{\perp 1}$ is perpendicular to $\mathbf{n}_{||}$ and $\mathbf{e}_3$, and $\mathbf{n}_{\perp 2}$ is perpendicular to $\mathbf{n}_{||}$ and $\mathbf{n}_{\perp}$. The particle frame is translated and rotated relative to the lab frame with a polar angle θ and azimuthal angle ϕ.

2. Unbounded sphere resistance and mobility tensor

For N spheres of radius a suspended in an unbounded incompressible Newtonian fluid in the low Reynolds number limit, the equation of motion is given by

$$\mathbf{U} = \mathbf{MF}, \tag{1}$$

where **U** is the concatenation of translational and rotational velocity vectors of N spheres, $\mathbf{U} = (\mathbf{U}^{(1)}, \mathbf{U}^{(2)}, \ldots, \boldsymbol{\Omega}^{(1)}, \boldsymbol{\Omega}^{(2)}, \ldots)$, **F** is the concatenation of forces and torques acting on the spheres, $\mathbf{F} = (\mathbf{F}^{(1)}, \mathbf{F}^{(2)}, \ldots, \mathbf{L}^{(1)}, \mathbf{L}^{(2)}, \ldots)$, where the superscript denotes the index of individual spheres, and **M** is the grand mobility tensor of size $6N \times 6N$. The corresponding resistance relationship is given as

$$\mathbf{F} = \mathbf{RU}, \tag{2}$$

where **R** is the grand resistance tensor and relates to the grand mobility tensor as

$$\mathbf{R} = \mathbf{M}^{-1} \tag{3}$$

which can be computed using[27]

$$\mathbf{R} = (\mathbf{M}^{\infty}_{\mathbf{PP}})^{-1} + \mathbf{R_{2B}} - \mathbf{R}^{\infty}_{\mathbf{2B}}, \tag{4}$$

which includes both far-field multi-body interactions [i.e., $(\mathbf{M}^{\infty}_{\mathbf{PP}})^{-1}$] and near-field pair-wise lubrication (i.e., $\mathbf{R_{2B}}$). The far-field pairwise resistance (i.e., $\mathbf{R}^{\infty}_{\mathbf{2B}}$) is subtracted since the far-field two-body interaction is already accounted for in $(\mathbf{M}^{\infty}_{\mathbf{PP}})^{-1}$. Details of these expressions are included in the supplementary material.

3. Sphere-wall resistance and mobility tensor

The grand resistance tensor for spheres above a planar no-slip wall is given as[9,29]

$$\mathbf{R} = (\mathbf{M}^{\infty}_{\mathbf{PW}})^{-1} + \mathbf{R_{2B}} + \mathbf{R_W} - (\mathbf{R_{2B,\infty}} + \mathbf{R_{W,\infty}}), \tag{5}$$

which includes both the multi-body far-field resistance tensor above a no-slip plane [i.e., $(\mathbf{M}^{\infty}_{\mathbf{PW}})^{-1}$], which is the inversion of many-bodied far-field mobility tensor, and pair-wise lubrication interactions. The pair-wise lubrication interaction is obtained by first adding the two-body particle-particle exact resistance tensor $\mathbf{R_{2B}}$ and the particle-wall exact resistance tensor $\mathbf{R_W}$, and then subtracting the far-field resistance tensor $\mathbf{R_{2B,\infty}} + \mathbf{R_{W,\infty}}$ to avoid the double counting of the far-field particle-particle and particle-wall interaction in $(\mathbf{M}^{\infty}_{\mathbf{PW}})^{-1}$ and $\mathbf{R_{2B}} + \mathbf{R_W}$. The elements in $\mathbf{R}_{2B}$ and $\mathbf{R}^{\infty}_{2B}$ are the same as Eq. (4). The explicit expressions for $(\mathbf{M}^{\infty}_{\mathbf{PW}})^{-1}$ can be found in Ref. 29. Details of these expressions are included in the supplementary material.

4. Chains-of-spheres-wall resistance and mobility tensor

We model rod-like particles as linear chains of touching spheres as depicted in Fig. 1. To model rod motion, the system is constrained to have six degrees of freedom (3 for translation and 3 for rotation). The rigid rod motion can be decomposed

into three degrees of translational motion of the center of mass and three degrees of rotational motion about the center of mass given by

$$\begin{pmatrix} \mathbf{F}_{rod} \\ \mathbf{L}_{rod} \end{pmatrix} = \mathbf{R}_{rod} \begin{pmatrix} \mathbf{U}_{rod} \\ \mathbf{\Omega}_{rod} \end{pmatrix}. \tag{6}$$

All quantities in Eq. (6) are calculated and measured in the particle frame. $\mathbf{R}_{rod}$ is a 6×6 resistance tensor for the six degrees of freedom of a single rod. The entries in $\mathbf{R}_{rod}$ can be calculated from Eqs. (2) and (6) by setting appropriate velocities to each sphere composing the rod. For example, if all spheres translate with unit velocity in the $\mathbf{n}_{\|}$ direction, then Eq. (2) can be used to calculate the $6N$ dimensional vector of forces and torques acting on the individual spheres. Those forces and torques can be converted to a 3-dimensional force $\mathbf{F}_{rod}$ and a 3 dimensional torque $\mathbf{L}_{rod}$ acting on the rod relative to its center of mass. Since the rod translates with velocity vector $\mathbf{U}_{rod}$ = (1,0,0) and zero rotational velocity $\mathbf{\Omega}_{rod}$ = (0,0,0), the first row elements in $\mathbf{R}_{rod}$ can be calculated by solving linear equations within Eq. (6). Other row elements in $\mathbf{R}_{rod}$ are calculated in the same scheme. The diffusivity tensor $\mathbf{D}_{rod}$ in the particle frame is related to $\mathbf{R}_{rod}$ by

$$\mathbf{D}_{rod} = k_B T (\mathbf{R}_{rod})^{-1}. \tag{7}$$

The diagonal components in $\mathbf{D}_{rod}$ are denoted as $D_{\|}^{t,b}, D_{\perp 1}^{t,b}, D_{\perp 2}^{t,b}, D_{\|}^{r,b}, D_{\perp 1}^{r,b}, D_{\perp 2}^{r,b}$ to represent primary translational and three rotational diffusivities along $\mathbf{n}_{\|}$, $\mathbf{n}_{\perp 1}$, and $\mathbf{n}_{\perp 2}$. Off-diagonal elements of $\mathbf{D}_{rod}$ are zero for bulk diffusion. A nearby wall introduces additional hydrodynamic interactions [i.e., Eq. (5)] for each sphere within the chain of spheres making up the rod particle. For interfacial diffusion, the diagonal components in $\mathbf{D}_{rod}$ are denoted as $D_{\|}^{t,w}, D_{\perp 1}^{t,w}, D_{\perp 2}^{t,w}, D_{\|}^{r,w}, D_{\perp 1}^{r,w}, D_{\perp 2}^{r,w}$ to represent primary translational and rotational diffusivities in the similar to bulk diffusion modes. Off-diagonal terms in $\mathbf{D}_{rod}$ are non-zero in the presence of the wall.

B. Equation of motion for dynamic simulations

1. Equation of motion under constraint

For N identical particles with coordinates $\mathbf{q} = (q_1, q_2, \ldots, q_{6N})$, including $3N$ positional coordinates $(x_1, y_1, z_1, \ldots, x_N, y_N, z_N)$ and $3N$ rotational coordinates $(\alpha_1, \beta_1, \gamma_1, \ldots, \alpha_N, \beta_N, \gamma_N)$, the equation of motion is

$$\frac{d\mathbf{q}}{dt} = \mathbf{U} = \mathbf{M} \cdot \mathbf{F}, \tag{8}$$

where $\mathbf{U}$ is a $6N$ dimensional velocity vector including $3N$ translational velocities and $3N$ rotational velocities. $\mathbf{M}$ is a $6N \times 6N$ grand mobility tensor obtained from the grand resistance tensor in Eq. (6) via $\mathbf{M} = (\mathbf{R})^{-1}$ (see the supplementary material for more details). $\mathbf{F}$ is a $6N$ dimensional force vector including $3N$ forces and $3N$ torques acting on the center of each particle, which is given by the sum of conservative forces, $\mathbf{F}^P$, and Brownian forces, $\mathbf{F}^B$, as

$$\mathbf{F} = \mathbf{F}^P + \mathbf{F}^B. \tag{9}$$

To model rods as chains-of-spheres that move together as a rigid body, the equation of motion [Eq. (8)] is modified to include additional constraint forces, $\mathbf{F}^C$, as

$$\mathbf{F} = \mathbf{F}^P + \mathbf{F}^B + \mathbf{F}^C. \tag{10}$$

2. Conservative forces

The $6N$ dimensional force vector $\mathbf{F}^P$ is the concatenation of $(\mathbf{F}_1{}^P, \mathbf{F}_2{}^P, \ldots, \mathbf{F}_N{}^P, \mathbf{L}_1{}^P, \mathbf{L}_2{}^P, \ldots, \mathbf{L}_N{}^P)$, where $\mathbf{F}_i{}^P$ and $\mathbf{L}_i{}^P$ represent the conservative force and torque experienced by sphere i. The system considered throughout this paper does not have conservative torques and $\mathbf{L}_i{}^P = 0$ (although constraining torques are included). The conservative forces on each sphere i composing the rod experience electrostatic forces and gravitation force[10]

$$\mathbf{F}_i^P = \kappa B^{pw} \exp(-\kappa(z_i - a))\mathbf{e}_3 + \sum_{j \neq i} \kappa B^{pp} \exp(-\kappa \left\|\mathbf{r}_{ij}\right\|) \frac{\mathbf{r}_{ij}}{\left\|\mathbf{r}_{ij}\right\|} + m\mathbf{g}, \tag{11}$$

where a is the radius of the sphere, z_i is the mass center height of the sphere, κ is the Debye length, B^{pw} is the pre-factor for electrostatic repulsion between the sphere and wall, B^{pp} is the pre-factor for electrostatic repulsion between spheres, $\boldsymbol{r}_{ij}$ is the vector from mass center of particle i to mass center of particle j, m is the buoyant sphere mass, and $\mathbf{g}$ is the acceleration due to gravity.

3. Constraint forces

The motion of a rod with aspect ratio p can be modeled by the motion of p spheres under two types of constraints: positional constraints and rotational constraints. The positional constraints are used to ensure that all the spheres are positioned in one line and each sphere is touching with its neighbors. The rotational constraints are that all the spheres can only rotate along the long axis of the rod with the same angular speed, whereas rotations perpendicular to the long axis are not allowed. The details of the constraints can be found in the supplementary material, but we provide a brief outline of how the constraint forces, $\mathbf{F}^C$, are determined. The K constraints, C_{μ}, on the coordinates $\mathbf{q}$ are given by[31]

$$C_\mu(q_1, q_2, \ldots, q_{6N}) = 0, \ \mu = 1, 2, \ldots, K \tag{12}$$

such that each coordinate q_j will experience an extra constraint force given as[30,31]

$$F_j{}^C = \sum_{\mu=1}^{K} \lambda_\mu \frac{\partial C_\mu}{\partial q_j}, \tag{13}$$

where λs are obtained by imposing the condition that the K constraints should be satisfied during the simulation to yield

$$\frac{\partial C_\mu}{\partial t} = \sum_{j=1}^{6N} \frac{\partial C_\mu}{\partial q_j} U_j = 0, \mu = 1, 2, \ldots, K \tag{14}$$

such that λ in Eq. (13) can be solved from Eqs. (8), (10), and (14).

4. Brownian forces

The Brownian forces $\mathbf{F}^B$ are obtained by first generating the regular Brownian force as

$$\left\langle \mathbf{F}^{B'} \right\rangle = 0, \left\langle \mathbf{F}^{B'} \mathbf{F}^{B'} \right\rangle = \frac{2k_B T}{\Delta t} \mathbf{R} \tag{15}$$

and then projecting the generated forces $\mathbf{F}^{B'}$ via

$$\mathbf{F}^{B} = \mathbf{P}\cdot\mathbf{F}^{B'}, P_{ij} = \delta_{ij} - \sum_{\nu=1}^{K}\sum_{\mu=1}^{K}\frac{\partial C_\mu}{\partial q_i}\left(\sum_{k=1}^{6N}\frac{\partial C_\mu}{\partial q_k}\frac{\partial C_\nu}{\partial q_k}\right)^{-1}\frac{\partial C_\nu}{\partial q_j} \tag{16}$$

such that Brownian forces will be locally tangent to the $6N$-K hyper-surface defined by the K constraints.[31] Please see the supplementary material for a detailed description.

5. Mid-point algorithm

With forces calculated, the mid-point algorithm is used to update the coordinate.[31] Specifically, the initial velocity and mid-point coordinate are first calculated as

$$\mathbf{U}^0 = (\mathbf{R}^0)^{-1}\cdot(\mathbf{F}^{P,0} + \mathbf{F}^{B,0} + \mathbf{F}^{C,0}), \tag{17}$$

$$\mathbf{q}^* = \mathbf{q}^0 + \frac{1}{2}\mathbf{U}^0\Delta t, \tag{18}$$

and then the intermediate velocity and finial position are calculated,

$$\mathbf{U}^* = (\mathbf{R}^*)^{-1}\cdot(\mathbf{F}^{P,*} + \mathbf{F}^{B,*} + \mathbf{F}^{C,*}), \tag{19}$$

$$\mathbf{q} = \mathbf{q}^0 + \mathbf{U}^*\Delta t, \tag{20}$$

where Δt is the integration time, and "0" and "*" denote the quantity that is calculated using the initial and mid-point configurations, respectively.

C. Equilibrium and dynamic analyses of rod diffusion

1. Equilibrium rod-wall distribution

For a rod levitated above a wall in nearly quasi-2D configurations (with the long-axis parallel to the wall), we characterize its configuration by the center-of-mass coordinates (x, y, z) and the polar angle θ (there is no dependence on the azimuthal angle). The net potential energy of a rod is the sum of potential energies for each sphere within the rod given by

$$U_{rod}(z,\theta) = \sum_{i=1}^{p} G_s z_i + B^{pw}\exp\left[-\kappa(z_i - a)\right], \tag{21}$$

where G_s is the buoyant weight of each sphere, z_i is the mass center of particle i composing the rod and can be related to z and θ by

$$z_i = z + 2a\cos(\theta)\left[i - (1 + p/2)\right]. \tag{22}$$

The equilibrium probability of a rod is given by a Boltzmann distribution as

$$\rho^{eq}(z,\theta) = N_0\sin(\theta)\exp\left[-U_{rod}(z,\theta)/k_BT\right], \tag{23}$$

where $\sin(\theta)$ is the factor accounting for the degeneracy when integrating out the variable of azimuth angle ϕ (there is no ϕ dependence), and N_0 is the normalizing factor to ensure the unit area for the integral of $\rho^{\mathrm{eq}}(z,q)$. The effective energy landscape then becomes

$$\frac{W(z,\theta)}{k_BT} = -\ln\left[\rho^{eq}(z,\theta)\right] + C, \tag{24}$$

where C is an integration constant related to a reference energy. The 2D energy landscape that can be converted to 1D effective energy landscape in either coordinate by integration is

$$\begin{aligned}\frac{W_\theta(\theta)}{k_BT} &= \int\exp\left[-W_{rod}(z,\theta)/k_BT\right]dz + C,\\ \frac{W_z(z)}{k_BT} &= \int\exp\left[-W_{rod}(z,\theta)/k_BT\right]d\theta + C.\end{aligned} \tag{25}$$

2. Rod diffusion far from an interface

The anisotropic diffusion behavior of a rod-shaped particle can be characterized by the mean squared positional displacement (MSPD) along directions parallel and perpendicular to the long axis. The displacement vector of the center of mass at time t can be decomposed into parallel and perpendicular components based on the initial orientation in the particle frame (Fig. 1). For MSPDs in parallel and perpendicular directions (see the supplementary material),

$$\begin{aligned}\langle\Delta r_\parallel(t)\Delta r_\parallel(t)\rangle &= 2D^t_{\perp1}t + \frac{2}{3}\left(D^t_\parallel - D^t_{\perp1}\right)t + \frac{4}{3}\left(D^t_\parallel - D^t_{\perp1}\right)\\ &\quad\times\frac{1}{6D^r_{\perp1}}\left[1 - \exp\left(-6D^r_{\perp1}t\right)\right],\\ \langle\Delta r_{\perp1}(t)\Delta r_{\perp1}(t)\rangle &= 2D^t_{\perp1}t + \frac{2}{3}\left(D^t_\parallel - D^t_{\perp1}\right)t - \frac{2}{3}\left(D^t_\parallel - D^t_{\perp1}\right)\\ &\quad\times\frac{1}{6D^r_{\perp1}}\left[1 - \exp\left(-6D^r_{\perp1}t\right)\right],\end{aligned} \tag{26}$$

where angle brackets indicate the ensemble average. For bulk diffusion, $\langle\Delta r_{\perp1}(t)\Delta r_{\perp1}(t)\rangle$ and $\langle\Delta r_{\perp2}(t)\Delta r_{\perp2}(t)\rangle$ are equivalent. If the MSPD is calculated by averaging over all trajectories with different initial orientations and all time scales, the results in Eq. (26) reduce to

$$\langle\Delta r(t)\Delta r(t)\rangle = 4D^t_{\perp1}t + 2D^t_\parallel t, \tag{27}$$

where $(\Delta r)^2 = (\Delta r_\parallel)^2 + (\Delta r_{\perp1})^2 + (\Delta r_{\perp2})^2$. 3D Brownian rotation is usually characterized by an orientation auto-correlation function related to rotational diffusivity as[32]

$$\langle\mathbf{n}_\parallel(t)\cdot\mathbf{n}_\parallel(0)\rangle = \exp(-2D^r_{\perp1}t), \tag{28}$$

where $\mathbf{n}_\parallel(t)$ is the rod's orientation vector at an elapsed time, t.

3. Rod diffusion parallel to a wall

For rods adjacent to a wall, the 2D projected MSPD and mean squared angular displacements (MSADs) are measurable quantities to characterize rod diffusion. Assuming the rod is strictly moving in 2D, the parallel and perpendicular MSPDs [from Eq. (26)] become[21]

$$\begin{aligned}\langle\Delta r_\parallel(t)\Delta r_\parallel(t)\rangle &= (D^t_\parallel + D^t_{\perp1})t - (D^t_{\perp1} - D^t_\parallel)\\ &\quad\times\frac{1}{4D^r_{\perp2}}\left[1 - \exp(-4D^r_{\perp2}t)\right],\\ \langle\Delta r_{\perp1}(t)\Delta r_{\perp1}(t)\rangle &= (D^t_\parallel + D^t_{\perp1})t + (D^t_{\perp1} - D^t_\parallel)\\ &\quad\times\frac{1}{4D^r_{\perp2}}\left[1 - \exp(-4D^r_{\perp2}t)\right],\end{aligned} \tag{29}$$

and similar to Eq. (27) for bulk diffusion, the MSPD averaged over all orientations is

$$\langle\Delta r(t)\Delta r(t)\rangle = 2(D^t_\parallel + D^t_{\perp1})t. \tag{30}$$

In the event that z and θ are not strictly constrained, the projected 2D MSPD is obtained by replacing diffusivities in Eq. (29) with probability-weighted diffusivities as[1]

$$\begin{aligned}\left\langle D^t_{\parallel}\right\rangle_{z,\theta} &= \int (D^t_{\parallel}\sin^2\theta + D^t_{\perp 2}\cos^2\theta)\rho^{eq}(z,\theta)d\theta dz,\\ \left\langle D^t_{\perp 1}\right\rangle_{z,\theta} &= \int D^t_{\perp 1}\rho^{eq}(z,\theta)d\theta dz,\end{aligned} \tag{31}$$

where subscripts denote averages over the indicated variables, where $\rho^{eq}(z,q)$ is the equilibrium distribution from Eq. (23).

4. Rod diffusion normal to wall

Rod diffusion normal to a wall is separation dependent via hydrodynamic interactions.[13,33] Diffusion coefficients are connected to the normal-to-wall component in the MSPD as[11]

$$D^t_3(z) = \frac{1}{2}\lim_{t\to 0}\frac{\left\langle(\Delta x_3(z,t))^2\right\rangle}{t}, \tag{32}$$

which can be used to extract the diffusion coefficient from particle trajectories. The diffusion coefficients can also be related to diffusion coefficients in the particle frame as

$$D^t_3(z) = \int (D^t_{\parallel}\cos^2\theta + D^t_{\perp 2}\sin^2\theta)\rho^{eq}(\theta)d\theta. \tag{33}$$

III. METHODS

We implemented CSD for two types of experiments: rod diffusion in bulk media and near a wall. In both cases, the rod material properties correspond to gold (Au) nano-rods of different aspects in aqueous media with 0.1 mM univalent electrolyte ($G_s/a = 0.297kT$, $B^{pw} = 486.6kT$, $\kappa^{-1} = 30$ nm) with the forces listed in the supplementary material. In both cases, the spheres composing the rod have a radius of $a = 200$ nm. For bulk diffusion, the rod aspect ratio is $p = 4$, rods are only subject to Brownian forces, the integration time step is 0.5 ms, and particle coordinates are recorded every 50 steps for 10 000 s. For rods adjacent to walls, rod aspect ratios include $p = 4$, 7, 12, and rods are subject to gravitational, electrostatic, and Brownian forces. For the rod-wall cases, the integration time step is 0.2 ms and particle coordinates are recorded every 50 steps for 2000 s. Boltzmann inversions of time averaged particle distributions [Eqs. (24) and (25)] are used to obtain energy landscapes from simulated trajectories. The vertical position, z, and polar angle, θ, are discretized with a resolution of 20 nm and 1°. For dynamic analyses, time-resolved MSPD and orientation auto-correlation function are calculated from simulated trajectories.

IV. RESULTS AND DISCUSSION

A. Rod bulk diffusivities

Figure 2 depicts the bulk diffusion modes for rods with aspect ratios of $p = 2$-30 calculated via the CSD method and its comparison with cylindrical rod results.[18] For a single rod far from any boundaries, off-diagonal terms of $\mathbf{D}_{rod}$ in the particle frame vanish since there are no correlations between different types of motion. In the bulk, translational and rotational diffusivities along $\mathbf{n}_{\perp 1}$ and $\mathbf{n}_{\perp 2}$ are equivalent, so results

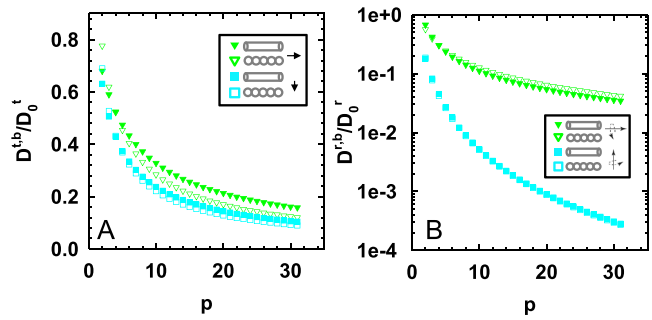

FIG. 2. Bulk diffusivities for chain-of-spheres vs. cylinders vs. aspect ratio (p = 2-30). (a) Translational diffusivities (normalized by $kT/6\pi\mu a$) along $\mathbf{n}_{\parallel}$ (green) for chain-of-spheres (open triangle) vs. cylinder model (filled triangles) and along $\mathbf{n}_{\perp 1}$ (cyan) for chain-of-spheres (open squares) vs. cylinder model (filled squares). (b) Rotational diffusivities (normalized by $kT/8\pi\mu a^3$) about $\mathbf{n}_{\parallel}$ (green) for chain-of-spheres (open triangle) vs. cylinder model (filled triangles) and about $\mathbf{n}_{\perp 1}$ (cyan) for chain-of-spheres (open squares) vs. cylinder model (filled squares).

are only shown for $\mathbf{n}_{\perp 1}$. In Fig. 2(a), translational diffusivities along $\mathbf{n}_{\perp 1}$ for chains-of-spheres show a systematic positive deviation (<10%) from the cylinder model for $p > 3$. The positive deviation can be understood through the fact that when a sphere translates through a quiescent flow, it experienced less drag than a cylindrical surface of length $2a$ translating perpendicular to its axis.

For translational diffusion along $\mathbf{n}_{\parallel}$, the chain-of-spheres model yields an overall smaller value (<20%) than the cylinder model. The cylinder model[18] is based on using many small spherical beads to model the cylinder shape. As such, it appears that the translational diffusivity along $\mathbf{n}_{\parallel}$ in the cylinder model is greater than the chain-of-spheres model because the density of smaller spherical beads composing the rod surface makes the cylinder smoother. Therefore, the difference is due to the finite size effect of the spheres in the chain-of-sphere rod, with the chain of spheres providing more friction as a corrugated surface.

In Fig. 2(b), we observed a close correspondence (<5%) between the two models for rotational diffusivities about $\mathbf{n}_{\perp 1}$. However, the rotational diffusivity about $\mathbf{n}_{\parallel}$ shows higher diffusivities for the chain-of-spheres computed to the cylinder model (<20%, difficult to see on the log scale). The reason for this discrepancy is likely the same as in the case of translation along $\mathbf{n}_{\parallel}$; the rotation of spheres experiences less drag than the rotation of a short cylindrical surface section of length $2a$. For convenience and ease of use of the theoretical results in Fig. 2, empirical fits to length and aspect ratio dependent bulk diffusivities, $D(L,p)$, are reported in the supplementary material with a general form with coefficients a_i given by

$$D(L,p) = \frac{kT}{2\pi\mu L}\left[\ln p + \frac{a_1p^2 + a_2p + a_3}{p^2 + a_4p + a_5}\right]. \tag{34}$$

B. Rod diffusivity near a wall

Figure 3 depicts height-dependent diffusivities for rods consisting of chains-of-spheres parallel to a wall for $p = 7$, 12. Each diffusivity is normalized by its bulk value so that all values approach zero as particle-wall surface separation, h, vanishes and unity as separation becomes large ($>50a$).

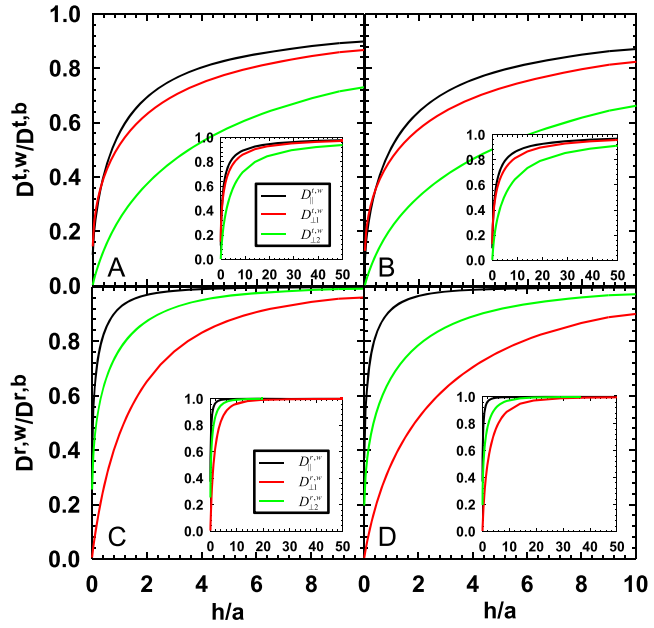

FIG. 3. Diffusivities for chain-of-spheres rod oriented parallel to wall. Height dependent coefficients in directions $\mathbf{n}_{\parallel}$ (black), $\mathbf{n}_{\perp 1}$ (red), $\mathbf{n}_{\perp 2}$ (green) for translational diffusivities of rods with aspect ratios (a) $p = 7$, (b) $p = 12$ and for rotational diffusivities with aspect ratios (c) $p = 7$, (d) $p = 12$.

Figure 3(a) shows translational diffusivities in the three directions each having a distinct elevation and aspect ratio dependence. Translational diffusivities for the chain-of-spheres follow trends for a single sphere approaching a wall.[13] All diffusivities decrease with decreasing separation, even when $h/a \sim 50$, which reflects far-field hydrodynamic interactions. Translational diffusivity decreases fastest along $\mathbf{n}_{\perp 2}$ as $O(h/a)$ and more slowly along $\mathbf{n}_{\parallel}$ and $\mathbf{n}_{\perp 1}$ as $O(\ln(h/a))$.

The hydrodynamic hindrance increases for longer rods. For chains-of-spheres above a wall, the contribution of each sphere to increasing drag can be understood by the addition of 2-body hydrodynamic interactions as well as multi-body interactions between particles and the wall. The increasing drag per unit length becomes smaller as the rod length increases ($p > 20$) since multi-body interactions between distant neighbors eventually become insignificant. Effects of multi-body hydrodynamics are most pronounced at intermediate separations ($1 < h/a < 10$). In the far-field ($h/a > 10$) and in the lubrication ($h/a \ll 1$) limits, the net interaction is dominated by pairwise interactions of the wall with each sphere within the chain-of-spheres.

Height dependent rotational diffusivities in the three directions are shown in Figs. 3(c) and 3(d). Rotations about $\mathbf{n}_{\perp 1}$ and $\mathbf{n}_{\perp 2}$ experience wall interactions when $h \approx$ 20-30a, whereas rotation about $\mathbf{n}_{\parallel}$ begins to deviate from bulk behavior for $h < 5a$. Although chain-of-sphere translation and rotation about $\mathbf{n}_{\perp 1}$ and $\mathbf{n}_{\perp 2}$ both involve translation of constituent spheres in the $\mathbf{n}_{\perp 1}$ and $\mathbf{n}_{\perp 2}$ directions, rotational hindrance is shorter-ranged compared to translational hindrance. This can be understood by considering the wall effect on the collective motion of spheres comprising the chain-of-spheres. Consider one sphere translating in bulk and generating a flow field along the translation direction; a nearby sphere will experience a higher mobility when it translates in the same direction and a lower mobility when translating in the opposite direction. When two spheres are near a wall, a no-slip boundary changes the flow field so that mobilities associated with collective motion decrease compared to the bulk, and mobilities for relative motion increase compared to the bulk (see hydrodynamic screening due to no-slip boundaries discussed elsewhere[34]). For translations along $\mathbf{n}_{\parallel}$, $\mathbf{n}_{\perp 1}$, and $\mathbf{n}_{\perp 2}$, all spheres move in the same direction, and the wall exerts a long-range hindrance. For rotations about $\mathbf{n}_{\perp 1}$ and $\mathbf{n}_{\perp 2}$, half the spheres move in the opposite direction to the other half; thus, the wall exerts a relatively weaker and short-ranged hindrance.

For rods much closer to the wall, near-field effects dominate a dramatic drop in diffusivities as they vanish near contact similar to the translational diffusivity. There are several interesting features in the height dependence of different rotational diffusivity modes. The rotation about $\mathbf{n}_{\perp 1}$ decreases faster than rotation about $\mathbf{n}_{\perp 2}$ since rotation about $\mathbf{n}_{\perp 1}$ involves translation of spheres normal to the wall. In the lubrication limit, rotation about $\mathbf{n}_{\parallel}$ and $\mathbf{n}_{\perp 2}$ vanishes slower as $O(\ln(h/a))$ but rotation about $\mathbf{n}_{\perp 1}$ vanishes faster as $O(h/a)$. The rotational diffusion along the $\mathbf{n}_{\parallel}$ direction generally has smaller and shorter-ranged interactions compared to other modes because the decrease of rotational diffusivity of constituent spheres along the $\mathbf{n}_{\parallel}$ direction scales as (h/a),[3] whereas the decrease of the translational diffusivity of constituent spheres scales as (h/a).[35]

To practically implement the theoretical results reported in Fig. 3, empirical fits are reported in the supplementary material. To illustrate the form of these corrections for a particular case, the correction for rod diffusion parallel to a wall is given by

$$f^{t}_{\parallel,p}(h) = \frac{D^{t,w}_{\parallel}(L,p,h)}{D^{t,b}_{\parallel}(L,p)}, \tag{35}$$

where both terms on the right hand side are given by Eq. (7). Based on this definition, Eq. (35) approaches 1 as h approaches infinity and 0 as h vanishes. The fit form of $f(h)$ is

$$f^{t}_{\parallel}(h) = \frac{a_1(h/a) + a_2(h/a)^2 + a_3(h/a)^3}{1 + a_4\,(h/a) + a_5(h/a)^2}, \tag{36}$$

where a_i are fitting coefficients. When $a < h < 10a$, an additional function [denoted as $g(p)$ in the supplementary material] is required to account for an additional weak aspect ratio dependence beyond the bulk dependence. As explained in more detail in the supplementary material, it is possible to compute all diffusivities with a general form given by $D(L,p,h) = D(L,p)f(h)g(p)$.

C. Translational and rotational coupling

In contrast with bulk diffusion, rod particles near surfaces have coupling between translational and rotational modes, which is captured by non-zero, off-diagonal terms in the diffusivity tensor. To characterize coupling, we define a correlation coefficient as

$$Corr_{ij} = D_{ij} \Big/ \sqrt{D_{ii}D_{jj}}, \tag{37}$$

where i and j have indices, T||, T⊥1, T⊥2 representing translation along $\mathbf{n}_{\parallel}$, $\mathbf{n}_{\perp 1}$, $\mathbf{n}_{\perp 2}$, and R||, R⊥1, R⊥2 representing rotation about $\mathbf{n}_{\parallel}$, $\mathbf{n}_{\perp 1}$, $\mathbf{n}_{\perp 2}$.

In Fig. 3 where the rod is parallel to a wall, the symmetric nature of this configuration produces little coupling, although some weak coupling exists between translation along $\mathbf{n}_{\parallel}$ and rotation about $\mathbf{n}_{\perp 1}$. To consider coupling in a more interesting configuration, Fig. 4 shows results for a rod of aspect ratio $p = 7$ at $\theta = 45°$ angle (i.e., angle between $\mathbf{n}_{\parallel}$ and $\mathbf{e}_3$ is 45°). Figures 4(a) and 4(b) show the diagonal terms of D vs. the distance of the closest approach between the lowest sphere and the wall, h. As the rod-wall separation decreases, all diffusive modes decrease monotonically similar to the overall trend for rods oriented parallel to a wall in Fig. 3. However, the exact coefficients have different functional forms. For example, translational diffusivities decrease faster than the parallel case because the motion along $\mathbf{n}_{\parallel}$ involves components of motion normal to the wall.

The translation-rotation coupling of rods near surfaces shows several interesting effects. Figure 4(c) shows height dependent correlation coefficients ($Corr_{\mathrm{T}\parallel,\mathrm{T}\perp 2}$, $Corr_{\mathrm{T}\parallel,\mathrm{R}\perp 1}$, $Corr_{\mathrm{T}\perp 1,R\perp 2}$, $Corr_{\mathrm{T}\perp 2,\mathrm{R}\perp 1}$) from Eq. (37) for off-diagonal/coupling terms in the diffusivity tensor. For example, the terms $Corr_{\mathrm{T}\parallel,\mathrm{T}\perp 2}$ and $Corr_{\mathrm{T}\parallel,\mathrm{R}\perp 1}$ show how translation along $\mathbf{n}_{\parallel}$ induces translation along $\mathbf{n}_{\perp 2}$ and rotation about $\mathbf{n}_{\perp 1}$ [Figs. 4(e) and 4(f)]. This has the net effect of the rod aligning itself with the wall and having an apparent attraction to the wall. As such, the rod moves a shorter distance compared to the case without coupling where only translation along $\mathbf{n}_{\parallel}$ is allowed.[36] In another case, coupling $Corr_{\mathrm{T}\perp 1,\mathrm{R}\perp 2}$ between translation along $\mathbf{n}_{\perp 1}$ with rotation about $\mathbf{n}_{\perp 2}$ [Fig. 4(g)] is due to non-uniform drag on the rod by the wall; lower end experiences more drag than the upper end. As such, when a lateral force is applied along $\mathbf{n}_{\perp 1}$, the upper end tends to move faster than the lower end and consequently the rod rotates. Similar reasoning applies to the coupling $Corr_{\mathrm{T}\perp 2,\mathrm{R}\perp 1}$ between translation in $\mathbf{n}_{\perp 2}$ and rotation about $\mathbf{n}_{\perp 1}$ [Fig. 4(h)]. All correlation coefficients become non-negligible for $h/a < 1$.

In Fig. 4(d), we investigate the angular dependence of correlation coefficients at fixed separation, $h/a = 0.05$. The coupling $Corr_{\mathrm{T}\parallel,\mathrm{T}\perp 2}$ of translation along $\mathbf{n}_{\parallel}$ with translation about $\mathbf{n}_{\perp 2}$ [Fig. 4(e)] has a maximum at ~30° and vanishes at both normal and parallel configurations. Similarly, the coupling of $Corr_{\mathrm{T}\parallel,\mathrm{R}\perp 1}$ translation along $\mathbf{n}_{\parallel}$ with rotation about $\mathbf{n}_{\perp 1}$ [Fig. 4(f)] is a maximum at ~30° and vanishes at both normal and parallel configurations. The coupling $Corr_{\mathrm{T}\perp 1,\mathrm{R}\perp 2}$ between translation along $\mathbf{n}_{\perp 1}$ and rotation about $\mathbf{n}_{\perp 2}$ [Fig. 4(g)] decreases monotonically from the normal configuration ($\theta = 0°$), where the imbalance of drag between the two ends is greatest, to the parallel configuration ($\theta = 90°$), where the imbalance disappears. For the coupling $Corr_{\mathrm{T}\perp 2,\mathrm{R}\perp 1}$ between translation along $\mathbf{n}_{\perp 2}$ and rotation about $\mathbf{n}_{\perp 1}$ [Fig. 4(h)], the correlation somewhat surprisingly peaks at ~80°. This arises from the reverse upward fluid flow when particles are moving towards a wall that induces a rotation about $\mathbf{n}_{\perp 1}$. Due to symmetry, there is no coupling between (1) translations along $\mathbf{n}_{\parallel}$ with translation along $\mathbf{n}_{\perp 1}$, (2) translation along $\mathbf{n}_{\parallel}$ with rotation about $\mathbf{n}_{\parallel}$, and (3) translation along $\mathbf{n}_{\perp 2}$ with rotation about $\mathbf{n}_{\parallel}$.

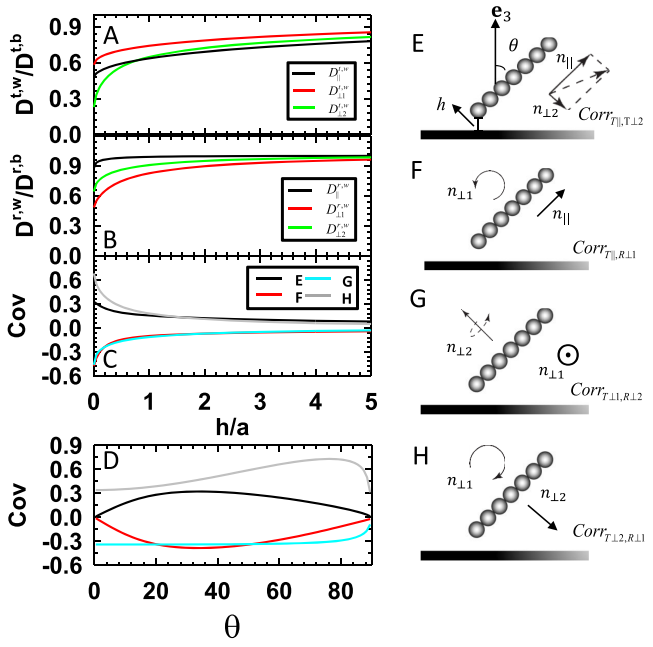

FIG. 4. Chain-of-spheres oblique ($\phi = 45°$) to the wall for $p = 7$. Height (distance of the closest approach) dependent coefficients for (a) translational and (b) rotational diffusivities along/about $\mathbf{n}_{\parallel}$ (black), $\mathbf{n}_{\perp 1}$ (red), and $\mathbf{n}_{\perp 2}$ (green). (c) Height and (d) angle dependent correlation coefficients [Eq. (37)] for coupled motions including (e) translation along $\mathbf{n}_{\parallel}$ and translation along $\mathbf{n}_{\perp 2}$ ($Corr_{\mathrm{T}\parallel,\mathrm{T}\perp 2}$, black), (f) translation along $\mathbf{n}_{\parallel}$ and rotation about $\mathbf{n}_{\perp 1}$ ($Corr_{\mathrm{T}\parallel,\mathrm{R}\perp 1}$, red), (g) translation along $\mathbf{n}_{\perp 1}$ and rotation about $\mathbf{n}_{\perp 2}$ ($Corr_{\mathrm{T}\perp 1,\mathrm{R}\perp 2}$, cyan), (h) translation along $\mathbf{n}_{\perp 2}$ and rotation about $\mathbf{n}_{\perp 1}$ ($Corr_{\mathrm{T}\perp 2,\mathrm{R}\perp 1}$, gray).

D. Analysis of bulk rod diffusion

With the ability to predict $\mathbf{D}$, dynamic simulations using $\mathbf{D}$ are used to show how analysis of rod trajectories, as in microscopy experiments, can be used to measure and model diffusion with connections to components of $\mathbf{D}$. Figure 5 reports results of the analysis of bulk diffusion trajectories of a single rod with $p = 5$. CSD was used to produce simulated random walk trajectories in bulk media [Fig. 5(a)] by considering only Brownian forces in Eq. (17). Vectors schematically depicted in Fig. 5(a) show how each three dimensional translational step in the lab frame is decomposed into components parallel and perpendicular to the rod axis in the particle frame. Figure 5(b) shows MSPD curves generated from simulated trajectories. Results in Fig. 5(b) include an MSPD for the center of mass in the lab frame as well as MSPDs parallel and perpendicular to the rod long axis in the particle frame. MSPD curves measured from simulated trajectories show agreement with theoretical predictions in Eqs. (26) and (27) for diffusion in the particle and laboratory frames.

The rotational diffusion characteristic time, $\tau_c = 1/2D^r_{\perp 2}$, captures the process of losing directional memory and the crossover from anisotropic translational diffusion to isotropic translational diffusion. In the short time limit ($t \ll \tau_c$), the anisotropic translational diffusion behavior is demonstrated by fast and slow MSPD curves in parallel (i.e., $\mathbf{n}_{\parallel}$ direction) and perpendicular (i.e., $\mathbf{n}_{\perp 1}$ direction) directions. For $t > t_c$, the two curves [represented in Eq. (29)] converge towards one curve [given by $(D^t_{\parallel} + D^t_{\perp 1})t$, see Eq. (27)], indicating the transition from anisotropic to isotropic diffusion. Figure 5(c)

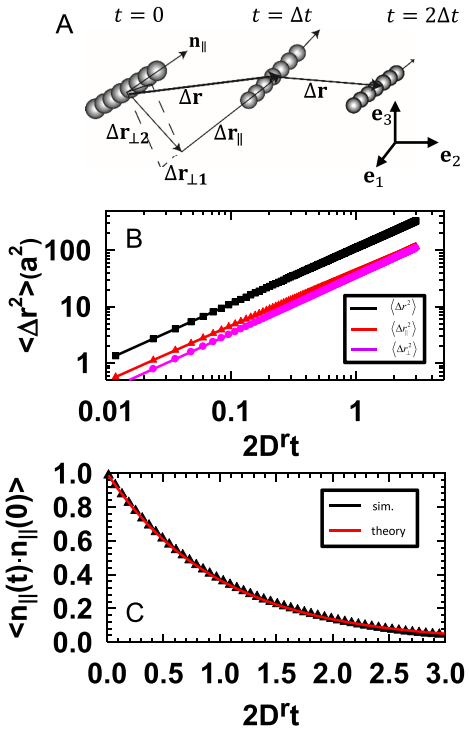

FIG. 5. MSPD and orientation autocorrelation function for bulk rod diffusion for $p = 5$. (a) Schematic of the rod trajectory with displacement vector $\Delta\mathbf{r}$ decomposed into components parallel and perpendicular to the rod axis in the particle frame with unit vectors in the lab frame shown for reference. (b) MSPD from simulation (points) vs. theory [Eqs. (26) and (27)] (lines) for translational diffusion (black) in the lab frame, (red) parallel to the rod long axis in the particle frame, and (pink) perpendicular to the rod long axis in the particle frame. (c) Orientation autocorrelation function from simulation (black triangles) and theory [Eq. (28)] (red line).

shows the orientation autocorrelation function calculated from simulation trajectories and the theoretical prediction from the right hand side of Eq. (28) [using D_r from Eq. (7)]. Excellent agreement is observed between measured simulation results and theoretical predictions. The autocorrelation function confirms rods lose orientational correlation on the characteristic time scale τ_c.

E. Analysis of rod diffusion near a wall

The simulations and analyses of bulk rod diffusion are extended here to rods near walls. Because dynamic analyses require information on how rod states are sampled near surfaces, our results first quantify time-averaged equilibrium distributions of rod elevation and orientation. Figure 6 shows equilibrium distributions of rods with $p = 4$, 7, 12 confined near a wall surface by gravity (normal to the underlying wall) while experiencing electrostatic repulsion. In particular, CSD simulations are performed with rods subject to gravitational, electrostatic, and Brownian forces. Energy landscapes parameterized by the rod elevation and azimuthal angle (z, θ) are used to characterize equilibrium distribution of states.

As shown in Figs. 6(a)–6(f), 2D energy landscapes from predictions [Eqs. (21)–(25)] and measured from simulations [via Boltzmann inversion, Eqs. (24) and (25)] show good agreement. For rods of all lengths, the most probable configuration is aligned parallel to the wall ($\theta = 90°$). Longer rods are more constrained in both z and θ. At the same height, longer rods are more constrained in θ due to electrostatic repulsion from the wall. In addition, longer rods are more constrained in z due to their increasing buoyant weight. Results in Figs. 6(g) and 6(h) also show projected one-dimensional energy landscapes vs. z and θ using Eq. (25). As p increases, the region of low energy/frequent sampling ($W < 5kT$) in height z is reduced from ~6a to ~2a. With regard to orientation dependence, a rod with $p = 4$ has a non-vanishing probability to be aligned normal to the interface ($\theta = 0°$), whereas a rod with

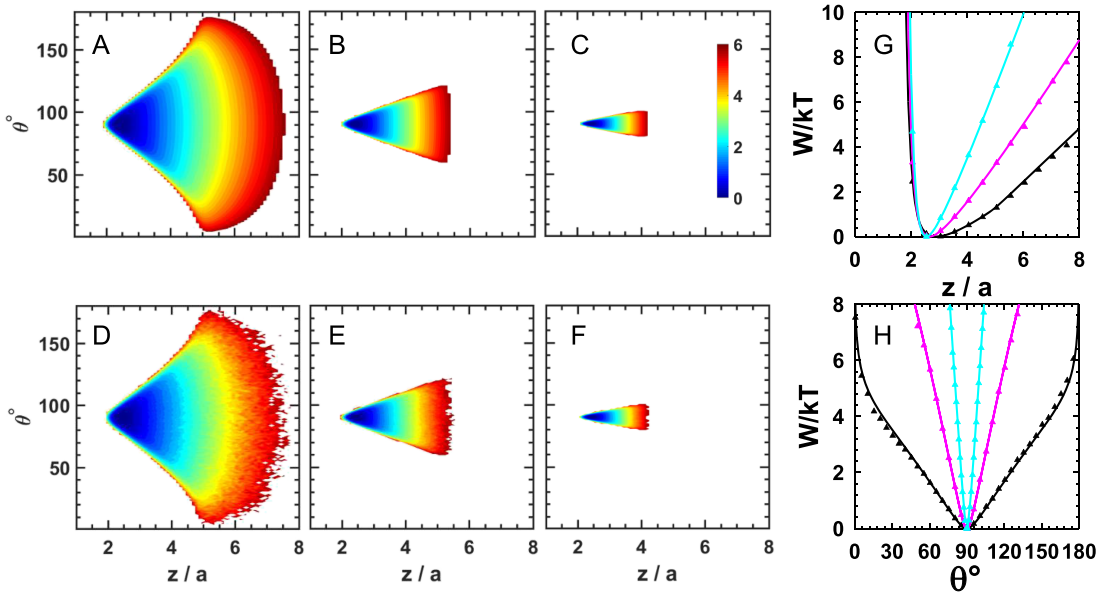

FIG. 6. Energy landscapes for a single rod above the wall for analyzing average diffusivities [via Eqs. (31) and (33), see Fig. 7]. For rods with $p = 4$, 7, 12, two dimensional energy landscapes vs. elevation z/a and θ as predicted from Eq. (24) [(a)-(c)] and as measured from CSD simulations via an inverse Boltzmann analysis in Eq. (24) [(d)-(f)]. One dimensional energy landscapes vs. (g) z/a and (h) θ for the same rods in (a)-(f) plotted as (black) $p = 4$, (pink) $p = 7$, and (cyan) $p = 12$ with (symbols) simulation results and (lines) from Eq. (25).

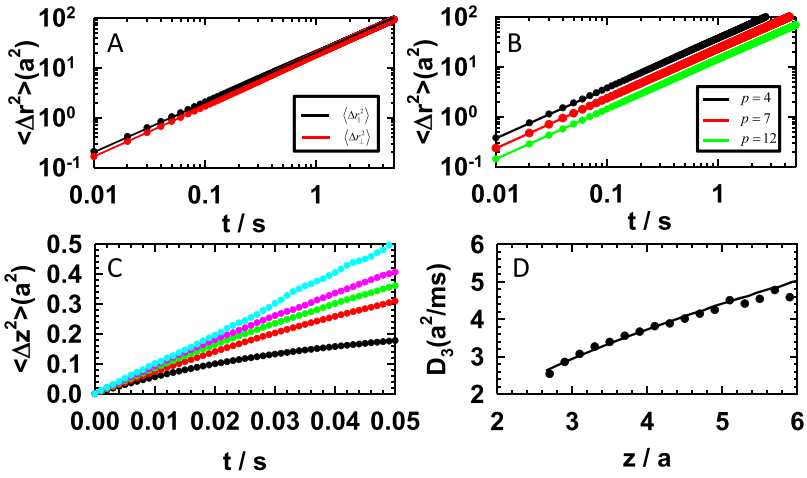

FIG. 7. Trajectory analysis for a single rod near a wall. (a) Rod with $p = 4$ near a wall for interactions in Fig. 6(a), MSPDs parallel (black) and perpendicular (red) to the rod long axis in the particle frame from simulated trajectory (symbols) and theory [lines, Eq. (29)]. (b) MSPDs for center of mass coordinates in the lab frame for rods with $p = 4$ (black), $p = 7$ (red), and $p = 12$ (green) from simulated trajectory [symbols, from Figs. 6(a)–6(f)] and theory [lines, Eq. (30)]. (c) MSPDs for center of mass for a rod with $p = 7$ [from Figs. 6(b) and 6(e)] normal to wall vs. elevation for starting coordinates at (bottom-to-top) $z = 2.9a$, $3.9a$, $4.9a$, $5.9a$, $6.9a$. (d) Normal particle-wall diffusivity vs. elevation [$D_3(z)$] from MSPDs in (c) via Eq. (32) (points) and theory in Eq. (33) (line).

p = 12 can only sample angles within ±10° of the parallel configuration.

For experiments where particle trajectories are measured adjacent to a wall, the MSPD is often used to quantify diffusion.[21] Figure 7(a) shows 2D parallel and perpendicular components of the MSPD in the particle frame for a rod with aspect ratio 4 from the simulation and the theoretical curves from Eq. (29). Similar to 3D bulk translational diffusion, faster diffusion is observed along the rod long axis at short times until the crossover to isotropic diffusion occurs on the characteristic time scale for rotational diffusion. Figure 7(b) shows how translational diffusion parallel to the wall varies for p = 4, 7, and 12. These data show that at longer times when diffusion is isotropic, higher aspect ratio rods have smaller average diffusivities as the result of their great size and their sampling lower elevations as the result of their greater buoyant weight.

Figure 7(c) shows diffusion normal to the wall for a rod with $p = 7$. The MSPDs are for different starting elevations[11] and show a systematic decrease as the rod elevation decreases. The decreasing diffusivity is due to increasing hydrodynamic hindrance as the rod is closer to the wall. As shown in Fig. 7(d), the diffusivities extracted from the initial slopes of the MSPD curves in Fig. 7(c) based on Eq. (32) have good agreement with theory prediction from Eq. (33). The significant change in diffusivity vs. elevation is similar to spheres[13] and indicates that treating rod diffusivities as a constant when approaching a surface can produce significant errors when either interpreting measurements or predicting interfacial or confined rod particle dynamics.

V. CONCLUSION

Our results include methods to compute diffusivities, simulate dynamics, and analyze trajectories for colloidal rods in bulk media and near wall surfaces by modelling rods as chains-of-spheres. Diffusion coefficients and simulated trajectories are based on a constrained Stokesian dynamics method to include hydrodynamic interactions, whereas trajectory analyses are general to any anisotropic particle near a wall. Bulk diffusivities show good correspondence with established literature results, and diffusivities near walls are summarized in terms of separation and aspect ratio dependent rational expressions fit to modeling results. Analyses of particle trajectories in terms of time-averaged equilibrium distribution functions and MSPDs show good agreement between measured quantities and theoretical predictions, including a crossover from anisotropic to isotropic translational diffusion. The methods reported in this work are sufficiently general that they should be readily extendable to other anisotropic particle shapes and many-particle concentrated systems near wall surfaces in future work.

SUPPLEMENTARY MATERIAL

See supplementary material for additional details of calculating resistance, mobility, and diffusion coefficients; implementing constraint dynamics and mean squared displacement analysis for bulk rod diffusion; and empirical fits to position dependent rod diffusion coefficients.

ACKNOWLEDGMENTS

We acknowledge the financial support by the National Science Foundation (No. CBET-1234981).

[1] G. Li and J. X. Tang, "Diffusion of actin filaments within a thin layer between two walls," Phys. Rev. E **69**(6), 061921 (2004).
[2] M.-H. Lu, L. Feng, and Y.-F. Chen, "Phononic crystals and acoustic metamaterials," Mater. Today **12**(12), 34–42 (2009).
[3] M. J. A. Hore and R. J. Composto, "Nanorod self-assembly for tuning optical absorption," ACS Nano **4**(11), 6941–6949 (2010).
[4] M. Rotunno, T. Bellini, Y. Lansac, and M. A. Glaser, "Phase behavior of polarizable spherocylinders in external fields," J. Chem. Phys. **121**(11), 5541–5549 (2004).
[5] A. Donev, I. Cisse, D. Sachs, E. A. Variano, F. H. Stillinger, R. Connelly, S. Torquato, and P. M. Chaikin, "Improving the density of jammed disordered packings using ellipsoids," Science **303**(5660), 990–993 (2004).
[6] M. J. Solomon and P. T. Spicer, "Microstructural regimes of colloidal rod suspensions, gels, and glasses," Soft Matter **6**(7), 1391–1400 (2010).
[7] K. Chaudhary, J. J. Juarez, Q. Chen, S. Granick, and J. A. Lewis, "Reconfigurable assemblies of Janus rods in AC electric fields," Soft Matter **10**(9), 1320–1324 (2014).
[8] H. Brenner, "The slow motion of a sphere through a viscous fluid towards a plane surface," Chem. Eng. Sci. **16**(3-4), 242–251 (1961).
[9] S. G. Anekal and M. A. Bevan, "Self diffusion in sub-monolayer colloidal fluids near a wall," J. Chem. Phys. **125**(3), 034906 (2006).

[10]S. G. Anekal and M. A. Bevan, "Interpretation of conservative forces from Stokesian dynamic simulations of interfacial and confined colloids," J. Chem. Phys. **122**, 034903 (2005).
[11]D. J. Beltran-Villegas, R. M. Sehgal, D. Maroudas, D. M. Ford, and M. A. Bevan, "Fokker–Planck analysis of separation dependent potentials and diffusion coefficients in simulated microscopy experiments," J. Chem. Phys. **132**(4), 044707 (2010).
[12]E. S. Pagac, R. D. Tilton, and D. C. Prieve, "Hindered mobility of a rigid sphere near a wall," Chem. Eng. Commun. **148-150**, 105 (1996).
[13]M. A. Bevan and D. C. Prieve, "Hindered diffusion of colloidal particles very near to a wall: Revisited," J. Chem. Phys. **113**(3), 1228–1236 (2000).
[14]R. J. Oetama and J. Y. Walz, "Simultaneous investigation of sedimentation and diffusion of a single colloidal particle near an interface," J. Chem. Phys. **124**(16), 164713 (2006).
[15]D. J. Beltran-Villegas, T. D. Edwards, and M. A. Bevan, "Self-consistent colloidal energy and diffusivity landscapes in macromolecular solutions," Langmuir **29**(40), 12337–12341 (2013).
[16]S. Broersma, "Viscous force and torque constants for a cylinder," J. Chem. Phys. **74**(12), 6989–6990 (1981).
[17]G. K. Batchelor, "Slender-body theory for particles of arbitrary cross-section in Stokes flow," J. Fluid Mech. **44**(03), 419–440 (1970).
[18]M. M. Tirado, C. L. p. Martínez, and J. G. a. de la Torre, "Comparison of theories for the translational and rotational diffusion coefficients of rod-like macromolecules. Application to short DNA fragments," J. Chem. Phys. **81**(4), 2047 (1984).
[19]S. R. Aragon and D. Flamik, "High precision transport properties of cylinders by the boundary element method," Macromolecules **42**(16), 6290–6299 (2009).
[20]M. L. Mansfield and J. F. Douglas, "Transport properties of rodlike particles," Macromolecules **41**(14), 5422–5432 (2008).
[21]Y. Han, A. M. Alsayed, M. Nobili, J. Zhang, T. C. Lubensky, and A. G. Yodh, "Brownian motion of an ellipsoid," Science **314**(5799), 626–630 (2006).
[22]D. Jeffrey and Y. Onishi, "The slow motion of a cylinder next to a plane wall," Q. J. Mech. Appl. Math. **34**(2), 129–137 (1981).
[23]N. J. De Mestre and W. B. Russel, "Low-Reynolds-number translation of a slender cylinder near a plane wall," J. Eng. Math. **9**(2), 81–91 (1975).
[24]J. T. Padding and W. J. Briels, "Translational and rotational friction on a colloidal rod near a wall," J. Chem. Phys. **132**(5), 054511–054518 (2010).
[25]M. Lisicki, B. Cichocki, and E. Wajnryb, "Near-wall diffusion tensor of an axisymmetric colloidal particle," J. Chem. Phys. **145**(3), 034904 (2016).
[26]M. De Corato, F. Greco, G. D'Avino, and P. L. Maffettone, "Hydrodynamics and Brownian motions of a spheroid near a rigid wall," J. Chem. Phys. **142**(19), 194901 (2015).
[27]J. F. Brady and G. Bossis, "Stokesian dynamics," Annu. Rev. Fluid Mech. **20**(1), 111–157 (1988).
[28]L. Durlofsky, J. F. Brady, and G. Bossis, "Dynamic simulation of hydrodynamically interacting particles," J. Fluid Mech. **180**, 21–49 (1987).
[29]J. W. Swan and J. F. Brady, "Simulation of hydrodynamically interacting particles near a no-slip boundary," Phys. Fluids **19**(11), 113306 (2007).
[30]E. J. Hinch, "Brownian motion with stiff bonds and rigid constraints," J. Fluid Mech. **271**, 219–234 (1994).
[31]A. Montesi, D. C. Morse, and M. Pasquali, "Brownian dynamics algorithm for bead-rod semiflexible chain with anisotropic friction," J. Chem. Phys. **122**(8), 084903 (2005).
[32]M. Doi and S. F. Edwards, *The Theory of Polymer Dynamics* (Oxford University Press, 1990).
[33]S. Kim and S. J. Karrila, *Microhydrodynamics: Principles and Selected Applications* (Dover Publications, 2005).
[34]P. P. Lele, J. W. Swan, J. F. Brady, N. J. Wagner, and E. M. Furst, "Colloidal diffusion and hydrodynamic screening near boundaries," Soft Matter **7**(15), 6844–6852 (2011).
[35]A. J. Goldman, R. G. Cox, and H. Brenner, "Slow viscous motion of a sphere parallel to a plane wall—I Motion through a quiescent fluid," Chem. Eng. Sci. **22**(4), 637–651 (1967).
[36]C. Sendner and R. R. Netz, "Hydrodynamic lift of a moving nano-rod at a wall," Europhys. Lett. **79**(5), 58004 (2007).

Journal of Colloid and Interface Science 449 (2015) 270–278

Contents lists available at ScienceDirect

Journal of Colloid and Interface Science

www.elsevier.com/locate/jcis

Modeling depletion mediated colloidal assembly on topographical patterns

Yuguang Yang, Tara D. Edwards, Michael A. Bevan *

Chemical & Biomolecular Engineering, Johns Hopkins University, Baltimore, MD 21218, United States

ARTICLE INFO

Article history:
Received 1 November 2014
Accepted 1 December 2014
Available online 6 December 2014

Keywords:
Tunable depletion attraction
Patterned excluded volume
Reconfigurable colloidal assembly
Monte Carlo simulations
Non-close packed structures

ABSTRACT

This work reports a model and Monte Carlo simulations of excluded volume mediated interactions between colloids and topographically patterned substrates in the presence of thermosensitive depletants. The model is matched to experiments to yield density, free energy, and potential energy landscapes that quantitatively capture particle microstructures varying from immobilized non-close packed configurations to random fluid states. A numerical model of local excluded volume affects is developed to enable computation of local depletion attraction in the presence of arbitrary geometries. Our findings demonstrate a quantitative modeling method to interpret and predict how surface patterns mediate local depletion interactions, which enables the design of colloidal based materials and devices.

1. Introduction

Depletion interactions arise between colloids and surfaces from "solute particles" being depleted, or excluded, from the gap between interacting objects [1]. When this occurs, pure solvent in the excluded volume has a different chemical potential from the solution outside the excluded volume. This produces an attraction between particles and surfaces proportional to the product of osmotic pressure and the excluded volume. Although depletion potentials become more complicated based on how solute particles interact with each other and surfaces [2], the basic picture presented above qualitatively captures the mechanism of colloidal depletion attraction for diverse solutes (*e.g.*, polymers, micelles, hydrogel particles, nanoparticles [3]). Because depletion interactions can occur in any mixture when a solute is excluded between surfaces, such interactions are expected to be ubiquitous in complex industrial formulations as well as biological systems [4].

By understanding the mechanism of depletion attraction, there is an opportunity to design such potentials by either controlling the osmotic pressure or designing the excluded volume. Examples of tuning the depletant osmotic pressure have included thermosensitive micelles [5], hydrogel particles [6,7], and polymer chains [8]. However, in each of these examples, the osmotic pressure changes because the depletant size changes, which also means the excluded volume changes (which depends on relative depletant and colloid dimensions). Beyond tuning depletant dimensions, exclude volume has been manipulated via surface geometries in several key examples including confining surfaces [9,10], surface features [11], templates for crystallization [12,13], surface roughness [14,15], and lock-and-key colloids (*i.e.*, local curvature) [16]. Although such studies demonstrate clever examples of tuning depletion interactions to affect colloidal assembly, accurate models have not been sufficiently developed to allow for systematic design and control of surface geometries that mediate local depletion potentials in colloidal materials and devices.

Here we report the development of a new method to compute local excluded volume and depletion interactions between particles and physically patterned surfaces. This method is used to analyze measurements of temperature dependent particle configurations on microfabricated surface topographies in the presence of thermosensitive depletants. Specifically, we analyze particles interacting with arrays of circles with sloping walls that produce additional local excluded volume (left side of Fig. 1, experiments reported elsewhere [17]). These measurements, and the new model reported here, are distinct from our prior study of patterned depletion mediated colloidal crystallization on an underlying gravitational energy landscape [7]. The present work is both scientifically and technologically novel by exploiting local excluded volume effects in conjunction with thermosensitive depletants to create non-close-packed reconfigurable structures. Such non-close-packed structures with length scales comparable to electromagnetic radiation have important applications as metamaterials and their reconfigurability can allow such systems to be used as static materials or programmable devices [18]. Ultimately, our findings demonstrate a quantitative modeling tool to

* Corresponding author.
E-mail address: mabevan@jhu.edu (M.A. Bevan).

http://dx.doi.org/10.1016/j.jcis.2014.12.002
0021-9797/

interpret and predict how local surface geometries alter local depletion interactions, which can enable new colloidal based materials and devices.

2. Theory

2.1. Net interaction potential

The net potential energy for colloidal particles interacting with each other, an underlying surface, and gravity (see Fig. 2) can be modeled as the superposition of independent potentials. For a charged colloidal particle i with radius, a, in the presence of non-adsorbing depletant particles, the net interaction potential is given by,

$$u_i(\mathbf{r}_i) = u_D^{pw}(\mathbf{r}_i) + u_E^{pw}(\mathbf{r}_i) + u_G^{pf}(z_i) + \sum_{j\neq i}\left[u_D^{pp}(r_{ij}) + u_E^{pp}(r_{ij})\right] \quad (1)$$

where $\mathbf{r}_i = (x_i, y_i, z_i)$ is position vector of particle i, z_i is the particle center-to-surface elevation relative to the underlying surface, and r_{ij} is center-to-center separation between particles i and j. Subscripts refer to: (E) electrostatic, (G) gravitational, and (D) depletion, and superscripts refer to: (pp) particle–particle, (pw) particle–wall, and (pf) particle–field. The range of electrostatic repulsion in this work is sufficient so that van der Waals interactions van be neglected.

2.2. Gravitational potential

The gravitational potential energy of each particle depends on its elevation above the reference surface multiplied by its buoyant weight, G, given by,

$$u_G^{pf}(z) = Gz = (4/3)\pi a^3(\rho_p - \rho_f)gz \quad (2)$$

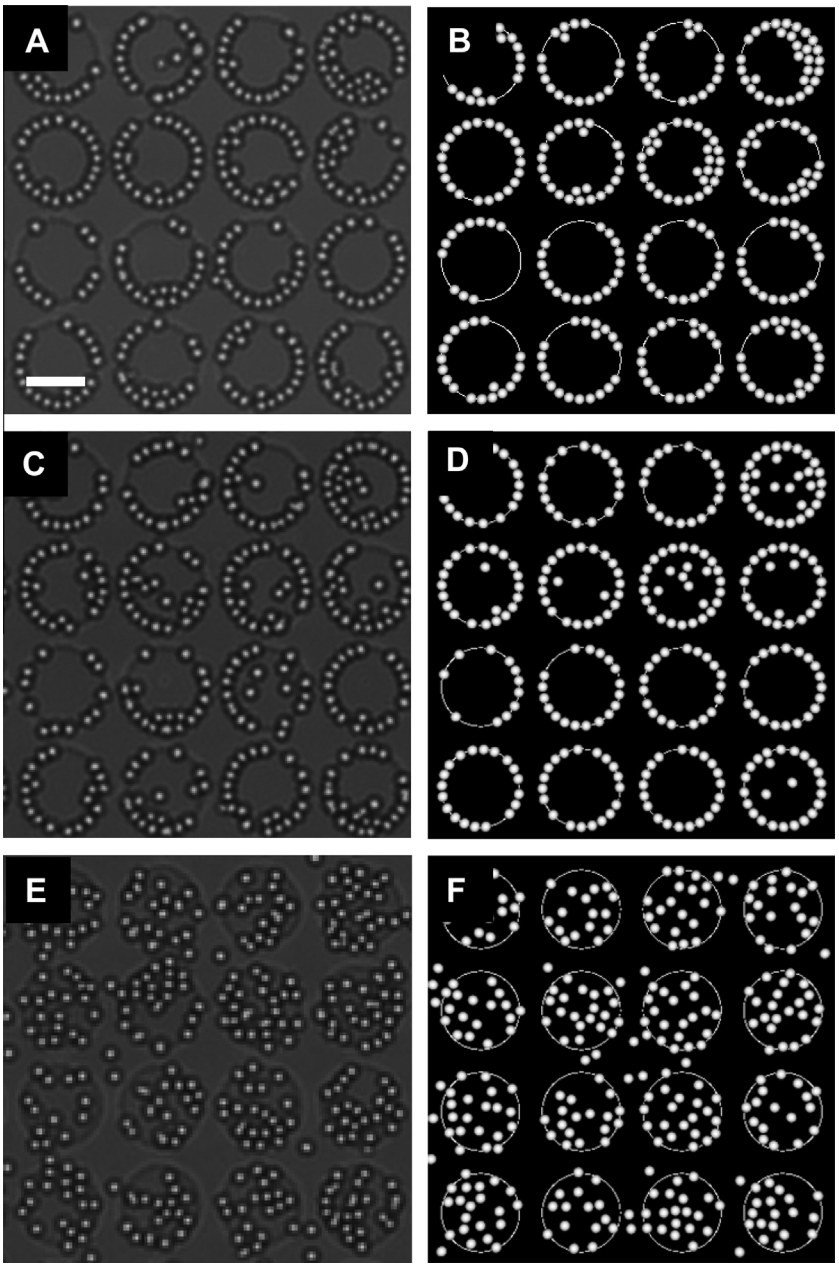

Fig. 1. Experimental images (A, C, E) and simulation renderings (B, D, F) of charged ~2 μm SiO_2 colloids at 0.18 area fraction experiencing depletion attraction with each other and a topographically patterned (well depth H = 285 nm) glass microscope slide surface. The depletion potential is tuned by the depletant size, $2L$, at 25 °C, $2L$ = 113 nm (A, B), 35 °C, $2L$ = 107 nm (C, D), 37 °C, $2L$ = 53 nm (E, F).

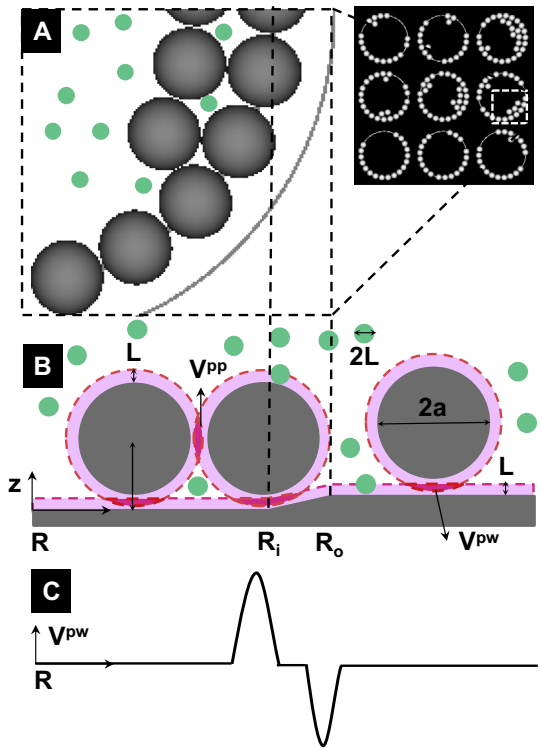

Fig. 2. Schematics of substrate geometry. (A) Snapshot (top views) of simulation rendering and magnified view of particles at pattern edge. (B) Cross sectional view of particles at pattern edge. Green and gray spheres are depletants and colloids. Red band (light) surrounding the gray sphere and the gray substrate is excluded volume (approximated via hard sphere repulsion). (C) Qualitative profiles of particle–wall excluded volume vs. radial coordinate from pattern feature center to edge and beyond (for colloidal sphere at constant elevation above substrate). (For interpretation of the references to color in this figure legend, the reader is referred to the web version of this article.)

where g is acceleration due to gravity, and ρ_p and ρ_f are the particle and fluid densities.

2.3. Electrostatic interaction potentials

The colloidal particles are electrostatically stabilized against aggregation and deposition due to van der Waals attraction. The interaction between electrostatic double layers on adjacent particle and planar wall surfaces are given by [19],

$$u_E^{pp}(r) = B\exp[-\kappa(r-2a)], u_E^{pw}(z) = 2B\exp[-\kappa(z-a)]$$
$$B = 32\pi\varepsilon a\left(\frac{kT}{e}\right)^2 \tanh\left(\frac{e\psi_1}{4kT}\right)\tanh\left(\frac{e\psi_2}{4kT}\right), \kappa = (2e^2N_AC/\varepsilon kT)^{1/2} \quad (3)$$

where κ is the inverse Debye length, ε is the solvent dielectric constant, k is Boltzmann's constant, T is absolute temperature, C is the 1:1 monovalent electrolyte molarity, N_A is Avogadro's number, e is the elemental charge, and ψ_1 and ψ_2 are the surface potentials.

2.4. AO depletion potentials

The depletion attraction between particles and underlying substrate surface can be given by a modified form of the usual AO depletion potential as [1],

$$u_D^{pp}(r) = -\Pi V_{EX}^{pp}(r) \quad (4)$$

$$u_D^{pw}(\mathbf{r}) = -\Pi V_{EX}^{pw}(\mathbf{r}) \quad (5)$$

where Π is the depletant osmotic pressure, and $V^{pp}{}_{EX}(r)$ and $V^{pw}{}_{EX}(\mathbf{r})$ are the excluded volume (see Fig. 1(b)) for particle–particle and particle–planar wall geometries given as [20–22],

$$V_{EX}^{pp}(r) = \pi\left[(4/3)(a+L)^3(1-(3/4)r(a+L)^{-1}+(1/16)r^3(a+L)^{-3})\right] \quad (6)$$

$$V_{EX}^{pp}(z) = \pi\left[(4/3)L^3+4L^2a-4La(z-a)+a(z-a)^2-L(z-a)^2 + (1/3)(z-a)^3\right] \quad (7)$$

where L is the depletant radius. For particles in the vicinity of a topographical pattern feature, the form of Eq. (5) remains the same in that the magnitude is determined by the depletant osmotic pressure, but the excluded volume term is computed numerically as described in the methods section of this paper. The numerical method is validated by producing the correct excluded volume terms given for particle–particle and particle–wall geometries in Eqs. (6) and (7).

2.5. Quasi-two dimensional models

In this paper, we perform quasi-2D measurements, simulations, and analyses of particles on patterned surfaces. The particles are assigned to a most probable elevation, z_M, above the substrate, which is the location of the net potential energy profile minimum normal to the substrate where the sum of the forces on the particle equal zero. This value can be determined as the value of z where the gradient of the net potential energy (z-dependent potentials in Eq. (1)) equals zero as given by,

$$\frac{\partial}{\partial z}\left[u_G^{pf}(z)+u_D^{pw}(z)+u_E^{pw}(z)\right] = 0 \quad (8)$$

This approach allows the position dependent elevation of each particle, $z(x_i, y_i)$, to be given as the sum of the local physical topography and the most probable height above the surface as,

$$z_i(x_i,y_i) = z_M + z(x_i,y_i) \quad (9)$$

which gives the net quasi-two dimensional potential energy (including a quasi-2D gravitational potential energy landscape [7,23]) for each particle as,

$$u_i(\mathbf{r}_i) = Gz_M(\mathbf{r}_i)+u_D^{pw}(\mathbf{r}_i)+\sum_{j\neq i}\left[u_E^{pp}(r_{ij})+u_D^{pp}(r_{ij})\right] \quad (10)$$

The goal of this work is to understand how particles sample the 2D energy landscape in the presence of gravity, depletion forces, and multi-particle packing effects. It has been shown that single particles (sufficiently dilute to only interact with surface but not each other) will sample the landscape in Eq. (10) via a Boltzmann relation (and its algebraic inverse) given by,

$$\rho(\mathbf{r})/\rho_{ref} = \exp\left[-(u(\mathbf{r})-u_{ref})/kT\right]$$
$$[u(\mathbf{r})-u_{ref}]/kT = -\ln[\rho(\mathbf{r})/\rho_{ref}] \quad (11)$$

where $u(\mathbf{r})$ is the potential energy landscape in Eq. (10), and ρ_{ref} and u_{ref} are the reference density and potential at a given state and location in the system (*e.g.*, single particle at the center of a pattern feature without any depletion attraction). For example, in the absence of particle–particle interactions or particle–wall depletion attraction, the potential energy landscape depends only on gravity and the height as,

$$u(x,y)-u_{ref} = G[z(x,y)-z_{ref}] \quad (12)$$

where z_{ref} is a reference height (*e.g.*, lowest or highest elevation on a surface). As particles begin to interact with each other and the underlying surface at finite concentration, the distribution of particles is related to the free energy landscape, $w(\mathbf{r})$, (and its algebraic inverse) given by,

$$\rho(\mathbf{r})/\rho_{\text{ref}} = \exp\left[-(w(\mathbf{r}) - w_{\text{ref}})/kT\right]$$
$$[w(\mathbf{r}) - w_{\text{ref}}]/kT = -\ln\left[\rho(\mathbf{r})/\rho_{\text{ref}}\right] \quad (13)$$

where ρ_{ref} and w_{ref} are again a reference density and potential at a given location (spatial position) and state (*i.e.*, global thermodynamic variables).

3. Methods

3.1. Excluded volume calculation

Considering the large ratio of the well diameter to the colloid diameter, we approximate the sloping well edge in Fig. 2 as a flat plane (R_iR_o section). The calculation of excluded volume is the intersection of colloidal particle excluded volume with the excluded volume from the three planes ($<R_i$, R_iR_o, $>R_o$ sections). The excluded volume of sphere and substrate are discretized with a resolution of $0.025a$ for each dimension (x, y, z), and then the volume elements inside the shaded region are added to obtain the overlap volume for the particle at each position (x, y, z). The accuracy of this method was validated by reproducing the particle–particle (Eq. (6)) and particle–wall (Eq. (7)) excluded volumes to <1% error.

3.2. Monte Carlo simulations

Quasi-2D experiments are modeled in 2D Monte Carlo (MC) simulations where colloids samples landscapes determine by gravity and substrate topography mediated depletion potentials. In 2D MC simulations, moves in x, y directions are accepted or rejected using the energy function in Eq. (10). In this implementation, real-time calculation of the excluded volume for every particle position would be computationally prohibitive. However, exploiting the natural system symmetry and periodicity (see Fig. 1), the particle position [x, y, $z(x, y)$] is converted to [R, $z(R)$], where R is the radial distance to the nearest well center. The excluded volume is then pre-calculated in a look-up table for use in the simulation. The MC simulations are performed at three different temperatures with all parameters listed in Table 1. Initial configurations for simulations were obtained from experimental images. Each MC simulation was performed for 2.5×10^6 steps with particle positions stored every 250 steps after an initial 10^6 step equilibration.

4. Results and discussion

4.1. 2D density landscapes

In experiments reported elsewhere [17] and shown in Fig. 1, temperature sensitive poly-N-isopropylacrylamide (PNIPAM) hydrogel particles were used as thermosensitive depletants to mediate depletion attraction between ~2 μm SiO_2 colloids and physically patterned surfaces. The temperature dependent PNIPAM depletant size produces tunable excluded volumes and depletant osmotic pressures to tune the net depletion potential. These tunable potentials provided the capability to control reconfiguration of colloidal particles between isotropic and non-close packed structures on a variety of topographical features. Here we report potentials and simulation methods that quantitatively capture these experimental observations and provide the capability to design new systems that exploit these tunable interactions and local excluded volume effects.

We first compare time-averaged equilibrium configurations from microscopy experiments and MC simulations for the three temperatures reported in Fig. 1. The 2D density profiles, $\rho(x, y)$, are normalized by the maximum density and are reported in Fig 3. The

Table 1
Parameters for MC simulations to match with experiments.

Variable	Theory/simulation
a/nm[a]	1100
κ^{-1}/nm[b]	9.54
ψ/mV[c]	−50
T/°C[d]	25, 35.0, 37.0
$2R$/μm[e]	17
D/μm[f]	21
H/nm[g]	285
$2L$/nm[h]	113, 107, 53
Π/kT (10^{-7} nm^{-3})[i]	26.0, 18.0, 5.4
ρ (10^{-7} nm^{-3})[j]	4.8, 4.6, 4.7
ϕ_D[k]	0.36, 0.30, 0.37
z_m/nm[l]	61, 66, 100
$\phi_{A,C}$[m]	0.178, 0.178, 0.175
N[n]	332, 332, 324

[a] Colloidal particle size.
[b] Debye screening length.
[c] Particle and wall electrostatic potential [26,27].
[d] Temperature.
[e] Patterned circle diameter.
[f] Center-to-center pattern spacing.
[g] Patterned depth.
[h] Depletant size.
[i] Depletant osmotic pressure.
[j] Depletant number density.
[k] Depletant volume fraction.
[l] Most probable height.
[m] Colloidal particle area fraction.
[n] Colloidal particle number.

experimental $\rho(x, y)$ were constructed from 50,156 images in 30 min videos (as reported in our separate experimental paper [17]). Most parameters used in the MC simulations were measured independently and reported in Table 1. To match experiment and MC simulations for each temperature, the particle-pattern excluded volume was computed using the numerical technique described in the methods section, which left the PNIPAM osmotic pressure as the sole adjustable parameter. The initial guess for the PNIPAM osmotic pressure was based on the Carnahan–Starling equation of state (CS-EOS) and DLS measured PNIPAM sizes [6,7]. Table 1 lists the temperature independent depletant number density and temperature dependent depletant volume fractions obtained from the fitted osmotic pressure values and the CS-EOS, which are reasonable based on the PNIPAM solution preparation.

Fig. 3 shows excellent agreement is observed between experiments and simulations at each temperature (within the statistical and spatial resolution of the experiments). Parts A, B in Figs. 1 and 3 show that for the largest depletant size ($2L$ = 113 nm) at the lowest temperature (T = 25 °C), particles preferentially stick to pattern feature edge where the excluded volume is the greatest. Depending on the number of particles in the well, a second ring of particle forms via lateral particle–particle depletion attraction. As temperature increases (T = 35 °C) and depletant size slightly decreases ($2L$ = 107 nm) in parts C, D in Figs. 1 and 3, particles near the pattern feature display an almost imperceptible increase in thermal motion and the second ring of particles now sample the pattern feature interior. Both effects show that reduced depletant size weakens the depletion attraction from a smaller excluded volume and a smaller depletant osmotic pressure (which scales as depletant volume, *e.g.*, second virial coefficient, volume fraction in equations of state [3,6,7,24,25]).

As the depletant size decreases considerably ($2L$ = 53 nm) at a slightly higher temperature (T = 37 °C) in parts E, F in Figs. 1 and 3, depletion attraction between particles with each other and all surface locations vanishes, since the excluded volume becomes identically zero in all potentials. In this case, particles explore potential energy landscapes determined by multi-particle packing effects

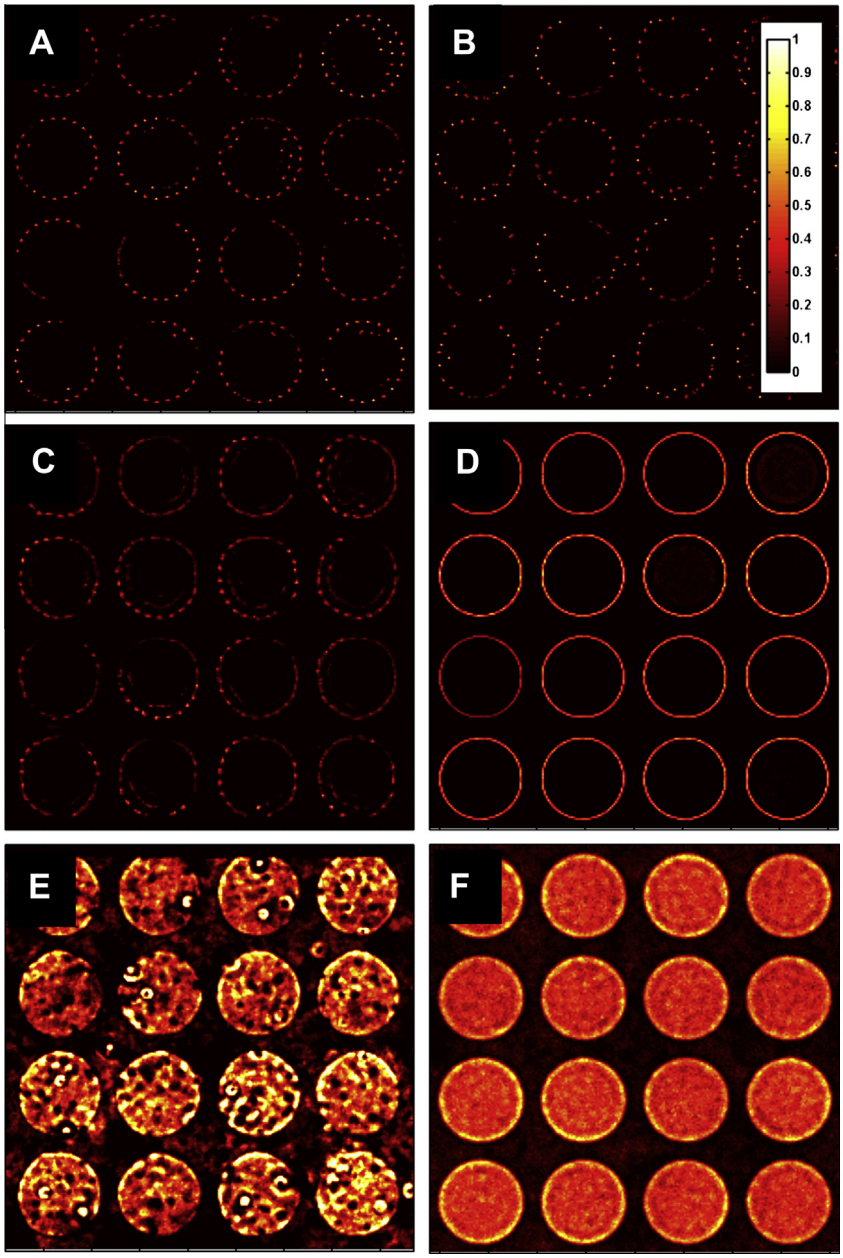

Fig. 3. 2D density landscapes from experiments (A, C, E) and simulations (B, D, F) at 25 °C, $2L$ = 113 nm (A, B), 35 °C, $2L$ = 107 nm (C, D), 37 °C, $2L$ = 53 nm (E, F).

and gravity (*i.e.* elevation), similar to our previous studies [6,7,23]. The depletant size changes continuously vs. temperature, although somewhat more steeply in the vicinity of 35–37 °C, so the excluded volume, depletion potentials, and particle configuration on the underlying pattern also change more dramatically in this temperature range.

4.2. 2D free energy landscapes

In addition to comparing the experimental and simulated density profiles, Fig. 4 shows a comparison of free energy landscapes, $w(x, y)$, for the three cases in Figs. 1 and 3. The $w(x, y)$ are obtained from a Boltzmann inversion (Eq. (13)) of the density profiles in Fig. 3, which produces energy minima at the highest density positions in Fig. 3. Because $\rho(x, y)$ were matched between experiment and simulation in Fig. 3, the $w(x, y)$ also naturally agree. For the 25 °C case in Fig. 4, the particles experience >10kT of depletion attraction with the pattern feature compared to all other locations on the surface. Because $w(x, y)$ can only be constructed where particles sample, and they do not sample significantly other regions beside the pattern feature edge, it is not possible to determine the absolute depth of the energy minimum relative to the rest of the surface; it is >10kT, but not clear by how much. In short, particles only sample pattern feature edges in wells that are deep enough that they do not escape, so they appear to be irreversibly bound on the observation time of our experiments.

As temperature is increased to 35 °C, the attraction of particles to the pattern feature is ~3kT lower energy than the interior of the pattern feature and >5kT lower than outside the pattern feature edge. Because particle–particle interactions become weak enough that particles can sample the pattern interior, the ~3kT difference is accurately measured. However, the depletion attraction between particles and the pattern edge plus the additional effect of gravity to escape the lower elevation interior region are too great to obtain sufficient statistics from particles outside the pattern feature. Finally, in the absence of depletion attraction at 37 °C, there is no

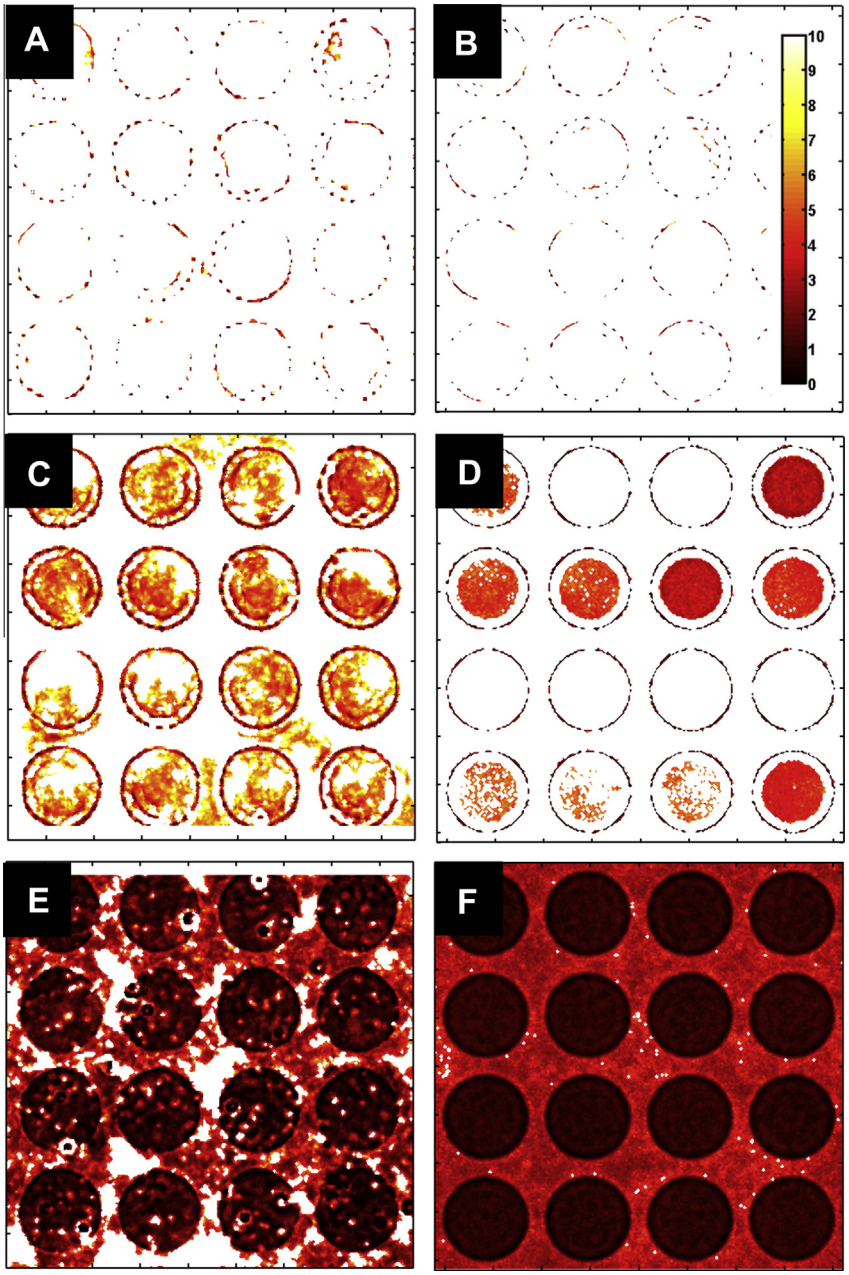

Fig. 4. 2D free energy landscapes from experiments (A, C, E) and simulations (B, D, F) at 25 °C, $2L$ = 113 nm (A, B), 35 °C, $2L$ = 107 nm (C, D), 37 °C, $2L$ = 53 nm (E, F).

attraction to the pattern feature edge, and the free energy difference between the well interior and well exterior is $\sim 4kT$, which is close to the gravitational potential energy of particles escaping the well. The differences between free energy and potential energy landscapes at each temperature are discussed in more detail in the followings sections.

4.3. 1D density and free energy landscapes

To generate more statistics in the experimental density and energy landscapes, and to take advantage of the pattern periodicity and circular symmetry, the density profiles in Fig. 3 are: (1) averaged over all features, which are considered to be nearly identical within the spatial limits of the microfabrication methods used to generate the pattern, and (2) after converting to polar coordinates, averaged over the angular coordinate, which the density and energy are not expected to have any dependence. This yields 1D radial density landscapes for each temperature, which are reported on the left hand side of Fig. 5. The 1D radial free energy landscapes are obtained from a Boltzmann inversion of the 1D density profiles and reported on the right hand side of Fig. 5. These results now show most clearly how the temperature dependent particle density and free energy vary relative to the pattern feature edge including the inner and outer radius of the sloped region. The oscillations in both landscapes clearly capture packing effects.

These results show at 25 °C that particles are attracted to the pattern feature edge and to each other as evident from the global energy minimum at the pattern periphery (particle-feature attraction) and the local minimum at $\sim 1.5a$ away from the edge towards the pattern interior (particle–particle attraction). The diminished single well at 35 °C quantifies the strength to which particles are attracted to the feature edge, and the absence of another well

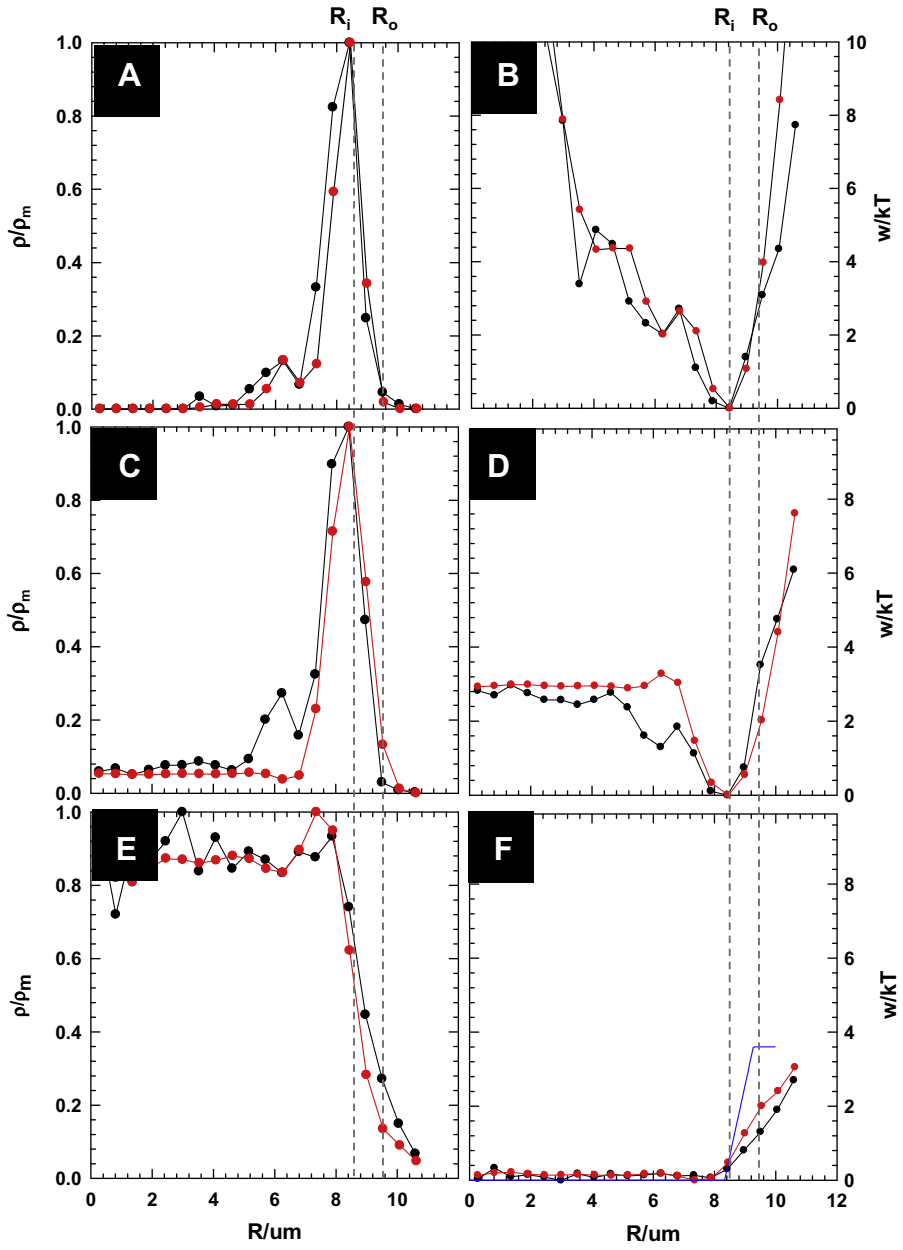

Fig. 5. 1D density (A, C, E) and free energy (B, D, F) landscapes from experiments (red lines and symbols) and simulations (black lines and symbols) at 25 °C, $2L$ = 113 nm (A, B), 35 °C, $2L$ = 107 nm (C, D), 37 °C, $2L$ = 53 nm (E, F). Blue line in (E) is gravitational potential energy landscape. Dash lines show inner (R_i) and outer (R_o) of pattern radius. (For interpretation of the references to color in this figure legend, the reader is referred to the web version of this article.)

shows that particle–particle attraction is negligible. In the absence of depletion attraction at 37 °C, particle are no longer preferentially attracted to the pattern edge. The free energy landscape depends on the balance of gravity and multi-particle packing effects, although the extent of multi-particle packing effects has yet to be determined. As a preliminary estimate, Fig. 5F shows the potential energy landscape due to single particles on the underlying pattern, which shows how multi-particle packing effects alter the interaction compared to single particles sampling. Although multi-particle packing effects were demonstrated to "push" particles out of patterned well features in more concentrated systems [23], here the effect is less obvious. This effect is explored in more detail in the potentials obtained from the inverse MC analysis used to match the images, density landscapes, and free energy landscapes in Figs. 1–5.

4.4. Potential energy landscapes

By matching the experimental and simulated images, density, and free energy landscape in Figs. 1 and 3–5, all contributing interaction potentials are determined, which means these can be discussed in addition to the free energy landscapes reported thus far. As described in the theory section, single particles can sample a potential energy landscape, $u(x, y)$, mediated by gravitational body forces and electrostatic and depletion colloidal forces. As particles become more concentrated, multi-particle packing influences how particle sample the underlying surface via a free energy landscape (that also includes an "entropy" landscape where $w(x, y) = u(x, y) - Ts(x, y)$). MC simulations naturally account for multi-particle packing effects, so that all particle–particle and particle–substrate interaction potentials are obtained unambiguously.

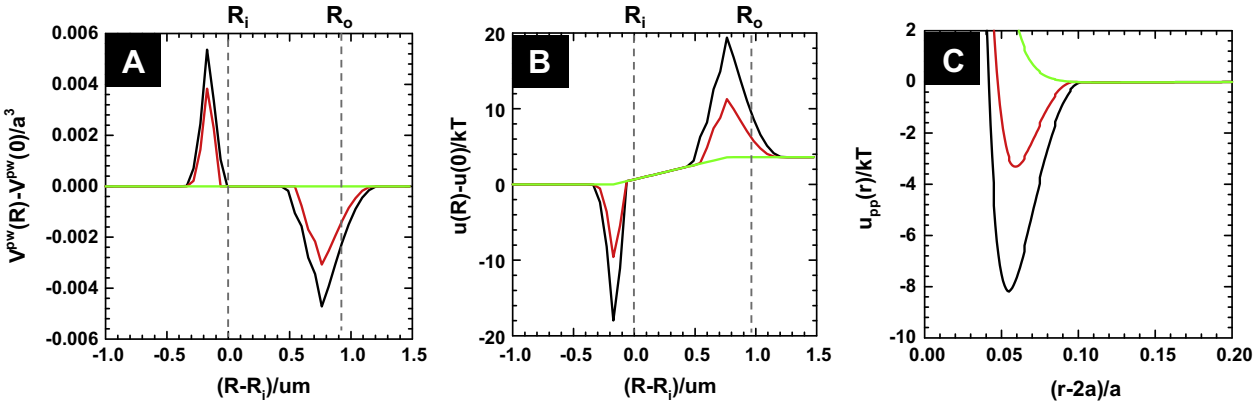

Fig. 6. Excluded volume difference (A), theoretical potential energy landscape (B), particle pair potential at 25 °C, $2L$ = 113 nm (black), 35 °C, $2L$ = 107 nm (red), 37 °C, $2L$ = 53 nm (green). (For interpretation of the references to color in this figure legend, the reader is referred to the web version of this article.)

To understand the relevant potential energy contributions, Fig. 6 shows the radial and temperature dependence of: (A) the particle–substrate excluded volume (that determines attraction), (B) the particle–substrate potential energy landscape including electrostatics, depletion, and gravity (u^{pw} and u^{pf} in Eq. (10), electrostatic u^{pw} omitted but effectively considered from most probable elevation in Eqs. (8) and (9)), and (C) the net particle–particle separation dependent potential energy including electrostatics and depletion (u^{pp} in Eq. (1)).

The results in Fig. 6A report the excluded volume as a difference between the value computed from the numerical method and the particle–wall value given in Eq. (7). This difference is reported as a function of lateral distance to the pattern feature edge for each temperature (*i.e.*, different depletant sizes, $2L$). When the particle is far away from the pattern edge ($R \ll R_i$, $R \gg R_o$), there is no excluded volume difference. At 37 °C, $\Delta V_{EX} = 0$ everywhere since the 53 nm PNIPAM particles are not excluded anywhere between the particles and patterned surface. At 35 °C and 25 °C, ΔV_{EX} increases with increasing $2L$ at the inner edge of the feature, where the concave surface curvature complements the particle, and decreases at the outer edge, where the convex curvature bends away from the particle surface.

Fig. 6B shows a plot of the potential energy landscape vs. the radial pattern feature coordinate. Potential energy is plotted related to the energy at the pattern feature center, where particle–wall electrostatics, depletion, and gravity balance each other to produce a most probable elevation (*i.e.*, Eq. (8)). For T = 37 °C, $\Delta V_{EX} = 0$ everywhere, and a purely gravitational potential energy landscape is obtained due to the elevation change of the surface. This explains the higher density of particle inside the pattern features. By multiplying the depletant osmotic pressure by ΔV_{EX} at 25 °C and 35 °C from Fig. 6A and adding it to the gravitational potential energy landscape, it is possible to obtain the potential energy landscape due to both contributions. It is now easy to see that single particles experience $\sim 10kT$ of attraction to the concave inner feature edge at 35C and nearly $\sim 20kT$ of attraction at 25 °C. In addition, the reduced excluded volume at the convex outer edge produce $\sim 5kT$ and $\sim 15kT$ potential energy barriers to single particles escaping the pattern outer edge. Together, the energy minimum at the inner edge and energy maximum at the outer edge produce energy changes (minimum depth to barrier maximum) of $\sim 15kT$ and $\sim 35kT$, which is effective at preventing particle escape immobilizing particles with energies $\gg kT$.

Finally, Fig. 6C also shows the pairwise particle–particle depletion attraction that contributes to the free energy landscapes in Fig. 5. The $\sim 8kT$ and $\sim 3kT$ particle–particle attraction at 25 °C and 35 °C are consistent with the degree of particle attachment to the first layer of particles immobilized at the pattern feature edge. In particular, the second layer of particles is completely immobile at 25 °C, whereas this layer shows intermittent attachment and detachment at 35 °C. At 37 °C, all depletion attraction vanishes including the particle–particle, particle–wall, and particle-edge feature attraction. The patterned surface mediated potential energy landscapes in combination with particle pair potentials reported in Fig. 6, when combined with multi-particle packing effects (*i.e.*, entropic contributions), clearly capture the free energy landscapes and density profiles obtained in the experimental studies reported in Fig. 1.

5. Conclusions

Our results demonstrate the ability to accurately interpret and predict excluded volume effects between colloids with each other and topographically patterned surfaces in the presence of depletants with thermosensitive sizes. A new modeling approach is reported to numerically compute the excluded volume between colloids interacting with arbitrary surface geometries. This approach enables the computation of depletion attraction with local surface pattern features in the presence of depletants with varying dimensions. This method is used to match Monte Carlo simulations to experiments to model the temperature dependent density, free energy, and potential energy landscapes that determine non-close-packed colloidal configurations on periodic arrays of circular features. Ultimately, the ability to quantitatively understand the interplay of electrostatic, gravitational, and tunable depletion interactions on topographically patterned substrates provides a basis to design and control colloidal based reconfigurable materials and devices for micro- and nano-technologies.

Acknowledgment

We acknowledge financial support by the National Science Foundation (CBET-1234981).

References

[1] S. Asakura, F. Oosawa, J. Chem. Phys. 22 (7) (1954) 1255–1256.
[2] H.N.W. Lekkerkerker, R. Tuinier, Colloids and the Depletion Interaction, Springer, Berlin, 2011, p. 234.
[3] T.D. Edwards, M.A. Bevan, Langmuir 28 (39) (2012) 13816–13823.
[4] D. Marenduzzo, K. Finan, P.R. Cook, J. Cell Biol. 175 (5) (2006) 681–686.
[5] J.R. Savage, D.W. Blair, A.J. Levine, R.A. Guyer, A.D. Dinsmore, Science 314 (2006) 795–798.
[6] G.E. Fernandes, D.J. Beltran-Villegas, M.A. Bevan, Langmuir 24 (2008) 10776–10785.

[7] G.E. Fernandes, D.J. Beltran-Villegas, M.A. Bevan, J. Chem. Phys. 131 (2009) 134705.
[8] L.T. Shelley, E. Robert, C.P. Royall, J. Phys.: Condens. Matter 24 (46) (2012) 464128.
[9] A. Trokhymchuk, D. Henderson, A. Nikolov, D.T. Wasan, J. Colloid Interface Sci. 243 (1) (2001) 116–127.
[10] A.D. Nikolov, D.T. Wasan, J. Colloid Interface Sci. 133 (1) (1989) 1–12.
[11] A.D. Dinsmore, A.G. Yodh, D.J. Pine, Nature 383 (6597) (1996) 239–242.
[12] K.-H. Lin, J.C. Crocker, V. Prasad, A. Schofield, D.A. Weitz, T.C. Lubensky, A.G. Yodh, Phys. Rev. Lett. 85 (8) (2000) 1770–1773.
[13] W. Lee, A. Chan, M.A. Bevan, J.A. Lewis, P.V. Braun, Langmuir 20 (13) (2004) 5262–5270.
[14] Sp. Badaire, Cc. Cottin-Bizonne, A.D. Stroock, Langmuir 24 (20) (2008) 11451–11463.
[15] K. Zhao, T.G. Mason, Phys. Rev. Lett. 101 (2008) 148301.
[16] S. Sacanna, W.T.M. Irvine, P.M. Chaikin, D.J. Pine, Nature 464 (7288) (2010) 575–578.
[17] T.D. Edwards, Y. Yang, M.A. Bevan, Reconfigurable multi-scale colloidal assembly on excluded volume patterns, 2014 (in preparation).
[18] K.A. Arpin, A. Mihi, H.T. Johnson, A.J. Baca, J.A. Rogers, J.A. Lewis, P.V. Braun, Adv. Mater. 22 (10) (2010) 1084–1101.
[19] G.M. Bell, S. Levine, L.N. McCartney, J. Colloid Interface Sci. 33 (3) (1970) 335–359.
[20] W.B. Russel, D.A. Saville, W.R. Schowalter, Colloidal Dispersions, Cambridge University Press, New York, 1989.
[21] A. Vrij, Pure Appl. Chem. 48 (1976) 471–483.
[22] A. Sharma, J.Y. Walz, J. Chem. Soc., Faraday Trans. 92 (24) (1996) 4997–5004.
[23] P. Bahukudumbi, M.A. Bevan, J. Chem. Phys. 126 (2007) 244702.
[24] T.D. Iracki, D.J. Beltran-Villegas, S.L. Eichmann, M.A. Bevan, Langmuir 26 (2010) 18710–18717.
[25] T.D. Edwards, M.A. Bevan, Macromolecules 45 (1) (2012) 585–594.
[26] H.J. Wu, M.A. Bevan, Langmuir 21 (4) (2005) 1244–1254.
[27] H.-J. Wu, T.O. Pangburn, R.E. Beckham, M.A. Bevan, Langmuir 21 (22) (2005) 9879–9888.

ACS NANO

www.acsnano.org

ARTICLE

Optimal Feedback Controlled Assembly of Perfect Crystals

Xun Tang,[‡] Bradley Rupp,[†] Yuguang Yang,[†] Tara D. Edwards,[†] Martha A. Grover,*[,‡] and Michael A. Bevan*[,†]

[‡]School of Chemical & Biomolecular Engineering, Georgia Institute of Technology, Atlanta, Georgia 30332, United States

[†]Department of Chemical & Biomolecular Engineering, Johns Hopkins University, Baltimore, Maryland 21218, United States

Supporting Information

ABSTRACT: **Perfectly ordered states are targets in diverse molecular to microscale systems involving, for example, atomic clusters, protein folding, protein crystallization, nanoparticle superlattices, and colloidal crystals. However, there is no obvious approach to control the assembly of perfectly ordered global free energy minimum structures; near-equilibrium assembly is impractically slow, and faster out-of-equilibrium processes generally terminate in defective states. Here, we demonstrate the rapid and robust assembly of perfect crystals by navigating kinetic bottlenecks using closed-loop control of electric field mediated crystallization of colloidal particles. An optimal policy is computed with dynamic programming using a reaction coordinate based dynamic model. By tracking real-time stochastic particle configurations and adjusting applied fields *via* feedback, the evolution of unassembled particles is guided through polycrystalline states into single domain crystals. This approach to controlling the assembly of a target structure is based on general principles that make it applicable to a broad range of processes from nano- to microscales (where tuning a global thermodynamic variable yields temporal control over thermal sampling of different states *via* their relative free energies).**

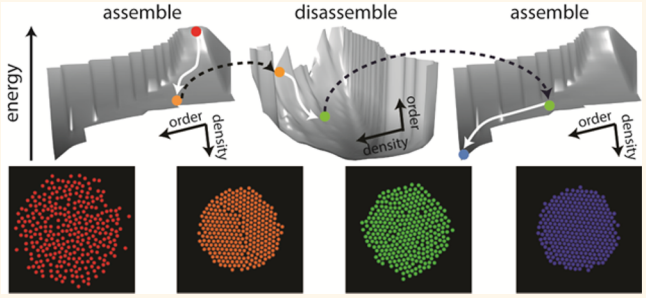

KEYWORDS: *colloidal assembly, low dimensional models, energy landscapes, stochastic ensemble control, Markov decision process*

Assembling colloidal nano- and microparticle components into perfectly ordered configurations could enable metamaterials with exotic properties that are otherwise unattainable.[1−4] Obtaining perfect structures is nontrivial at any scale (*e.g.*, atomic clusters, nanoparticle superlattices, folded proteins). Limited successful examples of perfect crystals on molecular scales include monocrystalline silicon for microelectronics *via* near-equilibrium directional growth from a seed crystal and single small protein crystals for X-ray crystallography *via* combinatorial screening. Such perfect atomic and molecular crystals are often obtained using open-loop control at near equilibrium conditions; that is, recipes based on slow nucleation, growth, and annealing to allow constituents to gradually assemble and relax into global free energy minimum perfect crystals. Like molecular crystallization, the capability to tune colloidal nano- and microparticle crystallization has been shown in a number of studies;[5−17] however, the controlled assembly of perfect thermodynamically stable colloidal crystals has not yet been demonstrated.

Crystallization kinetics depends on how constituents collectively assemble *via* diffusion. Molecular diffusion rates allow crystal growth near equilibrium to occur on time scales that are economically viable for manufacturing of high value-added materials. Colloidal nano- to microscale components, by virtue of their size, diffuse orders of magnitude more slowly than molecules, and hence colloidal assembly at near equilibrium conditions is impractical. The alternative, rapid out-of-equilibrium assembly, leads to defects (*e.g.*, polycrystals) and often arrested amorphous states. There appears to be an insurmountable gap between the limits of assembling perfect crystals *via* excessively long equilibrium processes and rapidly producing defective structures.

Here, we overcome the inherent drawbacks of open-loop controlled colloidal particle assembly processes by demonstrating rapid assembly of perfect crystals with closed-loop ("feedback") control based on a microscopic dynamic model. Practically, the experiment involves compressing charged colloids within a quadrupolar electric field (Figure 1). This is a self-assembly process in which a global thermodynamic variable (*i.e.*, electric field) changes the relative free energy of all configurations, causing particles to assemble *via* thermal motion to minimize their free energy. To enable feedback control,

Received: April 8, 2016
Accepted: July 5, 2016
Published: July 7, 2016

DOI: 10.1021/acsnano.6b02400
ACS Nano 2016, 10, 6791−6798

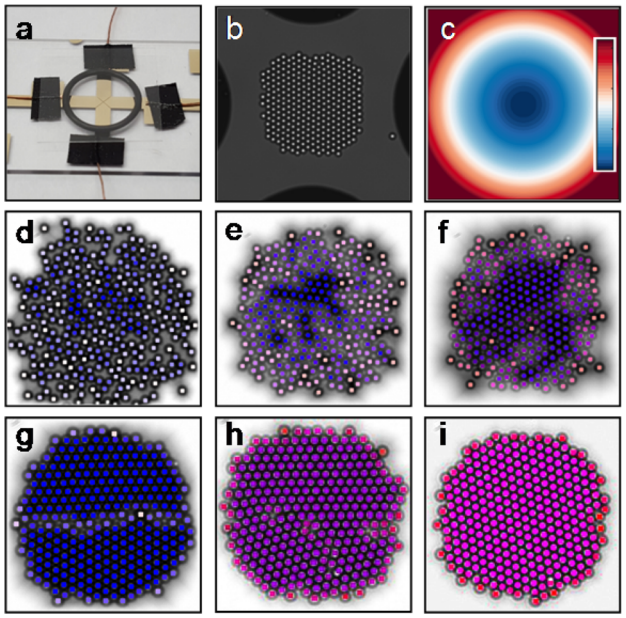

Figure 1. Quasi-2D colloidal crystal assembly in electric fields. (a) Microfabricated quadrupole electrode. (b) Optical microscopy image of particles within quadrupole. (c) Single particle-field potential (blue−red scale: 0−100kT). Images of 300 particles with centers colored to visualize reaction coordinates for local hexagonal order, C_6, and global hexagonal order, ψ_6, at electric field amplitudes of λ = (d) 0.2, (e) 0.9, (f) 2.0, and (g, h, i) 19.7. Representative microstructures include bicrystals with (g) large grain boundary (similar sized domains near max misorientation angle), (h) small grain boundary (dissimilar sized domains with smaller misorientation angle), and (i) no grain boundary, that is, perfect crystal. The 2.8 μm particles provide an internal scale bar.

essential real-time capabilities require (1) sensing the system state (*via* image analysis), (2) actuating particle interactions to navigate energy landscapes (*via* field mediated potentials), and (3) closing the loop to assign actuator settings based on sensor readings (*via* an optimal policy). This approach corrects defects in real-time to produce perfect crystals. While feedback control has been explored in microscopic systems including single particles,[18] colloidal assembly,[19] shear induced transitions,[20] nanostructure morphology,[21] and maximizing crystallinity,[22] none have produced perfect crystals using real-time defect correction.

Ultimately, this study is a proof-of-principle demonstration of controlling the navigation between two states in free energy space,[23] which we practically implement to create perfect 2D colloidal crystals. However, this approach could be used to navigate between any states including other colloidal microstructures (*e.g.*, gels, glasses, chains, clusters). Because colloidal particles thermally sample different configurations *via* diffusion based on their relative free energies and as such are often considered as models of atoms[24−26] (often in connection to the thermodynamics and kinetics of crystallization),[27−31] the physics underlying our approach is general across a range of length scales including molecular and nanoscales. As such, if correctly adapted (including appropriate methods to tune interactions[5−9] and to sense states, *e.g.*, *via* diffraction,[32,33] optical Fourier transforms,[34] super-resolution microscopy,[35,36] liquid cell electron microscopy[37]), the approach outlined in this work could be used to control states in systems of atoms, molecules, macromolecules, and nanoparticles. In addition to enabling the assembly of static, equilibrium target states, the ability to actively control particle ensembles between different nonequilibrium states could enable reconfigurable metamaterials (*i.e.*, metadevices).[38]

RESULTS AND DISCUSSION

Stochastic Polycrystal Assembly. Assembly is performed with 300 SiO_2 colloids (radius, a = 1.4 μm) confined by gravity into a quasi-2D layer within a quadrupole electrode (Figure 1a, see Methods and Supporting Information (SI)). A function generator controls the amplitude of a 1 MHz AC field, which determines the degree of localization of colloids at the field minimum in the quadrupole center (Figure 1b). The dipole-field potential characterizing the potential energy associated with confining particles is (Figure 1c)[39]

$$u(\mathbf{r}) = -\lambda f_{\mathrm{CM}}{}^{-1}[E(\mathbf{r})/E_0]^2 \quad (1)$$

where $\lambda = \pi_m a^3 (f_{\mathrm{CM}} E_0)^2/(kT)$ characterizes how strongly the radially varying field, $E(r)/E_0$, confines particles relative to thermal energy, kT, and f_{CM} depends on the particle, ε_p, and medium, ε_m, dielectric properties (see Methods and SI).[40] A balance of the field confinement against the quasi-2D dispersion osmotic pressure determines, for a given particle number, whether a fluid or solid phase will form *versus* λ (Figure 1d−i).[41] As system size increases, polycrystallinity (*i.e.*, misoriented crystal domains with grain boundaries, Figure 1g,h) becomes increasingly prevalent; this is the defect we aim to repair *via* feedback control.

To develop a sensor and model for grain boundary formation and motion, we employ a reaction coordinate based dynamic model.[42] Two reaction coordinates are necessary to quantify polycrystallinity: the degrees of global order, ψ_6, and local order, C_6. Values of ψ_6 and C_6 are computed in real-time from particle centers obtained *via* microscopy and image analysis (see Methods and SI). To briefly describe how reaction coordinates capture different states, $\psi_6 \approx 0$ for amorphous states (Figure 1d) and polycrystals (Figure 1g), whereas $\psi_6 \approx 1$ for perfect crystals (Figure 1h). C_6 captures the emergence of crystallinity during condensation and distinguishes amorphous (low C_6) and polycrystalline (high C_6) states (which both have $\psi_6 \approx 0$).

Polycrystallinity *versus* Uncontrolled Ramp Rate. We illustrate the need for feedback control by first showing examples without feedback control that demonstrate the trade-off between generating perfect crystals *via* slow, near-equilibrium ramps *versus* polycrystals *via* ramps too fast for relaxation into single crystals (Figure 2). Assembly trajectories are reported for N = 300 particles in Brownian Dynamic (BD) simulations matched to experiments[42] for several orders of magnitude in field ramp time. Nonequilibrium ψ_6 and C_6 trajectories averaged over 100 simulations for ramp times of 0, 1×10^3, 2×10^3, 5×10^3, and 10^4 s are shown alongside equilibrium ψ_6 (*i.e.*, free energy minima values at each λ, see SI). As expected, local ordering always precedes global ordering. The key result is that a ramp time greater than 10^4 s is required to achieve 100% perfect crystals in the near-equilibrium limit (*i.e.*, ramped ψ_6 passes through equilibrium ψ_6 values at long times). Faster ramps produce nonequilibrium polycrystals that do not relax to single crystals in the allotted times.

Feedback Controlled Navigation of Energy Landscapes. The (ψ_6, C_6) coordinates quantitatively capture nonequilibrium stochastic trajectories between states, which

DOI: 10.1021/acsnano.6b02400
ACS Nano 2016, 10, 6791−6798

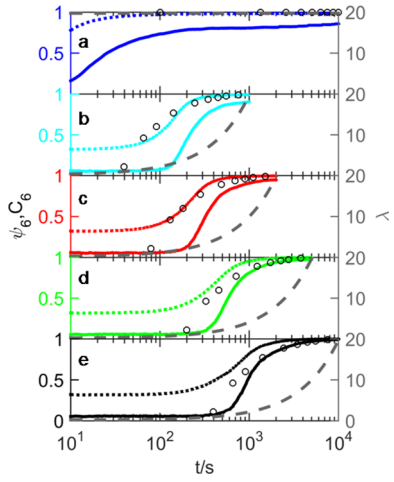

Figure 2. Ramping electric field at different rates without feedback control to understand effect of quench-rate on crystal assembly. Electric field amplitude, λ (long-dash gray), ramped from 0.2 to 19.7 over (a) 0 s (blue), (b) 1×10^3 s (cyan), (c) 2×10^3 s (red), (d) 5×10^3 s (green), and (e) 10^4 s (black). Local order, C_6 (dotted lines), emerges before global order, ψ_6 (solid lines). Equilibrium ψ_6 values (open circles) *vs* λ approach ψ_6 ramp trajectories only for the 10^4 s ramp.

provides a dynamic model to *close the loop* between *sensing* (determining the current state) and *actuation* (specifying λ to achieve a new state). A (ψ_6, C_6) based model quantifies field mediated crystallization dynamics *via* a Smoluchowski equation given as[42]

$$\frac{\partial p(\mathbf{x}, \lambda, t)}{\partial t} = \nabla \cdot \mathbf{D}(\mathbf{x}, \lambda) \cdot \left[\nabla + \frac{1}{kT} \nabla W(\mathbf{x}, \lambda) \right] p(\mathbf{x}, \lambda, t) \tag{2}$$

where p is probability, $\mathbf{x} = (\psi_6, C_6)$, $\mathbf{D}$ is a diffusivity landscape, and W is a free energy landscape. The dynamic model encapsulated in eq 2 enables formulating an optimal control scheme based on free energy gradients in W and hydrodynamic mediated friction in $\mathbf{D}$.[42]

Controlling crystallization is conceptually the navigation of free energy landscapes, W, at each electric field amplitude, λ (Figure 3a). The equilibrium ramp (Figure 2e) corresponds to slowly increasing $\lambda(t)$ so the configuration resides near the free energy minimum on each W. Faster ramps (Figure 2a–d) in $\lambda(t)$ cause sampling of nonequilibrium polycrystalline states on each W where vanishing gradients provide minimal driving force for relaxation.[42] The more sophisticated approach here is to determine the optimal $\lambda(t)$ based on current (ψ_6, C_6) coordinates to maximize the probability of moving from the initial fluid to the perfect crystal. Because the particle and grain boundary motion are stochastic, each process is unique, so no one $\lambda(t)$ is best every time; instead closed-loop control is required to obtain the optimal actuation.

To determine how to change the electric field *versus* time (*i.e.*, $\lambda(t)$) to best navigate the free energy landscapes, W, we use a Markov decision process based policy using dynamic programming.[43] This framework requires a discretized version of eq 2, known as a Markov state model,[44] which consists of a "probability transition matrix" to quantify the transition probability between all states during a time step, Δt, at each λ. The resulting policy, π, provides a mapping from the current measured state, $\mathbf{x}$, to the next action, λ, to be taken. Mathematically, $\lambda_{i+1} = \pi(\mathbf{x}_i)$, where i is the time step. The

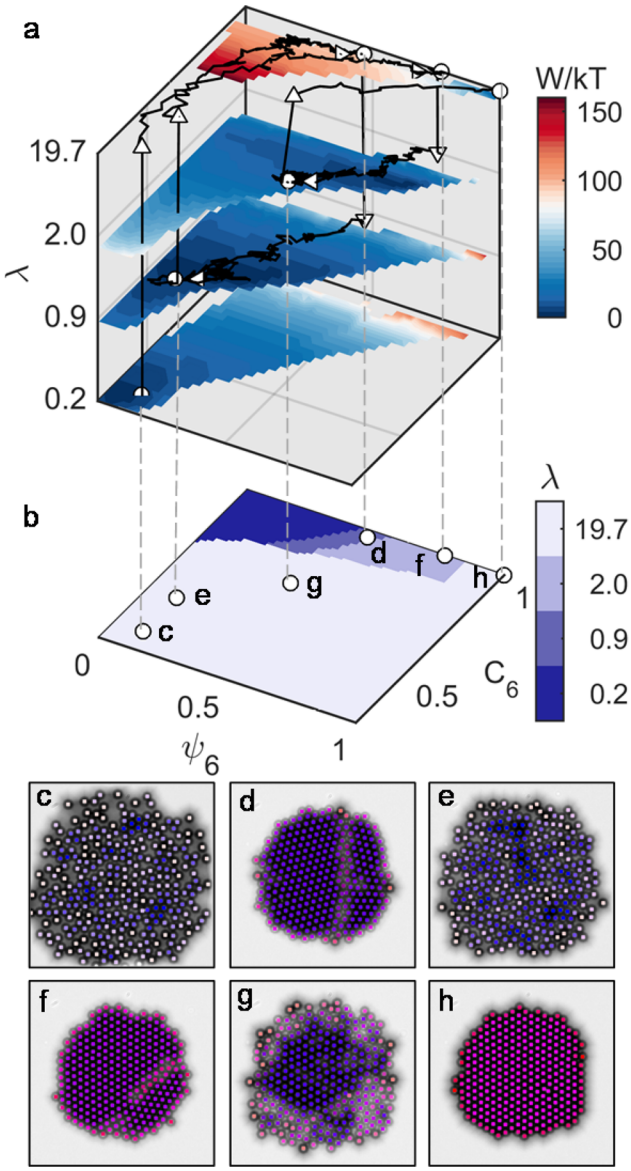

Figure 3. Assembly trajectory on energy landscapes under control (see Movie S1). (a) Free energy landscapes of 300 particles at the four λ's in policy. Example trajectory (black) with coordinates on policy (b) and corresponding images (c–h). (b) Optimal policy calculated using Markov decision process. Images showing representative configurations (same coloring scheme as Figure 1d–i) at (c) $\lambda = 0.2$ before compression, (d) first compression to $\lambda = 19.7$ with grain boundary, (e) relaxation at $\lambda = 0.9$, (f) recompression at $\lambda = 19.7$ with new grain boundary, (g) relaxation at $\lambda = 2.0$, and (h) perfect crystal at $\lambda = 19.7$.

optimal policy at each state $\mathbf{x}$ maximizes the objective function J^{π},[45]

$$J^{\pi}(\mathbf{x}) = X\{\sum_{i=0}^{\infty} \gamma^i R(\mathbf{x}_i, \lambda_i)\} \tag{3}$$

where X is the expectation operator and $R(\mathbf{x}_i, \lambda_i)$ is the reward function at time step i. In this work, $R = \psi_6^2$, such that a high global crystallinity is "rewarded". The discount factor γ ensures convergence of the policy calculation, and here is set to 0.99 (see Methods for details). The Markov decision process calculation provides the optimal policy (Figure 3b) in the form

DOI: 10.1021/acsnano.6b02400
ACS Nano 2016, 10, 6791–6798

of a look-up table, indicating the λ to use when assembly trajectories pass through each (ψ_6, C_6) coordinate.

A typical single experimental trajectory (Figure 3a,b) illustrates how the control policy is implemented. Practically, the feedback control is achieved in real-time *via* the following steps: (1) image analysis is used to locate particle centers and compute updated (ψ_6, C_6) coordinates every 100 ms, which are plotted as trajectories on the W at each λ (Figure 3a); (2) the current values of the (ψ_6, C_6) coordinates are found in the optimal control policy look-up table (Figure 3b); and (3) the new value of the quadrupole voltage (λ) found in the look-up table is updated every 100 s, which is shown by the trajectories jumping between the W in Figure 3a every time the λ value is changed. The policy update time of Δt = 100 s was determined by considering actuation times comparable to the inherent system response time.

The policy update time and inherent system response time depends on the cooperative short-range motion of particles necessary for grain boundary motion,[46,47] which can be estimated from the long time self-diffusivity as, $D_S^L = D_S^S[1 + 2\phi g(2a)]^{-1}$, where D_S^S is the short time self-diffusivity, ϕ is the particle area fraction, and $g(2a)$ is the radial distribution function contact value within the quasi-2D colloidal monolayer.[48] Using $D_S^S = 0.5D_0$ (D_0 is the Stokes−Einstein value) to account for particle-wall hydrodynamics,[49] and the hard disk fluid radial distribution function for $g(2a)$,[50] the time for particles to diffuse over a distance comparable to their own radius is $\tau = a^2/D_S^L \approx 100$ s at low concentrations. By considering how the soft electrostatic repulsion between particles significantly decreases $g(2a)$,[48] D_S^L becomes a weak function of ϕ, and as such, $\tau \approx 100$ s captures the characteristic structure relaxation time scale for all configurations and λ. Estimating D_S^L based on dense fluid properties can be rationalized since motion within grain boundaries has been compared to concentrated melt dynamics.[31,51,52] In addition, the different λ values in conjunction with the inhomogeneous field cause the dynamics to vary significantly from the concentrated interior of the particle ensemble to the vanishing density at its periphery.[41] Practically, the 100 s update time worked better than faster or slower times, consistent with the above analysis.

Movies (Movie S1) and images of particle configurations (Figures 3c−h) at start, end, and policy update points (Figure 3b) show that the policy uses (1) the highest field (λ = 19.7) for rapid initial assembly and to quench the final perfect crystal, (2) the lowest field (λ = 0.2) to partially disassemble large grain boundaries, and (3) intermediate field amplitudes (λ = 0.9, λ = 2.0) to assist relaxation of smaller grain boundaries. The control policy at most times drives rapid assembly at the highest field setting and is only reduced occasionally to eliminate defects without completely disassembling structures and restarting assembly.

Controlled *versus* Uncontrolled Assembly. Because colloidal assembly trajectories are stochastic, it is essential to collect sufficient statistics for a fair comparison of uncontrolled and controlled processes; to address this issue, 200 alternating uncontrolled and controlled cycles were obtained in a fully automated experiment over >31 h (see Methods and SI, Figure 4). Each cycle used feedback control to: (1) ensure initial disassembly, (2) execute either a step-quench without intervention or a series of 100 s control updates, and (3) terminate the process after either obtaining a perfect crystal or a period of 10^3 s. The first 10 cycles illustrate several scenarios

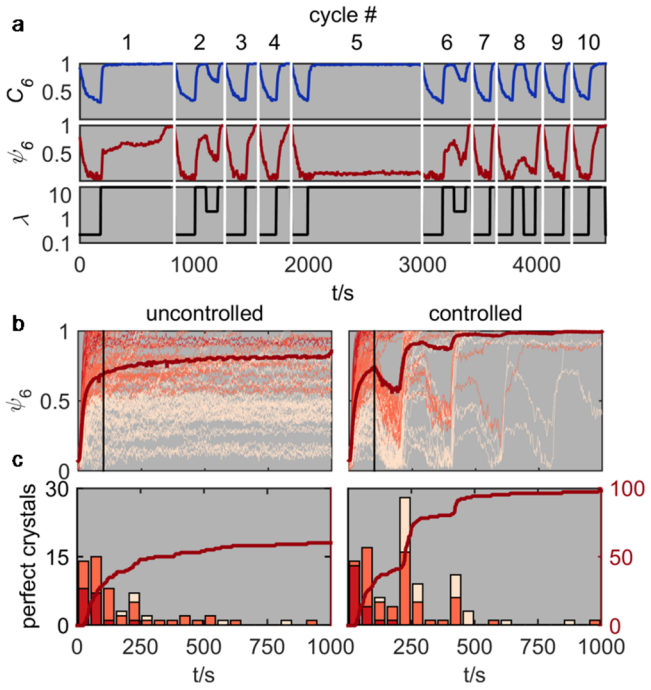

Figure 4. Controlled *vs* uncontrolled crystal assembly processes: 100 uncontrolled and 100 controlled trajectories shown as (a) first 10 cycles with C_6 (blue), ψ_6 (red), and λ (black) *vs* time, (b) ψ_6 *vs* time for 10^3 s for all experiments colored to indicate ensemble average (bold red), no grain boundary (red, $\psi_6 > 0.7$, $C_6 > 0.95$), small grain boundary (orange, $0.7 > \psi_6 > 0.4$, $C_6 > 0.95$), and large grain boundary (peach, $0.4 > \psi_6$, $C_6 > 0.95$), and (c) perfect crystals *vs* time as cumulative number (dark red) and instantaneous number (bars) with same color scheme as panel b.

(Movie S2, Figure 4a) including trajectories that (1) quickly relax for small grain boundaries (#3, #7, #9), (2) slowly relax to form a perfect crystal in <1000 s (#1), (3) form metastable crystals that never relax (#5), and (4) always form perfect crystals either without (#4, #10) or with (#2, #6, #8) several feedback corrections.

Analysis of all 200 ψ_6 *versus* time trajectories (Figure 4b) and number of perfect crystals *versus* time (Figure 4c) show key quantities to assess the controller's success at producing perfect crystals. A handful of perfect crystals form immediately during coalescence without grain boundaries (17 uncontrolled *vs* 19 controlled) by bypassing slow grain boundary motion on free energy plateaus (W at λ = 19.7 in Figure 3a).[42] The remaining ~160 trajectories illustrate how control removes grain boundaries by choosing lower λ. When removing small grain boundaries, perfect crystals are obtained in 100% (52/52) of trajectories after 1−2 corrective steps, whereas 78% (37/47) of small grain boundary bicrystals relax to perfect crystals without control. The ultimate test of the controller is for large grain boundaries; 93% (27/29) of controlled trajectories produce perfect crystals after 3−4 corrective steps *vs* 18% (6/34) of uncontrolled processes. In the final accounting, controlled processes produced perfect crystals 98% of the time, while uncontrolled processes were 60% successful.

CONCLUSIONS AND OUTLOOK

Our results demonstrate optimal feedback control to robustly assemble perfect colloidal crystals orders of magnitude faster than a slow quasi-equilibrium ramp and much more reliably

DOI: 10.1021/acsnano.6b02400
ACS Nano 2016, 10, 6791−6798

than rapid quenches. An optimal policy is computed with dynamic programming based on a low-dimensional reaction coordinate dynamic model. By tracking real-time stochastic particle configurations and employing the optimal policy to adjust applied electric fields *via* feedback, the evolution of unassembled particles is guided through polycrystal states into single domain crystals.

There are a number of ways this approach could be adapted and extended. For example, our approach could be implemented to constructively employ multiple complementary actuators (*e.g.*, magnetic fields to exert torques,[53] tunable depletion attraction to quench final states)[54] or be combined with other methods such as templated self-assembly (either unactuated[55,56] or actuatable[57]). Based on our prior work on nanoparticle assembly,[58] system size effects,[41] and three-dimensional assembly in electric[59] and gravitational fields,[60] our approach can also be adapted to (1) smaller nanoparticles (with different sensors; *e.g.*, attenuation based imaging,[58,60] scattering/diffraction),[32] (2) larger systems either through continuous processing (rather than batch processing; *e.g.*, a microfluidic device), parallelization (*e.g.*, electrode arrays),[61] or informing open-loop schemes (*e.g.*, toggling),[16] and (3) 3D crystals in thin films and possibly bulk crystals.

Further extensions of the methods and analyses developed in this work could be applied to other nano- and microscale processes involving anisotropic particles or multicomponent mixtures (with more states and bottlenecks), dynamical steady-states and out-of-equilibrium end points (where a Fokker–Planck equation describes the dynamics rather than a Smoluchowski equation), active micromachines and reconfigurable device elements (rather than static targets), and even synthetic materials systems that mimic basic control elements in biological systems (*e.g.*, chaperone control of protein folding and aggregation).[62] Our approach is based on first-principle concepts that are general to any molecular, nano-, or microscale assembly process where components thermally sample different configurations based on their relative free energies, states can be measured in real-time, an actuation mechanism exists to alter driving forces, and a dynamic model connects system responses to actuator settings.

METHODS

Sample Preparation. Coplanar quadrupole Au thin film electrodes were patterned on glass microscope coverslips that were sonicated in acetone for 30 min, sonicated in isopropanol (IPA) for 30 min, rinsed with deionized (DI) water, soaked in Nochromix (Godax) for 1 h, rinsed with DI water, sonicated in 0.1 M KOH for 30 min, rinsed with DI water, and dried with N_2. The electrodes were fabricated by spin coating photoresist (S1813, Shipley) onto microscope coverslips, UV exposure through a chrome photomask, and physical vapor deposition of a 15 nm chromium adhesive layer and a 35 nm gold layer. The photoresist liftoff was accomplished with agitation in 1165 Remover (Shipley). The electrode tips are separated by ~100 μm. Prior to experimentation, the coverslips with patterned quadrupole electrodes were sonicated in IPA for 30 min, acetone for 30 min, and IPA for 30 min, rinsed in DI water, then suspended in Nochromix for 20 min, rinsed with DI water, and dried with N_2.

Experiments were performed in batch cells consisting of Viton O-rings. To construct batch cells, O-rings were coated with vacuum grease and sealed between the coverslip with the electrode and a glass coverslip. Colloidal particle dispersion (100 μL) was dispensed into the batch cell and allowed to sediment for 5 min prior to sealing with a coverslip to obtain approximately 300 particles in the quadrupole. Twenty-two gauge copper wires were attached to the electrode using conductive carbon tape. The electrode was then connected in series with a function generator (Agilent 33220a) with one lead attached to the north–south poles and another to the east–west poles.

Microscopy. Microscopy was performed on an inverted optical microscope with a 63× Zeiss air objective lens (0.6 numerical aperture) at 1.25 magnification. A 12-bit CCD camera captured 336 pixel × 256 pixel (104 μm × 79 μm) digital images at rate of 10 frames/s. Image capture and analysis were performed using MATLAB Image Processing and Image Acquisition Toolboxes. Image analysis algorithms coded in MATLAB were used to simultaneously locate and track particle centers, as well as compute local and global order parameters in real time,[19] Experimental values of ψ_6 and C_6 were normalized by constants $\psi_{6,\max} = 0.8$ and $C_{6,\max} = 0.95$ to account for particle tracking errors.

Feedback Control. The electric field amplitude and frequency were controlled *via* the function generator using a device driver written in the MATLAB Instrument Control Toolbox. A sinusoidal voltage with a 1 MHz frequency was varied among $\lambda = 0.2$, 0.9, 2.0, and 19.7 for controlled cycles and held at a constant $\lambda = 19.7$ for uncontrolled cycles. The value of λ is related to the electric field and peak to peak voltage as

$$\lambda = \pi\varepsilon_m a^3 (f_{CM} E_0)^2/(kT) \qquad E_0 = 8^{-0.5} V_{pp}/d_g \tag{4}$$

where λ has the same definition as the main manuscript, d_g is the electrode gap, and V_{pp} is the peak-to-peak voltage set in the function generator. For $d_g = 100$ μm in this and previous work, the value of V_{pp} at which all particles crystallize in a system of N particles was determined to be

$$V_{pp} = a_0 N^{-b_0} \qquad a_0 = 7.15 + 4.10 \times 10^{-3}\kappa^{-1}$$
$$b_0 = 0.219 + 4.24 \times 10^{-4}\kappa^{-1} \tag{5}$$

where κ^{-1} is the Debye length. Values of V_{pp} and λ used in this work are reported in Supplementary Table 1.

Several properties could change in the course of a ~31 h experiment, such as particle stability, solvent conditions, and evaporation. However, there is no evidence that any of these factors changed the experimental conditions by plotting any measured quantity *versus* time. This is shown by the fact that the probability that an uncontrolled cycle would form a perfect crystal remains for all practical purposes constant for the experiment duration.

The radius of gyration, R_g, was used to measure the degree of melting between individual cycles. After a perfect crystal was obtained or 1000 s had elapsed, the system was melted at $\lambda = 0.2$ until $R_g = 25.5$ μm, at which point the next crystallization cycle was started. R_g is given by

$$R_g = 0.5 N^{-1} [\sum |r_i - r_j|^2]^{0.5}/R_{g,HEX} \tag{6}$$

where $R_{g,HEX}$ is the radius of gyration for two-dimensional hexagonally close packed particles with regular polygon morphologies given by

$$R_{g,HEX} = 5^{0.5} 3^{-1} a N^{0.5} \tag{7}$$

Reaction Coordinates. Reaction coordinates are computed for different system sizes to include edge effects. The global 6-fold bond orientational order, ψ_6, is given by[54,63,64]

$$\psi_6 = \left| \frac{1}{N} \sum_{j=1}^{N} \psi_{6,j} \right| \tag{8}$$

where N is the total number of particles in the ensemble, and $\psi_{6,j}$ is the local 6-fold bond orientation order of particle j given as

$$\psi_{6,j} = \frac{1}{N_{C,j}} \sum_{k=1}^{N_{C,j}} e^{i6\theta_{jk}} \tag{9}$$

where $N_{C,j}$ is the number of neighbors within the first $g(r)$ peak (coordination radius) of particle j, and θ_{jk} is the angle between particle j and each neighboring particle k with an arbitrary reference direction. Connectivity between crystalline particles, $\chi_{6,jk}$, is given by

DOI: 10.1021/acsnano.6b02400
ACS Nano 2016, 10, 6791–6798

$$\chi_{6,jk} = \frac{|\mathrm{Re}[\psi_{6,j}\psi_{6,k}^{*}]|}{|\psi_{6,j}\psi_{6,k}^{*}|} \tag{10}$$

where $\psi_{6,j}^{*}$ is the complex conjugate of $\psi_{6,j}$. This is used to compute the local order parameter for 6-fold connectivity, $C_{6,j}$, which produces integer values between zero and six. The number of crystalline nearest neighbors, $C_{6,j}$, for particle j is determined using the criterion[65]

$$C_{6,j} = \sum_{k=1}^{N_{C,j}} \begin{bmatrix} 1 & \chi_{6,jk} \geq 0.32 \\ 0 & \chi_{6,jk} < 0.32 \end{bmatrix} \tag{11}$$

$$C_6 = \frac{1}{N}\sum_{i=1}^{N} C_{6,i}/\langle C_6\rangle_{\mathrm{HEX}} \tag{12}$$

where C_6 is the average normalized local 6-fold connectivity, normalized by $\langle C_6\rangle_{\mathrm{HEX}}$, the C_6 value for 2D hexagonal close packed particles with a hexagonal morphology given by[19]

$$\langle C_6\rangle_{\mathrm{HEX}} = N^{-1}6(3S^2 + S) \tag{13}$$

$$S = -(1/2) + [(1/3)(N-1) + (1/4)]^{1/2} \tag{14}$$

Markov State Model Construction. A Markov state model (MSM)[44] is characterized by a set of discretized states S, and a probability transition matrix $P(\lambda)$ for each input λ. $P(\lambda)$ is composed of transition probability $P(\lambda)_{ij}$, which denotes the probability of the system to be in state j after a transition time of Δt given the current state as i under an input λ. The state space is defined by the reaction coordinates (ψ_6, C_6). The discretization is fine enough to distinguish configurations that lead to different dynamics but not too fine to lead to sampling issues in building the transition matrix and computational issues in solving for the control policy.[66] We discretized the reaction coordinate ψ_6 into 50 intervals and C_6 into 120 intervals after trial-and-error inspection. A total of 6000 discrete states were defined.

We generated sample data from the BD simulations to build four MSMs for each of our four input levels: λ = 0.2, 0.9, 2.0, 19.7. For each model, BD simulations were initialized in different discrete states to cover a commonly visited region of the state space. The simulations were repeated to ensure that the important states have enough samples to account for stochastic effects. Simulations were conducted under both constant and time-varying inputs to enrich sampling, with voltage switching at intervals of Δt = 100 s, corresponding to the transition time used in the MSM. To preserve the Markovity of the system, a large transition time Δt is desired for better accuracy[66−68] but at the cost of intermediate information loss. After an investigation over a range of transition times on the model accuracy, the transition time Δt = 100 s was chosen to balance the MSM accuracy with the ability to actuate at useful time intervals (see main text for discussion of inherent system response time).

Markov Decision Process Based Optimal Control Policy Calculation. A Markov decision process (MDP) is composed of a MSM, a set t of discrete time epoch i, and a set A of discrete actions λ.[43,69] If t is a finite set, the MDP is called finite-horizon MDP, and it is called infinite-horizon MDP if t is an infinite set. An optimal control policy associated with an infinite-horizon MDP is a time-independent policy, that is, the control policy is stationary at each update interval. Considering the convenience in practical use as well as its ability for visualization and understanding, we investigated the infinite-horizon MDP based optimization problem to solve for a stationary optimal control policy. In the infinite-horizon MDP, the optimization is achieved over an infinite number of time steps, i, and the objective function is defined as

$$J^{\pi}(\mathbf{x}) = X\{\sum_{i=0}^{\infty}\gamma^{i}R(\mathbf{x}_i, \lambda_i)\} \tag{15}$$

where X is the expectation operator, π:$S \rightarrow A$, is a feasible policy composed of control actions $\lambda_i \in A$, $\mathbf{x}_i \in S$ is the discrete state, i is the discrete time instant, and $\gamma \in (0,1)$ is the discount factor introduced to ensure the convergence to optimality in dynamic programming. $R(\mathbf{x}_i,\lambda_i)$:$S \times A \rightarrow \mathbf{R}$ is the one-stage reward function obtained when the system is in state $\mathbf{x}$, and a control action λ is taken. The optimal value function J^* and the optimal policy π^* are defined in eq 16, where "sup" indicates the supremum, and Π^s is the set of all feasible control policies,

$$J^{*}(\mathbf{x}) = \sup_{\pi\in\Pi^s} J^{\pi}(\mathbf{x}) \qquad \pi^{*}(\mathbf{x}) = \arg\{\sup_{\pi\in\Pi^s} J^{\pi}(\mathbf{x})\} = \arg J^{*}(\mathbf{x}) \tag{16}$$

In our particular calculation, the one-stage reward function is defined as $R(\mathbf{x}_i, \lambda_i) = \psi_6^2$, with a discount factor of γ = 0.99. With a discount factor so close to 1, the future values of the reward are nearly as important as the initial reward, over the ten control intervals considered here. The objective function was selected to achieve the highest possible ψ_6 value, which corresponds to a highly ordered, single domain crystalline state of the system. C_6 is not included explicitly in the objective function, but a high ψ_6 value state automatically requires a high C_6 value due to physical constraints. The optimal control policy was solved with dynamic programming in the MDP framework, using a policy iteration algorithm embedded in the MDP Toolbox from MATLAB central distribution.[70]

ASSOCIATED CONTENT

Supporting Information

The Supporting Information is available free of charge on the ACS Publications website at DOI: 10.1021/acsnano.6b02400.

Additional materials and methods and simulation and analytical methods (PDF)
Supplementary movie S1 (MOV)
Supplementary movie S2 (MOV)

AUTHOR INFORMATION

Corresponding Authors

*E-mail: martha.grover@chbe.gatech.edu.
*E-mail: mabevan@jhu.edu.

Author Contributions

X.T., B.R., and Y.Y. contributed equally.

Notes

The authors declare no competing financial interest.

ACKNOWLEDGMENTS

We acknowledge financial support provided by AFOSR (Grant FA9550-12-1-0090), NSF Cyber Enabled Discovery and Innovation grants (Nos. CMMI-1124648 and CMMI-1124678), an NSF unsolicited grant (No. CBET-1234981), and ONR (Grant N000141210134).

REFERENCES

(1) Ozbay, E. The Magical World of Photonic Metamaterials. *Opt. Photonics News* **2008**, *19*, 22−27.
(2) Stebe, K. J.; Lewandowski, E.; Ghosh, M. Oriented Assembly of Metamaterials. *Science* **2009**, *325*, 159−160.
(3) Arpin, K. A.; Mihi, A.; Johnson, H. T.; Baca, A. J.; Rogers, J. A.; Lewis, J. A.; Braun, P. V. Multidimensional Architectures for Functional Optical Devices. *Adv. Mater.* **2010**, *22*, 1084−1101.
(4) Engheta, N. 150 Years of Maxwell's Equations. *Science* **2015**, *349*, 136−137.
(5) Kalsin, A. M.; Fialkowski, M.; Paszewski, M.; Smoukov, S. K.; Bishop, K. J. M.; Grzybowski, B. A. Electrostatic Self-Assembly of Binary Nanoparticle Crystals with a Diamond-Like Lattice. *Science* **2006**, *312*, 420−424.
(6) Henzie, J.; Grünwald, M.; Widmer-Cooper, A.; Geissler, P. L.; Yang, P. Self-Assembly of Uniform Polyhedral Silver Nanocrystals into

DOI: 10.1021/acsnano.6b02400
ACS Nano 2016, 10, 6791−6798

Densest Packings and Exotic Superlattices. *Nat. Mater.* **2011**, *11*, 131−137.
(7) Nykypanchuk, D.; Maye, M. M.; van der Lelie, D.; Gang, O. DNA-Guided Crystallization of Colloidal Nanoparticles. *Nature* **2008**, *451*, 549−552.
(8) Shevchenko, E. V.; Talapin, D. V.; Kotov, N. A.; O'Brien, S.; Murray, C. B. Structural Diversity in Binary Nanoparticle Superlattices. *Nature* **2006**, *439*, 55−59.
(9) Macfarlane, R. J.; Lee, B.; Jones, M. R.; Harris, N.; Schatz, G. C.; Mirkin, C. A. Nanoparticle Superlattice Engineering with DNA. *Science* **2011**, *334*, 204−208.
(10) Cheng, Z.; Russel, W. B.; Chaikin, P. M. Controlled Growth of Hard-Sphere Colloidal Crystals. *Nature* **1999**, *401*, 893−895.
(11) Biancaniello, P. L.; Kim, A. J.; Crocker, J. C. Colloidal Interactions and Self Assembly Using DNA Hybridization. *Phys. Rev. Lett.* **2005**, *94*, 058302.
(12) Savage, J. R.; Blair, D. W.; Levine, A. J.; Guyer, R. A.; Dinsmore, A. D. Imaging the Sublimation Dynamics of Colloidal Crystallites. *Science* **2006**, *314*, 795−798.
(13) Yan, J.; Bloom, M.; Bae, S. C.; Luijten, E.; Granick, S. Linking Synchronization to Self-Assembly Using Magnetic Janus Colloids. *Nature* **2012**, *491*, 578−581.
(14) Koenig, G. M.; Lin, I.-H.; Abbott, N. L. Chemoresponsive Assemblies of Microparticles at Liquid Crystalline Interfaces. *Proc. Natl. Acad. Sci. U. S. A.* **2010**, *107*, 3998−4003.
(15) Soyka, F.; Zvyagolskaya, O.; Hertlein, C.; Helden, L.; Bechinger, C. Critical Casimir Forces in Colloidal Suspensions on Chemically Patterned Surfaces. *Phys. Rev. Lett.* **2008**, *101*, 208301.
(16) Swan, J. W.; Vasquez, P. A.; Whitson, P. A.; Fincke, E. M.; Wakata, K.; Magnus, S. H.; Winne, F. D.; Barratt, M. R.; Agui, J. H.; Green, R. D.; Hall, N. R.; Bohman, D. Y.; Bunnell, C. T.; Gast, A. P.; Furst, E. M. Multi-Scale Kinetics of a Field-Directed Colloidal Phase Transition. *Proc. Natl. Acad. Sci. U. S. A.* **2012**, *109*, 16023−16028.
(17) Kim, Y.; Shah, A. A.; Solomon, M. J. Spatially and Temporally Reconfigurable Assembly of Colloidal Crystals. *Nat. Commun.* **2014**, *5*, 3676.
(18) Armani, M. D.; Chaudhary, S. V.; Probst, R.; Shapiro, B. Using Feedback Control of Microflows to Independently Steer Multiple Particles. *J. Microelectromech. Syst.* **2006**, *15*, 945−956.
(19) Juarez, J. J.; Bevan, M. A. Feedback Controlled Colloidal Self-Assembly. *Adv. Funct. Mater.* **2012**, *22*, 3833−3839.
(20) Vezirov, T. A.; Gerloff, S.; Klapp, S. H. L. Manipulating Shear-Induced Non-Equilibrium Transitions in Colloidal Films by Feedback Control. *Soft Matter* **2015**, *11*, 406−413.
(21) Solis, E. O. P.; Barton, P. I.; Stephanopoulos, G. Controlled Formation of Nanostructures with Desired Geometries. 2. Robust Dynamic Paths. *Ind. Eng. Chem. Res.* **2010**, *49*, 7746−7757.
(22) Klotsa, D.; Jack, R. L. Controlling Crystal Self-Assembly Using a Real-Time Feedback Scheme. *J. Chem. Phys.* **2013**, *138*, 094502.
(23) Branduardi, D.; Gervasio, F. L.; Parrinello, M. From A to B in Free Energy Space. *J. Chem. Phys.* **2007**, *126*, 054103.
(24) Gast, A. P.; Russel, W. B. Simple Ordering in Complex Fluids - Colloidal Particles Suspended in Solution Provide Intriguing Models for Studying Phase Transitions. *Phys. Today* **1998**, *51*, 24−30.
(25) Anderson, V. J.; Lekkerkerker, H. N. W. Insights into phase transition kinetics from colloid science. *Nature* **2002**, *416*, 811−815.
(26) Poon, W. Colloids as Big Atoms. *Science* **2004**, *304*, 830−831.
(27) Pusey, P. N.; van Megen, W. Phase Behaviour of Concentrated Suspensions of Nearly Hard Colloidal Spheres. *Nature* **1986**, *320*, 340−342.
(28) Gasser, U.; Weeks, E. R.; Schofield, A.; Pusey, P. N.; Weitz, D. A. Real-Space Imaging of Nucleation and Growth in Colloidal Crystallization. *Science* **2001**, *292*, 258−262.
(29) Pertsinidis, A.; Ling, X. S. Diffusion of Point Defects in Two-Dimensional Colloidal Crystals. *Nature* **2001**, *413*, 147−150.
(30) Schall, P.; Cohen, I.; Weitz, D. A.; Spaepen, F. Visualization of Dislocation Dynamics in Colloidal Crystals. *Science* **2004**, *305*, 1944−1948.
(31) Alsayed, A. M.; Islam, M. F.; Zhang, J.; Collings, P. J.; Yodh, A. G. Premelting at Defects Within Bulk Colloidal Crystals. *Science* **2005**, *309*, 1207−1210.
(32) Ackerson, B. J.; Clark, N. A. Shear-Induced Partial Tranlational Ordering of a Colloidal Solid. *Phys. Rev. A: At., Mol., Opt. Phys.* **1984**, *30*, 906−918.
(33) Lumsdon, S. O.; Kaler, E. W.; Velev, O. D. Two-Dimensional Crystallization of Microspheres by a Coplanar AC Electric Field. *Langmuir* **2004**, *20*, 2108−2116.
(34) Goldenberg, L. M.; Wagner, J.; Stumpe, J.; Paulke, B.-R.; Görnitz, E. Simple Method for the Preparation of Colloidal Particle Monolayers at the Water/Alkane Interface. *Langmuir* **2002**, *18*, 5627−5629.
(35) Schermelleh, L.; Heintzmann, R.; Leonhardt, H. A Guide to Super-Resolution Fluorescence Microscopy. *J. Cell Biol.* **2010**, *190*, 165−175.
(36) Leung, B. O.; Chou, K. C. Review of Super-Resolution Fluorescence Microscopy for Biology. *Appl. Spectrosc.* **2011**, *65*, 967−980.
(37) Chen, Q.; Smith, J. M.; Park, J.; Kim, K.; Ho, D.; Rasool, H. I.; Zettl, A.; Alivisatos, A. P. 3D Motion of DNA-Au Nanoconjugates in Graphene Liquid Cell Electron Microscopy. *Nano Lett.* **2013**, *13*, 4556−4561.
(38) Zheludev, N. I.; Kivshar, Y. S. From Metamaterials to Metadevices. *Nat. Mater.* **2012**, *11*, 917−924.
(39) Juarez, J. J.; Liu, B. G.; Cui, J.-Q.; Bevan, M. A. kT-Scale Colloidal Interactions in High-Frequency Inhomogeneous AC Electric Fields. II. Concentrated Ensembles. *Langmuir* **2011**, *27*, 9219−9226.
(40) Adriani, P. M.; Gast, A. P. A Microscopic Model of Electrorheology. *Phys. Fluids* **1988**, *31*, 2757−2768.
(41) Edwards, T. D.; Beltran-Villegas, D. J.; Bevan, M. A. Size Dependent Thermodynamics and Kinetics in Electric Field Mediated Colloidal Crystal Assembly. *Soft Matter* **2013**, *9*, 9208−9218.
(42) Edwards, T. D.; Yang, Y.; Beltran-Villegas, D. J.; Bevan, M. A. Colloidal Crystal Grain Boundary Formation and Motion. *Sci. Rep.* **2014**, *4*, 6132.
(43) Chang, H.; Fu, M.; Hu, J.; Marcu, S. *Simulation-Based Algorithms for Markov Decision Processes*; Springer-Verlag: New York, 2006.
(44) Bowman, G.; Pande, V. S.; Noe, F. *An Introduction to Markov State Models and Their Application to Long Timescale Molecular Simulation*; Springer: Dordrecht, the Netherlands, 2014.
(45) Puterman, M. L. *Markov Decision Processes: Discrete Stochastic Dynamic Programming*; John Wiley & Sons: New York, 2014.
(46) Zhang, H.; Srolovitz, D. J.; Douglas, J. F.; Warren, J. A. Characterization of Atomic Motion Governing Grain Boundary Migration. *Phys. Rev. B: Condens. Matter Mater. Phys.* **2006**, *74*, 115404.
(47) Skinner, T. O. E.; Aarts, D. G. A. L.; Dullens, R. P. A. Grain-Boundary Fluctuations in Two-Dimensional Colloidal Crystals. *Phys. Rev. Lett.* **2010**, *105*, 168301.
(48) Anekal, S.; Bevan, M. A. Self Diffusion in Sub-Monolayer Colloidal Fluids Near a Wall. *J. Chem. Phys.* **2006**, *125*, 034906.
(49) Goldman, A. J.; Cox, R. G.; Brenner, H. Slow Viscous Motion of a Sphere Parallel to a Plane Wall – I. Motion Through a Quiescent fluid. *Chem. Eng. Sci.* **1967**, *22*, 637−651.
(50) Yuste, S. B.; Santos, A. A Heuristic Radial-Distribution Function for Hard Disks. *J. Chem. Phys.* **1993**, *99*, 2020−2023.
(51) Nagamanasa, K. H.; Gokhale, S.; Ganapathy, R.; Sood, A. K. Confined Glassy Dynamics at Grain Boundaries in Colloidal Crystals. *Proc. Natl. Acad. Sci. U. S. A.* **2011**, *108*, 11323−11326.
(52) Zhang, H.; Srolovitz, D. J.; Douglas, J. F.; Warren, J. A. Grain Boundaries Exhibit the Dynamics of Glass-Forming Liquids. *Proc. Natl. Acad. Sci. U. S. A.* **2009**, *106*, 7735−7740.
(53) Du, D.; Li, D.; Thakur, M.; Biswal, S. L. Generating an *in situ* Tunable Interaction Potential for Probing 2-D Colloidal Phase Behavior. *Soft Matter* **2013**, *9*, 6867−6875.
(54) Fernandes, G. E.; Beltran-Villegas, D. J.; Bevan, M. A. Interfacial Colloidal Crystallization *via* Tunable Hydrogel Depletants. *Langmuir* **2008**, *24*, 10776−10785.

DOI: 10.1021/acsnano.6b02400
ACS Nano 2016, 10, 6791−6798

(55) Lee, W.; Chan, A.; Bevan, M. A.; Lewis, J. A.; Braun, P. V. Nanoparticle-Mediated Epitaxial Assembly of Colloidal Crystals on Patterned Substrates. *Langmuir* **2004**, *20*, 5262−5270.
(56) Ferraro, M. E.; Bonnecaze, R. T.; Truskett, T. M. Graphoepitaxy for Pattern Multiplication of Nanoparticle Monolayers. *Phys. Rev. Lett.* **2014**, *113*, 085503.
(57) Edwards, T. D.; Yang, Y.; Everett, W. N.; Bevan, M. A. Reconfigurable Multi-Scale Colloidal Assembly on Excluded Volume Patterns. *Sci. Rep.* **2015**, *5*, 13612.
(58) Bahukudumbi, P.; Everett, W. N.; Beskok, A.; Huff, G. H.; Lagoudas, D.; Ounaies, Z.; Bevan, M. A. Colloidal Microstructures, Transport, and Impedance Properties within Interfacial Microelectrodes. *Appl. Phys. Lett.* **2007**, *90*, 224102.
(59) Juarez, J. J.; Feicht, S. E.; Bevan, M. A. Electric Field Mediated Assembly of Three Dimensional Equilibrium Colloidal Crystals. *Soft Matter* **2012**, *8*, 94−103.
(60) Beckham, R. E.; Bevan, M. A. Interfacial Colloidal Sedimentation Equilibrium I. Intensity Based Confocal Microscopy. *J. Chem. Phys.* **2007**, *127*, 164708.
(61) Beltran-Villegas, D. J.; Schultz, B. A.; Nguyen, N. H. P.; Glotzer, S. C.; Larson, R. G. Phase behavior of Janus colloids determined by sedimentation equilibrium. *Soft Matter* **2014**, *10*, 4593−4602.
(62) Liberek, K.; Lewandowska, A.; Ziętkiewicz, S. Chaperones in Control of Protein Disaggregation. *EMBO J.* **2008**, *27*, 328−335.
(63) Fernandes, G. E.; Beltran-Villegas, D. J.; Bevan, M. A. Spatially Controlled Reversible Colloidal Self-Assembly. *J. Chem. Phys.* **2009**, *131*, 134705.
(64) Nelson, D. R.; Halperin, B. I. Dislocation-Mediated Melting in Two Dimensions. *Phys. Rev. B: Condens. Matter Mater. Phys.* **1979**, *19*, 2457−2484.
(65) Rein ten Wolde, P.; Ruiz-Montero, M. J.; Frenkel, D. Numerical Calculation of the Rate of Crystal Nucleation in a Lennard-Jones System at Moderate Undercooling. *J. Chem. Phys.* **1996**, *104*, 9932.
(66) Sarich, M.; Noé, F.; Schütte, C. On the Approximation Quality of Markov State Models. *Multiscale Model. Simul.* **2010**, *8*, 1154−1177.
(67) Prinz, J.-H.; Wu, H.; Sarich, M.; Keller, B.; Senne, M.; Held, M.; Chodera, J. D.; Schütte, C.; Noé, F. Markov Models of Molecular Kinetics: Generation and Validation. *J. Chem. Phys.* **2011**, *134*, 174105.
(68) Pande, V. S.; Beauchamp, K.; Bowman, G. R. Everything You Wanted to Know About Markov State Models but Were Afraid to Ask. *Methods* **2010**, *52*, 99−105.
(69) Bertsekas, D. P. *Dynamic Programming and Optimal Control*, 3rd ed.; Athena Scientific: Nashua, NH, 2012.
(70) Chadès, I.; Cros, M.; Garcia, F.; Sabbadin, R. Markov Decision Processes (MDP) Toolbox. https://www.mathworks.com/matlabcentral/fileexchange/25786-markov-decision-processes--mdp--toolbox.

DOI: 10.1021/acsnano.6b02400
ACS Nano 2016, 10, 6791−6798

ACS NANO
Cite This: ACS Nano 2018, 12, 10712−10724
www.acsnano.org

ARTICLE

Optimal Navigation of Self-Propelled Colloids

Yuguang Yang and Michael A. Bevan*

Chemical & Biomolecular Engineering, Johns Hopkins University, Baltimore, Maryland 21218, United States

Supporting Information

ABSTRACT: Controlling the navigation of self-propelled, Brownian colloids in complex microstructured environments (*e.g.*, porous media and tumor vasculature) is important to emerging applications (*e.g.*, enhanced oil recovery and drug delivery). Here, we report a feedback control strategy by which to navigate self-propelled colloids through free space and increasingly complex mazes. Colloid rod position and orientation within mazes is sensed in real time, and instantaneous propulsion along the rod long axis can be actuated via light intensity. However, because uncontrolled rod rotational diffusion determines the propulsion direction, feedback control based on a policy is required to decide how to actuate propulsion magnitude versus colloid position and orientation within mazes. By considering stochastic rod dynamics including self-propulsion, translational−rotational diffusion, and rod−maze interactions, a Markov decision process framework is used to determine optimal control policies to navigate between start and end points in minimal time. The free-space navigation optimal policy effectively reduces to a simple heuristic in which propulsion is actuated only when particles point toward the target. The emergent structure of optimal control policies in mazes is based on the practice of globally following the shortest geometric paths; however, locally, propulsion is actuated to either follow paths toward the target or to produce collisions with maze features as part of generating more-favorable positions and orientations. Findings show how the coupled effects of maze size, propulsion speed, control update time, and relative particle translational and rotational diffusivities influence navigation performance.

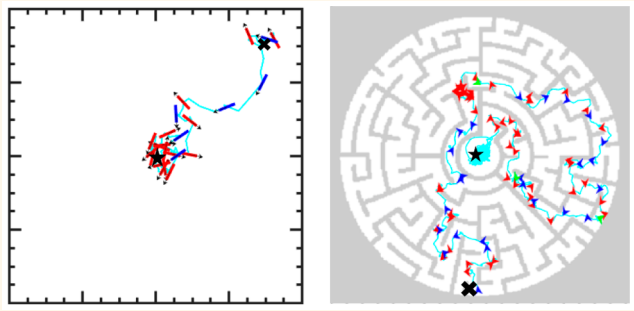

KEYWORDS: *active colloids, feedback control, Markov decision process, fractal mazes, first passage time*

Inspired by the natural microscopic swimmers, such as bacteria and sperm, recent efforts have been made to fabricate synthetic self-propelled particles.[1−3] Such self-propelled particles take various forms, such as bimetallic spheres and rods as well as chains of particles,[4] which function via different propulsion mechanisms such as catalytic osmotic flows[1] or field-mediated artificial flagellar motion.[5] A number of studies have investigated the behavior of self-propelled particles in homogeneous bulk systems,[6] in inhomogeneous environments with random or patterned obstacles,[7] and within assembled clusters.[8,9] By controlling the trajectories of self-propelled particles to perform tasks such as localization, targeting, and collective motion, it is anticipated that applications could be realized involving drug delivery,[10] environmental remediation,[11] oil recovery,[12] and functioning micromachinery.[13−16] To date, the control of self-propelled particles has generally involved simple feedback control to position particles at prescribed locations in free space.[6,17−20] However, the navigation of self-propelled particle trajectories within microstructured environments containing obstacles and dead ends, as in mazes, has not been addressed. Such control is essential to enable self-propelled particles to navigate porous networks (*e.g.*, tissue and soil).

Here, we develop a general approach to enacting robust optimal feedback control of self-propelled colloidal particle trajectories in complex microstructured media. Optimal path planning generally requires minimizing geometric path lengths and avoiding dead-end pathways (*e.g.*, self-driving cars) to efficiently navigate between start and end points. For potential applications that require self-propelled colloid navigation in large-scale microstructured environments, optimal path planning is essential to minimize passage times, traversed distances, and consumption of scarce resources. While generic optimal path-planning algorithms for deterministic and stochastic systems are well-established,[21,22] developing optimal path-planning algorithms specifically for self-propelled colloids requires careful consideration of Brownian translation and rotation. In particular, random Brownian motion drives colloids to uniformly sample all positions and orientations in free space and mazes as part of maximizing entropy.

The ability to control actuation of rod propulsion is necessary to bias stochastic trajectories along designated geometric paths connecting start and end points. In one trivial

Received: July 16, 2018
Accepted: September 25, 2018
Published: September 25, 2018

DOI: 10.1021/acsnano.8b05371
ACS Nano 2018, 12, 10712−10724

limit, the ability to actuate propulsion amplitude on short time scales and in all degrees of freedom could be used to completely suppress Brownian motion to produce deterministic trajectories (like traditional robots). However, the more likely situation encountered in nano- and microscale systems is that feedback control updates occur on time scales slower than those associated with Brownian motion, and under-actuation does not enable arbitrary forces and torques to control all degrees of freedom. Optimal feedback control of self-propelled particles in mazes is a nontrivial problem that has not been solved to the authors' knowledge, particularly where the objective is a minimum passage-time using an approach to directly address the effects of stochasticity and under-actuation.

Based on the aforementioned considerations as well as the types of self-propelled particles that have been practically demonstrated in experiments, here, we report the results for optimal control policies in simulated experiments for the case depicted in Figure 1. We consider the quasi-2D motion of

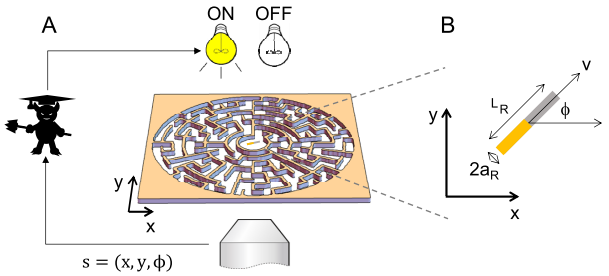

Figure 1. Feedback-controlled navigation of self-propelled rods in mazes. (A) (1) An imaging system senses the particle state, $s = (x, y, \phi)$, within a maze, (2) which is transferred to the controller (a "Maxwell demon"-like entity who knows the optimal control policy) at control update time interval, t_C, (3) where it is determined whether to turn a light on or off to actuate particle propulsion. The controller uses an optimal control policy determined using a MDP framework based on the particle's state-dependent transition probability. (B) The lab frame coordinate system used to track the rod center of mass position and orientation. The self-propelled rod with length of $L_R = 2\ \mu$m, and diameter of $2a_R = 0.4\ \mu$m is propelled along its long axis with speed, v, that is proportional to light intensity.

micron sized colloidal rods with a propulsion magnitude that is tunable via light intensity[23−32] or other globally actuatable mechanisms[23,32−34] and a propulsion direction along the rod's long axis that is determined by uncontrolled Brownian rotation. Results are reported for optimal control of such particles in free space and increasingly complex mazes using a feedback scheme consisting of (1) a sensor based on a microscope and camera to track rods' positions and orientations, (2) an actuator that uses a light source to tune rod propulsion speed (but not direction) at a given control update time, and (3) a control policy that closes the loop by specifying real-time propulsion actuation based on the rod state to rapidly navigate between points. By developing a probabilistic model (Markov chain model) of the rod dynamics under different propulsion settings, a Markov decision process (MDP)[33] framework is used offline to determine the optimal control policy for various geometries including free-space to increasingly complex mazes. After essential navigation control principles are identified in a series of case studies, findings are generalized to show how optimal control policies scale with maze feature size, control update time, and relative rates of colloid propulsion and diffusion. By using the MDP framework, the approach to optimal control investigated in this work is rigorous, robust, and general and can be easily adapted to other propulsion mechanisms beyond light-controlled self-propulsion.

To provide some additional context for the conceptual approach in this work, the proposed strategy can be compared to Maxwell's demon. In Maxwell's thought experiment, a demon controls a door between two halves of a container; the opening and closing of the door after sensing approaching molecules' speeds is employed with the objective to separate slower and faster molecules between the two halves. Because this process would raise one side's temperature and lower the other side's temperature from an initially uniform temperature, the second law of thermodynamics appears to be violated (via an apparent net entropy decrease; the second law is probably not violated because the demon's efforts likely increase entropy elsewhere). We find inspiration from the demon's ability to exploit control of thermal motion to achieve a nontrivial outcome. Instead of actuating a door to separate molecules with different thermal energies, here, we actuate the self-propulsion of thermally rotating colloids to navigate mazes. The natural tendency without control in both experiments is for entropy to be maximized via random sampling of states within the container (to produce a uniform temperature) or maze (to produce a random walk or diffusion). In the case of Maxwell's demon, sensing molecular speed is used to decide whether to actuate a door, whereas in the present case, sensing particle position and orientation is used to decide whether to actuate propulsion. However, as will be shown, the decision to actuate propulsion (*i.e.*, the control policy) in maze navigation is less obvious than for Maxwell's demon, who simply actuates a door based on a threshold molecular speed. In the following, we report a method to determine and demonstrate optimal control policies for actuating Brownian self-propelled colloids with the objective of optimally navigating mazes.

RESULTS AND DISCUSSION

Colloidal Dynamics to Optimal Control. To pose a well-formulated control problem, we first introduce a sufficiently realistic Brownian dynamics (BD) simulation model of self-propelled colloidal rod particles to capture the dominant physics commonly observed in experiments.[34] Although more-rigorous and more-complex models of rod−boundary hydrodynamic and colloidal interactions (including translation−rotation coupling)[35] and propulsion mechanisms[36−38] could introduce quantitative changes to the following results, the conceptual problem and algorithms are not expected to differ significantly based on such model variations. Practically, an equation of motion containing different or additional terms could be used to obtain optimal control policies using the general method illustrated in this work. The equation of motion for the lab frame position vector, $\mathbf{r}$, and orientation, ϕ, of a self-propelled Brownian colloidal rod in two dimensions is given by coupled equations as:

$$\mathbf{r}(t+\Delta t) = \mathbf{r}(t) + \frac{\mathbf{D}_t}{kT}\cdot\mathbf{F}\Delta t + \Delta\mathbf{r}^B + v\cos(\phi)\mathbf{e}_1 + v\sin(\phi)\mathbf{e}_2$$

$$\phi(t+\Delta t) = \phi(t) + \frac{D_r}{kT}\Gamma\Delta t + \Delta\phi^B \quad (1)$$

DOI: 10.1021/acsnano.8b05371
ACS Nano 2018, 12, 10712−10724

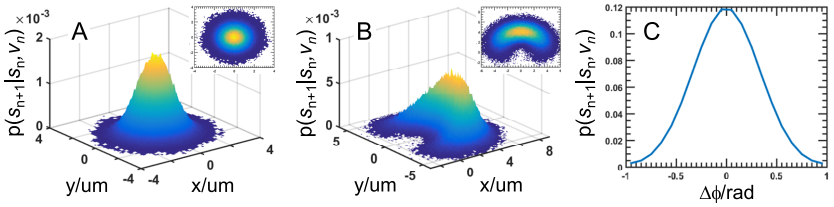

Figure 2. Transition probability in free space for diffusion and self-propulsion. (A) Plot of $p(s_{n+1}|s_n,v_n)$ shown for position coordinates (x, y) without self-propulsion (*i.e.*, diffusion) after a 1 s time step starting from the initial state $s = (x, y, \phi) = (0, 0, 0)$. (B) Plot of $p(s_{n+1}|s_n,v_n)$ with the same parameters as in panel A except with $v = 4.5$ μm/s. (C) Plot of $p(s_{n+1}|s_n,v_n)$ shown for angular coordinate (ϕ) with and without self-propulsion after 1 s. Note that the rotational probability is not influenced by self-propulsion because there is no angular contribution.

where $\mathbf{D}_t$ is the translational diffusivity tensor containing coefficients for different directions,[35,39] D_r is the rotational diffusivity, $\mathbf{F}$ and Γ are forces and torques due to rod−obstacle electrostatic interactions, v is propulsion speed (*e.g.*, actuated by light or another mechanism), kT is thermal energy, Δt is the time step, and $\mathbf{e}_1$ and $\mathbf{e}_2$ are orthogonal unit vectors in the Cartesian coordinate lab frame (see the calculation of coefficients and additional details in the Methods section). This model assumes gravity and substrate repulsion confine rod particles in a quasi-2D layer.[35,39] The cylindrical rod particles are uniaxial (2 μm in length and 0.4 μm in cylindrical cross-sectional diameter) so that the only degrees of freedom are the particle center-of-mass and orientation angle in the lab frame. A key aspect of this model from a control perspective is that the orientation, *i.e.*, the direction of the propulsion, is not controlled, which is determined to be realistic based on self-propelled particle experiments.[40] As a result, when there is nonzero propulsion velocity ($v > 0$), directed deterministic motion occurs at short times ($t \ll 1/D_r$), whereas stochastic motion occurs at longer times ($t \gg 1/D_r$).[40]

To navigate a rod through a maze using only controlled propulsion, an intuitive strategy is to actuate propulsion when orientation and position favorably influence trajectories to avoid obstacles and dead ends. Such a strategy could be quantified by a control policy, π, which is a set of rules that close the loop between an actuatable velocity, v, and observable system states, $s = (x, y, \phi)$, to achieve a navigation objectives using control update time, t_C. However, it is difficult to guarantee that such a control policy would be effective or produce an "optimal" trajectory. The optimal control policy, π^*, is a policy that navigates between states with a minimum integrated process cost, where the cost can be expressed as a quantifiable metric, *e.g.*, total time, distance traveled, energy consumed, *etc.*

Here, we use a MDP framework to compute the optimal control policy.[33] The MDP framework is appropriate in the present problem to consider the nonlinear, coupled stochastic Brownian rotation and self-propulsion. To implement MDP, a discrete-time Markov chain model is constructed to capture the rod's transition probability between different states at different self-propulsion speeds. Then the optimal control policy is obtained by minimizing a cost function associated with the entire integrated process of moving between different states based on the Markov chain model. The MDP framework is general and can be employed to develop optimal control policies for different equations of motion and actuation mechanisms (*e.g.*, see examples of tunable depletion[41] and electric-field-mediated[42−44] colloidal assembly). Uncertainty in particle states in experiments from imaging limitations can be considered within the MDP framework using signal processing strategies (*e.g.*, filters).[22] Details regarding the computation of the Markov chain model, transition probability, and optimal control policy are reported in the Methods section.

Free-Space Navigation. We first demonstrate optimal control of a self-propelled colloidal rod in quasi-2D free space (*i.e.*, the absence of obstacles or confinement). The essential input to the MDP framework is a Markov chain model of the rod dynamics characterized by a transition probability, $p(s_{n+1}|s_n,v_n)$, from state s_n to state s_{n+1} for a given propulsion velocity, v_n, and control update time, t_C. Here the subscript n and $n+1$ denotes the state and speed are measured at time t_n and $t_{n+1} = t_n + t_C$. For navigating quasi-2D free space, Figure 2 shows a plot of $p(s_{n+1}|s_n,v_n)$ constructed from BD simulations for a starting state of $s_n = (x, y, \phi) = (0, 0, 0)$, a control update time, $\Delta t_C = 1$ s, and two velocity states $v = 0$ μm/s and $v = 4.5$ μm/s (*i.e.*, light intensity "off" and "on").

In the absence of propulsion, the transition probability has a Gaussian distribution in the x, y and ϕ coordinates with the expected mean (at the origin) and variances for 2D translational ($4D_t t_C$) and rotational ($2D_r t_C$) diffusion.[39] For a propulsion of $v = 4.5$ μm/s, the transition probability is a distorted Gaussian in the particle coordinate system along the propulsion direction (a "banana" distribution[45]) with the mode at $(x, y, \phi) = (4.5, 0, 0)$. The angular displacement distribution (Figure 2C) is unaffected by propulsion and is based solely on rotational diffusion (*i.e.*, Gaussian with zero mean and variance of $2D_r t_C \approx 60$ degrees). The relatively large angular displacement variance produces the large spread in the position probability (Figure 2B) due to coupling.

The free-space transition probability (Figure 2) can be used in eq 14 to compute the optimal control policy to navigate a self-propelled Brownian rod between two points in free space. A representative trajectory (Figure 3A and Movie S1) for controlled navigation between initial and final coordinates demonstrates how propulsion is actuated based on the rod's position and orientation relative to the target. The optimal policy specifies propulsion versus eight discretely partitioned rod states, which are plotted in a coordinate frame referenced to the target state (Figure 3B; zero angle indicates the rod pointing directly toward the target). The optimal policy, $\pi^*(x, y, \phi)$, is compactly expressed via projection of the target-rod distance vector onto the rod long axis, d_n (which effectively accounts for orientation via compact notation), as:

$$\pi^*(d_n) = \begin{cases} \text{ON } (v = 4.5\ \mu\text{m/s}), & d_n > 2.3\mu\text{m} \\ \text{OFF } (v = 0\ \mu\text{m/s}), & d_n \le 2.3\mu\text{m} \end{cases} \quad (2)$$

which shows that only the orientation and distance of the rod relative to the target are important. This policy could be non-dimensionalized to scale for other v and t_C, but dimensions are

DOI: 10.1021/acsnano.8b05371
ACS Nano 2018, 12, 10712−10724

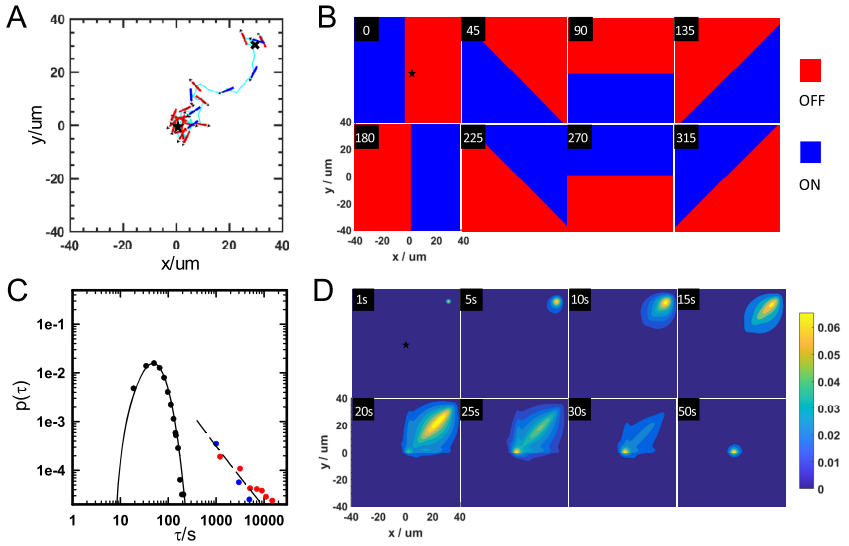

Figure 3. Optimal navigation of self-propelled colloids in free space. (A) Simulated optimally controlled trajectory for a 200 s period with starting state $(x, y, \phi) = (30, 30, 0)$ (×) and target position $(x, y) = (0, 0)$ (★) (animated in Movie S1). The blue shaded rod indicates self-propulsion in the on state ($v = 4.5\ \mu$m/s), and red indicates the off state corresponding to Brownian diffusion ($v = 0\ \mu$m/s). (B) Visualization of optimal control policy calculated using eq 14 as a function of states in (x, y, ϕ); states are discretized into a Cartesian grid in particle position (x, y) and octants (in 0° and 45° increments) in the particle orientation relative to the forward direction of the particle long axis relative to the target. Blue indicates the self-propelled on state ($v = 4.5\ \mu$m/s), and red indicates the off state corresponding to Brownian diffusion ($v = 0\ \mu$m/s). (C) First-passage time distributions, $p(\tau)$, from simulation (points) for controlled (black) and uncontrolled diffusion (red) and uncontrolled propulsion (blue). First-passage time distribution from models (lines) for controlled (eq 17) and uncontrolled diffusion and propulsion (asymptotic limit of $1/t\ \ln^2(t)$). (D) Theoretical probability evolution from eq 16 under optimal control as a function of time.

retained for explicit connection to the example in Figure 1. Practically, the optimal control policy adjusts propulsion speed to minimize distance between the rod position and the target at each control update time step. The intuitive picture underlying the control policy is that when the target is in front of the rod and relatively far away, propulsion is turned on to reduce distance to the target; if the target is either behind the rod or nearby (*i.e.*, $d_n \lesssim 0.5\ vt_C \approx L_R$), propulsion is turned off to avoid increasing distance to the target or overshooting. As already previewed, this policy has some similarities to that employed by Maxwell's demon; a single action is taken when the desired system state appears via stochastic thermal fluctuations, and the action is based on information to drive an apparent entropy decreasing process. For free-space navigation, the optimal policy effectively reduces to a simple heuristic; actuate propulsion when the particle is pointing toward the target. Such a simple control scheme is not obviously expected to be the case for particles interacting with obstacles and features within a maze.

To evaluate performance and utility of the optimal free-space control policy (eq 2), the time for rods to traverse between initial and target positions or the first-passage time, τ, is characterized for several cases. The target in this and all cases is defined as $S^{target} = [(x, y): |x - x^{target}| + |y - y^{target}| < 0.5L_R]$. Trajectories ($\sim 10^3$) are measured for 3 different cases: (1) no propulsion (*i.e.*, rod diffusion), (2) propulsion engaged at all times, and (3) optimally controlled propulsion (Figure 3C). For each case, first passage time histograms are reported to account for stochastic rod motion and distributed passage times. The key finding from these results is that the optimally controlled trajectories have a finite, compact distribution and, hence, a finite mean first passage time of $\langle\tau\rangle \approx 60$ s. In contrast, either in the absence of propulsion or for full uncontrolled propulsion, the τ distributions are heavy tailed (*i.e.*, tails not exponentially bounded), which results in unbounded means (*i.e.*, $\langle\tau\rangle$). Rods experience random walks in both uncontrolled cases, where full propulsion has a higher effective translational diffusivity[40] of $D_{eff} = D_t + v^2/4D_r$. The long-time asymptotic limit for an unbounded first passage time distribution is expected to scale as $\sim\tau^{-1}\ \ln^2(\tau)$,[46] which agrees with simulated results for both uncontrolled cases.

The time evolution of the rod's positional probability provides a means to visualize the rod's stochastic motion as the optimal policy controls propulsion velocity and navigation from initial to target coordinates (Figure 3D). Results for positional probability at different time points are obtained by evolving the Markov chain model via eq 16 (see the Methods section). The probability of the controlled trajectories evolves from an initial δ function at the starting position and then, at longer times, stretches along the shortest geometric path toward the target. The probability distribution first reaches the target by ~20 s and then concentrates at the target until it reaches a compact distribution that becomes increasingly centered on the target at >60 s. Because the controlled process remains stochastic, the probability evolution is consistent with both the τ distribution (Figure 3C; ~10 s < τ < ~200 s with $\langle\tau\rangle \approx 60$ s) and the single rendered trajectory (Figure 3A and Movie S1; $\tau \approx 120$s). In contrast to the optimally controlled probability evolution, a 2D random walk (*i.e.*, no propulsion or uncontrolled full propulsion) is simply a Gaussian distribution spreading uniformly from the starting coordinates.

Simple Obstacle to Complex-Maze Navigation. After understanding self-propelled colloidal navigation in free space, we next consider how a single obstacle within a bounded region, as the simplest maze feature, alters the optimal control policy (Figure 4 and Movie S2). A representative trajectory is shown (Figure 4A) for controlled navigation between initial $(x, y, \phi) = (3, 3, 0)$ and target $(x^{target}, y^{target}) = (3, 25)$ states in the

DOI: 10.1021/acsnano.8b05371
ACS Nano 2018, 12, 10712−10724

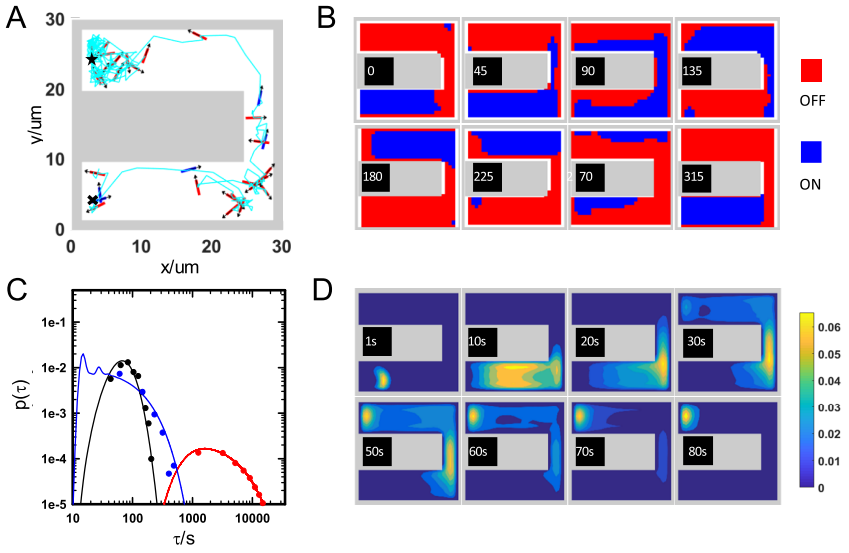

Figure 4. Optimal navigation of self-propelled colloids in simple mazes. (A) Simulated optimally controlled trajectory for a 200 s period with a starting state of $(x, y, \phi) = (2, 3, 0)$ (×) and a target position of $(x, y) = (2, 25)$ (★) (animated in Movie S2). (B) Visualization of optimal control policy calculated using eq 14 as a function of states in (x, y, ϕ); formatting is identical to that of Figure 3B. (C) First-passage time distributions from simulation (points) for controlled (black) and uncontrolled diffusion (red) and uncontrolled propulsion (blue) and a model for all cases (lines) (eq 17). (D) Theoretical probability evolution from eq 16 under optimal control as a function of time.

presence of a rectangular obstacle with two dead-ends. The optimal policy, π^*, is calculated as in free-space via eq 14 but now using parameters characterizing the navigation task in the simple maze: (1) S^{target} is set to the target region as defined in the free-space case; (2) the transition matrix $P(s_{n+1}|s_n, v_n)$ is set such that the rod's configuration cannot overlap with maze walls (see details in the Methods section); (3) the state space S is set as all feasible rod configurations that do not overlap with maze features.

The resulting optimal policy (Figure 4B) cannot be compactly captured by a single parameter as in the free-space policy in eq 2 (*i.e.*, no simplifying reduction was identified). However, the policy can be depicted as in the free-space case, where $\pi^*(x, y, \phi)$ is plotted for eight discretely partitioned angles ϕ and a grid of x, y, coordinates within the maze. This policy essentially has a global and a local structure. Globally, the policy acutates propulsion to follow the shortest geometric path from any point toward the target. Locally, propulsion is turned ON to either direct particles directly along the path toward the target or to propel particles to collide with maze features as part of redirecting particles to positions and orientations that get to the target faster (*e.g.*, by escaping corners). Otherwise, propulsion is turned OFF to wait for desirable positions and orientations to appear via stochastic thermal translation and rotation. Examples indicating propulsion into the wall can be observed for each of the eight discretized orientations in Figure 4B; these are apparent as "on" states (blue) when particles are adjacent to and pointing toward surfaces (*e.g.*, blue in corners in 0° and 180° cases). The strategy to favor particle-boundary collisions in the control policy within mazes emerges in a manner that is not obvious *a priori* and is not easily captured with a simple heuristic.

The first-passage time distribution for controlled navigation of the simple maze can be compared to uncontrolled diffusion or propulsion (Figure 4C). The distributions from BD simulations via eq 1 and a theoretical Markov chain model via eq 17 (see the Methods section) show excellent agreement. The first-passage time distributions for the uncontrolled cases are also now both finite, in contrast to the free-space problem because rods cannot diffuse outside of the maze. Optimal control causes the rod to reach the target ∼10× faster than the uncontrolled diffusive process (self-propulsion OFF). The uncontrolled self-propelled process arrives at the target on comparable times to the optimally controlled case (*i.e.*, wider distribution but similar $\langle\tau\rangle$). This demonstrates that fast random motion is an effective strategy for quickly reaching targets in relatively simple and small-scale mazes by rapidly sampling all available states (in contrast to infinite states in free-space and large state spaces in complex mazes). The short time modes in the uncontrolled self-propelled first passage time distribution are not artifacts but real effects likely due to the characteristic rod and maze geometry. As a final contrast between controlled and uncontrolled propulsion, control maintains particles at the target after arrival, whereas uncontrolled process continue random sampling of all available states after their first arrival at the target.

The spatial probability evolution of the optimally controlled rod is depicted in Figure 4D. A new feature in the simple maze is the temporary accumulation of probability at the entrance to the thin channel section for $t \approx 10-20$ s but not at the channel outlet. This indicates the rod's rate of leaving the channel is greater than the rod's rate of entering the channel. The wider opening immediately outside the narrow channel allows uniform sampling of all orientations, whereas confinement within the channel favors rod orientations aligned with channel walls. This produces an entropic barrier to rods entering the narrower channel, both with and without propulsion. In the case of control, alignment of rods with channel walls produces more favorably oriented states in which propulsion can be actuated, thus resulting in a faster exit from the channel.

The approach to optimal navigation of self-propelled colloids in the simple mazes can be extended to larger-scale, complex mazes. These are conceptually similar but demonstrate additional features of maze size scaling and the importance of control. Here, we systematically increase the number of rectangular obstacles features based on repetition of

DOI: 10.1021/acsnano.8b05371
ACS Nano 2018, 12, 10712−10724

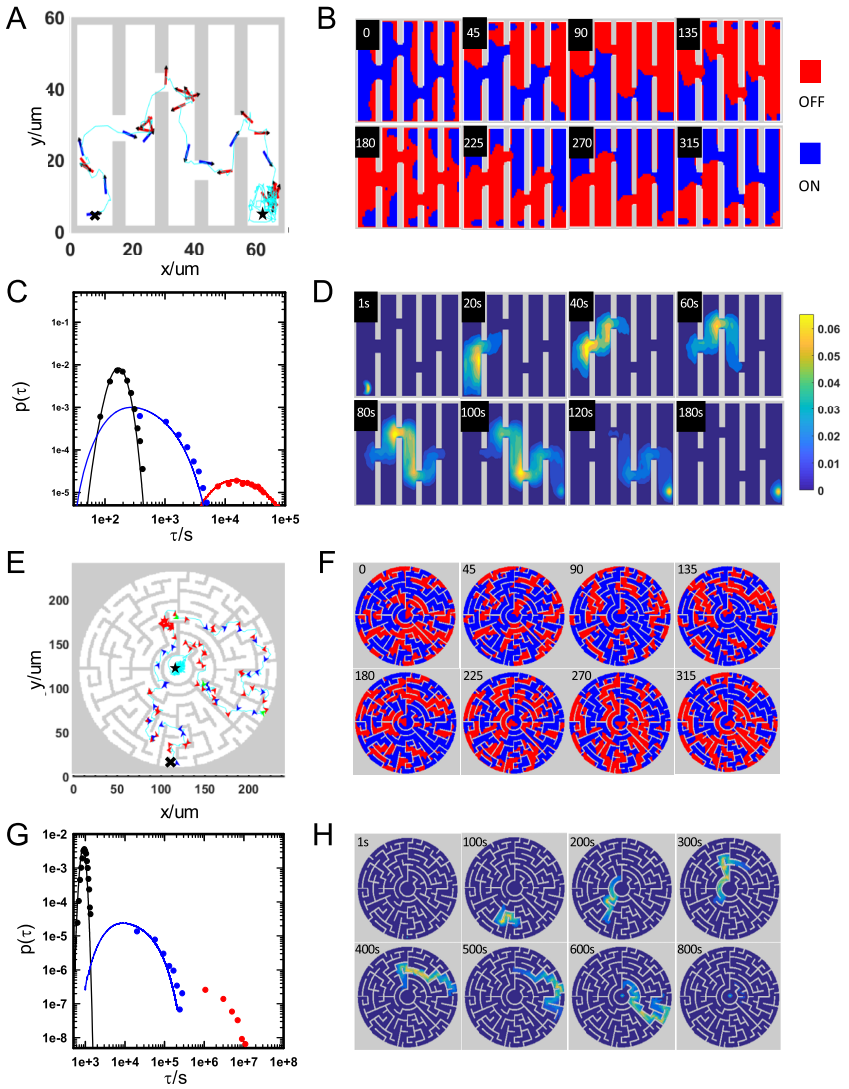

Figure 5. Optimal navigation of self-propelled rods in complex mazes. Simulated trajectory, control policy, first-passage time distributions, and probability evolution for (A−D) a maze with multiple obstacles with similar features to Figure 4 and (E−H) a large-scale maze. Descriptions of panels are the same as panels in Figures 3 and 4. Trajectories in panels A and F are animated in Movie S3 and Movies S4 and S5, respectively. The model-based first-passage time distribution (eq 17) for the uncontrolled diffusion case in panel G is not available due to the prohibitive computational time cost. Note: the initial distribution in panel H at 1s is nearly a δ function, so it is difficult to see at the rendered image size and resolution.

local geometry in Figure 4. As in the free-space and simple mazes, a representative trajectory (Figure 5A and Movie S3) shows the controlled navigation between a starting state (4, 4, 0) and a target position (67, 5). Locally, the optimal control policy (Figure 5B) shares similar features to the simple maze policy, whereas globally, the path depends on the maze solution. In this case, the first-passage time distribution (Figure 5C) shows that optimally controlled self-propelled particles reach the target ∼100× faster than the uncontrolled diffusive process (propulsion OFF) and 3× faster than the uncontrolled self-propelled process (propulsion ON). The probability evolution (Figure 5D) again illustrates the optimal control and, again, show accumulation of probability at channel inlet as in the simple maze example.

The results for the most-complex maze considered in this work (Figure 5E, Movie S4) follow from a systematic extension of the approach and findings for simpler mazes. Generally, as mazes become larger and more complex, the advantages of optimal control become increasingly pronounced compared to the uncontrolled self-propelled process (*i.e.*, self-propulsion on the entire time). The control policy (Figure 5F) again reflects the strategy of optimizing stochastic trajectories around local features (including favorable collisions and alignment with maze features), which is superimposed on the global strategy of finding the shortest path between start and end points (which also avoids dead ends, *i.e.*, non-solutions). In particular, the first-passage time distribution, and the mode in particular (Figure 5G), shows optimally controlled self-propelled particles reach the target ∼80× faster than the uncontrolled self-propelled process (propulsion ON) (and ∼8000× faster than the uncontrolled diffusive process (propulsion off)). Finally, the probability evolution (Figure 5H) helps visualize the progress of the stochastic process as rods navigate the maze both locally and globally. Although the simpler mazes demonstrate the same basic features of the control problem relative to control in free-space and uncontrolled random transport processes, the capability of controlling self-propelled

DOI: 10.1021/acsnano.8b05371
ACS Nano 2018, 12, 10712−10724

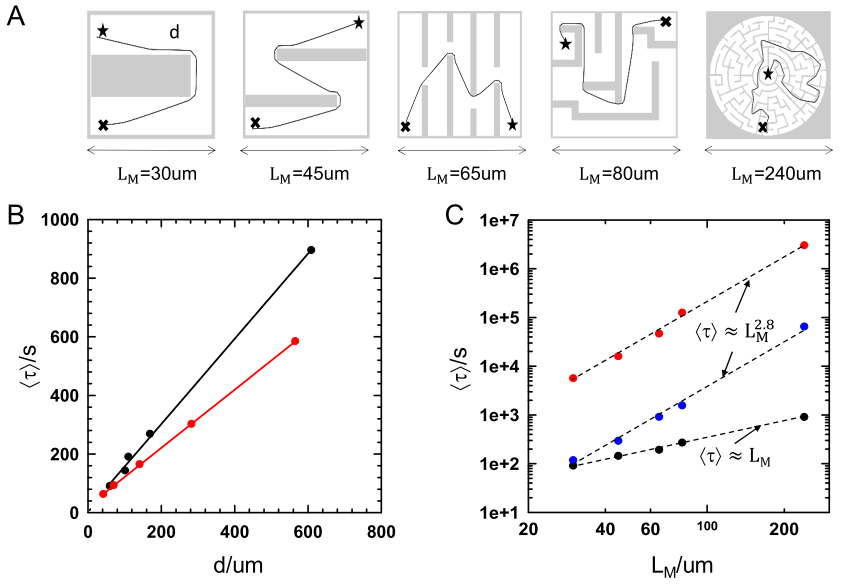

Figure 6. Mean first-passage time scaling for rod navigation under different control strategies and maze dimensions. (A) Mazes of increasing size, L_M, showing the starting and end points and the shortest total traversed path length, d. Mean first-passage time, $\langle\tau\rangle$, as a function of: (B) the shortest path length, d, for the optimal control of (red circles) maze navigation and (black squares) free-space navigation; and (C) maze size, L_M, for different control policies including (black circles) optimal control, (blue circles) uncontrolled propulsion (v = 4.5 μm/s), and (red circles) uncontrolled diffusion (v = 0 μm/s). Lines indicate approximate power law scaling for $\langle\tau\rangle$ as a function of L_M for each control strategy.

particles to enable rapid navigation becomes increasingly apparent in larger mazes.

Size Scaling and Generalization. To systematically quantify navigation of self-propelled colloids through porous media across multiple scales (*e.g.*, tumor vasculature to oil reservoirs), we investigate scaling of optimal control performance versus maze size L_M and traversed path length, d (Figure 6A). We compare scaling for different overall travel distances in two types of optimally controlled self-propelled colloid navigation tasks, including: (1) navigation in free space with increasing Euclidian distance between starting and target locations and (2) navigation in mazes with similar local features (*e.g.*, fractal dimension) and increasing traversed distances (Figure 6A).

Results show that mean first passage time, $\langle\tau\rangle$, under optimal control varies linearly versus total traversed path length, d, (*i.e.*, contour length) both in free space and in mazes (Figure 6B). One finding that emerges is that free-space optimal navigation is more costly compared to maze navigation in terms of time to traverse equivalent distances. The basic explanation is that flat channel features enhance directed motion by aligning rod-shaped particles parallel to confining walls. Practically, this increases the persistence length over which propulsion can be actuated to arrive at the target more quickly. The slope of the linear scaling for optimally controlled navigations in free space and in mazes, and their differences are not obviously predicted by simple models but rather emerge as clear trends.

Comparing uncontrolled and controlled $\langle\tau\rangle$ in free space is not possible because uncontrolled free-space first passage time distributions, $p(\tau)$, and their means are unbounded. When comparing uncontrolled and controlled $\langle\tau\rangle$ values in different-sized mazes (Figure 6C), a dramatic improvement in navigation performance was observed with optimal control. In particular, results can be summarized by power law scaling relationships in which $\langle\tau\rangle \propto L_M$ for optimal control and $\langle\tau\rangle \propto L_M^{2.8}$ for uncontrolled cases. The observed power law can be rationalized for the optimal control case because $\langle\tau\rangle \propto d$ and $d \propto L_M$; hence, $\langle\tau\rangle \propto L_M$. As for the uncontrolled case, diffusion in bounded porous media is know to scale as[47] $\langle\tau\rangle \approx A_{free}\Delta r^{(dv/dp)}$, where A_{free} is void space area fraction, Δr is Euclidean distance between the start and end points, and d_v and d_p are fractal dimensions of the void space and the particle random walk. Because $A_{free} \propto L_M^{dv}$ and $\Delta r \propto L_M$, and $(d_v/d_p) \approx 1-2$,[47] the fit value of $\langle\tau\rangle \propto L_M^{2.8}$ is within expectations. In short, scaling of $\langle\tau\rangle$ either with path length, d, in free-space or mazes or maze size, L_M, grows more slowly with control than without control (smaller linear increase versus path length and smaller power versus maze size). These results show how the control of self-propelled colloid navigation scales with maze size and complexity.

The specific navigation problems investigated in this work depend on several control parameters, which are not easily explored in an exhaustive parametric analysis. As a result, we vary control parameters for several model cases, with the goal of generalizing our findings and understanding limitations of optimally controlled self-propelled colloids. We hypothesize that minimizing $\langle\tau\rangle$ associated with navigating between points is closely related to minimizing error when controlling the steady-state position. As such, we attempt to understand both control about a position and navigation between points. To aid analysis of positioning and navigation performance, a non-dimensional control update time, τ_C, is defined as:[6]

$$\tau_C = \frac{t_C}{\tau_r} = D_r t_C \tag{3}$$

where τ_r is the Brownian rotational time given by D_r^{-1}, and, t_C is the dimensional control update time. This characterizes how the time for control updates compares to the time for particles to reorient via rotation based on their characteristic relaxation time. In addition, a non-dimensional propulsion rate is defined

DOI: 10.1021/acsnano.8b05371
ACS Nano 2018, 12, 10712−10724

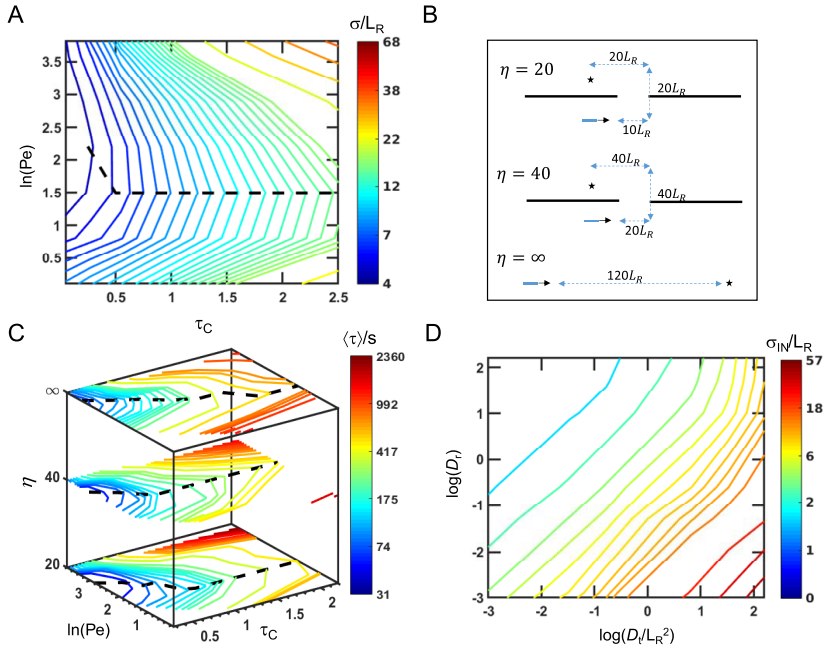

Figure 7. Generalization of optimal control for different non-dimensional control update times (τ_C), propulsion rates (Pe), and maze feature sizes (η). (A) Average positioning error (σ/L_R) (eq 5) about target point at steady-state as a function of τ_C and Pe. The black dashed line again indicates the optimal combinations of propulsion and update time to minimize error. (B) Schematics for different navigation tasks characterized by η ($\eta \equiv L_O/L_R$; ratio of obstacle size, L_O, to rod length, L_R). (C) Summary of $\langle\tau\rangle$ under optimal control in navigation tasks in B vs ln(Pe) and non-dimensional control update time, τ_C. The black dash line passes through the minimum point on each contour line; this locus of points indicates the optimal propulsion (Pe) at a given control update time (τ_C) to minimize the travel time from starting to target coordinates ($\langle\tau\rangle$). (D) Intrinsic position error (σ_{IN}/L_R) as a function of D_r and D_t [where (0,0) corresponds to D_t and D_r values used in the rest of the paper], found by searching τ_C and Pe at each D_t and D_r coordinate to find the minimum error as in panel A.

in terms of a Peclet number, Pe, using a standard definition of:[34]

$$\mathrm{Pe} = \frac{v\tau_r}{\sqrt{2D_t\tau_r}} = \frac{v}{\sqrt{2D_tD_r}} \tag{4}$$

which characterizes the ratio of the propulsion rate and translational diffusion rate or the ratio of the self-propelled drift distance to the translational diffusion distance (during the time interval for rotation, τ_r) ($D_t = 0.5(D_{t,\parallel} + D_{t,\perp}$; see Table 1 in the Methods section). Because the characteristic distances over which self-propulsion and translational diffusion become random walks both depend on the time for particles to reorient,[40,48] the rotational diffusion coefficient appears in both terms. Lastly, a non-dimensional positioning accuracy is characterized by:

$$\sigma(\tau_C, \mathrm{Pe}) = \left[\int [(x - x_{target})^2 + (y - y_{target})^2] p^{\pi^*(\tau_C,\mathrm{Pe})}(x, y)\mathrm{d}x\ \mathrm{d}y\right]^{0.5} \tag{5}$$

where $p^{\pi^*(\tau_C,\mathrm{Pe})}$ is the steady-state position distribution under the optimal policy $\pi^*(\tau_C, \mathrm{Pe})$ as a function of τ_C and Pe. Eq 5 approaches unity as the error term in the integrand vanishes.

Using these non-dimensional quantities, positioning and navigation performance are quantified as a function of τ_C and Pe. We first consider positioning error, σ, in free space from the steady-state control of a particle about a target (Figure 7A). This provides a basis to understand how control parameters influence navigation between points. Positioning error results show a smaller τ_C produces better accuracy. This is consistent with expectations in that more frequent feedback enables faster error correction, and at the same time, there is no penalty for maintaining the previous actuator setting. In experiments, the choice of τ_C will practically depend on hardware or software limitations (*e.g.*, image acquisition and analysis, spatiotemporal resolution, memory requirements, algorithm expense, *etc.*).

In contrast to the control update time dependence, the dependence on Pe is nonmonotic at any given τ_C. In the following discussion, we define Pe* as the minimum error at each τ_C, which forms a locus of points that tend toward an asymotically flat trend at high τ_C. For a given control update time, either making the propulsion rate significantly slower or faster than the diffusion rate increases error. Practically, backward sloping contours along Pe ≈ Pe* indicate a cooperative relationship between decreasing τ_C and increasing Pe to produce minimum error. When Pe is >Pe*, faster propulsion together with larger control update times increases positioning error, analogous to driving a car at high speed with slow reaction time. The larger position error when Pe is <Pe* arises because slower propulsion does not reduce positioning error due to Brownian motion, and the process tends toward uncontrolled diffusion. In short, simply varying Pe away from Pe* while keeping τ_C fixed degrades positioning performance, but varying both together produces the minimum positioning error.

With an understanding of positioning error, we now assess navigation performance versus τ_C and Pe. We consider $\langle\tau\rangle$ for different navigation tasks including navigation in free space and around different-sized obstacles. Specifically, we investigate navigation between two points in free space and between two points around obstacles of different dimensions compared to the rod dimension (Figure 7B) (where $\eta = L_O/L_R$; ratio of obstacle size, L_O, to rod length, L_R). Plots of $\langle\tau\rangle$ versus τ_C and

DOI: 10.1021/acsnano.8b05371
ACS Nano 2018, 12, 10712−10724

Pe are reported for three values of η = 20, 40, and ∞ (Figure 7C).

Similar to the trends for positioning performance (σ versus τ_C and Pe in Figure 7A), it is also found that $\langle\tau\rangle$ continuously decreases with increasing Pe and decreasing τ_C in a cooperative fashion to a lower limit. This is again because faster feedback and faster propulsion together enable colloids to increasingly follow optimal local and global paths. In general, self-propelled colloids under optimal control arrive more quickly at targets by using smaller τ_C (*i.e.*, more-frequent feedback updates). If τ_C is allowed to become too large at low Pe, $\langle\tau\rangle$ values diverge, indicating that the system becomes uncontrollable (except for the smallest obstacle feature, where confinement appears to help guide particles). As Pe $\rightarrow$ 0 or $\tau_C \gg 1$, the self-propelled particle essentially becomes either an unpropelled Brownian random walker or a constant propulsion random walker, which both lead to an unbounded $\langle\tau\rangle$. Finally, the optimal Pe at fixed τ_C gradually increases versus increasing obstacle size; this can be understood based on the fact that smaller obstacles (η) benefit from finer control associated with less propulsion (smaller Pe).

However, it is important to note in all the above cases that continuously decreasing τ_C, while increasing Pe does not completely eliminate positioning error or continuously improve navigation performance. This is an intrinsic error inherent to the control system that cannot be eliminated by choice of τ_C and Pe. The intrinsic error can be defined as σIN = min $\sigma(\tau_C$,Pe), which indicates σ_{IN} is also a function of D_r and D_t (based on eqs3 and 4). To quantify σ_{IN} at different combinations of D_r and D_t, values of Pe and τ_C were varied to find the minimum position error in free space, which can be plotted versus D_r and D_t (Figure 7D). The error is observed to increase as $\sigma_{IN} \approx (D_t/D_r)^{0.5}$, which appears as diagonal contour lines on a log−log plot. This indicates that even after optimal values of τ_C and Pe are determined for a given set of D_r and D_t, finite error remains and depends on the relative ratio of the diffusivities as well as their absolute values. This intrinsic positioning error reflects the uncontrollable elements even under feedback control (*i.e.*, rotation is uncontrollable in the current problem), which provides insight on the fundamental limitations of controlling the position or navigation of self-propelled colloids. As such, any system that requires positioning error below this limit will not be efficiently controllable.

In summary, under optimal control, positioning accuracy (Figure 7A) and navigation performance (Figure 7C) share similar dependencies on control update time and propulsion speed. Control update time and propulsion speed need to be chosen in a cooperative manner to maximize positioning accuracy and minimize navigation $\langle\tau\rangle$. In addition, there are limits associated with both positioning accuracy and navigation performance due to intrinsic uncontrollable elements. The close connections between positioning accuracy and navigation performance can be understood via the optimal control principles revealed in the example cases (Figures 3−5). The ability to optimally navigate between start and end points is achieved by accurately and rapidly controlling colloid positions to subtargets along the globally shortest path.

CONCLUSIONS AND OUTLOOK

We reported a general rigorous framework to determine optimal control policies for navigation of self-propelled colloids in free space and mazes. In free space, a strategy is employed in which the real-time sensing of colloid position and orientation is used to determine the propulsion rate; in this case, the control policy effectively reduces to one in which propulsion is turned on only when the rod is pointing toward the target. In mazes, obstacles obstruct paths between self-propelled colloids and targets, which alters the resulting control policy. Globally, the strategy identifies the shortest path between start and end points, and locally, propulsion is controlled to often follow paths avoiding collisions but in some cases to promote collisions with maze features. Propulsion into boundaries appears to redirect particles to positions and orientations relative to maze features that favor a higher probability of reaching targets faster. While controlling trajectories to avoid collisions is consistent with intuition, promoting particle-boundary collisions emerges in a manner that is not obvious *a priori* and is not captured with a simple heuristic.

The optimal control policy enables orders-of-magnitude faster first-passage times between points compared to either Brownian motion or uncontrolled propulsion. The optimal control performance scales linearly with the traveled path length in both free space and mazes, which contrasts a nearly cubic dependence for uncontrolled random walks. Control parameters are generalized in terms of non-dimensional control update times, propulsion rate, and obstacle dimensions based on rod diffusion rates and dimensions. Findings show using small update times coupled with high propulsion rates provides optimal control over the closely connected tasks of minimizing steady-state colloid positioning error and minimizing colloid navigation times between points. Preliminary studies showed continuous propulsion settings and finer angular discretization did not alter policies compared with the ones reported in this paper.

Our findings are general and can easily be adapted to different actuators and navigation problems using the MDP framework. In future work, the goal is to implement the reported control method using actuation mechanisms cited in this paper as well as approaches we have previously reported (where practical implementation issues are addressed related to imaging, noise, resolution, *etc.*).[43,49−51] Extensions of these concepts could be applied to ensembles of self-propelled colloids using distributed actuators (*e.g.*, electrode arrays,[52] liquid crystal displays, and lasers) to perform additional tasks such are cargo capture and transport in free space and mazes. In such approaches, dynamic target positions and actuation of each particle could be controlled by navigating each particle's trajectory relative to its neighbors (*e.g.*, parallel maze problems).

METHODS

Brownian Dynamics. To model the forces and torques acting on rods due to electrostatic interactions with obstacles, the rod is modeled as a chain of touching spherical beads. Forces acting on the beads that composing the rod will then be transformed to the equivalent forces and torques acting the mass center of the rod. For a rod with position and orientation characterized by $(\mathbf{r}, \phi) = (x, y, \phi)$, the positions of its m spherical beads (where $m = L_R/2a_R$) of radius a_R are given as:

$$\mathbf{r}_i^s = \mathbf{r} + 2a_R\mathbf{n}_1\left(i - \frac{1+m}{2}\right) \qquad i = 1, 2, \ldots, m \tag{6}$$

where $\mathbf{n}_1$ is the unit direction vector of the rod. Obstacles are also represented by a collection of spherical beads such that the interaction between the rod and the obstacles can be easily calculated. R denotes the set of indices for beads composing the rod, and O denotes the set

DOI: 10.1021/acsnano.8b05371
ACS Nano 2018, 12, 10712−10724

of indices for beads composing the obstacles. The forces due to rod−obstacle interactions are simply the summation of interaction forces spherical beads with the obstacle beads, given as:

$$\mathbf{F} = \sum_{i\in R} \mathbf{F}_i^s,\ \mathbf{F}_i^s = \sum_{j\in O} \frac{\mathbf{r}_{ij}^s}{r_{ij}^s} B^{pp}\kappa \exp[-\kappa(r_{ij}^s - 2a_R)] \qquad i \in R \tag{7}$$

where $\mathbf{F}$ is the force on the rod, $\mathbf{F}^s$ is the force on the spherical beads, B^{pp} is the prefactor for electrostatic interactions, κ^{-1} is the Debye length, $\mathbf{r}_{ij}^s = \mathbf{r}_j^s - \mathbf{r}_i^s$ is the vector pointing from bead i to bead j, and r_{ij}^s is the magnitude of $\mathbf{r}_{ij}^s$. The torque on the rod can be related to forces on beads as:

$$\Gamma = \sum_{j\in R} (\mathbf{r}_j^s - \mathbf{r}) \times \mathbf{F}_j^s \tag{8}$$

The forces and torques in eqs 7 and 8 then can be plugged into eq 1 for simulation. Random Brownian translational and rotational displacement vectors $\Delta\mathbf{r}^B$ and $\Delta\phi^B$ obey the relationships:

$$\langle \Delta\mathbf{r}^B \rangle = 0,\ \langle \Delta\mathbf{r}^B (\Delta\mathbf{r}^B)' \rangle = 2\mathbf{D}_t \Delta t$$
$$\langle \Delta\phi^B \rangle = 0,\ \langle \Delta\phi^B \Delta\phi^B \rangle = 2D_r \Delta t \tag{9}$$

where D_r is the rotational diffusivity, and $\mathbf{D}_t$ is the translational diffusivity tensor obtained as $\mathbf{D}_t = \mathbf{nn}D_{t,\parallel} + (\mathbf{I} - \mathbf{nn})D_{t,\perp}$, where $\mathbf{I}$ is the indentity tensor, $\mathbf{n}$ is $(\cos(\phi),\sin(\phi))$ and the orientation vector, and $D_{t,\parallel}$ and $D_{t,\perp}$ are translational diffusivity coefficients parallel and perpendicular to the rod long axis.[35] BD simulations are used to construct transition probabilities and to test the efficacy of optimal control policies. When constructing $p(\tau)$ for different control strategies, ∼1000 simulated trajectories were run from the specified initial state until each trajectory reached the target. The histograms for τ are obtained on linear scale. The integration time step in all cases is 0.1 ms, and all other simulated parameters are reported in Table 1.

Table 1. Parameters Used in BD Simulations of Self-Propelled Colloidal Rods[a]

parameter	eq	value	parameter	eq	value
a_R (nm)[b]	6	200	$D_{t,\parallel}$ (m^2/s)[g]	1, 9	5.13×10^{-13}
B_{pp} (a/kT)[c]	7	2.2974	$D_{t,\perp}$ (m^2/s)[h]	1, 9	4.02×10^{-13}
κ^{-1} (nm)[d]	7	30	D_r (rad^2/s)[i]	1, 9	0.55
m ($L_R/2a_R$)[e]	6	5	v (m/s)[j]	1	4.5×10^{-6}
L_R (nm)[f]		2000			

[a]Parameters are indicated with footnotes. [b]Cylindrical rod cross-sectional radius. [c]Electrostatic potential pre-factor. [d]Debye screening length. [e]Rod aspect ratio. [f]Rod length. [g]Translation diffusivity along the rod long axis. [h]Translation diffusivity perpendicular to the rod long axis. [i]Rotational diffusivity about the rod long axis. [j]Self-propulsion speed.

Transition Probability and Markov Chain Model. A discrete-time Markov chain for the rod's dynamics under different propulsion velocities is fully characterized by the transition probability, $p(s_{n+1}|s_n,v_n)$, where s_n and s_{n+1} are states at time t_n and $t_{n+1} = t_n + t_C$, and v_n is the self-propulsion speed during time t_n and t_{n+1}. The Markov chain model and the transitional probabilities are the critical inputs for designing an optimal control policy using MDP. The transition probabilities can be obtained directly by (1) running multiple short BD simulations starting at every state in S and then (2) collecting statistics for the resulting states after a discrete time step. However, such an approach is time-consuming and is not easily scalable to larger system sizes. To overcome this issue, an approximate but numerically accurate approach (*a posteriori*) we devised is to distinguish state transitions into two general cases, including: (1) rods moving in free space (*i.e.*, no rod-obstacle interaction), and (2) rods moving near obstacles.

To implement this approach, free space transition probabilities are constructed by translating and rotating about a single initial state because $p(s_{n+1}|s_n,v_n)$ depends only on differences between consecutive states(*i.e.*, $x_n - x_{n-1}$, $y_n - y_{n-1}$, and $\phi_n - \phi_{n-1}$). The state space is constructed by discretizing the 2D Cartesian space as grids with resolution $5a$ (half of the length of a rod) in the x and y directions, and the angular space with resolution $\pi/8$ (45°). With this resolution, rods approximately occupy two to three 2D grid elements. The state space, S, consists of all configurations that do not overlap with obstacles.

Transition probabilities near obstacles differ from free-space transition probabilities due to rod−obstacle interactions and thus depend on rod and obstacle geometries, positions, and orientations. Capturing all details of rod transition probabilities near obstacles is impractical and, in many cases, unnecessary; here, we approximate transition probabilities involving rod−obstacle collisions by equating the transition probability to zero for inadmissible overlapping states (*i.e.*, forbidden positions and orientations because rods cannot penetrate obstacles) and renormalizing the remaining probability for admissible states. This simplifies the transition probability near boundaries with minimal but sufficient details of rod−obstacle interactions.

When employing this estimate of the transition probability in the control scheme in this work, it was found that simply disallowing propulsion when the probability of overlapping states exceeds a threshold (∼70%) was sufficient for control purposes. It appears unnecessary for the problems investigated in this work to more accurately quantify the transition probability corresponding to rod-obstacle interactions. However, care should be taken when extending such a simplification to other geometries in which overlapping states dominate (*e.g.*, more-confined geometries). Despite using a convenient approximation for the transition probability to minimize computational expense (<1 s on a desktop computer), the approach reported in this work is general and can also be applied using more-accurate transition probability estimates.

Optimal Control Framework and Probability Evolution. We use a MDP framework to compute optimal control policies in this work.[33] To implement a MDP framework, a discrete-time Markov chain model is first constructed to capture the rod transition probability (see the previous section). The optimal control policy is then obtained by minimizing the expected "cost" over all trajectories obtained by actuating propulsion under candidate control policies. Any control policy, π, is a function mapping from state space to the set of admissible self-propulsion velocities. In other words, given a current state, $s_n = (x_n, y_n, \phi_n)$, π is used in a feedback scheme to determine a propulsion velocity, v, at the next control update time step, t_C. The expected cost accumulated during a navigation process, or cost-to-go function, $J^\pi(s_0)$, for a given π and initial state, s_0, is:

$$J^\pi(s_0) = \mathbf{E}[C(s_0) + \gamma^1 C(s_1) + \cdots + \gamma^N C(s_N)] = \mathbf{E}\sum_{n=0}^{N} \gamma^n [C(s_n)] \tag{10}$$

where $\mathbf{E}$ is the expectation with respect to the distribution of trajectories under a control policy, π, n is the discrete time step index, N is the integer time horizon (*i.e.*, number of steps for path planning, C is the one-step cost function, and γ is the discount factor (number between 0 and 1). In this work, N is selected as $+\infty$, such that obtained optimal control policy is time-independent, and C is set equal to 1 for all states that are not within a threshold of the target state and is 0 for all states within the target-state threshold (which is common in path-planning algorithms).[21] The constant discount factor, γ, is also equated to 0.99 in this work. The relationship between consecutive states (*i.e.*, s_n and s_{n+1}) in eq 10 is characterized by the one-step transition probability given by:

$$p(s_{n+1}) = p(s_{n+1}|s_n, \pi(s_n))p(s_{n-1}) \tag{11}$$

where $\pi(s_n)$ determines the value of propulsion, v_n. Note that the dynamic model of the self-propelled rod captured by the continuous-time Langevin equation in eq 1 is now represented by a discrete-time

DOI: 10.1021/acsnano.8b05371
ACS Nano 2018, 12, 10712−10724

Markov chain model captured by the one-step transition probability in eq 11. By understanding how to compute the cost-to-go function for an arbitrary policy, π, it is possible to determine the optimal policy, π^*, by minimizing the cost-to-go function as:[33]

$$\pi^* = \arg\min_{\pi} J^{\pi}(s_0) = \arg\min_{\pi} \mathbf{E}\sum_{n=0}^{\infty} \gamma^n [C(s_n)] \tag{12}$$

where the argument π of the objective function is implicitly included in the expectation operator because π affects the future state probability distribution via eq 11. Practically, the optimal cost-to-go function, J^*, and optimal control policy, π^*, given by:

$$J^* = \min_{\pi} J^{\pi}, \qquad \pi^* = \arg\min_{\pi} J^{\pi} \tag{13}$$

can be obtained numerically using Bellman's principle of optimality via the recursive relationship:

$$J^*(s) = \min_{\pi(s)}\left[\gamma \sum_{s'} p(s'|s, \pi(s)) J^*(s') + C(s)\right] \tag{14}$$

which can be solved iteratively to yield J^* and π^*. Briefly, starting with an initial guess, $J^{(0)}$, and solving for $J^{(1)}$ and $\pi^{(1)}$ using:

$$J^{(k+1)}(s) = \min_{\pi^{(k+1)}}\left[\gamma \sum_{s'} p(s'|s, \pi^{(k+1)}(s)) J^{(k)}(s') + C(s)\right] \tag{15}$$

it can be shown that $J^{(k)}$ and $\pi^{(k)}$ converge to J^* and π^* as k becomes large.[53]

Control Policy Effectiveness. The effectiveness of the control policy can be evaluated by quantifying the time it takes rods to travel between initial and target points, or the first passage time. Becasuse of stochastic rod motion, there is naturally a distribution of first-passage times, which can be quantified as a histogram from experiments or a modeled probability distribution. To model the first-passage time distribution, the first step is to obtain the probability evolution under a given control policy by iterating the Markov chain model as:

$$p(s_n|s_0) = \left\{\prod_{i=0}^{n-1} p(s_{i+1}|s_i, \pi(s_i))\right\} p(s_0)$$
$$p(s_0) = I(s_0, s_{\text{init}}) \tag{16}$$

where $p(s_n|s_0)$ is the conditional probability distribution, represented as a vector of the state s_n given the initial state s_0, $p(s_{i+1}|s_i,\pi(s_i))$ is the transition probability matrix under the control policy π, $p(s_0)$ is the initial probability distribution represented as a vector, $s_{\text{init}} = (x_{\text{init}}, y_{\text{init}}, \phi_{\text{init}})$, is the initial state, and $I(s_0, s_{\text{init}})$ is the indicator function that equals 1 for $s_0 = s_{\text{init}}$ and is otherwise equal to zero. Based on eq 16, first passage time distribution, $p(\tau)$, can be computed as:

$$p(\tau) = p(n\Delta t) \approx \sum_{s_n \in S^{\text{target}}} p(s_n|s_0) - \sum_{s_{n-1} \in S^{\text{target}}} p(s_{n-1}|s_0) \tag{17}$$

where S^{target} is the target region. Note that eq 17 can be viewed as a discrete-time version of the result for continuous systems given by:[54]

$$p(\tau) = \frac{d}{d\tau}\int_0^{\tau} dt \int_{s \in S^{\text{target}}} p(s(t)|s_0)\, ds \tag{18}$$

Positioning Error. Positioning error in free space was characterized by controlling the particle position about a fixed point. Results were first obtained for a fixed D_t and D_r corresponding to the rod investigated in Figures 2–6 with properties reported in Table 1. Simulations were performed for logarithmic sampling of a grid with τ_C between 0.0275 and 2.75 and Pe between 0.09 and 71.8. At each grid point, 10^3 BD simulations were performed each with a total time of 10^4 s and an integration time of $0.01\tau_C$. Particle positions for analysis were collected at time steps corresponding to τ_C. To characterize positioning error in navigation tasks, the simulation and data sampling parameters are the same as in the free space.

Free-space intrinsic position error was further characterized as a function of self-propelled rods' values of D_t and D_r. Simulations were performed for logarithmic sampling of a grid with both D_t and D_r varying from 0.01 to 100 (where 0 corresponds to the rod value used in Figures 2–6). To generate the intrinsic positioning error data in Figure 7, at each (D_t, D_r) coordinate, the minimum error was found by logarithmically varying τ_C from 0.005 to 1 and Pe from 1 to 100. The simulation parameters were that same as those used to determine position error versus (τ_C, Pe).

ASSOCIATED CONTENT

Supporting Information

This material is available free of charge at The Supporting Information is available free of charge on the ACS Publications website at DOI: 10.1021/acsnano.8b05371.

A video showing simulated optimally controlled trajectory in free space for the experimental results in Figure 3 (AVI)

A video showing simulated optimally controlled trajectory in simple maze for the experimental results in Figure 4 (AVI)

A video showing simulated optimally controlled trajectory in intermediate maze for the experimental results in Figure 5A–D (AVI)

A video showing simulated optimally controlled trajectory in complex maze for the experimental results in Figure 5E–H (AVI)

High-quality rendering of maze navigation experiment in Figure 5E–H and Supplementary Movie S4. (AVI)

AUTHOR INFORMATION

Corresponding Author

*E-mail: mabevan@jhu.edu.

ORCID

Michael A. Bevan: 0000-0002-9368-4899

Author Contributions

The manuscript was written through contributions of all authors. Y.Y. and M.B. designed the computer experiments and their analysis. Y.Y. performed and analyzed the simulated computer experiments. Y.Y. and M.B. interpreted the data.

Notes

The authors declare no competing financial interest.

ACKNOWLEDGMENTS

We acknowledge financial support provided by a NSF Cyber Enabled Discovery and Innovation grant (CMMI-1124648). We acknowledge Martin Rietveld and Allan Doyle for assistance rendering the last Supporting Information movie.

REFERENCES

(1) Sánchez, S.; Soler, L.; Katuri, J. Chemically Powered Micro- and Nanomotors. *Angew. Chem., Int. Ed.* **2015**, *54*, 1414–1444.

(2) Li, J.; Rozen, I.; Wang, J. Rocket Science at the Nanoscale. *ACS Nano* **2016**, *10*, 5619–5634.

(3) Mallouk, T. E.; Sen, A. Powering Nanorobots. *Sci. Am.* **2009**, *300*, 72–77.

(4) Duan, W.; Wang, W.; Das, S.; Yadav, V.; Mallouk, T. E.; Sen, A. Synthetic Nano-and Micromachines in Analytical Chemistry: Sensing, Migration, Capture, Delivery, and Separation. *Annu. Rev. Anal. Chem.* **2015**, *8*, 311–333.

(5) Dreyfus, R.; Baudry, J.; Roper, M. L.; Fermigier, M.; Stone, H. A.; Bibette, J. Microscopic Artificial Swimmers. *Nature* **2005**, *437*, 862–865.

(6) Qian, B.; Montiel, D.; Bregulla, A.; Cichos, F.; Yang, H. Harnessing Thermal Fluctuations for Purposeful Activities: The Manipulation of Single Micro-Swimmers by Adaptive Photon Nudging. *Chem. Sci.* **2013**, *4*, 1420−1429.
(7) Volpe, G.; Buttinoni, I.; Vogt, D.; Kümmerer, H.-J.; Bechinger, C. Microswimmers in Patterned Environments. *Soft Matter* **2011**, *7*, 8810.
(8) Zhang, J.; Yan, J.; Granick, S. Directed Self-Assembly Pathways of Active Colloidal Clusters. *Angew. Chem., Int. Ed.* **2016**, *55*, 5166−5169.
(9) Palacci, J.; Sacanna, S.; Steinberg, A. P.; Pine, D. J.; Chaikin, P. M. Living Crystals of Light-Activated Colloidal Surfers. *Science* **2013**, *339*, 936−940.
(10) Kagan, D.; Laocharoensuk, R.; Zimmerman, M.; Clawson, C.; Balasubramanian, S.; Kang, D.; Bishop, D.; Sattayasamitsathit, S.; Zhang, L.; Wang, J. Rapid Delivery of Drug Carriers Propelled and Navigated by Catalytic Nanoshuttles. *Small* **2010**, *6*, 2741−2747.
(11) Soler, L.; Magdanz, V.; Fomin, V. M.; Sanchez, S.; Schmidt, O. G. Self-Propelled Micromotors for Cleaning Polluted Water. *ACS Nano* **2013**, *7*, 9611−9620.
(12) Kar, A.; Chiang, T.-Y.; Ortiz Rivera, I.; Sen, A.; Velegol, D. Enhanced Transport into and out of Dead-End Pores. *ACS Nano* **2015**, *9*, 746−753.
(13) Stenhammar, J.; Wittkowski, R.; Marenduzzo, D.; Cates, M. E. Light-Induced Self-Assembly of Active Rectification Devices. *Sci. Adv.* **2016**, *2*, e1501850.
(14) Tasci, T. O.; Herson, P. S.; Neeves, K. B.; Marr, D. W. Surface-Enabled Propulsion and Control of Colloidal Microwheels. *Nat. Commun.* **2016**, *7*, 10225.
(15) Takagi, D.; Palacci, J.; Braunschweig, A. B.; Shelley, M. J.; Zhang, J. Hydrodynamic Capture of Microswimmers into Sphere-Bound Orbits. *Soft Matter* **2014**, *10*, 1784.
(16) Ozin, G. A.; Manners, I.; Fournier-Bidoz, S.; Arsenault, A. Dream Nanomachines. *Adv. Mater.* **2005**, *17*, 3011−3018.
(17) Bregulla, A. P.; Yang, H.; Cichos, F. Stochastic Localization of Microswimmers by Photon Nudging. *ACS Nano* **2014**, *8*, 6542−6550.
(18) Haeufle, D. F. B.; Bäuerle, T.; Steiner, J.; Bremicker, L.; Schmitt, S.; Bechinger, C. External Control Strategies for Self-Propelled Particles: Optimizing Navigational Efficiency in the Presence of Limited Resources. *Phys. Rev. E: Stat. Phys., Plasmas, Fluids, Relat. Interdiscip. Top.* **2016**, *94*, 012617.
(19) Mano, T.; Delfau, J.-B.; Iwasawa, J.; Sano, M. Optimal Run-and-Tumble−Based Transportation of a Janus Particle with Active Steering. *Proc. Natl. Acad. Sci. U. S. A.* **2017**, *114*, E2580.
(20) Selmke, M.; Khadka, U.; Bregulla, A. P.; Cichos, F.; Yang, H. Theory for Controlling Individual Self-Propelled Micro-Swimmers by Photon Nudging I: Directed Transport. *Phys. Chem. Chem. Phys.* **2018**, *20*, 10502−10520.
(21) LaValle, S. M. *Planning Algorithms*; Cambridge University Press: New York, 2006.
(22) Bertsekas, D. P. *Dynamic Programming and Optimal Control*; Athena Scientific: Nashua, NH, 2005.
(23) Palacci, J.; Sacanna, S.; Kim, S. H.; Yi, G. R.; Pine, D. J.; Chaikin, P. M. Light-Activated Self-Propelled Colloids. *Philos. Trans. R. Soc., A* **2014**, *372*, 20130372.
(24) Ghosh, A.; Fischer, P. Controlled Propulsion of Artificial Magnetic Nanostructured Propellers. *Nano Lett.* **2009**, *9*, 2243−2245.
(25) Esplandiu, M. J.; Afshar Farniya, A.; Bachtold, A. Silicon-Based Chemical Motors: An Efficient Pump for Triggering and Guiding Fluid Motion Using Visible Light. *ACS Nano* **2015**, *9*, 11234−11240.
(26) Buttinoni, I.; Volpe, G.; Kümmel, F.; Volpe, G.; Bechinger, C. Active Brownian Motion Tunable by Light. *J. Phys.: Condens. Matter* **2012**, *24*, 284129.
(27) Duan, W.; Ibele, M.; Liu, R.; Sen, A. Motion Analysis of Light-Powered Autonomous Silver Chloride Nanomotors. *Eur. Phys. J. E: Soft Matter Biol. Phys.* **2012**, *35*, 77.
(28) Li, W.; Wu, X.; Qin, H.; Zhao, Z.; Liu, H. Light-Driven and Light-Guided Microswimmers. *Adv. Funct. Mater.* **2016**, *26*, 3164−3171.
(29) Enachi, M.; Guix, M.; Postolache, V.; Ciobanu, V.; Fomin, V. M.; Schmidt, O. G.; Tiginyanu, I. Light-Induced Motion of Microengines Based on Microarrays of Tio2 Nanotubes. *Small* **2016**, *12*, 5497−5505.
(30) Chen, C.; Mou, F.; Xu, L.; Wang, S.; Guan, J.; Feng, Z.; Wang, Q.; Kong, L.; Li, W.; Wang, J.; et al. Light-Steered Isotropic Semiconductor Micromotors. *Adv. Mater.* **2017**, *29*, 1603374.
(31) Zhou, D.; Li, Y. C.; Xu, P.; McCool, N. S.; Li, L.; Wang, W.; Mallouk, T. E. Visible-Light Controlled Catalytic Cu2o-Au Micromotors. *Nanoscale* **2017**, *9*, 75−78.
(32) Solovev, A. A.; Smith, E. J.; Bof Bufon, C. C.; Sanchez, S.; Schmidt, O. G. Light-Controlled Propulsion of Catalytic Microengines. *Angew. Chem., Int. Ed.* **2011**, *50*, 10875−10878.
(33) Puterman, M. L. *Markov Decision Processes: Discrete Stochastic Dynamic Programming*; Wiley: Hoboken, NJ, 2014.
(34) Bechinger, C.; Di Leonardo, R.; Löwen, H.; Reichhardt, C.; Volpe, G.; Volpe, G. Active Particles in Complex and Crowded Environments. *Rev. Mod. Phys.* **2016**, *88*, 045006.
(35) Yang, Y.; Bevan, M. A. Interfacial Colloidal Rod Dynamics: Coefficients, Simulations, and Analysis. *J. Chem. Phys.* **2017**, *147*, 054902.
(36) Moran, J. L.; Posner, J. D. Phoretic Self-Propulsion. *Annu. Rev. Fluid Mech.* **2017**, *49*, 511−540.
(37) Mozaffari, A.; Sharifi-Mood, N.; Koplik, J.; Maldarelli, C. Self-Propelled Colloidal Particle near a Planar Wall: A Brownian Dynamics Study. *Physical Review Fluids* **2018**, *3*, 014104.
(38) Uspal, W. E.; Popescu, M. N.; Dietrich, S.; Tasinkevych, M. Self-Propulsion of a Catalytically Active Particle near a Planar Wall: From Reflection to Sliding and Hovering. *Soft Matter* **2015**, *11*, 434−438.
(39) Bitter, J. L.; Yang, Y.; Duncan, G.; Fairbrother, H.; Bevan, M. A. Interfacial and Confined Colloidal Rod Diffusion. *Langmuir* **2017**, *33*, 9034−9042.
(40) Howse, J. R.; Jones, R. A. L.; Ryan, A. J.; Gough, T.; Vafabakhsh, R.; Golestanian, R. Self-Motile Colloidal Particles: From Directed Propulsion to Random Walk. *Phys. Rev. Lett.* **2007**, *99*, 048102.
(41) Bevan, M. A.; Ford, D. M.; Grover, M. A.; Shapiro, B.; Maroudas, D.; Yang, Y.; Thyagarajan, R.; Tang, X.; Sehgal, R. M. Controlling Assembly of Colloidal Particles into Structured Objects: Basic Strategy and a Case Study. *J. Process Control* **2015**, *27*, 64−75.
(42) Tang, X.; Zhang, J.; Bevan, M. A.; Grover, M. A. A Comparison of Open-Loop and Closed-Loop Strategies in Colloidal Self-Assembly. *J. Process Control* **2017**, *60*, 141−151.
(43) Tang, X.; Rupp, B.; Yang, Y.; Edwards, T. D.; Grover, M. A.; Bevan, M. A. Optimal Feedback Controlled Assembly of Perfect Crystals. *ACS Nano* **2016**, *10*, 6791−6798.
(44) Xue, Y.; Beltran-Villegas, D. J.; Tang, X.; Bevan, M. A.; Grover, M. A. Optimal Design of a Colloidal Self-Assembly Process. *IEEE Trans. Control Sys. Technol.* **2014**, *22*, 1956.
(45) Long, A. W.; Wolfe, K. C.; Mashner, M. J.; Chirikjian, G. S. The Banana Distribution Is Gaussian: A Localization Study with Exponential Coordinates. *Robotics: Science and Systems VIII*; MIT Press: Cambridge, MA, 2013, 265−272.
(46) Redner, S. *A Guide to First-Passage Processes*; Cambridge University Press: New York, 2007.
(47) Condamin, S.; Benichou, O.; Tejedor, V.; Voituriez, R.; Klafter, J. First-Passage Times in Complex Scale-Invariant Media. *Nature* **2007**, *450*, 77−80.
(48) Han, Y.; Alsayed, A. M.; Nobili, M.; Zhang, J.; Lubensky, T. C.; Yodh, A. G. Brownian Motion of an Ellipsoid. *Science* **2006**, *314*, 626−630.
(49) Juarez, J. J.; Bevan, M. A. Feedback Controlled Colloidal Self-Assembly. *Adv. Funct. Mater.* **2012**, *22*, 3833−3839.
(50) Juarez, J. J.; Mathai, P. P.; Liddle, J. A.; Bevan, M. A. Multiple Electrokinetic Actuators for Feedback Control of Colloidal Crystal Size. *Lab Chip* **2012**, *12*, 4063−4070.
(51) Edwards, T. D.; Bevan, M. A. Controlling Colloidal Particles with Electric Fields. *Langmuir* **2014**, *30*, 10793−10803.

DOI: 10.1021/acsnano.8b05371
ACS Nano 2018, 12, 10712−10724

(52) Lu, J. P.; Thompson, J. D.; Whiting, G. L.; Biegelsen, D. K.; Raychaudhuri, S.; Lujan, R.; Veres, J.; Lavery, L. L.; Völkel, A. R.; Chow, E. M. Open and Closed Loop Manipulation of Charged Microchiplets in an Electric Field. *Appl. Phys. Lett.* **2014**, *105*, 054104.
(53) Powell, W. B. *Approximate Dynamic Programming: Solving the Curses of Dimensionality*; Wiley: Hoboken, NJ, 2011.
(54) Risken, H.; Frank, T. *The Fokker-Planck Equation: Methods of Solution and Applications*, 2nd ed; Springer: Berlin, Germany, 1996.

DOI: 10.1021/acsnano.8b05371
ACS Nano 2018, 12, 10712−10724

Pattern Recognition Letters 86 (2017) 76–81

Contents lists available at ScienceDirect

Pattern Recognition Letters

journal homepage: www.elsevier.com/locate/patrec

An M-estimator for reduced-rank system identification

Shaojie Chen[a,*], Kai Liu[b], Yuguang Yang[c], Yuting Xu[a], Seonjoo Lee[d], Martin Lindquist[a], Brian S. Caffo[a], Joshua T. Vogelstein[e,f]

[a] Department of Biostatistics, Johns Hopkins Bloomberg School of Public Health, Baltimore 21205, USA
[b] Department of Neuroscience, Johns Hopkins University, Baltimore 21205, USA
[c] Department of Chemical and Biomolecular Engineering, Johns Hopkins University, Baltimore 21205, USA
[d] Department of Psychiatry and Department of Biostatistics, Columbia University, New York City 10027, USA
[e] Child Mind Institute, Baltimore 21205, USA
[f] Department of Biomedical Engineering and Institute for Computational Medicine, Johns Hopkins University, Baltimore 21205, USA

ARTICLE INFO

Article history:
Received 8 August 2016
Available online 19 December 2016

Keywords:
High dimension
Image processing
Parameter estimation
State-space model
Time series analysis

ABSTRACT

High-dimensional time-series data from a wide variety of domains, such as neuroscience, are being generated every day. Fitting statistical models to such data, to enable parameter estimation and time-series prediction, is an important computational primitive. Existing methods, however, are unable to cope with the high-dimensional nature of these data, due to both computational and statistical reasons. We mitigate both kinds of issues by proposing an M-estimator for Reduced-rank System IDentification (MR. SID). A combination of low-rank approximations, ℓ_1 and ℓ_2 penalties, and some numerical linear algebra tricks, yields an estimator that is computationally efficient and numerically stable. Simulations and real data examples demonstrate the usefulness of this approach in a variety of problems. In particular, we demonstrate that MR. SID can accurately estimate spatial filters, connectivity graphs, and time-courses from native resolution functional magnetic resonance imaging data. MR. SID therefore enables big time-series data to be analyzed using standard methods, readying the field for further generalizations including non-linear and non-Gaussian state-space models.

1. Introduction

High-dimensional time-series data are becoming increasingly abundant across a wide variety of domains, spanning economics [13], neuroscience [10], and cosmology [28]. Fitting statistical models to such data, to enable parameter estimation and time-series prediction, is an important computational primitive. Linear dynamical system (LDS) models are amongst the most popular and powerful, because of their intuitive nature and ease of implementation [15]. The famous Kalman Filter-Smoother is one of the most popular and powerful tools for time-series prediction with an LDS, given known parameters [14].

In practice, however, for many LDS's, the parameters are unknown and must be estimated in a process often called *system identification* [17]. To the best of our knowledge, currently there does not exist a methodology that provides parameter estimates and predictions for ultra-high-dimensional time-series data (e.g. the dimension of the time series, $p > 10,000$).

The challenges associated with high-dimensional time-series estimation and prediction are multifold. First, naïvely, such models include dense $p \times p$ matrices, which are often too large to store, much less invert in memory. Several recent efforts to invert large sparse matrices using a series of computational tricks show promise, though they are still extremely computationally expensive [4,12].

Second, estimators behave poorly due to numerical instability. Reduced-rank LDS models can partially address this problem by reducing the number of latent states. [7]. However, without further constraints, the dimensionality of the latent states would be reduced to such an extent that it would significantly decrease the predictive capacity of the resulting model. Third, even after addressing these problems, the time to compute all the necessary quantities can be overly burdensome. Distributed memory implementations, such as those built with Spark, might help overcome this problem. However, it would lead to additional costs and set-up burden, as it would require a Spark cluster [29].

* Corresponding author.
E-mail address: pzcsj76@gmail.com (S. Chen).

http://dx.doi.org/10.1016/j.patrec.2016.12.012

We address all three of these issues with our M-estimator for Reduced-rank System IDentification (MR. SID). By assuming the dimensionality of the latent state space is small (i.e. reduced-rank), relative to the observed space dimensionality, we can significantly improve computational tractability and estimation accuracy. By further penalizing the estimators, with ℓ_1 and/or ℓ_2 penalties, via utilizing prior knowledge on the structure of the parameters, we gain further estimation accuracy in this high-dimensional but relatively low-sample size regime. Finally, by employing several numerical linear algebra tricks, we can reduce the computational burden significantly.

These three techniques combined enable us to obtain highly accurate estimates in a variety of simulation settings. MR. SID is, in fact, a generalization of the now classic Baum-Welch expectation maximization algorithm, commonly used for system identification in much lower dimensional linear dynamical systems [20]. We show numerically that the hyperparameters can be selected to minimize prediction error on held-out data. Finally, we use MR. SID to estimate functional connectomes from the motor cortex. MR. SID enables us to estimate the regions, rather than imposing some prior parcellation on the data, as well as estimate sparse connectivity between regions. MR. SID reliably estimates these connectomes, as well as predicts the held-out time-series data. To our knowledge, this is the first time a single unified approach has been used to estimate partitions and functional connectomes directly from the high-dimensional data.

This work presents a new analysis of a model which has only been implemented in low-dimensional settings, and paves the way for high-dimensional implementation. Though primitive, it is a first step for essentially any high-dimensional time series analysis, control system identification, and spatiotemporal analysis. To enable extensions, generalizations, and additional applications, the code for the core functions and generating each of the figures is freely available on Github (https://github.com/shachen/PLDS/).

2. The model

In statistical data analysis, one often encounters some observed variables, as well as some unobserved latent variables, which we denote as $\boldsymbol{Y} = (\boldsymbol{y}_1, \ldots, \boldsymbol{y}_T)$ and $\boldsymbol{X} = (\boldsymbol{x}_1, \ldots, \boldsymbol{x}_T)$ respectively. By the Bayes rule, the joint probability of $\boldsymbol{X}$ and $\boldsymbol{Y}$ is $P(\boldsymbol{X}, \boldsymbol{Y}) = P(\boldsymbol{Y}|\boldsymbol{X})P(\boldsymbol{X})$. The conditional distribution $P(\boldsymbol{Y}|\boldsymbol{X})$ and prior $P(\boldsymbol{X})$ can both be represented as a product of marginals:

$$P(\boldsymbol{Y}|\boldsymbol{X}) = \prod_{t=1}^{T} P(\boldsymbol{y}_t|\boldsymbol{y}_0, \ldots, \boldsymbol{y}_{t-1}, \boldsymbol{x}_0, \ldots, \boldsymbol{x}_{t-1}),$$

$$P(\boldsymbol{X}) = P(\boldsymbol{x}_0) \prod_{t=1}^{T} P(\boldsymbol{x}_t|\boldsymbol{x}_0, \ldots, \boldsymbol{x}_{t-1}).$$

The generic time-invariant state-space model (SSM) makes the following simplifying assumptions:

$$\begin{aligned} P(\boldsymbol{y}_t|\boldsymbol{y}_0, \ldots, \boldsymbol{y}_{t-1}, \boldsymbol{x}_0, \ldots, \boldsymbol{x}_t) &\approx P(\boldsymbol{y}_t|\boldsymbol{x}_t), \\ P(\boldsymbol{x}_t|\boldsymbol{x}_0, \ldots, \boldsymbol{x}_{t-1}) &\approx P(\boldsymbol{x}_t|\boldsymbol{x}_{t-1}). \end{aligned} \tag{1}$$

A linear dynamical system (LDS) further assumes that both terms in (1) are linear Gaussian functions, which when written as an iterative random process, yield the standard matrix update rules:

$$\begin{aligned} &\boldsymbol{x}_{t+1} = A\boldsymbol{x}_t + \mathbf{w}_t, \quad \mathbf{w}_t \sim N(\mathbf{0}, Q), \quad \boldsymbol{x}_0 \sim N(\pi_0, V_0), \\ &\boldsymbol{y}_t = C\boldsymbol{x}_t + \mathbf{v}_t, \quad \mathbf{v}_t \sim N(\mathbf{0}, R), \end{aligned}$$

where A is a $d \times d$ state transition matrix and C is a $p \times d$ generative matrix. $\boldsymbol{x}_t$ is a $d \times 1$ vector and $\boldsymbol{y}_t$ is a $p \times 1$ vector. The output noise covariance R is $p \times p$, while the state noise covariance Q is $d \times d$. Initial state mean $\boldsymbol{\pi}_0$ is $d \times 1$ and covariance V_0 is $d \times d$.

The model can be thought of as a continuous version of the hidden Markov model (HMM), where the columns of C stand for the hidden states and one observes a single state at time t. Unlike HMM, LDS (1) allows one to observe a linear combination of multiple states. A is the analogy of the state transition matrix, which describes how the weights $\boldsymbol{x}_t$ evolve over time. Another difference is that LDS contains two white noise terms, which are captured by the Q and R matrices.

Without applying further constraints, the LDS model itself is unidentifiable. Three minimal constraints are introduced for identifiability:

Constraint 1: Q is the identity matrix

Constraint 2: the order of C' s columns is fixed based on their norms

Constraint 3: $V_0 = \mathbf{0}$

Note that the first two constraints follow directly from Roweis and Ghahramani (1999), which try to eliminate the degeneracy in the model. Additionally, V_0 is set to zero, meaning the starting state $\boldsymbol{x}_0 = \pi_0$ is an unknown constant instead of a random variable. We put this constraint on, because in the application that follows only one single chain of time series observed. To estimate V_0, multiple series of observations are required.

The following three constraints are further applied to achieve a more useful model:

Constraint 4: R is a diagonal matrix

Constraint 5: A is sparse

Constraint 6: C has smooth columns

The constraint on R is natural. Consider the case where the observations are high dimensional, which means that the R matrix is very large. One cannot accurately estimate the many free parameters in R with a limited amount of observations. Therefore, some constraints on R will help with inferential accuracy, by virtue of significantly reducing variance while not adding too much bias. For example, R can be set to multiples of the identity matrix, or more generally, a diagonal matrix. A static LDS model with a diagonal R is equivalent to Factor Analysis, while one with multiples of the identity R matrix leads to Principal Component Analysis (PCA) [21].

The A matrix is the transition matrix of the hidden states. In many applications, it is desirable for A to be sparse. An ℓ_1 penalty on A is used to impose the sparsity constraint. In the applications that follow, A is a central construct of interest representing a so-called connectivity graph, and the graph is expected to be sparse.

Similarly, in many applications, it is desirable for the columns of C to be smooth. For example, in neuroimaging data analysis, each column of C can be a signal in the brain. Having the signals spatially smooth can help extract meaningful information from the noisy neuroimaging data. In this context, an ℓ_2 penalty on columns of C is used to enforce smoothness.

With all those constraints, the model becomes:

$$\begin{aligned} &\boldsymbol{x}_{t+1} = A\boldsymbol{x}_t + \mathbf{w}_t, \quad \mathbf{w}_t \sim N(\mathbf{0}, \mathbf{I}), \quad \boldsymbol{x}_0 = \pi_0, \\ &\boldsymbol{y}_t = C\boldsymbol{x}_t + \mathbf{v}_t, \quad \mathbf{v}_t \sim N(\mathbf{0}, R), \end{aligned} \tag{2}$$

where A is a sparse matrix and C has smooth columns.

Let $\theta = \{A, C, R, \pi_0\}$ represent all unknown parameters, while $P(\boldsymbol{X}, \boldsymbol{Y})$ represents the full likelihood. Then, combining model 2 and the constraints on A and C leads us to an optimization problem:

$$\hat{\theta} = \underset{\theta}{\operatorname{argmin}} \left\{ -\log P_\theta(\boldsymbol{X}, \boldsymbol{Y}) + \lambda_1 \|A\|_1 + \lambda_2 \|C\|_2^2 \right\} \tag{3}$$

where λ_1 and λ_2 are tuning parameters and $\|\cdot\|_p$ represents the p-norm of a vector. Equivalently, this problem has the following dual

form:

$$\begin{aligned} &\text{minimize} && \{-\log P_\theta(\boldsymbol{X},\boldsymbol{Y})\} \\ &\text{subject to:} && \alpha\|A\|_1+(1-\alpha)\|C\|_2^2 \le \varphi \text{ for some } \varphi; \\ & && A\in\mathcal{A}_{d\times d},\ C\in\mathcal{C}_{p\times d}, R\in\mathcal{R}_{p\times p}, \pi_0\in\pi_{d\times 1} \end{aligned}$$

where $\alpha=\frac{\lambda_1}{\lambda_1+\lambda_2}$. $\mathcal{A}_{d\times d}$ and $\mathcal{C}_{p\times d}$ are $d\times d$ and $p\times d$ dimensional matrix spaces respectively. $\mathcal{R}_{p\times p}$ is the $p\times p$ diagonal matrix space and $\pi_{d\times 1}$ is the d dimensional vector space.

3. Parameter estimation

Replacing $\log P(\boldsymbol{X},\boldsymbol{Y})$ in problem (3) with its concrete form, one gets

$$\begin{aligned} \hat{\theta}=\underset{\theta}{\operatorname{argmin}}\ \Bigg\{ &\sum_{t=1}^{T}\left(\frac{1}{2}[\boldsymbol{y}_t-C\boldsymbol{x}_t]^{\top}R^{-1}[\boldsymbol{y}_t-C\boldsymbol{x}_t]\right)-\frac{T}{2}\log|R| \\ &+\sum_{t=1}^{T}\left(\frac{1}{2}[\boldsymbol{x}_t-A\boldsymbol{x}_{t-1}]^{\top}[\boldsymbol{x}_t-A\boldsymbol{x}_{t-1}]\right)-\frac{T}{2}\log|\mathbf{I}| \\ &-\log(\mathbb{1}_{\pi_0}(\boldsymbol{x}_0))+\lambda_1\|A\|_1+\lambda_2\|C\|_2^2\Bigg\} \end{aligned} \tag{4}$$

Denote the target function in the curly braces as $\boldsymbol{\Phi}(\theta,\ \boldsymbol{Y},\ \boldsymbol{X})$. Then a parameter estimation algorithm is one that optimizes $\boldsymbol{\Phi}(\theta,\ \boldsymbol{Y},\ \boldsymbol{X})$ with regard to $\theta=\{A,C,R,\pi_0\}$.

Parameter estimation for LDS has been investigated extensively in statistics, machine learning, control theory, and signal processing research. For example, in machine learning, the exact and variational inference algorithms for general Bayesian networks can be applied to LDS. In control theory, the corresponding area of study is known as system identification.

Specifically, one way to search for the maximum likelihood estimation (MLE) is through iterative methods such as Expectation-Maximization (EM) [22]. The EM algorithm for a standard LDS is detailed in Zoubin and Geoffrey (1996) [11]. An alternative is to use subspace identification methods such as N4SID and PCA-ID, which give asymptotically unbiased closed-form solutions [8,27]. In practice, determining an initial solution with subspace identification and then refining it with EM is an effective approach [6].

However, the above approaches are not directly applicable to optimization problem (3) due to the introduced penalty terms. We therefore developed an algorithm called M-estimation for Reduced-rank System IDentification (MR. SID), as described below. MR. SID is a generalized Expectation-Maximization (EM) algorithm.

3.1. E Step

The E step of EM requires computation of the expected log likelihood, $\Gamma=E[\log P(\boldsymbol{X},\boldsymbol{Y})|\boldsymbol{Y}]$. This quantity depends on three expectations: $E[\boldsymbol{x}_t|\boldsymbol{Y}]$, $E[\boldsymbol{x}_t\boldsymbol{x}_t^{\top}|\boldsymbol{Y}]$ and $E[\boldsymbol{x}_t\boldsymbol{x}_{t-1}^{\top}|\boldsymbol{Y}]$. For simplicity, we denote their finite sample estimators by:

$$\hat{\boldsymbol{x}}_t\equiv E[\mathbf{x_t}|\boldsymbol{Y}],\ \ \hat{P}_t\equiv E[\boldsymbol{x}_t\boldsymbol{x}_t^{\top}|\boldsymbol{Y}],\ \ \hat{P}_{t,t-1}\equiv E[\boldsymbol{x}_t\boldsymbol{x}_{t-1}^{\top}|\boldsymbol{Y}]. \tag{5}$$

Expectations (5) are estimated with a Kalman filter/smoother (KFS), which is detailed in the Appendix. Notice that all expectations are taken with respect to the current estimations of parameters.

3.2. M Step

Each of the parameters in $\theta=\{A,C,R,\pi_0\}$ is estimated by taking the corresponding partial derivatives of $\boldsymbol{\Phi}(\theta,\ \boldsymbol{Y},\ \boldsymbol{x})$, setting them to zero, and then solving the equations. The details of derivations can be found in the Appendix.

Table 1
The complete EM algorithm.

Algorithm EM Algorithm for MR. SID
1. Initialize $\theta=\{A,C,R,\pi_0\}$ with SVD
2. While convergence criteria are unmet **E Step**
3. Update the expectations in Eq. (5) with the KFS **M Step**
4. $R^{\text{new}}=\text{diag}\left\{\frac{1}{T}\sum_{t=1}^{T}(\boldsymbol{y}_t\boldsymbol{y}_t^{\top}-C^{\text{old}}\hat{\boldsymbol{x}}_t\boldsymbol{y}_t^{\top})\right\}$, as in Eq. 6
5. $\pi_0^{\text{new}}=\hat{\boldsymbol{x}}_0$
6. Update C^{new}, as in Eq. (7)
7. Update A^{new} with FISTA, as in Eq. (8)

Let the estimations from the previous step be denoted as $\theta^{\text{old}}=\{A^{\text{old}},C^{\text{old}},R^{\text{old}},\pi_0^{\text{old}}\}$ and the current estimations as $\theta^{\text{new}}=\{A^{\text{new}},C^{\text{new}},R^{\text{new}},\pi_0^{\text{new}}\}$. The estimation for the R matrix has a closed form, as follows:

$$R^{\text{new}}=\text{diag}\left\{\frac{1}{T}\sum_{t=1}^{T}(\boldsymbol{y}_t\boldsymbol{y}_t^{\top}-C^{\text{new}}\hat{\boldsymbol{x}}_t\boldsymbol{y}_t^{\top})\right\} \tag{6}$$

where diag extracts the diagonal of the in-bracket term, as we constrain R to be diagonal in Constraint 4.

The estimation for $\boldsymbol{\pi}_0$ has a closed form. The relevant term $\log(\mathbb{1}_{\pi_0}(\hat{\boldsymbol{x}}_0))$ is minimized only when $\pi_0^{\text{new}}=\hat{\boldsymbol{x}}_0$.

The estimation for the C matrix also has a closed form. Using a vectorization trick as in [25], one can derive C's closed form solution with the Tikhonov regularization [24]

$$C^{\text{new}}=\text{Solve with Tikhonov regularization} \tag{7}$$

For matrix A, its estimation is similar to that of C, but slightly more complex. The complexity is that A does not have a closed form solution due to the ℓ_1 penalty term. However, it can be solved numerically with a Fast Iterative Shrinkage-Thresholding Algorithm (FISTA) [5]. The FISTA algorithm is detailed in the Appendix.

With FISTA, matrix A updates as follows:

$$A^{\text{new}}=\text{Solve with FISTA} \tag{8}$$

The parameters in the EM algorithm are initialized with the singular value decomposition (SVD). In addition, several matrix computation techniques are utilized to make the algorithm highly efficient and scalable. The details can be found in the Appendix. Combining the initialization, E-step, and M-step, a complete EM algorithm for MR. SID is addressed in Table 1.

4. Simulations

4.1. Simulation setup

Two simulations of different dimensions are performed to demonstrate the parameter estimations, computational efficiency, and predicting ability of MR. SID. In the low dimensional setting, $p=300$, $d=10$, and $T=100$. A is first generated from a random matrix, then elements with small absolute values are truncated to zero to make it sparse. Afterwards, a multiple of the identity matrix is added to A. Finally, A is scaled to make sure its eigenvalues fall within $[-1,1]$, thus avoiding diverging time series. Matrix C is then generated as follows. Each column contains random samples from a standard Gaussian. Then, each column is sorted in ascending order. Covariance Q is the identity matrix and covariance R is a multiple of the identity matrix. Initial state $\pi_0=\mathbf{0}$ is a zero vector. Pseudocode for data generation can be found in the Appendix.

In the high-dimensional setting, $p=10000$, $d=30$, and $T=100$. The parameters are generated in the same manner. To evaluate the accuracy of estimations, we elect to define the distance between two matrices A and B as

$$d_{A,B}=\underset{P\in P(n)}{\operatorname{argmin}}\left\{\log\left[\frac{n}{\text{Trace}(P\times C_{A,B})}\right]\right\} \tag{9}$$

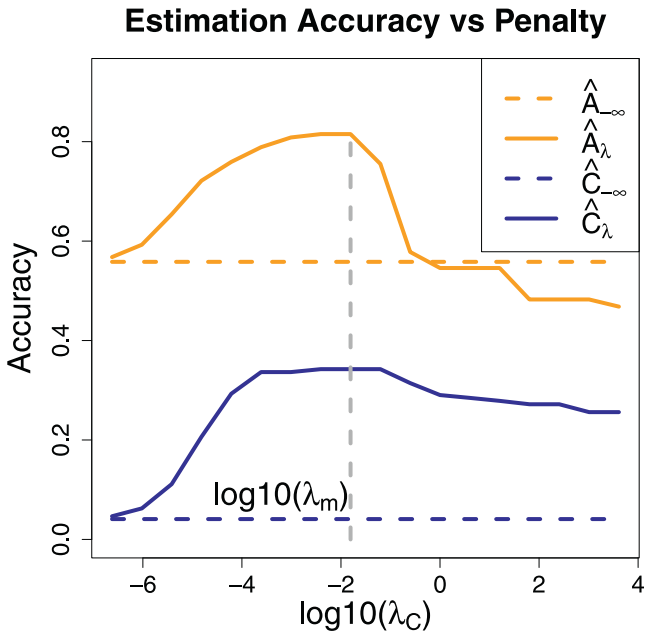

(a) Low dimensional setting

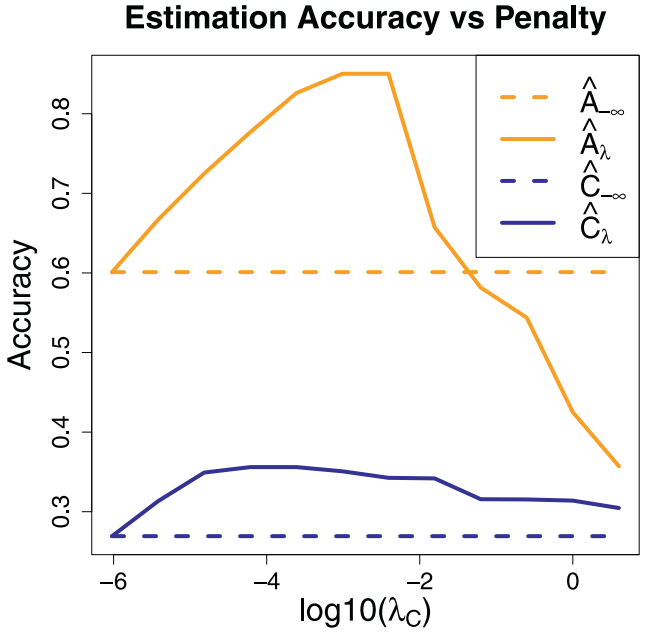

(b) High dimensional setting

Fig. 1. x axis is tuning parameter λ_C under log scale and y axis is the distance between truth and estimations; λ_A is increasing proportionally with λ_C. One can see that in both the low dimensional and hight dimensional setting, estimation accuracies for A and C first increase then decrease as penalty increases.

where $C_{A,B}$ is the correlation matrix between columns of A and B, $P(n)$ is a collection of all the permutation matrices of order n, and P is a permutation matrix.

Both the standard LDS and MR. SID are applied to the simulation data. Estimation accuracies are plotted against penalty sizes in Fig. 1. From the plot, one sees that the prediction accuracy first improves, then drops when the penalties increase. MR. SIDis also used for time series prediction, and the result is plotted in Fig. 2. The prediction accuracy peaks when the penalty coefficients λ_A

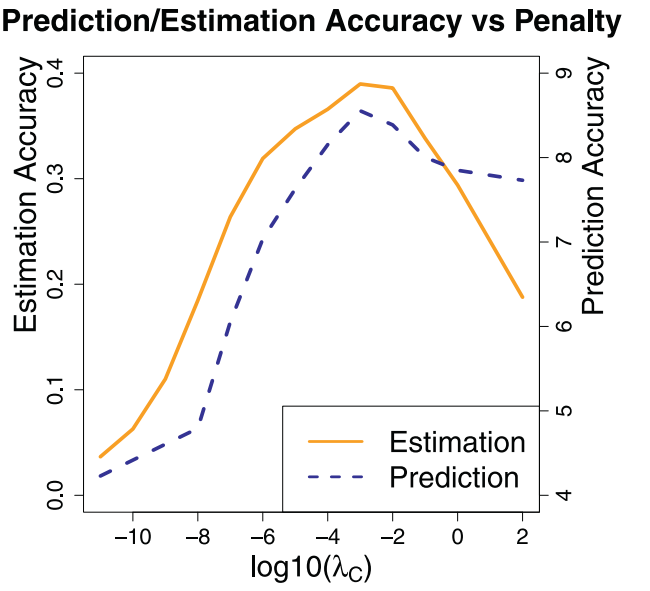

Fig. 2. Estimation and prediction accuracies. The x-axis represents the penalty size on a log scale. The y-axis represents the estimation and prediction accuracies. Note that the penalty which yields the most accurate estimation also gives the best prediction.

and λ_C are around 10^{-3}. This makes sense, as the same (λ_A, λ_C) pair also gives the best estimations of A and C, as seen in Fig. 1. The latter observation provides us a way to pick tuning parameters in real applications: one can use a collection of tuning parameter pairs (λ_A, λ_C) for estimations (with train data) and subsequently for predictions (with test data). The pair that gives the most accurate out-of-sample predictions is picked. This trick is used in Section 5.

5. Application

5.1. Data and motivation

MR. SID is applied to two datasets in this section: the Kirby 21 data and the Human Connectome Project (HCP) data.

The Kirby 21 data were acquired from the FM Kirby Research Center at the Kennedy Krieger Institute, an affiliate of Johns Hopkins University [16]. Twenty-one healthy volunteers with no history of neurological disease each underwent two separate resting state fMRI sessions on the same scanner. The data are preprocessed with FSL, a comprehensive library of analysis tools for fMRI, MRI, and DTI brain imaging data [23]. Specifically, FSL is used for spatial smoothing with a Gaussian kernel. Then MR. SID was applied on the smoothed data. The number of scans was $T = 210$.

The Human Connectome Project (HCP) is a systematic effort to map macroscopic human brain circuits and their relationship to behavior in a large population of healthy adults [9,18,26]. All scans consist of 1200 time points. A comprehensive introduction of the dataset is given by [26].

Extensive research has been done to analyze the above datasets. Methods such as PCA and ICA (Independent Component Analysis) have been applied to obtain spatial decompositions of the brain, as well as the functional connectivity among the decomposed regions. Thus, for our first application, we applied MR. SID to the Kirby 21 data with the intent of obtaining both a spatial decomposition graph and a connectivity graph. As a second application, MR. SID was applied to the HCP data to predict brain activities. For both datasets, the motor cortex, which contains $p = 7396$ voxels, is analyzed instead of the whole brain.

Table 2
Similarities among estimated A matrices.

$d_{A,B}$	A_{11}	A_{12}	A_{21}	A_{22}
A_{11}	0			
A_{12}	**0.076(0.88)**	0		
A_{21}	0.105(1.05)	0.095(1.08)	0	
A_{22}	0.095(1.02)	0.095(1.09)	**0.085(0.98)**	0

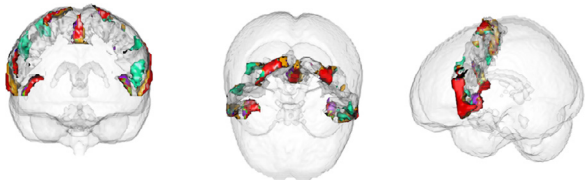

Fig. 3. 3D rendering of columns of matrix C_{11}: estimation for the first scan of subject one.

5.2. Results

MR. SID is first applied to two subjects (four scans) from the Kirby 21 dataset. To pick the optimal penalty size, different values of $\lambda_A = \lambda_C$ were attempted. Their values range from 10^{-10} to 10^4. Then the estimated models with each combination were used to make predictions. We use the value of 10^{-5}, as it gives the most accurate out-of-sample predictions. To determine the number of latent states, d, the profile likelihood method proposed by Zhu et al. [30] is utilized. The method assumes the eigenvalues of the data matrix follow a Gaussian mixture, and uses profile likelihood to pick the optimal number of latent states. Apply the method to all four scans, the numbers of latent states are 11, 6, 14 and 15 respectively. Their average, $d = 11$, is used.

First, let's look at the estimations of A matrix. Let A_{12} stand for the estimated A matrix for the second scan of subject one. Similar logic applies to the A_{11}, A_{21}, A_{22}, and C matrices. These matrices contain subject-specific information. 4 matrices leads to 6 unique pairs. Intuitively, the pair (A_{11}, A_{12}) and (A_{21}, A_{22}) should have the highest similarity, as each comes from two scans of the same subject. This idea is validated by Table 2, which summarize similarities among the 4 matrices. The distance measure in Eq. (9) was used. The Amari error [2], which is another permutation-invariant measure of similarity, is also provided. A smaller $d(A, B)$ or Amari error means higher similarity.

Next, let's look at the C matrices. 3D renderings of the columns of C_{11} are shown in Fig. 3. The 3D regions in the plot are comparable to existing parcellations of the motor cortex. As an example, the blue region in Fig. 3 accurately matches the dorsomedial (DM) parcel of the five-region parcellation proposed by Nebel MB et al. [19].

Matrix A and C have natural interpretation here. Each $\boldsymbol{y}_t$ is a snapshot of brain activity at time t. The columns of C are interpreted as time-invariant brain "point spread functions". At each time point, the observed brain image, $\boldsymbol{y}_t$, is a linear mixture of latent co-assemblies of neural activity $\boldsymbol{x}_t$. Matrix A describes how $\boldsymbol{x}_t$ evolves over time. A is a directed graph if one treats each neural assembly as a vertex. Each neural assembly is spatially smooth, and connectivity across them is empirically sparse. This naturally fits into the sparsity and smoothness assumptions of MR. SID.

To summarize, MR. SID gives a spatial decomposition of the motor cortex, as well as the sparse connectivity among the decomposed regions. The connectivity graph contains subject-specific information and can correctly group scans by subject. The decomposed regions are spatially smooth and are comparable to existing parcellations of the motor cortex.

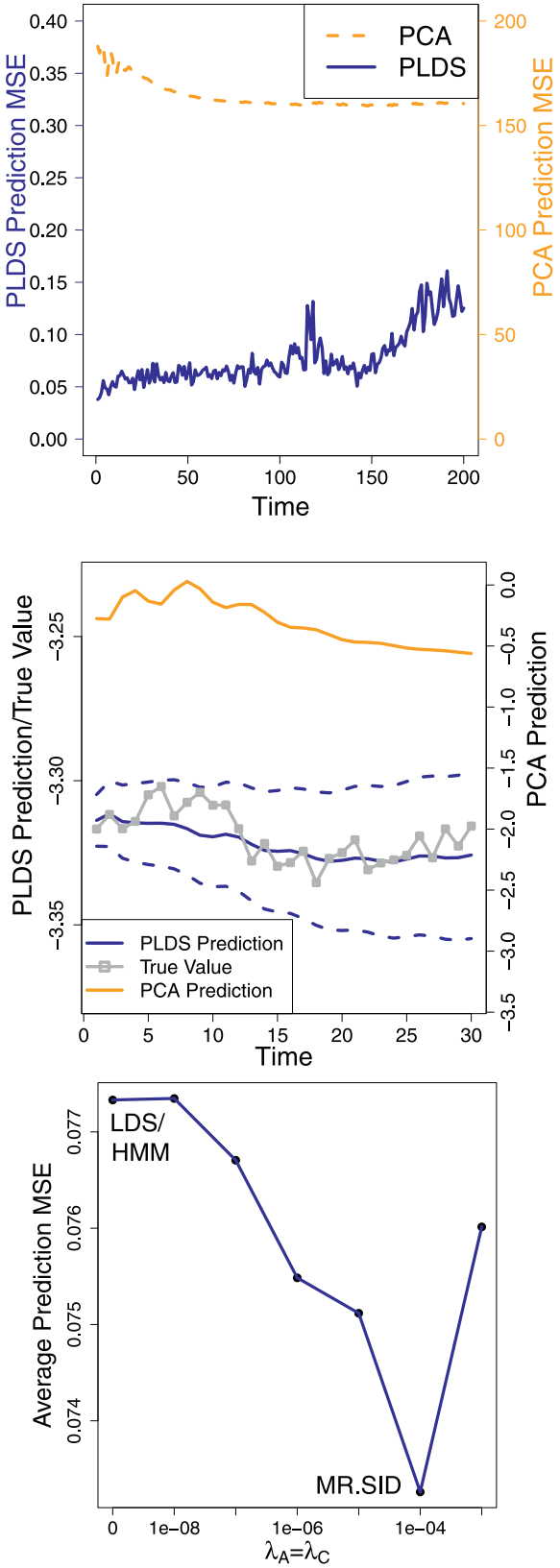

Fig. 4. Predictions on HCP data: *(1)* MR. SID and SVD predictions over time, with accuracies measured as mean squared error (MSE). *(2)* Sample time series plot. True signals and predictions are both averaged over a sample of 20 voxels. The dotted blue lines represents the 60% prediction interval of MR. SID. Values were log-scaled for plotting. *(3)* Prediction accuracies of LDS/HMM and MR. SID.

As a second application, MR. SID is applied to the HCP data. The goal is to predict future brain signals using historical data. HCP data has $T = 1200$ time points. The first $N = 1000$ (about 80%) were used as training data, while the rest were used for out-of-sample test. For comparison purposes, the PCA/SVD method (to initialize MR. SID) and the LDS/HMM model are also fitted. Parameter estimations are first performed for all three methods, then the estimated parameters were fed into Eq. (2) to make k-step predictions into the future. Pseudocode for k-step ahead predictions is given in the Appendix.

The prediction accuracies are shown in Fig. 4. From the top panel, one can see that MR. SID has significantly higher prediction accuracies than SVD for the first 150 steps. Considering that SVD is used to initialize MR. SID, this observation demonstrates that MR. SID makes real improvement on top of SVD. The middle panel is a sample plot of the true time series and predictions. MR. SID gives more accurate predictions and its prediction interval covers the true signal. Note that the interval gets wider for longer term predictions, as the errors from each step accumulate. The bottom panel compares MR. SID models of different penalties: when there is no penalty, MR. SID gives identical result as LDS/HMM; with the optimal penalty picked with training data, it gives more accurate predictions than LDS.

6. Discussion

We have taken a first step towards the modeling and estimation of high-dimensional time-series data. The proposed method balances both statistical and computational considerations. Indeed, much like the Kalman Filter-Smoother for modeling time-series data, and the Baum-Welch algorithm for system identification act as "primitives" for time-series data analysis, MR. SID can act as a primitive for similar time-series analysis when the dimensionality is significantly larger than the number of time steps. Via simulations we demonstrated the efficacy of our methods. Then, by applying the proposed approach to fMRI scans of the motor cortex of healthy adults, we identified limited sub-regions (networks) from the motor cortex.

In the future, this work could be extended in two important directions. First, the assumption of conditionally independent observations given latent states remains a challenge. The covariance structures in the observation equation, R, should be generalized and prior knowledge could be incorporated into it [1]. The idea is that R should be general enough to be flexible, but sufficiently restricted to make the model useful. Many other methods, e.g. those that use tridiagonal and upper triangular matrices, could also be considered. Mohammad et al. have discussed the impact of autocorrelation on functional connectivity, which also provides some direction for extension [3]. In addition, the work can also be extended on the application side. Currently, only data from a few subjects have been analyzed. As a next step, the model can generalize to a group version and be used to analyze more subjects. The A matrix estimated by MR. SID could potentially be used as a measure of fMRI scan reproducibility.

Acknowledgments

This work is graciously supported by the Defense Advanced Research Projects Agency (DARPA) SIMPLEX program through SPAWAR contract N66001-15-C-4041 and DARPA GRAPHS N66001-14-1-4028.

Supplementary material

Supplementary material associated with this article can be found, in the online version, at 10.1016/j.patrec.2016.12.012.

References

[1] G.I. Allen, L. Grosenick, J. Taylor, A generalized least-square matrix decomposition, J. Am. Stat. Assoc. 109 (505) (2014) 145–159.
[2] S.-i. Amari, A. Cichocki, H.H. Yang, et al., A new learning algorithm for blind signal separation, Adv. Neural Inf. Process Syst. (1996) 757–763.
[3] M.R. Arbabshirani, E. Damaraju, R. Phlypo, S. Plis, E. Allen, S. Ma, D. Mathalon, A. Preda, J.G. Vaidya, T. Adali, et al., Impact of autocorrelation on functional connectivity, NeuroImage (2014).
[4] A. Banerjee, J.T. Vogelstein, D.B. Dunson, Parallel inversion of huge covariance matrices, arXiv preprint (2013).
[5] A. Beck, M. Teboulle, A fast iterative shrinkage-thresholding algorithm for linear inverse problems, SIAM J. Imaging Sci. 2 (1) (2009) 183–202.
[6] B. Boots, Learning stable linear dynamical systems, Ph.D. thesis. MS Thesis in Machine Learning, Carnegie Mellon University, 2009.
[7] S. CHEN, S.A. BILLINGS, W. LUO, Orthogonal least squares methods and their application to non-linear system identification, Int. J. Control 50 (5) (1989) 1873–1896, doi:10.1080/00207178908953472.
[8] G. Doretto, A. Chiuso, Y.N. Wu, S. Soatto, Dynamic textures, Int. J. Comput. Vis. 51 (2) (2003) 91–109.
[9] D.A. Feinberg, S. Moeller, S.M. Smith, E. Auerbach, S. Ramanna, M. Gunther, M.F. Glasser, K.L. Miller, K. Ugurbil, E. Yacoub, Multiplexed echo planar imaging for sub-second whole brain fmri and fast diffusion imaging, PloS one 5 (12) (2010) e15710.
[10] K. Friston, L. Harrison, W. Penny, Dynamic causal modelling, NeuroImage 19 (4) (2003) 1273–1302, doi:10.1016/S1053-8119(03)00202-7.
[11] Z. Ghahramani, G.E. Hinton, Parameter estimation for linear dynamical systems, Technical Report, Technical Report CRG-TR-96-2, University of Totronto, Dept. of Computer Science, 1996.
[12] C.-J. Hsieh, M.A. Sustik, I.S. Dhillon, P.K. Ravikumar, R. Poldrack, BIG & QUIC: Sparse Inverse Covariance Estimation for a Million Variables, in: Advances in Neural Information Processing Systems, 2013, pp. 3165–3173.
[13] S.r. Johansen, Statistical analysis of cointegration vectors, J. Econ. Dyn. Control 12 (2–3) (1988) 231–254, doi:10.1016/0165-1889(88)90041-3.
[14] R.E. Kalman, A new approach to linear filtering and prediction problems, J. Basic Eng. 82 (1) (1960) 35, doi:10.1115/1.3662552.
[15] R.E. Kalman, Mathematical description of linear dynamical systems, J. Soc. Ind. Appl. Math. Series A Control 1 (2) (1963) 152–192, doi:10.1137/0301010.
[16] B.A. Landman, A.J. Huang, A. Gifford, D.S. Vikram, I.A.L. Lim, J.A. Farrell, J.A. Bogovic, J. Hua, M. Chen, S. Jarso, et al., Multi-parametric neuroimaging reproducibility: a 3-t resource study, Neuroimage 54 (4) (2011) 2854–2866.
[17] L. Ljung, System Identification, in: A. Procházka, J. Uhlí?, P.W.J. Rayner, N.G. Kingsbury (Eds.), Signal Analysis and Prediction, Applied and Numerical Harmonic Analysis, Birkhäuser Boston, Boston, MA, 1998, doi:10.1007/978-1-4612-1768-8.
[18] S. Moeller, E. Yacoub, C.A. Olman, E. Auerbach, J. Strupp, N. Harel, K. Uğurbil, Multiband multislice ge-epi at 7 tesla, with 16-fold acceleration using partial parallel imaging with application to high spatial and temporal whole-brain fmri, Magn. Reson. Med. 63 (5) (2010) 1144–1153.
[19] M.B. Nebel, S.E. Joel, J. Muschelli, A.D. Barber, B.S. Caffo, J.J. Pekar, S.H. Mostofsky, Disruption of functional organization within the primary motor cortex in children with autism, Hum. Brain Mapp. 35 (2) (2014) 567–580.
[20] L.R. Rabiner, A tutorial on hidden markov models and selected applications in speech recognition, Proc. IEEE 77 (2) (1989) 257–286.
[21] S. Roweis, Z. Ghahramani, A unifying review of linear gaussian models, Neural Comput. 11 (2) (1999) 305–345.
[22] R.H. Shumway, D.S. Stoffer, An approach to time series smoothing and forecasting using the em algorithm, J. Time Series Anal. 3 (4) (1982) 253–264.
[23] S.M. Smith, M. Jenkinson, M.W. Woolrich, C.F. Beckmann, T.E. Behrens, H. Johansen-Berg, P.R. Bannister, M. De Luca, I. Drobnjak, D.E. Flitney, et al., Advances in functional and structural mr image analysis and implementation as fsl, Neuroimage 23 (2004) S208–S219.
[24] A.N. Tikhonov, On the stability of inverse problems, in: Dokl. Akad. Nauk SSSR, 39, 1943, pp. 195–198.
[25] B.A. Turlach, W.N. Venables, S.J. Wright, Simultaneous variable selection, Technometrics 47 (3) (2005) 349–363.
[26] D.C. Van Essen, S.M. Smith, D.M. Barch, T.E. Behrens, E. Yacoub, K. Ugurbil, W.-M.H. Consortium, et al., The wu-minn human connectome project: an overview, Neuroimage 80 (2013) 62–79.
[27] P. Van Overschee, B. De Moor, N4sid: Subspace algorithms for the identification of combined deterministic-stochastic systems, Automatica 30 (1) (1994) 75–93.
[28] Y. Xie, J. Huang, R. Willett, Change-point detection for high-dimensional time series with missing data, IEEE J. Sel. Top Signal Process 7 (1) (2013) 12–27, doi:10.1109/JSTSP.2012.2234082.
[29] M. Zaharia, M. Chowdhury, M.J. Franklin, S. Shenker, I. Stoica, Spark: cluster computing with working sets, in: Proceedings of the 2nd USENIX conference on Hot topics in cloud computing, 10, 2010, p. 10.
[30] M. Zhu, A. Ghodsi, Automatic dimensionality selection from the scree plot via the use of profile likelihood, Comput. Stat. Data Anal. 51 (2) (2006) 918–930.

ChemComm

COMMUNICATION

View Article Online
View Journal | View Issue

Cite this: *Chem. Commun.*, 2017, 53, 12438

Received 25th September 2017,
Accepted 27th October 2017

DOI: 10.1039/c7cc07465d

rsc.li/chemcomm

Chemical antagonism between photodynamic agents and chemotherapeutics: mechanism and avoidance†

Qingshuo Meng,‡[ab] Jia Meng,‡[ab] Wei Ran,[ab] Jinghan Su,[ab] Yuguang Yang,[c] Pengcheng Zhang *[ab] and Yaping Li *[ab]

We report a photochemical reaction-induced antagonism between the photodynamic agent (PS) and anti-cancer drugs during combined therapy. The annihilation of singlet oxygen and alkene-containing drugs into inactive drug hydroperoxides is responsible for the antagonism, and results in decreased efficacy against several cancer cell lines. Experimental and simulation results reveal that the annihilation abates with increasing distance between the PS and drugs *via* confining the PS and drugs into separated vehicles. As a result, antagonism can be switched to synergism in treating both drug sensitive and resistant cancer cells.

Photosensitizers (PSs) have shown great potential in photocatalysis and cancer therapy due to their capability to conduct light-powered chemical reactions.[1–4] Given their controllable and potent activity, PS-based nanoparticles have served as both drugs and carriers, which include titanium dioxide,[5] plasmonic vesicles,[6,7] upconversion nanoparticles,[8] gold nanorods,[9] PS-conjugated antibodies,[10] porphysomes,[11,12] and PS-loaded liposomes.[13,14] However, the treatment effect induced by PSs is transient and is also limited by the depth of tissue penetration of the laser, which hampers the application of PS-based therapy.[15] Many efforts have been devoted to developing PSs with absorbance in the second near-infrared window, as lasers in this range show high tissue penetration.[16] An alternative and effective strategy to address this issue is combination therapy, exemplified by nanoparticles with both chemotherapy and photodynamic therapy (PDT) activities.[13,17–27] These nanoparticles are effective for cancer therapy because localized singlet oxygen ($^1O_2$) or reactive oxygen species (ROS) produced by the PS can facilitate extravasation and tissue penetration of chemotherapeutics *via* triggering the apoptosis of both cancerous and endothelial cells.[28–30] Also, the short-lived $^1O_2$ or ROS can control the release of chemotherapeutics enveloped by carriers and subcellular vesicles to realize long-term inhibition of tumor growth and metastasis.[13,17–22] However, the same strategy would also generate, in nanoparticles, a high local concentration of $^1O_2$/ROS that are reactive to drugs in the same carrier. The interaction between the PS and drugs during the treatments is largely unclear, in contrast to tremendous efforts and successes in the development of such nanoparticles for combination therapy. So far, only a few studies have reported pharmacologic or pharmacokinetic antagonism between PDT and chemotherapy.[31,32] It is crucial to understand the photochemistry behind the interactions between PS generated $^1O_2$ and drugs before clinical translation of these nanomedicines.[33]

In this communication, we report a chemical antagonism between the PS chlorin e6 trimethyl ester (Ce6tM) and chemotherapeutics (Fig. 1a). Drugs of different structures, including curcumin (polyphenol), docetaxel (taxane), mertansine (maytansinoid), vinorelbine (vinca alkaloids), and rapamycin (macrolide) were used as model drugs (Fig. 1b), among which the latter four are being used or tested in the clinic for cancer therapy. Regardless of their different structures, they were all deposited together with Ce6tM in the lipid bilayers (~5 nm in thickness) of vesicles (60–70 nm in diameter) formed by dipalmitoyl-*sn*-glycero-3-phosphocholine (DPPC) (dual-drug loaded liposomes, DL-X), revealed by cryogenic transmission electron microscopy (cryo-TEM) and confocal laser scanning microscopy (CLSM) (Fig. S1 and S2, ESI†). The hydrodynamic size of the vesicles (~80 nm) determined by dynamic light scattering (DLS) was consistent with that determined by cryo-TEM (Table S1, ESI†). Quantitative encapsulation of Ce6tM and drugs also suggested preferential drug accumulation in the hydrophobic membrane of the vesicles (Tables S2 and S3, ESI†). Mono-drug loaded liposomes (ML-X) containing either Ce6tM or drug were prepared, and were similar to DL-X in morphology and size (Fig. S3 and Tables S1–S3, ESI†). These results revealed that Ce6tM and drugs were concentrated in the membrane of the vesicles.

The close deposition of Ce6tM and drugs in the lipid bilayer of the vesicles would enable possible chemical reactions. We,

[a] *State Key Laboratory of Drug Research & Center of Pharmaceutics, Shanghai Institute of Materia Medica, Chinese Academy of Sciences, 501 Haike Road, Shanghai 201203, China. E-mail: pzhang@simm.ac.cn, ypli@simm.ac.cn*
[b] *University of Chinese Academy of Sciences, 19 Yuquan Road, Beijing 100049, China*
[c] *Department of Chemical and Biomolecular Engineering, Johns Hopkins University, 3400 North Charles Street, MD 21218, USA*

† Electronic supplementary information (ESI) available. See DOI: 10.1039/c7cc07465d
‡ These authors contributed equally to this work.

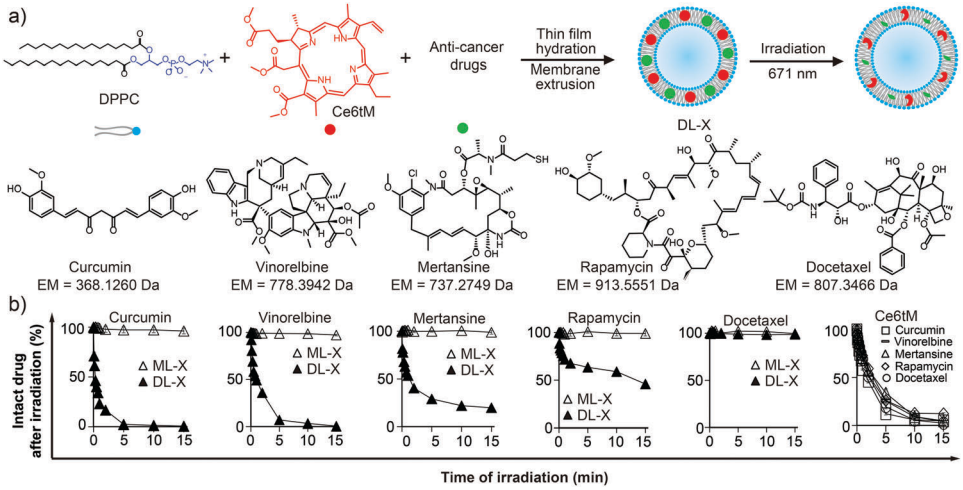

Fig. 1 Preparation and irradiation-induced drug decomposition of DL-X. (a) Schematic illustration of the preparation and irradiation-induced drug decomposition in DL-X. The chemical structures and their exact mass (EM) were listed. (b) Time-dependent degradation of anti-cancer drugs and Ce6tM in different vesicles under laser irradiation (671 nm, 2 W cm^{-2}). The initial concentrations of Ce6tM and anti-cancer drugs were 235 and 118 μM, respectively.

therefore, irradiated the liposomes with a 671 nm laser and monitored their changes using multiple techniques. We first observed a dramatic change (colored to colorless) in the color of DL-X (Fig. S4, ESI†). The qualitative observation suggested that both the drugs and PS degraded during irradiation (Fig. 1a), which urged us to perform a quantitative study. Fig. 1b shows the degradation profiles of anti-cancer drugs in DL-X and ML-X under laser irradiation using high-performance liquid chromatography (HPLC). The rates of drug decomposition varied for different DL-X, with 76%, 51%, 46%, 22%, 0.3% and ~30–40% of curcumin, vinorelbine, mertansine, rapamycin, docetaxel, and Ce6tM decomposed within 1 min, respectively. Drug decomposition accelerated when the amount of Ce6tM relative to drug increased (Table S4, ESI†) or when higher irradiation power was applied to the solutions (Fig. S5, ESI†). These results demonstrated the existence of chemical antagonism between PDT and chemotherapy. Though fast and dramatic drug and Ce6tM decomposition was recorded, cryo-TEM imaging and DLS analysis revealed no obvious change in the morphology, size, size distribution, surface charge and bilayer structure of DL-X before and after irradiation, or when compared with ML-X (Fig. S6, S7 and Table S1, ESI†).

We then explored the mechanism that led to the chemical antagonism. It turned out that $^1O_2$ was the dominant if not the only factor driving the process, as significant and fast $^1O_2$ production was detected using an SOSG-based method (SOSG is a $^1O_2$ activatable fluorescent probe) in DL-SOSG but not ML-SOSG (Fig. 2a). Synchronized $^1O_2$ production and drug decomposition was always observed under conditions of varying Ce6tM-to-drug ratios and irradiation powers (Fig. S5, S8, S9 and Table S4, ESI†). When $^1O_2$ was quenched by 30 mM sodium azide (NaN_3, a scavenger of $^1O_2$[34]) (Fig. S10, ESI†), degradation of the drugs in DL-X was also prohibited (Fig. 2b). All these results confirmed the pivotal role of $^1O_2$ in the observed chemical antagonism.

It has been reported that $^1O_2$ can react with biomacromolecules and alkene-containing chemicals to generate hydroperoxides whose

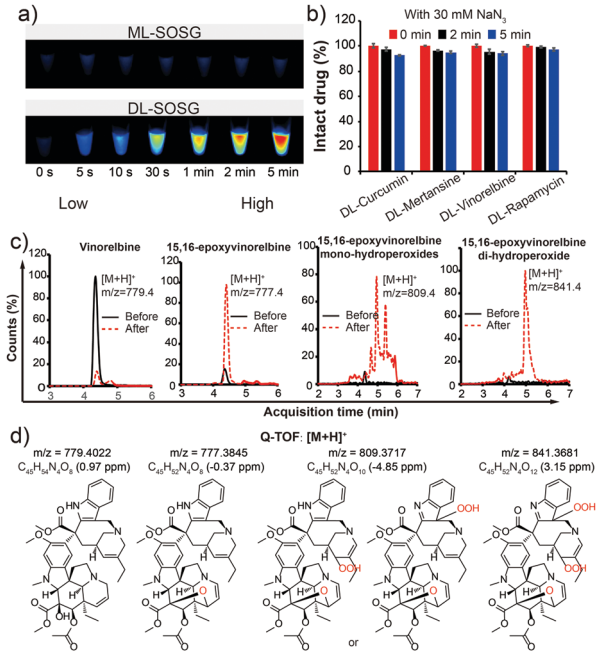

Fig. 2 The mechanism of photo-induced drug decomposition. (a) Fluorescence images of irradiated ML-SOSG and DL-SOSG solutions (Epi illumination: 455–485 nm, emission filter: 530/28 nm). (b) Anti-cancer drugs remained intact in co-delivery liposomes in the presence of 30 mM NaN_3. (c) LC-MS spectrum of DL-vinorelbin before and after irradiation. (d) The exact mass of generated species and the most plausible formulas (mass accuracy) and structures.

exact masses are ~32*n* Da (*n* = 1, 2, 3, *etc.*) larger than those of the parental molecules.[35,36] We, therefore, monitored the mass change using liquid chromatography–mass spectrometry (LC-MS). In irradiated DL-vinorelbine, we observed a dramatic conversion of vinorelbine to species whose exact masses were 2.0 Da less or 30.0 and 62.0 Da larger than that of vinorelbine (Fig. 2c). Further quad-time-of-flight (Q-TOF) LC-MS-MS analysis revealed that the 2.0177 Da mass loss was due to the deprivation of 2 hydrogen atoms associated with the formation of 15,16-epoxyvinorelbine

(a major metabolite of vinorelbine[37]) (Fig. 2d). The 31.9872 and 63.9846 Da mass increase from that of 15,16-epoxyvinorelbine suggested the addition of 2 and 4 oxygen atoms (Fig. 2d). There were two possible mono-hydroperoxide isomers of different retention times in the LC-MS spectrum. However, we were unable to assign the peaks to the corresponding isomers, as each captured fragment could not be exclusively associated with one reaction site (Fig. S11, ESI†). Similar studies were performed on other DL-X, and the results strongly indicated that curcumin, mertansine-Pyr (use instead of mertansine, EM = 846.2735 Da) and rapamycin were all converted into the corresponding hydroperoxides (Fig. S12–S14, ESI†), while no drug conversion was observed in DL-docetaxel (Fig. S15, ESI†). To investigate the exact structures of the hydroperoxides, techniques such as nuclear magnetic resonance (NMR) will be required. Unfortunately, due to their reactivity, the purification of hydroperoxides would be challenging, and it might be necessary to develop suitable online NMR reaction monitoring technologies.[38]

The $^1O_2$, while decomposing drugs, was simultaneously quenched by them. We compared the release of $^1O_2$ from DL-X relative to ML-Ce6tM, using SOSG-based fluorometry. We found that DL-X released significantly less $^1O_2$ than ML-Ce6tM ($p < 0.0005$), and the more susceptible a co-encapsulated drug to $^1O_2$, the less $^1O_2$ released from the corresponding DL-X (Fig. S16, ESI†). Since $^1O_2$ was the executor of PDT, the result here suggested that co-delivered chemotherapeutics could also antagonize the efficacy of PDT.

Given the great potential of combined PDT and chemotherapy in cancer management,[13,39] it is necessary to develop a strategy that allows simultaneous use of the two modalities with minimized annihilation. One possible strategy is placing drugs some distance (l) away from the PS (Fig. 3a) so that short-lived $^1O_2$ (lifespan = 3.5 ms[40]) could destroy cancer cells before annihilating with drugs. To test our hypothesis, the rates of drug decomposition in DL-X and physical mixtures of ML-X and ML-Ce6tM were compared. Reduced drug degradation was observed when l = 488 nm (0.6 mg mL^{-1} in DPPC) (Fig. 3b) but not when l = 157 nm (18 mg mL^{-1} in DPPC) (Fig. S17, ESI†). Meanwhile, no such big difference was observed for DL-X under the same concentrations. To understand the observed phenomenon, we estimated the mean first collision time (MFCT) of liposomes under Brownian motion (the detailed method is provided in the ESI†). The collision was defined when $l < 90$ nm (the nearest distance between Ce6tM and anti-cancer drug molecules would be shorter than 20 nm[40]). The MFCTs of liposomes under the two conditions were 473 ± 74 and 12.5 ± 1.7 μs (15626 liposomes each experiment, average from 200 experiments for each condition), respectively, indicating a more frequent collision of liposomes in concentrated solution. We simulated the random walks of 216 liposomes (2 types mixed at a 1 : 1 ratio) under the two conditions (Movies S1 and S2, ESI†), and ~50-fold faster collision of liposomes was recorded in concentrated solution (Fig. 3c). These results proved that using a physical mixture instead of DL-X could be a feasible and effective strategy to mitigate the antagonism between PS and drugs.

We finally evaluated the *in vitro* activity of vinorelbine-loaded liposomes against human A549 non-small cell lung cancer cells, B16-F10 melanoma cancer cells, HT29 colon cancer cells, and MCF-7 breast cancer cells, after confirming that only marginal drug release

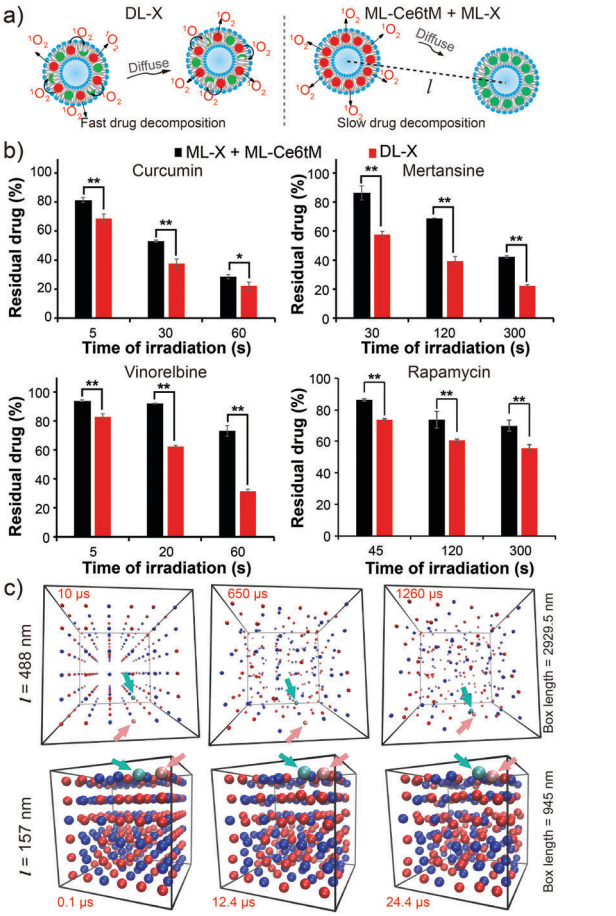

Fig. 3 Effect of distance between the PS and drugs on chemical antagonism. (a) Schematical illustration of the effect of distance between the PS and drugs on drug decomposition. (b) The comparison of drug decomposition rates in DL-X and a corresponding mixture of ML-X and ML-Ce6tM. (c) Snapshots of 216 liposomes (red: ML-Ce6tM; blue: ML-X) before 2 of them (light red and light blue ones, indicated by arrows) collided. The data were represented as mean ± s.d. (n = 3). *$p < 0.05$, **$p < 0.005$.

within 8 h of incubation (Table S5, ESI†). We first investigated the effect of hydroperoxide formation on vinorelbine activity and found that the two were negatively correlated (Table S6, ESI†), indicating that hydroperoxides of vinorelbine are not active. Similar results were observed from the formulations of the remaining three drugs on the 4 cell lines (Tables S7–S9, ESI†). We further evaluated the synergistic effect of combined therapies on A549 and MCF-7, as well as their drug resistant strains (A549T and MCF-7/ADR, about 20- and 7-fold more resistant to vinorelbine than the parental cell lines, respectively, Table S10, ESI†). Hydroperoxides of vinorelbine were much less active and unable to kill >50% of the resistant cells under 30 μg mL^{-1} (Table S10, ESI†). After confirming the resistance, the cells were irradiated after a 4 h incubation period. On drug resistant cell lines, the IC50 of DL-vinorelbine was ~1.5-fold that of ML-Ce6tM (Fig. 4). In sharp contrast, the physical mixture (ML-vinorelbine + ML-Ce6tM) was ~5-fold more effective than ML-Ce6tM, while ML-vinorelbine alone was ineffective under the same conditions (Fig. 4). A similar trend was observed on drug sensitive A549 and MCF-7 cells (Fig. S18, ESI†). These results proved the existence of antagonism between closely deposited PS and drugs. The antagonism effect is

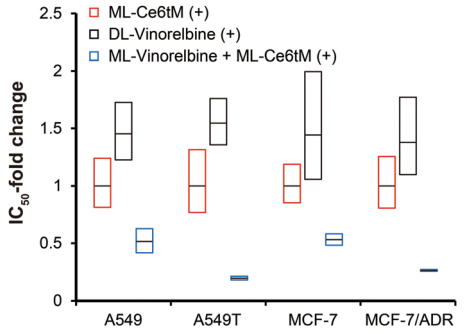

Fig. 4 Change in the IC_{50} of vinorelbine-containing formulations relative to ML-Ce6tM. Boxes show 95% confidence ranges with the median in black.

rooted in the chemical susceptibility of drugs and the consequent annihilation of $^1O_2$ and alkene-containing drugs (Fig. 3a and Fig. S16, ESI†). The rate of annihilation will drop dramatically in the presence of steric hindrance near the alkene group,[41] which may cause the ultra-slow degradation of docetaxel (Fig. 1). These results also demonstrated that a profound synergistic effect could be achieved using a physical mixture strategy, probably due to an enhanced cytosol delivery of chemotherapeutics during PDT.[13,14,17–24,30,42] Since the combined use of PDT and other treatments is among the fastest growing fields of nano-medicine,[43] we believe that the knowledge acquired herein would facilitate the rational design and development of new and powerful combined nano-therapeutics.

In conclusion, we have reported the chemical antagonism between Ce6tM and drugs, which could be generalize to any generator of $^1O_2$ and therapeutics (small molecules, proteins/peptides, and nucleotides[35,36,44]) containing susceptible moieties such as phenol, indole, or alkene groups. More importantly, we have shown that the chemical antagonism could be addressed by encapsulating the two modalities into separated liposomes. The findings here highlight that chemical compatibility of combined drugs, in addition to compatibilities in their mechanism of action and pharmacokinetic properties, should be taken into consideration when designing new combined therapies.

This work was financially supported by the National Natural Science Foundation of China (81521005, 81270047, and 81671808) and the Youth Innovation Promotion Association of CAS (2017335). We are grateful to the National Centre for Protein Science Shanghai (Electron Microscopy system) for their instrument support and technical assistance.

Conflicts of interest

There are no conflicts to declare.

Notes and references

1 W. J. Youngblood, S. H. Lee, K. Maeda and T. E. Mallouk, *Acc. Chem. Res.*, 2009, **42**, 1966–1973.
2 P. Wu, C. He, J. Wang, X. Peng, X. Li, Y. An and C. Duan, *J. Am. Chem. Soc.*, 2012, **134**, 14991–14999.
3 M. Ethirajan, Y. Chen, P. Joshi and R. K. Pandey, *Chem. Soc. Rev.*, 2011, **40**, 340–362.
4 J. F. Lovell, T. W. Liu, J. Chen and G. Zheng, *Chem. Rev.*, 2010, **110**, 2839–2857.
5 N. Kotagiri, G. P. Sudlow, W. J. Akers and S. Achilefu, *Nat. Nanotechnol.*, 2015, **10**, 370–379.
6 J. Song, P. Huang, H. Duan and X. Chen, *Acc. Chem. Res.*, 2015, **48**, 2506–2515.
7 J. Lin, S. Wang, P. Huang, Z. Wang, S. Chen, G. Niu, W. Li, J. He, D. Cui, G. Lu, X. Chen and Z. Nie, *ACS Nano*, 2013, **7**, 5320–5329.
8 N. M. Idris, M. K. Gnanasammandhan, J. Zhang, P. C. Ho, R. Mahendran and Y. Zhang, *Nat. Med.*, 2012, **18**, 1580–1585.
9 J. Conde, N. Oliva, Y. Zhang and N. Artzi, *Nat. Mater.*, 2016, **15**, 1128–1138.
10 M. Mitsunaga, M. Ogawa, N. Kosaka, L. T. Rosenblum, P. L. Choyke and H. Kobayashi, *Nat. Med.*, 2011, **17**, 1685–1691.
11 J. F. Lovell, C. S. Jin, E. Huynh, H. Jin, C. Kim, J. L. Rubinstein, W. C. Chan, W. Cao, L. V. Wang and G. Zheng, *Nat. Mater.*, 2011, **10**, 324–332.
12 E. Huynh, B. Y. Leung, B. L. Helfield, M. Shakiba, J. A. Gandier, C. S. Jin, E. R. Master, B. C. Wilson, D. E. Goertz and G. Zheng, *Nat. Nanotechnol.*, 2015, **10**, 325–332.
13 B. Q. Spring, R. Bryan Sears, L. Z. Zheng, Z. Mai, R. Watanabe, M. E. Sherwood, D. A. Schoenfeld, B. W. Pogue, S. P. Pereira, E. Villa and T. Hasan, *Nat. Nanotechnol.*, 2016, **11**, 378–387.
14 A. Y. Rwei, J. J. Lee, C. Zhan, Q. Liu, M. T. Ok, S. A. Shankarappa, R. Langer and D. S. Kohane, *Proc. Natl. Acad. Sci. U. S. A.*, 2015, **112**, 15719–15724.
15 P. Zhang, C. Hu, W. Ran, J. Meng, Q. Yin and Y. Li, *Theranostics*, 2016, **6**, 948–968.
16 G. Hong, A. L. Antaris and H. Dai, *Nat. Biomed. Eng.*, 2017, **1**, 0010.
17 C. He, D. Liu and W. Lin, *ACS Nano*, 2015, **9**, 991–1003.
18 C. He, X. Duan, N. Guo, C. Chan, C. Poon, R. R. Weichselbaum and W. Lin, *Nat. Commun.*, 2016, **7**, 12499.
19 D. Luo, N. Li, K. A. Carter, C. Lin, J. Geng, S. Shao, W. C. Huang, Y. Qin, G. E. Atilla-Gokcumen and J. F. Lovell, *Small*, 2016, **12**, 3039–3047.
20 D. Luo, K. A. Carter, A. Razi, J. Geng, S. Shao, D. Giraldo, U. Sunar, J. Ortega and J. F. Lovell, *Biomaterials*, 2016, **75**, 193–202.
21 Y. Yuan, J. Liu and B. Liu, *Angew. Chem., Int. Ed.*, 2014, **53**, 7163–7168.
22 T. T. Wang, D. G. Wang, H. J. Yu, M. W. Wang, J. P. Liu, B. Feng, F. Y. Zhou, Q. Yin, Z. W. Zhang, Y. Z. Huang and Y. P. Li, *ACS Nano*, 2016, **10**, 3496–3508.
23 C. Wang, X. Sun, L. Cheng, S. Yin, G. Yang, Y. Li and Z. Liu, *Adv. Mater.*, 2014, **26**, 4794–4802.
24 Q. Chen, X. Wang, C. Wang, L. Z. Feng, Y. G. Li and Z. Liu, *ACS Nano*, 2015, **9**, 5223–5233.
25 L. Feng, L. Cheng, Z. Dong, D. Tao, T. E. Barnhart, W. Cai, M. Chen and Z. Liu, *ACS Nano*, 2017, **11**, 927–937.
26 Y. Wang, Y. Xie, J. Li, Z. H. Peng, Y. Sheinin, J. Zhou and D. Oupicky, *ACS Nano*, 2017, **11**, 2227–2238.
27 Y. Li, Y. Deng, X. Tian, H. Ke, M. Guo, A. Zhu, T. Yang, Z. Guo, Z. Ge, X. Yang and H. Chen, *ACS Nano*, 2015, **9**, 9626–9637.
28 I. Rizvi, J. P. Celli, C. L. Evans, A. O. Abu-Yousif, A. Muzikansky, B. W. Pogue, D. Finkelstein and T. Hasan, *Cancer Res.*, 2010, **70**, 9319–9328.
29 B. W. Henderson and T. J. Dougherty, *Photochem. Photobiol.*, 1992, **55**, 145–157.
30 D. Luo, K. A. Carter, A. Razi, J. Geng, S. Shao, C. Lin, J. Ortega and J. F. Lovell, *J. Controlled Release*, 2015, **220**, 484–494.
31 E. Crescenzi, A. Chiaviello, G. Canti, E. Reddi, B. M. Veneziani and G. Palumbo, *Mol. Cancer Ther.*, 2006, **5**, 776–785.
32 M. F. Zuluaga and N. Lange, *Curr. Med. Chem.*, 2008, **15**, 1655–1673.
33 K. Glusac, *Nat. Chem.*, 2016, **8**, 734–735.
34 T. Maisch, J. Baier, B. Franz, M. Maier, M. Landthaler, R. M. Szeimies and W. Baumler, *Proc. Natl. Acad. Sci. U. S. A.*, 2007, **104**, 7223–7228.
35 M. J. Davies, *Biochem. Biophys. Res. Commun.*, 2003, **305**, 761–770.
36 M. Prein and W. Adam, *Angew. Chem., Int. Ed. Engl.*, 1996, **35**, 477–494.
37 K. Yamaguchi, T. Yasuzawa, T. Sakai and S. Kobayashi, *Xenobiotica*, 1998, **28**, 281–291.
38 D. A. Foley, E. Bez, A. Codina, K. L. Colson, M. Fey, R. Krull, D. Piroli, M. T. Zell and B. L. Marquez, *Anal. Chem.*, 2014, **86**, 12008–12013.
39 S. W. Morton, M. J. Lee, Z. J. Deng, E. C. Dreaden, E. Siouve, K. E. Shopsowitz, N. J. Shah, M. B. Yaffe and P. T. Hammond, *Sci. Signaling*, 2014, **7**, ra44.
40 S. Hatz, J. D. Lambert and P. R. Ogilby, *Photochem. Photobiol. Sci.*, 2007, **6**, 1106–1116.
41 C. W. Jefford and A. F. Boschung, *Helv. Chim. Acta*, 1974, **57**, 2242–2257.
42 J. G. Shiah, Y. G. Sun, C. M. Peterson, R. C. Straight and J. Kopecek, *Clin. Cancer Res.*, 2000, **6**, 1008–1015.
43 L. Cheng, C. Wang, L. Feng, K. Yang and Z. Liu, *Chem. Rev.*, 2014, **114**, 10869–10939.
44 S.-j. Park, W. Park and K. Na, *Adv. Funct. Mater.*, 2015, **25**, 3472–3482.

Journal of Process Control 27 (2015) 64–75

Contents lists available at ScienceDirect

Journal of Process Control

journal homepage: www.elsevier.com/locate/jprocont

Controlling assembly of colloidal particles into structured objects: Basic strategy and a case study

Michael A. Bevan[a], David M. Ford[b,*], Martha A. Grover[c], Benjamin Shapiro[d], Dimitrios Maroudas[b], Yuguang Yang[a], Raghuram Thyagarajan[b], Xun Tang[c], Ray M. Sehgal[b]

[a] Department of Chemical & Biomolecular Engineering, Johns Hopkins University, United States
[b] Department of Chemical Engineering, University of Massachusetts, Amherst, United States
[c] Department of Chemical & Biomolecular Engineering, Georgia Institute of Technology, United States
[d] Department of Bioengineering, University of Maryland, United States

ARTICLE INFO

Article history:
Received 31 March 2014
Received in revised form
26 November 2014
Accepted 26 November 2014
Available online 8 January 2015

Keywords:
Self-assembly
Colloidal particles
Diffusion map
Markov decision processes
Smoluchowski equation

ABSTRACT

A computational study is presented in which real-time manipulation of the interaction potential between particles in a colloidal system is used to control their assembly into a close-packed crystalline object. The basic model used throughout the study is a high-fidelity representation of a real experimental system in which 32 colloidal silica particles are suspended in aqueous solution with polymer hydrogel providing a temperature-tunable attractive force between the particles. Diffusion mapping is used to determine a set of coarse variables that provide an appropriate low-dimensional representation of this system at four discrete values of the attraction strength. In this case the diffusion mapping process identified two dimensions; one correlates well with the radius of gyration of the entire set of particles and the other correlates well with the average distance between distinct clusters of particles. Two different stochastic models are then built in the two-dimensional (2D) space of these variables, using data from a large number of short Brownian dynamics simulations of the full 32-particle system. The first 2D model is based on a Smoluchowski framework and is used to characterize the overall equilibrium and diffusive properties of the system. The second 2D model is based on a transition rate matrix and is used for process control. A control policy based on an infinite-horizon Markov decision process is developed using the four different attraction strengths as the input variables. The resulting policy is non-trivial; rather than simply selecting the strongest level of attraction, some mix of weak and strong attractions generally provides the optimal approach to the target close-packed state. This study, while focused on the particular mechanism of tunable depletion attraction, suggests a general strategy that could be adapted to different mechanisms of actuating colloidal assembly.

1. Introduction and background

1.1. Purpose

The purpose of this paper is to outline a general framework for controlling the self-assembly of a finite collection of colloidal particles into useful structures, and to demonstrate the application of that framework on a simple but physically relevant example.

Prior work in manipulating particle ensembles has largely separated into either self-assembly without real-time feedback control, or feedback control without self-assembly. Self-assembly is a well-studied field documented in multiple review articles [1–3]. During self-assembly, particle–particle interactions may cause them to assemble into ordered ensembles, and that assembly can be guided by varying external parameters that modulate the strength of interactions, by patterning the substrate on which ensemble formation occurs, or by choosing and/or modifying the properties of the particles. Usually, the number of particles is large and their behavior is most naturally described by statistical models. In contrast, real-time feedback control of micro- and nano-scale particles has been applied to systems with just a few particles whose behavior is modeled deterministically and where control actuation is essentially considered per-particle. Researchers have modulated dielectrophoretic (DEP) forces [4–6], optoelectronic actuation [7],

* Corresponding author. Tel.: +1 4135770134.
E-mail address: ford@ecs.umass.edu (D.M. Ford).

http://dx.doi.org/10.1016/j.jprocont.2014.11.011
0959-1524/

magnetic fields [8–11], and fluid flow and electrokinetic forces [12–17], to control the position and orientation of one and a few (<10) micro/nano particles and rods. Several approaches have been developed to tune colloidal interactions to mediate crystallization of small ensembles in a reversible manner [18–24], which are amenable to control via feedback schemes. Our recent work [22,25] suggests that these two approaches could be combined, and our goal in this paper is to demonstrate that feedback can improve ensemble self-assembly in a high-fidelity model of the assembly process.

1.2. Colloidal systems

Colloidal particles with dimensions ranging from nanometers (nm) to microns provide the basic building blocks to control material structures on length scales larger than molecular dimensions but smaller than macroscopically visible dimensions. While standard chemistry deals with building atomic and molecular structures, and microfabrication and granular material processing provide routes toward manipulating miniaturized structures on the order of 10–1000 μm, colloidal assembly provides unique access to material architectures with characteristic dimensions from 1 nm to 10 μm. Although controlling microstructure is important to determining emergent material properties in any colloidal system (such as in paint and mud) [26], it becomes increasingly important and justified for creating high value-added materials with exotic electromagnetic properties. In particular, the ability to assemble defect-free colloidal crystals provides a potential scalable manufacturing method to create materials for advanced applications, such as solar-cell coatings, as well as futuristic technologies based on optical computing and cloaking devices. Methods to model and control colloidal crystallization have been developed in recent years [18–22].

2. Theory

We first provide some basic physical theory of the thermodynamics and dynamics of colloidal solutions. We take a microscopic approach and describe both the conservative and non-conservative forces that act on the particles, with an emphasis on a certain type of attractive conservative force that is sensitive to temperature. We then discuss how high-dimensional data at the level of the particle coordinates, as generated by simulation (using the forces mentioned above) or experiment, can be used to create low-dimensional stochastic models of the system dynamics. Finally we describe how control of an assembly process can be achieved by using the low-dimensional stochastic models as a real-time guide to manipulating the forces. The flowchart in Fig. 1 provides an overview of the strategy.

2.1. Basic physics of colloids

In its simplest form a colloidal solution has two components: the colloid particles and the solvent molecules. There may be more components if the solvent is a mixture of molecular species, or if there is more than one type (or size) of colloid particle. For simplicity the basic two-component case is presented here, and the particle and solvent species are both assumed to be spherical. Relaxation of either of these restrictions poses no additional conceptual difficulty.

Statistical mechanics [27] provides the basic underlying theory of how the colloid particles and solvent molecules sample positions in space and time, at fixed values of global thermodynamic parameters. There are large differences in size and mass of the two components, as well as the time scales associated with their motion [28]; this significant asymmetry will allow certain simplifications to be made in the modeling.

The forces acting on the colloid particles are the key elements in a dynamical model. Section 2.1.1 presents a framework for describing the net conservative forces between the particles. Section 2.1.2 presents the important non-conservative (hydrodynamic) forces that arise in colloidal systems. Section 2.1.3 presents a full dynamical model in particle positions and time that incorporates both types of force.

2.1.1. Conservative forces and interaction potentials in colloidal solutions

This section is based on a review by Frenkel [29], which goes back to the work of Onsager [30], and another by Belloni [31], which uses McMillan–Mayer solution theory [32,33].

Assume that a colloidal solution is composed of N_C colloid particles, occupying positions $\mathbf{r}^{(N_C)}$, and N_S solvent molecules, occupying positions $\mathbf{r}^{(N_S)}$, at a fixed volume V and temperature T. The total potential energy may be written as the sum of colloid–colloid (CC), colloid–solvent (CS), and solvent–solvent contributions (SS),

$$U_{\text{tot}}(\mathbf{r}^{(N_C)}, \mathbf{r}^{(N_S)}) = U_{\text{CC}}(\mathbf{r}^{(N_C)}) + U_{\text{CS}}(\mathbf{r}^{(N_C)}, \mathbf{r}^{(N_S)}) + U_{\text{SS}}(\mathbf{r}^{(N_S)}). \quad (1)$$

(Note that this decomposition does not necessarily imply a pairwise additivity of the potential energy at the particle-molecule level.) The positions of the solvent molecules change much more rapidly than the positions of the colloid particles due to the asymmetry in size, mass, and time scales of the two species. This leads to the reasonable assumption that the positions of the solvent molecules may be averaged over, to obtain an effective potential based on colloid particle positions only. The resulting potential of mean force W has the general form

$$W(\mathbf{r}^{(N_C)}) = U_{\text{CC}}(\mathbf{r}^{(N_C)}) - kT \ln \left\langle \exp\left[-\frac{U_{\text{CS}}(\mathbf{r}^{(N_C)}, \mathbf{r}^{(N_S)})}{kT} \right] \right\rangle_{\mathbf{r}^{(N_S)}}, \quad (2)$$

where k is the Boltzmann constant, T is the temperature, and the brackets denote an average value from Boltzmann sampling over the positions of the solvent molecules (In fact this sampling is done most conveniently at fixed chemical potential of the solvent μ_S rather than at fixed N_S. See either Frenkel [29] or Belloni [31] for a complete derivation at the level of statistical mechanical partition functions.). The quantity W is not equivalent to U_{tot}; it does not include a solvent–solvent contribution, and the dependence of the colloid–solvent contribution on $\mathbf{r}^{(N_S)}$ has been averaged out. However, W does provide the basis for a complete description of the thermodynamic properties of the colloidal particles in an effective one-component model (OCM) in which they interact through an implicit solvent medium. The force on a given particle i due to these interactions, which is of use when computing dynamic trajectories of particles as discussed in Section 2.1.3, is straightforwardly computed from the potential of mean force as

$$\mathbf{f}_i(\mathbf{r}^{(N_C)}) = -\nabla_i W. \quad (3)$$

Predicting or measuring the potential of mean force in a given colloidal solution is not a simple task, even within the OCM. To make the problem more tractable the potential is often treated as pairwise additive, so that

$$W(\mathbf{r}^{(N_C)}) = \sum_{i<j} w(r_{ij}), \quad (4)$$

where the sum is over all pairs of colloid particles and $r_{ij} = |\mathbf{r}_i - \mathbf{r}_j|$ is the center-to-center distance between particles i and j. In most pairwise interaction models there are additive contributions representing repulsion and attraction, as

$$w(r) = w_{\text{rep}}(r) + w_{\text{att}}(r) \quad (5)$$

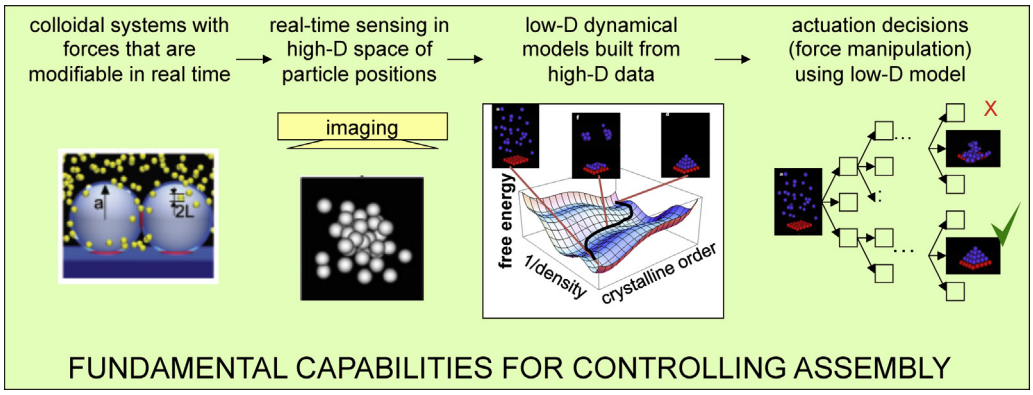

Fig. 1. An overview of how colloidal assembly can be controlled by real-time manipulation of interaction forces.

The repulsion typically arises from the fact that colloidal particles have some net surface charge in solution due to the dissociation of functional groups and/or preferential adsorption of certain charged species from solution. The basic principle of repulsion between like charges then causes repulsion between particles; however, the magnitude and range of this repulsion is modulated by the presence of ions in solution, and the development of accurate models for $w_{rep}(r)$ has been the subject of much study [31]. Even in the absence of significant surface charge there will be steric repulsion due to overlaps at the atomic level upon close approach ($r = 2a$ with a the particle radius) of two particles; this type of repulsion is often modeled in $w_{rep}(r)$ by a simple hard sphere potential.

An attractive component $w_{att}(r)$ in the potential may arise from several different physical phenomena. Dispersion, or van der Waals, attraction is due to interactions between permanent or fluctuating dipoles in the two particles. The combination of these attractive forces with electrostatic repulsion via Eq. (5) yields the well-known Derjaguin, Landau, Verwey, and Overbeek (DLVO) potential, which is a common model for understanding colloidal stability; the attractive forces create an infinitely deep potential well near particle–particle contact ($r = 2a$), but the electrostatic repulsion forms a positive potential barrier at intermediate r that reduces the rate at which particle pairs "fall into" the well and irreversibly aggregate [28].

There are other sources of attractive interactions $w_{att}(r)$ in colloidal systems. An interesting example, and the one of the main interest here, is the introduction of a third component (called the depletant) into the system. The depletant is typically another colloidal species, much smaller in size than the main one, that causes an attraction between the larger particles through an entropic mechanism originally described by Asakura and Oosawa [34]. Fig. 2a depicts the mechanism. A single isolated large particle excludes the centers of the small particles from a sphere of volume $(4/3)\pi(a+L)^3$, where a is the large particle radius and L is the depletant radius. However, when the surface-to-surface separation $(r - 2a)$ of two large particles becomes less than or equal to the diameter $2L$ of the depletant particle, the excluded volumes of the two spheres partially overlap (red region in Fig. 2a) and the net volume available to the depletant particles is increased by the overlap amount. This effect, which increases the entropy of the total system, is (perhaps surprisingly) strong enough to cause the particles of the main colloidal species to preferentially sample such separations. From the point of view of the colloidal particles, this preferential sampling is equivalent to a pairwise attraction that acts when $r \le 2(a+L)$. Recently one of our laboratories [20,21] has implemented an experimental realization of this concept using ~2 μm silica particles as the main colloidal species and ~200 nm poly-*N*-isopropylacrylamide (PNIPAM) gel particles as the depletant. They found that the pairwise potential of mean force was modeled well by the traditional Asakura–Oosawa expression

$$w(r) = w_{rep}(r) - \Pi\left[\left(\frac{4\pi}{3}\right)(a+L)^3\left(1 - \frac{3r}{4(a+L)} + \frac{r^3}{16(a+L)^3}\right)\right] \quad (6)$$

where $w_{rep}(r)$ is given by a common expression for charge-based repulsion and Π is the osmotic pressure of the depletant species. The quantity Π, which sets the magnitude of the entire depletion-based attraction, is proportional to the volume fraction of solution occupied by the depletant species and therefore proportional to L^3, the cube of the depletant radius. The radius L of the PNIPAM particles is highly sensitive to temperature in the neighborhood of 25 °C, so small changes in temperature can cause large changes in Π as shown in Fig. 2b. This type of attraction is interesting for the present contribution because it can be changed over a broad range by using the solution temperature as an input variable. Of course

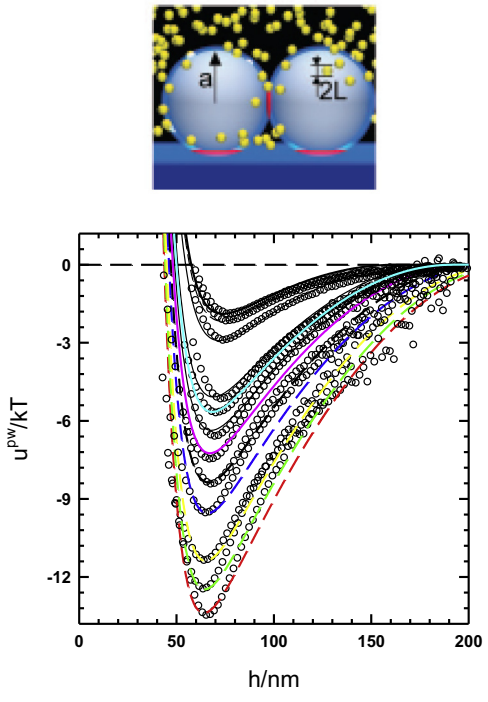

Fig. 2. (a) Schematic of charged 2.34 μm SiO_2 colloidal particles with particle–wall or particle–particle surface separation, h, experiencing depletion attraction with each other and a glass microscope slide due to the exclusion of spherical depletants (yellow) with radius, L. Depletants can approach the SiO_2 surfaces within a distance, Δ_{EV}. Depletants can approach each other within a distance, Δ_{OP} [63]. (b) Particle–wall potential energy profiles obtained using total internal reflection microscopy [20]. (For interpretation of the references to color in this figure legend, the reader is referred to the web version of this article.)

in a real system one must consider issues such as the response time of the system temperature to a change in the desired set point and the role of transient states with temperature gradients; in this paper we consider an idealized model in which system temperature changes are instantaneous and uniform. It should be noted that the potentials in Fig. 2b were directly measured using total internal reflection microscopy [20,21], which can directly measure kT-scale and nanometer-scale colloidal interactions [35,36] in contrast to other established force measurement techniques such as the Surface Forces Apparatus [37] or the Atomic Force Microscope [38].

2.1.2. Non-conservative forces and hydrodynamics in colloidal solutions

The particles also experience non-conservative hydrodynamic and stochastic forces as they move through the solvent. The formalism for modeling these forces [39,40] starts with the Liouville equation for the probability distribution function of the colloid particles and solvent molecules in phase space, i.e. the complete set of position and momentum coordinates. The large difference in mass between the two species is invoked to justify an integration over the solvent positions and momenta; the result is a Fokker–Planck equation in the phase space of the colloid particles only, with the potential of mean force W describing the conservative forces and a phenomenological friction tensor characterizing the hydrodynamic forces. Furthermore the time scale for momentum relaxation of a colloid particle is assumed to be very short compared to that for position relaxation, so the colloidal particle momentum variables may also be eliminated yielding the Fokker–Planck equation,

$$\frac{\partial p}{\partial t} = \nabla \cdot \mathbf{D}_{\text{diff}} \cdot \left(\nabla - \frac{1}{kT} \mathbf{F}^{\text{con}} \right) p, \tag{7}$$

where $p(\mathbf{r}^{(N_C)}, t)$ is the probability distribution for the positions of the colloidal particles at time t, $\mathbf{F}^{\text{con}} = -\nabla W$ is the vector of conservative forces acting on the particles, and $\mathbf{D}_{\text{diff}}$ is the diffusion tensor. This specific version of the Fokker–Planck equation, which has the equilibrium solution $p_{\text{eq}} \sim \exp(-W/kT)$, is often called the Smoluchowski equation.

The tensor $\mathbf{D}_{\text{diff}}$ captures the hydrodynamic and stochastic forces and is generally not diagonal, as the diffusive motions of the particles are coupled by interactions through the liquid solvent. These off-diagonal hydrodynamic interactions are many-body in nature and can be quite challenging to model in concentrated colloidal solutions. Approximate models, usually involving pairwise additivity at some level, are available and have proven useful [41]. Hydrodynamic interactions have a much longer range than most pairwise potentials of mean force $w(r)$ and are therefore much more costly to compute. The simplest level of approximation is to completely ignore hydrodynamic coupling between particles but retain the stochastic Brownian forces (arising from collisions with the solvent molecules) on each individual particle. In that limit $\mathbf{D}_{\text{diff}} = D_0\mathbf{I}$, where $\mathbf{I}$ is the identity matrix and $D_0 = kT/(6\pi\mu a)$ with μ the solvent viscosity.

2.1.3. Dynamical modeling at the particle level

2.1.3.1. Theory and numerical simulation. In principle the solution to Eq. (7), $p(r^{(N_C)}, t)$, provides the basis for a complete description of the equilibrium and dynamic properties of a system with specified N_C, V, T, W, and $\mathbf{D}_{\text{diff}}$. However, solving Eq. (7) directly is not convenient in practice because the partial differential equation has $3N_C$ spatial dimensions. The more common strategy is to perform dynamic simulations of the system using a discrete-time version of the Langevin equation that corresponds to Eq. (7); any desired properties may then be computed as averages over the simulated trajectories. In colloidal systems this approach has been named Stokesian dynamics (SD), in analogy with molecular dynamics (MD) for atomistic systems [41]. Eq. (8) shows the form of a typical SD time-stepper [42]

$$\mathbf{r} = \mathbf{r}^0 + (\nabla \cdot \mathbf{D}^0_{\text{diff}})\Delta t + (kT)^{-1}\mathbf{D}^0_{\text{diff}} \cdot (\mathbf{F}^{\text{con},0} + \mathbf{F}^{\text{B},0})\Delta t \tag{8}$$

where Δt is the time interval, the superscript 0 indicates quantities computed at the beginning of the time interval, $\mathbf{r}$ is the vector of particle positions, and $\mathbf{F}^{\text{B}}$ is a vector of stochastic forces characterized by a mean $\langle F^{\text{B}} \rangle = 0$ and a variance $\langle \mathbf{F}^{\text{B}}(0)\mathbf{F}^{\text{B}}(t) \rangle = 2(kT)^2\mathbf{D}^{-1}_{\text{diff}}\delta(t)$, where $\delta(t)$ is the Dirac delta function. As noted in Section 2.1.2, $\mathbf{D}_{\text{diff}}$ becomes a diagonal matrix independent of particle positions when the hydrodynamic coupling between particles is neglected; in this limit the second term on the right-hand-side of Eq. (8) is zero and SD reduces to the simpler Brownian dynamics (BD). BD is the technique employed in this paper for all basic particle-level dynamical simulations.

SD time-steppers like Eq. (8) provide the means to carry out a dynamical simulation of the colloidal system at the particle-coordinate level, limited only by the accuracy of the conservative potentials and the hydrodynamic diffusion tensors. However, using SD directly in a process control scheme is not feasible because of the long time required to compute trajectories. Ultimately, one is limited by the maximum allowable time step Δt in the SD equation and the speed of the available computer. The former depends somewhat on the nature of the conservative forces in the system but is, typically, on the order of 10^{-4} s or less. The latter of course depends on the computational resources available. As a concrete example, we observed a roughly 12:1 ratio of computing time to simulated time in our BD simulations of the 32-particle system in this paper, using a single core of an AMD Opteron processor.

2.1.3.2. Verification of simulations against experiments. If we are to build low-dimensional models (Section 2.2) based on trajectories from detailed time-steppers like those just described, we must have some level of confidence in the accuracy of the force models employed in the time-steppers. The AO-depletion interaction potential model used in this work, Eq. (6), was carefully constructed in previous studies by fitting the model parameters so that BD simulations reproduced certain thermodynamic and transport properties measured in microscopy experiments. Specifically, inverse Monte Carlo methods (including image resolution limiting effects) [43–45] were used to determine parameters by matching measured and simulated radial distribution functions [20] and mean square displacement statistics [21]. We are therefore confident that the BD simulations employed here, using the conservative force model of Eq. (6), provide quite accurate representations of trajectories observed in real laboratory experiments.

2.2. Dimensionality reduction techniques

Since controlling colloidal assembly with trajectory data from real-time direct numerical simulation is not feasible (Section 2.1.3.1), we pursue the alternative strategy of using such data off-line to build models of reduced dimensionality. We view the problem as consisting of two parts: identifying the minimum dimensionality needed to represent the system and choosing appropriate coordinates for those dimensions, and then building a model in those coordinates. We typically refer to the coordinates as "coarse variables" or "order parameters" (OPs), although they may not necessarily reflect order in the conventional sense.

2.2.1. Identifying reduced dimensionality and coordinates

Diffusion map (DMap) analysis, sometimes referred to as the nonlinear analog of principal component analysis, provides a route to identifying low-dimensional representations of a data set [46–48]. In DMap analysis a Markov matrix is constructed from the data set based on transition probabilities, derived from

a chosen distance metric, between points in the set. If the data, comprising points of dimension n, are indeed embedded in some lower-dimensional manifold, then the eigenvalue spectrum of the matrix will exhibit a gap after the first $(k+1)$ eigenvalues where $k<n$ (note that the first eigenvalue is trivially 1 for a Markov matrix). The top k non-trivial eigenvectors then provide a mapping to the lower-dimensional space, wherein the k coordinates of a given data point are given by the corresponding entries in these eigenvectors. In past applications to colloidal assembly [49–51] we have found k values in the range 2–5 for colloidal systems with n ~30–300 (10–100 particles in 3D), using a Hausdorff distance metric on data sets of $\sim 10^3$–10^4 snapshots sampled from dynamic trajectories. While DMap analysis does provide a value of k and an accompanying set of reduced-space coordinates for each data point in the set, unfortunately it does not provide an explicit mapping between the n-dimensional and k-dimensional coordinates. The task of identifying useful OPs in the n-dimensional space therefore requires some empiricism.

In the past [49–51] we have approached this problem by proposing a set of physically meaningful functions of the n-dimensional coordinates and evaluating the correlation between their values and the values of the top eigenvectors, across the data set. Here we consider three such functions. The first two, $R_g{}^*$ and $\langle C_6\rangle$, have been used in past publications [49–51] to which we refer the reader for more detail. $R_g{}^*$ is the radius of gyration of the particle assembly normalized by the radius of a single particle; it is expected to be a useful metric for discriminating between diffuse and condensed phases. $\langle C_6\rangle$ is the average number of crystalline bonds per particle, with a crystalline bond between two particles defined by both spatial proximity and degree of similarity in a sixfold orientational order parameter. As a metric of crystallinity, $\langle C_6\rangle$ is expected to be useful for discriminating between solid-like and fluid-like condensed configurations (and in some cases between solid phases of different lattice structure). The third OP, $D_{cc}{}^*$, is introduced here for the first time and defined as the average pairwise distance between distinct clusters in the system normalized by the radius of a single particle. A cluster is defined as a subset of particles that are mutually connected by pairwise bonds. In the example problem studied here, a pair of colloidal particles is defined as bonded if they are close enough to experience the mutual attractive entropic interaction caused by the depletant particles as defined in Section 2.1.1. The number of distinct clusters in an n-particle system may range from 1 to n. The pairwise distance between two clusters is defined as the smallest distance between any pair of particles, with the pair comprising one particle from each cluster. In the case of only one distinct cluster, $D_{cc}{}^*$ is set to a value that corresponds to the maximum bonded length for a particle pair; this makes $D_{cc}{}^*$ an essentially continuous function with a lower bound equal to the maximum bonded length.

Fig. 3 illustrates four trajectories of the model system, each for a different value of the attraction strength, plotted in the three OPs. While the physical insight derived from these plots will become more apparent later, one can immediately see the relevant range of each OP and the stochastic nature of the trajectories in the OP variables.

2.2.2. Constructing models in the OPs

In past work [49,50] we have constructed Smoluchowski models in the low-dimensional space of the chosen order-parameter set $\mathbf{X}$,

$$\frac{\partial \rho(\mathbf{X},t)}{\partial t} = \nabla \cdot e^{-\frac{F(\mathbf{X})}{kT}} \mathbf{D}(\mathbf{X}) \cdot \nabla e^{\frac{F(\mathbf{X})}{kT}} \rho(\mathbf{X},t) \tag{9}$$

where $\rho(\mathbf{X},t)$ is the probability of the system being at location $\mathbf{X}$ in order parameter space at time t, $F(\mathbf{X})$ is the free energy landscape (FEL), and $\mathbf{D}(\mathbf{X})$ is the diffusivity landscape (DL). In writing such a model, we have assumed that the system undergoes a Markov process in the coarse-variable space. While we have not rigorously proven that this is true, it seems a reasonable starting point based on the fact that the colloidal system under consideration follows a Markov process in its basic coordinates $\mathbf{r}^{(N_C)}$. Previously we have constructed the models of Eq. (9) by fitting the coefficients F and $\mathbf{D}$ to direct BD simulations of the colloidal system using either a linear fit to many localized short trajectories [52] or a fit to discretized transition rate matrices using Bayesian inference on longer trajectories [53]. The FEL and DL provide an overview of the coarse thermodynamic and kinetic characteristics of the system.

To assess the quantitative accuracy of candidate low-dimensional Smoluchowski models, we compared probability propagator $\rho(\mathbf{X},t)$ obtained by particle-scale BD simulations and low-dimensional Langevin dynamic (LDLD) simulations. The LDLD simulations are based on a Langevin equation given as

$$\mathbf{X}(t+\Delta t) = \mathbf{X}(t) - \mathbf{D}(\mathbf{X}) \cdot (kT)^{-1} \nabla F(\mathbf{X}) \Delta t + \nabla \cdot \mathbf{D}(\mathbf{X}) + [2\mathbf{D}(\mathbf{X})\Delta t]^{1/2} \Gamma(t), \tag{10}$$

where the coefficients are the same as in Smoluchowski model, Δt is the integration time step, and $\Gamma(t)$ is a Gaussian noise variable. An accurate Smoluchowski model will reproduce $\rho(\mathbf{X},t)$ obtained from high-dimensional particle-scale BD simulations and LDLD.

2.3. Process control

Recent studies have demonstrated the success of the Markov decision process (MDP) in simulating and controlling the dynamics of stochastic and many-body systems [54,55]. In our previous studies on colloidal assembly, we used MDP to achieve a highly ordered colloidal crystal in a Markov chain transition state model of the assembly process [25,56,57], using electric field [25,56] and depletion force [57] as the control input. Given these successes, in this paper, we construct a Markov decision process framework to study the control of the colloidal crystals to form a single crystalline state using the system osmotic pressure as the control variable, and implementing the control in a BD simulation.

As a version of dynamic programming, the Markov decision process is characterized by $\{K, S, A_s, P_a\}$ [58,59]. Here K is the collection of the discrete time steps k; S is the state space of the system; and A_s is the collection of all admissible control actions for state s. In this study, there are four states of the system that correspond to four different values of the attraction strength Π defined by Eq. (6). Specifically, $A_s = \{\Pi_1^*, \Pi_2^* \ \Pi_3^* \ \Pi_4^*\} = \{1.05, \ 1.11, \ 1.30, \ 1.90\} \times 10^{-7}\,\mathrm{nm}^{-3}$ for all states $s \in S$, where $\Pi^* = \Pi/(kT)$. P_a is the parameterized probability transition matrix for control action $a \in A_s$, which contains the probability $P_{a,ij}$ for the system to be in state j after a time step of Δt under control action a, given the current state of i.

The steps for constructing the transition matrices P_a include: first, to identify and discretize the continuous system state into a finite number of discrete states; second, to approximate the transitions between the discrete states using samples of the full system [60]. These samples may come from a dynamic simulation or from experimental measurements; here the BD simulation provides the samples. The DMap analysis (Section 3.2) identifies the order parameters $R_g{}^*$ and $D_{cc}{}^*$ as an appropriate low-dimensional set of coarse variables for this system, so the system state is described by these variables with $R_g{}^* \in [2.6\ 4.5]$ and $D_{cc}{}^* \in [2\ 8]$ (ranges are defined by physical meaning). $R_g{}^*$ is discretized into 96 evenly spaced intervals with an increment of $\Delta R_g{}^* = 0.02$, while $D_{cc}{}^*$ is discretized into 61 evenly spaced intervals with increment $\Delta D_{cc}{}^* = 0.1$. These increments were selected by constructing transition rate models with different levels of discretization, to determine the optimal size to accurately represent the BD simulation.

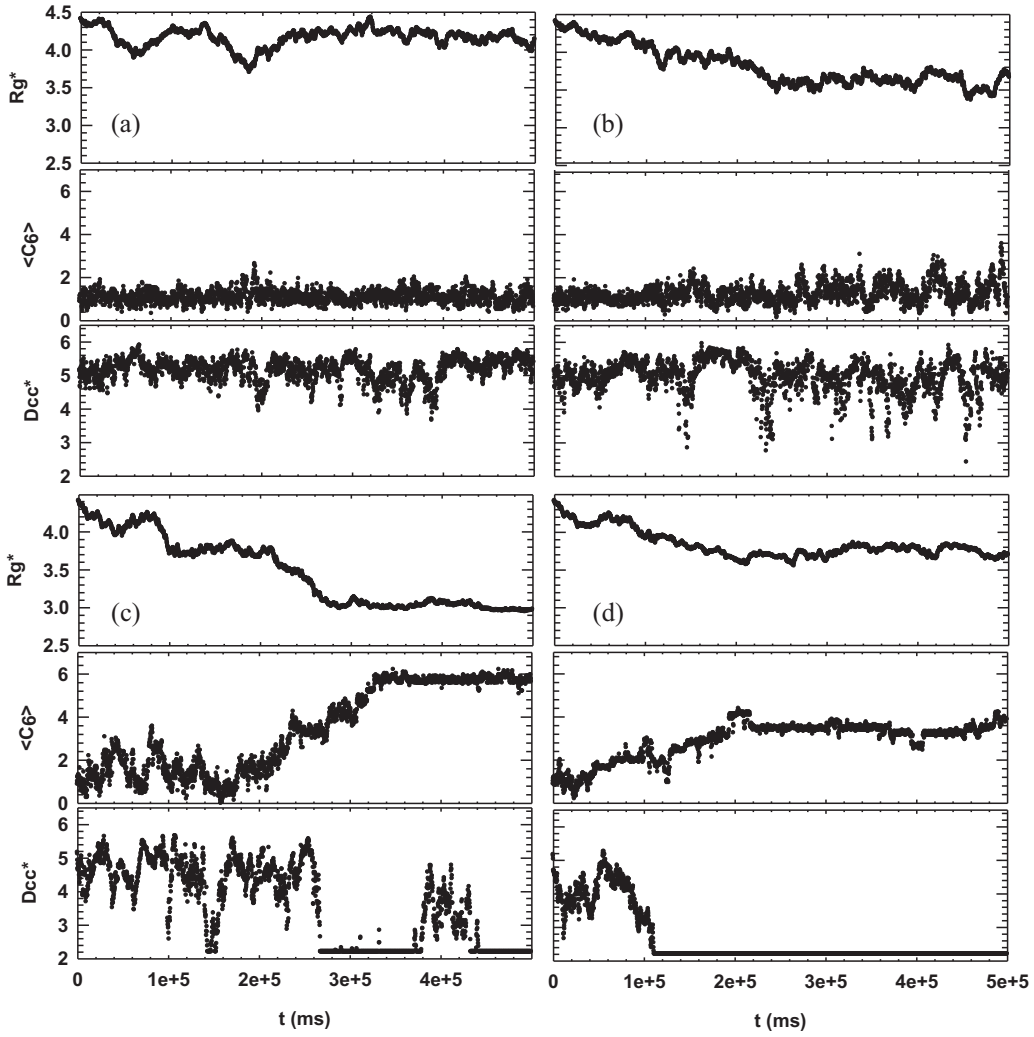

Fig. 3. Four different representative dynamic trajectories of the model colloidal system. Each trajectory is plotted in terms of the three coarse variables considered in this study: radius of gyration R_g*, crystallinity metric $\langle C_6 \rangle$, and average cluster-to-cluster distance D_{cc}*. The trajectories are for different values of osmotic pressure $\Pi^* = 1.05$ (a), 1.11 (b), 1.30 (c), and 1.90 (d), with Π^* defined later in the text.

Independent Brownian dynamics simulations are conducted under each of the four constant Π^* values to cover the effective state space that can be visited by the system. Based on the Brownian dynamics simulations, four independent Markov transition matrices P_a are constructed, having a time step of $\Delta t = 5$ s for each of the four Π^* values.

We designed an infinite-horizon MDP to obtain the optimal control policy [58,59]. To formulate the optimization problem, the objective function J_a is defined as

$$J_a(x) = E\left\{\sum_{k=0}^{\infty} \gamma^k R(x_k, a_k)\right\} \tag{11}$$

where E is the expectation operator needed to account for the stochasticity of the system. $a_k \in A_s$ is the control action at time step k, and $x_k \in S$ is the system state at time step k. γ is the discount factor, which ensures the convergence of the optimal policy calculation, and is chosen as 0.99.

$R(x_k,a_k)$ is the one-stage reward function when action a is used, given the system state in x. The one-stage-reward function $R(x_k,a_k)$ is defined to drive the system simultaneously to a state with low D_{cc}* and low R_g* values, which corresponds to a single highly ordered crystal.

$$R(x_k, a_k) = \frac{1}{R_g^{*2}} + \frac{1}{D_{cc}^{*2}} \tag{12}$$

The optimal control policy is achieved by obtaining an input trajectory a that maximizes the objective function J_a over an infinite number of time steps, via dynamic programming; and the optimal policy $a^*(x) \in A$ is defined as

$$a^*(x) = arg\{\sup J_a(x)\} \tag{13}$$

3. Example problem

3.1. Model system

We modeled a system of 32 colloidal particles interacting via the AO-depletion potential of Eq. (6). As mentioned in Section 2.3, we employed four specific values of the attraction strength, $\Pi^* = \Pi/kT = 1.05$, 1.11, 1.3, and 1.9 (all in units of 10^{-7} nm^{-3}). This variation in Π^* is sufficient to take the system from a state where it is purely fluid-like (1.05) to a state where it coexists in fluid- and solid-like states (1.11) and finally to a state where

it is purely solid-like (1.3 and 1.9). At $\Pi^* = 1.9$, the crystalline state is a deep energy well, effectively locking in the desired state. With respect to the other parts of the AO depletion potential, including the repulsive contribution, we used exactly the same mathematical forms and parameter values employed in previous work [49–51,61].

3.2. Diffusion map results

In our earlier work [50] we used trajectory data sets obtained from Brownian-dynamics simulations as the input to the DMap analysis. However, the time required to generate trajectories that sample all relevant regions of phase space, i.e. detailed particle coordinate space, can be prohibitively long. In this work, we have adopted the idea of integrating diffusion mapping with Monte Carlo umbrella sampling (MC-US) as proposed by Ferguson and coworkers [62]. The umbrella sampling ensures a more complete coverage of the phase space, although the biased nature of the sampling must be accounted for when preparing the trajectory data set for the DMap analysis. We implemented the method as follows.

We chose $R_g{}^*$ and $\langle C_6 \rangle$ as the starting order parameter set. This pair of variables has been used in our past studies and serves as a reasonable starting point. We also employed the specific attraction strength value $\Pi^* = 1.11$ because this value is known to produce the most complex free energy landscape, with local minima representing both fluid-like and crystalline-like states [50]. We carried out umbrella sampling on a grid spacing of (0.01, 0.0625) in the OP space $\psi = (R_g^*, \langle C_6 \rangle)$. Partially overlapping windows with side length equal to 10 times the grid spacing were used to cover the OP space, with hard walls used to constrain the system within a window during an MC run. We ran 50 million Monte Carlo steps per window and, by stitching together the free energy profiles in adjacent windows, produced a free energy landscape (FEL), $F(\psi)$, at the resolution of the grid. From this process we also naturally obtained a large collection of detailed particle configurations, or snapshots, that span the range of ψ. We then associated with each snapshot a Boltzmann weight given by

$$P(\psi_i) = \frac{e^{-\beta F(\psi_i)}}{\sum_{i=1}^{n} e^{-\beta F(\psi_i)}} \tag{14}$$

We used two-dimensional interpolation on the grid to compute each $F(\psi_i)$. Under this probability distribution, we scaled up our data set using

$$c_i = \text{round}([sP(\psi_i)]) \tag{15}$$

where s is a scaling factor and c_i is the multiplicity of each snapshot i. In the data set, each snapshot was then replicated a number of times equal to c_i ($c_i = 0$ essentially removes that snapshot from the data set). This procedure transformed the inherently biased set of snapshots from MC-US into a set that is consistent with what an unbiased MC walk would have produced, assuming that the underlying choice of coarse variables provides a meaningful FEL. We set the scaling factor s equal to 10^6 and subsampled to generate a data set containing $\sim 10^4$ snapshots. We employed this pseudo-unbiased set of snapshots as the input to the DMap analysis (We note that other procedures for generating the pseudo-unbiased data set, which would take advantage of the fact that the configurations within a given window already have the correct relative weighting, are possible.). We also analyzed two subsets of this master data set; one subset included only those snapshots located in the fluid-like well on the FEL, and the other included only those snapshots located in the crystalline-like well. This allowed us to understand certain features of the DMap results.

Fig. 4(a)–(c) shows the eigenvalue spectra for the fluid well, crystalline well, and two-well (master) data set, respectively. A spectral gap is observed after the first non-trivial eigenvalue in (a) and the first two non-trivial eigenvalues in (b) and (c), which indicates a dimensionality of at most two. Fig. 5 shows the data sets plotted in the coordinates of the first two non-trivial eigenvectors, i.e., in $\nu_2 - \nu_3$ space. The data points are colored by the value of the order parameter $R_g{}^*$ (a, d, g), $\langle C_6 \rangle$ (b, e, h), or $D_{cc}{}^*$ (c, f, i). The first row (a–c) shows the data from the fluid well. The DMap coordinate ν_2, corresponding to the single non-trivial eigenvalue in Fig. 5(a), correlates best with $R_g{}^*$. The second row (d–f) shows the data from the solid well. The data points are clustered by both $R_g{}^*$ and $\langle C_6 \rangle$, but $D_{cc}{}^*$ shows an excellent correlation with ν_2 as indicated by the continuous change of color from left to right in Fig. 5(f). The two-well (master) data set is shown in the third row (g–i). By comparing this row with the rows above, we see that the fluid data are localized near the vertex of the angle formed by the two branches of the crystalline data. As with the crystalline well data, $D_{cc}{}^*$ correlates best with ν_2. For the data sets that include the crystalline well, Fig. 5(d–i), we observe a symmetry about the $\nu_3 = 0$ axis. This symmetry suggests that this coordinate is capturing some inversion degrees of freedom, which are not of particular interest in this study. Overall, the DMap analysis leads us to conclude that the OP space $\psi = (R_g^*, D_{cc}^*)$ will provide a better coarse-grained representation than the originally chosen space $(R_g{}^*, \langle C_6 \rangle)$. $R_g{}^*$ correlates best with the only important coordinate in the fluid well. $D_{cc}{}^*$ correlates best with the first important coordinate in the crystalline well, while the second important coordinate in this well seems to be associated with an inversion symmetry that is not of interest. Fig. 5(d) and (e) and (g) and (h) indicate redundancy of information contained by $R_g{}^*$ and $\langle C_6 \rangle$, suggesting that the latter variable may be replaced. The work below will therefore employ the low-dimensional variable set $(R_g{}^*, D_{cc}{}^*)$.

3.3. Free energy and diffusivity landscapes

By fitting the trajectories in the order parameter space from BD simulations, we obtained $F(\mathbf{X})$ and $\mathbf{D}(\mathbf{X})$ in the Smoluchowski model, as shown in Figs. 6 and 7. The FEL provides thermodynamic information on the likelihood of the system being in different regions of the order parameter space $(R_g{}^*, D_{cc}{}^*)$. The free energy differences capture the thermodynamic driving force that influences trajectory drift between different states. At $\Pi^* = 1.05$, there is a global minimum located around (4.2, 4.9), which corresponds to fluid-like structures. As Π^*, increases to 1.11, the appearance of the two wells located at (3.8, 4.9) and (3.1, 4.1) indicates the coexistence of fluid-like structure and solid-like structures. At higher Π^*, large FEL gradients drive fluid-like structures toward solid-like structure with low $D_{cc}{}^*$ and low $R_g{}^*$. At regions around (3.1, 3.5), there exist a local minimum with kT scale barrier prior to assembly trajectories entering the global minimum near (3.0, 2.2).

The $\mathbf{D}(\mathbf{X})$ shown in Fig. 7 characterize the drift and diffusion mediated by the free energy gradient. We present only the diagonal terms of the tensor $\mathbf{D}$, as the cross terms that characterize coupling between $D_{cc}{}^*$ and $R_g{}^*$ are basically negligible. For each Π^*, the $D_{cc}{}^*D_{cc}{}^*$ component shows higher values at $D_{cc}{}^* \sim 2$–3, which characterize the larger fluctuations due to particles attaching to or breaking apart from a cluster. For the highest Π^* case, the region near $D_{cc}{}^* \sim 3$–5, $R_g{}^* \sim 3.0$–3.2 also has a higher diffusivity in the $D_{cc}{}^*D_{cc}{}^*$ component. For the $R_g{}^*R_g{}^*$ component, higher values appear at moderate extent of condensation ($R_g{}^* \sim 3.2$–4.0), where particle arrangement results in strong fluctuations in $R_g{}^*$. Both the $D_{cc}{}^*D_{cc}{}^*$ and $R_g{}^*R_g{}^*$ components generally show decreasing values at lower $R_g{}^*$ as the configuration is more condensed, with little room for the particle arrangement.

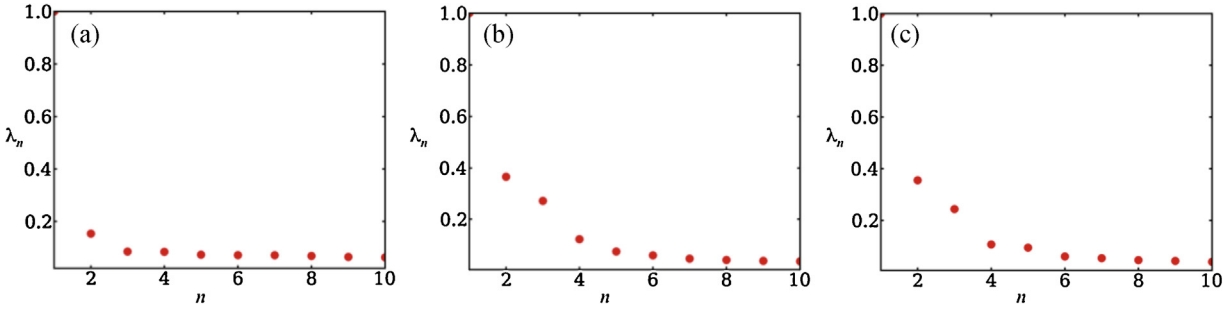

Fig. 4. Eigenvalue spectra for data sets comprising (a) fluid, (b) crystal and (c) both fluid and crystal states. For the fluid data set there is a spectral gap after the first non-trivial eigenvalue, but for the crystal and combined data sets there is a spectral gap after the first two non-trivial eigenvalues. These findings indicate a requirement of at most two dimensions in the low-dimensional model.

The validity of the low-dimensional Smoluchowski models are examined by comparing the probability propagator constructed from particle-scale BD simulation and order-parameter-scale LDLD simulations. As an example, Fig. 8 shows results for $\Pi^* = 1.11$ and an observation time $t = 10$ s for two starting points. The time scale is smaller than the global relaxation time (i.e., order 10^3 s) and larger than the Brownian time scale (i.e., order 10^{-1} s) and is expected to capture transient assembly dynamics. Fig. 8 shows good agreement between BD and LDLD simulations starting at (4.4, 5.2) and (3.2, 4.5), which are the locations of the two wells at $\Pi^* = 1.11$. Similar comparisons for the fluid well at lower Π^* and similar FEL at higher Π^* confirm the high-dimensional particle scale model can be well approximated by low dimensional order parameter based dynamic models.

3.4. Process control using MDP

Following the methods described in Section 2.3, we constructed four transition matrices, one for each of the four osmotic pressure values Π^* in the action space. To evaluate the accuracy of these transition matrices, Fig. 9 shows the 1000-realization averaged Markov chain Monte Carlo simulation based on sampling of the transition matrices, compared to 1000-realization averaged Brownian dynamics simulations. All these simulations are run under a constant Π^* value, i.e., without control.

In Fig. 9, 'BDUnCon' denotes the uncontrolled Brownian-dynamics simulation and 'MCUnCon' denotes the uncontrolled Markov chain Monte Carlo simulation. All the simulations started from the same fluid-like initial state with $R_g{}^* = 4.4$ and $D_{cc}{}^* = 5.15$,

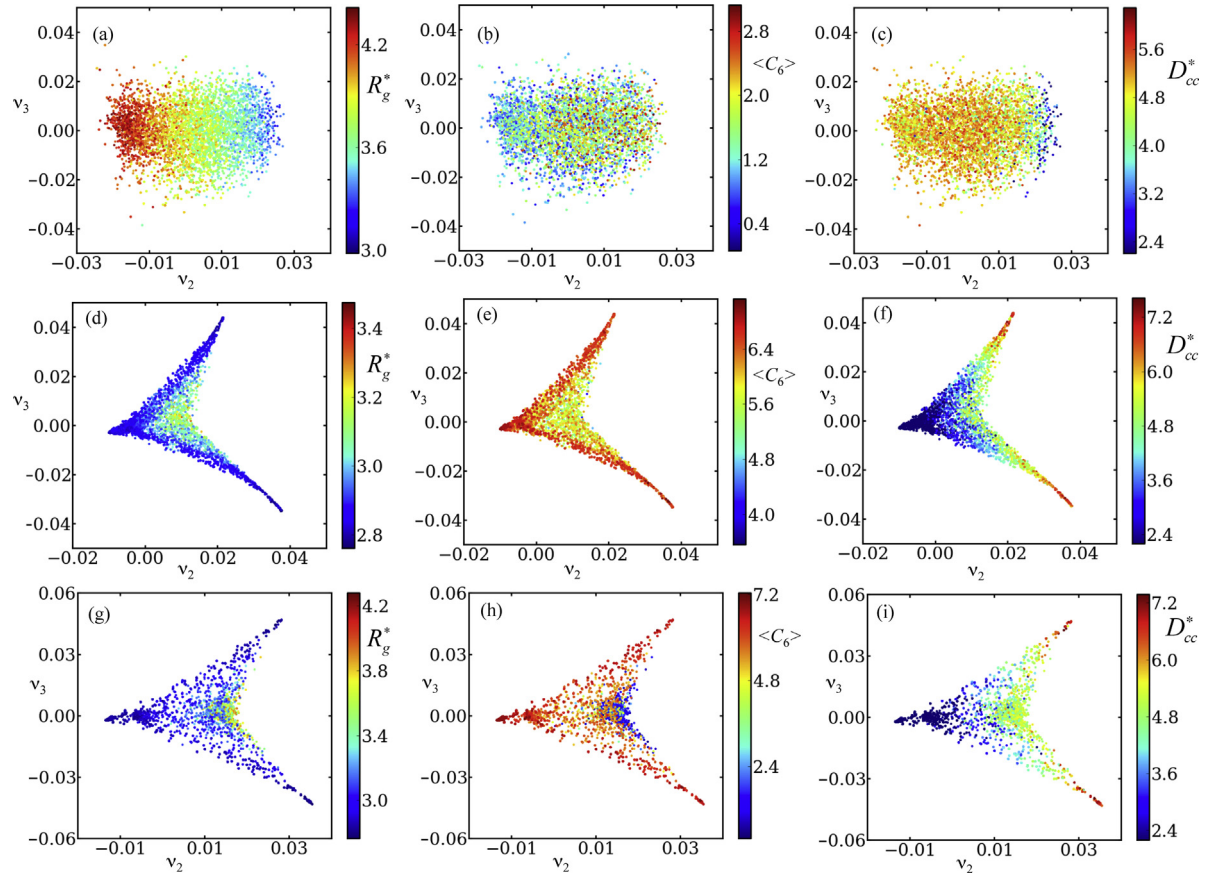

Fig. 5. Diffusion map representation of the three data sets described in the text, in the space of the first two eigenvectors. The top row (a–c) is for the fluid data set, the middle row (d–f) is for the crystal data set, and the bottom row (g–i) is for the combined data set. In the first column (a, d, g) the data points are colored by $R_g{}^*$, in the second column (b, e, h) the data points are colored by $\langle C_6 \rangle$, and in the third column (c, f, i) the data points are colored by $D_{cc}{}^*$. (For interpretation of the references to color in this figure legend, the reader is referred to the web version of this article.)

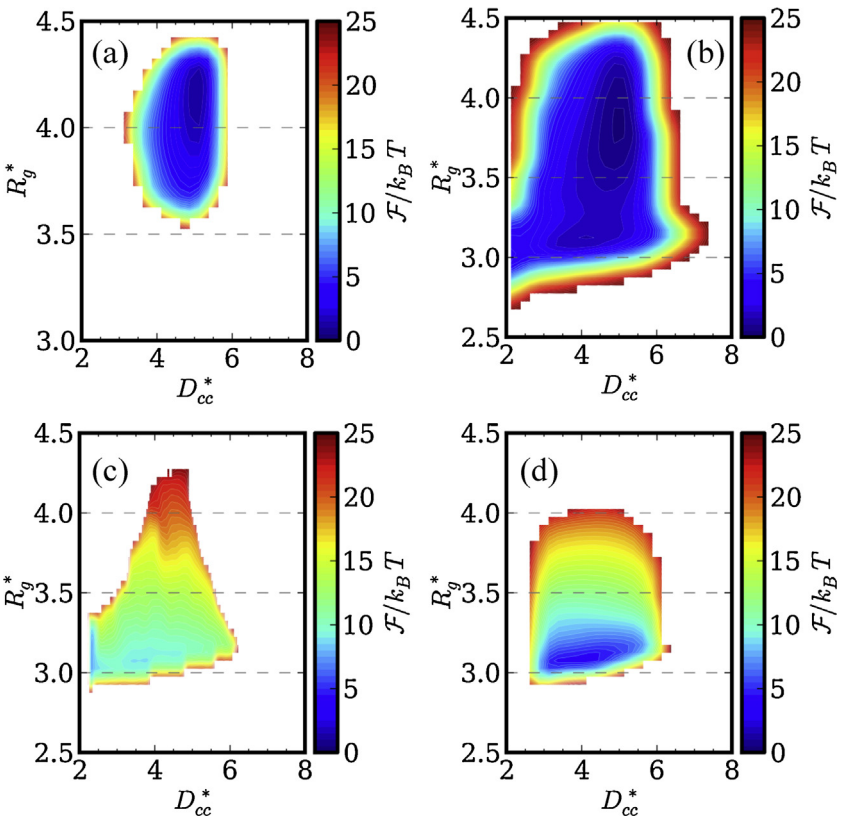

Fig. 6. Free energy landscapes $F(\mathbf{X})/kT$ as a function of $D_{cc}{}^*$ and $R_g{}^*$ obtained by fitting trajectories to the Smoluchowski equation at $\Pi^* = 1.05$ (a), 1.11 (b), 1.30 (c), and 1.90 (d).

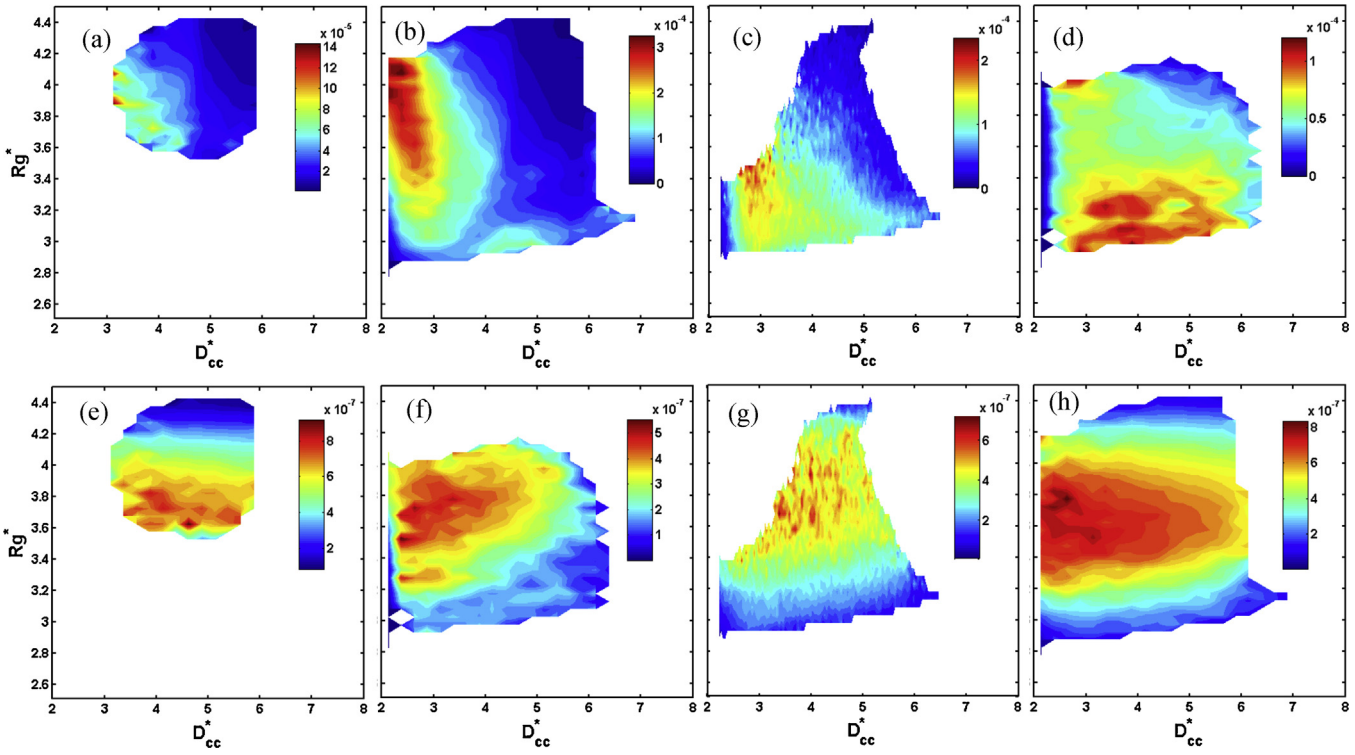

Fig. 7. Diagonal components $D_{D_{cc}^*D_{cc}^*}$ (upper row) and $D_{R_g^*R_g^*}$ (lower row) of the diffusivity landscape, in units of s^{-1}, obtained by fitting trajectories to Smoluchowski equation at $\Pi^* = 1.05$ (a, e), 1.11 (b, f), 1.30 (c, g), and 1.90 (d, h).

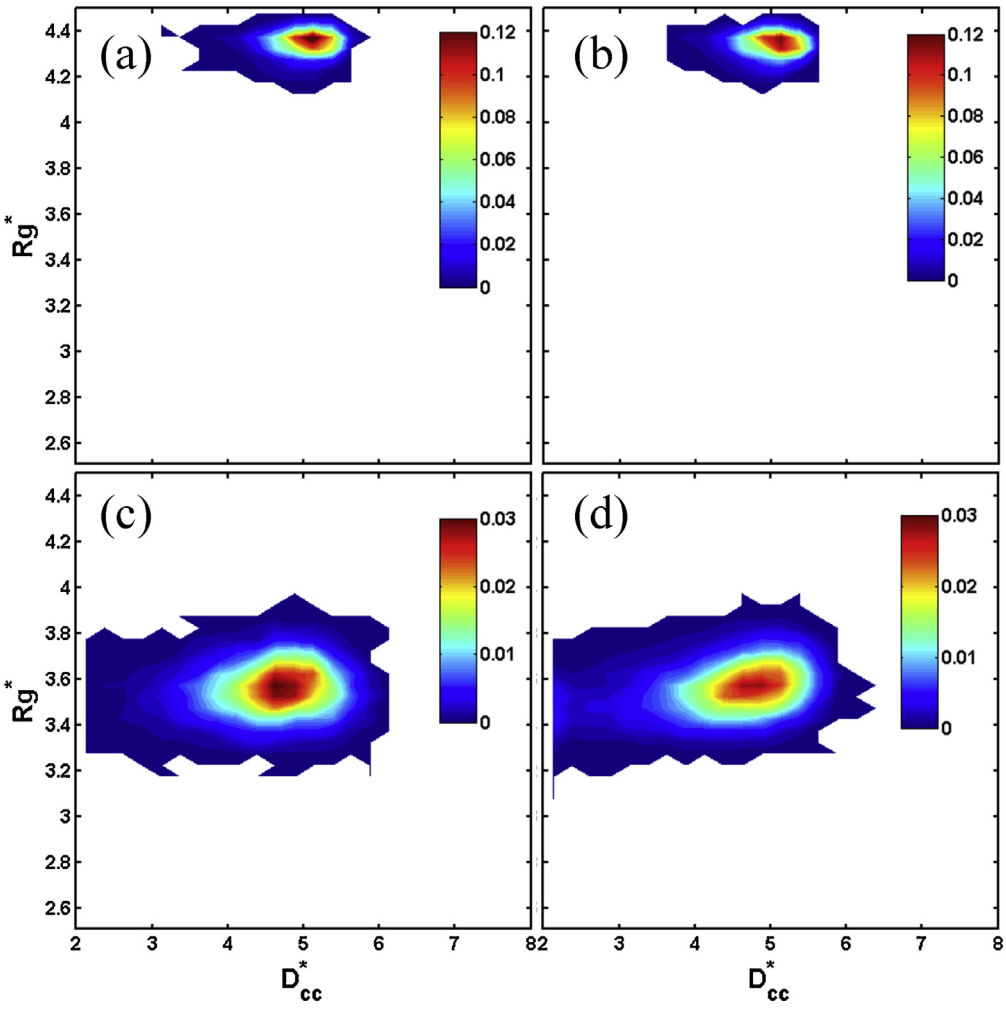

Fig. 8. Probability propagator $\rho(\mathbf{X}, t)$ obtained from BD and LDLD at $\Pi^* = 1.11$ with starting point (4.4, 5.2) (a) BD (b) LDLD and starting point (3.2, 4.5) (c) BD (d) LDLD with observation time 10 s.

and were simulated for 500 s. According to this comparison, the transition matrices P_a are able to approximate the BD simulation qualitatively and with reasonable quantitative accuracy, capturing the differences between the four osmotic pressures. Under high Π^* values (Π_3^* and Π_4^*), the system is able to reach a more crystalline final state (given the same amount of simulation time), indicated by lower $R_g{}^*$ and $D_{cc}{}^*$ values. Meanwhile, the system under Π_3^* can achieve greater condensation indicated by $R_g{}^*$, compared to Π_4^*. On the other hand, the system is able to achieve a lower $D_{cc}{}^*$ value under Π_4^* relative to Π_3^*. Given these observations, some combination of Π_3^* and Π_4^* might be desirable, in order to accomplish the goals of low $R_g{}^*$ and $D_{cc}{}^*$.

Given the transition matrix models, we constructed a time-independent optimal control policy with dynamic programming using the policy iteration algorithm. This two-dimensional control

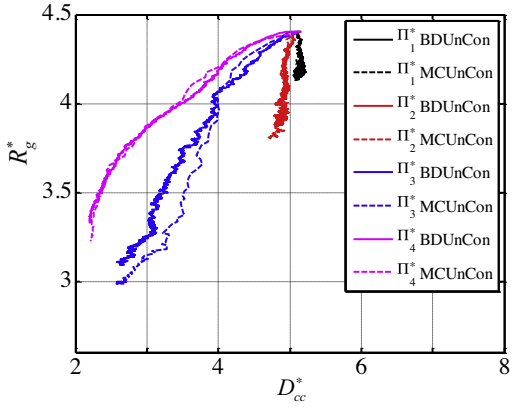

Fig. 9. Comparison between averaged MCMC and BD simulation order parameter trajectories for different constant input Π^* values from a system without feedback control.

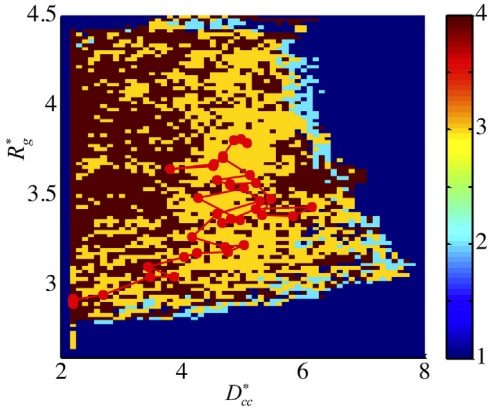

Fig. 10. Optimal control policy computed based on Markov chain model using dynamic programming.

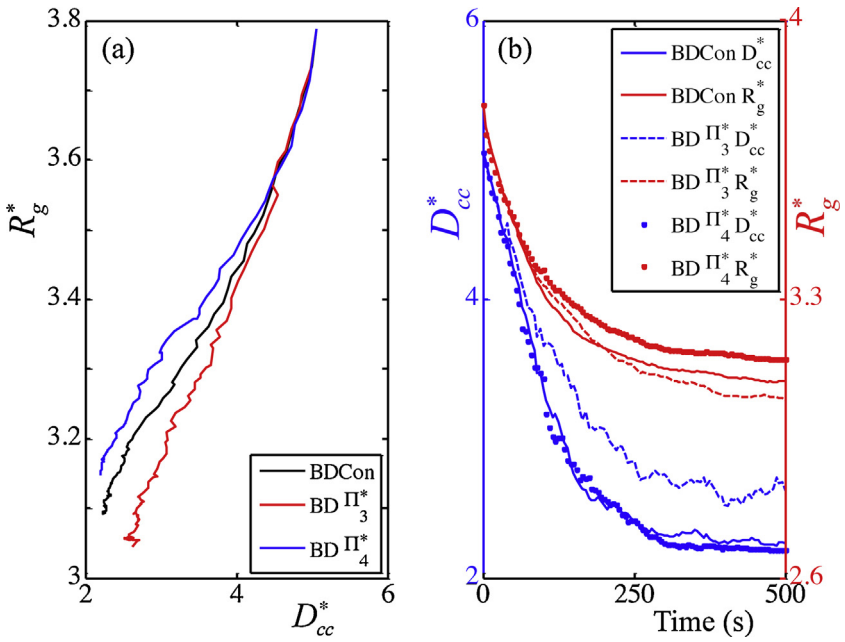

Fig. 11. Comparison between 500-s 250-realization-averaged order parameter trajectories with and without the control policy.

policy is shown in Fig. 10 as a lookup table. The numbers in the color bar stand for the control action Π^* values, increasing from Π_1^* to Π_4^* accordingly. Given its time-independent property, with the current R_g^* and D_{cc}^* values known, the corresponding control action can be taken directly from this table. With approximately 10,000 discrete states, the policy calculation can be achieved in only a few minutes.

According to Fig. 10, the optimal control policy chooses the high Π^* value, Π_3^* and Π_4^*, in most of the order-parameter state space. When the system is close to the global minimum point around $R_g^* = 2.8$ and $D_{cc}^* = 2.2$, indicated by the FELs, Π_4^* control is used in order to lock the system in the global minimum state. On top of the control policy is plotted a single controlled BD simulation result, starting from a fluid-like state of $R_g^* = 3.78$ and $D_{cc}^* = 5.0$. By switching between Π_3^* and Π_4^*, the system is able to reach a final state of $R_g^* = 2.9$ and $D_{cc}^* = 2.2$.

Moreover, the effectiveness of the control policy is evaluated by applying it to both the Markov chain transition matrix model and the BD simulation. A comparison of 250-realization-averaged order parameter simulation results with and without control in Brownian dynamics is given in Fig. 11.

In Fig. 11, the trajectory labeled as 'BDCon' stands for the 250-realization-averaged BD simulations with control. Trajectories labeled preceded with 'BDΠ^*' are 250-realization averaged Brownian dynamics simulation under constant Π^* values. All these trajectories are simulated for 500 s, starting from the same initial fluid-like state of $R_g^* = 3.78$ and $D_{cc}^* = 5.0$. Fig. 11(a) shows the averaged trajectories in the order-parameter phase plane. Inspection of the controlled trajectory reveals a decrease in the final D_{cc}^* value, compared to that under Π_3^*, as well as a lower R_g^* value compared to that under Π_4^*. Fig. 11(b) shows the same results as in Fig. 11(a), but now as a function of time. In all three cases the system responds on approximately the same timescale, but achieves different long-term states.

4. Conclusion

Application of feedback control in colloidal assembly is challenging, due to the nonlinear, stochastic, and high-dimensional dynamics, as well as the difficulty of real-time measurement. However, recent advantages in computation and in situ sensing make optimal model-based feedback control feasible. Reduced-order state representations and dynamic models link naturally to the framework of the Markov decision process, providing the optimal policy in a table-lookup form that requires virtually no online computation. Application of this approach to a Brownian Dynamics simulation of depletion-force mediated self-assembly demonstrates the feasibility of the approach, as well as the ability of a time-varying input to drive the system to a more desirable crystalline state.

Acknowledgments

M.A.B., D.M.F., M.A.G. and B.S. acknowledge financial support by the National Science Foundation through a set of collaborative Cyber Enabled Discovery and Innovation Grants (awards nos. CMMI-1124648, CMMI-1125188, CMMI-1124678, and CMMI-1261938). D.M. and R.M.S. acknowledge support by the U.S. Department of Energy, Office of Basic Energy Sciences, Division of Materials Sciences and Engineering, under award no. DE-FG02-07ER46407.

References

[1] O.D. Velev, S. Gupta, Adv. Mater. 21 (19) (2009) 1897–1905.
[2] M. Grzelczak, J. Vermant, E.M. Furst, L.M. Liz-Marzán, ACS Nano 4 (7) (2010) 3591–3605.
[3] S.C. Glotzer, M.J. Solomon, Nat. Mater. 6 (7) (2007) 557–562.
[4] D.E. Chang, N. Petit, Int. J. Robust Nonlinear Control 15 (16) (2005) 769–784.
[5] B. Edwards, N. Engheta, S. Evoy, J. Appl. Phys. 102 (2) (2007) 024913.
[6] M.P. Melnyk, D.E. Chang, Asian J. Control 13 (4) (2011) 480–491.
[7] G.J. Shah, A.T. Ohta, E.P.Y. Chiou, M.C. Wu, C.-J.C.J. Kim, Lab Chip 9 (12) (2009) 1732–1739.
[8] J.K. Fisher, J. Cribb, K.V. Desai, L. Vicci, B. Wilde, K. Keller, R.M. Taylor, J. Haase, K.E.T. Bloom, O. Brien, R. Superfine, Rev. Sci. Instrum. 77 (2) (2006), 023702.
[9] C. Gosse, V. Croquette, Biophys. J. 82 (6) (2002) 3314–3329.
[10] M.P. Kummer, J.J. Abbott, B.E. Kratochvil, R. Borer, A. Sengul, B.J. Nelson, IEEE Trans. Robot. 26 (6) (2010) 1006–1017.
[11] H. Lee, Y. Liu, R.M. Westervelt, D. Ham, IEEE J. Solid-State Circuits 41 (6) (2006) 1471–1480.
[12] M. Armani, S. Chaudhary, R. Probst, B. Shapiro, uTAS, Malmo, Sweden, 2004, pp. 26–30.
[13] M. Armani, S. Chaudhary, R. Probst, B. Shapiro, J. Micro-Electro-Mech. Syst. 15 (4) (2006) 945–956.
[14] A.E. Cohen, W.E. Moerner, Opt. Express 16 (10) (2008) 6941–6956.

[15] M.D. Curtis, G.J. Sheard, A. Fouras, Lab Chip 11 (14) (2011) 2343–2351.
[16] R. Probst, Z. Cummins, C. Ropp, E. Waks, B. Shapiro, IEEE Control Syst. Mag. 32 (2) (2012) 26–53.
[17] M. Tanyeri, M. Ranka, N. Sittipolkul, C.M. Schroeder, Lab Chip 11 (24) (2011) 4181–4186.
[18] P.L. Biancaniello, A.J. Kim, J.C. Crocker, Phys. Rev. Lett. 94 (2005), 058302.
[19] F. Soyka, O. Zvyagolskaya, C. Hertlein, L. Helden, C. Bechinger, Phys. Rev. Lett. 101 (20) (2008), 208301.
[20] G.E. Fernandes, D.J. Beltran-Villegas, M.A. Bevan, Langmuir 24 (2008) 10776–10785.
[21] G.E. Fernandes, D.J. Beltran-Villegas, M.A. Bevan, J. Chem. Phys. 131 (2009), 134705.
[22] J.J. Juarez, M.A. Bevan, Adv. Funct. Mater. 22 (18) (2012) 3833–3839.
[23] J.J. Juarez, S.E. Feicht, M.A. Bevan, Soft Matter 8 (1) (2012) 94–103.
[24] J.J. Juarez, P.P. Mathai, J.A. Liddle, M.A. Bevan, Lab Chip 12 (20) (2012) 4063–4070.
[25] Y. Xue, D.J. Beltran-Villegas, X. Tang, M.A. Bevan, IEEE Trans. Control Syst. Technol. (2014), http://dx.doi.org/10.1109/TCST.2013.2296700.
[26] C.F. Zukoski, Chem. Eng. Sci. 50 (24) (1995) 4073–4079.
[27] D.A. McQuarrie, Statistical Mechanics, HarperCollins, New York, 1976.
[28] W.B. Russel, D.A. Saville, W.R. Schowalter, Colloidal Dispersions, Cambridge University Press, New York, 1989.
[29] D. Frenkel, Physica A 313 (1–2) (2002) 1–31.
[30] L. Onsager, Ann. N. Y. Acad. Sci. 51 (4) (1949) 627–659.
[31] L. Belloni, J. Phys.: Condens. Matter 12 (46) (2000) R549–R587.
[32] T.L. Hill, An Introduction to Statistical Thermodynamics, Dover, New York, 1986.
[33] W.G. Mcmillan, J.E. Mayer, J. Chem. Phys. 13 (7) (1945) 276–305.
[34] S. Asakura, F. Oosawa, J. Chem. Phys. 22 (7) (1954) 1255–1256.
[35] D.C. Prieve, Adv. Colloid Interface Sci. 82 (1–3) (1999) 93–125.
[36] M.A. Bevan, S.L. Eichmann, Curr. Opin. Colloid Interface Sci. 16 (2) (2011) 149–157.
[37] J. Israelachvili, Y. Min, M. Akbulut, A. Alig, G. Carver, W. Greene, K. Kristiansen, E. Meyer, N. Pesika, K. Rosenberg, H. Zeng, Rep. Prog. Phys. 73 (3) (2010), 16.
[38] W.A. Ducker, T.J. Senden, R.M. Pashley, Nature 353 (6341) (1991) 239–241.
[39] D.L. Ermak, J.A. Mccammon, J. Chem. Phys. 69 (4) (1978) 1352–1360.
[40] T.J. Murphy, J.L. Aguirre, J. Chem. Phys. 57 (5) (1972), 2098.
[41] J.F. Brady, G. Bossis, Annu. Rev. Fluid Mech. 20 (1988) 111–157.
[42] D.J. Beltran-Villegas, R.M. Sehgal, D. Maroudas, D.M. Ford, M.A. Bevan, J. Chem. Phys. 132 (2010) 044707.
[43] H.-J. Wu, T.O. Pangburn, R.E. Beckham, M.A. Bevan, Langmuir 21 (22) (2005) 9879–9888.
[44] T.O. Pangburn, M.A. Bevan, J. Chem. Phys. 123 (2005), 174904.
[45] T.O. Pangburn, M.A. Bevan, J. Chem. Phys. 124 (2006), 054712.
[46] R.R. Coifman, S. Lafon, A.B. Lee, M. Maggioni, B. Nadler, F. Warner, S.W. Zucker, Proc. Natl. Acad. Sci. U. S. A. 102 (21) (2005) 7426–7431.
[47] A.L. Ferguson, A.Z. Panagiotopoulos, I.G. Kevrekidis, P.G. Debenedetti, Chem. Phys. Lett. 509 (1–3) (2011) 1–11.
[48] B. Nadler, S. Lafon, R.R. Coifman, I.G. Kevrekidis, Appl. Comput. Harmon. A 21 (1) (2006) 113–127.
[49] D.J. Beltran-Villegas, R.M. Sehgal, D. Maroudas, D.M. Ford, M.A. Bevan, J. Chem. Phys. 135 (2011) 154506.
[50] D.J. Beltran-Villegas, R.M. Sehgal, D. Maroudas, D.M. Ford, M.A. Bevan, J. Chem. Phys. 137 (2012) 134901.
[51] R.M. Sehgal, J.G. Cogan, D.M. Ford, D. Maroudas, Appl. Phys. Lett. 102 (2013) 201905.
[52] D.I. Kopelevich, A.Z. Panagiotopoulos, I.G. Kevrekidis, J. Chem. Phys. 122 (2005) 044908.
[53] G. Hummer, New J. Phys. 7 (1) (2005), 34.
[54] A. Banerjee, A. Pomerance, W. Losert, S. Gupta, IEEE Trans. Autom. Sci. Eng. 7 (2010) 218–227.
[55] Y. Xue, M.A. Grover, 2011 American Control Conference, San Francisco, CA, 2011, pp. 3269–3274.
[56] X. Tang, Y. Yang, M.A. Bevan, M.A. Grover, 2014 American Control Conference, Portland, OR, 2014, pp. 1120–1125.
[57] Y. Xue, D. Beltran-Villegas, M.A. Bevan, M.A. Grover, 2013 American Control Conference, Washington, DC, 2013, pp. 3334–3339.
[58] D.P. Bertsekas, Dynamic Programming and Optimal Control, vol. 2, Athena Scientific, Belmont, MA, 2012.
[59] M.L. Puterman, Markov Decision Processes Discrete Stochastic Dynamic Programming, Wiley-Interscience, Hoboken, NJ, 2005.
[60] J.-H. Prinz, H. Wu, M. Sarich, B. Keller, M. Senne, M. Held, J.D. Chodera, C. Schutte, F. Noe, J. Chem. Phys. 134 (2011), 174105.
[61] D.J. Beltran-Villegas, M.A. Bevan, Soft Matter 7 (7) (2011) 3280–3285.
[62] A.L. Ferguson, A.Z. Panagiotopoulos, P.G. Debenedetti, I.G. Kevrekidis, J. Chem. Phys. 134 (2011), 135103.
[63] T.D. Edwards, M.A. Bevan, Langmuir 28 (39) (2012) 13816–13823.

Soft Matter

PAPER

View Article Online
View Journal | View Issue

Cite this: *Soft Matter*, 2018, **14**, 934

Energy landscapes for ellipsoids in non-uniform AC electric fields†

Isaac Torres-Díaz, Bradley Rupp, Yuguang Yang and Michael A. Bevan *

Received 20th November 2017,
Accepted 24th December 2017

DOI: 10.1039/c7sm02287e

rsc.li/soft-matter-journal

We report a closed-form analytical model for energy landscapes of ellipsoidal particles in non-uniform high-frequency AC electric fields to identify all possible particle positions and orientations. Three-dimensional equilibrium positions and orientations of prolate ($r_x = r_y < r_z$), oblate ($r_x = r_z > r_y$), and scalene ($r_x \neq r_y \neq r_z$) ellipsoids are reported *vs.* field frequency and amplitude, which are determined from energy landscape minima. For ellipsoids within non-uniform electric fields between co-planar parallel electrodes, the number of configurations of position and orientation is 6 for prolate, 5 for oblate, and 9 for scalene ellipsoids. In addition, for coplanar electrodes, conditions are identified when particles can be treated using a quasi-2D analysis in the plane of their most probable elevation near an underlying surface. The reported expressions are valid for time-averaged interactions of ellipsoid particles in arbitrary AC electric field configurations, such that our results are applicable to electromagnetic tweezers interacting with particles having an appropriate material property contrast with the medium in the frequency range of interest.

Introduction

The ability to manipulate the position and orientation of microscopic objects with external fields without direct mechanical intervention is an enabling capability for many aspects of nano- and micro-technologies. An important precedent is the use of electromagnetic radiation to manipulate colloidal particles in various forms including optical fields (*e.g.*, optical tweezers[1]), electric fields (*e.g.*, dielectrophoresis[2]), and magnetic fields (*e.g.*, magnetic tweezers[3,4]). A key aspect to all of these approaches is understanding very accurately how the applied field interacts with the object of interest. For example, understanding particle interactions with a focused laser beam is critical to designing and operating optical tweezer apparatus and optimizing for different particle material properties.[5] The same is true of manipulating magnetic particles with various magnetic field configurations.[6]

Here, we are concerned with ellipsoidal particles, having up to the three different axes (*i.e.*, tri-axial), interacting with non-uniform high frequency AC electric fields (Fig. 1). The ability to measure and model such particle–field interactions provides a basis to manipulate the position and orientation of anisotropic particles. Although a significant body of research has focused on transport of particles in AC electric fields,[7,8] which is referred to as dielectrophoresis, here we are specifically interested in the time-averaged interaction of induced dipoles with non-uniform AC electric fields. For example, previous work on spherical particles has shown how dipole-field interactions produce energy landscapes (energy *vs.* position) that dictate the forces, torques, and thermal sampling of particles about equilibrium positions located at either electric field maxima or minima at different field frequencies.[9–11]

For anisotropic colloidal particles, it is commonly understood that particles often align with their long-axis parallel to the dominant electric field direction during transport[7,8] and in concentrated systems.[12–15] However, it has also been known for some time, from at least two prior studies, that single uni-axial particles in AC electric fields can orient both parallel and perpendicular to field lines (for anisotropic cells).[16,17] The theory underlying this phenomena pre-dates these experimental observations,[18] but other than being used to capture frequency dependent cell orientations, it has not been used to model potential energy landscapes in colloidal systems with well-defined material properties. In particular, the authors are unaware of any previous studies that report the position and orientation dependent energy landscapes of anisotropic colloidal particles as a function of field frequency and amplitude.

In this work, we report closed-form energy landscapes for dielectric ellipsoids in non-uniform, high-frequency AC electric fields between coplanar electrodes (Fig. 1). Results are reported for prolate, oblate, and scalene ellipsoids as a function of field frequency and amplitude. In general, for scalene (*i.e.*, tri-axial) ellipsoids, net potential energy landscapes from superposition

Chemical & Biomolecular Engineering, Johns Hopkins University, Baltimore, MD 21218, USA. E-mail: mabevan@jhu.edu

† Electronic supplementary information (ESI) available. See DOI: 10.1039/c7sm02287e

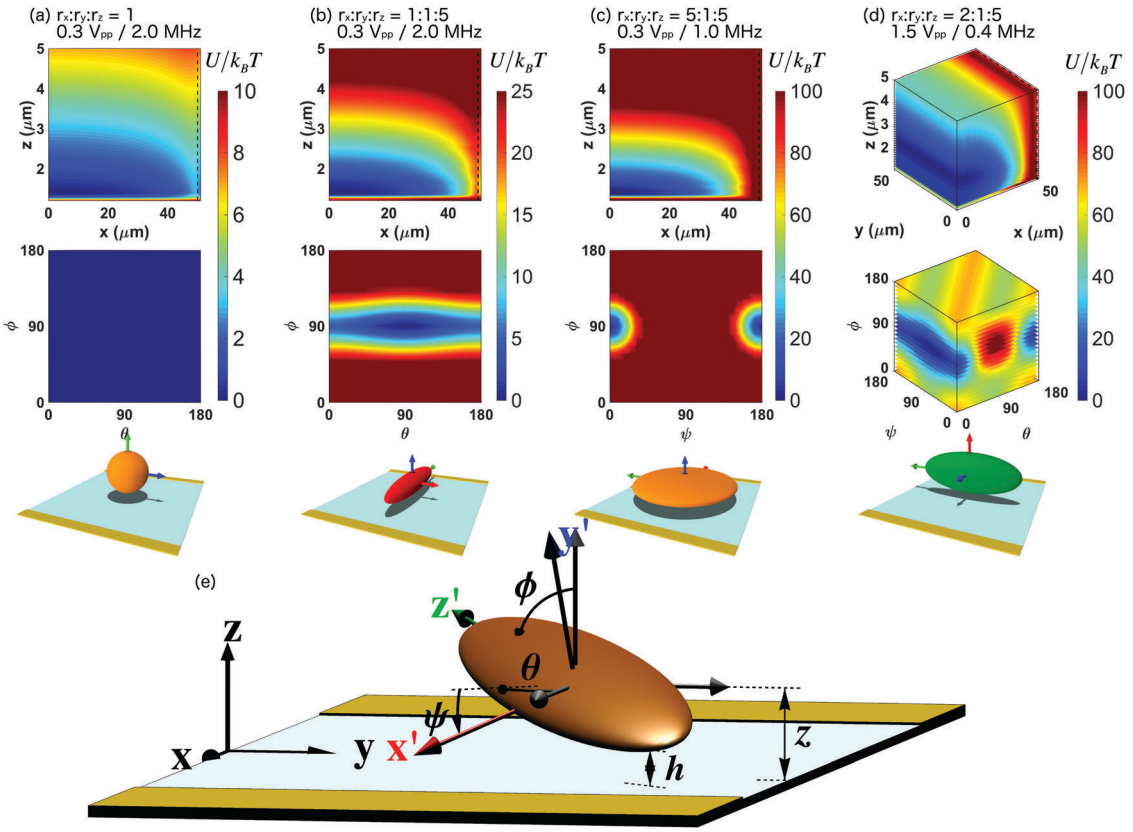

Fig. 1 Projected net potential energy for position and orientation of ellipsoids in non-uniform high-frequency AC electric fields between coplanar parallel electrodes (100 μm gap). (a) x–z and θ–ϕ projections for sphere ($r_x : r_y : r_z = 1$ μm) in 2 MHz 0.3 V_{pp} AC field. (b) x–z and θ–ϕ projections for prolate ellipsoid ($r_x : r_y : r_z = 1 : 1 : 5$ μm) in 2 MHz 0.3 V_{pp} AC field. (c) x–z and ψ–ϕ projections for oblate ellipsoid ($r_x : r_y : r_z = 5 : 1 : 5$ μm) in 1.0 MHz 0.3 V_{pp} AC field. (d) x–y–z and θ–ψ–ϕ projections for scalene ellipsoid ($r_x : r_y : r_z = 2 : 1 : 5$ μm) in 0.4 MHz 1.3 V_{pp} AC field. Equilibrium particle configuration (not to scale) is depicted at each condition. Particle x', y' and z' axes are represented as red, blue and green arrows. Material parameters are reported in Table 1. (d) Schematic of scalene ellipsoid arbitrarily orientated relative to coplanar parallel electrodes (not at scale) with orientation given by Euler angles (ϕ, θ, ψ). Colored primed coordinates attached to particle semi-axes are referred to as particle coordinates. Black unprimed coordinates attached to the planar surface are referred to as laboratory coordinates. Also labeled are the particle surface-wall minimum distance, h, and particle center elevation relative to the wall, z.

of substrate,[19] gravity, and electric field mediated interactions depend on six variables, with three for position and three for orientation as,

$$u^{\text{net}}(\mathbf{X}, \mathbf{\Theta}) = u^{\text{net}}(x, y, z, \theta, \phi, \psi), \quad (1)$$

where $\mathbf{X} = (x, y, z)$ represents the particle center of mass position, and $\mathbf{\Theta} = (\theta, \phi, \psi)$ the particle orientation. In contrast, the symmetry of prolate and oblate ellipsoids requires fewer orientation variables, and spheres have no orientation dependence. The present analysis of the time average potential energy landscapes for minimum energy states yields all available combinations of position and orientation for different field conditions and for different particle shapes. Results and findings include representative example energy landscapes, visual and plotted state diagrams of possible states, and an analysis of conditions where quasi-two dimensional behavior is a reasonable approximation of the six dimensional dependence in eqn (1). The theoretical potentials presented in this work are general to other electrode configurations and should be extensible to describe particle–field potentials and orientations in concentrated systems.

Theory

Laboratory & particle coordinates

Consider an ellipsoidal colloidal particle near a planar surface (Fig. 1(e)). The colloid is under the influence of a non-uniform AC electric field generated between parallel thin electrodes of negligible thickness. The ellipsoid principal semi-axes (r_x, r_y, r_z) are directed along the x', y', and z' axes, which is the particle frame. The unprimed axes x, y, and z represent the laboratory coordinates with origin between the symmetry plane electrode gap center. The relative orientation of the particle is defined by the Euler angles (θ, ϕ, ψ), where ϕ represents the polar angle, θ the azimuthal angle, and ψ the rotation angle around the z' axis. The variable x represents the particle position relative to the electrode gap center, z is the elevation of the particle center relative the planar wall surface, and h represents the distance of closest

approach between the particle and wall. In the following, it will be shown how to relate variables in the laboratory (x, y, z) and particle (x', y', z') frames by a rotation transformation matrix.

Net potential energy landscape

The net potential energy of a particle near a planar wall (Fig. 1(e)) under the influence of an AC electric field is given by particle–wall (pw) and particle–field (pf) interactions

$$u^{\text{net}}(\mathbf{X}, \mathbf{\Theta}) = u^{\text{pw}}(\mathbf{X}, \mathbf{\Theta}) + u^{\text{pf}}(\mathbf{X}, \mathbf{\Theta}), \tag{2}$$

where $\mathbf{X} = (x, y, z)$ and $\mathbf{\Theta} = (\theta, \phi, \psi)$. In this work, due to the symmetry of electrodes, there is no dependence in the y-direction. For axisymmetric particles, like prolate ($r_x = r_y < r_z$) and oblate ($r_x = r_z > r_y$) ellipsoids, the net potential energy does not depend on the angle ψ and θ, respectively (Fig. 1). For uniform spherical particles, the angular dependence vanishes.[10] The present study is concerned only with particles within the non-uniform electric field between electrodes, so that particle-electrode interactions are not considered.

Particle–wall potential

The particle–wall potential allows particles to sample different positions and orientations without touching the substrate. Particle–wall interactions are considered to be dominated by electrostatic repulsion with a negligible van der Waals contribution. The net particle–wall interaction energy is given by electrostatic interaction[19–21]

$$u^{\text{pw}}(z, \phi, \theta, \psi) = \frac{Z \exp(-\kappa h)}{\sqrt{\Gamma}}, \tag{3}$$

$$Z = 64\pi\varepsilon_{\text{m}}\left(\frac{k_{\text{B}}T}{z_{\text{v}}e}\right)^2 \tanh\left(\frac{z_{\text{v}}e\psi_{\text{p}}}{4k_{\text{B}}T}\right)\tanh\left(\frac{z_{\text{v}}e\psi_{\text{w}}}{4k_{\text{B}}T}\right), \tag{4}$$

where κ^{-1} is the Debye length, ε_{m} is the medium dielectric constant, k_{B} is Boltzmann's constant, T is the absolute temperature, e is the electron charge, z_{v} is electrolyte valence, and ψ_{p} and ψ_{w} are particle and wall surface potentials. Γ is the Gaussian curvature of the particle where the distance between surfaces, h, is minimum. For ellipsoidal particles, h is function of both particle position and orientation, and Γ is a function only of the relative particle orientation given by[19]

$$h(z, \phi, \theta, \psi) = z - \sqrt{(r_x A_{13})^2 + (r_y A_{23})^2 + (r_z A_{33})^2},$$

$$\Gamma(\phi, \theta, \psi) = \frac{\left[(r_x A_{13})^2 + (r_y A_{23})^2 + (r_z A_{33})^2\right]^2}{r_x^2 r_y^2 r_z^2},$$

$$A_{13} = \sin\psi\sin\phi, \quad A_{23} = \cos\psi\sin\phi, \quad A_{33} = \cos\phi. \tag{5}$$

Particle–field potentials

The net particle–field interaction includes the gravitational potential energy and the interaction of the induced dipole with the applied electric field given by superposition as

$$u^{\text{pf}}(\mathbf{X}, \mathbf{\Theta}) = u_{\text{g}}^{\text{pf}}(z) + u_{\text{de}}^{\text{pf}}(\mathbf{X}, \mathbf{\Theta}), \tag{6}$$

where the gravitational potential energy relative to the substrate is given by

$$u_{\text{g}}^{\text{pf}}(z) = v_{\text{p}}(\rho_{\text{p}} - \rho_{\text{m}})gz, \tag{7}$$

where $v_{\text{p}} = 4\pi r_x r_y r_z/3$ is the particle volume, g is acceleration due to gravity, ρ_{p} and ρ_{m} are the particle and medium densities. For a dielectric ellipsoidal particle, the interaction energy between the induced dipole and the applied electric field is[18]

$$u_{\text{de}}^{\text{pf}} = -k_{\text{B}}T\lambda\sum_{i=1}^{3}\left[\frac{f_{\text{CM},i}}{|f_0|^2}\left(E_i^{*\prime}\right)^2\right], \tag{8}$$

$$\lambda \equiv (3/4)(\varepsilon_{\text{m}}v_{\text{p}}/k_{\text{B}}T)|f_0|^2(E_0^{*})^2, \tag{9}$$

where λ is a dimensionless ratio of the magnitude of the time-average induced dipole–field interaction energy and the thermal energy. The index i = 1, 2, 3 (x', y', z') represents the particle principal axes, $f_{\text{CM},i}$ is the Clausius–Mossotti factor along the particle's i-axis, and f_0 is the f_{CM} of the shortest axis at zero frequency. The f_{CM} along the i-axis of the particle is defined by[18]

$$f_{\text{CM},i} = \text{Re}\left[\frac{1}{3}\frac{\tilde{\varepsilon}_{\text{p},i} - \tilde{\varepsilon}_{\text{m}}}{\tilde{\varepsilon}_{\text{m}} + (\tilde{\varepsilon}_{\text{p},i} - \tilde{\varepsilon}_{\text{m}})L_i}\right], \tag{10}$$

where $\tilde{\varepsilon}_{\text{m}}$ is the complex medium permittivity, $\tilde{\varepsilon}_{\text{p},i}$ is the complex particle permittivity along the i-axis of the particle. Both are expressed as $\tilde{\varepsilon} = \varepsilon - i\sigma/\omega$, where σ is conductivity, and ω is the electric field frequency. L_i is a parameter defined in the solution of Laplace's equation in ellipsoidal coordinates, which quantifies the anisotropy of the particle along the i-axis[18]

$$L_i = \frac{r_x r_y r_z}{2}\int_0^\infty \frac{\text{d}\alpha}{(\alpha + r_i^2)\sqrt{(\alpha + r_x^2)(\alpha + r_y^2)(\alpha + r_z^2)}}. \tag{11}$$

In eqn (9), $E_i^{*\prime} = E_i'/(V_{\text{pp}}/\pi d_{\text{g}})$ is the normalized electric field in the direction of the i-axis of the particle, where $V_{\text{pp}} = 2V_0$ is the peak-to-peak voltage, and d_g is the electrode gap. The electric field in the particle coordinates $\mathbf{E}'$ is related to the field in laboratory coordinates $\mathbf{E}$ by

$$\mathbf{E}' = \mathbf{A}\cdot\mathbf{E}, \tag{12}$$

where the rotation transformation matrix $\mathbf{A}$ is defined by

$$\mathbf{A} = \begin{pmatrix} A_{11} & A_{12} & A_{13} \\ A_{21} & A_{22} & A_{23} \\ A_{31} & A_{32} & A_{33} \end{pmatrix} = \begin{pmatrix} \cos\psi\cos\theta - \cos\phi\sin\theta\sin\psi & \cos\psi\sin\theta + \cos\phi\cos\theta\sin\psi & \sin\psi\sin\phi \\ -\sin\psi\cos\theta - \cos\phi\sin\theta\cos\psi & -\sin\psi\sin\theta + \cos\phi\cos\theta\cos\psi & \cos\psi\sin\phi \\ \sin\phi\sin\theta & -\sin\phi\cos\theta & \cos\phi \end{pmatrix} \tag{13}$$

where in the present work, we use Euler angles, although an alternative way to describe this system is using quaternion parameters (e_0, e_1, e_2, e_3).[22] The electric field, **E**, between coplanar electrodes is[23]

$$E_x = \frac{2V_0}{\pi d}\left[\tan^{-1}\left(\frac{\sin\hat{x}}{\sinh\hat{z}}\right) - \tan^{-1}\left(\frac{\cos\hat{x}}{\sinh\hat{z}}\right)\right],$$
$$E_z = \frac{V_0}{\pi d}\left[\ln\left(\frac{\cosh\hat{z}+\cos\hat{x}\cosh\hat{z}+\sin\hat{x}}{\cosh\hat{z}-\cos\hat{x}\cosh\hat{z}-\sin\hat{x}}\right)\right], \quad (14)$$

where $\hat{x} = \pi(x + d)/2d + \pi/4$ and $\hat{z} = \pi z/2d$, where d is the electrode gap. In eqn (8), the electric field can be expressed in normalized form as $\mathbf{E}^* = \mathbf{E}/(V_{pp}/\pi d)$.

Probability distributions & potentials

For particles near infinite dilution, the probability $p(\mathbf{X}, \mathbf{\Theta}) = p(x, y, z, \phi, \theta, \psi)$ of sampling different positions and orientations is related to potential energy by Boltzmann's equation as

$$p(\mathbf{X}, \mathbf{\Theta}) = p(\mathbf{X}_r, \mathbf{\Theta}_r)\exp[-(u^{net}(\mathbf{X}, \mathbf{\Theta}) - u^{net}(\mathbf{X}_r, \mathbf{\Theta}_r))/k_BT], \quad (15)$$

where $u^{net}(\mathbf{X}, \mathbf{\Theta})$ is the net potential energy in eqn (2), and $\mathbf{X}_r$ and $\mathbf{\Theta}_r$ are the reference position and orientation in the relative potential energy. Since the net potential energy of the anisotropic particle has a dependence on six variables, it is necessary to reduce the dimensionality of probability distributions and potentials for visualization and comparison with experimental data. The angle-averaged distribution $\langle p(\mathbf{X})\rangle_{\mathbf{\Theta}}$ can be calculated by[24]

$$\langle p(\mathbf{X})\rangle_{\mathbf{\Theta}} = \int_{\psi_i}^{\psi_f}\int_{\phi_i}^{\phi_f}\int_{\theta_i}^{\theta_f} p(x,y,z,\phi,\theta,\psi)\sin\phi\,d\theta\,d\phi\,d\psi \Big/ \int_{\psi_i}^{\psi_f}\int_{\phi_i}^{\phi_f}\int_{\theta_i}^{\theta_f}\sin\phi\,d\theta\,d\phi\,d\psi, \quad (16)$$

where the integration limits are 0 and 180 degrees due to particles' orientational symmetry. Eqn (16) can be used to determine the effective position dependent, or angle-averaged, potential $\langle u^{net}(\mathbf{X})\rangle_{\mathbf{\Theta}}$ *via* an inverse Boltzmann's relation as

$$\frac{\langle u^{net}(\mathbf{X})\rangle_{\mathbf{\Theta}} - \langle u^{net}(\mathbf{X}_r)\rangle_{\mathbf{\Theta}}}{k_BT} = \ln\left[\langle p(\mathbf{X}_r)\rangle_{\mathbf{\Theta}}/\langle p(\mathbf{X})\rangle_{\mathbf{\Theta}}\right]. \quad (17)$$

and, in a similar way, the position-averaged distribution $\langle p(\mathbf{\Theta})\rangle_{\mathbf{X}}$ can be calculated by

$$\langle p(\mathbf{\Theta})\rangle_{\mathbf{X}} = \frac{1}{(z_f - z_i)(y_f - y_i)(x_f - x_i)}\int_{z_i}^{z_f}\int_{y_i}^{y_f}\int_{x_i}^{x_f} p(x,y,z,\phi,\theta,\psi)\,dx\,dy\,dz, \quad (18)$$

where the integration limits in x and y are defined by the electrode geometry and z must be greater than the longest particle axis. Eqn (18) can be used to determine the effective orientation dependent, or position-averaged potential $\langle u^{net}(\mathbf{\Theta})\rangle_{\mathbf{X}}$ as a function particle orientation as

$$\frac{\langle u^{net}(\mathbf{\Theta})\rangle_{\mathbf{X}} - \langle u^{net}(\mathbf{\Theta}_r)\rangle_{\mathbf{X}}}{k_BT} = \ln\left[\langle p(\mathbf{\Theta}_r)\rangle_{\mathbf{X}}/\langle p(\mathbf{\Theta})\rangle_{\mathbf{X}}\right]. \quad (19)$$

Another lower-dimensional case of interest is the quasi-2D distribution of states projected onto a surface, which is often the case with optical microscopy measurements.[25–27] For the position, x, and orientation angle, θ, of the particle, the average probability is expressed as

$$\langle p(x,\theta)\rangle_{y,z,\phi,\psi} = \frac{\int_{z_i}^{z_f}\int_{y_i}^{y_f}\int_{\phi_i}^{\phi_f}\int_{\psi_i}^{\psi_f} p(x,y,z,\phi,\theta,\psi)\,dz\,dy\,d\phi\,d\psi}{(z_f - z_i)(y_f - y_i)(\phi_f - \phi_i)(\psi_f - \psi_i)}, \quad (20)$$

which can be used to calculate the effective projected potential $\langle u^{net}(x,\theta)\rangle_{y,z,\phi,\psi}$ by

$$\frac{\langle u^{net}(x,\theta)\rangle_{y,z,\phi,\psi} - \langle u^{net}(x_r,\theta_r)\rangle_{y,z,\phi,\psi}}{k_BT} = \ln\left[\langle p(x_r,\theta_r)\rangle_{y,z,\phi,\psi}\Big/\langle p(x,\theta)\rangle_{y,z,\phi,\psi}\right]. \quad (21)$$

Quasi-2D analysis

In the following, an estimate is provided for the maximum applied voltage when a quasi-2D analysis is appropriate. For a particle at the middle of the gap at a fixed orientation parallel to the x-component of the field, the net potential energy of the particle (eqn (2)) reduces to

$$\frac{u^{net}(z)}{k_BT} = B_e\frac{\exp(-\kappa h)}{\sqrt{r_m^2\Gamma}} + G\frac{z}{r_m} - 4\lambda\frac{f_{cm,i}}{|f_0|^2}\tan^{-1}\left(\frac{1}{\sqrt{2}}\mathrm{csch}\left(\frac{\pi z}{2d}\right)\right)^2, \quad (22)$$

where $G \equiv \nu_p(\rho_p - \rho_m)gr_m/k_BT$, $B_e \equiv Zr_m/k_BT$, and r_m is the minimum semi-axis length of the particle. Eqn (22) shows that in the middle of the gap at a fixed orientation, the equilibrium position is determined by a balance between gravity, electrostatic repulsion, and the gradient of the x-component of the field along the z-axis. For conditions where the particle is not close to the surface where electrostatic interactions are negligible, the minimum energy state (where the gradient of eqn (22) vanishes) yields the maximum ratio between electrical and gravitational energy required for quasi-2D behavior as

$$\frac{\lambda}{G} = \frac{1}{4}\left|\frac{f_0^2}{f_{cm,i}}\right|\frac{\sqrt{2}}{\pi^2}\frac{d_g}{r_m}\frac{d_g}{d_g - 2z}, \quad (23)$$

which upon further simplification after inserting λ and G yields the maximum applied voltage as

$$V_{pp,max} = \pi d_g\sqrt{\frac{\sqrt{2}}{\pi^2}\frac{(\rho_p - \rho_m)g}{3\varepsilon_m}\frac{d_g}{|f_{cm,i}|}\left(\frac{d_g}{d_g - 2z}\right)}, \quad (24)$$

where in eqn (23) and (24) the analytical form is simplified *via* the following approximation

$$\frac{d}{dz}\left[\tan^{-1}\left(\frac{1}{\sqrt{2}}\mathrm{csch}\left(\frac{\pi z}{2d_g}\right)\right)^2\right] \approx \frac{\pi^2}{\sqrt{2}d_g}\left(1 - \frac{2z}{d_g}\right) \quad (25)$$

Since eqn (24) is an estimated value of the maximum voltage for a quasi-2D analysis, the position of the particle can be evaluated as the axis length perpendicular to the wall (*e.g.*, $z = r_x$).

Results & discussion

Particle shapes & physical parameters

The equilibrium position and orientation of ellipsoidal particles are investigated in non-uniform AC electric fields for different aspect ratios and typical material properties (Table 1). We consider three representative particle shapes with aspect ratios of: (a) $r_x : r_y : r_z$ = 1 : 1 : 5 μm (prolate), (b) 5 : 1 : 5 μm (oblate), and (c) 2 : 1 : 5 μm (scalene). The particle and medium dielectric constants were fixed to $\varepsilon_m = 78\varepsilon_0$ and $\varepsilon_p = 3.2\varepsilon_0$, which are typical values reported for water and polymer colloids (*e.g.*, SU8 photoresist particles). The conductivities along different axes for each ellipsoid type in Table 1 are motivated by parameters identified in preliminary experimental results (unpublished). Finally, in an initial parametric search, the medium conductivity was systematically varied from 1 to 10 μS cm^{-1} (while fixing all other properties) to identify conditions for the maximum number of states for each case, which produced the medium conductivities in Table 1. The material parameters reported in Table 1 are realistic for dielectric particles in low ionic strength aqueous media and are useful for analyzing how f_{CM} along different particle axes influence equilibrium positions and orientations *vs.* field frequency and amplitude.

Fig. 2 shows the f_{CM} for the principal axes of the ellipsoidal particles as a function of medium conductivity and AC field frequency. Due to the shape anisotropy, the f_{CM} associated with different particle axes have different crossover frequencies. Fig. 2 shows the interval of crossover frequencies is shorter as the conductivity of the surrounding medium increases. For isotropic spherical particles, the three axes have the same f_{CM} with the same crossover frequency.[7] In the following, we show the conditions that generate a greater number of positions and orientations between the parallel electrodes as a function of the field frequency.

Energy landscape for prolate ellipsoids

Prolate particles have symmetry along the z'-axis, which eliminates any ψ-angle dependence. Since the y-component of the field is zero there is no dependence along that coordinate. In Fig. 3, results are shown for the projected 2D position (x, z) and orientation (θ, ϕ) energy landscapes (eqn (2), (17) and (19)) for a prolate particle ($r_x : r_y : r_z$ = 1 : 1 : 5 μm) at four different field

Table 1 Properties of media and ellipsoids investigated in this study. For each aspect ratio, columns report surface conductivities of each particle axis as well as the medium conductivity. The medium and particle dielectric constants in call cases are $\varepsilon_m = 78\varepsilon_0$ and $\varepsilon_p = 3.2\varepsilon_0$

Shape	$r_x : r_y : r_z$	σ_x (μS cm^{-1})	σ_y (μS cm^{-1})	σ_z (μS cm^{-1})	σ_m (μS cm^{-1})
Prolate	1 : 1 : 5	20	20	40	3
Oblate	5 : 1 : 5	30	10	30	1
Scalene	2 : 1 : 5	20	12	26	2

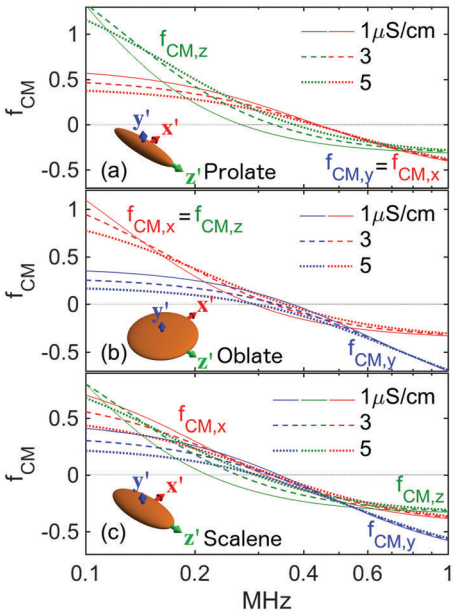

Fig. 2 Clausius–Mossotti factors, f_{CM}, for principal axes of ellipsoids *vs.* electric field frequency and medium conductivity (see inset legends). The particle aspect ratios are $r_x : r_y : r_z$ = (a) 1 : 1 : 5 μm, (b) 5 : 1 : 5 μm, and (c) 2 : 1 : 5 μm, which are depicted in the panel insets. Material parameters are in Table 1.

conditions, and the renderings for the minimum energy landscape. For field conditions of 100 kHz and 0.3 V_{pp}, Fig. 3(a), the minimum of the projected energy landscape indicates that the equilibrium state of the particle center is located close to the edge of the electrode gap, as in the case of spherical particles.[10] However, due to the particle aspect ratio, the projected energy landscape of the particle position possesses three relative energy minima at different elevations (Fig. 3(a)). These energy minima are not reflected in the orientational projection of the energy landscape, where it is shown that the long axis of the particle is oriented parallel to the field x-component. This corresponds to the configuration shown in red in the bottom rendering.

For field conditions of 300 kHz and 0.3 V_{pp}, Fig. 3(b) shows the positional and orientational projections of the energy landscape, which indicate that the equilibrium state of the particle center is located close to the edge of the electrode gap, and the long axis is perpendicular to the field x-component. Here, the minimum appears at $\theta = 0^\circ$ or 180°, indicating that the z'-axis of the particle could be oriented along the positive or negative y-direction in the laboratory coordinates. The change in the particle orientation between 100 and 300 kHz is correlated with the crossover frequency between the f_{CM} along the long axis (z-axis) and short axis (x-axis), as depicted in Fig. 2. Again, this effect is not seen in spheres[10] since they are isotropic.

For a further frequency increase, at 500 kHz and 0.3 V_{pp}, the minimum of the positional and orientational projections of the energy landscape indicate that the equilibrium state of the particle keeps the same orientation as for 300 kHz, but it is now located in the middle of the electrode gap as shown in Fig. 3(c). Here, the transition between the particle position at the edge of

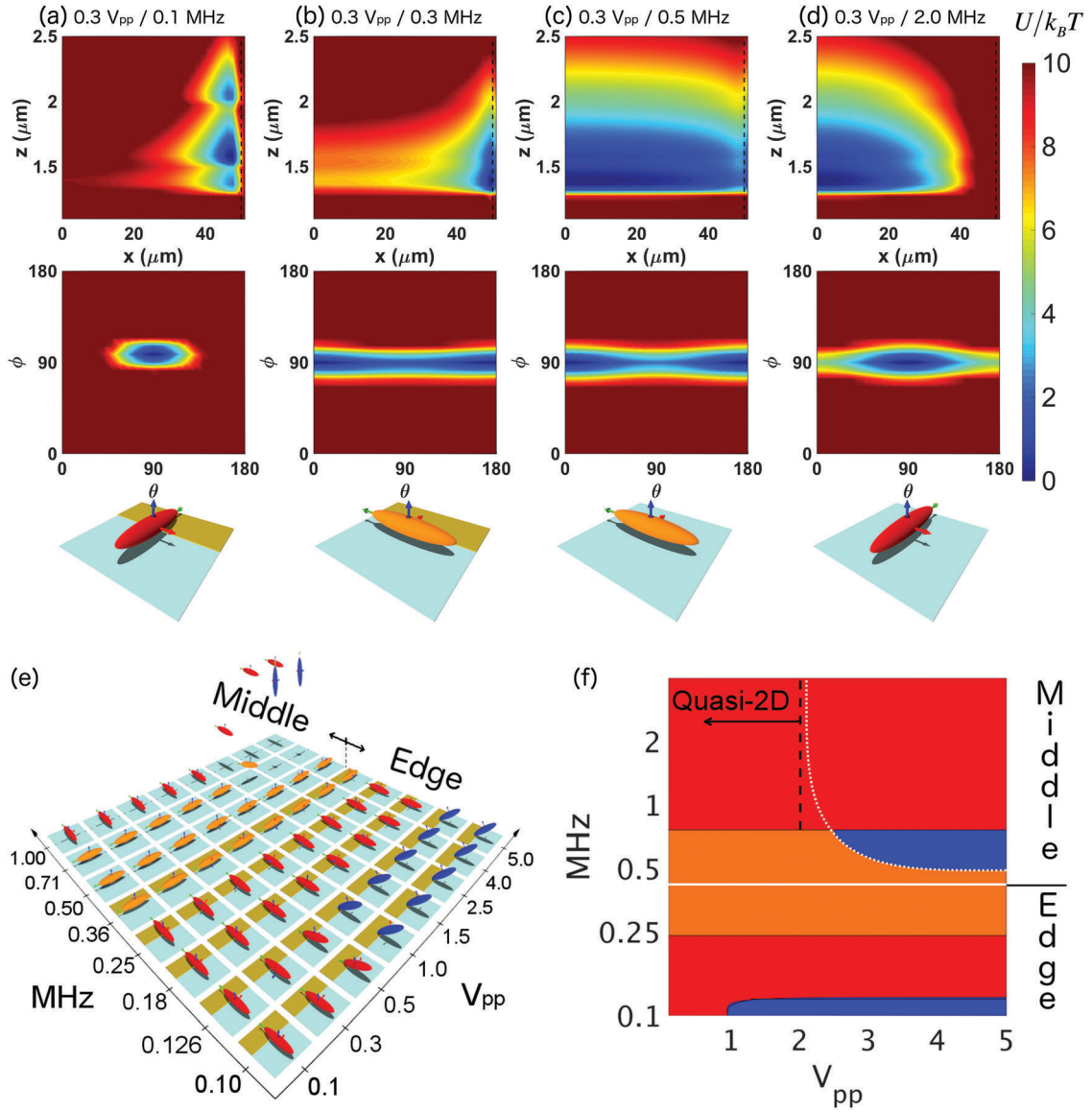

Fig. 3 Position and orientation projected energy landscapes for prolate ellipsoids ($r_x : r_y : r_z$ = 1 : 1 : 5) from 0–10k_BT relative to the global energy minimum. Field conditions are for 0.3 V_{pp}, and frequencies of (a) 0.1, (b) 0.3, (c) 0.5, and (d) 2 MHz. The lowest energy state is rendered under energy landscape plots. Material parameters are listed in Table 1. (e) Discrete rendered states *vs.* voltage and frequency category axes. (f) Continuous state diagram *vs.* field strength and frequency. Solid white line indicates the transition in position from the electrode edges to electrode center. Dashed white line indicates when particles move away from the surface. Dashed black line is maximum V for quasi-2D analysis (eqn (24)).

the electrode gap (300 kHz) and in the middle of the electrode gap (500 kHz) is correlated with the change in the sign of the f_{CM} as shown in Fig. 2(a). In the two first cases in Fig. 3(a) and (b) the value of f_{CM} is positive, indicating that the particle is more polarizable that the surrounding medium, and it is located at the electric field maximum. In contrast, at 500 kHz, the particle is less polarizable than the surrounding medium and is located at the electric field minimum. At still higher frequencies, 2 MHz and 0.3 V_{pp}, the Fig. 3(d) shows that the particle is still in the middle of the electrode gap since the f_{CM} is negative, and the long axis is oriented along the x-component of the electric field. The change in orientation between 500 kHz and 1 MHz is correlated with the crossover frequency between the f_{CM} of the short and long axes, as seen in Fig. 2(a). It determines which axis is aligned with the electric field.

To understand the orientation of single prolate particles in a non-uniform electric field, we calculated the minimum of the energy landscape at different applied voltages. Fig. S1 (ESI†) shows the equilibrium position and orientation of a prolate particle at different medium conductivity values as a function of the voltage and frequency of the applied field. It is seen that as the medium conductivity increases, *i.e.* the difference between particle and medium conductivities decreases, the particle can reach perpendicular position at the edge of the electrode at high voltages, *i.e.* there is a change in the absolute minimum as shown in Fig. 3(a). However, its equilibrium position is shifted

towards the middle of the electrode gap. Additionally, for greater medium conductivity values, the range of crossover frequencies between different orientations decreases and the particle reaches fewer configurations at different field conditions.

Results in Fig. S1(b) (ESI†) yield the position/orientation state diagram for the prolate particle (Fig. 3(f)). Some representative conditions are depicted in Fig. 3(e). In Fig. 3(f), the black dashed line corresponds with the approximated conditions (eqn (24)) that limits the quasi-2D analysis, *i.e.* when the long axis of the particle is parallel to the substrate. The white dotted line corresponds to the calculated conditions where the particle moves away from the substrate. Here, it is seen that the prolate particle can be controlled in a quasi-2D conditions at low voltages, and in three-dimensional space at higher voltages. From Fig. S1 (ESI†), it is seen that the number of states for a prolate particle can change depending of the particle and medium properties, *i.e.* depending of the f_{CM} along the particle axes. It is seen that a prolate ellipsoid ($r_x : r_y : r_z = 1 : 1 : 5$ μm) can reach the maximum number of six states by varying the field amplitude and frequency. The six total configurations include three at the electrode gap middle and three at the electrode edge. The prolate ellipsoid long axis can be oriented parallel and perpendicular to the field direction, and at higher field strengths it can also be aligned perpendicular to the wall.

Energy landscape for oblate ellipsoids

A similar analysis to that for the prolate particle in Fig. 3 has been conducted to understand the behavior of oblate particles ($r_x : r_y : r_z = 5 : 1 : 5$ μm). It has symmetry along the y'-axis, and as shown in Fig. 1, the energy landscape has no dependence on the θ-angle. In Fig. 4, we show the results for the projected 2D position (x, z) and orientation (ψ, ϕ) energy landscapes (eqn (2), (17) and (19)) for an oblate particle at four different field conditions, where the particle configuration at the minimum energy landscape for each condition is depicted at the bottom.

For 0.3 V_{pp}, the particle has two different positions at the edge and in the middle of the electrode gap. The first condition is at low frequencies where f_{CM} is positive (Fig. 2(b)); *i.e.* that particle is more polarizable than the surrounding medium, and it is located at the electric field maximum. At higher field frequencies, where f_{CM} is negative (Fig. 2(b)), the particle is located in the middle of the electrode gap where the field is minimum. Due to the symmetry of the oblate particle along the y'-axis, it behaves similar to a spherical particle, when the short axis is perpendicular to the substrate. Even though that under these conditions the particle is oriented parallel to the wall, there is a small variation in the location of the energy landscape minimum, and the local gradient around it, as shown in Fig. 4(a)–(d). However, it is clear that this particle shape can be analyzed in quasi-2D conditions at low field strengths.

The oblate particle behavior has been characterized at different medium conductivities and field strengths. Fig. 4(f) shows the conditions for a large number of states where its properties are listed on Table 1. It is shown the equilibrium state configuration as a state diagram as a function of the field frequency and voltage, and some representative states are depicted in Fig. 4(e). In Fig. 4(f), the black dashed line corresponds to the conditions (eqn (24)) that can be approximated by the quasi-2D analysis, *i.e.* when the short axis of the particle is perpendicular to the substrate. The white dotted line corresponds to the limit where the particle moves away from the substrate, and it describes the required conditions for a three-dimensional control on the particle.

It is seen that the short axis of a particle with oblate shape ($r_x : r_y : r_z = 5 : 1 : 5$ μm) is preferentially aligned perpendicular to the wall at low voltages. It can reach five different states at different field amplitude and frequency conditions. When the short axis of the particle is perpendicular (y-direction) to the field direction, the particle energy along the z-axis overcomes the gravitational energy making the particle moves away from the substrate. Interestingly, the frequency when the oblate particle moves from the edge to the middle of the electrode gap is dependent on the magnitude of the field strength. This is a result of the different crossover frequencies of the particle axes in Fig. 2(b). The short axis of the particle is less polarizable the medium, while the long axis still being more polarizable than the medium. For this case at high voltages, the dipole–field interaction energy overcomes gravitational energy, and the short axis is aligned with the field x-component, thus determining the equilibrium position. The orientation of oblate-like particles with different electric field conditions has been reported,[28] where the short axis of the plate-like particles is oriented parallel to the wall and perpendicular to the main component of the field. The present study shows the required and necessary conditions to control the position and orientation of such oblate particles at different field conditions.

Energy landscape for scalene ellipsoids

Before describing the net potential energy landscape for scalene ellipsoids, the possible states are discussed for tri-axial particles at different field conditions. For a given field frequency, the net potential energy for anisotropic particles depends on position and orientation. To describe the equilibrium particle state, Fig. S2 (ESI†) schematically depicts different particle configurations at the electrode edge where positional and orientational coordinates are plotted separately. Fig. S2(a) (ESI†) illustrates the most probable position of the particle center in the vicinity of the energy landscape minimum in each case and its projections onto different spatial planes. Similarly, Fig. S2(b) (ESI†) illustrates the most probable orientations of particle in the vicinity of the energy landscape minimum in each case including projections. Here, we show only the angular variation between 0 and 180°, since the ellipsoidal particle has three perpendicular planes of symmetry.[29] The states in Fig. S2(a) and (b) (ESI†) are color coded according the rendered configurations in Fig. S2(c) (ESI†).

The six different possible configurations in Fig. S2(c) (ESI†) are different from previous predictions for scalene anisotropic particles, which have shown that particles could only be oriented along the three principal axes.[16,17,30] The main difference is that the field generated in the parallel electrode configuration has components in the x- and z-directions, which increases the possible particle configurations. For scalene particles, the maximum number of possible orientational states is equal to the product

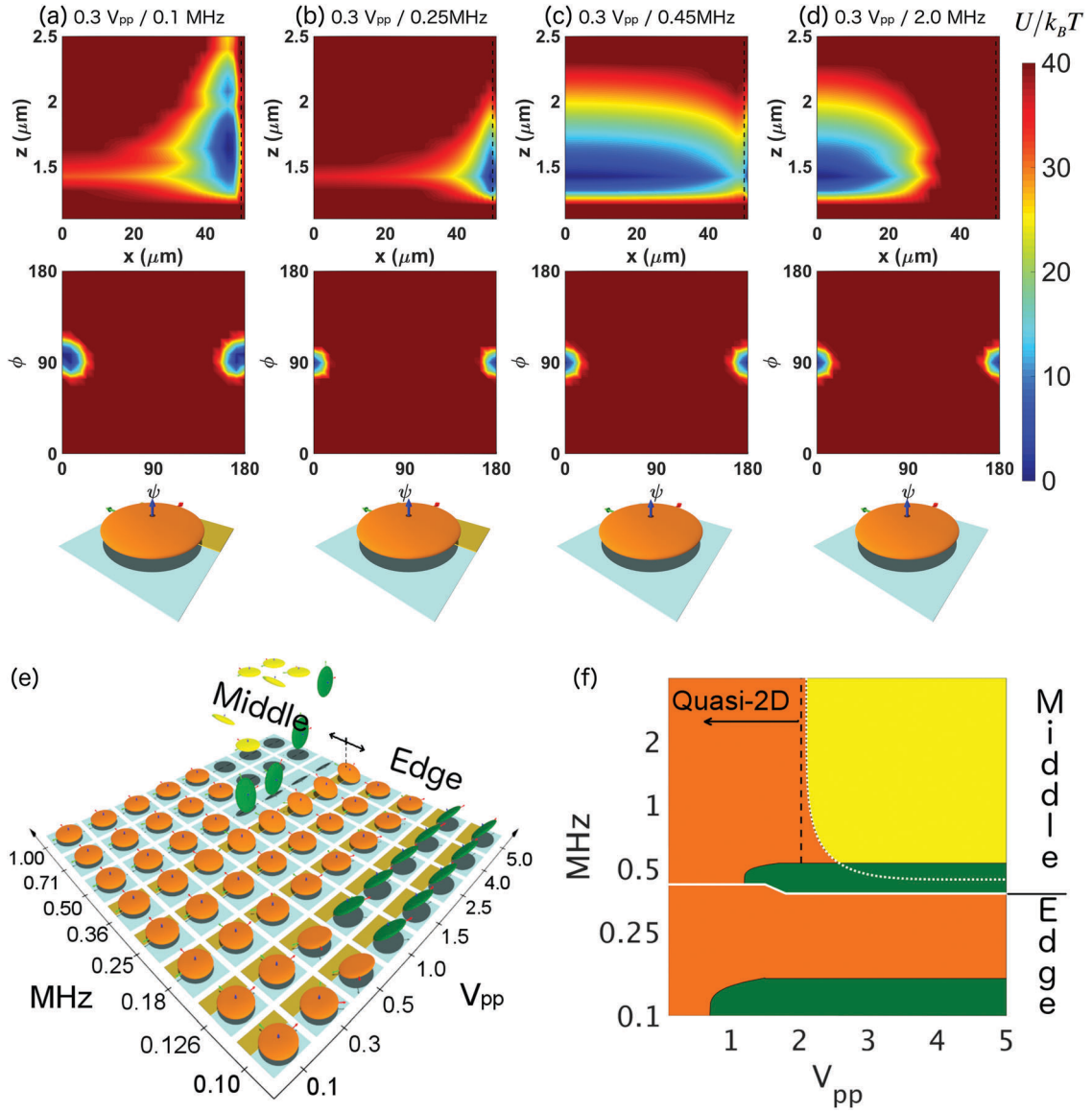

Fig. 4 Position and orientation projected energy landscapes for oblate ellipsoids ($r_x:r_y:r_z$ = 5 : 1 : 5) from 0–100 k_BT relative to the global energy minimum. Field conditions are for 0.3 V_{pp}, and frequencies of (a) 0.1, (b) 0.25, (c) 0.45, and (d) 1 MHz. The lowest energy state is rendered under energy landscape plots. Material parameters are listed in Table 1. (e) Discrete rendered states *vs.* voltage and frequency category axes. (f) Continuous state diagram *vs.* field strength and frequency. Solid white line indicates the transition in position from the electrode edges to electrode center. Dashed white line indicates when particles move away from the surface. Dashed black line is maximum *V* for quasi-2D analysis (eqn (24)).

of the number of field components and the number of different axes of the particle. Due to the symmetry of prolate and oblate particles, the maximum number states at the electrode is three, and of course, spheres have a single state because of their isotropic shape. The states in Fig. S2(c) (ESI†) are also possible at the center of the electrode gap. We use the same color scheme to define particle's orientational configurations whether they are at the electrode edge or electrode gap center. Based on this information, a scalene particle can be positioned and oriented in a maximum of twelve different states between parallel electrodes.

In Fig. 5, results are shown for the projected 3D position and orientation energy landscapes (eqn (2), (17) and (19)) for a scalene particle ($r_x:r_y:r_z$ = 2 : 1 : 5 μm) at four different field conditions. In this case, there is no rotational symmetry along any particle axis, so position and orientation averaged energy landscapes cannot be shown as 2D surfaces. Each case must consider three spatial and orientational axes for each case. Even though there is no field gradient along the *y*-axis, the orientation averaged energy landscape in a three dimensional space is plotted to show the generality of the analysis, which can be applied to any other electrode configuration. For field conditions of 100 kHz and 0.3 V_{pp} (λ = 0.8), Fig. 5(a) shows that the minimum of the projected energy landscape indicates that the equilibrium state of the particle center is located close to the edge of the electrode gap, as in the case of spherical particles.[10] Under these conditions, the position averaged energy landscape

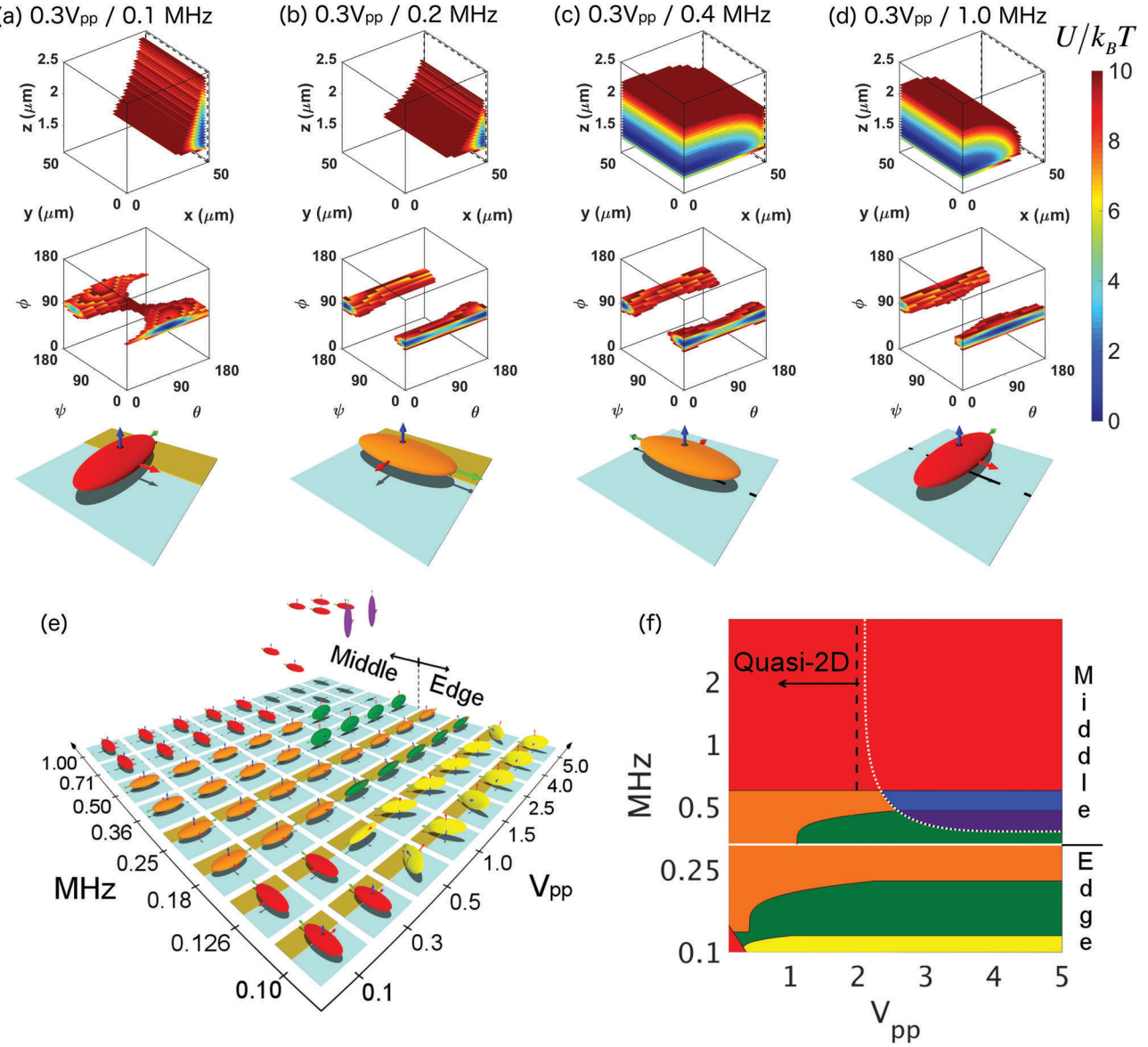

Fig. 5 Position and orientation projected energy landscapes for scalene ellipsoids ($r_x : r_y : r_z$ = 2 : 1 : 5) from 0–10 k_BT relative to the global energy minimum. Field conditions are for 0.3 V_{pp}, and frequencies of (a) 0.1, (b) 0.2, (c) 0.4, and (d) 1.0 MHz. (bottom) The lowest energy state is rendered under energy landscape plots. Material parameters are listed in Table 1. Low dimensional energy landscape projections are shown In Fig. S3 and S4 (ESI†). (e) Discrete rendered states *vs.* voltage and frequency category axes. (f) Continuous state diagram *vs.* field strength and frequency. Solid white line indicates the transition in position from the electrode edges to electrode center. Dashed white line indicates when particles move away from the surface. Dashed black line is maximum *V* for quasi-2D analysis (eqn (24)).

shows that the long axis of the particle is oriented parallel to the *x*-component of the electric field, and the short axis is oriented perpendicular to the surface. This corresponds to the configuration shown in red depicted at the bottom of Fig. 5(a).

Fig. 5(b) shows the projected 3D position and orientation landscapes at 200 kHz and 0.3 V_{pp}. Here, the particle center's most probable location is close to the edge of the electrode. The long axis of the particle is oriented perpendicular to the *x*-component of the field, and the short axis is oriented normal to the wall. For both 100 and 200 kHz, the f_{CM} has a positive value, which means that the particle is more polarizable than the surrounding medium, and located in the higher field region near the electrode edge. At 100 kHz the long axis is more polarizable than the short axis, but at 200 kHz the short axis is more polarizable than the long axis. At low fields, the ellipsoidal particle preferred orientation is correlated with the greater f_{CM} value; *i.e.* the axis of the particle that has the greater polarization will be oriented along the *x*-component of the field, and the shortest axis will be oriented perpendicular to the wall.

The projected 3D position and orientation landscapes at 0.3 V_{pp} and 0.4 MHz, and 1.0 MHz are shown in Fig. 5(c) and (d), respectively. At these conditions, the f_{CM} is negative, making the particle less polarizable than the medium to give a most probable location at the electrode gap center. From the projected

orientational landscape at 0.4 MHz (Fig. 5(c)), it is seen that the particle long-axis is oriented perpendicular to the *x*-component of the field with the short axis oriented normal to the wall. However, for higher frequencies, the orientation of the long axis of the particle changes to be parallel with the applied electric field. Even though in these cases the f_{CM} is negative, the orientation of the long axis is correlated to the higher polarization of the particle axis at every frequency. When the f_{CM} is negative, the absolute minimum of the energy landscape is located outside of the electrode gap on top of the electrode. However, an energy barrier located at the electrode edge practically keeps particles within the electrode gap. As such, our analysis is for particles at this local minimum, which is practically useful for manipulating particles within the electrode gap region.

Under this field strength (0.3 V_{pp}), the particle can be oriented in the same two orientational states at the electrode edge and the electrode center like prolate particles. The characteristic dipole–field interaction energy (λ = 0.8) is significantly less than the characteristic gravitational potential energy (G = 20, eqn (22)). This causes to the particle short-axis to always be aligned perpendicular to the surface. Eqn (24) predicts that a voltage <1.33 V_{pp} is required to maintain quasi-2D conditions. Even though the f_{CM} of the short axis has a larger value between 150 and 200 kHz, the applied voltage is not enough to rotate the particle to different orientational states.

To determine the maximum number of states for particles under different field conditions and medium conductivities, we repeat the analysis described in Fig. 3 and 4 for many energy landscapes *vs.* applied voltage (electric field) and frequency. Fig. 5(f) shows the equilibrium position and orientation of a scalene ellipsoid ($r_x : r_y : r_z$ = 2 : 1 : 5 μm). Fig. 5(e) depicts some representative voltage and frequency values of the entire analyzed spectrum, which is shown in Fig. 5(e) as a state diagram. The color scheme corresponds to the orientations and scheme in Fig. S2 (ESI†). Fig. 5 shows how the particle's orientation depends on voltage and frequency. As explained previously, at low voltages the particle short axis stays perpendicular to the wall allowing two orientational states at the electrode edge and two in the electrode gap center. As the voltage increases, particles realize different orientations since the dipole–field interaction energy along the *z*-axis (in the lab coordinate) becomes comparable to the gravitational energy as predicted by eqn (22) (*i.e.* the equilibrium position shifts to higher elevations). For a scalene particle, equilibrium states are reached when any of the particle axes is aligned perpendicular to the wall (Fig. 5(f)), which depends on the f_{CM} and applied voltage, or the polarization along the different particle axes.

At low frequencies, the particle is more polarizable than the surrounding medium and is located at the electrode gap edge. Here, it has four orientational configurations. Two of these states correspond to the long axis aligned and two of them perpendicular to the *x*-component of the field. Under these conditions, the short axis of the particle could be parallel or perpendicular to the wall. At high frequencies, the particle is located in the middle of the electrode gap. Here, we can distinguish five different orientational states, where the short axis is parallel in two of them and perpendicular to the wall in the others. The long axis is aligned parallel and perpendicular to the *x*-component of the field, and it can also be oriented normal to the surface. The predicted voltage (eqn (24)) for the quasi-2D threshold at high frequencies is represented as a dashed black line in Fig. 5, which is consistent with the particle orientations obtained from the most probable states in the energy landscapes.

Generality of energy landscapes

Based on the analysis in Fig. 3–5 and result in eqn (24), quasi-2D behavior is generally observed only at low field strengths. In particular, for applied voltages $<V_{pp,max}$ in eqn (24), the results in Fig. 3–5 show that the f_{CM} can predict the most probable position and orientation of dielectric ellipsoids at different frequencies. This finding shown that the axis with the highest polarization is aligned with the *x*-component of the field. In all of these cases the gravitational energy causes the short axis to be perpendicular to the underlying wall under low field strengths, so the particle orientation is defined by the f_{CM} of the remaining two axes.

The present analysis shows results for ellipsoidal particles with different aspect ratios, corresponding to prolate ($r_x : r_y : r_z$ = 2 : 1 : 5 μm), oblate ($r_x : r_y : r_z$ = 5 : 1 : 5 μm), and scalene ($r_x : r_y : r_z$ = 2 : 1 : 5 μm). The equations reported here are valid for arbitrary ellipsoidal particle shapes, including spheres. Our results show the main phenomenological characteristics of the position/orientation projected energy landscape for ellipsoidal particles, and the analytical description can be used to predict the behavior for different electrode configurations, such as spiral electrodes,[31] parallel plate electrodes,[13,32,33] quadrupole or octupole electrodes,[34] and others.[35,36] The behavior and number of positional and orientational states in every case depend on the f_{CM} and the relative components of the field in the laboratory coordinates. However, particles under the influence of non-uniform fields with azimuthal symmetry[31,36] will have a similar behavior along the radial direction as our present results. For parallel plate electrodes, the field is uniform and perpendicular to the plates, so the particle behavior is only limited by the gravitational energy, which results in two and three states for uni-axial and tri-axial particles. As such, our results are perhaps most useful for non-uniform AC electric fields with spatially varying gradients that produce local maxima and minima with frequency dependent orientations.

Here we list assumptions, limitations, and issues that might arise when comparing the models here with direct experimentally accessible information. The model here is based on uniform polarizable anisotropic ellipsoids at each position and orientation. This is a valid assumption if the particle size is smaller than the characteristic dimension of the field gradient. In the parallel electrode configuration, field gradients along the *x*-direction are greater at the edge of the electrode, which can generate an underestimation of the potential well at those locations (by neglecting higher multi-poles that have finite contributions[37]). Our results include analytical results for the particle position and orientation based on material and geometric properties of particle and the surrounding medium. However, in experiments, it is not necessarily a simple task to estimate conductivities along

particle axes. In future work, we plan to report how such parameters can be obtained by fitting optical microscopy measurements of energy landscapes *vs.* field frequency and amplitude to the expressions reported in this work.

Conclusions

Analytical expressions are reported for the time-average energy landscapes of prolate, oblate, and scalene ellipsoids in non-uniform AC electric fields between coplanar electrodes. Ellipsoid particle equilibrium positions and orientations are obtained from global minima of net potential energy landscapes computed from superposition of dipole-field, gravity, and ellipsoid-substrate electrostatic repulsion. This analysis yields the maximum number of possible states for ellipsoidal particles *vs.* field frequency and amplitude for the coplanar electrode configuration. Results indicate up to 9 states for scalene ellipsoids (4 orientations at field maximum, 5 orientations at field minimum), 6 states for prolate ellipsoids (3 orientations at field maximum, 3 orientations at field minimum), and 5 states for oblate ellipsoids (2 orientations at field maximum, 3 orientations at field minimum). To facilitate comparisons with experiments, a criterion is reported for the highest voltage or electric field, when particles can be reliably analyzed as quasi-2D (thermally sampled degrees of freedom are within a plane adjacent to underlying substrate). The analytical potential energy landscapes reported in the paper are general and can be used with different electrode geometries and electric field shapes.

Conflicts of interest

There are no conflicts to declare.

Acknowledgements

We acknowledge financial support by the National Science Foundation (CBET-1434993).

References

1 D. G. Grier, *Nature*, 2003, **424**, 810–816.
2 A. Ramos, H. Morgan, N. G. Green and A. Castellanos, *J. Electrost.*, 1999, **47**, 71–81.
3 C. Gosse and V. Croquette, *Biophys. J.*, 2002, **82**, 3314–3329.
4 J. V. I. Timonen and B. A. Grzybowski, *Adv. Mater.*, 2017, **29**, 1603516.
5 J. Fu, Q. Zhan, M. Y. Lim, Z. Li and H. D. Ou-Yang, *Opt. Lett.*, 2013, **38**, 3995–3998.
6 A. C. H. Coughlan and M. A. Bevan, *Phys. Rev. E*, 2016, **94**, 042613.
7 T. B. Jones, *Electromechanics of Particles*, Cambridge University Press, Cambridge, 1995.
8 H. Morgan and N. G. Green, *AC electrokinetics: colloids and nanoparticles*, Research Studies Press, Philadelphia, PA, 2003.
9 J. J. Juarez and M. A. Bevan, *J. Chem. Phys.*, 2009, **131**, 134704.
10 J. J. Juarez, J.-Q. Cui, B. G. Liu and M. A. Bevan, *Langmuir*, 2011, **27**, 9211–9218.
11 J. J. Juarez, B. G. Liu, J.-Q. Cui and M. A. Bevan, *Langmuir*, 2011, **27**, 9219–9226.
12 J. P. Singh, P. P. Lele, F. Nettesheim, N. J. Wagner and E. M. Furst, *Phys. Rev. E: Stat., Nonlinear, Soft Matter Phys.*, 2009, **79**, 050401.
13 A. A. Shah, H. Kang, K. L. Kohlstedt, K. H. Ahn, S. C. Glotzer, C. W. Monroe and M. J. Solomon, *Small*, 2012, **8**, 1551–1562.
14 A. Kuijk, T. Troppenz, L. Filion, A. Imhof, R. van Roij, M. Dijkstra and A. van Blaaderen, *Soft Matter*, 2014, **10**, 6249–6255.
15 S. J. Boehm, L. Lin, K. Guzmán Betancourt, R. Emery, J. S. Mayer, T. S. Mayer and C. D. Keating, *Langmuir*, 2015, **31**, 5779–5786.
16 M. Saito, H. P. Schwan and G. Schwarz, *Biophys. J.*, 1966, **6**, 313–327.
17 R. D. Miller and T. B. Jones, *Biophys. J.*, 1993, **64**, 1588–1595.
18 J. A. Stratton, *Electromagnetic Theory*, McGraw-Hill Book Company, Inc., New York, 1941.
19 I. Torres-Diaz and M. A. Bevan, *Langmuir*, 2017, **33**, 4356–4365.
20 L. R. White, *J. Colloid Interface Sci.*, 1983, **95**, 286–288.
21 P. Schiller, S. Krüger, M. Wahab and H. J. Mögel, *Langmuir*, 2011, **27**, 10429–10437.
22 D. J. Evans, *Mol. Phys.*, 1977, **34**, 317–325.
23 H. Morgan, A. García Izquierdo, D. Bakewell, N. G. Green and A. Ramos, *J. Phys. D: Appl. Phys.*, 2001, **34**, 1553–1561.
24 S. Singh, *Liquid Crystals: Fundamentals*, World Scientific, River Edge, NJ, 2002.
25 M. P. Lettinga, E. Barry and Z. Dogic, *EPL*, 2005, **71**, 692.
26 Y. Han, A. M. Alsayed, M. Nobili, J. Zhang, T. C. Lubensky and A. G. Yodh, *Science*, 2006, **314**, 626–630.
27 M. A. Bevan and S. L. Eichmann, *Curr. Opin. Colloid Interface Sci.*, 2011, **16**, 149–157.
28 D. Rossi, J. H. Han, W. Jung, J. Cheon and D. H. Son, *ACS Nano*, 2015, **9**, 8037–8043.
29 H. Brenner, *J. Colloid Interface Sci.*, 1981, **80**, 548–588.
30 H. Morgan and N. G. Green, *J. Electrost.*, 1997, **42**, 279–293.
31 X. B. Wang, Y. Huang, X. Wang, F. F. Becker and P. R. Gascoyne, *Biophys. J.*, 1997, **72**, 1887–1899.
32 B. W. Kwaadgras, T. H. Besseling, T. J. Coopmans, A. Kuijk, A. Imhof, A. V. Blaaderen, M. Dijkstra and R. V. Roij, *Phys. Chem. Chem. Phys.*, 2014, **16**, 22575–22582.
33 M. Suga, A. Kunimoto and H. Shinohara, *Biosens. Bioelectron.*, 2017, **97**, 53–58.
34 Y. Huang and R. Pethig, *Meas. Sci. Technol.*, 1991, **2**, 1142.
35 K. A. Collins, X. Zhong, P. Song, N. R. Little, M. D. Ward and S. S. Lee, *Langmuir*, 2015, **31**, 10411–10417.
36 J. J. Crassous and A. F. Demirors, *Soft Matter*, 2017, **13**, 88–100.
37 E. Liang, R. L. Smith and D. S. Clague, *Phys. Rev. E: Stat., Nonlinear, Soft Matter Phys.*, 2004, **70**, 066617.

2014 American Control Conference (ACC)
June 4-6, 2014. Portland, Oregon, USA

Grain Boundary Control in Colloidal Self-Assembly with Dynamic Programming

Xun Tang[1], Yuguang Yang[2], Michael A. Bevan[2], and Martha A. Grover[1,3]

Abstract— **We propose a Markov decision based dynamic programming method to manipulate the self-assembly of a quadrupole colloidal system for grain-boundary-free two-dimensional crystals. To construct the optimal control policy, we developed a Markov chain model, based on information extracted from a Langevin dynamics simulation model, which originated from a more complicated Brownian dynamics model. An infinite-horizon Markov decision process is defined, and the optimal control policy is solved with dynamic programming using policy iteration. Both the Markov chain Monte Carlo and the Langevin dynamics simulation results demonstrate that the control strategy is able to significantly accelerate the crystallization of a SiO_2 colloidal self-assembly process for a grain-boundary-free, highly ordered crystal. Future work will focus on implementation of the control policy on the Brownian dynamics simulation and the experiments.**

I. INTRODUCTION

Colloidal self-assembly refers to the process by which colloidal particles converge into an ordered structure with or without external interference. Periodically regular colloidal crystals, also called photonic crystals, have wide applications in various fields, including chemical and biological sensors [1], semiconductors [2], and photonic devices [3], due to their ability to manipulate the propagation of light. This unique feature of photonic crystals stimulated intense study on the techniques for its fabrication such as chemical stimuli-induced molecular interaction directed self-assembly, sedimentation, evaporation, adsorption, and external field directed self-assembly. Comprehensive literature reviews on the fabrication and applications of photonic crystals can be found in Ref. [4], [5], [6].

In spite of these many aforementioned techniques for photonic crystal fabrication, most self-assembling processes still suffer from defects, including vacancies and grain boundaries. Getting rid of these defects still remains one of the biggest challenges before the large-scale production of photonic crystals can be realized. In Ref. [7], the authors demonstrated that by periodically applying and removing the electric field during the self-assembly process, they were able to achieve a single-crystal monolayer in a microfluidic chamber. The authors' findings give a good example of using a time-varying external electric field to achieve single domain colloidal crystals. However, the crystals are not achieved in any optimized way, and there is no feedback.

[1] School of Chemical & Biomolecular Engineering, Georgia Institute of Technology, 311 Ferst Dr. NW, Atlanta, GA. 30332-0100.

[2] The Department of Chemical and Biomolecular Engineering, Johns Hopkins University, 221 Maryland Hall 3400 North Charles Street, Baltimore, MD 21218.

[3] Corresponding author: martha.grover@chbe.gatech.edu

In addition, using feedback control policies has emerged as a viable approach [8], [9], [10]. In Ref. [8], model predictive control was applied to a stochastic simulation of colloidal self-assembly to rapidly achieve a highly ordered crystalline state. In Ref. [9], dynamic programming was applied to a similar stochastic colloidal self-assembly process as in Ref. [8] for a rapid formation of a highly ordered crystalline state. Besides, in Ref. [10], Juarez and Bevan designed a proportional controller to enable the connection between the real-time sensing of this dynamic assembly process (via a crystalline order parameter named C_6) and the external tunable electric potential. They further demonstrated the development of the crystalline colloidal assembly from a fluid state under feedback control [10].

Recent study has shown the Markov chain model as a promising representative for micro scale processes [9], [11]. The robustness of a Markov decision process based control policy was demonstrated on a stochastic colloidal self-assembly process in Ref. [9] to produce a highly ordered colloidal crystal. In this paper, we introduce a Markov decision process based optimal control strategy to a SiO_2 self-assembly system for grain-boundary-free, and highly ordered two-dimensional crystals. In our past work [8], [9], we studied optimal control on a system with 174 particles with a one-dimensional Langevin model. This system did not exhibit persistent grain boundaries due to the small number of particles; however, in this study, 210 particles are used, and this leads to grain boundary formation and persistence during the assembly process. Fig. 1 depicts results from a Brownian dynamics simulation [13]. In Fig. 1(a) the system is in a fluid-like state, while in Fig. 1(c) the system is in the desired crystalline state. The system in Fig. 1(b) has a grain boundary, a condensed yet defected state.

In this paper, we constructed Markov chain models from a two-dimensional Langevin dynamics model, which originated from a Brownian dynamics simulation, to simulate the dynamics of the colloidal assembly process. Based on the Markov chain model, dynamic programming was used to design an optimal control policy. The purpose of this paper is to introduce a control strategy to robustly control the formation of a single domain colloidal crystal in a system where grain-boundary formation is prevalent. Detailed descriptions of the experimental system, the simulation models and the analysis of the control results are given in the following sections.

II. PROBLEM STATEMENT

In order to study the reliability of a Markov decision process based optimal controller for the colloidal self-assembly

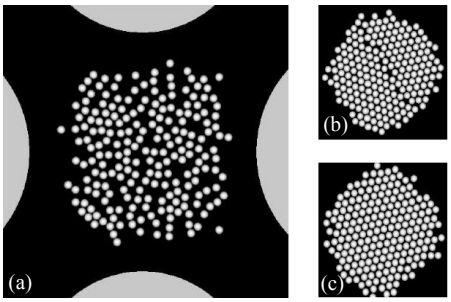

Fig. 1. (a) top view of dispersed colloidal particles in Brownian dynamics simulation; (b) colloidal ensemble with grain boundary; (c) colloidal ensemble without grain boundary

process, we consider a SiO_2 particle colloidal experiment developed by one of the authors (Bevan) [11]. In this system, 210 identical SiO_2 particles with a nominal size of 1.5 μm are suspended in deionized water in a container made of glass microscope cover slips (50 mm x 24 mm x 150 μm) [12]. Four separate, tunable 1 MHz AC electrode tips are attached to the edge of the container to generate a non-homogeneous electric field inside the container [12]. Details of the particle-particle and particle-field interaction forces have been studied and are simulated with a Brownian Dynamics (BD) model [13]. Previous studies have shown that by changing the magnitude of the voltage potential, the movement of the particles can be controlled, and thus the formation of the crystals [12]. Both laboratory experimental results and simulation results indicate that, for such a large colloidal system (with a particle number of 210), grain boundaries can be easily formed, thus posing an obstacle in achieving a single-domain, highly ordered crystal. Given these observations, we aim to develop a control policy with dynamic programming based on a Markov chain model, to rapidly form a grain-boundary-free SiO_2 crystal.

III. Theory and Methods

In order to more effectively study the dynamics of the colloidal assembly system considered in our study, and to more conveniently construct a control policy, we developed mathematical models for the system simulation and prediction. Based on the physical analysis of the interactions inside the system, we constructed a Brownian dynamics (BD) model which is able to accurately describe the experiments. However, considering its high computational time, we further developed a Langevin dynamics (LD) model to simplify the simulation. To enable the use of dynamic programming for our control policy, we further developed Markov chain models based the Langevin dynamics model.

In a colloidal assembly system, where the state variables are the coordinates of all the particles, the state space dimension can be prohibitively large. To reduce the state space dimension, we define an approximate system state using order parameters [14]. In the colloidal self-assembly system, a pair of order parameters is identified to describe the instantaneous state of the assembly process: ψ_6, which is a six-fold bond orientational order parameter, captures the occurrence of the grain boundary [12]; Rg, the radius of gyration, captures the condensation of the system [15]. A high Rg value together with a low ψ_6 value indicates a fluid-like state of the system, while a low Rg value together with a high ψ_6 value indicates a highly ordered, grain-boundary-free crystalline state. Therefore, the objective of the control is to achieve a state with the highest possible ψ_6 value and the lowest possible Rg value at the same time. These order parameters can be both theoretically calculated with a dynamics model and experimentally measured with a laboratory microscope, and this enables optimal control over both a simulation model and a laboratory experiment. With the help of a MATLAB program, Rg and ψ_6 values can be accurately calculated online every 0.125 s from the particle coordinates captured by a microscope in the laboratory experiments. The definitions of these two order parameters are specified in the following section.

Parameter	Value
$2a$ (nm)[a]	2920
κ^{-1} (nm)[b]	10
ψ (mV)[c]	-50.0
λ[d]	1.31
f_{CM}[e]	-0.4667
$\varepsilon_m/\varepsilon_0$[f]	78
d_g (μm)[g]	100

Table 1. Parameters for Brownian Dynamics simulation: (a) colloidal particle size, (b) Debye screening length, (c) particle and wall Stern potential, (d) peak voltage applied to electrodes, (e) Clausius-Mosotti factor for an AC field frequency at 1 MHz, (f) medium dielectric permittivity, (g) electrode spacing.

A. Brownian dynamics and Langevin dynamics model

In this paper, BD simulations in the canonical ensemble are performed for 210 colloidal particles for six different constant voltages: 0.3V, 0.4V, 0.45V, 0.5V, 0.7V, and 1V, where 'V' stands for the maximum possible voltage of 2 volts. The time step used to update the particle configuration is set as 0.1 ms. These simulations were run for 10^7 time steps with an initial equilibration time of 2×10^6 time steps. Configurations were stored every 10^3 time steps and used to calculate the order parameters Rg and ψ_6. The parameters used in the BD simulation are summarized in Table 1, while the detailed construction of the BD simulation is elaborated in Ref. [16].

Although the BD model describes the dynamics of the system accurately, it takes hours to finish even a single realization of the simulation. Considering the simplicity of Langevin dynamics and its success at microscopic-level crystallization simulation [7], [8], [17], we further developed an LD model to shorten the computational time. The Langevin equation of motion specifying the evolution of the coordinate vector in order parameter space is given as:

$$\frac{\partial x}{\partial t} = -\beta D(x)\cdot\bigtriangledown W(x) + \bigtriangledown\cdot D(x) + \zeta(x,t) \qquad (1)$$

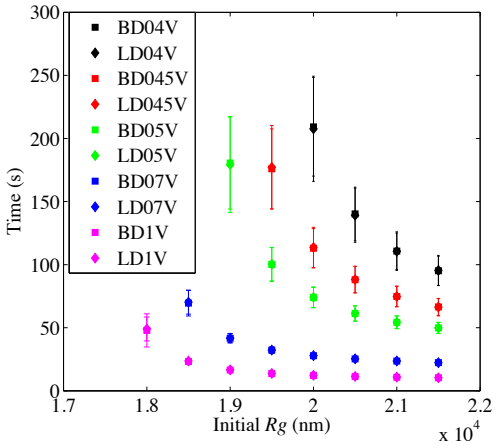

Fig. 2. 1000-realization averaged BD and LD mean first passage times starting from different Rg values under different constant voltages

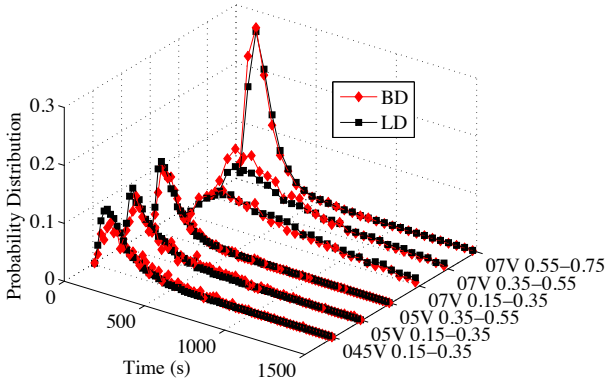

Fig. 3. 1000-realization averaged BD and LD mean first passage time distributions starting from different ψ_6 values under different constant voltages

where $x = (Rg, \psi_6)$ is the coordinate vector, tensor field $D(x)$ and scalar potential field $W(x)$ are diffusivity landscape (DL) and free energy landscape (FEL) which depend on the coordinates. ζ is the random noise variable with zero mean and variance $\langle \zeta_i(x,t)\zeta_j(x,t')\rangle = 2D_{ij}(x)\delta(t-t')$, as required by the Einstein relation, where i, j stand for Rg and ψ_6 respectively. $\bigtriangledown$ is a gradient operator, and $\bigtriangledown\cdot$ is a divergence operator. The DL and FEL, as the input quantities of the LD equation, are derived from particle scale Brownian dynamics via the linear fitting method [18]. To evaluate the accuracy of the LD simulation model, we compared the mean first passage time of both order parameters, under several constant voltages, against the results from the BD simulation.

Fig. 2 shows the comparison of the time needed for the system to decrease by 1000 nm in the Rg coordinate, from different initial points. In Fig. 2, the mean first passage time under 0.4V from Brownian dynamics is labeled as 'BD04V', and that from Langevin dynamics is labeled as 'LD04V', etc. The error bar in the plots shows the standard deviation at each point. The comparison demonstrates a good agreement between the LD and the BD model.

Fig. 3 shows the comparison of the distribution of the time needed for the system to increase by 0.2 in the ψ_6 coordinate, from different initial points. For example, the distribution labeled as '045V 0.15–0.35' denotes the time distribution of a 1000-realization-simulation for the system to travel 0.2 in ψ_6 from $\psi_6 = 0.15$ to $\psi_6 = 0.35$ under a constant voltage of 0.45V. With these mean first passage time comparisons, we validate the accuracy of our Langevin dynamics.

B. Markov Chain Model

Considering the construction of the simulation model described in the above sections, together with the observation from the laboratory experiments, the state of the assembly process at each instant depends only on the previous system state and the voltage used at that state. Therefore, we can use a parameterized-time-independent Markov chain model to simulate the system, and at the same time to enable the development of an optimal control policy.

A first step in building a Markov chain model is to define the discrete state space S, transition matrix P_a, and the discrete actuation space A. In this SiO_2 colloidal self-assembly system, we discretize the order parameter ψ_6 into $N_1 = 40$ evenly spaced grid cells, with $\psi_6 \in [0,1]$; and order parameter Rg into $N_2 = 156$ evenly spaced grid cells, with $Rg \in [16200, 24000]$. Therefore, the final state space is discretized into $N = N_1 \times N_2$ grid cells. The choice of the bounds on these two order parameters are based on the effective space that can be visited by the system according to the free energy landscape analysis. The actuation space A is defined as $A = \{0.3V, 0.4V, 0.45V, 0.5V, 0.7V, 1.0V\}$.

The transition matrix P_a contains the probabilities $p_{a_{ij}}$ for the system to be in state j, given the current state of i and action of a after a time step of Δt. The Δt value plays a significant role in determining the accuracy of the Markov chain model. By doing in-depth mean first passage time analysis for different Δt values, $\Delta t = 10$ s is found to give an accurate Markov chain model to capture the dynamics of the system, and is used in all the following calculations. Given the Δt value, the probability transition matrix P_a is constructed by running 50 independent Langevin dynamics simulations at each of 2070 distinct initial points. These initial points are chosen to cover the effective space of the colloidal system. With all the LD simulations, the $N \times N$ transition matrix P_a for each of the six actuators was achieved. A model characterized by the pair $\{S, P_a\}$ is referred to as a finite-state Markov chain model [19].

C. Markov Decision Process Based Dynamic Programming

A Markov decision process (MDP) is characterized by $\{T, S, A, P_a\}$ [20], where S, A, and P_a are defined as in the previous section. T is the collection of the discrete time epoch k. If T is finite, the MDP is called finite-horizon MDP, and it is called infinite-horizon MDP if T is infinite. Given the fact that an optimal control policy for a discounted infinite-horizon MDP is time-independent [18], we decided to adopt a discounted infinite-horizon MDP in our system for

the control policy. The control policy is solved with dynamic programming using policy iteration.

In infinite-horizon MDP, the optimization is achieved over an infinite number of time steps, and the objective function for an infinite-horizon MDP is defined as:

$$J_a(x) = E\left\{\sum_{k=0}^{\infty} \gamma^k R(x_k, a_k)\right\} \tag{2}$$

where E is the expectation operator, $a \in A$ is the control action, $x \in S$ is the discrete system state, $k \in T$ is the discrete time instant, and $\gamma \in (0,1)$ is the discount factor introduced to ensure the convergence of the optimization [21]. $R(x,a)$ is the one-stage reward function obtained when the system is in state x and a control action a is taken according to the optimality criterion, and it follows that $R(x,a) : S \times A \to \mathbb{R}$. The optimal value function and the optimal policy $a^*(x) \in A$ are defined as:

$$\begin{aligned} J^*(x) &= \sup_{a \in A} J_a(x) \\ a^*(x) &= \arg\{\sup_{a \in A} J_a(x)\} = \arg J^*(x) \end{aligned} \tag{3}$$

In our particular system, the one-stage-reward function is defined as:

$$R(x_k, a_k) = {\psi_6}^2 \tag{4}$$

The optimal control policy is obtained by solving for the input a trajectory that maximizes the sum of this one-stage-reward function over an infinite time horizon via policy iteration with discount factor $\gamma = 0.99$. The design of the reward function is aimed to achieve the highest possible ψ_6 value, which corresponds to a highly ordered, single domain crystalline state of the system. Rg is not included in the reward function, because it is impossible to achieve a high value of ψ_6 without a low value of Rg.

IV. RESULT AND DISCUSSION

Based on the methods described in Section III, we constructed six Markov chain models for each of the six actuation voltages: 0.3V, 0.4V, 0.45V, 0.5V, 0.7V, and 1V. To evaluate the accuracy of these models, in Fig. 4, we compared the 300-second uncontrolled simulation results under each of these six voltages for both the Markov chain model and the LD model. The legend 'MCMC', and 'LD' stands for Markov chain Monte Carlo simulation and Langevin dynamics simulation respectively. '03V' through '1V' denotes the voltage under which the simulations are conducted. All these trajectories are averages over 1000 independent simulations from the same initial point of $Rg = 20000$ nm, and $\psi_6 = 0.1$, which corresponds to a fluid-like state of the system. According to this comparison, although the Markov chain model tends to overpredict the dynamics in the aspect of ψ_6, the differences are slight. One noticeable phenomenon in these uncontrolled trajectories is, as the magnitude of the voltage increases, the system would reach a better, more crystalline state, which is defined by a high ψ_6 value and a low Rg value. Intuitively, one would expect to use the highest possible voltage all the time to most efficiently form

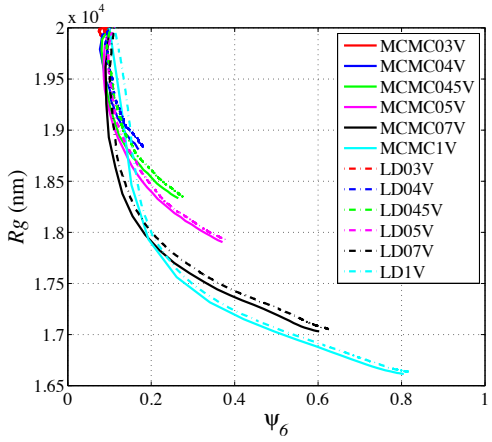

Fig. 4. Comparison between 1000-realization averaged MCMC and LD simulation order parameter trajectories for different constant input a from a system without the optimal control policy

the crystals. However, experimental results show that under a high potential, like 0.7V and 1V, the particles are pushed together too quickly, which leaves less time for the system to self-correct for defects. Once the system gets stuck in a disordered state, it will take a long time for the system to relax through self-corrections, and this makes it impractical for a real world production. Therefore, using a high voltage all the time might not be the optimal policy.

With these six Markov chain models, a time-independent optimal control policy was developed using dynamic programming. Fig. 5 shows the control policy in a two-dimensional plot. The numbers in the color bar stand for the control actions in an increasing order, where 1 stands for voltage 0.3V, and 6 stands for voltage 1V. This policy is interpreted as a look-up table. To use it, for example, when the system is in state of $Rg = 1.8 \times 10^4$ nm and $\psi_6 = 0.4$, the voltage of 1V should be used, which is colored as red and labeled as 6 in Fig. 5. In the control policy, the highest voltage of 1V is optimal in most of the effective space; this observation meets the expectation in Fig. 4 that a high voltage would result in a higher crystalline state than a lower voltage. However, one important point in the control policy is the use of lower voltages in the region of $Rg \leq 1.7 \times 10^4$ nm and ψ_6 around 0.6. These lower voltages are used to give the system long enough relaxation time for self-corrections in order to avoid getting stuck in the disordered state.

The implementations of the control policy onto both the Markov chain model and the Langevin dynamics simulation demonstrate that the control policy shown in Fig. 5 is able to yield a better crystalline state than an uncontrolled process. Detailed comparison results are given in Fig. 6. In Fig. 6, we only showed the LD uncontrolled trajectories for comparison, considering the agreement between the uncontrolled LD and MCMC simulations illustrated in Fig. 4.

Fig. 6 shows the comparison of 1000-realization averaged controlled Langevin dynamics (LDcontrolled) and Markov chain Monte Carlo (MCcontrolled) simulations against the uncontrolled Langevin dynamics (LD03V through LD1V)

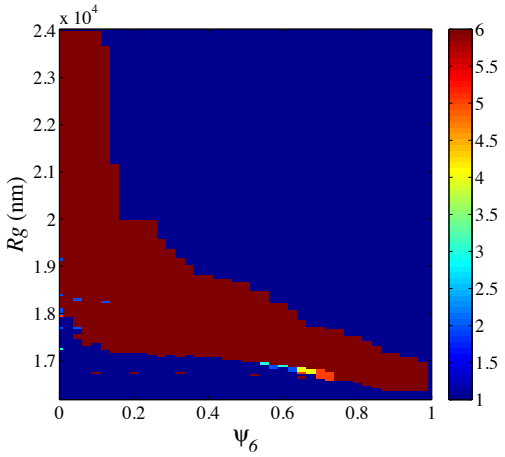

Fig. 5. Optimal control policy computed using Markov decision based dynamic programming

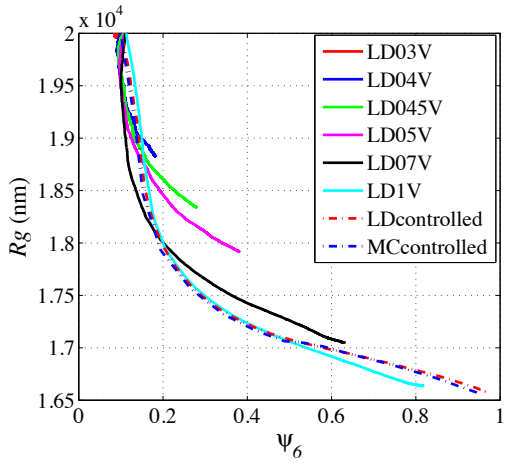

Fig. 6. Comparison between 1000-realization averaged order parameter trajectories with and without optimal control policy

results over 300 seconds. All the trajectories are averages over 1000 independent realizations starting from the same initial point of $Rg = 20000$ nm and $\psi_6 = 0.1$.

From the comparison, we conclude the effectiveness of the control policy by noticing the system reached ψ_6 of around 0.95 and Rg of around 1.65×10^4 nm after 300 seconds under the control. The highest possible ψ_6 value that can be achieved without control is around 0.8 under 1V. The comparison reveals an obvious divergence between the controlled trajectory and the 1V uncontrolled trajectory around the point of $\psi_6 = 0.5$ and Rg around 1.7×10^4 nm due to the use of 0.3V. Because of this use of a low voltage, the system enjoys a boost in ψ_6 by correcting defects introduced by the high voltages. Therefore it leads to a higher final ψ_6 value after 300 seconds of simulation. All these observations meet the expectation that high voltages should be used most of the time according to Fig. 5, while low or intermediate voltages should also be used to provide corrections during the process. Besides, the controlled Markov chain Monte Carlo simulation and the controlled Langevin dynamics simulation demonstrate a high similarity with each other, which further confirms the accuracy of the Markov chain model in approximating the LD model.

In addition, the evolution of the order parameters over time for both the Markov chain Monte Carlo and the Langevin dynamics simulations are investigated for a better understanding of the performance with respect to time. Results are summarized in Fig. 7.

Fig. 7 shows the evolution of the order parameters over time, with the system started from a fluid-like state with a low ψ_6 value and a high Rg value, and developed into a highly ordered crystalline state with a high ψ_6 value and a low Rg value after 300 seconds of simulation. In Fig. 7, all these four order parameter trajectories are averaged over 1000 independent realizations. From this figure, we can see that both Rg and ψ_6 reach a steady state after about 250 seconds of simulation in the LD model. While ψ_6 achieves its steady state after about 150 seconds, Rg stabilizes after about

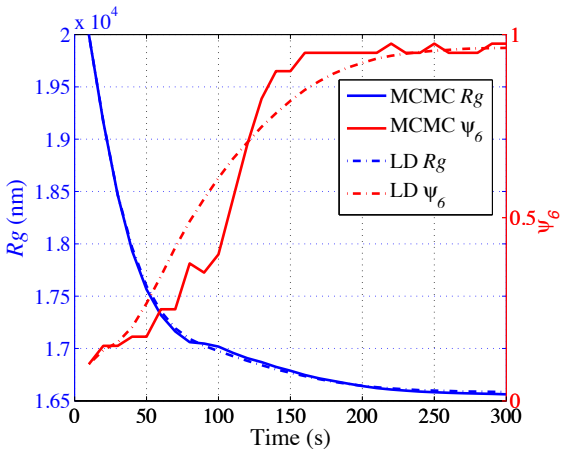

Fig. 7. 1000-realization averaged MCMC and LD simulation: order parameter evolution over time, under the optimal policy in Fig. 5

250 seconds in the MCMC simulation. These observations indicate the actual time needed for the system to reach a highly ordered, grain-boundary-free crystalline state is shorter than 300 seconds under the control policy.

Besides, the analysis of the averaged optimized control actions demonstrates that the use of high voltages for most of the time together with the use of low or intermediate voltages at times of around 70 seconds is able to give a better crystalline state. Both the optimized voltage trajectories from Markov chain Monte Carlo simulation (solid red line) and Langevin dynamics simulation (solid blue line) are summarized in Fig. 8.

Fig. 8 shows the 1000-realization optimized control action for both the Markov chain model and the LD model over 300 seconds of simulation. A similar trend can be observed in both of these two trajectories: at the beginning of the simulation, the highest voltage 1V was used to give the system a strong momentum to initialize the crystallization. However, when the system evolves to Rg of 1.7×10^4 nm and ψ_6 around 0.4, a low voltage is sometimes used to

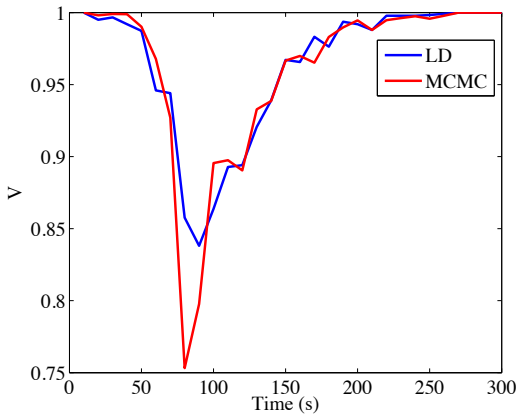

Fig. 8. 1000-realization averaged MCMC and LD simulation: input voltage evolution in time, under the optimal policy

correct defects that are caused by the strong electric forces induced by applying a high voltage. This strategy is well demonstrated in the control policy given in Fig. 5. Once the defects get resolved, the system chooses to use higher and higher voltages towards the end of the simulation to further speed up the process. The use of high voltage in the end is also justified physically, that a strong electric force is better able to maintain the system in a highly ordered state than a lower voltage. However, the optimized control policy trajectories from the MCMC and the LD simulation shows a noticeable difference between each other. This is due to the fact that the number of the realizations that used a non-trivial control policy (a control that is not using a constant voltage V) differs in the two sets of 1000 realization simulations. Specifically, 361 out of 1000 realizations used a non-trivial control policy in the LD simulation, while 631 out 1000 realizations used a non-trivial control policy in the MCMC simulation. This observation further demonstrates that using a highest constant voltage throughout the simulation does not necessarily guarantee an optimal result, in both the MCMC and the LD simulation.

The ultimate goal of this work is to feasibly produce grain-boundary-free crystals in the lab with the control policy shown in this paper. Given the simulation results, our next step is to apply the control policy in the BD simulation and in the laboratory experiment for the production of single domain, defect-free SiO_2 colloidal crystals.

V. CONCLUSIONS

Using Markov decision process based dynamic programming for a SiO_2 colloidal self-assembly process, we are able to achieve a single domain, highly ordered colloidal crystal in simulations. From all the analysis of the controlled and uncontrolled MCMC and LD simulation results, we conclude that a Markov chain model is suitable for simulating the dynamics of the stochastic self-assembly system. We further conclude that the controlled system gives significantly better results than the uncontrolled system, and a grain-boundary-free crystalline state can be achieved within about 250 seconds of simulation time under the control. Given the required policy updating time, $\Delta t = 10$ s, and the laboratory order parameter calculation time, 0.125 s, the in-lab control experiments are practical and are ongoing.

ACKNOWLEDGMENT

Acknowledgment is made to the National Science Foundation for support of this research, through collaborative grant Grant #1124678 (Grover) and #1124648 (Bevan) through the Cyber-Enabled Discovery and Innovation program.

REFERENCES

[1] Q.-H. Wei, D. M. Cupid and X. L. Wu, Controlled assembly of two-dimensional colloidal crystals, Applied Phys. Letters, vol. 77 pp. 1641 Sep. 2000.
[2] O. D. Velev and A. M. Lenhoff, Colloidal crystals as templates for porous materials, Curr. Opin. Colloid Interface Sci. vol. 5 pp. 56, 2000.
[3] S. O. Lumsdon, E. W. Kaler and O. D. Velev, Two-dimensional crystallization of microspheres by a coplanar AC electric field, Langmuir, vol. 20 pp. 2108-2116 Jan. 2004.
[4] M. Grzelczak, J. Vermant, E. M. Furst and L.M. Liz-Marzán, Directed self-assembly of nanoparticles, ACS Nano, vol. 4 pp. 3591-3605 Jun. 2010.
[5] K. A. Arpin, A. Mihi, H. T. Johnson, A. J. Baca, J. A. Rogers, J. A. Lewis, and P. V. Braun, Multidimensional architectures for functional optical devices, Adv. Mater., vol. 22 pp. 1084-1101 Feb. 2010.
[6] O. D. Velev and S. Gupta, Materials fabricated by micro- and nanoparticle assembly – the challenging path from science to engineering, Adv. Mater., vol. 21 pp. 1897-1905 Feb. 2009.
[7] S. Kim, R. Asmatulu, H. L. Marcus and F. Papadimitrakopoulos, Dielectrophoretic assembly of grain-boundary-free 2D colloidal single crystals, J. Colloid and Interface Sci., vol. 354 pp. 448-454 Nov. 2010.
[8] X. Tang, Y. Xue, and M. A. Grover, Colloidal self-assembly with model predictive control, Proceedings of the 2013 American Control Conference Jun. 2013.
[9] Y. Xue, D. J. Beltran-Villegas, X. Tang, M. A. Bevan and M. A. Grover, Optimal design of colloidal self-assembly process, IEEE Trans. on Control Systems Technology, 2014, doi: 10.1109/TCST.2013.2296700.
[10] J. J. Juárez and M. A. Bevan, Feedback controlled colloidal self-assembly, Adv. Funct. Mater., vol. 22 pp. 3833-3839 Sep. 2012.
[11] A. Banerjee, A. Pomerance, W. Losert and S. Gupta, Developing a stochastic dynamic programming framework for optical tweezer based automated particle transport operations, IEEE Trans. on Automation Science and Engineering, vol. 7 pp. 218-227 Apr. 2010.
[12] J. J. Juárez, S. E. Feicht and M. A. Bevan, Electric field mediated assembly of three dimensional equilibrium colloidal crystals, Soft Matter, vol. 8 pp. 94-103, 2012.
[13] J. J. Juárez and M. A. Bevan, Interactions and microstructures in electric field mediated colloidal assembly, J. Chem. Phys., vol. 131 pp. 134704 Oct. 2009.
[14] D. J. Beltran-Villegas, R. Sehgal, D. M. Maroudas, D. M. Ford and M. A. Bevan, Fokker-Planck analysis of separation dependent potentials and diffusion coefficients in simulated microscopy experiments, J. Chem. Phys. vol. 123 pp. 044707 Jan. 2010.
[15] D. J. Beltran-Villegas and M. A. Bevan, Free energy landscapes for colloidal crystal assembly, Soft Matter vol. 7 pp. 3280-3285 Feb. 2011.
[16] S. G. Anekal and M. A. Bevan, Interpretation of conservative forces from Stokesian dynamic simulations of interfacial and confined colloids, J. Chem. Phys., vol. 112 pp. 34903 Jan. 2005.
[17] C. Liu and M. Muthukumar, Langevin dynamics simulations of early-stage polymer nucleation and crystallization, J. Chem. Phys., vol. 109 pp. 2536 Aug. 1998.
[18] D. I. Kopelevich, A. Z. Panagiotopoulos and I. G. Kevrekidis, Coarse-grained kinetic computations for rare events: application to micelle formation, J. Chem. Phys., vol. 122 pp. 044908 Jan. 2005.
[19] D. P. Bertsekas, Dynamic Programming and Optimal Control. Nashua, NH: Athena Scientific, 2005.
[20] M. L. Puterman, Markov Decision Processes Discrete Stochastic Dynamic Programming. Hoboken, NJ: Wiley-Interscience, 2005.
[21] H. Chang, M. Fu, J. Hu and S. Marcus, Simulation-Based Algorithms for Markov Decision Processes. New York, NY: Springer, 1989.

LANGMUIR

Article

pubs.acs.org/Langmuir

Interfacial and Confined Colloidal Rod Diffusion

Julie L. Bitter,[†] Yuguang Yang,[‡] Gregg Duncan,[‡] Howard Fairbrother,[†] and Michael A. Bevan*[,‡]

[†]Chemistry and [‡]Chemical & Biomolecular Engineering, Johns Hopkins University, Baltimore, Maryland 21218, United States

ABSTRACT: Optical microscopy is used to measure translational and rotational diffusion of colloidal rods near a single wall, confined between parallel walls, and within quasi-2D porous media as a function of rod aspect ratio and aqueous solution ionic strength. Translational and rotational diffusivities are obtained as rod particles experience positions closer to boundaries and for larger aspect ratios. Models based on position dependent hydrodynamic interactions quantitatively capture diffusivities in all geometries and indicate particle−wall separations in agreement with independent estimates based on electrostatic interactions. Short-time translational diffusion in quasi-2D porous media is insensitive to porous media area fraction, which appears to arise from a balance of hydrodynamic hindrance and enhanced translation due to parallel alignment along surfaces. Findings in this work provide a basis to interpret and predict interfacial and confined colloidal rod transport relevant to biological, environmental, and synthetic material systems.

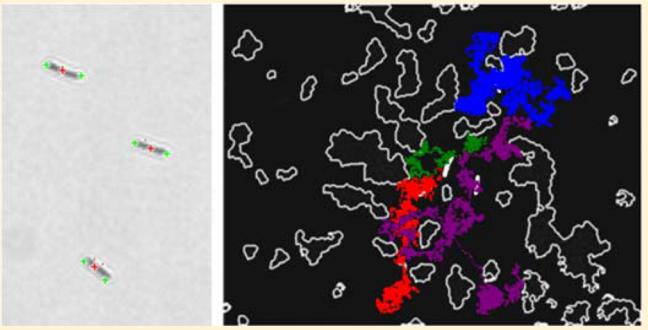

INTRODUCTION

Anisotropic colloidal particles are present in biological, medical, environmental, and synthetic material systems. Transport of anisotropic particles in interfacial and confined geometries is important to problems involving, for example, biological[1−4] and drug[5,6] particle transport within tissues, nanoparticle fate within environmental porous media,[7−12] and deposition and assembly on substrates of particle-based surface coatings.[13−15] Colloidal particle transport near surfaces in general depends on conservative colloidal forces (e.g., electrostatic, van der Waals, gravity) and nonconservative hydrodynamic forces (e.g., Stokes drag, lubrication). Conservative colloidal forces determine how close particles get to surfaces, which determines position dependent hydrodynamic forces that govern how much a particle's motion is impeded by fluid friction. For anisotropic particles, and rod shaped particles, the situation becomes more complex; conservative forces determine both position and orientation, which controls net hydrodynamic interactions as well as coupling between translational and rotational motion.[16]

Colloidal rod diffusion in bulk systems is reasonably well understood based on close correspondence between models[17−20] and measurements.[21−24] Likewise, position dependent diffusion of spherical colloids adjacent to surfaces has also been shown in high resolution measurements[25−29] to agree with models that self-consistently consider conservative and nonconservative colloidal forces.[30,31] However, analysis of measured colloidal rod diffusion near boundaries[3,32−35] has been restricted based on the limitations of available models. For example, many studies have used numerical results for bulk rod diffusion[17−20] modified by approximate lubrication corrections for cylinders adjacent to single planar wall surfaces.[36] Models of colloidal rods as "chains-of-spheres" more accurately consider position and orientation dependent hydrodynamic interactions, but the results are limited to a single aspect ratio and a single wall surface.[37] In short, easy-to-use, parametric, experimentally validated models are not currently available to interpret and predict boundary effects on colloidal rod diffusion.

In this work, we use optical microscopy to measure translational and rotational diffusion of colloidal rods versus aspect ratio, solution ionic strength, and geometries (Figure 1). We investigate gold (Au) rods with cross-sectional diameters of $d = 2a = 300$ nm and lengths of $L \approx 2-6$ μm to probe aspect ratios of $p = L/d \approx 7-20$. Rod-wall geometries studies include (1) particles levitated above single planar wall surfaces via a balance of gravity and electrostatic repulsion, (2) particles confined in a quasi-two-dimensional gap between two nominally parallel walls in a slit pore geometry, and (3) particles confined within a quasi-two-dimensional porous media that is formed by 2 μm spherical silica colloid spacers in random amorphous configurations at different area fractions. The solution ionic strength is varied from the minute ionic strength of deionized water (0.03 mM) up to 5 mM NaCl, to mediate electrostatic repulsion and the average rod−wall separation distance (without causing deposition or contact). Measured diffusivities are compared to a recent model developed by us[38] using a Stokesian dynamic method of computing diffusion tensors for rigid chains-of-spheres near surfaces. In particular, closed-form expressions fit to computational simulations for translational and rotational diffusivities are compared to experimental measurements as a function of rod−wall separation and rod aspect ratio.

Received: May 21, 2017
Revised: July 23, 2017
Published: August 9, 2017

DOI: 10.1021/acs.langmuir.7b01704
Langmuir 2017, 33, 9034−9042

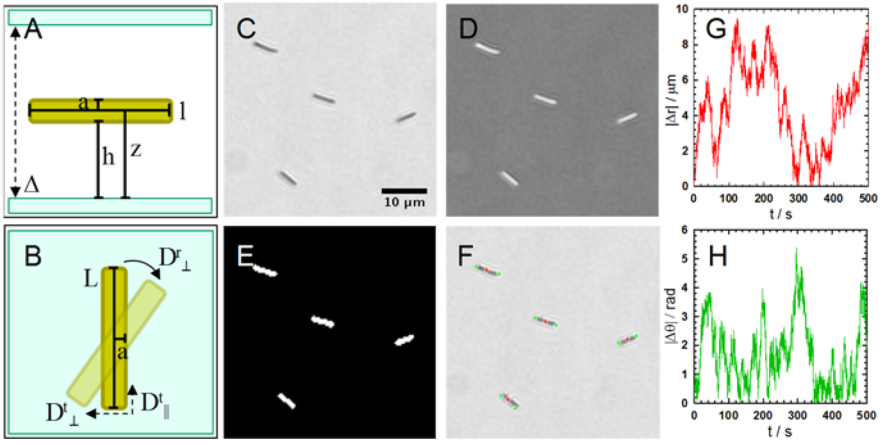

Figure 1. Rod-wall schematics, image analysis, and raw trajectories. Schematics of colloidal rod particle adjacent to planar surface with defined variables from (A) side and (B) top views. Representative images of Au colloidal rods and depiction of key image analysis steps showing (C) raw transmitted light image, (D) inversion, (E) binary thresholding, and (F) center and end point labeling. Plots of magnitude of displacement of center of mass position (G) and angular orientation (H) with respect to origin in laboratory coordinates for a single rod particle, corresponding to labels from (F).

THEORY

Bulk Translational and Rotational Diffusion. The translational diffusivity of an isolated rod particle far from any boundaries with long axis, L, and diameter, $d = 2a$, can be expressed in terms of its aspect ratio, $p = L/d$ (Figure 1). Expressions reported here, for the bulk diffusion of chains-of-spheres,[38] agree with established models of Tirado and co-workers for cylindrical particles.[19,39,40] The diffusion coefficient for translational diffusion parallel to the long axis is given by[38]

$$D_{\parallel}^{t,b}(p) = (kT/2\pi\eta L) f_{\parallel}^{t,b}(p) \tag{1}$$

where

$$f_{\parallel}^{t,b}(p) = \ln(p) + \frac{-0.4536p^2 - 1.772p + 41.5}{p^2 + 34.38p + 18.96} \tag{2}$$

and the coefficient for translational diffusion perpendicular to the long axis is given by

$$D_{\perp}^{t,b}(p) = (kT/2\pi\eta L) f_{\perp}^{t,b}(p) \tag{3}$$

where

$$f_{\perp}^{t,b}(p) = \ln(p) + \frac{-0.3604p^2 + 28.36p + 72.63}{p^2 + 36.29p + 34.9} \tag{4}$$

and η is the fluid medium viscosity, k is Boltzmann's constant, and T is absolute temperature. The three-dimensional center of mass translational diffusion coefficient is given by

$$D^{t,b}(p) = (1/3)D_{\parallel}^{t,b}(p) + (2/3)D_{\perp}^{t,b}(p) \tag{5}$$

The rotational diffusivity of an isolated rod particle perpendicular its long axis is given by

$$D_{\perp}^{r,b}(p) = (3kT/\pi\eta L^3) f_{\perp}^{r,b}(p) \tag{6}$$

$$f_{\perp}^{r,b}(p) = \ln(p) + \frac{-1.373p^3 - 19.39p^2 - 148.1p + 265.2}{p^3 + 56.43p^2 + 54.35p - 268.4} \tag{7}$$

Interfacial Translational and Rotational Diffusion. Here we summarize expressions for diffusion of chains of spheres as a function of distance relative to a planar interface when the chain's long axis is oriented parallel to the interface.[38] The results converge to the bulk diffusivities in eqs 1−7 for large separations, and to asymptotic results for infinitely long cylinders near a wall[36] at vanishing separations. The translational diffusivity of a rod particle parallel to its long axis and parallel to a no-slip planar interface, for $h < a$ and $6 < p < 16$, is given by

$$D_{\parallel}^{t,i}(p, h) = D_{\parallel}^{t,b}(p) g_{\parallel}^{t,i}(h) \tag{8}$$

where using the definition for $z = h + a$ (see Figure 1), the function $g(h)$ is given as

$$g_{\parallel}^{t,i}(h) = \frac{0.9909(z/a)^3 + 0.3907(z/a)^2 - 0.1832(z/a) - 0.001815}{(z/a)^3 + 2.03(z/a)^2 - 0.3874(z/a) - 0.07533} \tag{9}$$

and the coefficient for translational diffusion perpendicular to the long axis, again for $h < a$ and $6 < p < 16$, is given by

$$D_{\perp}^{t,i}(p, h) = D_{\perp}^{t,b}(p) g_{\perp}^{t,i}(h) \tag{10}$$

where

$$g_{\perp}^{t,i}(h) = \frac{0.9888(z/a)^3 + 0.788(z/a)^2 - 0.207(z/a) - 0.004766}{(z/a)^3 + 3.195(z/a)^2 - 0.09612(z/a) - 0.1523} \tag{11}$$

and the two-dimensional center of mass translation diffusion coefficient at a given surface to surface separation is given by

$$D^{t,i}(p, h) = (1/2)D_{\parallel}^{t,i}(p, h) + (1/2)D_{\perp}^{t,i}(p, h) \tag{12}$$

The rotational diffusivity of a rod shaped particle perpendicular its long axis as a function of its aspect ratio and height above the planar surface, interface, for $h < a$ and $6 < p < 16$, is given by

$$D_{\perp}^{r,i}(p, h) = D_{\perp}^{r}(p) g_{\perp}^{r,i}(h) \tag{13}$$

where

$$g_{\perp}^{r,i}(h) = \frac{0.998(z/a)^3 + 131.1(z/a)^2 + 21.25(z/a) + 0.01275}{(z/a)^3 + 128.7(z/a)^2 + 121.1(z/a) + 2.897} \tag{14}$$

Confined Translational and Rotational Diffusion. For a single colloid confined between two parallel planar surfaces with separation, δ, the hydrodynamic hindrance to lateral diffusion can be described using

$$D^{2w}(z, a, \delta) = D^{b} f^{2w}(z, a, \delta) \tag{15}$$

where a number of approximate solutions exist for $f^{2w}(z,a,\delta)$. The simplest of these is the linear superposition approximation (suggested

DOI: 10.1021/acs.langmuir.7b01704
Langmuir 2017, 33, 9034−9042

by Oseen),[41] which includes hydrodynamic hindrance of each wall from the single wall results as given by

$$f^{2w}(z, a, \delta) = [f^{1w}(z, a)^{-1} + f^{1w}(\delta - z, a)^{-1} - 1]^{-1} \quad (16)$$

which can be applied with any of the separation-dependent diffusivities in eqs 1−14.

Measured Average Diffusion Coefficients. Measurements of average diffusivities can be obtained via mean squared positional displacements (MSPD), in one-dimension, $\langle x^2 \rangle$ (or $\langle y^2 \rangle$), as

$$\langle x^2 \rangle = \frac{1}{N_p} \sum_{i=1}^{N_p} [x_i(t) - x_i(0)]^2 = 2\langle D^t \rangle t + \Delta^2 \quad (17)$$

or in polar coordinates, $\langle r^2 \rangle$ (where $r^2 = x^2 + y^2$), as

$$\langle r^2 \rangle = \frac{1}{N_p} \sum_{i=1}^{N_p} [r_i(t) - r_i(0)]^2 = 4\langle D^t \rangle t + \Delta^2 \quad (18)$$

and for mean squared angular displacements (MSAD), $\langle \theta^2 \rangle$, as

$$\langle \theta^2 \rangle = \frac{1}{N_p} \sum_{i=1}^{N_p} [\theta_i(t) - \theta_i(0)]^2 = 2\langle D^r \rangle t + \Delta^2 \quad (19)$$

where N_p is the number of particles, and Δ^2 is related to the square of the uncertainty in either the particle center position or long-axis orientation due to limited spatial resolution (i.e., the CCD camera pixel size is approximately equal to Δ).

Potential Energy Profiles. The potential energy for an isolated rod particle with L parallel to an underlying planar surface can be calculated by the sum of contributing potentials as

$$U(z) = U_G(z) + U_E(z) \quad (20)$$

where the subscripts refer to the gravitational (G) and electrostatic (E) interactions, $z = h + a$ is the particle center to the wall surface (Figure 1), h is the particle surface to wall surface separation, and a is the rod short-axis radius. van der Waals attraction is expected to be negligible based on our previous studies of Au−silica interactions.[42]

The gravitational potential energy of each rod depends on its buoyant weight, G, as the product of particle volume and density mismatch with the medium as given by

$$U_G(z) = Gz = mg(h + a) = \pi a^2 L(\rho_p - \rho_f)\, g(h + a) \quad (21)$$

where m is buoyant mass, g is acceleration due to gravity, and ρ_p and ρ_f are particle and fluid densities, respectively. For rods where the potential energy associated with elevating one end relative to the other is $>5kT$, the long axis will remain parallel to the underlying wall. For this orientation, the rod−wall electrostatic interaction depends on the nondimensional double layer thickness. In particular, for thin double layers ($\kappa a \gg 1$) and a 1:1 electrolyte, we consider a solution based on the nonlinear Poison−Boltzmann equation to model the electrostatic double layer on flat plates. Used with the Derjaguin approximation for geometry correction, this gives a potential as[43]

$$U_E^{ND}(z) = 64\pi LB(\kappa a/2\pi)^{0.5} \exp[-\kappa z] \quad (22)$$

where

$$B = \varepsilon \left(\frac{kT}{e}\right)^2 \tanh\left(\frac{e\psi_p}{4kT}\right) \tanh\left(\frac{e\psi_w}{4kT}\right) \quad (23)$$

and

$$\kappa = \left[\frac{e^2 N_A}{\varepsilon kT} \sum_i C_i\right]^{1/2} \quad (24)$$

where κ is the inverse Debye screening length, ε is the solvent dielectric constant, e is the elemental charge, ψ_p and ψ_w are the surface potentials of the particle and the wall, respectively, N_A is Avogadro's number, and C_i is electrolyte molarity.

For thick double layers ($\kappa a \approx 1$) and a 1:1 electrolyte, we approximate the interaction by considering a chain of touching spheres, each of radius, a, and total number of L/a, and use the linear superposition approximation for sphere−plate interactions[44] to give

$$\begin{aligned} U_E^{LS}(z) &= (L/2a) U_{E,PW}^{LS}(h) \\ &= (L/2a) 16\pi aB \exp(-\kappa z) \\ &= 8\pi LB \exp(-\kappa z) \end{aligned} \quad (25)$$

Average Particle−Wall Separation and Diffusivities. Colloidal rods experience Brownian motion and sample a range of heights relative to underlying wall surfaces in the presence of the colloidal interactions and gravity given in eqs 20−25. By considering the balance of electrostatic and gravitational interactions, the rod's most probable elevation, h_m, can be determined where the gradient of the potential vanishes (i.e., where the sum of the forces is zero). Using the potential in eq 22, the value of h_m is

$$h_m^{ND} = \kappa^{-1} \ln\left[\frac{64(\kappa^3 a/2\pi)^{0.5} B}{a^2(\rho_p - \rho_f)g}\right] \quad (26)$$

whereas using the potential in eq 25 gives the value of h_m as

$$h_m^{LS} = \kappa^{-1} \ln\left[\frac{8\kappa B}{a^2(\rho_p - \rho_f)g}\right] \quad (27)$$

For comparison, it is also possible to compute the average elevation, $\langle h \rangle$, from the particle−wall interactions by considering the Boltzmann weighted integral average as

$$\langle h \rangle = \frac{\int h p(h)\, dh}{\int p(h)\, dh} \quad (28)$$

where $p(h)$ is the probability of rod−wall separations given by a Boltzmann distribution as

$$p(h) = p(h_m) \exp[-(U(h) - U(h_m))/kT] \quad (29)$$

While the position dependent diffusivities in eqs 1−16 can be evaluated at discrete elevations such as h_m or $\langle h \rangle$ in eqs 26−28, the average diffusivity, $\langle D \rangle$, for each diffusion mode is accurately predicted as an average over the equilibrium distribution of heights sampled by confined particles as given by[25,30,42]

$$\langle D \rangle = \frac{\int D(h)\, p(h)\, dh}{\int p(h)\, dh} \quad (30)$$

MATERIALS AND METHODS

Colloids and Surfaces. Hydrochloric acid, potassium hydroxide, sodium chloride, and colloidal SiO_2 (2.34 μm) were used as received without further purification. Au rods were electrochemically grown to prescribed lengths in 300 nm pores of anodic aluminum oxide membranes (that determine the Au rod diameter from SEM[45]). The alumina template was dissolved in base, and rods were freed from a thin film using nitric acid.[45] Rods were dispersed in deionized water. Zeta potential (ζ) was used as an estimation of the surface potential for the Au rods (ψ_p), and was measured at four ionic strength conditions using electrophoretic mobility.

For quasi-2D porous media experiments, dilute silica spacer particle dispersions were prepared by adding 0.5 μL of the stock to 4 mL of DI water, whereas concentrated dispersions for spin coating were prepared by diluting 100 μL of stock silica in 1 mL of 0.1 mM NaCl. The addition of NaCl aided in adhering the silica particles to the coverslips during spin coating. Au rod dispersions were prepared by diluting 60 μL of stock into 136 μL of electrolyte solution and 4 μL silica particle spacers. For two-wall experiments, this dispersion was used as is to confine the rods, and for one-wall experiments the dispersion was diluted to achieve the desired ionic strength. The silica

DOI: 10.1021/acs.langmuir.7b01704
Langmuir 2017, 33, 9034−9042

spacer particles have previously been shown to have a diameter of 2.1 μm,[46,47] which then also sets the two-wall experiment gap dimension.

Sample Cells. Glass microscope coverslips (24 mm × 60 mm) were wiped clean with lens paper, and then sonicated for 30 min in acetone and 30 min in isopropanol before being soaked in Nochromix overnight. Small glass coverslips (18 mm × 18 mm) were wiped with lens paper and placed directly into Nochromix. All coverslips were rinsed with deionized (DI, 18.3 MΩ) water and soaked in 0.1 M KOH for 30 min, and then rinsed with DI water again and dried with nitrogen before use.

O-Ring sample cells for one-wall experiments were constructed by using vacuum grease to adhere a 5 mm ID O-ring to a clean long coverslip. Afterward, dilute Au rod dispersions were pipetted into the O-ring, a small coverslip was placed on top and then sealed with vacuum grease. Confined cells were created by adding 10 μL of the Au/silica spacer particle mixture onto the center of a coverslip. A coverslip was placed on top of the droplet to confine particles between the two walls. Lens paper was used to wick away extraneous solution from between the coverslips until interference patterns were observed. The two coverslips were sealed together using epoxy.

Porous media sample cells were prepared by spin coating 100 μL of concentrated silica particle dispersion onto a long glass coverslip at 1000 rpm for 40 s. After spin coating, the coverslip was placed on a hot plate and dried overnight at 50 °C. Silica colloid coated coverslips were gently rinsed with DI water three to five times to remove any crystallized salt and then dried for 10 min on a hot plate. After drying, 12 μL of the Au rod stock was deposited onto the center of the coated coverslip and sealed in the same manner as the confined sample cells.

Microscopy. The two-wall experiments were performed using transmitted light on an upright microscope with a 63× objective (NA = 0.75). The one-wall and quasi-2D porous media experiments were performed on an inverted microscope with a 63× objective (NA = 0.75) using transmitted light and dark field, respectively. A dry dark field condenser attachment (NA = 0.8/0.95) was used to image experiments performed with concentrated porous media. Particle trajectories were monitored with a 12bit CCD camera in 4-binning mode for 30 000 frames at ≈27.6 fps for one-wall and two-wall experiments and at ≈10 fps for porous media experiments.

Particle Tracking. A new image analysis algorithm coded in FORTRAN 77 and MATLAB 2015a was developed to track particle translation and rotation. Rods appear dark on a bright background in transmitted light illumination (Figure 1C), and subsequent inversion (Figure 1D) and binary thresholding (Figure 1E) to identify all pixels comprising the rod. After identification of the coordinates of all pixels comprising a rod, x_i and y_i, the coordinates of the center of mass (red points in Figure 1F) of each rod, x_{cm} and y_{cm}, can be calculated as

$$x_{cm} = n^{-1} \sum_{i}^{n} x_i \tag{31}$$

$$y_{cm} = n^{-1} \sum_{i}^{n} y_i \tag{32}$$

Rod end points (green points in Figure 1F) were identified as the maximum distance from the center-of-mass coordinates and used to track the distance, R_i, and angle, θ_i, of each end point as

$$R_i = [(x_{cm} - x_i)^2 + (y_{cm} - y_i)^2]^{0.5} \tag{33}$$

$$\theta_i = \arctan[(y_{cm} - y_i)/(x_{cm} - x_i)] \tag{34}$$

which were used to compute MSPD and MSAD curves using the eqs 17−19 and the multiple time origin method.[30] Figure 1G, H shows the magnitude of the center-of-mass position displacement and angular displacement vs time for a single rod. The instantaneous length of each rod is obtained by calculating the distance between the center and each end point and summing the two radii. The reported rod lengths are the most probable values obtained from histograms of all measured lengths for each particle.

For porous media experiments, a separate algorithm in MATLAB was used to identify silica microsphere positions and perimeters in dark field microscopy images using algorithms adapted for tracking cells.[48,49] The scheme is created by thresholding the silica particles based on a "solidity" factor (based on a percentage of white pixels). The solidity factor distinguishes the spheres, which appear as white halos around darker centers, from the much brighter Au rods. Boundaries were drawn around the silica particles that met the required solid percentage (but not around Au rods), which were overlaid in images and videos. The area fraction (ϕ) of the image contained within the silica particle boundaries was also calculated.

RESULTS AND DISCUSSION

Measuring Rod Translational and Rotation Diffusion.

Figure 2 shows mean squared positional displacements (MSPD) and mean squared angular displacements (MSAD) versus time from analyzing optical microscopy videos of ≈10 Au rods in 0.1 mM NaCl. Results are obtained for particles near a single wall, where they are confined by gravity, and for particles confined between two parallel walls separated by ≈2 μm diameter silica spacers. Each curve is fit via linear regression to eqs 18 and 19 to obtain $D^{t,i}$ and $D^{r,i}$. The measured values of $D^{t,i}$ and $D^{r,i}$ in Figure 2 show that shorter rods translate and rotate more quickly than longer rods having the same short-axis diameter (300 nm), consistent with expectations.

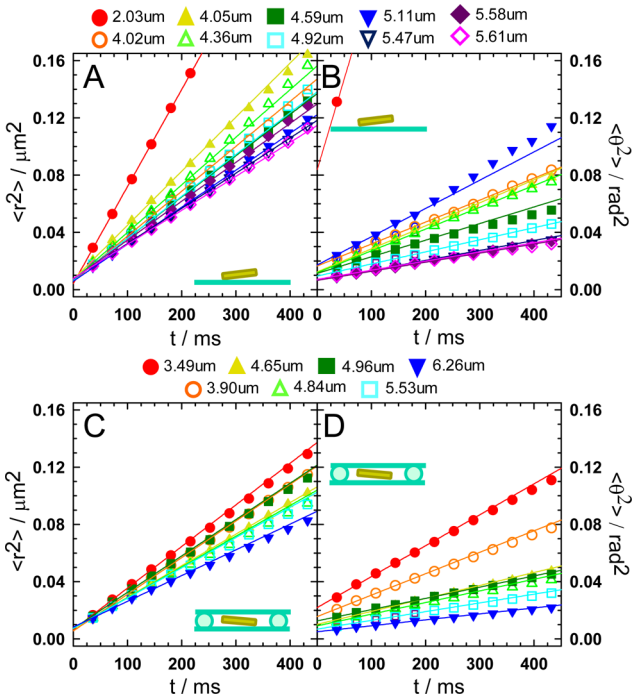

Figure 2. Mean square displacement date vs rod length and wall geometry. Mean squared (A, C) positional and (B, D) angular displacement vs time for Au colloidal rod particles with cross-sectional diameters of $d = 2a = 300$ nm. Results are reported for [NaCl] = 0.1 mM and varying rod lengths (see legend) adjacent to one wall (A, B) or confined between parallel walls separated by ≈2 μm (C, D). Symbols show particle tracking data, and lines are fits using eqs 18 and 19.

Deviations from the expected monotonic trends in Figure 2 may be the result of irregularities in the cylindrical rod shape, heterogeneities on the surfaces of the gold or silica, and spatiotemporal resolution limits in the experimental recordings. For example, blue triangles in Figure 2B correspond to a rod

DOI: 10.1021/acs.langmuir.7b01704
Langmuir 2017, 33, 9034−9042

having L = 5.11 μm with a higher than expected rotational diffusion. In this specific instance, a slight curve to the rod shape may produce rolling motion at the rod ends that appears as faster rotation. In another case, the 4.02 and 4.05 μm rods are simply two different rods, with lengths that are not significantly different relative to the image pixel size, and as such, differences in their measured diffusivities are also attributed to nonuniformities. Finally, the red circles for the shortest ~2 μm rod in Figure 2 show an inadequate combination of spatial and temporal resolution necessary to capture the fast rotation of the smallest rod in this study. The last case is perhaps also most susceptible to out-of-plane 3D motion that could also make the apparent projected 2D rotation appear faster.

When comparing the two experimental geometries (one-wall versus two-walls) in Figure 2, the rods in the one-wall experimental system (Figure 2A) display faster translational diffusion than in the two-wall experiments (Figure 2C). The second confining wall (≈2 μm separation) introduces an additional drag that can be expected to slow diffusion, consistent with expectations, results for spherical nanoparticles and nanotubes,[26,27,35] and simulations of anisotropic particles.[38] However, this effect is much less pronounced for rotational diffusion, which shows comparable rates for similar sized rods in both geometries (Figure 2B, D). Previous experiments have also observed limited effects of confinement on rotational diffusion.[34]

Diffusivity vs Aspect Ratio, Ionic Strength, and Geometry. Many measurements of particle diffusion for one-wall and two-wall configurations, like the ones reported in Figure 2, were performed versus ionic strength to vary how particles sample positions near the wall surface via differing strengths of electrostatic interactions.[26,27,35] Figure 3 reports diffusivities versus aspect ratio, $p = L/d$, from $p \approx 10$ to 20 (where $d = 2a$ = 300 nm) and ionic strengths corresponding to deionized water (≈ 0.03 mM NaCl) up to 5 mM NaCl. Diffusivities for each of the four cases in Figure 3 were fit using the expressions in eqs 8−16, where the only adjustable parameter for each ionic strength was the elevation, h, of the Au rod above the surface. For the translational diffusivities in Figure 3A and C, the solid lines are least squared error fits, and the two types of dashed lines capture the maximum and minimum values necessary to enclose all data for each ionic strength. For the rotational diffusivities in Figure 3B and D, the theoretical curves are relatively insensitive to elevation and aspect ratio. As such, given the error bars in the measured data, we plot theoretical curves using the elevations fit to the translational diffusivities (rather than performing an independent least-squares fit to the measured rotational diffusivities). Using this approach, there is good agreement between the measurements and predictions. The fit values of h for each case are reported in Figure 4.

The translational diffusion of rods is faster for shorter aspect ratios, lower ionic strength solutions, and one-wall configurations as shown by the theoretical curves in Figure 3A and C. For example, the DI and 0.1 mM diffusivities are ≈30% higher for the one-wall than for the two-wall geometry, and the 1 and 5 mM conditions are ≈20% higher for one-wall than two-wall configurations. There is also a decrease in the spread of the diffusivities measured, and thus the heights sampled by the rods, with the more confined geometry as is observed for both D^t and D^r. As Figure 2 shows, the rotational diffusivities in Figure 3 exhibit a relative insensitivity to the one- or two-wall

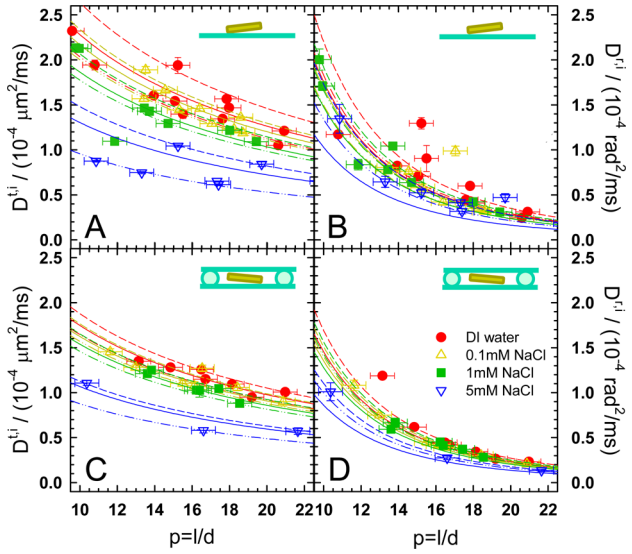

Figure 3. Rod diffusion vs solution ionic strength and wall geometry. Translational (A, C) and rotational (B, D) diffusion coefficients versus aspect ratio (abscissa) and ionic strength (see inset legend). The data points are the initial slopes of measured mean squared positional and angular displacements shown in Figure 2. For the translational diffusivities (A, C), the solid lines are least squared error fits to the D^t using particle−wall separation, h, as the sole adjustable parameter in eq 12 for one wall and eq 15 for two walls; the dashed and dot-dot-dashed lines are the same equations fit to enclose the maximum and minimum values, respectively, within each ionic strength data set. For the rotational diffusivities (B, D), the lines are computed using the values of h fit to translational diffusion data as input into eq 13 for one wall and eq 15 for two walls. Error bars are for each rod measured and are obtained as one pixel length at binning 4 (385 nm) for p, and the standard deviation of the slope in Figure 2 for D^t and D^r.

configurations, but show a clear dependence on rod aspect ratio, as well as ionic strength.

The decreasing diffusivities for increasing ionic strength are the result of decreasing electrostatic repulsion that allows particles to approach wall surfaces more closely, and thus increases hydrodynamic resistance on particle motion. The decrease in translational diffusion is greater than the decrease in rotational diffusion, with particle−wall separation mediated by the solution ionic strength. This observed insensitivity in D^r is consistent with a prior modeling study of rods as chains of spheres,[50] which is similar to the hydrodynamic model developed in our work.[38] The explanation for the difference between the separation dependence of the translational and rotational diffusivities can be explained by considering the rods as chains-of-spheres. Translation of chains-of-spheres are governed by the collective diffusion of the spheres comprising the chain, which decrease significantly with decreasing particle−wall separation. In contrast, rotation of chains-of-spheres depends on the diffusion of spheres relative to each other, which is insensitive to particle−wall separation for the elevations probed in this study.

Measured vs Modeled Diffusivities. The predicted diffusivities show good correspondence with the measured diffusivities for a single adjustable parameter, h. To test the accuracy of the fit separation estimates, and hence the elevation-dependent diffusivity models, we compare fits to predictions based on the conservative forces acting on the rods. Figure 4 shows the values of the rod particle−wall surface-to-surface separation from experiment and theory. Rod separations

DOI: 10.1021/acs.langmuir.7b01704
Langmuir 2017, 33, 9034−9042

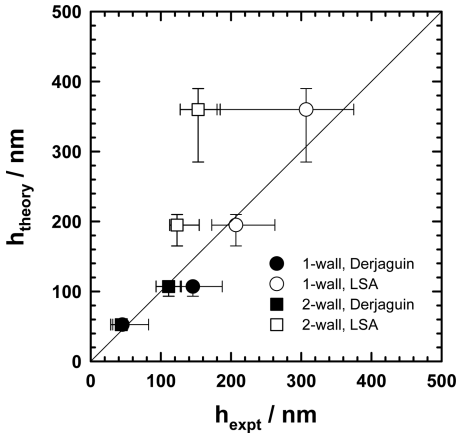

Figure 4. Rod–wall separations from measured diffusivity analysis vs colloidal force predictions. Values of particle–wall surface-to-surface separation from experiments, h_{expt}, in Figures 2 and 3 and from theoretical models, h_{theory}, using eqs 26 and 27. Values of h_{expt} were obtained by fitting translational diffusivities near one wall (circles) to eq 12 and between two walls (squares) to eq 15. Error bars on h_{expt} were obtained from the limiting lines in Figure 3 that contain all data points for each ionic strength. Values of h_{theory} were obtained for double layers that are thin relative to the rod radius ($\kappa a \gg 1$; 1–5 mM, filled points) using eq 26 and for double layers that are comparable to the rod radius and particle separation ($\kappa a \approx \kappa h \approx 1$; 0.03–0.1 mM, open points) using eq 27 (based on conditions for most accurate models for electrostatic interactions between spheres[51]). Surface potentials used to compute h_{theory} were chosen as $\psi_p = \zeta_p$ for the rod based on ionic strength dependent measurements in Figure 3 and as $\psi_w = -50$ mV for the glass slide with error bars based on low and high estimates of −10 and −100 mV.[52]

from fits to translational diffusion experiments, h_{expt}, for the one-wall and two-wall cases in Figure 3 are plotted on the x-axis, and separations from theoretical models, h_{theory}, using eqs 26 and 27 are shown on the y-axis.

Values of h_{expt} are indicated as single points in Figure 4 and represent the best-fit separation for each $D^{t,i}$ versus p curve for each ionic strength in Figure 3. The error bars in Figure 4 are taken from the extreme (dashed, dot-dot-dashed) curves of Figure 3. Values of h_{theory} are computed using eq 26 for the higher ionic strengths ([NaCl] = 1 mM, 5 mM) and eq 27 for lower ionic strengths ([NaCl] = 0.03 mM, 0.1 mM), based on constraints determined by the relative thickness of the double layer to the rod radius, κa, and rod–wall separation, κh, as noted in the Theory section.[53] The points for h_{theory} are based on wall surface potentials of $\psi_w = -50$ mV, obtained from prior measurements,[52] and error bars are based on more extreme surface potentials of $\psi_w = -10$ mV and $\psi_w = -100$ mV (with the rest of the model parameters reported in Table 1).

Agreement is good between the rod–wall separations inferred from model fits to translational diffusion data and predictions based on a balance of electrostatic repulsion and gravity (within error bars in Figure 4). This agreement is excellent at higher ionic strengths where the rod is closer to the bottom wall for both the one-wall and two-wall configurations. The agreement is worse (error bars do not account for discrepancies) for the systematically higher elevations predicted for the two-wall configuration at low ionic strengths. This could occur for a variety of reasons including (1) the electrostatic repulsion exerted by the top-wall is neglected in eq 27 and could cause particles to sample lower elevations than predicted, (2) the Brownian rotation perpendicular to the wall increases as it gets further away from the bottom wall; this effect is neglected (because it is nontrivial to include) both in terms of its influence on rod elevation as well as rod transport in the plane parallel to the bottom wall, and (3) the two-wall hydrodynamic correction in eq 16 based on one-wall is approximate (as discussed for spheres[26,35,54,55]), and could introduce some uncertainty in the elevation inferred from translational diffusion measurements.

Table 1. Constants Used in Theoretical Fits

variable (units)	value
$d = 2a$ (μm)	0.3
ρ_p (g/cm^3)	19.3
ρ_f (g/cm^3)	1.00
ε_w	78
T (K)	294
η (Pa·s)	1.002×10^{-3}
δ (μm)	2.1
NaCl (mM)	≈0.03, 0.1, 1, 5
κ^{-1} (nm)	55, 27, 9.3, 4.3
$\psi_p = \zeta_p$ (mV)	−24, −24, −20, −15
ψ_w (mV)	−50

As a final note, a rigorous consideration of the separation-dependent diffusion should include an average over all elevations[25,30] (eq 30) rather than a single elevation (e.g., most probable (eqs 26, 27) or average elevation (eq 28)). Although evaluation of $D(h)$ at a fixed elevation appears sufficient to generate agreement for most results in Figure 4, the potential energy ($U(h)$ in eq 29) could become asymmetric versus separation and include angular dependence (e.g., $U(h,\theta,\phi)$). A significantly different rod–wall interaction potential could cause the average over the probability ($p(h)$ in eq 29) to produce a value of $\langle D \rangle$ that is different from evaluating $D(h)$ at the mode or mean of $p(h)$. Such an effect could become more pronounced as particles move further from the bottom wall and also interact with the top wall. In any case, further efforts to test this idea by constructing models for a possible $U(h,\theta,\phi)$ are beyond the scope of the present work, and ultimately do not appear necessary to explain the agreement observed for the majority of the data in Figure 4. In short, diffusivities from evaluating the position dependent expressions at the most probable or average elevation, or by computing an average diffusivity over all sampled elevations, are all practically the same, with the exception of the low ionic strength cases.

Translational Diffusion in Quasi-2D Porous Media. Based on the agreement between experiments and models for rod diffusion near one and two walls, an experiment was designed to measure diffusion in quasi-2D porous media (Figure 5). These experiments measured short-time diffusion specifically as a probe of hydrodynamic interactions,[28,31,56,57] which are the main interest of this paper, without probing the role of pore microstructure on long-time diffusion (e.g., as studied by others[58,59]). Figure 5 shows trajectories and MSPD for translational diffusion of Au rods in very low ionic strength solution within a randomly oriented 2D porous media consisting of silica particles spin-coated onto a bottom coverslip and acting as spacers between a top coverslip. Similar to the two-wall case in Figures 2–4 (which is practically the infinitely dilute case for the experiments in Figure 5), the gap space is determined by the silica spacer particles to be ≈2.1 μm. Dark field microscopy was used to obtain contrast to simultaneously

DOI: 10.1021/acs.langmuir.7b01704
Langmuir 2017, 33, 9034–9042

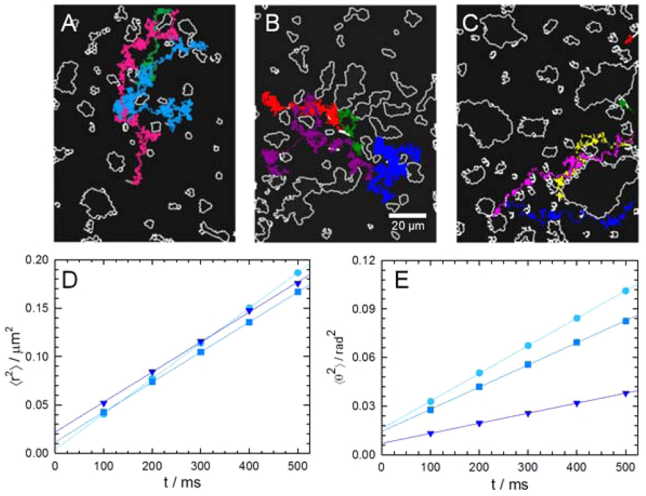

Figure 5. Short-time rod diffusion in quasi-2D porous media. Processed images from dark field microscopy experiments of Au rod diffusion in quasi-2D porous media with area fractions of (A) 0.085, (B) 0.156, and (C) 0.245. Colored trajectories of different Au rods illustrate translational diffusion in the course of the 50 min observation time. (D) MSPDs and (E) MSADs for the three blue trajectories in (A)−(C), which all correspond to rods of L = 3.3−3.4 μm with points indicating area factions of (circles) 0.085, (squares) 0.156, and (triangles) 0.245.

track Au particle diffusion and silica particle porous media boundaries.

Figure 5A−C shows trajectories for diffusion in quasi-2D porous media with area fractions of 0.085, 0.156, and 0.245. Overlaid in different colors are trajectories for individual rods for 50 min. Figure 5D shows short-time limit MSPDs for three rods with comparable lengths of ≈3.4 μm in Figure 5A−C designated by blue trajectories. For all three porous media area fractions tested, the resulting translational diffusivity is $\approx D$ = 2 μm^2/ms, which is essentially the same as the two-wall results in Figure 3 for $p = l/d$ = 3.4 μm/0.3 μm ≈ 11 and deionized water (where again, the results in Figure 3 are a quasi-2D porous media experiment with an area fraction near zero). Figure 5E shows short-time limit MSADs for the same three rods in Figure 5D. The resulting rotational diffusivities are near the two-wall results for the lowest area fraction but drop by a factor of ∼3 for the highest area fraction investigated here. In short, the translational diffusivities for the three porous medium area fractions are not obviously distinguishable from each other, whereas the rotational diffusivities show a clear decrease with increasing area fraction.

The short-time translational diffusivity (Figure 5D) exhibits the hydrodynamic effects of the confining walls, but is insensitive to the local environments determined by the porous medium area fraction. This effect could arise from simply from averaging over rod positions far from the porous media surfaces that contribute to the net average diffusivity similar to the case without porous media. However, the reduced short-time rotational diffusivity (Figure 5E) with increasing area fraction indicates that interactions between rods and porous media surfaces do hinder rotational motion, which is perhaps to be expected. To explain both translational and rotational diffusivity trends in a self-consistent manner, electrostatic repulsion between the rod and porous media may produce alignment of the rod's long-axis parallel to the porous medium surface. As a result, rotation will be hindered, but the resulting translation is dominated by this fastest diffusion mode for these configurations (eq 8).[60] This may be an example of how position and orientation are correlated, and how translational and rotational diffusion can be coupled,[16] as determined by interactions with the local porous media structure. This effect appears to produce about the same translational diffusivity in Figure 5 as confinement between two walls without porous media (Figure 3) (where the average motion parallel and perpendicular to the major axes determine the net diffusivity).

The long-time diffusivity for the trajectories in Figure 5A−C varies for the different quasi-2D porous media area fractions. However, in this initial study, we focused on the short-time behavior that is dominated by hydrodynamic interactions, which are relevant to the models being explored in this work. Practically, much more temporal and spatial sampling is required to obtain sufficient statistics and averaging of rod trajectories over locally heterogeneous media to obtain more general results for long-time diffusion.[61] It is also important to note that the short-time diffusivity investigated in this work, by necessity, always has a critical role in long-time diffusion; i.e., diffusion over longer times and distances necessarily requires many diffusive steps over short times and distances. For example, diffusion in dense suspensions[57] or porous media[62] includes a short-time diffusion term (accounting for local hydrodynamic interactions) multiplied by a term associated with long-time diffusion through surrounding microstructures (accounting for global energy landscapes). Our findings in this work on the role of hydrodynamic interactions in interfacial and confined diffusion of rod shaped colloidal particles can eventually be incorporated into more complex models for long-time diffusion that consider additional complexities of porous media microstructure (e.g., as studied by others[58,59]).

CONCLUSIONS

Measurements and models of interfacial and confined diffusion show agreement for different confinement geometries, rod aspect ratios, and electrostatic interactions. Measurements of translational and rotational diffusion of rods with aspect ratios of $p = l/d \approx$ 10−20 near one wall and confined between two walls agree quantitatively within the limits of uncertainty with models we developed to include position dependent hydrodynamic interactions. Significant reductions in translational and rotational diffusivities are observed as rod particles experience positions closer to boundaries. Aqueous solution ionic strength was investigated to mediate electrostatic repulsion between rods and surfaces. Ionic strength dependent diffusivities show that rod−wall separations predicted by theories for electrostatic repulsion (balanced by gravity) show good correspondence with separations inferred by fitting measured diffusivities to separation dependent models.

Finally, we show that short-time translational diffusion in quasi-2D porous media produces results nearly independent of porous media area fraction (whereas long-time diffusion is expected to be sensitive to porous media microstructure). In contrast, the short-time rotational diffusivity decreases with increasing porous media area fraction presumably due to rod interactions with porous media surfaces. The net neutral effect of porous media on short-time translation diffusion may be explained by hydrodynamic hindrance being compensated by faster translational diffusion along rod particles' long axes due to parallel alignment along porous media surfaces. Future studies will incorporate findings from this work on the role of hydrodynamic interactions on interfacial and confined diffusion

DOI: 10.1021/acs.langmuir.7b01704
Langmuir 2017, 33, 9034−9042

of rod particles into models for long-time diffusion that consider porous media microstructure. Ultimately, findings from this work provide a basis to interpret and predict colloidal rod transport in numerous applications relevant to biological, environmental, and synthetic material systems.

AUTHOR INFORMATION

Corresponding Author

*E-mail: mabevan@jhu.edu.

ORCID

Howard Fairbrother: 0000-0003-4405-9728

Michael A. Bevan: 0000-0002-9368-4899

Notes

The authors declare no competing financial interest.

ACKNOWLEDGMENTS

We acknowledge financial support by the National Science Foundation (CBET-1066254, CHE-1112335, and an IGERT traineeship). We thank Wei Wang and Tom Mallouk from Pennsylvania State University for providing the Au rods used in this study.

REFERENCES

(1) Berg, H. C. *Random Walks in Biology*; Princeton University Press: Princeton, NJ, 1993.

(2) Tavaddod, S.; Charsooghi, M. A.; Abdi, F.; Khalesifard, H. R.; Golestanian, R. Probing passive diffusion of flagellated and deflagellated Escherichia coli. *Eur. Phys. J. E: Soft Matter Biol. Phys.* **2011**, *34* (2), 1−7.

(3) Hunt, A. J.; Gittes, F.; Howard, J. The force exerted by a single kinesin molecule against a viscous load. *Biophys. J.* **1994**, *67* (2), 766−781.

(4) Li, G. L.; Tang, J. X. Diffusion of actin filaments within a thin layer between two walls. *Phys. Rev. E* **2004**, *69*, 061921.

(5) Geng, Y.; Dalhaimer, P.; Cai, S.; Tsai, R.; Tewari, M.; Minko, T.; Discher, D. E. Shape effects of filaments versus spherical particles in flow and drug delivery. *Nat. Nanotechnol.* **2007**, *2* (4), 249−255.

(6) Barua, S.; Yoo, J.-W.; Kolhar, P.; Wakankar, A.; Gokarn, Y. R.; Mitragotri, S. Particle shape enhances specificity of antibody-displaying nanoparticles. *Proc. Natl. Acad. Sci. U. S. A.* **2013**, *110* (9), 3270−3275.

(7) Weiss, T. H.; Mills, A. L.; Hornberger, G. M.; Herman, J. S. Effect of Bacterial Cell Shape on Transport of Bacteria in Porous Media. *Environ. Sci. Technol.* **1995**, *29* (7), 1737−1740.

(8) Liu, Q.; Lazouskaya, V.; He, Q.; Jin, Y. Effect of Particle Shape on Colloid Retention and Release in Saturated Porous Media. *J. Environ. Qual.* **2010**, *39* (2), 500−508.

(9) Salerno, M. B.; Flamm, M.; Logan, B. E.; Velegol, D. Transport of Rodlike Colloids through Packed Beds. *Environ. Sci. Technol.* **2006**, *40* (20), 6336−6340.

(10) Xu, S.; Liao, Q.; Saiers, J. E. Straining of Nonspherical Colloids in Saturated Porous Media. *Environ. Sci. Technol.* **2008**, *42* (3), 771−778.

(11) Fakhri, N.; MacKintosh, F. C.; Lounis, B.; Cognet, L.; Pasquali, M. Brownian Motion of Stiff Filaments in a Crowded Environment. *Science* **2010**, *330* (6012), 1804−1807.

(12) He, K.; Retterer, S. T.; Srijanto, B. R.; Conrad, J. C.; Krishnamoorti, R. Transport and Dispersion of Nanoparticles in Periodic Nanopost Arrays. *ACS Nano* **2014**, *8* (5), 4221−4227.

(13) Arpin, K. A.; Mihi, A.; Johnson, H. T.; Baca, A. J.; Rogers, J. A.; Lewis, J. A.; Braun, P. V. Multidimensional Architectures for Functional Optical Devices. *Adv. Mater.* **2010**, *22* (10), 1084−1101.

(14) Velev, O. D.; Gupta, S. Materials Fabricated by Micro- and Nanoparticle Assembly − The Challenging Path from Science to Engineering. *Adv. Mater.* **2009**, *21* (19), 1897−1905.

(15) Glotzer, S. C.; Solomon, M. J. Anisotropy of building blocks and their assembly into complex structures. *Nat. Mater.* **2007**, *6* (7), 557−562.

(16) Neild, A.; Padding, J. T.; Yu, L.; Bhaduri, B.; Briels, W. J.; Ng, T. W. Translational and rotational coupling in Brownian rods near a solid surface. *Phys. Rev. E* **2010**, *82* (4), 041126.

(17) Broersma, S. Viscous force and torque constants for a cylinder. *J. Chem. Phys.* **1981**, *74* (12), 6989−6990.

(18) Tirado, M. M.; de la Torre, J. G. Translational friction coefficients of rigid, symmetric top macromolecules. Application to circular cylinders. *J. Chem. Phys.* **1979**, *71* (6), 2581−2587.

(19) Tirado, M. M.; de la Torre, J. G. Rotational dynamics of rigid, symmetric top macromolecules. Application to circular cylinders. *J. Chem. Phys.* **1980**, *73* (4), 1986−1993.

(20) Brenner, H. Rheology of a dilute suspension of axisymmetric Brownian particles. *Int. J. Multiphase Flow* **1974**, *1* (2), 195−341.

(21) Wilcoxon, J.; Schurr, J. M. Dynamic light scattering from thin rigid rods: Anisotropy of translational diffusion of tobacco mosaic virus. *Biopolymers* **1983**, *22* (3), 849−867.

(22) Schumacher, G. A.; van de Ven, T. G. M. Brownian motion of rod-shaped colloidal particles surrounded by electrical double layers. *J. Chem. Soc., Faraday Trans.* **1991**, *87* (7), 971−976.

(23) Cush, R.; Dorman, D.; Russo, P. S. Rotational and Translational Diffusion of Tobacco Mosaic Virus in Extended and Globular Polymer Solutions. *Macromolecules* **2004**, *37* (25), 9577−9584.

(24) Mukhija, D.; Solomon, M. J. Translational and rotational dynamics of colloidal rods by direct visualization with confocal microscopy. *J. Colloid Interface Sci.* **2007**, *314* (1), 98−106.

(25) Bevan, M. A.; Prieve, D. C. Hindered Diffusion of Colloidal Particles Very Near to A Wall: Revisited. *J. Chem. Phys.* **2000**, *113* (3), 1228−1236.

(26) Eichmann, S. L.; Anekal, S. G.; Bevan, M. A. Electrostatically confined nanoparticle interactions and dynamics. *Langmuir* **2008**, *24*, 714−721.

(27) Eichmann, S. L.; Bevan, M. A. Direct Measurements of Protein Stabilized Gold Nanoparticle Interactions. *Langmuir* **2010**, *26*, 14409−14413.

(28) Beltran-Villegas, D. J.; Edwards, T. D.; Bevan, M. A. Self-Consistent Colloidal Energy and Diffusivity Landscapes in Macromolecular Solutions. *Langmuir* **2013**, *29* (40), 12337−12341.

(29) Zettner, C. M.; Yoda, M. Particle velocity field measurements in a near-wall flow using evanescent wave illumination. *Exp. Fluids* **2003**, *34*, 115−121.

(30) Anekal, S.; Bevan, M. A. Self Diffusion in Sub-Monolayer Colloidal Fluids Near a Wall. *J. Chem. Phys.* **2006**, *125*, 034906.

(31) Beltran-Villegas, D. J.; Sehgal, R. M.; Maroudas, D.; Ford, D. M.; Bevan, M. A. Fokker−Planck Analysis of Separation Dependent Potentials and Diffusion Coefficients in Simulated Microscopy Experiments. *J. Chem. Phys.* **2010**, *132*, 044707.

(32) Klein, J. D.; Clapp, A. R.; Dickinson, R. B. Direct measurement of interaction forces between a single bacterium and a flat plate. *J. Colloid Interface Sci.* **2003**, *261* (2), 379−385.

(33) Li, G.; Tang, J. X. Diffusion of actin filaments within a thin layer between two walls. *Phys. Rev. E* **2004**, *69* (6), 061921.

(34) Marshall, B.; Davis, V.; Lee, D.; Korgel, B. Rotational and translational diffusivities of germanium nanowires. *Rheol. Acta* **2009**, *48* (5), 589−596.

(35) Eichmann, S. L.; Smith, B.; Meric, G.; Fairbrother, D. H.; Bevan, M. A. Imaging Carbon Nanotube Interactions, Diffusion, and Stability in Nanopores. *ACS Nano* **2011**, *5* (7), 5909−5919.

(36) Jeffrey, D.; Onishi, Y. The slow motion of a cylinder next to a plane wall. *Q. J. Mech. Appl. Math.* **1981**, *34* (2), 129−137.

(37) Padding, J. T.; Briels, W. J. Translational and rotational friction on a colloidal rod near a wall. *J. Chem. Phys.* **2010**, *132* (5), 054511−8.

(38) Yang, Y.; Bevan, M. A. Interfacial Colloidal Rod Diffusion: Coefficients, Simulations & Analysis. *J. Chem. Phys.* **2017**, *147*, 054902.

(39) Tirado, M. M.; de la Torre, J. G. Translational friction coefficients of rigid, symmetric top macromolecules. Application to circular cylinders. *J. Chem. Phys.* **1979**, *71* (6), 2581−2587.

DOI: 10.1021/acs.langmuir.7b01704
Langmuir 2017, 33, 9034−9042

(40) Tirado, M. M.; Martinez, C. L.; de la Torre, J. G. Comparison of theories for the translational and rotational diffusion coefficients of rod-like macromolecules. Application to short DNA fragments. *J. Chem. Phys.* **1984**, *81* (4), 2047−2052.
(41) Happel, J.; Brenner, H. *Low Reynolds Number Hydrodynamics*; Prentice-Hall: Englewood Cliffs, NJ, 1965.
(42) Wu, H.-J.; Everett, W. N.; Anekal, S. G.; Bevan, M. A. Mapping Patterned Potential Energy Landscapes with Diffusing Colloidal Probes. *Langmuir* **2006**, *22*, 6826−6836.
(43) Israelachvilli, J. *Intermolecular and Surface Forces*, 3rd ed.; Academic Press: New York, 2011.
(44) Adamczyk, Z.; Warszynski, P. Role of electrostatic interactions in particle adsorption. *Adv. Colloid Interface Sci.* **1996**, *63*, 41−149.
(45) Yu, J.-S.; Kim, J. Y.; Lee, S.; Mbindyo, J. K. N.; Martin, B. R.; Mallouk, T. E. Template synthesis of polymer-insulated colloidal gold nanowires with reactive ends. *Chem. Commun.* **2000**, *24*, 2445−2446.
(46) Wu, H.-J.; Bevan, M. A. Direct Measurement of Single and Ensemble Average Particle-Surface Potential Energy Profiles. *Langmuir* **2005**, *21* (4), 1244−1254.
(47) Wu, H.-J.; Pangburn, T. O.; Beckham, R. E.; Bevan, M. A. Measurement and Interpretation of Particle−Particle and Particle−Wall Interactions in Levitated Colloidal Ensembles. *Langmuir* **2005**, *21* (22), 9879−9888.
(48) Duncan, G. A.; Fairbrother, D. H.; Bevan, M. A. Diffusing colloidal probes of cell surfaces. *Soft Matter* **2016**, *12* (21), 4731−4738.
(49) Duncan, G. A.; Gerecht, S.; Fairbrother, D. H.; Bevan, M. A. Diffusing Colloidal Probes of kT-Scale Biomaterial−Cell Interactions. *Langmuir* **2016**, *32* (46), 12212−12220.
(50) Lele, P. P.; Swan, J. W.; Brady, J. F.; Wagner, N. J.; Furst, E. M. Colloidal diffusion and hydrodynamic screening near boundaries. *Soft Matter* **2011**, *7* (15), 6844−6852.
(51) Glendinning, A. B.; Russel, W. B. The electrostatic repulsion between charged spheres from exact solutions to the linearized poisson-boltzmann equation. *J. Colloid Interface Sci.* **1983**, *93* (1), 95−104.
(52) Bitter, J. L.; Duncan, G. A.; Beltran-Villegas, D. J.; Fairbrother, D. H.; Bevan, M. A. Anomalous Silica Colloid Stability and Gel Layer Mediated Interactions. *Langmuir* **2013**, *29*, 8835−8844.
(53) Russel, W. B.; Saville, D. A.; Schowalter, W. R. *Colloidal Dispersions*; Cambridge University Press: New York, 1989.
(54) Ganatos, P.; Pfeffer, R.; Weinbaum, S. A strong interaction theory for the creeping motion of a sphere between plane parallel boundaries. Part 2. Parallel motion. *J. Fluid Mech.* **1980**, *99*, 755−783.
(55) Pawar, Y.; Anderson, J. L. Hindered Diffusion in Slit Pores: An Analytical Result. *Ind. Eng. Chem. Res.* **1993**, *32*, 743−746.
(56) Medina-Noyola, M. Long-Time Self-Diffusion in Concentrated Colloidal Dispersions. *Phys. Rev. Lett.* **1988**, *60* (26), 2705−2708.
(57) Brady, J. F. The Long-Time Self-Diffusivity in Concentrated Colloidal Dispersions. *J. Fluid Mech.* **1994**, *272*, 109−133.
(58) He, K.; Babaye Khorasani, F.; Retterer, S. T.; Thomas, D. K.; Conrad, J. C.; Krishnamoorti, R. Diffusive Dynamics of Nanoparticles in Arrays of Nanoposts. *ACS Nano* **2013**, *7* (6), 5122−5130.
(59) Skaug, M. J.; Wang, L.; Ding, Y.; Schwartz, D. K. Hindered Nanoparticle Diffusion and Void Accessibility in a Three-Dimensional Porous Medium. *ACS Nano* **2015**, *9* (2), 2148−2156.
(60) Han, Y.; Alsayed, A. M.; Nobili, M.; Zhang, J.; Lubensky, T. C.; Yodh, A. G. Brownian Motion of an Ellipsoid. *Science* **2006**, *314* (5799), 626−630.
(61) Elliott, L. C. C.; Barhoum, M.; Harris, J. M.; Bohn, P. W. Trajectory analysis of single molecules exhibiting non-Brownian motion. *Phys. Chem. Chem. Phys.* **2011**, *13* (10), 4326−4334.
(62) Saxton, M. J. Lateral Diffusion in an Archipelago - Single-Particle Diffusion. *Biophys. J.* **1993**, *64* (6), 1766−1780.

DOI: 10.1021/acs.langmuir.7b01704
Langmuir 2017, 33, 9034−9042

Langmuir

ARTICLE

pubs.acs.org/Langmuir

Modulating the Structure and Properties of Poly(sodium 4-styrenesulfonate)/Poly(diallyldimethylammonium chloride) Multilayers with Concentrated Salt Solutions

Lulu Han, Zhengwei Mao, He Wuliyasu, Jindan Wu, Xiao Gong, Yuguang Yang, and Changyou Gao*

MOE Key Laboratory of Macromolecular Synthesis and Functionalization, Department of Polymer Science and Engineering, Zhejiang University, Hangzhou 310027, China

Supporting Information

ABSTRACT: Poly(sodium 4-styrenesulfonate) (PSS)/poly(diallyldimethylammonium chloride) (PDADMAC) multilayers were treated with 1−5 M NaCl solutions, resulting in continuous changes in the physicochemical properties of the multilayers. Significant mass loss was observed when the salt concentration was higher than 2 M and reached as high as 72% in a 5 M NaCl solution. The disassembly occurred initially in the superficial layers and then developed in the bulk multilayers. For the multilayers with PDADMAC as the outmost layer, the molar ratio of PSS/PDADMAC was increased and the surface chemistry was changed from PDADMAC domination below 2 M NaCl to PSS domination above 3 M NaCl. Owing to the higher concentrations of uncompensated for polyelectrolytes at both lower and higher salt concentrations, the swelling ratio of the multilayers was decreased until reaching 3 M NaCl and then was increased significantly again. The salt-treated PSS/PDADMAC thin films are expected to show different behaviors in terms of the physical adsorption of various functional substances, cell adhesion and proliferation, and chemical reaction activity.

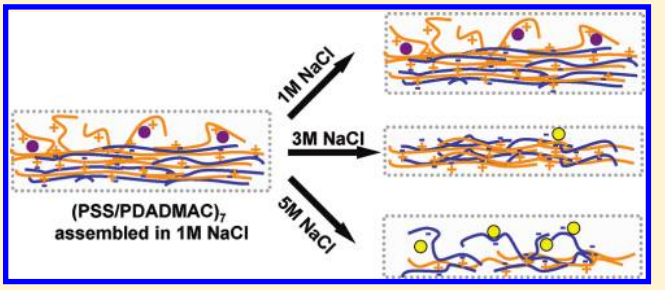

Layer-by-layer (LbL) assembly is a versatile method of building up thin polymer films on various substrates.[1−5] In particular, the polyelectrolyte multilayers (PEMs) are assembled by the alternative adsorption of polycations and polyanions via electrostatic attraction.[6,7] Their well-defined nanostructures and properties, including compositions, thicknesses, surface functional groups, and internal linkages between layers, can be governed by many parameters during the building process and post-treatment, for example, the types of polyelectrolytes and salts, salt concentration, temperature, and pH.[8−15] Therefore, PEMs have attracted much interest with respect to their applications in chemical and biological sensors,[16−18] drug-delivery carriers,[19−21] microelectronics,[22,23] nano-optics,[24,25] biomimetics,[26] and tissue engineering.[27−30]

Many previous studies have reported that the PEMs can be regarded as insoluble polyelectrolyte complexes (PECs) bound to a surface, and the phase behavior of PECs can be controlled by the salt strength and the stoichiometry of polycations and polyanions.[31−37] Generally, the charge interaction between polyelectrolytes is more strongly screened at a higher salt strength, leading to a lower solubility of PECs. However, post-treatment of the multilayers in a salt solution with a critical high ionic strength will redistribute the charge and multilayer structure and soften, swell, and even dissolve the PEMs.[12,38−44] However, the decomposition behaviors of the multilayers are also dependent on the building blocks. For weak polyelectrolyte multilayers such as poly(acrylic acid) (PAA)/(allylamine hydrochloride) (PAH), their thickness is decreased progressively in 1−5 M NaCl solutions. The degree of etching is also tuned by the molecular weight of the building blocks and the pH value during assembly that influences the ionic cross-linking density of the PEMs. In this process, the chemical composition and properties of PAA/PAH are not changed after salt treatment, and thereby the swelling ratio of the multilayers is kept constant in water.[45] In contrast, the mass loss of poly(sodium 4-styrenesulfonate) (PSS)/PAH multilayers occurs only in NaCl solution above 3 M, and the multilayer swelling in salt solution is shown.[38]

The strong polyelectrolyte multilayers assembled from PSS and poly(diallyldimethylammonium chloride) (PDADMAC) are stable in salt solutions that are less concentrated than 2 M.[39] The distribution of charges and the intrinsic persistence length of the PDADMAC chain mismatch that of PSS,[46] leading to the strong responses of the multilayers to the salt solution. For example, both the thickness and hydration of the PDADMAC/PSS multilayers are greater and more sensitive than those of the PAH/PSS system built up or post-treated at a relatively high salt concentration such as 1 M NaCl, with a more obvious odd−even effect.[11,12,47] More recently, the salt-induced fusion of PSS/PDADMAC multilayer

Received: September 2, 2011
Revised: November 21, 2011
Published: November 26, 2011

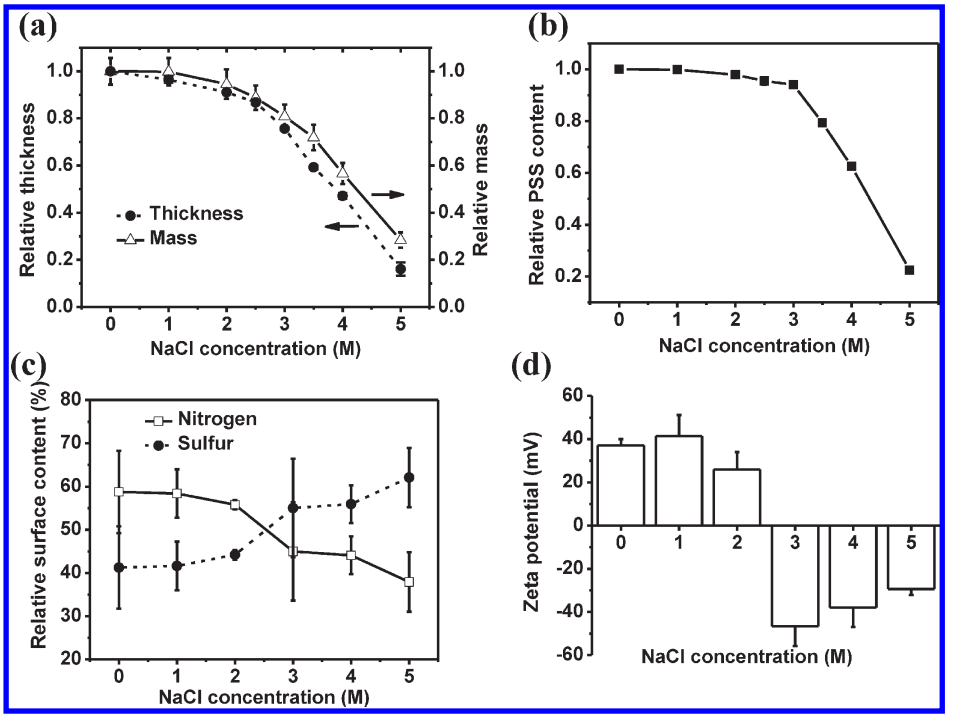

Figure 1. Mass and surface properties of $(PSS/PDADMAC)_7$ multilayers post-treated with different concentrations of NaCl solutions. (a) Alteration of mass and thickness as a function of NaCl concentration as determined by QCM-D and ellipsometry. The mass and thickness are normalized to those of the pristine multilayers, which are 38.5 $\mu g/cm^2$ and 190 nm, respectively. (b) Integrated value over 215−240 nm in the UV−vis absorption spectra of the multilayers after incubation in different concentrations of NaCl solutions. The value is proportional to the PSS content in the multilayers. (c) Relative surface contents of nitrogen and sulfur as determined by XPS, which denote the relative PDADMAC and PSS surface contents, respectively. (d) Surface zeta potential of the multilayers post-treated with different concentrations of NaCl solutions. The measurement was conducted in a 10 mM NaCl solution.

microcapsules at increasing salt concentration above 3 M has been reported.[48] However, less attention is paid to alterations in the chemical composition and physicochemical properties of PSS/PDADMAC multilayers after post-treatment in higher concentrations of salt solutions.

In this study, we shall make use of the well-acknowledged salt treatment method to post-treat the PSS/PDADMAC multilayers in 0−5 M NaCl solutions. The changes in mass, thickness, chemical composition, surface charge, counterions, and viscoelastic properties are investigated by means of ellipsometry, UV−vis and X-ray photoelectron spectroscopy, the zeta potential, and the quartz crystal microbalance. Some interesting phenomena (until now, only in these PE pairs) are found, and the underlying mechanism is elucidated. The resulting ultrathin films with unique features are expected to find diverse applications in surface engineering and biological fields.

MATERIALS AND METHODS

Materials. Polyethyleneimine (PEI, M_w = 25 kDa), poly(diallyldimethylammonium chloride) (PDADMAC, M_w = 200−350 kDa), and poly(sodium 4-styrenesulfonate) (PSS, M_w = 70 kDa) were obtained from Sigma-Aldrich. The water used in the experiments was purified by a Milli-Q water system (Millipore, U.S.A.). The polyelectrolytes were prepared as 1 mg/L aqueous solutions. PEI was dissolved in water, and PSS and PDADMAC were supplemented with 1 M NaCl. Quartz, glass, and silicon wafers were cleaned in piranha solution (7:3 v/v% H_2SO_4/H_2O_2). (***Caution!*** *Piranha is a strong oxidizer and should not be stored in a closed container.*) After being copiously rinsed with water, they were dried under a smooth stream of N_2.

Multilayer Assembly. To ensure successful adsorption, a precursory layer of PEI was deposited onto the silicon wafers. PSS and PDADMAC in a 1 M NaCl solution were then alternately assembled by autodipping at 20 °C. Between alternate exposures to the two kinds of polymer solutions for 20 min, there were three rinses with 0.1 M NaCl solution for 3 min. In the last step, the films were immersed in water for at least 5 min to eliminate the adsorbed salt. In total, seven bilayers were assembled, and the multilayers are expressed as $(PSS/PDADMAC)_7$ if not otherwise stated.

Post-treatment of the Multilayers. The $(PSS/PDADMAC)_7$ multilayers were incubated in NaCl solutions of different concentrations at room temperature for 2 h and were then rinsed with water and dried under a smooth stream of N_2.

Spectroscopic Ellipsometry. The thickness and refractive index of the multilayers were determined in air from a spectroscopic ellipsometer (model M2000D, J. A. Woollam Inc., Lincoln, NE) at an incident angle of 75° within a wavelength range of 300−1700 nm. The thickness was calculated from the ellipsometric parameters, Δ and ψ, using a Cauchy model. The measurement in water was carried out in a liquid cell within a wavelength range of 300−1100 nm.

UV−Vis Spectroscopy. Quartz slides were used as the substrates to assemble the multilayers. UV−vis spectra were obtained from a UV−vis spectrophotometer (Shimadzu, UV2550) within a wavelength range of 200−360 nm. The absorbance between 215 and 240 nm, which is assigned to the benzene ring of PSS, was integrated for quantitative comparison.

X-ray Photoelectron Spectroscopy (XPS). The compositions of the multilayers after salt treatment were detected by an Axis Ultra spectrometer (Kratos Analytical, U.K.) with a monochromated Al Kα source at pass energies of 160 eV for survey spectra and 80 eV for core-level spectra.

dx.doi.org/10.1021/la2040533 |*Langmuir* 2012, 28, 193–199

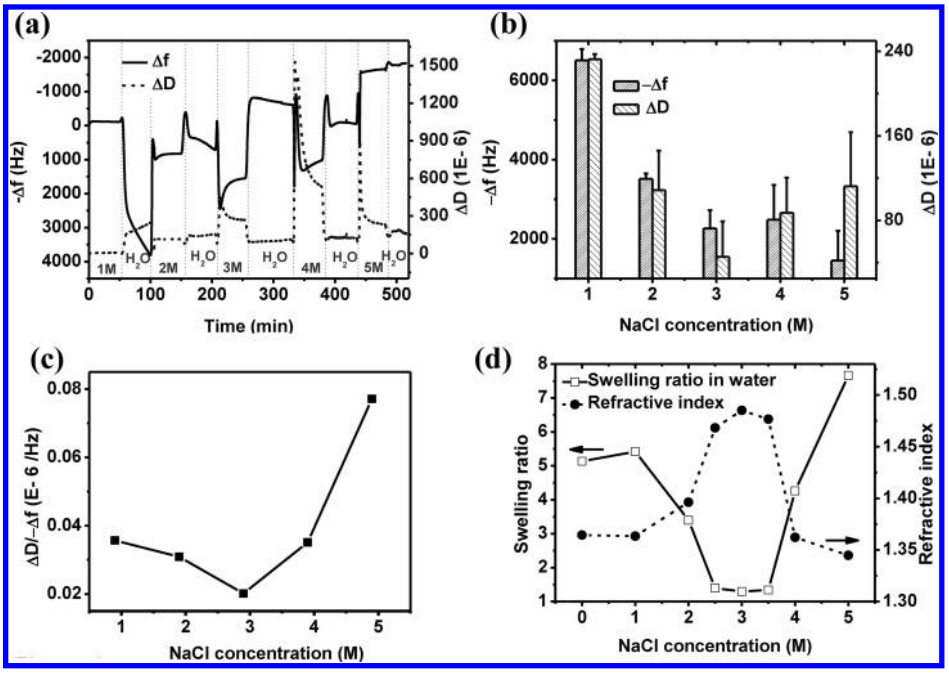

Figure 2. Viscoelastic properties of the multilayers post-treated with different concentrations of NaCl solutions. (a) The alteration of $(PSS/PDADMAC)_7$ multilayers was monitored stepwise in situ in 1, 2, 3, 4, and 5 M NaCl solutions by QCM-D. After each exposure of the salt solution, the sample was rinsed with ultrapure water. (b) Values of $-\Delta f$ and ΔD of the multilayers in water as a function of NaCl concentration. The data represent the differences between the values of the multilayers in water after each salt treatment and the blank substrate (gold-coated quartz crystal). (c) Viscoelastic parameters $\Delta D/-\Delta f$ of the multilayers in water as a function of salt concentration. (d) Swelling ratio and refractive index of the salt-treated multilayers in water as measured by ellipsometry.

The binding energy was corrected for static charging of the C 1s peak at 284.8 eV. Data analysis was performed with Kratos Vision Processing.

Zeta Potential. The surface zeta potentials of the multilayers were measured in 10 mM NaCl using a Delsa Nano Series zeta potential/submicrometer particle size analyzers (Beckman Coulter, U.S.A.) via electrophoresis technology.

Quartz Crystal Microbalance with Dissipation (QCM-D). Changes in both the dissipation (D) and resonance frequency (f) of the quartz crystal assembled with multilayers after salt treatment were monitored by QCM-D (model Q-SENSE E4, Sweden) using gold-coated quartz crystals (5 MHz) as the substrates. In situ ΔD and Δf (Figure 2a) were expressed as the directly measured values, and others were calculated from the differences between the values of measured samples and blank substrates. The mass change in air was calculated by using the Sauerbrey relation with QTools software.

RESULTS

Changes in Mass and Surface Properties. After the $(PSS/PDADMAC)_7$ multilayers (PDADMAC as the outmost layer) were post-treated in different concentrations of NaCl solutions, their mass and thickness were measured by QCM and ellipsometry in a dry state. Figure 1a shows that they were both gradually decreased along with the increase in salt concentration from 1 to 5 M and became more serious above 2 M NaCl. Only 28% mass and 16% thickness were retained after 5 M NaCl treatment. The mass loss is known to be caused by the disassembly of the multilayers as a result of the electrostatic screening by NaCl solution of the charge interaction.[49]

To identify the loss of each component, UV−vis absorption spectra were recorded and the value in the range from 215 to 240 nm was integrated (Figure 1b). This value is solely attributed to PSS, which was largely retained at a lower salt concentration. For example, at 3 M, 94% PSS remained (Figure 1b), which was much larger than the retained total mass of 81% (Figure 1a). Therefore, the mass loss at lower concentrations of salt solutions ($\leq$3 M) is mainly contributed by PDADMAC. When the salt concentration was greater than 3 M, PSS was dissolved significantly as well. For example, at 5 M NaCl only 25% PSS was retained (Figure 1b), which conveys that both PSS and PDADMAC are dissolved simultaneously, compared with the 28% remaining mass.

The loss of the polyelectrolytes shall inevitably cause a change in the surface chemistry, which was verified by XPS measurement (Figure 1c). The S/N molar ratio, which is proportional to the PSS and PDADMAC contents on the surface, was found to be 41:59 in the pristine multilayers. This is consistent with the PDADMAC-terminated surface of the multilayers. The S/N ratio remained almost unchanged after 1 M treatment (42:58), which is in good agreement with the constant mass and thickness. After 2 M NaCl treatment, the S/N ratio was improved slightly to 44:56 and then increased substantially to 55:45, 56:44, and 62:38 after 3, 4, and 5 M NaCl treatments, respectively, indicating that PDADMAC molecules are released more significantly from the multilayers at critical high salt concentrations.

Along with the alteration of the PSS/PDADMAC ratio, small balanced ions (e.g., Cl^- and Na^+) must be changed correspondingly to compensate for the extra charge in the multilayers.[50] XPS characterization indeed found that the Cl/N ratios were 10:59, 9:58, and 6:56 for the pristine multilayers and the multilayers treated with 1 and 2 M NaCl solutions, respectively. No Na^+ was found in these multilayers. By contrast, no Cl^- was found in the multilayers treated with $\geq$3 M NaCl solutions. In the multilayers treated with 3, 4, and 5 M NaCl solutions, the S/Na ratios were

dx.doi.org/10.1021/la2040533 |*Langmuir* 2012, 28, 193–199

55:3, 56:22, and 62:34, respectively. If we assume that the counterions (SO_3^-/Cl^-, or $N(R)_4^+$/Na^+) shall compensate for each other regardless of their types, then the overall ratios between the anions and cations are roughly equal, except in the 4 M NaCl-treated multilayers (multilayers 4 and 5 M) in which about 17% of the cations were present in excess. The reason is not known but is likely caused by the stronger interaction between sulfonic and sodium ions, which surpasses that of ammonium chloride and sulfonic ammonium ion pairs.[51]

The change in the surface zeta potential is in good agreement with the above results. Figure 1d shows that the surfaces of the pristine and 1 M NaCl-treated multilayers were positively charged with a zeta potential of +40 mV, which is consistent with the multilayer structure of the PDADMAC-dominated surface. This value was decreased to +25 mV after the partial release of PDADMAC in 2 M NaCl. Along with the increase in salt concentration, the surface charge was reversed to negative with values of -47 ± 9, -39 ± 7, and -29 ± 3 mV for multilayers 3, 4, and 5 M, respectively.

It is worth mentioning that the QCM measured 81 and 28% remaining mass at 3 and 5M, respectively, which were smaller and almost equal to the PSS mass (94 and 25% at 3 and 5M, respectively) as measured by UV−vis. This result implies that the increase in the ionic strength from 0 to 3 M results in the depletion of PDADMAC and the enrichment of PSS in the multilayers. Further increases in the salt concentration from 3 to 5 M should shift the balance back. However, XPS data demonstrated statistically significant increases in the PSS/PDADMAC ratio only upon changing the salt concentration from 2 to 3M. Further increases in the salt concentration to 5 M never changed this ratio back. The reason for such a discrepancy could be the fact that QCM and UV−vis spectroscopy analyze the bulk but XPS is a true surface analytical method that shows just the top few nanometers of the surface. Zeta potential measurements show that the surface charge changed from positive to negative when the salt concentration increased from 2 to 3M, conveying that the terminal layer changes from PDADMAC to PSS. These results suggest the possible different properties of the bulk and the outmost surface of the multilayers after salt etching.

Changes in Viscoelasticity. As a result of the change in chemical composition, the physical properties should be reasonably altered, especially their viscoelasticity. In this regard, QCM-D was used to record the resonance frequency (Δf) and dissipation factor (ΔD) of each treated multilayer, which can provide information about the internal structure and viscoelastic properties of the thin films. It is known that $-\Delta f$ is proportional to the mass increase and a dense/rigid (e.g., dehydrated) or swollen/flexible (e.g., highly hydrated) film has a small or large ΔD value, respectively. When the pristine $(PSS/PDADMAC)_7$ multilayers were incubated in pure water, no meaningful data could be collected by QCM-D. It is likely that the larger film thickness (190 nm) and high swelling nature (Figure 2d) surpass the measuring limit. Therefore, the measurement started from 1 M NaCl solution and thereby the $-\Delta f$ and ΔD values were normalized to those measured in 1 M NaCl solution (Figure 2a). When the medium was changed to water, the $-\Delta f$ increased sharply within the first few minutes and then increased slowly. Equilibrium was not achieved within the 1 h measuring time. Correspondingly, ΔD was improved. This result reveals that a large amount of water diffuses into the multilayers and the process lasts for a very long time. After the medium was changed to the 2 M NaCl solution, both $-\Delta f$ and ΔD were decreased, implying the loss of the infiltrated water. No large change was found after the multilayers were rinsed with water again. However, when the medium was changed to a 3 M NaCl solution, $-\Delta f$ increased immediately and then decreased slowly to a new balanced state, thus confirming the greater amount of swelling of the multilayers and the gradual mass loss in 3 M NaCl solution. Unlike their counterparts of multilayers 1 and 2 M, the $-\Delta f$ and ΔD values of multilayer 3 M decreased substantially in water, implying a huge loss of infiltrated water. A similar alteration regime was found in a 4 M NaCl solution, whereas in a 5 M NaCl solution water rinsing did not bring about changes in terms of the $-\Delta f$ and ΔD values.

To quantify the real $-\Delta f$ and ΔD values in water, the data of the substrate (gold-coated quartz crystal) were subtracted by the measured data in Figure 2a. Figure 2b shows that $-\Delta f$ decreased monotonously along with the increase in salt concentration whereas ΔD decreased initially until 3 M NaCl and increased again above 3 M NaCl. It is known that $\Delta D/-\Delta f$ is proportional to the water content per mass unit in the multilayer films.[52] Figure 2c confirms that the water content in the multilayers was decreased until 3 M NaCl and then was increased. Therefore, multilayer 3 M possesses the lowest swelling structure. By contrast, multilayer 5 M is highly hydrated.

The difference in swelling of the salt-treated multilayers was further confirmed by ellipsometry. For each multilayer film, its thickness in both the dry and wet states was independently measured. The ratio of wet thickness to dry thickness thus directly reflects the swelling ratio, which showed a V shape with a minimum value at 3 M NaCl in water (Figure 2d). Again, the maximum swelling appeared at 5 M NaCl. By contrast, the refractive index, which is an average of the polymer matrix ($\sim$ 1.52) and water (1.33) values and thereby proportional to the polymer content, showed perfect reverse alteration regimes to those of the swelling ratios.

Surface Morphology. Figure S1 shows the surface morphology of the salt-treated multilayers detected by AFM in PBS. (In water, no images could be recorded except for multilayer 3 M because of the very hydrated, soft structure.) Compared to the pristine layers and multilayers treated with lower concentrations of salt solutions (Figure S1a,b), fewer vermiculate structures existed on the multilayers treated with higher concentrations of the NaCl solution (Figure S1c−f). Nonetheless, the overall roughness (rms) in PBS was varied within a small range (i.e., 12.1 $\pm$ 2.8, 11.0 $\pm$ 1.7, 4.1 $\pm$ 1.3, 3.6 $\pm$ 2.2, 6.4 $\pm$ 0.1, and 4.6 $\pm$ 0.4 nm for the multilayers treated in 0, 1, 2, 3, 4, and 5 M NaCl solutions, respectively).

DISCUSSION

Many previous studies reported that the ionic strength plays a significant role in the multilayer structures and that post-treatment in salt solution can soften, swell, and even dissolve the PEMs because salt can screen the charge interaction between polyelectrolytes.[12,38−42] The decomposition behaviors of the multilayers are strongly dependent on the building blocks. According to the schematic stability diagram for polyelectrolyte multilayers proposed by Kovacevic et al.,[31] the polyelectrolyte chains become sufficiently mobile and multilayer dissolution occurs at a certain salt concentration (c_{cr}). The c_{cr} of polyelectrolyte pairs is low for the weak interactions (for example, 0.45 M for poly(*N*-ethyl-4-vinylpyridinium bromide)/poly(methacrylic acid) (PVP/PMAA) multilayers), and the polyelectrolyte multilayers can be formed only in a narrow range of the polycation/polycation ratio

(~1:1).[32,50,53] PSS is one of the strongest binders to polycations because of its abundant SO_3^- groups, and those polyamines containing primary amino groups have the strongest interactions with polyanions. Therefore, PSS/poly(allylamine hydrochloride) (PAH) multilayers can resist decomposition in highly concentrated NaCl solution (3 M).[33] By contrast, the dissolution of both types of PSS/PDADMAC and poly(acrylic acid) (PAA)/PAH multilayers occurs in a salt solution at around 2 M.[45] Nonetheless, the chemical composition of the PAA/PAH multilayers remained constant as a result of a similar extent of PAA and PAH release. Compared to those PAH/PAA and PSS/PAH polyelectrolyte pairs, the interaction between PSS/PDADMAC polyelectrolytes pairs is weaker,[46,54] leading to the change in the chemical compositions and thereby the physicochemical properties as demonstrated in this study.

Herein, we found that for the pristine layers and multilayers treated with 1 and 2 M NaCl solutions, the original structure and properties of the multilayers are mostly retained because of little electrostatic repulsion, with a PDADMAC-dominated positively charged surface and a larger swelling ratio in water. The extra charge on PDADMAC is balanced by Cl^- ions. The hardly swollen multilayer 3 M film, by contrast, has roughly equal amounts of PDADMAC and PSS and a PSS-dominated negatively charged surface as a result of the larger loss of PDADMAC. For the multilayer 4 and 5 M films, as a result of the substantial mass loss, PSS becomes abundant and the swelling ratio is very high, especially for the multilayer 5 M film, which has the highest hydration in water. The extra charge of PSS is balanced by Na^+ ions in these multilayers.

According to previous results, the basic structure of a multilayer film can be subdivided into three zones: a few layers deposited onto the substrate (zone I), a "bulk" film (polyelectrolyte complexes, zone II), and an outer region (uncompensated for polyion, zone III).[55] The XPS result (Figure 1c) shows that N is present in excess on the assembled $(PSS/PDADMAC)_7$ multilayers. Hence, it is reasonable to assume that the less-fixed PDADMAC is easier to dissociate than the internal polyelectrolytes. In addition, the swelling behaviors between the outer region and the bulk film are different: zone II swells in salt solutions owing to the broken ionic bonds between polyanions and polycations but collapses in water; zone III, however, is more similar to that of the classic polyions and shows a reverse alteration in response to salt solution and water.[55,56] Therefore, the larger swelling behaviors (namely, the large ΔD values) in water after treatment in 1 and 2 M NaCl (Figure 2a) convey that zone III should exist and dominate the swelling behavior. Compared to that of multilayers 1M, the ΔD value in water is increased only slightly for multilayers 2 M, implying that the effect of zone III is largely reduced. This result is consistent with the fact that the electrostatic screening length of PDADMAC is slightly larger (~1 nm) than the average distance between the effective charge (~0.7 nm), causing little electrostatic repulsion of the polyelectrolyte in 2 M NaCl solution, which is not enough to dissociate the bulk.[44,57] After a substantial loss of mass along with the increase in the salt concentration, the regular multilayer structure of three zones is reasonably destroyed and therefore zone III no longer remains. The larger swelling of multilayers 4 and 5 M in water should result from the uncompensated for PSS molecules, which possess the same physicochemical behavior as that of free polyions.

To confirm this explanation, we compared the mass loss per layer. The mass of the terminal PDADMAC layer and the last PSS/PDADMAC bilayers contributed 15 and 33% of the total mass of the multilayers as measured by QCM, respectively. The 6% mass loss of multilayer 2 M (Figure 1a) is smaller than the mass of the terminal PDADMAC layer, confirming that the outside PDADMAC is only partially removed from the surface. After the treatment in 3 M NaCl solution, a 19% mass loss was found on the multilayers, which is larger than the mass of terminal PDADMAC but smaller than that of the last bilayers. The results thus reflect that the last PDADMAC layer is completely etched off but part of the last PSS layer remains on the surface. All of the results are in good agreement with the fact that the outmost layer is first removed, resulting in the increasing S/N ratio, and then the bulk of the multilayers is exposed and broken sharply along with the increase in salt concentration, leading to 43 and 72% mass losses in multilayers 4 and 5 M, respectively. This huge mass loss (>70%) is much larger than that of the PAA/PAH (~50%) and PSS/PAH multilayers (~15%) treated in the same 5 M salt solution[45] because of the weaker interaction.[46,54]

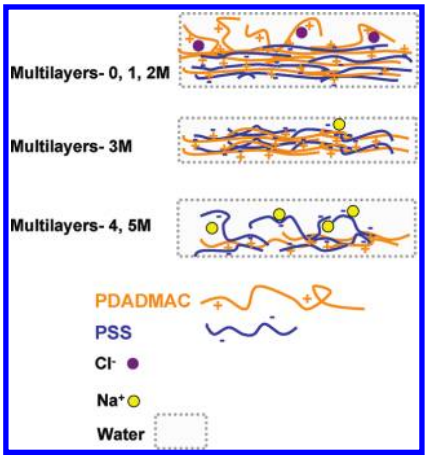

Figure 3. Schematic illustrations showing the typical physicochemical properties of the $(PSS/PDADMAC)_7$ multilayers treated with different concentrations of NaCl solutions.

By applying the salt treatment to PSS-terminated multilayers (i.e., $(PSS/PDADMAC)_7PSS$), we obtained a similar result. The film surface was dominated by PSS, with an S/N ratio of 61:39, which was decreased to 53:67 and 47:53 after treatment with 1 and 2 M NaCl solutions, respectively. This result further proves that the uncompensated for polyions on the superficial layers are more easily etched off. After the $(PSS/PDADMAC)_7PSS$ multilayers were treated in 3, 4, and 5 M NaCl solutions, however, the S/N ratios on the surfaces (55:45, 60:40, and 65:35) were almost the same as those of the salted, treated PDADMAC-dominated multilayers (i.e., multilayers 3, 4, and 5 M (55:45, 56:44 and 62:38), respectively). Therefore, when the dissolution occurs, the remaining film structure is controlled thermodynamically by the chemical nature of the building blocks but is not influenced by the chemical structure of the last layer. The larger loss of PDADMAC on the surface in concentrated NaCl solution (>3 M) can be explained by the fact that the distances between monomer units of PSS and PDADMAC are 2.6 and 5.2 Å,[58] respectively, which implies that PDADMAC has a smaller charge density than PSS and therefore is more sensitive to salt screening.[57]

CONCLUSIONS

The salt treatment can easily change the structure and physicochemical properties of the PSS/PDADMAC multilayers, resulting

in thin films with various features. Because the polyanion/polycation stoichiometry in bulk multilayers is observed to be 1:1 or at least close to this value,[55] multilayer 3 M can be regarded as the bulk film because of the roughly equal amounts of PSS and PDADMAC. As a result of the better compensation (5% counterions), the largest cross-linking density is expected among others, leading to the smallest swelling behavior in water (Figure 3). For the thin films with larger numbers of uncompensated for polyions such as multilayers 1 and 5 M, a swollen, hydrated structure is formed. Moreover, because the slight mass loss does not obviously change the multilayer structure, multilayers 0, 1, and 2 M can basically maintain their initial physicochemical structure (a PDADMAC-dominated surface). By contrast, the massive loss of polyelectrolytes completely destroys the layered structure of multilayers 4 and 5 M, leading to a surface chemistry reversal. In such a case, the structure is not composed of multilayers any longer. The obtained polymer thin films with various structures and properties are expected to find diverse applications in the fields of biomaterials, medicine, and nanotechnology.

■ ASSOCIATED CONTENT

Supporting Information. Atomic force microscopy. Morphology of the $(PSS/PDADMAC)_7$ multilayers in PBS. Relative thickness of $(PSS/PPDADMAC)_7$ multilayers treated in 3 and 5 M NaCl solutions as a function of time. This material is available free of charge via the Internet at http://pubs.acs.org.

■ AUTHOR INFORMATION

Corresponding Author
*E-mail: cygao@mail.hz.zj.cn.

■ ACKNOWLEDGMENT

This study was financially supported by the Natural Science Foundation of China (20934003) and the Major State Basic Research Program of China (2011CB606203).

■ REFERENCES

(1) Iler, R. K. *J. Colloid Interface Sci.* **1966**, *21*, 569–572.
(2) Decher, G.; Hong, J. D.; Schmitt, J. *Thin Solid Films* **1992**, *210*, 831–835.
(3) Decher, G. *Science* **1997**, *277*, 1232–1237.
(4) Sukhorukov, G. B.; Donath, E.; Lichtenfeld, H.; Knippel, E.; Knippel, M.; Budde, A.; Möhwald., H. *Colloids Surf., A* **1998**, *137*, 253–266.
(5) Donath, E.; Sukhorukov, G. B.; Caruso, F.; Davis, S. A.; Möhwald., H. *Angew. Chem., Int. Ed.* **1998**, *37*, 2202–2205.
(6) Cheung, J. H.; Stockton, W. B.; Rubner, M. F. *Macromolecules* **1997**, *30*, 2712–2716.
(7) Caruso, F.; Lichtenfeld, H.; Donath, E.; Möhwald., H. *Macromolecules* **1999**, *32*, 2317–2328.
(8) Buscher, K.; Graf, K.; Ahrens, H.; Helm, C. A. *Langmuir* **2002**, *18*, 3585–3591.
(9) Mendelsohn, J. D.; Barrett, C. J.; Chan, V. V.; Pal, A. J.; Mayes, A. M.; Rubner, M. F. *Langmuir* **2000**, *16*, 5017–5023.
(10) Dubas, S. T.; Schlenoff, J. B. *Macromolecules* **1999**, *32*, 8153–8160.
(11) Dubas, S. T.; Schlenoff, J. B. *Langmuir* **2001**, *17*, 7725–7727.
(12) Ramos, J. J. I.; Stahl, S.; Richter, R. P.; Moya, S. E. *Macromolecules* **2010**, *43*, 9063–9070.
(13) Llarena, I.; Ramos, J. J. I.; Donath, E.; Moya, S. E. *Macromol. Rapid Commun.* **2010**, *31*, 526–531.
(14) Gao, C. Y.; Leporatti, S.; Moya, S.; Donath, E.; Möhwald., H. *Chem.—Eur. J.* **2003**, *9*, 915–920.
(15) Antipov, A. A.; Sukhorukov, G. B.; Möhwald., H. *Langmuir* **2003**, *19*, 2444–2448.
(16) Lvov, Y. M.; Lu, Z. Q.; Schenkman, J. B.; Zu, X. L.; Rusling, J. F. *J. Am. Chem. Soc.* **1998**, *120*, 4073–4080.
(17) Campas, M.; O'Sullivan, C. *Anal. Lett.* **2003**, *36*, 2551–2569.
(18) Kim, H.; Doh, J.; Irvine, D. J.; Cohen, R. E.; Hammond, P. T. *Biomacromolecules* **2004**, *5*, 822–827.
(19) Izumrudov, V. A.; Kharlampieva, E.; Sukhishvili, S. A. *Biomacromolecules* **2005**, *6*, 1782–1788.
(20) Berg, M. C.; Zhai, L.; Cohen, R. E.; Rubner, M. F. *Biomacromolecules* **2006**, *7*, 357–364.
(21) Wood, K. C.; Boedicker, J. Q.; Lynn, D. M.; Hammond, P. T. *Langmuir* **2005**, *21*, 1603–1609.
(22) Fou, A. C.; Onitsuka, O.; Ferreira, M.; Rubner, M. F.; Hsieh, B. R. *J. Appl. Phys.* **1996**, *79*, 7501–7509.
(23) Eckle, M.; Decher, G. *Nano Lett.* **2001**, *1*, 45–49.
(24) Nolte, A. J.; Rubner, M. F.; Cohen, R. E. *Langmuir* **2004**, *20*, 3304–3310.
(25) Lukkari, J.; Salomaki, M.; Viinikanoja, A.; Aaritalo, T.; Paukkunen, J.; Kocharova, N.; Kankare, J. *J. Am. Chem. Soc.* **2001**, *123*, 6083–6091.
(26) Li, B. Y.; Haynie, D. T. *Biomacromolecules* **2004**, *5*, 1667–1670.
(27) Boudou, T.; Crouzier, T.; Ren, K. F.; Blin, G.; Picart, C. *Adv. Mater.* **2010**, *22*, 441–467.
(28) Elbert, D. L.; Herbert, C. B.; Hubbell, J. A. *Langmuir* **1999**, *15*, 5355–5362.
(29) Chluba, J.; Voegel, J. C.; Decher, G.; Erbacher, P.; Schaaf, P.; Ogier, J. *Biomacromolecules* **2001**, *2*, 800–805.
(30) Tang, Z. Y.; Wang, Y.; Podsiadlo, P.; Kotov, N. A. *Adv. Mater.* **2006**, *18*, 3203–3224.
(31) Kovacevic, D.; van der Burgh, S.; de Keizer, A.; Stuart, M. A. C. *Langmuir* **2002**, *18*, 5607–5612.
(32) Kovacevic, D.; van der Burgh, S.; de Keizer, A.; Stuart, M. A. C. *J. Phys. Chem. B* **2003**, *107*, 7998–8002.
(33) Sukhishvili, S. A.; Kharlampieva, E.; Izumrudov, V. *Macromolecules* **2006**, *39*, 8873–8881.
(34) Sui, Z. J.; Salloum, D.; Schlenoff, J. B. *Langmuir* **2003**, *19*, 2491–2495.
(35) Sui, Z. J.; Jaber, J. A.; Schlenoff, J. B. *Macromolecules* **2006**, *39*, 8145–8152.
(36) Sui, Z. J.; Schlenoff, J. B. *Langmuir* **2004**, *20*, 6026–6031.
(37) Dubas, S. T.; Schlenoff, J. B. *Macromolecules* **2001**, *34*, 3736–3740.
(38) Heuvingh, J.; Zappa, M.; Fery, A. *Langmuir* **2005**, *21*, 3165–3171.
(39) Von Klitzing, R.; Wong, J. E.; Jaeger, W.; Steitz, R. *Curr. Opin. Colloid Interface Sci.* **2004**, *9*, 158–162.
(40) Irigoyen, J.; Moya, S. E.; Iturri, J. J.; Llarena, I.; Azzaroni, O.; Donath, E. *Langmuir* **2009**, *25*, 3374–3380.
(41) Kohler, K.; Biesheuvel, P. M.; Weinkamer, R.; Möhwald., H.; Sukhorukov, G. B. *Phys. Rev. Lett.* **2006**, 97.
(42) McAloney, R. A.; Dudnik, V.; Goh, M. C. *Langmuir* **2003**, *19*, 3947–3952.
(43) Sukhishvili, S. A.; Granick, S. *J. Am. Chem. Soc.* **2000**, *122*, 9550–9551.
(44) Kiryukhin, M. V.; Man, S. M.; Sadovoy, A. V.; Low, H. Y.; Sukhorukov, G. B. *Langmuir* **2011**, *27*, 8430–8436.
(45) Nolte, A. J.; Takane, N.; Hindman, E.; Gaynor, W.; Rubner, M. F.; Cohen, R. E. *Macromolecules* **2007**, *40*, 5479–5486.
(46) Von Klitzing, R. *Phys. Chem. Chem. Phys.* **2006**, *8*, 5012–5033.
(47) Jaber, J. A.; Schlenoff, J. B. *Langmuir* **2007**, *23*, 896–901.
(48) Zhang, R. J.; Kohler, K.; Kreft, O.; Skirtach, A.; Möhwald., H.; Sukhorukov, G. *Soft Matter* **2010**, *6*, 4742–4747.
(49) Schlenoff, J. B.; Ly, H.; Li, M. *J. Am. Chem. Soc.* **1998**, *120*, 7626–7634.
(50) Hoogeveen, N. G.; Stuart, M. A. C.; Fleer, G. J.; Bohmer, M. R. *Langmuir* **1996**, *12*, 3675–3681.

(51) Qiao, B. F.; Cerda, J. J.; Holm, C. *Macromolecules* **2010**, *43*, 7828–7838.
(52) Hemmersam, A. G.; Foss, M.; Chevallier, J.; Besenbacher, F. *Colloids Surf., B* **2005**, *43*, 208–215.
(53) Izumrudov, V.; Kharlampieva, E.; Sukhishvili, S. A. *Macromolecules* **2004**, *37*, 8400–8406.
(54) Han, L. L.; Zhou, J.; Gong, X.; Yang, J.; Gao, C. Y. *Macromol. Mater. Eng.* **2010**, *295*, 716–725.
(55) Ladam, G.; Schaad, P.; Voegel, J. C.; Schaaf, P.; Decher, G.; Cuisinier, F. *Langmuir* **2000**, *16*, 1249–1255.
(56) Feldoto, Z.; Varga, I.; Blomberg, E. *Langmuir* **2010**, *26*, 17048–17057.
(57) Guzman, E.; Ritacco, H.; Rubio, J. E. F.; Rubio, R. G.; Ortega, F. *Soft Matter* **2009**, *5*, 2130–2142.
(58) McAloney, R. A.; Sinyor, M.; Dudnik, V.; Goh, M. C. *Langmuir* **2001**, *17*, 6655–6663.

SCIENTIFIC REPORTS

OPEN

Reconfigurable multi-scale colloidal assembly on excluded volume patterns

Received: 03 February 2015
Accepted: 30 July 2015
Published: 02 September 2015

Tara D. Edwards[1], Yuguang Yang[1], W. Neil Everett[2] & Michael A. Bevan[1]

The ability to create multi-scale, periodic colloidal assemblies with unique properties is important to emerging applications. Dynamically manipulating colloidal structures *via* tunable *kT*-scale attraction can provide the opportunity to create particle-based nano- and microstructured materials that are reconfigurable. Here, we report a novel tactic to obtain reconfigurable, multi-scale, periodic colloidal assemblies by combining thermoresponsive depletant particles and patterned topographical features that, together, reversibly mediate local *kT*-scale depletion interactions. This method is demonstrated in optical microscopy experiments to produce colloidal microstructures that reconfigure between well-defined ordered structures and disordered fluid states as a function of temperature and pattern feature depth. These results are well described by Monte Carlo simulations using theoretical depletion potentials that include patterned excluded volume. Ultimately, the approach reported here can be extended to control the size, shape, orientation, and microstructure of colloidal assemblies on multiple lengths scales and on arbitrary pre-defined pattern templates.

Ordered multi-scale colloidal assemblies can generate periodic and resonant structures comparable to or smaller than wavelengths of electromagnetic radiation to create metamaterials[1,2]. Metamaterials have emergent aggregate material properties that affect their interaction with elecromagnetic radiation (*e.g.*, absorbance, reflection, transmission) that are observed in nature (*e.g.*, butterflies, beetles[3,4]) and could be created in synthetic materials for emerging applictions (*e.g.*, sensing, solar cells, imaging, cloaking, antennas[5–7]). Colloidal assembly provides a possible method to fabricate large-area hierarchical structures required for metamaterials, including ensemble particle responses (that differ from single particles and bulk materials[8]) and patterning of resonant structures (*e.g.*, split rings)[1,9]. In addition to using colloidal assembly for metamaterial fabrication, reversible assembly schemes can enable switching multi-scale structures between two or more configurations as a basis to develop reconfigurable metamaterials for use in devices.

It is important to consider a number of factors to design colloidal interactions and assembly schemes suitable for reconfigurable multi-scale metamaterials. While colloids can easily be assembled into amorphous, irreversible, static, arrested structures by strong attractive interactions[10] and can be coaxed into close-packed crystalline configurations by carefully tuning attractive interactions on the order of the thermal energy (kT)[11,12], generating multi-scale structures is much more challenging. For example, it is possible to assemble space-filling, non-close packed configurations using templated sedimentation[13], magnetic[14,15] and electrostatic[16,17] attraction, capillary forces[18], laser tweezers[19], chemical synthesis[20], site-specific bonding[21–23], spin coating[24], and tri-block colloids[25]. Generating colloidal microstructures *via* tunable kT-scale attraction provides the opportunity for material/device reconfiguration, which has been achieved *via* external stimuli, including opto-electrical effects[26,27], high frequency AC electric fields[28–31], and thermosensitive depletion interactions[11,12,32,33]. For the specific case of depletion interactions, it has also been possible to develop local and directional attraction by designing local surface features[34], templates for crystallization[35,36], surface roughness[37–39], and lock-and-key colloids (*i.e.*, local curvature)[40].

[1]Chemical & Biomolecular Engineering, Johns Hopkins University, Baltimore, MD 21218. [2]Exoteric Instruments, 604 Basie Bend, Cedar Park, TX 78613. Correspondence and requests for materials should be addressed to M.A.B. (email: mabevan@jhu.edu)

In this work, we demonstrate the reversible assembly/disassembly of micron scale colloidal chains at the edges of ciruclar features patterned into an array, which represents a basic periodic arrangement of resonant structures that could be developed into a large-area reconfigrable metamaterial. In particular, we report a tactic to generate reconfigurbale multi-scale colloidal assemblies by combining thermosensitive depletion interactions and patterned surface topographical features that, together, reversibly mediate local *kT*-scale depletion interactions (Fig. 1a,b and Supplementary Fig. S1). In brief, depletion interactions, which rely on the exclusion of solute particles between surfaces, are manipulated by: (1) thermoresponsive poly-N-isoproplyacrylamide (PNIPAM) hydrogel depletant particles that alter depletion attraction *via* their temperature-dependent size, and (2) systematically varying physical surface patterns that lead to local excluded volume effects that mediate depletion attraction between colloids and pattern features. Using a model recently developed by us[41] (including previous high-resolution particle-wall and particle-particle potentials[11,12]), we measure, analyze, simulate, and design depletant and pattern dimensions to understand the net interactions that control colloidal assembly.

While thermoresponsive depletion has been used to reversibly assemble close-packed colloidal crystals[12,32,33], and surface patterns have been used to create local depletion attraction[34] (including templates for close-packed colloidal crystals[11,35,36]), we are unaware of a precedent to exploit a synergistic combination of such methods to control multi-scale colloidal assembly. By investigating local depletion mediated interactions and assembly on model surface topographies, it is possible to understand the fundamental mechanisms underlying the net depletion interaction; it depends on both changing the depletant osmotic pressure and the excluded volume determined by the depletant size in combination with local topographical feature dimensions. Our results demonstrate how size tunable depletants produce comparable changes in solution osmotic pressure and local excluded volume to generate reconfigurable multi-scale colloidal assemblies on topographically patterned substrates. Ultimately, our findings include the development of accurate quantitative models of locally tunable depletion interactions that could enable the rational design, control, and optimization of particle based reconfigurable materials and devices.

Results and Discussion

Depletion interactions on patterned surfaces. PNIPAM hydrogel nanoparticles were synthesized (see Supplementary Methods) for use as depletant particles. In aqueous media, their diameter, $2L$, varies as a function of temperature, T. PNIPAM particles are swollen with water at low temperatures but become continuously desolvated as their lower critical solution temperature is approached. Dynamic light scattering measurements were used to measure the hydrodynamic diameter of the PNIPAM particles vs. temperature (Fig. 1c)[12,42]. The continuous change in PNIPAM size vs. temperature suggests a continuous "knob" for tuning depletion attraction and the associated self-assembly (rather than a "switch" for a first-order transition); we revisit whether a continuous transition in the assembly process is possible at the end of our discussion.

Video microscopy was used to directly measure quasi-two dimensional (2D) configurations of nominal $2a = 2.34\,\mu m$ diameter SiO_2 colloids with PNIPAM hydrogel depletant particles in 1 mM NaCl sedimented onto periodic arrays of physically patterned wells of different shapes and sizes. Gravity concentrates the SiO_2 colloids within 285 nm deep patterned wells while 112.7 nm ($T = 25\,°C$) diameter PNIPAM depletants caused the SiO_2 particles to outline the inner well side walls. Figure 1d–f displays different types of periodic multi-scale colloidal structures obtained by combining depletion interactions with locally patterned excluded volume.

In all cases, assembly initiates along feature edges due to a local increase in excluded volume (*via* the sloped 13° walls, Supplementary Fig. S2b), and hence increased depletion attraction that localizes particles at feature edges[34]. Because particles also experience depletion attraction with each other, the localized particles first tend to form chains at pattern edges, and then layer into 2D crystalline states as more particles are added. Samples at lower colloid area concentrations form incomplete rings of partial chains *via* lateral particle-particle attraction (Fig. 1e), whereas higher concentrations produce multilayers within the wells (also in Fig. 1e). The average concentration inside and outside features is expected to have a Boltzmann dependent partitioning based on the free energy difference determined by gravity and multi-particle packing effects[11,43]. Finally, crystals unattached to the pattern edge were never observed for any combination of pattern depth, depletant size, or particle concentration described in the following study.

Colloidal assembly vs. pattern feature depth. Colloidal assembly as a function of well depth was investigated by using the same system described in Fig. 1d–f with features etched to various depths. The far left column in Fig. 2 shows images of colloidal configurations extracted from video microscopy measurements (Supplementary Videos S1–S3) for three different well depths: $H = 285$ nm, 90 nm, and 35 nm. Consistent with the results in Fig. 1d–f, Fig. 2a,b shows colloidal SiO_2 outlining the inner periphery of features within 285 nm and 90 nm deep wells (again, with multilayers forming in some cases *via* particle-particle depletion attraction). In Fig. 2c, where $H = 35$ nm, the additional excluded volume at feature edges becomes negligible, and particles formed an equilibrium fluid microstructure across the entire substrate surface, demonstrating that particle-particle depletion attraction was insufficient to induce quasi-2D crystallization in the absence of significant surface topographical features.

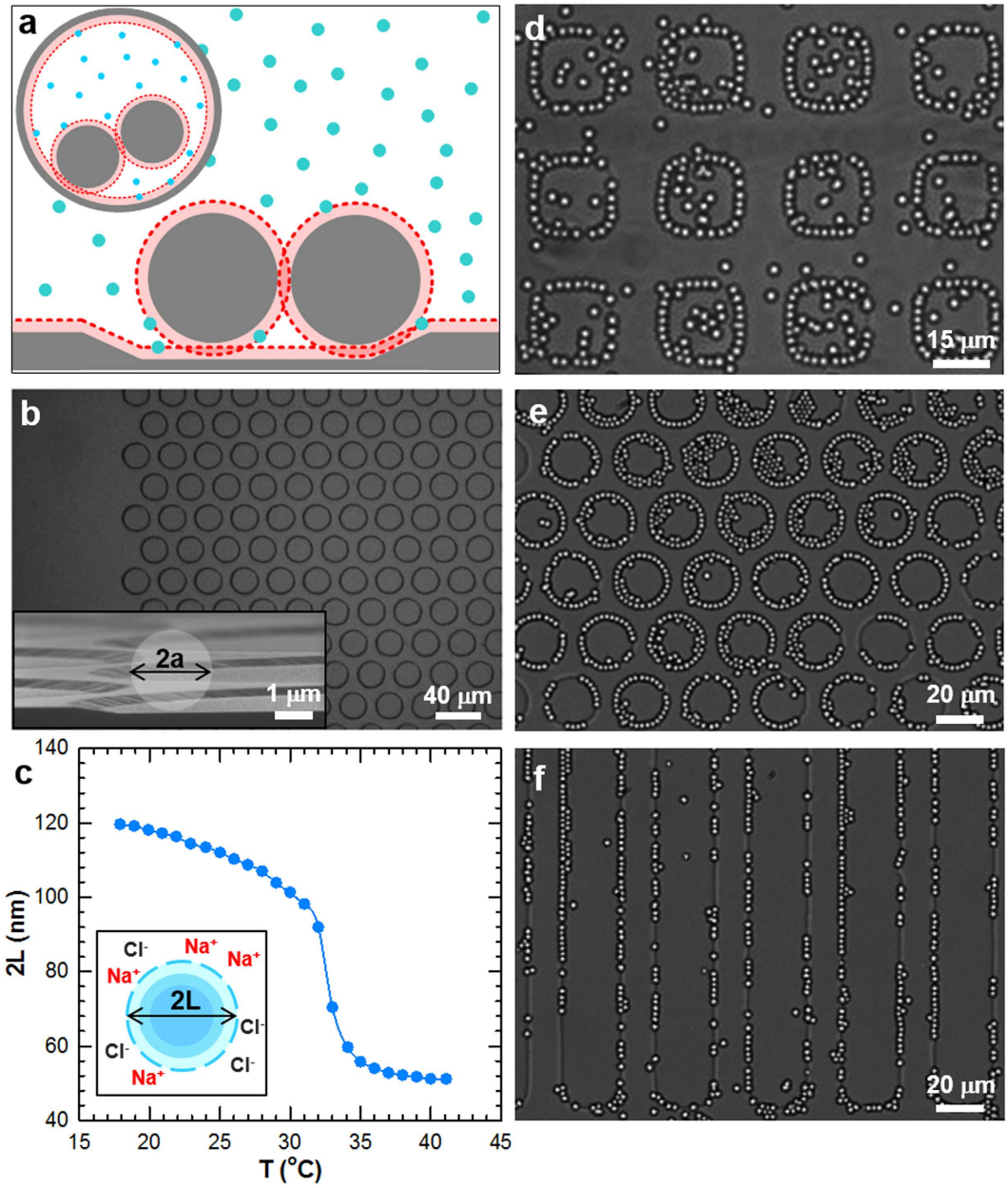

Figure 1. Reversible multi-scale assembly of charged ~2 μm diameter SiO_2 colloids above topographical surface patterns resulting from thermoresponsive hydrogel nanoparticle-mediated depletion interactions. (**a**) Schematic of charged SiO_2 colloids (gray circles) experiencing depletion attraction with each other and a topographical feature due to the exclusion of the smaller spherical depletants (cyan circles). When the surface-to-surface separation between particles or particles and the underlying feature is less than the depletant diameter, $2L$, (light red areas) the depletants are excluded from the overlapping regions (darker red areas). Inset is a top-down view of SiO_2 colloids experiencing depletion interactions with a circular patterned feature. (**b**) Microscopy image of etched circles arranged on a hexagonal lattice. Inset is an SEM image of a cross-section showing the resulting sidewall geometry with an overlaid representation of a silica colloid. (**c**) Hydrodynamic diameter of PNIPAM depletant nanoparticles in 1 mM NaCl as a function of temperature. (**d**–**f**) Experimental images extracted from video microscopy measurements of equilibrated multi-scale self-assembled SiO_2 particles at 25 °C (PNIPAM $2L \cong 113$ nm) localized to the edges of ~285 nm deep (**d**) 20 μm × 20 μm squares, (**e**) 20 μm circles on a hexagonal lattice, and (**f**) 20 μm wide channels.

The second column of Fig. 2 shows 2D particle trajectories for the first ~36 s extracted from video microscopy measurements for the three well depths. These plots trace the positions sampled by each particle within each well feature as a function of time to convey the degree of particle motion vs. feature depth (for readers without access to Supplementary Videos S1–S3). The data at $H = 285$ nm shows that

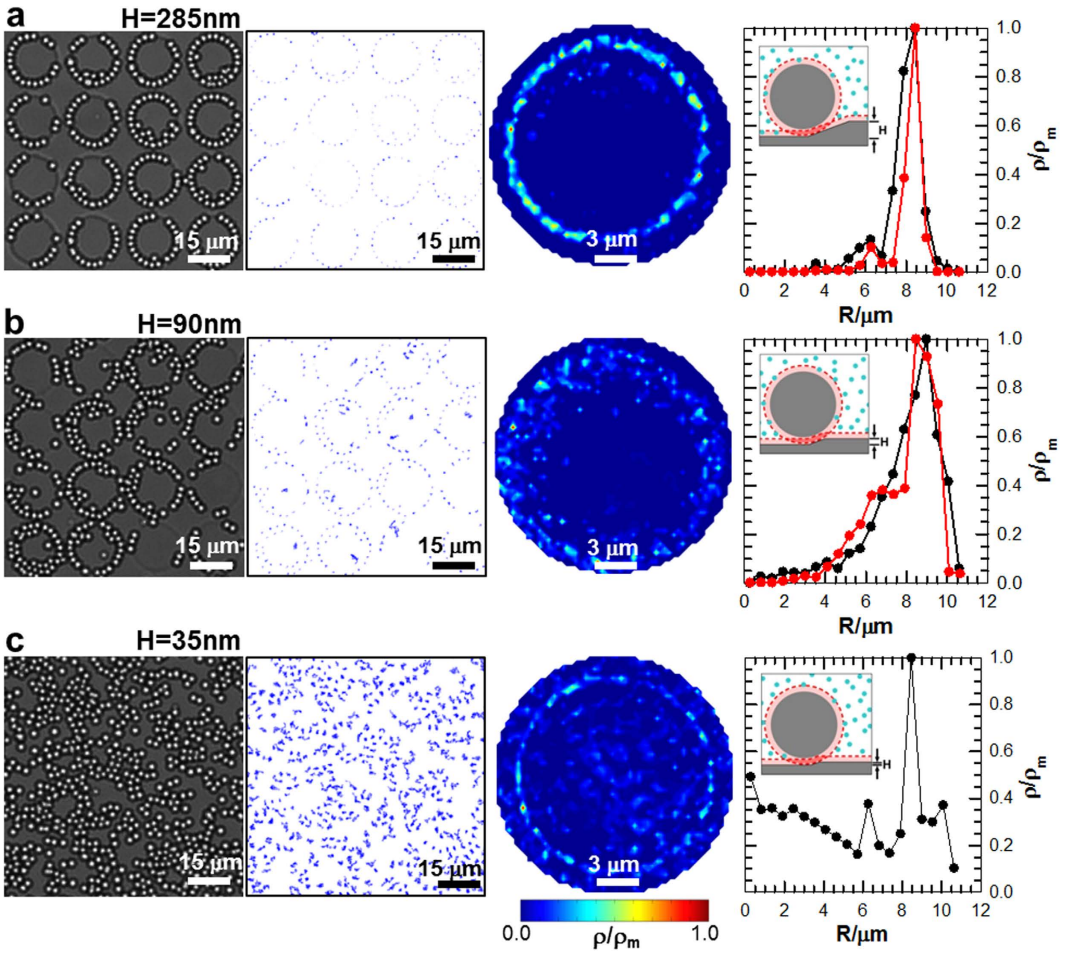

Figure 2. Structural, spatial, and statistical information obtained from video microscopy of equilibrated colloidal assembly as a function of topographical surface pattern depth. Results shown for patterned 12 μm circles arranged on a square lattice with (**a**) $H = 285$ nm, (**b**) $H = 90$ nm, (**c**) $H = 35$ nm deep at ~25 °C in the presence of ~113 nm diameter PNIPAM hydrogel nanoparticles. (left-to-right) Experimental images extracted from video microscopy, dynamic traces of 2D particle trajectories over patterns from the first 1,000 experimental frames (~36 s), contour plots of 2D density profiles with experimental particle center coordinates averaged over all features, and 1D radial density profiles from experiments (red) and MC simulations (black) (except for $H = 35$ nm experiment where pattern edges could not be resolved).

particles are arranged near the inside perimeter of the features. At $H = 90$ nm, occasional particle excursions away from the sidewalls can be observed, but otherwise, the plots indicate that the particles prefer to be situated proximal to other particles and along the interior well edges. At $H = 35$ nm, trajectories in Fig. 2c show particles diffusing over the patterned surface with only minor effects of particle-particle attraction and gravity.

To model the combined colloid, depletion, and patterned surface interactions as a function of H, Monte Carlo (MC) simulations were performed at each of the three well depths using a novel method reported by us elsewhere[41]. Details of the model are provided in this previous paper, but we provide some key information here for convenience. The depletion potential, U_D, vs. seperation, r, was modeled using a modified form of the usual Asakura-Oosawa (AO) depletion potential as[12,42,44],

$$U_D = -\Pi(\rho, L)\, V_X(r, L, H)$$

where the depletant osmotic pressure, Π, and excluded volume, V_X, both depend on the thermoresponsive depletant size, L, and ρ is the depletant number density. Direct measurements have shown this potential accurately captures particle-wall and particle-particle depletion interactions (for a variety of material systems)[12] using the Carnahan-Starling hard sphere equation of state[45] for Π (accurate equations of state are critical to quantitative depletion potentials[42]) and the usual hard sphere excluded volume terms[46]. We use the particle-particle and particle-wall potentials from this previous work without modification, since they were shown to accurately capture particle-wall potentials at high-spatial resolution and

Variable	Value
a^a [nm]	1100
$\rho_p{}^b$[g cm^{-3}]	1.92
$\rho_f{}^c$ [g cm^{-3}]	1.0
κ^{-1d} [nm]	9.5
ψ^e [mV]	−50
T^f [°C]	25, 25, 25, 25, 35, 37
$2L^g$ [nm]	113, 113, 113, 113, 107, 53
$2R^h$ [μm]	17
D^i [μm]	21
H^j [nm]	35, 90, 285, 285, 285, 285
N^k	672, 332, 332, 332, 332, 324
$\phi_A{}^l$	0.36, 0.18, 0.18, 0.18, 0.18, 0.18
$z_m{}^m$	61, 61, 61, 61, 66, 100
Π^n [kT 10^{-6} nm^{-3}]	2.6, 2.6, 2.6, 2.6, 1.8, 0.54
$\rho_m{}^o$ [μm^{-2}]	7.46e^{-3}, 2.10e^{-2}, 2.03e^{-2}, 2.26e^{-2}, 1.17e^{-2}, 6.67e^{-4}

Table 1. Parameters for experimental analysis and MC simulations in Figs 2–4 at each etched circular pattern well depth, *H*, and each temperature, *T* (*i.e.*, depletant diameter, 2*L*). [a]particle radius previously obtained from measured gravitational potential using Total Internal Reflection Microscopy[12]; [b]SiO_2 colloid density (for Stöber SiO_2)[55]; [c]water density; [d]Debye screening length calculated (Eq. (S3)) and from conductivity; [e]particle and wall electrostatic potential previously fit to potential energy profiles in previous work[48,56]; [f]temperature from *in situ* thermocouple; [g]depletant particle diameter from dynamic light scattering (Fig. 1c); [h]patterned circle diameter and [i]center-to-center pattern spacing from scanning electron microscopy; [j]patterned well depth from ten averaged profilometry measurements; [k]number of particles from image analysis; [l]colloid area fraction from image analysis; [m]most probable height calculated using Eqs. (S6)-(S7); [n]osmotic pressure calculated using Carnahan-Starling equation of state[11,12,45]; [o]maximum colloid density value from image analysis.

infinite dilution as well as quasi-2D phase behavior without any adjustable parameters[11,12]. In this work, V_X is computed for particles and underlying surfaces using the same hard sphere expressions; however, it is computed numerically to consider local pattern features (see Supplementary Theory)[41]. The origin and value of all independently measured parameters used in interaction potentials (see Supplementary Theory Eq. (S1)-(S8)) are reported in Table 1.

Because V_X depends on the surface-to-surface separation, r, between colloidal particles and the substrate, for particles interacting with a pattern feature's side wall, it also depends on the pattern feature's height, H. The potential for U_D indicates that at a given temperature (*i.e.*, fixed depletant size, L), the value of Π is fixed and V_X increases with increasing H for $r < 2aL$; this increases depletion attraction between particles and patterned features. This is verified by the agreement of our experimental and simulation results in Fig. 2 that show depletion attraction between colloidal particles and pattern edges decreasing with decreasing feature depth.

To capture time-averaged particle microstructures, quasi-2D particle density landscapes, $\rho(x, y)$, were constructed relative to each circular pattern center by averaging particle center coordinates over 16 pattern features in both experiments and MC simulations for each well depth[43]. In this work, it is not necessary to consider other distribution functions since the particle-wall and particle-particle potentials are already known from previous work[11,12]. The third column of Fig. 2 gives contour plots of $\rho(x, y)$ from the experiments normalized by the maximum density, ρ_m, for the three well depths investigated. A ring of density at the radial distance corresponding to particle centers about one radius away from the pattern edge clearly captures particle attraction to this feature.

In addition to the radial density dependence showing particles at the pattern feature edge, there is a slight angular dependence (as indicated by the peaks in the experimental landscapes) within the radial ring closest to the edge. This suggests some structural correlation or alignment between adjacent patterns. This effect is very weak and does not create any issues when matching simulations and experiments using the reported potential for U_D, but could arise from: (1) insufficient averaging to generate perfect 2D distribution functions, (2) a component of gravity parallel to the surface due to mis-leveling, (2) weak convection causing shear alignment during assembly, (3) some small scale surface texture resulting from the wet etching patterning method producing local excluded volume[37–39]. However, with regard to the latter effect, the Supplementary Videos also clearly show single particles coexisting with particle chains

that are freely mobile along the pattern edges demonstrating that roughness is insufficient to localize particles at specific angular positions. Aside from the small angular density fluctuations, the experimental and MC simulated 2D density landscapes are indistinguishable within the experimental resolution limits and materials nonuniformities (*e.g.*, particle polydispersity, pattern heterogeneity).

Density landscapes for the two deeper well depths, $H = 285$ nm and 90 nm, in Fig. 2a,b show particles concentrated around the interior periphery of pattern features and that there are very few, if any, excursions of the particles away from the sidewalls or each other. However, whereas particle-surface interactions keep the ring of particles in the first layer around the inside pattern edges immobile, the second layer of particles appear to intermittently break free and reform long lifetime bonds for $H = 90$ nm but not for $H = 285$ nm. Because the particle-particle depletion attraction does not obviously depend on H, it appears that a weakened particle-edge attraction allows more thermal motion in the first layer that occasionally causes a particle in the second layer to break free. This effect is accurately captured in the MC simulations without any modifications to the particle-particle depletion attraction, which supports an explanation of a multi-particle packing effect in conjunction with thermal motion in the first layer.

The density landscape for the shallowest well depth ($H = 35$ nm), where there is minimal depletion attraction, shows that gravity slightly concentrates the particles to the inside of the circular wells. The concentration inside the feature is determined by a Boltzmann distribution dependent on the free energy difference of residing at the lower elevation inside the well compared to outside the pattern feature[11,43]. Otherwise, the particles are randomly distributed over the pattern surface as an inhomogeneous fluid phase.

The 2D density profiles in Fig. 2 can be plotted as one-dimensional (1D) density landscapes (far right column) by converting to polar coordinates and averaging over the angular coordinate. Results are shown for both the microscopy experiments and Monte Carlo simulations, except for the $H = 35$ nm experiment where the pattern edges were difficult to resolve under the randomly distributed particles. These results most clearly quantify how the particle density varies relative to the patterned feature edge vs. feature depth. Good correspondence is observed between the experimental and simulations results. The presence of multiple peaks in the 1D density profiles of Fig. 2a–c captures particle packing effects. The 1D density profiles of Fig. 2a and b for $H = 285$ nm and 90 nm have a maximum peak occurring at the inside edge of the pattern feature R, and a secondary peak at ~1.5a toward the feature center. This verifies that particles are more attracted to the inside perimeter of the pattern features and to each other when the well depth is between $H = 285$ nm and 90 nm[41]. The 1D density profiles of Fig. 2c have multiple peaks corresponding to particle clusters distributed inhomogeneously over the surface. Thus, at $H = 35$ nm, there is not enough attraction for the particles to display a significant energetic preference for feature edges.

At this point, we note that although the sloped side walls of the pattern features exhibit some roughness (*e.g.*, Fig. 1b inset), which could potentially increase the local excluded volume and depletion attraction[37–39], modeling the sloping wall edges as flat planes produces excellent agreement between simulations and experiments[41]. This finding indicates the effect of the roughness is negligible and makes sense based on the relative size of the surface asperities compared to the colloidal particles and depletant particles. In particular, the roughness is sufficiently small that it does not change how depletants are excluded between the colloidal particles and the pattern feature compared to smooth surfaces.

Colloidal assembly vs. depletant size. Based on PNIPAM's T-dependent size (Fig. 1c)[11,12], we investigated assembly at feature edges vs. T for arrays of 285 nm deep wells. The depletion attraction, U_D, decreases with decreasing depletant size since both Π and V_X decrease with decreasing depletant size. Depletant size decreases with increasing T in the present work so that U_D, Π, and V_X also all decrease with increasing T. This is tested for a fixed well depth of $H = 285$ nm in Fig. 3 and Supplementary Videos S4–S6. Figure 3 shows in a similar format to Fig. 2 how particle ordering varies at three different T. By switching the temperature between 25 °C and 37 °C, it was possible to control the degree of colloidal ordering within the pattern features and reconfigure colloidal assemblies between disordered fluid and multi-scale patterned states. The change in particle assembly with changing T in Fig. 3 occurred in ~10 min. A total of ~30 min was allowed for equilibration before analyzing particle configurations for Fig. 3. This process was completely reversible for all pattern feature sizes, depths, and geometries in this work.

In Fig. 3a, snapshots from video microscopy clearly show that particles outline the inside edges of the patterned circular well features at 25 °C, as was previously shown in Figs 1d–f and 2a,b. Again, colloidal concentrations greater than that needed to entirely outline the inside circumference of the pattern feature resulted in the start of a second ring of particles within the first. Likewise, no freestanding crystals were observed in the pattern interior. Colloidal 2D trajectories display the degree of particle motion away from the inner pattern feature edge as a function of time. The 2D trajectory plot of the second column in Fig. 3a shows that particles at 25 °C deviate minimally from the inside periphery of the wells. At this temperature, PNIPAM depletant particles are 113 nm in diameter (Fig. 1c), which gives rise to a significant depletion attraction at the well periphery and colloidal chain assembly.

Similar to the well depth results in Fig. 2a, particle-particle depletion attraction at this temperature is also significant relative to kT so that the 2D colloidal trajectories show particles comprising the second ring are also immobile. In Fig. 3b, at $T = 35$ °C ($2L \cong 107$ nm), the depletion attraction is reduced (*i.e.*, maximum particle–wall attraction decreases from 19kT at 25 °C to 10kT at 35 °C and particle-particle

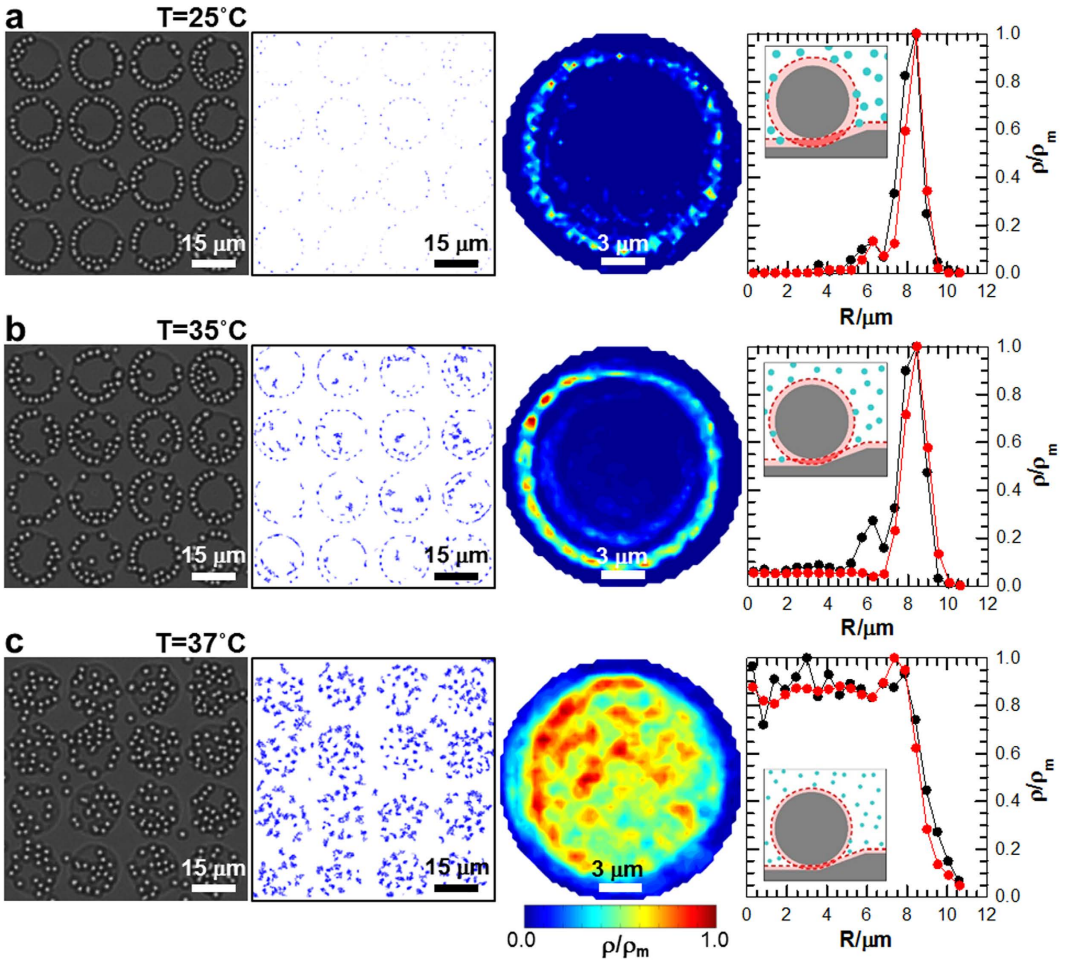

Figure 3. Structural, spatial, and statistical information obtained from video microscopy of equilibrated colloidal assembly as a function of temperature (*i.e.*, depletant size). Results shown for patterned 12 μm diameter circles arranged on a square lattice with $H = 285$ nm deep in the presence of PNIPAM hydrogel nanoparticle depletants at (**a**) 25 °C ($2L \cong 113$ nm), (**b**) 35 °C ($2L \cong 107$ nm), and (**c**) 37 °C ($2L \cong 53$ nm). (left-to-right) Experimental images extracted from video microscopy, dynamic traces of 2D particle trajectories over patterns from the first 1,000 experimental frames (~36 s), contour plots of 2D density profiles with experimental particle center coordinates averaged over all features, and 1D radial density profiles from experiments (red) and MC simulations (black).

attraction decreases from $8kT$ to $3kT$, respectively). Video microscopy images of equilibrium particle positions and 2D particle trajectories on the patterned substrate demonstrate sufficient depletion attraction for assembly, although a small increase in particle diffusion provides some evidence for a temperature-dependent reduction in the attraction. The 2D particle trajectories also show particles within the second layer in pattern features occasionally attaching and detaching due to reduced particle-particle depletion attraction. Finally, at 37 °C when depletant particles deswell to $2L \cong 53$ nm (Fig. 3c), depletion attraction is negligible, and particles diffuse freely except for the small gravitational energy difference inside and outside features[43].

To quantify the spatially varying particle distributions in these experiments, quasi-2D density landscapes, $\rho(x, y)/\rho_m$, were constructed from particle centers from video microscopy experiments averaged over ~30 min at each T. As in Fig. 2, assuming all pattern features to be identical within microfabrication limits, the density landscapes were averaged over all features. The resulting time-averaged 2D density landscapes appear as contour plots in the third column of Fig. 3. The density landscapes clearly show particles: assembling along feature edges at 25 °C, assembling but with increased local thermal motion at 35 °C, and disassembling with uniform diffusion within wells at 37 °C. The density landscapes capture the slight substrate tilt, evidenced by the increased sampling of the upper left quadrant of each feature. This illustrates how it is possible to bias the location of colloidal chain assembly within each feature with a lateral gravitational potential or another external field (which may be related to the weak angular correlations in Fig. 2).

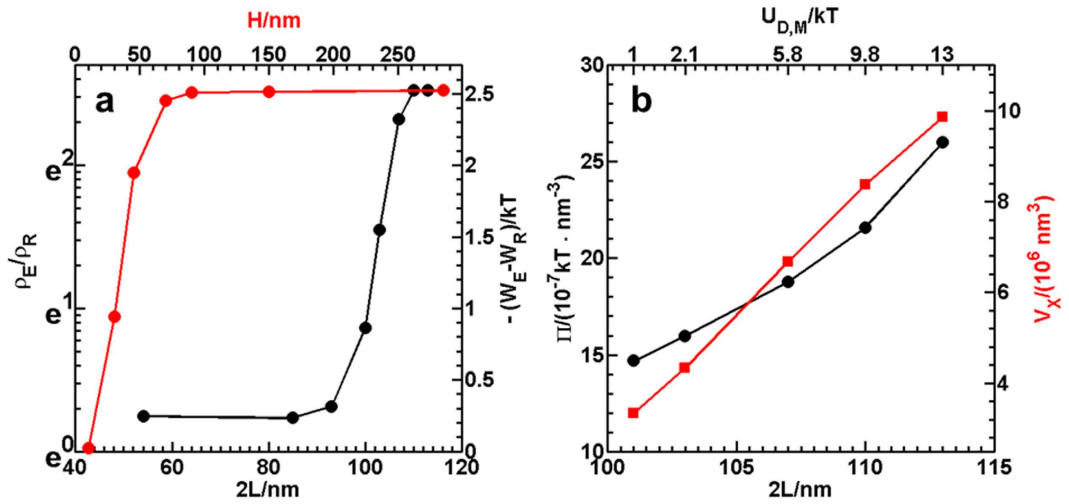

Figure 4. Density, free energy, and potential energy (with osmotic pressure/excluded volume contributions) for particles at pattern feature edge vs. depletant size and feature depth. (**a**) Density at pattern edge, ρ_E, relative to density on pattern interior as reference state, ρ_R, vs. depletant size, $2L$, for $H = 285$ nm and vs. pattern depth, H, for $2L = 113$ nm. Ratio of densities plotted on the right-hand-side on an exponential scale to show Boltzmann relationship, $\rho_E/\rho_R = \exp[-(W_E - W_R)/kT]$, to the left-hand-side showing free energy difference between particles at the pattern edge, W_E, compared to the pattern interior, W_R (*i.e.*, reference state). (**b**) Osmotic pressure, Π, and excluded volume, V_X, vs. depletant size, $2L$, and vs. depletion attraction minimum, $U_{D,M}$, based on particle-wall depletion attraction, which is related by a factor to depletion attraction at the pattern edge (*i.e.*, pattern edge V_X can be considered as some combination of 2 walls) for different H and wall angles. Note that the scale for $U_{D,M}$ has a non-linear relationship to the $2L$ scale and is plotted as text to simply show values corresponding to $U_{D,M}$.

To quantify how temperature-dependent depletion affects colloidal assembly within features, MC simulations were performed[41], using the parameters reported in Table 1. One-dimensional density profiles constructed from time-averaged particle coordinates are plotted in Fig. 3a–c to show radial particle density vs. temperature. For $T = 25$ °C and 35 °C in Fig. 3a and b, respectively, the 1D density shows a maximum peak at the feature sidewall and a secondary peak at ~1.5a, resulting from colloidal assembly in the pattern interior. Although the secondary interior peak is absent from the experimental profile in Fig. 3b, we attribute this discrepancy to inadequate statistical sampling in the experiment (*i.e.*, accurately quantifying this small peak depends strongly on observing a small number of particles bound to the interior of colloidal chains attached to the pattern edge). In contrast, the peak is clearly present in the experiments at $T = 25$ °C in Fig. 3a for stronger particle-particle attraction.

The 1D density profile at 37 °C in Fig. 3c shows that the particle density is evenly distributed within wells as the result of vanishing depletion attraction. The 1D density profiles in Figs 2 and 3 from experiments and MC simulations show excellent agreement within the spatial resolution and sampling limits in the optical microscopy measurements[47] as well as the particle and microfabricated pattern uniformity[43,48–51].The results in Figs 2 and 3 generally validate the interpretive/predictive capability of the interaction potential for U_D and our numerical routine for computing excluded volume[41].

Colloidal assembly vs. local depletion attraction. We now use the MC simulations matched to experiments to further explore in Fig. 4 how the density of particles attached to the pattern feature edge, ρ_E, varies as a function of depletant size and well depth. In particular, we invstigate more values than were probed in the experiments to get a better sense of how the assembly transitions from disordered fluids to chains lining pattern edges. In Fig. 4, we are also able to relate density changes in assembled particles at the pattern edge to the free energy and potential energy of colloid attachment to the well edge, as well as changes in osmotic pressure and excluded volume.

Figure 4a plots ρ_E/ρ_R vs. depletant size, $2L$, for $H = 285$ and vs. pattern depth, H, for $2L = 113$ nm, where ρ_R is the reference density in the pattern interior. Values of ρ_E and ρ_R are taken directly from MC simulated 1D densitry profiles like those reported in column 4 of Figs 2 and 3. The quantity ρ_E/ρ_R is plotted on an exponential scale so it can be related to a second linear axis for the free energy of attachment of particles to the pattern edge *via* a Boltzmann relationship, $\rho_E/\rho_R = \exp[-(W_E - W_R)/kT]$. In this relationship, $W_E - W_R$ is the difference in the free energy of particles at the pattern edge, W_E, compared to the free energy of particles in the pattern interior, W_R (*i.e.*, the reference state in this case).

The quantities ρ_E/ρ_R and $-(W_E - W_R)/kT$ in Fig. 4a show a sharp transition of particles not being associated with the pattern edge or each other (no obvious attraction) to being highly localized at the

edge in chains (attraction to the edge and other particles) for changes in both $2L$ and H. As such, the reconfiguration mechanism associated with colloidal chain assembly at the topographical pattern edges has a first-order "type" transition both with changing depletant size and changing pattern well depth. Although a truly one-dimensional fluid-solid transition is not expected to display first-order behavior, quasi-1D freezing experiments and simulations routinely show abrupt phase changes indistinguishable from first-order transitions[52]. Because the particle-topographical pattern interaction in this work is clearly 3D in nature, it does not make sense to consider our observation of disordered fluid states condensing into near equilibrium colloidal chains as a 1D or even quasi-1D phenomenon. As such, the observation of a first-order "type" of transition between fluids and patterned chains is not at odds with expectations for 1D phase transitions (that are not obviously applicable to this work).

We can examine U_D more closely to better understand the mechanism associated with depletant size producing a relatively sharp transition in the reconfiguration of particles between inhomogeneous fluids and patterned chains. Figure 4b plots the PNIPAM solution Π vs. $2L$ using the Carnahan-Starling hard sphere equation of state[45]. Figure 4b also shows the particle-wall V_X vs. $2L$ using the standard particle-wall equation[46] (also see Eq. (S5)) for separations values of z_m in Table 1, which is the particles' most probable height above the substrate due to a balance of gravity and electrostatic repulsion (see Supplementary Theory and Eq. (S6)). For the feature geometry used in this work (see Fig. 1b), the feature V_X is always approximately some factor times the particle-wall value; for example, it is $\sim 1V_X$ as the angle goes to zero and closer to $\sim 2V_X$ (in some cases) as the angle goes to 90°. As such, the percent change in the particle-wall V_X will also be the percent change in the particle-feature V_X, even if the absolute values differ. On the top axis, the values of the net potential minimum, $U_{D,M}$, are plotted vs. $2L$, which does not have a straightforward linear relationship, so they are simply plotted as text values for reference. In short, as the depletant sizes changes from 100 nm to 115 nm, the depletion attraction changes from $1kT$–$13kT$. This is the result of Π increasing $\sim 2\times$ and V_X increasing $\sim 3\times$ over the same range of depletant size.

The results in Fig. 4, taken together, show that the potential indeed changes continuously vs. depletant size with comparable effects due to the changes in Π and V_X, which also change continuously. Because $2L$, Π, V_X, and $U_{D,M}$ all change continuously, ultimately the abrupt change from fluid states to patterned chains occurs with a critical level of attraction in what appears to be a first-order "type" transition. At least for the types of tunable depletants and patterned excluded volume investigated in this work, the colloidal assembly undergoes a switching behavior to enable a potential two-state metamaterial with on- and off- configurations. More continuous or multi-state transitions could eventually enable further tuning of multi-scale metamaterials.

In conclusion, we present a novel approach to reconfigurable colloidal assembly of multi-scale structures that combines thermoresponsive depletion attraction with topographically patterned surface features. Changing both the temperature and topography was shown to reconfigure colloidal microstructures between two well-defined states: multi-scale periodic structures and disordered fluid states. Spatial- and time-averaged density profiles characterized how the degree of colloidal ordering can be controlled as a function of patterned feature depth and temperature, which was quantitatively captured by theoretical depletion potentials. Our findinsg show the formation of patterned colloidal chains occurs *via* a first-order "type" transition depsite the continously tunable depletant size, osmotic pressure, excluded volume, and local depletation attraction. The ability to dynamically manipulate multi-scale colloidal assemblies provides a basis for the development of micro- and nano- scale periodic and resonant structured materials and devices. Ultimately, the approach reported here can be extended to control the size, shape, orientation, and microstructure of colloidal assemblies on multiple lengths scales and in arbitrary pre-defined pattern templates.

Methods

Surface patterning. Topographical features were wet etched into microscope slides (Gold Seal, VWR), using patterned photoresist (S1818, Microchem) as the etch mask. All etching was carried out under agitation at 25 °C in a mixture of oxide etchants (1:1 Timetch:Buffer-HF-Improved, Transene Company), with the resulting depth controlled by etch time. Feature depths were measured with a stylus profilometer (Dektak 6M) at ten positions across the array. The feature sidewalls had sloping edges due to the isotropic nature of the wet etch (Fig. 1b inset and Supplementary Fig. S2).

Particles. Nominal 2.34 μm diameter SiO_2 colloids (Bangs Laboratories) and NaCl were used as received. Uncharged PNIPAM hydrogel particles were synthesized using a standard literature procedure (see Supplementary Methods)[53]. Patterned microscope slides were sonicated in acetone, isopropanol, and then deionized (DI) water, followed by 1 h of immersion in piranha (3:1 H_2SO_4:30% H_2O_2,), a DI water rinse, sonication in 100 mM KOH for 30 min, a DI water rinse, and then dried with N_2 prior to each experiment. Dispersions of 2.34 μm SiO_2, PNIPAM, aqueous NaCl, and DI water were prepared to yield 1 mM NaCl with a 17.5% stock PNIPAM volume fraction and ~18% SiO_2 interfacial area fraction.

Video microscopy. All experiments were performed in ~100 μm thick, epoxy-sealed sample cells consisting of a microscope slide substrate and a glass coverslip. Temperature control was achieved using a heating stage with a Bionomic System BC-110 temperature controller (20/20 Technology, Inc.). Patterned substrates were coupled to the heating stage using a silicone-based heat sink compound (RadioShack).

A 12-bit CCD camera (ORCA-ER, Hamamatsu) on an inverted optical microscope (Axio Observer A1, Zeiss) was operated in 4-binning mode with a 63× objective to yield 28 frame/s and 385 nm/pixel. Image analysis algorithms coded in Fortran were used to track lateral colloid motion in all experiments[11,43,51,54].

Monte Carlo simulations. VM experiments were modeled in 2D MC simulations, where colloids sampled landscapes determined by gravity and substrate topography-mediated depletion potentials, using a novel approach to compute local excluded volume effects, which is described in detail elsewhere[41]. MC simulations were performed using parameters provided in Table 1, and initial configurations were obtained from experimental images. Each MC simulation was performed for 2.5×10^6 steps with particle positions stored every 250 steps after an initial equilibration of 10^6 steps.

References

1. Ozbay, E. The Magical World of Photonic Metamaterials. *Opt. Photon. News* **19,** 22–27, doi: 10.1364/OPN.19.11.000022 (2008).
2. Boltasseva, A. & Shalaev, V. M. All that glitters need not be gold. *Science* **347,** 1308–1310, doi: 10.1126/science.aaa8282 (2015).
3. Biró, L. P. & Vigneron, J. P. Photonic nanoarchitectures in butterflies and beetles: valuable sources for bioinspiration. *Laser Photonics Rev* **5,** 27–51, doi: 10.1002/lpor.200900018 (2011).
4. Sharma, V., Crne, M., Park, J. O. & Srinivasarao, M. Structural Origin of Circularly Polarized Iridescence in Jeweled Beetles. *Science* **325,** 449–451, doi: 10.1126/science.1172051 (2009).
5. Zhang, J., Li, Y., Zhang, X. & Yang, B. Colloidal Self-Assembly Meets Nanofabrication: From Two-Dimensional Colloidal Crystals to Nanostructure Arrays. *Adv. Mat.* **22,** 4249–4269, doi: 10.1002/adma.201000755 (2010).
6. Ye, X. & Qi, L. Two-dimensionally patterned nanostructures based on monolayer colloidal crystals: Controllable fabrication, assembly, and applications. *Nano Today* **6,** 608–631, doi: 10.1016/j.nantod.2011.10.002 (2011).
7. Shipway, A. N., Katz, E. & Willner, I. Nanoparticle Arrays on Surfaces for Electronic, Optical, and Sensor Applications. *ChemPhysChem* **1,** 18–52, doi: 10.1002/1439-7641(20000804)1:1<18::aid-cphc18>3.0.co;2-l (2000).
8. Bahukudumbi, P. *et al.* Colloidal Microstructures, Transport, and Impedance Properties within Interfacial Microelectrodes. *Appl. Phys. Lett.* **90,** 224102, doi: 10.1063/1.2744480 (2007).
9. Gay-Balmaz, P. & Martin, O. J. F. Electromagnetic resonances in individual and coupled split-ring resonators. *J. Appl. Phys.* **92,** 2929–2936, doi: 10.1063/1.1497452 (2002).
10. Lin, M. Y. *et al.* Universality in colloid aggregation. *Nature* **339,** 360–362, doi: 10.1038/339360a0 (1989).
11. Fernandes, G. E., Beltran-Villegas, D. J. & Bevan, M. A. Spatially Controlled Reversible Colloidal Self-Assembly. *J. Chem. Phys.* **131,** 134705, doi: 10.1063/1.3243686 (2009).
12. Fernandes, G. E., Beltran-Villegas, D. J. & Bevan, M. A. Interfacial Colloidal Crystallization via Tunable Hydrogel Depletants. *Langmuir* **24,** 10776–10785, doi: 10.1021/la802025d (2008).
13. Khanh, N. N. & Yoon, K. B. Facile Organization of Colloidal Particles into Large, Perfect One- and Two-Dimensional Arrays by Dry Manual Assembly on Patterned Substrates. *J. Am. Chem. Soc.* **131,** 14228–14230, doi: 10.1021/ja905534k (2009).
14. Erb, R. M., Son, H. S., Samanta, B., Rotello, V. M. & Yellen, B. B. Magnetic assembly of colloidal superstructures with multipole symmetry. *Nature* **457,** 999–1002, doi: 10.1038/nature07766 (2009).
15. Demirors, A. F., Pillai, P. P., Kowalczyk, B. & Grzybowski, B. A. Colloidal assembly directed by virtual magnetic moulds. *Nature* **503,** 99–103, doi: 10.1038/nature12591 (2013).
16. Leunissen, M. E. *et al.* Ionic colloidal crystals of oppositely charged particles. *Nature* **437,** 235–240, doi: 10.1038/nature03946 (2005).
17. Aizenberg, J., Braun, P. V. & Wiltzius, P. Patterned colloidal deposition controlled by electrostatic and capillary forces. *Phys. Rev. Lett.* **84,** 2997–3000 (2000).
18. Yin, Y., Lu, Y., Gates, B. & Xia, Y. Template-Assisted Self-Assembly; A Practical Route to Complex Aggregates of Monodispersed Colloids with Well-Defined Sizes, Shapes, and Structures. *J. Am. Chem. Soc.* **123,** 8718–8729, doi: 10.1021/ja011048v (2001).
19. Ognysta, U., Nych, A., Nazarenko, V., Škarabot, M. & Muševič, I. Design of 2D Binary Colloidal Crystals in a Nematic Liquid Crystal. *Langmuir* **25,** 12092–12100, doi: 10.1021/la901719t (2009).
20. Perro, A. *et al.* A Chemical Synthetic Route towards "Colloidal Molecules". *Angewandte Chemie* **121,** 367–371, doi: 10.1002/ange.200802562 (2009).
21. Wang, Y. *et al.* Colloids with valence and specific directional bonding. *Nature* **491,** 51–55, doi: 10.1038/nature11564 (2012).
22. McGinley, J. T., Jenkins, I., Sinno, T. & Crocker, J. C. Assembling colloidal clusters using crystalline templates and reprogrammable DNA interactions. *Soft Matter* **9,** 9119–9128, doi: 10.1039/c3sm50950h (2013).
23. Feng, L. *et al.* Cinnamate-based DNA photolithography. *Nat Mater* **12,** 747–753, doi: 10.1038/nmat3645 (2013).
24. Jiang, P., Prasad, T., McFarland, M. J. & Colvin, V. L. Two-dimensional nonclose-packed colloidal crystals formed by spincoating. *Appl. Phys. Lett.* **89,** 011908, doi: 10.1063/1.2218832 (2006).
25. Chen, Q. *et al.* Triblock Colloids for Directed Self-Assembly. *J. Am. Chem. Soc.* **133,** 7725–7727, doi: 10.1021/ja202360g (2011).
26. Kim, Y., Shah, A. A. & Solomon, M. J. Spatially and temporally reconfigurable assembly of colloidal crystals. *Nat Commun* **5,** doi: 10.1038/ncomms4676 (2014).
27. Hayward, R. C., Saville, D. A. & Aksay, I. A. Electrophoretic assembly of colloidal crystals with optically tunable micropatterns. *Nature* **404,** 56–59, doi: 10.1038/35003530 (2000).
28. Chaudhary, K., Juarez, J. J., Chen, Q., Granick, S. & Lewis, J. A. Reconfigurable assemblies of Janus rods in AC electric fields. *Soft Matter* **10,** 1320–1324, doi: 10.1039/c3sm52418c (2014).
29. Juarez, J. J., Mathai, P. P., Liddle, J. A. & Bevan, M. A. Multiple electrokinetic actuators for feedback control of colloidal crystal size. *Lab on a Chip* **12,** 4063–4070, doi: 10.1039/C2LC40692F (2012).
30. Juarez, J. J. & Bevan, M. A. Feedback Controlled Colloidal Self-Assembly. *Adv. Funct. Mater.* **22,** 3833–3839, doi: 10.1002/adfm.201200400 (2012).
31. Juarez, J. J., Feicht, S. E. & Bevan, M. A. Electric field mediated assembly of three dimensional equilibrium colloidal crystals. *Soft Matter* **8,** 94–103, doi: 10.1039/C1SM06414B (2012).
32. Savage, J. R., Blair, D. W., Levine, A. J., Guyer, R. A. & Dinsmore, A. D. Imaging the Sublimation Dynamics of Colloidal Crystallites. *Science* **314,** 795–798, doi: 10.1126/science.1128649 (2006).
33. Shelley, L. T., Robert, E. & Royall, C. P. Temperature as an external field for colloid–polymer mixtures: 'quenching' by heating and 'melting' by cooling. *J. Phys. Condens. Matter* **24,** 464128 (2012).
34. Dinsmore, A. D., Yodh, A. G. & Pine, D. J. Entropic control of particle motion using passive surface microstructures. *Nature* **383,** 239–242, doi: 10.1038/383239a0 (1996).
35. Lin, K.-H. *et al.* Entropically Driven Colloidal Crystallization on Patterned Surfaces. *Phys. Rev. Lett.* **85,** 1770–1773, doi: 10.1103/PhysRevLett.85.1770 (2000).

36. Lee, W., Chan, A., Bevan, M. A., Lewis, J. A. & Braun, P. V. Nanoparticle-Mediated Epitaxial Assembly of Colloidal Crystals on Patterned Substrates. *Langmuir* **20,** 5262–5270, doi: 10.1021/la035694e (2004).
37. Badaire, S. p., Cottin-Bizonne, C. c. & Stroock, A. D. Experimental Investigation of Selective Colloidal Interactions Controlled by Shape, Surface Roughness, and Steric Layers. *Langmuir* **24,** 11451–11463, doi: 10.1021/la801718j (2008).
38. Zhao, K. & Mason, T. G. Suppressing and Enhancing Depletion Attractions between Surfaces Roughened by Asperities. *Phys. Rev. Lett*. **101,** 148301, doi: 10.1103/PhysRevLett.101.148301 (2008).
39. Kraft, D. J. *et al.* Surface roughness directed self-assembly of patchy particles into colloidal micelles. *PNAS* **109,** 10787–10792, doi: 10.1073/pnas.1116820109 (2012).
40. Sacanna, S., Irvine, W. T. M., Chaikin, P. M. & Pine, D. J. Lock and key colloids. *Nature* **464,** 575–578, doi: 10.1038/nature08906 (2010).
41. Yang, Y., Edwards, T. D. & Bevan, M. A. Modeling depletion mediated colloidal assembly on topographical patterns. *J. Coll. Interfac. Sci*. **449,** 270–278, doi: 10.1016/j.jcis.2014.12.002 (2015).
42. Edwards, T. D. & Bevan, M. A. Depletion-Mediated Potentials and Phase Behavior for Micelles, Macromolecules, Nanoparticles, and Hydrogel Particles. *Langmuir* **28,** 13816–13823, doi: 10.1021/la302805n (2012).
43. Bahukudumbi, P. & Bevan, M. A. Imaging Energy Landscapes using Concentrated Diffusing Colloidal Probes. *J. Chem. Phys.* **126,** 244702, doi: 10.1063/1.2739548 (2007).
44. Asakura, S. & Oosawa, F. On Interaction between 2 Bodies Immersed in a Solution of Macromolecules. *J. Chem. Phys.* **22,** 1255–1256, doi: 10.1063/1.1740347 (1954).
45. Carnahan, N. F. & Starling, K. E. Equation of state for nonattracting rigid spheres. *J. Chem. Phys.* **51,** 635, doi: 10.1063/1.1672048 (1969).
46. Lekkerkerker, H. N. W. & Tuinier, R. *Colloids and the Depletion Interaction*. (Springer, 2011).
47. Bevan, M. A. & Eichmann, S. L. Optical Microscopy Measurements of kT-Scale Colloidal Interactions. *Curr. Opin. Colloid Interface Sci*. **16,** 149–157, doi: 10.1016/j.cocis.2010.12.006 (2011).
48. Wu, H.-J., Pangburn, T. O., Beckham, R. E. & Bevan, M. A. Measurement and Interpretation of Particle−Particle and Particle−Wall Interactions in Levitated Colloidal Ensembles. *Langmuir* **21,** 9879–9888, doi: 10.1021/la050671g (2005).
49. Pangburn, T. O. & Bevan, M. A. Anomalous potentials from inverse analyses of interfacial polydisperse attractive colloidal fluids. *J. Chem. Phys.* **124,** 054712, doi: 10.1063/1.2162536 (2006).
50. Pangburn, T. O. & Bevan, M. A. Role of polydispersity in anomalous interactions in electrostatically levitated colloidal systems. *J. Chem. Phys.* **123,** 174904, doi: 10.1063/1.2074887 (2005).
51. Wu, H.-J., Everett, W. N., Anekal, S. G. & Bevan, M. A. Mapping Patterned Potential Energy Landscapes with Diffusing Colloidal Probes. *Langmuir* **22,** 6826–6836, doi: 10.1021/la060501j (2006).
52. Koga, K. Freezing in one-dimensional liquids. *The Journal of Chemical Physics* **118,** 7973–7980, doi: 10.1063/1.1564049 (2003).
53. Pelton, R. H. & Chibante, P. Preparation of Aqueous Lattices with N-Isopropylacrylamide. *Colloids Surf.* **20,** 247–256, doi: 10.1016/0166-6622(86)80274-8 (1986).
54. Crocker, J. C. & Grier, D. G. Methods of Digital Video Microscopy for Colloidal Studies. *J. Colloid. Interface Sci.* **179,** 298–310, doi: 10.1006/jcis.1996.0217 (1996).
55. Stober, W., Fink, A. & Bohn, E. Controlled Growth of Monodisperse Silica Spheres in the Micron Size Range. *J. Coll. Interfac. Sci*. **26,** 62–69, doi: 10.1016/0021-9797(68)90272-5 (1968).
56. Wu, H. J. & Bevan, M. A. Direct Measurement of Single and Ensemble Average Particle-Surface Potential Energy Profiles. *Langmuir* **21,** 1244–1254, doi: 10.1021/la047892r (2005).

Acknowledgements

We acknowledge financial support from the National Science Foundation (CBET-1234981).

Author Contributions

T.E., W.E., Y.Y. and M.B. designed the experiments and their analyses. W.E. designed and fabricated the topographically patterned subtrates. T.E. synthesized PNIPAM and performed the experiments. T.E. and Y.Y. analyzed the experiments. Y.Y. and M.B. designed the simulations and their analyses. Y.Y. performed and analyzed the simulations. T.E., W.E., Y.Y. and M.B. interpreted the data. T.E., W.E., Y.Y. and M.B. wrote the manuscript.

Additional Information

Supplementary information accompanies this paper at http://www.nature.com/srep

Competing financial interests: The authors declare no competing financial interests.

How to cite this article: Edwards, T. D. *et al.* Reconfigurable multi-scale colloidal assembly on excluded volume patterns. *Sci. Rep.* **5**, 13612; doi: 10.1038/srep13612 (2015).

About AACC

The American Automatic Control Council (AACC) is an association of the control systems divisions of nine member societies to represent the United States (U.S.) to the world control community and to support the mission of the individual member societies in enhancing the role and contributions of automation to the benefit of humankind.

The AACC hosts the annual, 3-day, interdisciplinary American Control Conference (ACC) with about 1600 participants and over 1100 refereed papers. The ACC is an internationally recognized quality venue for dissemination of ideas, methodology, networking for leaders within academe, research labs, and industry. Additionally, the AACC provides annual awards to recognize and honor individuals who have made substantial contributions to both control theory and practice, supports control education from K-12 through post graduate studies, and provides delegates from the U.S. to the International Federation of Automatic Control (IFAC). At any one time there are about 200 individual volunteers working to make AACC and ACC events successful, providing them opportunities for personal and professional development and recognition.

Activities of the AACC are governed by a Board of Directors. Each director is a delegate from and appointed by each member society. Daily activities of the AACC are executed by 5 AACC officers, reporting to the Board. Operating committees for the conferences, awards committees, etc. report to the officers. All directors, officers, and committee members are volunteers.

AIAA (http://www.aiaa.org/)	American Institute of Aeronautics and Astronautics (**AIAA** (http://www.aiaa.org/)) (See also AIAA Guidance Navigation and Control Technical Committee (http://www.aiaa.org/participate/tcs/index.hfm?GetComm=66&tc=tc).)
AIChE (http://www.aiche.org/)	American Institute of Chemical Engineers (**AIChE** (http://www.aiche.org/))
Applied Probability Society of INFORMS informs	Applied Probability Society (APS, a subdivision of INFORMS (https://connect.informs.org/aps/home))

(http://www.asce.org/)	American Society of Civil Engineers (**ASCE** (http://www.asce.org/))
(http://www.asme.org/)	American Society of Mechanical Engineers (**ASME** (https://www.asme.org/)) (See also ASME Dynamic System and Control Division (https://community.asme.org/dynamic_systems_control/w/wiki/4235.events.aspx).)
(http://www.ieee.org/)	Institute of Electrical and Electronics Engineers (**IEEE** (http://www.ieee.org/)) (See also IEEE Control Systems Society (http://www.ieeecss.org/).)
(http://www.isa.org/)	International Society of Automation (**ISA** (http://www.isa.org/))
(http://www.scs.org/)	Society for Modeling & Simulation International (**SCS** (http://www.scs.org/))
(http://www.siam.org/)	Society for Industrial and Applied Mathematics (**SIAM** (http://www.siam.org/))(See also SIAM Activity Group on Control and Systems Theory (http://www.siam.org/activity/cst/))

The AACC is the US National Member Organization of the International Federation of Automatic Control (**IFAC** (http://www.ifac-control.org/)).

The main technical activity of the AACC is to sponsor, organize and run the annual "American Control Conference" (**ACC** (http://acc2015.a2c2.org/)). The ACC is usually held during the month of June, and occasionally in May or July.

The AACC publishes individual news articles on the website. Please contact the News Editor, John Hedengren at john_hedengren@byu.edu (mailto:john_hedengren@byu.edu), for announcement of relevant events.

Search A2C2

Search A2C2

Community

(https://www.linkedin.com/groups/13510485/profile)

History Book

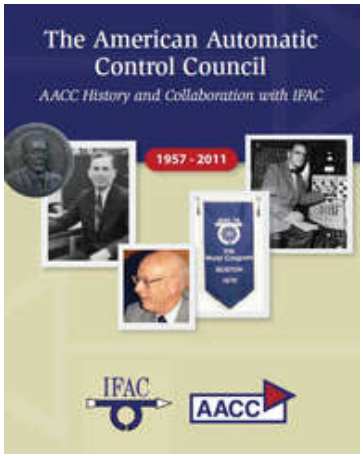

(/sites/a2c2.org/files/BookWithCover.pdf)

(http://www.aiaa.org/) (http://www.aiche.org/) (http://www.informs.org/Community/APS) (http://www.asce.org/) (http://www.asme.org/) (http://www.ieee.org/) (https://www.isa.org/) (http://scs.org/) (http://www.siam.org/)

A2C2.org Webmaster: John Hedengren (http://apm.byu.edu/prism/index.php/Members/JohnHedengren)

(https://www.linkedin.com/groups/American-Automatic-Control-Council-13510485/about)

About the Journal

Editor-in-Chief: Paul S. Weiss
University of California, Los Angeles
E-mail: editor@nano.ucla.edu
Print Edition ISSN: 1936-0851
Web Edition ISSN: 1936-086X

View Publication Information in Current Issue

2017 Impact Factor: 13.709
2017 Total Citations: 134,596

Indexed/Abstracted in: CAS, SCOPUS, MEDLINE/PubMed and Web of Science.

ACS Nano received the 2008 Association of American Publishers' Award for Best New Journal in the category of Science, Technology, and Medicine.

Journal Scope

Published monthly, *ACS Nano* is an international forum for the communication of comprehensive articles on nanoscience and nanotechnology research at the interfaces of chemistry, biology, materials science, physics, and engineering. Moreover, the journal helps facilitate communication among scientists from these research communities in developing new research opportunities, advancing the field through new discoveries, and reaching out to scientists at all levels.

ACS Nano publishes comprehensive articles on synthesis, assembly, characterization, theory, and simulation of nanostructures (nanomaterials and assemblies, nanodevices, and self-assembled structures), nanobiotechnology, nanofabrication, methods and tools for nanoscience and nanotechnology, and self- and directed-assembly.

In addition to comprehensive, original research articles, *ACS Nano* offers thorough reviews, perspectives on cutting-edge research, conversations with nanoscience and nanotechnology thought leaders, and discussions of topics that provide distinctive views about the future of nanoscience and nanotechnology.

Select Decade
Select Volume
Select Issue
List of Issues Go

1155 Sixteenth Street N.W.
Washington, DC 20036

Products

Journals A-Z
eBooks
C&EN
C&EN Archives
ACS Legacy Archives
ACS Mobile
Video

User Resources

About Us
ACS Members
Librarians
ACS Publishing Center
Website Demos
Privacy Policy
Mobile Site

Support

Get Help
For Advertisers
Institutional Sales

Live Chat

Partners

ChemComm

Read this journal

(http://pubs.rsc.org/en/journals/journalissues/cc?&_ga=2.70573268.533760951.1534757065-1046491195.1532073717#!recentarticles&adv)

Submit your article

(https://mc.manuscriptcentral.com/chemcomm)

Impact factor: 6.290*
Publishing frequency: 100 issues per year
Indexed in Science Citation Index (SCI) and MEDLINE
Chair: Veronique Gouverneur

Scope

ChemComm (*Chemical Communications*) is renowned as the fastest publisher of articles providing information on new avenues of research, drawn from all the world's major areas of chemical research.

ChemComm publishes 100 issues per year, the first chemistry journal to do this, resulting in even faster times to publication and increased visibility.

The journal publishes a number of web themed issues on cutting edge areas of chemical research. From 2011, an Emerging Investigator issue is published on an annual basis.

ChemComm is now offering authors the option of double-blind peer review, in addition to single-blind peer review.

Volume 51 | Number 3 | 11 January 2015 | Pages 437–608

ChemComm

Chemical Communications
www.rsc.org/chemcomm

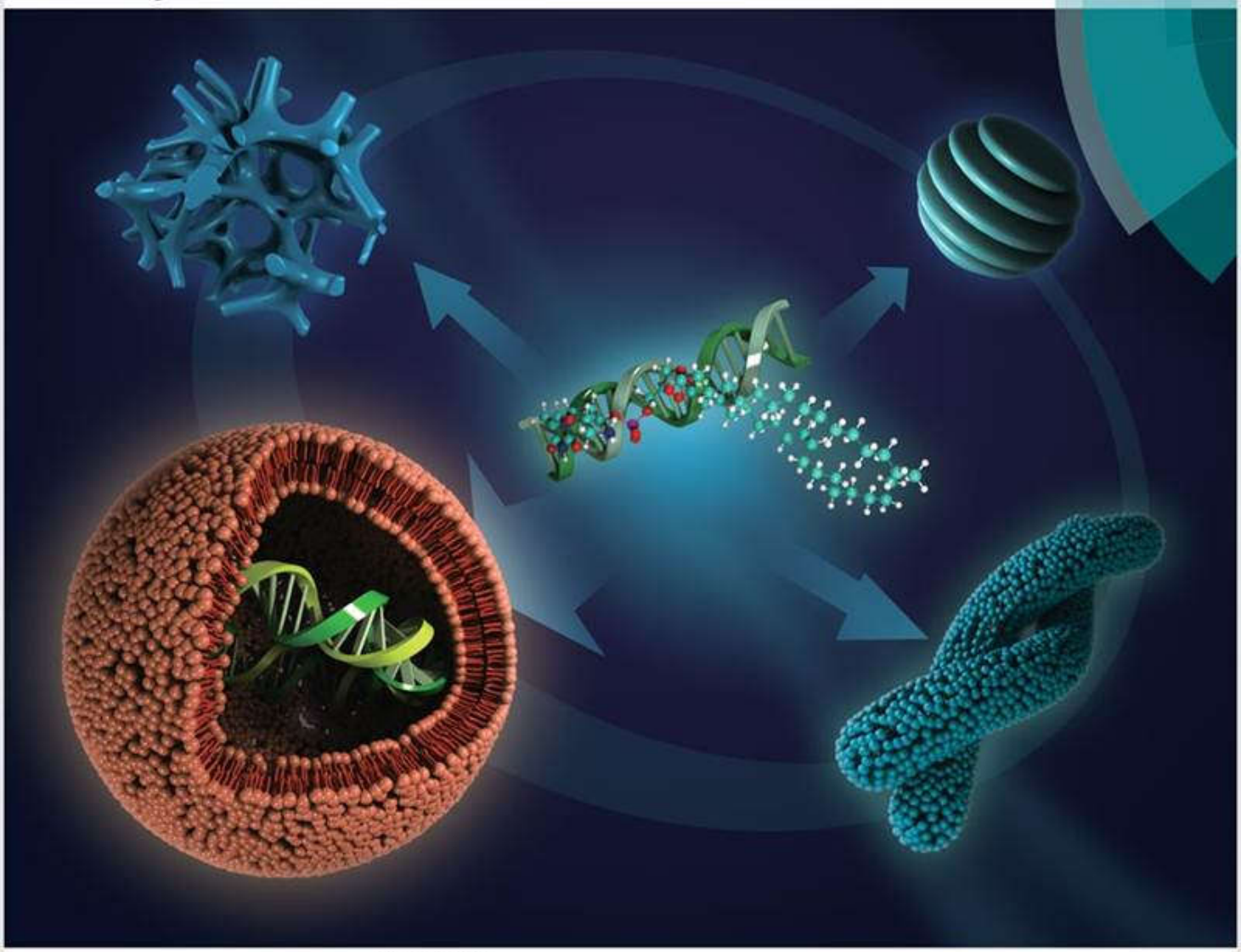

ISSN 1359-7345

ROYAL SOCIETY OF CHEMISTRY

COMMUNICATION
Zhenjun Yang *et al.*
Supramolecular assemblies of novel aminonucleoside phospholipids and their bonding to nucleic acids

Editorial board Advisory board Editorial office Lectureship

Chair

Véronique Gouverneur (/journals-books-databases/about-journals/chemcomm/editorial-board-members/#cc_gouverneur), University of Oxford, UK

Associate editors

Penny Brothers (/journals-books-databases/about-journals/chemcomm/editorial-board-members/#cc_brothers), The University of Auckland, New Zealand

Rachel Caruso (/journals-books-databases/about-journals/chemcomm/editorial-board-members/#cc_caruso), RMIT University, Australia

Steven De Feyter (/journals-books-databases/about-journals/chemcomm/editorial-board-members/#cc_de_feyter), KU Leuven, Belgium

Antonio Echavarren (/journals-books-databases/about-journals/chemcomm/editorial-board-members/#cc_echavarren), Institute of Chemical Research of Catalonia, Spain

Daniel Gamelin (/journals-books-databases/about-journals/chemcomm/editorial-board-members/#cc_gamelin), University of Washington, USA

Itaru Hamachi (/journals-books-databases/about-journals/chemcomm/editorial-board-members/), Kyoto University, Japan

Michael Krische (/journals-books-databases/about-journals/chemcomm/editorial-board-members/#cc_krische), University of Texas at Austin, USA

Can Li (/journals-books-databases/about-journals/chemcomm/editorial-board-members/#cc_li), Dalian Institute of Chemical Physics, China

Amy Prieto (/journals-books-databases/about-journals/chemcomm/editorial-board-members/#cc_prieto), Colorado State University, USA

S Ramakrishnan (/journals-books-databases/about-journals/chemcomm/editorial-board-members/#cc_ramakrishnan), Indian Institute of Science, India

Jean-Louis Reymond (/journals-books-databases/about-journals/chemcomm/editorial-board-members/#cc_reymond), University of Berne, Switzerland

Manfred Scheer (/journals-books-databases/about-journals/chemcomm/editorial-board-members/#cc_scheer), University of Regensburg, Germany

Jonathan L Sessler (/journals-books-databases/about-journals/chemcomm/editorial-board-members/#cc_sessler), University of Texas at Austin, USA

Jonathan W Steed (/journals-books-databases/about-journals/chemcomm/editorial-board-members/#cc_steed), Durham University, UK

T Don Tilley (/journals-books-databases/about-journals/chemcomm/editorial-board-members/#cc_tilley), University of California, Berkeley, USA

Sandeep Verma (/journals-books-databases/about-journals/chemcomm/editorial-board-members/), Indian Institute of Technology Kanpur, India

Article types

Chemical Communications publishes:

- Communications
- Feature articles
- Highlights

See more information about these article types +

Journal specific guidelines

The following guidelines are journal specific. For general guidance on preparing an article please visit our Prepare your article (/journals-books-databases/journal-authors-reviewers/prepare-your-article/) page, the content of which is relevant to all of our journals.

Double-blind peer review option

ChemComm is now offering authors the option of double-blind peer review. Both single- and double-blind peer review are now available to authors.

- Single-blind peer review - where reviewers are anonymous but author names and affiliations are known to reviewers. (This is the traditional peer review model used on *ChemComm*.)

- Double-blind peer review - where authors and reviewers' identities are concealed from each other.

Guidelines for authors and reviewers can be found below.

Guidelines for authors and reviewers +

Experimental guidelines

Experimental information must be provided to enable other researchers to reproduce accurately the work. The experimental details and the characterisation data should preferably be provided as electronic supplementary information (ESI), although on occasion it may be appropriate to include some or all of this within the body of the communication. This will depend on the nature of the research being reported.

The synthesis of all new compounds must be described in detail. Synthetic procedures must include the specific reagents, products and solvents and must give the amounts (g, mmol, for products: %) for all of them, as well as clearly stating how the percentage yields are calculated. They must also include all the characterisation data for the prepared compound or material. For multistep synthesis papers, spectra of key compounds and the final product should be included. For a series of related compounds, at least one representative procedure which outlines a specific example that is described in the text or in a table and which is representative for the other cases must be provided.

Characterisation of new compounds & computational results +

Readership information

ChemComm is for academic and industrial chemists in all areas of the chemical sciences.

Subscription information

ChemComm is part of collections RSC Gold, Core Chemistry and General Chemistry.

Print + online 2018: ISSN 1359-7345, £3,563 / $6,273
Online only 2018: ISSN 1364-548X, £3,393 / $5,975

*2017 Journal Citation Reports ® (Clarivate Analytics, June 2018)

ChemComm

Pre-submission queries please contact Philippa Ross, Executive Editor
Email:Send us an email

Post-submission queries please contact Helen Saxton, Editorial Production Manager
Email:Send us an email

Share

Not a member?

Apply for membership (/membership-and-community/join/)

books-databases/) (/membership-and- contacts/)

About the Journal

Editor-in-Chief: Françoise Winnik
University of Helsinki
E-mail: eic@langmuir.acs.org

Print Edition ISSN: 0743-7463
Web Edition ISSN: 1520-5827

View Publication Information in Current Issue

2017 Impact Factor: 3.789
2017 Total Citations: 118,255

Indexed/Abstracted in: CAS, SCOPUS, EBSCOhost, British Library, PubMed, Web of Science, and SwetsWise.

Journal Scope

Langmuir is the leading journal focusing on the fundamental science of systems and materials in which the interface dominates structure and function. Submissions on original advances in the understanding of interfaces including novel concepts and emerging areas are welcome. The following topics are within the scope of *Langmuir.*

- Surfaces and interfaces (synthetic and natural): adsorption, surfactants, emulsions, ultrathin films, forces and dynamics.
- Surface chemistry of interface-rich systems and nanoparticles/colloids.
- Interface-driven stability; response, organization and self-organization of (nano)particle suspensions and structures.
- Charge transfer at interfaces: electrochemistry, processes related to energy use and production.
- Bio-interfaces: synthetic surfaces in vivo and in vitro.
- Measurements on interfaces and colloids.
- Understanding of fundamental interfacial properties aided by theory & computations.

Reviewers of Langmuir manuscripts will be asked the following questions.

- Does the manuscript report novel scientific findings relevant to the broad field of interface science?
- Are the claims adequately supported with appropriate data, control experiments, and statistics?

1155 Sixteenth Street N.W.
Washington, DC 20036

Products

Journals A-Z
eBooks
C&EN
C&EN Archives
ACS Legacy Archives
ACS Mobile
Video

User Resources

About Us
ACS Members
Librarians
ACS Publishing Center
Website Demos
Privacy Policy
Mobile Site

Support

Get Help
For Advertisers
Institutional Sales

Live Chat

Partners

(https://www.sciencedirect.com/science/journal/01678655)

ISSN: 0167-8655

Pattern Recognition Letters

An official publication of the International Association for Pattern Recognition

Editors-in-Chief: G. Borgefors (https://www.journals.elsevier.com:443/pattern-recognition-letters/editorial-board/g-borgefors), G. Sanniti di Baja (https://www.journals.elsevier.com:443/pattern-recognition-letters/editorial-board/g-sanniti-di-baja), S. Sarkar (https://www.journals.elsevier.com:443/pattern-recognition-letters/editorial-board/s-sarkar)

› View Editorial Board (https://www.journals.elsevier.com:443/pattern-recognition-letters/editorial-board)

Submit Your Paper (https://ees.elsevier.com/patrec)

Supports Open Access (http://www.elsevier.com/journals/pattern-recognition-letters/0167-8655/open-access-options)

View Articles (https://www.sciencedirect.com/science/journal/01678655)

Guide for Authors

Abstracting/ Indexing (http://www.elsevier.com/journals/pattern-recognition-letters/0167-8655/abstracting-indexing)

Track Your Paper

Order Journal (https://www.elsevier.com/journals/institutional/pattern-recognition-letters/0167-8655)

Journal Metrics

- CiteScore: **3.00**

Impact Factor: **1.952**

5-Year Impact Factor: **2.350**

Source Normalized Impact per Paper (SNIP): **1.580**

SCImago Journal Rank (SJR): **0.662**

- View More on Journal Insights

Your Research Data

- Share your research data (https://www.elsevier.com/authors/author-services/research-data)
- Visualize your data (http://www.elsevier.com/authors/author-services/data-visualization)
- Data in Brief co-submission (https://www.elsevier.com/authors/author-services/research-data/data-articles/DIB-co-submission)
- MethodsX co-submission (https://www.elsevier.com/authors/author-services/research-data/materials-and-methods/mex-co-submission)

Related Links

- Author Stats
- Researcher Academy
- Author Services (https://www.elsevier.com/authors/author-services)
- Try out personalized alert features

Pattern Recognition Letters aims at rapid publication of concise articles of a broad interest in **pattern recognition.**
Subject areas include all the current fields of interest represented by the Technical Committees of the International Association of Pattern Recognition, and other developing themes involving...

Read more

Most Downloaded | Recent Articles | Most Cited | Open Access Articles

Data clustering: 50 years beyond K-means
Anil K. Jain

A review of unsupervised feature learning and deep learning for time-series modeling
Martin Längkvist | Lars Karlsson | ...

An introduction to ROC analysis
Tom Fawcett

> View All Most Downloaded Articles (https://www.journals.elsevier.com:443/pattern-recognition-letters/most-downloaded-articles)

Most Downloaded Articles

Recent Articles

Most Cited Articles

Recent Open Access Articles

(/pat tern- (http s://w

Announcements (https://www.journals.elsevier.com:443/pattern-recognition-letters/announcements)

Heliyon Partner Journal

This journal has partnered with *Heliyon*, an open access journal from Elsevier publishing quality peer reviewed research across all disciplines. *Heliyon*'s team of experts provides editorial excellence, fast publication, and high visibility for your paper. Authors can quickly and easily transfer their research from a Partner Journal to *Heliyon* without the need to edit, reformat or resubmit.

>Learn more at Heliyon.com

> View All (https://www.journals.elsevier.com:443/pattern-recognition-letters/announcements)

Article Selections (https://www.journals.elsevier.com:443/pattern-recognition-letters/article-selections)

Article Selections

Article selection Big Data@Elsevier.Computer Science (https://www.journals.elsevier.com:443/pattern-recognition-letters/article-selections/virtual-special-issue-big-dataelseviercomputer-science)

> View All (https://www.journals.elsevier.com:443/pattern-recognition-letters/article-selections)

News (https://www.journals.elsevier.com:443/pattern-recognition-letters/news)

Computer Science Catalogue 2018-2019 (https://www.journals.elsevier.com:443/pattern-recognition-letters/news/computer-science-catalogue-2018-2019)

MARIA PETROU PRIZE (https://www.journals.elsevier.com:443/pattern-recognition-letters/news/maria-petrou-prize)

Executable Papers - improving the article format in computer science (https://www.journals.elsevier.com:443/pattern-recognition-letters/news/introducing-executable-papers)

> View All (https://www.journals.elsevier.com:443/pattern-recognition-letters/news)

Call for Papers (https://www.journals.elsevier.com:443/pattern-recognition-letters/call-for-papers)

Pattern Recognition and Artificial Intelligence Techniques for Cultural Heritage special issue (https://www.journals.elsevier.com:443/pattern-recognition-letters/call-for-papers/pattern-recognition-and-artificial-intelligence-techniques)

Virtual Special Issue on “Pattern Recognition and Cognitive Assistants (PRCA)” at Pattern Recognition Letters Journal (https://www.journals.elsevier.com:443/pattern-recognition-letters/call-for-papers/vsi-pattern-recognition-and-cognitive-assistants)

Special Issue on Deep Multi-source Data Analysis (DMDA) (https://www.journals.elsevier.com:443/pattern-recognition-letters/call-for-papers/special-issue-on-deep-multi-source-data-analysis-dmda)

> View All (https://www.journals.elsevier.com:443/pattern-recognition-letters/call-for-papers)

PlumX Metrics (https://www.journals.elsevier.com:443/pattern-recognition-letters/top-articles)

Below is a recent list of 2017/2018 articles that have had the most social media attention. The Plum Print next to each article shows the relative activity in each of these categories of metrics: Captures, Mentions, Social Media and Citations. Go here to learn more about PlumX Metrics.

A BA-based algorithm for parameter optimization of Support Vector Machine

Generalized mean based back-propagation of errors for ambiguity resolution

Analysis of human tissue densities: A new approach to extract features from medical images

> View All (https://www.journals.elsevier.com:443/pattern-recognition-letters/top-articles)

Special Issues (https://www.journals.elsevier.com:443/pattern-recognition-letters/special-issues)

Special issues published in Pattern Recognition Letters.

Multimodal Fusion for Pattern Recognition

Zubair Khan | Shishir Kumar | ...

Data Representation and Representation Learning for Video Analysis

William Robson Schwartz | Larry Davis

Integrating Biometrics and Forensics

Michele Nappi | Nasir Memon | ...

> View All (https://www.journals.elsevier.com:443/pattern-recognition-letters/special-issues)

Tweets by @comp_science

Tweets by @comp_science

Computer Science
@comp_science

New Editorial Team for Systems & Control Letters
bit.ly/2PHk4Fp

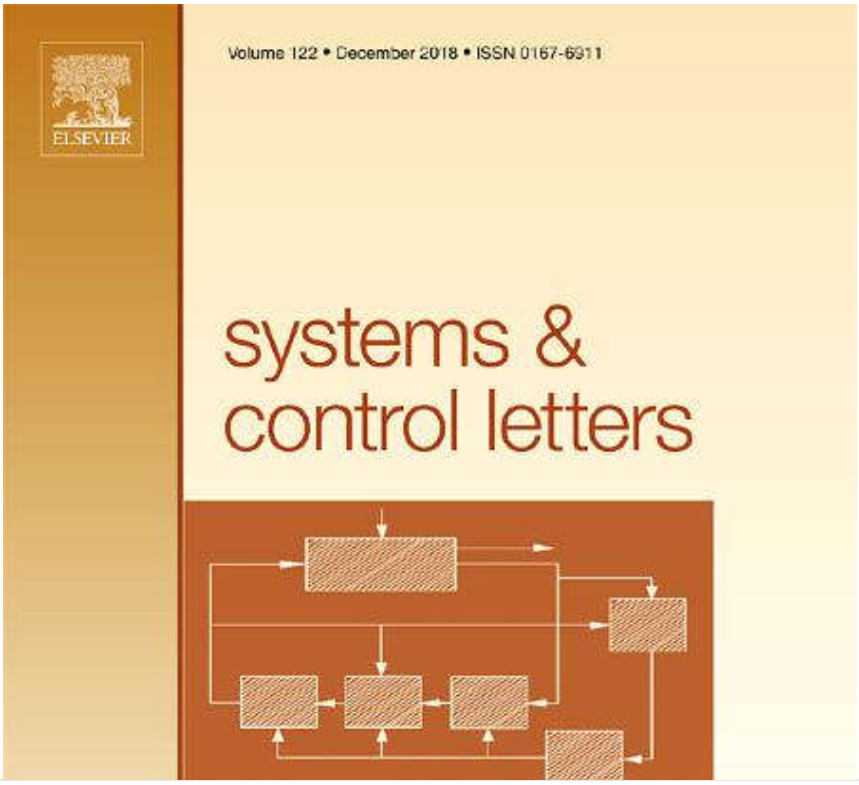

Embed View on Twitter

Pattern Recognition Letters

Readers
View Articles
Volume/ Issue Alert
Personalized Recommendations

Authors (http://www.elsevier.com/authors/home)
Author Information Pack (http://www.elsevier.com/journals/pattern-recognition-letters/0167-8655?generatepdf=true)
Submit Your Paper
Track Your Paper
Early Career Resources (http://www.elsevier.com/early-career-researchers/training-and-workshops)
Rights and Permissions (https://www.elsevier.com/about/policies/copyright/permissions)
Webshop

Support Center

Librarians (https://www.elsevier.com/librarians)
Ordering Information and Dispatch Dates (http://www.elsevier.com/journals/pattern-recognition-letters/0167-8655/order-journal)
Abstracting/ Indexing (http://www.elsevier.com/journals/pattern-recognition-letters/0167-8655/abstracting-indexing)

Editors (http://www.elsevier.com/editors/home)
Publishing Ethics Resource Kit (http://www.elsevier.com/editors/perk)
Guest Editors (http://www.elsevier.com/editors/guest-editors)
Support Center

Reviewers (http://www.elsevier.com/reviewers/home)
Reviewer Guidelines (http://www.elsevier.com/reviewersguidelines)
Log in as Reviewer
Reviewer Recognition (https://www.elsevier.com/reviewers/becoming-a-reviewer-how-and-why#recognizing)
Support Center

Advertisers Media Information (https://www.elsevier.com/advertisers)

Societies (http://www.elsevier.com/societies/home)

(https://www.elsevier.com)

(https://www.elsevier.com) (http://www.reedelsevier.com/)

(http://www.reedelsevier.com/)

(https://twitter.com/ElsevierConnect) (https://www.facebook.com/ElsevierConnect) (https://www.linkedin.com/company/reed-elsevier) (https://www.mendeley.com/groups/)

About the journal

Scientific Reports is an online, open access journal from the publishers of *Nature*. We publish scientifically valid primary research from all areas of the natural and clinical sciences. Visit this page to find out about the quality, rigour, reach and service offered by *Scientific Reports*.

The 2017 journal metrics for *Scientific Reports* are as follows:

- 2-year impact factor: 4.122
- 5-year impact factor: 4.609
- Immediacy index: 0.576
- Eigenfactor ® score: 0.71896
- Article influence score: 1.356
- 2-year median: 2

Visit the Nature Research journals metrics page for a description of these metrics.

Aims and scope

More on the aims and scope of *Scientific Reports* is available in this section, as well as indexing and archiving information.

Editorial Advisory Panel and Editorial Board

Scientific Reports' Editorial Advisory Panel and Editorial Board of researchers spans the spectrum of science, and is at the heart of what we do. Find out more, and see the Editorial Board Members in your research area in this section.

Open access

Scientific Reports is a fully open access journal. More on Creative Commons Attribution licenses and the benefits of publishing open access can be found in this section.

Article processing charges

To allow immediate global open access to all articles, *Scientific Reports* levies an article processing charge (APC). Current APCs and waiver information are available in this section.

FAQs

Answers to common questions about *Scientific Reports* can be found in this section.

Article Alerts

Sign up to article alerts and stay up-to-date with our latest content.

Scientific Reports ISSN 2045-2322 (online)

ROYAL SOCIETY OF CHEMISTRY

(/)

Journals, books & databases

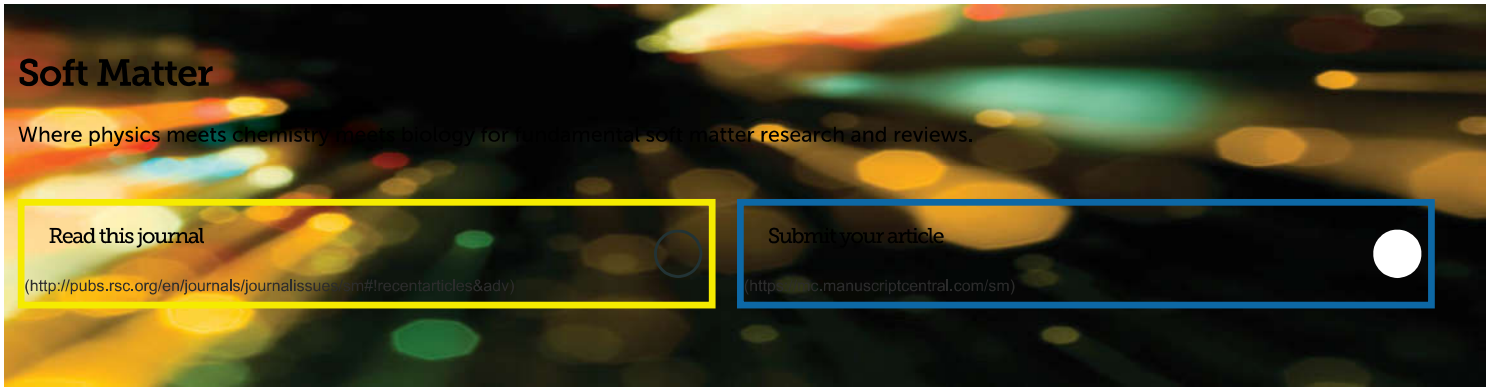

Impact factor: 3.709*
Publishing frequency: 48 issues per year
Immediacy index: 0.824
Indexed in MEDLINE
Editor-in-Chief: Darrin Pochan

Scope

Soft Matter provides a unique forum for the communication of fundamental science underpinning the behaviour of soft matter. There is a particular focus on the interface between physics, materials science, biology, chemical engineering and chemistry.

The scope of *Soft Matter* covers the following.

• Bulk soft matter assemblies, including colloids, granular matter, liquid crystals, polymers and active matter
• Soft nanotechnology and self-assembly
• Biological aspects of soft matter
• Surfaces, interfaces, and interactions
• Theory, modelling, and simulation

Volume 11 | Number 19 | 21 May 2015 | Pages 3737–3948

Soft Matter

www.softmatter.org

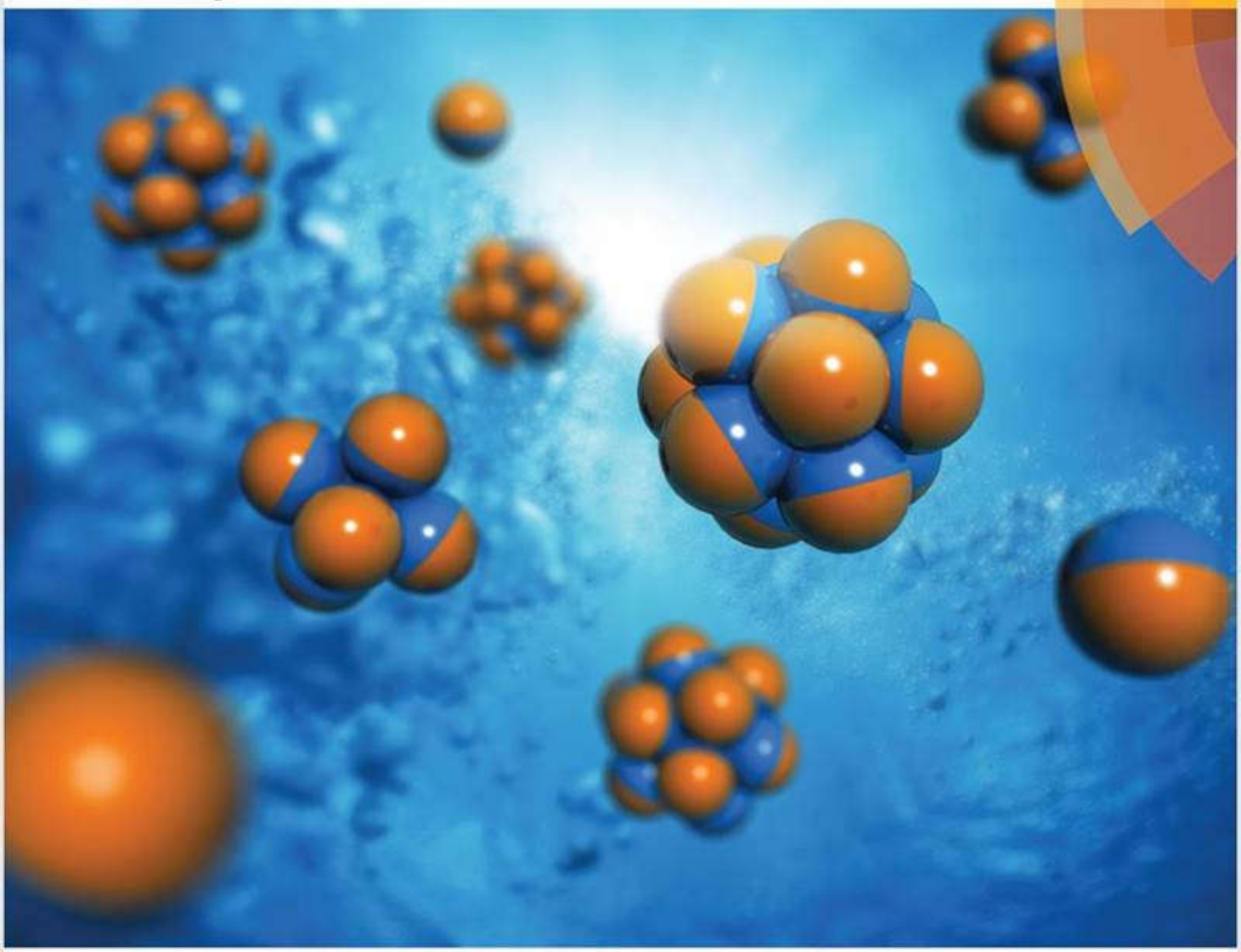

ISSN 1744-683X

ROYAL SOCIETY OF CHEMISTRY

COMMUNICATION
Arash Nikoubashman *et al.*
Self-assembly of Janus particles under shear

Editorial board Advisory board Editorial office Lectureship

Editor-in-Chief

Darrin Pochan (/journals-books-databases/about-journals/soft-matter/editorial-board-members/), University of Delaware, USA

Associate editors

Tommy Angelini (/journals-books-databases/about-journals/soft-matter/editorial-board-members/#sm_angelini), University of Florida, USA

Alfred Crosby (/journals-books-databases/about-journals/soft-matter/editorial-board-members/#sm_crosby), University of Massachusetts Amherst, USA

Jan Dhont (/journals-books-databases/about-journals/soft-matter/editorial-board-members/#sm_dhont), Forschungszentrum Jülich, Germany

Jianbin Huang (/journals-books-databases/about-journals/soft-matter/editorial-board-members/#sm_huang), Peking University, China

Paul Janmey (/journals-books-databases/about-journals/soft-matter/editorial-board-members/#sm_janmey), University of Pennsylvania, USA

Sanat Kumar (/journals-books-databases/about-journals/soft-matter/editorial-board-members/#sm_kumar), Columbia University, USA

Oleg Lavrentovich (/journals-books-databases/about-journals/soft-matter/editorial-board-members/#sm_lavrentovich), Kent State University, USA

Christos Likos (/journals-books-databases/about-journals/soft-matter/editorial-board-members/#sm_likos), University of Vienna, Austria

Kathleen Stebe (/journals-books-databases/about-journals/soft-matter/editorial-board-members/#sm_stebe), University of Pennsylvania, USA

Dimitris Vlassopoulos (/journals-books-databases/about-journals/soft-matter/editorial-board-members/), FORTH-IESL, Greece

Editorial Board Members

Gijsje Koenderink (/journals-books-databases/about-journals/soft-matter/editorial-board-members/#sm_koenderink), AMOLF, Netherlands

Emanuela Zaccarelli (/journals-books-databases/about-journals/soft-matter/editorial-board-members/#sm_zaccarelli), Sapienza University of Rome, Italy

Xuehua Zhang (/journals-books-databases/about-journals/soft-matter/editorial-board-members/#sm_zhang),University of Alberta, Canada

Article types

Soft Matter publishes:

- Communications
- Full papers
- Reviews
- Tutorial reviews
- Perspectives

See more information about these article types +

Article templates

To help authors publish their research with us we host our Soft Matter LaTeX template (https://www.overleaf.com/latex/templates/royal-society-of-chemistry-template-for-preparing-your-submission-to-soft-matter-using-overleaf/pctnxvqjxfzb#.WdJXeeRTF9A) in the Overleaf authoring tool. Overleaf simplifies LaTeX authorship by enabling collaborators to easily prepare and edit their manuscripts with realtime format previewing, simple document sharing and collaboration, and user support and LaTeX help.

With one-click, the PDF of your manuscript and a ZIP file of the LaTeX source files are sent directly to the Soft Matter submission system without the need to download and re-upload files, making the process quicker and easier.

A free introductory course (https://www.overleaf.com/latex/learn/free-online-introduction-to-latex-part-1) is available to authors who are new to LaTeX and Overleaf. Our Microsoft Word templates are located in our author guidelines. (/journals-books-databases/journal-authors-reviewers/author-tools-services/)

Journal guidelines

For guidance on preparing your article please visit our Prepare your article (/journals-books-databases/journal-authors-reviewers/prepare-your-article/) page, the content of which is relevant to all of our journals. Note that some journals have additional specific guidelines.

Readership information

Soft Matter has a global circulation and interdisciplinary audience.

- Physicists
- Biophysicists
- Bioengineers
- Biological scientists
- Biochemists
- Chemical engineers
- Materials scientists
- Surface scientists
- Physical, organic and theoretical chemists

Subscription information

Soft Matter is part of collections RSC Gold and Materials Science

Online only 2018: ISSN 1744-6848, £1,468 / $2,586

*2017 Journal Citation Reports ® (Clarivate Analytics, June 2018)

Soft Matter

Pre-submission queries please contact Neil Hammond, Executive Editor
Email:Send us an email

Post-submission queries please contact Lucy Argyle, Editorial Production Manager
Email:Send us an email

Share

Recently viewed

ChemComm (/journals-books-databases/about-journals/chemcomm/)

Not a member?

Apply for membership (/membership-and-community/join/)

books-databases/) (/membership-and- contacts/)

community/)

Focus and Coverage

The Journal of Chemical Physics publishes quantitative and rigorous science of long-lasting value in methods and applications of chemical physics. The Journal also publishes brief Communications of significant new findings, Perspectives on the latest advances in the field, and Special Topic issues. The Journal focuses on innovative research in experimental and theoretical areas of chemical physics, including spectroscopy, dynamics, kinetics, statistical mechanics, and quantum mechanics. In addition, topical areas such as polymers, soft matter, materials, surfaces/interfaces, and systems of biological relevance are of increasing importance.

Topical coverage includes:

- Theoretical Methods and Algorithms
- Advanced Experimental Techniques
- Atoms, Molecules, and Clusters
- Liquids, Glasses, and Crystals
- Surfaces, Interfaces, and Materials
- Polymers and Soft Matter
- Biological Molecules and Networks

For examples of the scope and type of articles published in JCP, please see the 2017 JCP Editors' Choice Collection.

2017 Journal Citation Reports® (Clarivate Analytics, 2018)*:

Five-Year Impact Factor	2.743
Impact Factor	2.843
Immediacy Index	0.786
Cited Half-Life	>10.0
EigenFactor Score	0.14777
Article Influence Score	0.849

* Data from the *2017 Journal Citation Reports® Science Edition* (Clarivate Analytics, 2018).

ISSN

The international standard serial number (ISSN) for *Journal of Chemical Physics* is 0021-9606 for the printed edition and the electronic ISSN (E-ISSN) is 1089-7690 for the online edition.

The CODEN is **JCPSA6**.

Resources

AUTHOR

LIBRARIAN

ADVERTISER

General Information

ABOUT

CONTACT

HELP

PRIVACY POLICY

TERMS OF USE

FOLLOW AIP PUBLISHING:

Grain Boundary Formation and Motion in Colloidal Crystals

Yuguang Yang, Tara D. Edwards, Daniel J. Beltran-Villegas, Michael A. Bevan
Department of Chemical and Biomolecular Engineering, Johns Hopkins University, Baltimore, Maryland 21218

I. Motivation & background

Kinetic problem: evolution of the structure & kinetic traps

Dynamic models

Self-Propelled Colloids Navigating Mazes & Organizing into Machines

Michael A. Bevan and Yuguang Yang
Department of Chemical and Biomolecular Engineering, Johns Hopkins University, Baltimore, Maryland 21218

abstract

Controlling navigation of self-propelled microscopic 'robots' subject to random Brownian motion in complex microstructured environments (e.g., porous media, tumor vasculature) is important to many emerging applications (e.g., enhanced oil recovery, drug delivery). In this work, we design an optimal feedback policy to navigate an active self-propelled colloidal rod in complex mazes with various obstacle types. Actuation of the rods is modeled based on a light-controlled osmotic flow mechanism, which produces different propulsion velocities along the rod's long axis. Actuator-parameterized Langevin equations, with soft rod-obstacle repulsive interactions, are developed to describe the system dynamics. A Markov decision process (MDP) framework is used for optimal policy calculations with design goals of colloidal rods reaching target end points in minimum time. Simulations show that optimal MDP-based policies are able to control rod trajectories to reach target regions order-of-magnitudes faster than uncontrolled rods, which diverges as maze complexity increases. An efficient multi-graph based implementation for MDP is also presented, which scales linearly with the maze dimension.
After understanding optimal control of single self-propelled colloids, we extend our approaches to ensembles of self-propelled particles to actuate motion of movable objects, such as cargo or other device parts (as opposed to static maze obstacles). In this case, we develop a multi-agent coordinated optimal control algorithm for application to systems of many self-propelled particles. We show that such algorithm can drive particles to form arbitrary geometrical shapes, including topologically complex structures, and perform effectively rigid collective motions, including translation and rotation. For demonstration purposes, we show particle swarms transporting inert cargo particles as well as the assembly and controlled spin of a gear, as a basic element in a micro mechanical machine.

background & motivation

control of self propelled particles in nano, bio, & energy applications

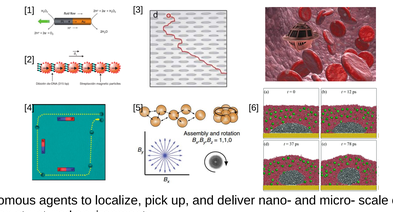

- Autonomous agents to localize, pick up, and deliver nano- and micro- scale objects in complex structured environments
- Functional nano- and micro- machines from cooperative motion of particle ensembles

problem statement

equation of motion & transition probability for 3 propulsion rates

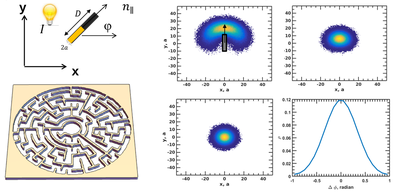

$$\mathbf{r}(t+\Delta t) = \mathbf{r}(t) + \frac{\mathbf{D}_t}{kT}\cdot\mathbf{F}\Delta t + \Delta\mathbf{r}^B + v(l)\cos(\varphi)\mathbf{e}_1 + v(l)\sin(\varphi)\mathbf{e}_2$$

$$\varphi(t+\Delta t) = \varphi(t) + \frac{D_r}{kT}\mathbf{T}\cdot\mathbf{e}_3\Delta t + \Delta\varphi^B$$

$$\langle\Delta\mathbf{r}^B\rangle = 0, \langle\Delta\mathbf{r}^B(\Delta\mathbf{r}^B)^\gamma\rangle = 2\mathbf{D}_t\Delta t$$

$$\langle\Delta\varphi^B\rangle = 0, \langle\Delta\varphi^B\Delta\varphi^B\rangle = 2D_r\Delta t$$

- D=10a
- $v = 0$ pure diffusion
- $v = 1.5um/s$, slow
- $v = 5\ um/s$, fast

single particle control theory

Markov decision process & dynamic programming

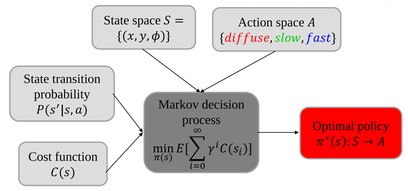

[7] Optimization formulation to minimize expected trajectory cost considering known state transition probability

$$J^*(s_0) = \min \mathbb{E}\{\sum_{n=0}^{\infty} \gamma^n C(s_n, \pi(s_n))\}, C(s_n) = \begin{cases} 0, \text{if } s_n = s^{target} \\ 1, \text{otherwise} \end{cases}$$

$$P(s_n) = P(s_n \mid s_{n-1}, a) P(s_{n-1})$$

Solve coupled equations to generate optimal policy via iteration over J* (dynamic programming)

$$J^*(s) = \min_{\pi(s)}\{\gamma \sum_{s'} P(s' \mid s, \pi(s)) J^*(s') + C(s)\}$$

$$\pi^*(s) = \arg\min_{\pi(s)}\{\gamma \sum_{s'} P(s' \mid s, \pi(s)) J^*(s') + C(s)\}$$

single particle → single target

particle navigation in free space

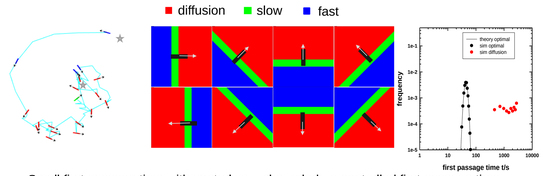

- Small first passage time with control vs. unbounded un-controlled first passage time
- Optimal control policy can maintain particle around target
- Estimate first passage time distribution via $\rho(n\Delta t) \approx \sum_{s_n \in s^{target}} P(s_n \mid s_0) - \sum_{s_{n-1} \in s^{target}} P(s_{n-1} \mid s_0)$

single particle → single target with single obstacle

single particle to single target in simple maze

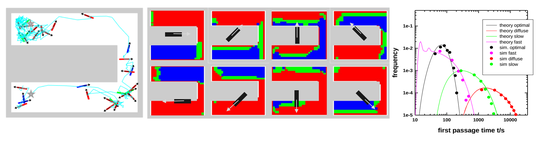

- Optimally controlled particles reach target orders of magnitude faster than diffusion
- Fast propulsion without control has similar arrival time compared to optimal control
- First passage time distribution in agreement from theory and simulation

single particle → single target with multiple obstacles

single particle to single target in increasingly complex mazes

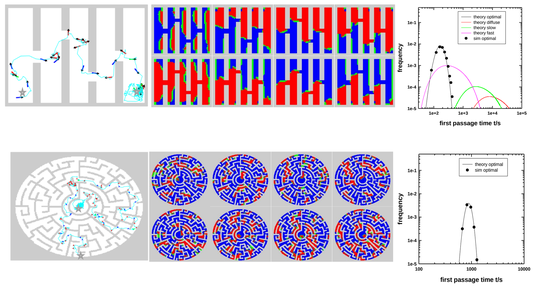

- Optimal policy shows similar actuation for similar local geometry in different scale mazes
- Optimal navigation is orders-of-magnitude faster compared to all uncontrolled cases
- First passage time distribution via simulation for large mazes are computationally prohibitive.

first passage time scaling

first passage time vs. complexity-invariant maze size

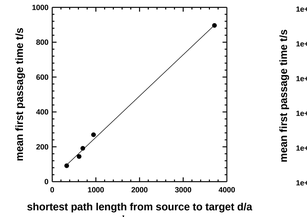

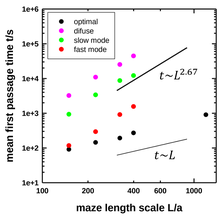

$$\langle t \rangle = \frac{d}{p v_{max}} \sim d \sim L$$

d: contour length of shortest trajectory
p: probability to take fast propulsion v_{max}
A_{free}: available area within maze

[8] $\langle t \rangle \sim A_{free} \times \Delta r^{\beta} \sim L^{d_f} L^{\beta} \sim L^{\gamma}$

[9] $D_{eff} \sim D_t + \frac{v^2}{4D_r}$

Δr: Euclidean distance between source and target

- Mean first passage time in optimal navigation linearly increases with maze size
- Mean first passage time in uncontrolled navigation scale as maze size to power 2.67

multi-particle control

iteration between optimal assignment and optimal planning

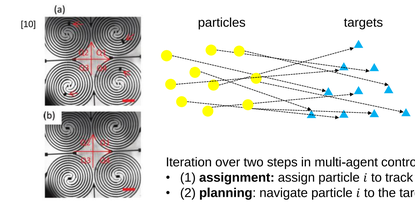

Iteration over two steps in multi-agent control:
- (1) **assignment:** assign particle i to track target $g(i)$
- (2) **planning**: navigate particle i to the target $g(i)$

[11] Assignment:

$$\min_g \sum_{i=0}^{N} J^*(s_i, s_{g(i)}^{target}), g: \{1,2,...N\} \to \{1,2,...N\}$$

g: 1-1 assignment function

Planning:

$$J^*(s_i, s_{g(i)}^{target}) = \min_{\pi_i} \mathbb{E}\{\sum_{i=0}^{\infty} \gamma^n C(s_i, s_{g(i)}^{target})\},$$

$$C(s_i, s_{g(i)}^{target}) = \begin{cases} 0, \text{if } s_i = s_{g(i)}^{target} \\ 1, \text{otherwise} \end{cases}$$

$$P(s_i^n) = P(s_i^n \mid s_i^{n-1}, a) P(s_i^{n-1})$$

multiple particles → multiple targets

microstructure & morphology control via active assembly

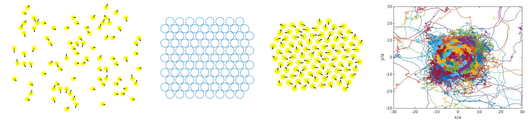

applications in cargo delivery & functional machines

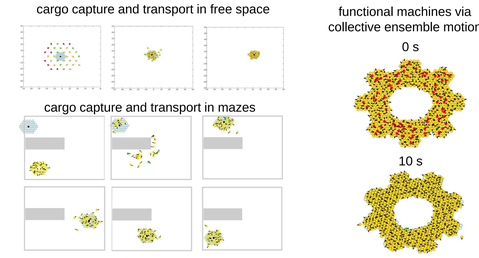

- Cargo capture: particles assemble around inert cargo and capture it
- Cargo transport: assembled particles collectively move captured cargo

conclusions

- Optimally navigating colloidal objects through complex environments can achieve orders-of-magnitude improvement in arrival time target
- Extension to multi-particle control to achieve active assembly, cargo capture, cargo transport, and dynamic functional machines.

Literature cited

1. Wang, Y., et al. (2006). "Bipolar Electrochemical Mechanism for the Propulsion of Catalytic Nanomotors in Hydrogen Peroxide Solutions†." Langmuir 22(25): 10451-10456.
2. Dreyfus, R., et al. (2005). "Microscopic artificial swimmers." Nature 437(7060): 862-865.
3. Volpe, G., et al. (2011). "Microswimmers in patterned environments." Soft Matter 7(19): 8810.
4. Baraban, L., et al. (2012). "Catalytic Janus Motors on Microfluidic Chip: Deterministic Motion for Targeted Cargo Delivery." ACS Nano 6(4): 3383-3389.
5. Tasci, T. O., et al. (2016). "Surface-enabled propulsion and control of colloidal microwheels." Nat Commun 7: 10225.
6. Wang, F.-C. and H.-A. Wu (2013). "Enhanced oil droplet detachment from solid surfaces in charged nanoparticle suspensions." Soft Matter 9(33): 7974-7980.
7. Bellman, R.E. 1957. Dynamic Programming. Princeton University Press, Princeton, NJ. Republished 2003: Dover
8. Howse, J. R., et al. (2007). "Self-motile colloidal particles: From directed propulsion to random walk." Physical Review Letters 99(4)
9. Condamin, S., et al. (2007). "First-passage times in complex scale-invariant media." Nature 450(7166): 77-80.
10. Lu, J. P. et al (2014). Open and closed loop manipulation of charged microchiplets in an electric field. Applied Physics Letters, 105(5), 054104.
11. Shoham, Y. and K. Leyton-Brown (2008). Multiagent Systems: Algorithmic, Game-Theoretic, and Logical Foundations, Cambridge University Press.

Acknowledgments

We acknowledge financial support by the National Science Foundation through Cyber Enabled Discovery and Innovation grants and DARPA Atoms to Products program.

For additional information

E-mail:
Michael A. Bevan mabevan@jhu.edu
Yuguang Yang yyang@jhu.edu

Bevan group web page:
http://www.jhu.edu/bevan

Literature cited

1. W. Lee, A. Chan, M.A. Bevan, J.A. Lewis, P.V. Braun, Nanoparticle-mediated epitaxial assembly of colloidal crystals on patterned substrates. *Langmuir* **2004**, 20 (13), 5262-5270.
2. L.B. Jerrim, O.D. Velev, Deposition of coatings from live yeast cells and large particles by "convective-sedimentation" assembly. *Langmuir* **2009**, 25, 5692-5702.
3. Yethiraj A. Tunable colloids: control of colloidal phase transitions with tunable interactions. *Soft Matter*. 2007;3(9):1099. doi:10.1039/b704251p.
4. J.J. Juarez, J.Q. Cui, B.G. Liu, M.A. Bevan, *kT*-scale colloidal interactions in high frequency inhomogeneous AC electric fields I. Single particles. *Langmuir* **2011**, 27 (15), 9211-9218.
5. J.J. Juarez, M.A. Bevan, Interactions and microstructures in electric field mediated colloidal assembly. *Journal of Chemical Physics* **2009**, 131 (13).
6. J.J. Juarez, J.Q. Cui, B.G. Liu, M.A. Bevan, *kT*-scale colloidal interactions in high frequency inhomogeneous AC electric fields II. Concentrated ensembles. *Langmuir* **2011**, 27 (15), 9219-9226.
7. J.J. Juarez, S.E. Feicht, M.A. Bevan, Electric field mediated assembly of three dimensional equilibrium colloidal crystals. *Soft Matter* **2012**, 8 (1), 94-103.
8. J.J. Juarez, M.A. Bevan, Feedback controlled colloidal self-assembly. *Advanced Functional Materials* **2012**, 22 (18), 3833-3839.
9. J.J. Juarez, P.P. Mathai, J.A. Liddle, M.A. Bevan, Multiple electrokinetic actuators for feedback control of colloidal crystal size. *Lab on a Chip* **2012**, 12 (20), 4063-4070.
10. T.D. Edwards, D.J. Beltran-Villegas, M.A. Bevan, Size dependent thermodynamics and kinetics in electric field mediated colloidal assembly. *Soft Matter* **2013**, 9, 9208-9218.
11. D.J. Beltran-Villegas, R.M. Sehgal, D. Maroudas, D.M. Ford, M.A. Bevan, Smoluchowski model of crystallization dynamics of small colloidal clusters. *Journal of Chemical Physics* **2011**, 135 (15), 154506.
12. D.J. Beltran-Villegas, M.A. Bevan, Free energy landscapes for colloidal crystal assembly. *Soft Matter* **2011**, 7, 3280-3285.

Acknowledgments

We acknowledge financial support by the National Science Foundation through Cyber Enabled Discovery and Innovation grants (CMMI-0835549, CMMI-1124648) and unsolicited grants (CBET-0932973, CBET-1234981).

We thank our CDI collaborators: Ford & Thyagarajan (UMass) for contributing work on dimensionality reduction, as well as Grover & Tang (GaTech) for contributing work on optimal control.

For additional information

E-mail:
Yuguang Yang yyang60@jhu.edu
Tara D. Edwards tiracki1@jhu.edu
Daniel J. Beltran-Villegas daniel.jose.beltran@gmail.com
Michael A. Bevan mabevan@jhu.edu

Bevan group web page:
http://www.jhu.edu/bevan

State transition probability at different speed

- state distribution $P(s'|s,a)$ after 1s
- Initial state $s_0 = (x, y, \phi) = (0,0,0)$
- Constructed from BD simulations

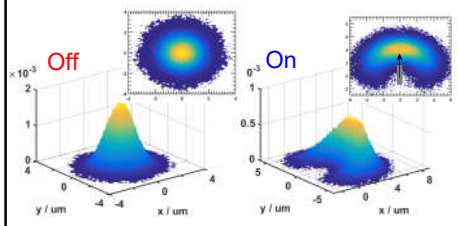

$P(x, y|s_0, a)$

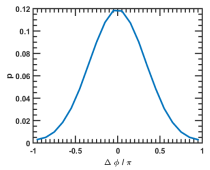

$P(\phi|s_0, a)$

Markov decision framework for optimal policy

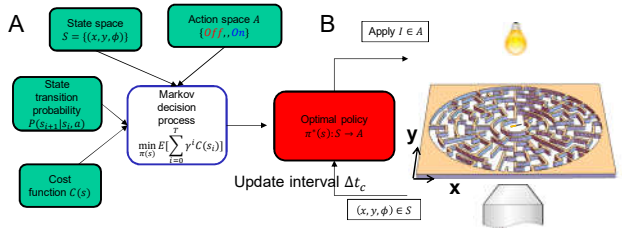

[7] Optimal cost-to-go $J^*(s) = \min_{\{\pi(s)\}} J(s) = \mathbf{E} \sum_{t=0..T} \gamma^t C(s, \pi(a))$

Optimal policy: $\pi^*(s) = \underset{\{\pi(s)\}}{argmin}\, J(s), \quad C(s,a) = \begin{cases} 0, \text{if } s = s^{target} \\ 1, \text{otherwise} \end{cases}$

[7]Bellman, R.E. 1957. Dynamic Programming Dover

Optimal navigation in free space

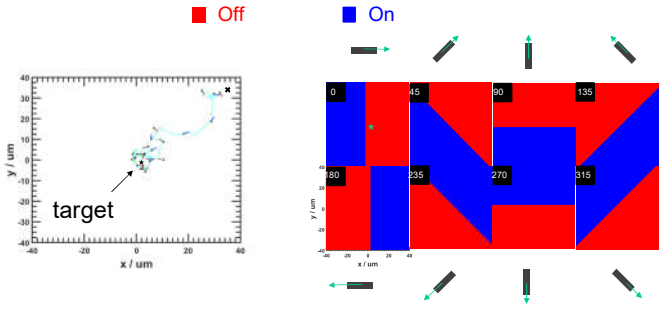

- An optimal policy indicates which action to take when at state (x, y, ϕ)
- **Maxwell demon-like** control policy: turn On when position&direction are "correct"

Optimal navigation in free space

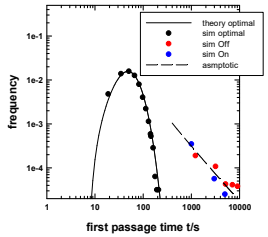

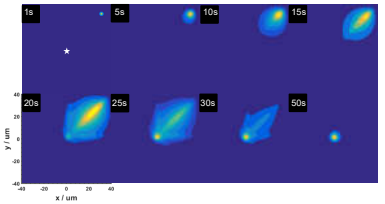

[8]

- Asymptotic first passage distribution $\sim \frac{1}{t\,(\ln t)^2}$ for uncontrolled (random walking)rod, with unbounded infinite mean.

$$P(s_n) = P(s_n \mid s_{n-1}, \pi^*(s_n))P(s_{n-1})$$
$$P(s_0) = \delta(s_0 - s_{init})$$

- Theoretically estimate first passage time distribution via

$$\rho(n\Delta t) \approx \sum_{s_n \in S^{target}} P(s_n \mid s_0) - \sum_{s_{n-1} \in S^{target}} P(s_{n-1} \mid s_0)$$

[8] Redner, S. (2007). A Guide to First-Passage Processes, Cambridge University Press

Optimal navigation in simple maze

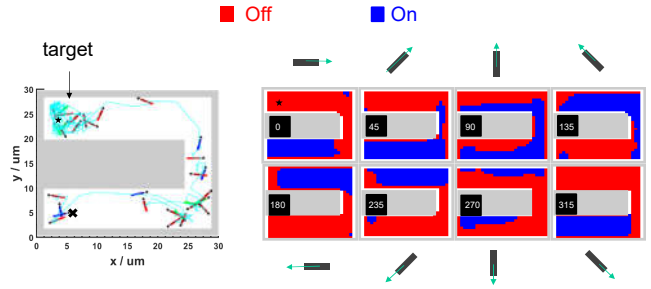

- Locally Maxwell demon-like control policy
- Globally following “shortest” geometric path

slide 9

Optimal control in simple maze

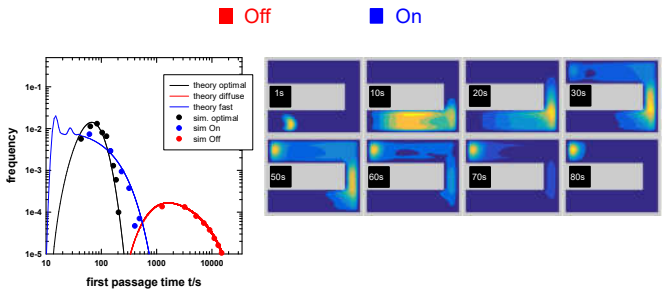

- Optimally controlled particles reach target **~100X faster** than diffusion
- Constant **On** mode has **similar arrival time** compared to optimal control in **simple geometry**

slide 10

Optimal control in complex maze I

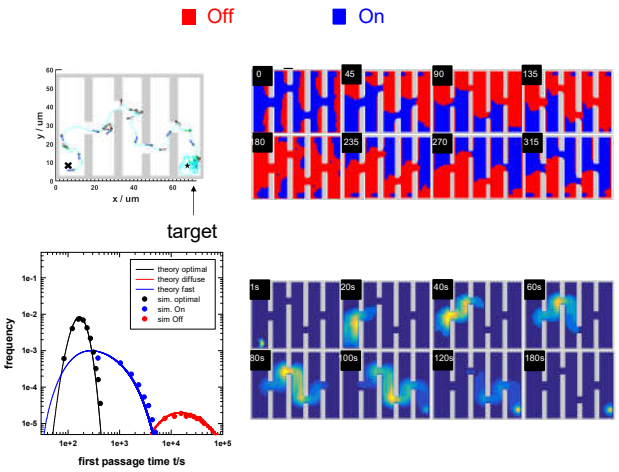

slide 11

Optimal control in complex maze II

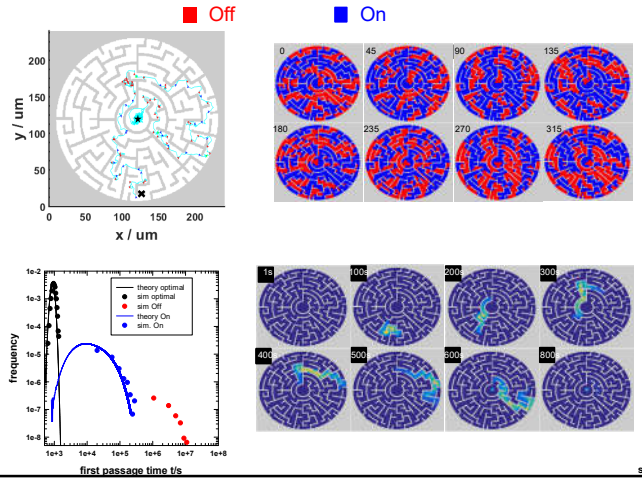

slide 12

Scaling analysis of navigation performance

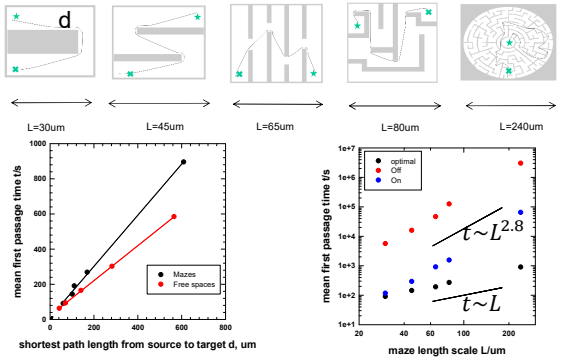

$\langle t \rangle_{optimal} \sim d \sim L$

[8] $\langle t \rangle_{noncontrol} \sim L^{\gamma}$

d: contour length of shortest trajectory

[8] Condamin, S., et al. (2007). Nature 450(7166): 77-80.

slide 13

Generalization on navigation performance

How does control update time, Δt_c, and speed, v, affect performance?

Non-dimensionalization:
- Characterized time scale $t^* = 1/D_r$
- $\lambda = \Delta t_c / t^*$, $Pe = vt^* / \sqrt{D_t t^*}$

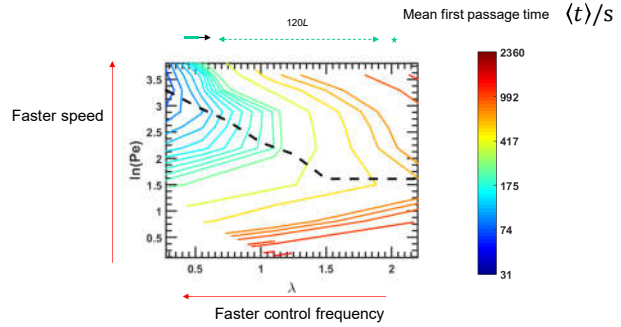

- Navigation performance can be tuned by Pe, λ

slide 14

Generalization on navigation performance

How does control update time, Δt_c, and speed, v, affect performance?

Non-dimensionalization:
- Characterized time scale $t^* = 1/D_r$
- $\lambda = \Delta t_c / t^*$, $Pe = vt^* / \sqrt{D_t t^*}$

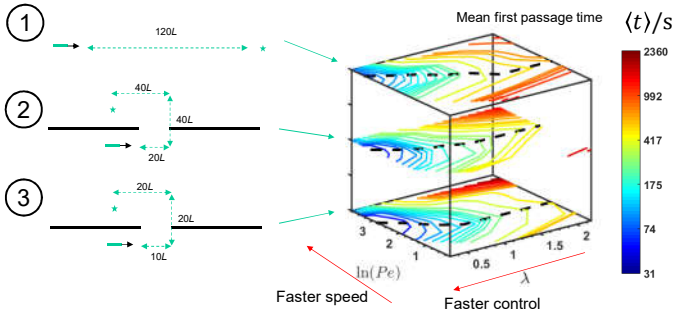

- Navigation performance can be tuned by Pe, λ at different tasks.

slide 15

Conclusions & ongoing work

Conclusion

- Investigate **the principle of optimal navigations** in free space and mazes
- Optimally navigating can achieve **orders-of-magnitude** improvement in arrival time
- Performance will **scale well** as the size of mazes increases
- Control algorithm can **generalize** to different settings

Ongoing

-Multi-agent control for active assembly

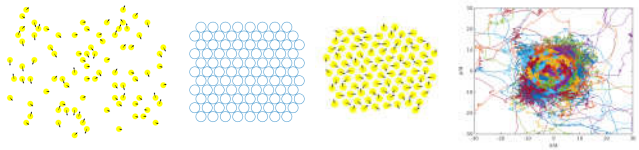

initial state | target state | assembled state | assembly trajectories

slide 16

Ongoing work

What is the principle for multi-agent control?

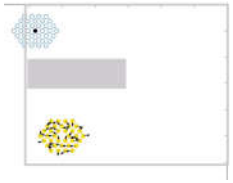

cargo capture and transport in mazes

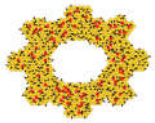

functional machines (gear) via collective coordinated motion

References

Literature cited

1. Wang, Y., et al. (2006). "Bipolar Electrochemical Mechanism for the Propulsion of Catalytic Nanomotors in Hydrogen Peroxide Solutions†." Langmuir 22(25): 10451-10456.
2. Dreyfus, R., et al. (2005). "Microscopic artificial swimmers." Nature 437(7060): 862-865.
3. Volpe, G., et al. (2011). "Microswimmers in patterned environments." Soft Matter 7(19): 8810.
4. Baraban, L., et al. (2012). "Catalytic Janus Motors on Microfluidic Chip: Deterministic Motion for Targeted Cargo Delivery." ACS Nano 6(4): 3383-3389.
5. Tasci, T. O., et al. (2016). "Surface-enabled propulsion and control of colloidal microwheels." Nat Commun 7: 10225.
6. Wang, F.-C. and H.-A. Wu (2013). "Enhanced oil droplet detachment from solid surfaces in charged nanoparticle suspensions." Soft Matter 9(33): 7974-7980.
7. Bellman, R.E. 1957. Dynamic Programming. Princeton University Press, Princeton, NJ. Republished 2003: Dover
8. Redner, S. (2007). A Guide to First-Passage Processes, Cambridge University Press.
9. Howse, J. R., et al. (2007). "Self-motile colloidal particles: From directed propulsion to random walk." Physical Review Letters 99(4)
10. Condamin, S., et al. (2007). "First-passage times in complex scale-invariant media." Nature 450(7166): 77-80.

Finite system and continuous system

Proof of concept

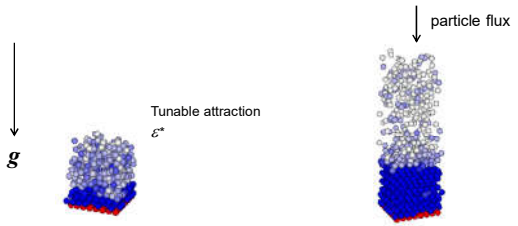

Controlled crystallization via
--sedimentation
--tunable attraction

Controlled growth in
continuous system

slide 21 of 17

Yuguang Yang

Johns Hopkins University

stochastic modeling
optimal control
chemical physics

	All	Since 2013
Citations	149	145
h-index	6	6
i10-index	5	5

TITLE	CITED BY	YEAR
Modulating the structure and properties of poly (sodium 4-styrenesulfonate)/poly (diallyldimethylammonium chloride) multilayers with concentrated salt solutions L Han, Z Mao, H Wuliyasu, J Wu, X Gong, Y Yang, C Gao Langmuir 28 (1), 193-199	45	2011
Colloidal crystal grain boundary formation and motion TD Edwards, Y Yang, DJ Beltran-Villegas, MA Bevan Scientific reports 4, 6132	27	2014
Optimal feedback controlled assembly of perfect crystals X Tang, B Rupp, Y Yang, TD Edwards, MA Grover, MA Bevan ACS nano 10 (7), 6791-6798	21	2016
Controlling assembly of colloidal particles into structured objects: Basic strategy and a case study MA Bevan, DM Ford, MA Grover, B Shapiro, D Maroudas, Y Yang, ... Journal of Process Control 27, 64-75	19	2015
Reconfigurable multi-scale colloidal assembly on excluded volume patterns TD Edwards, Y Yang, WN Everett, MA Bevan Scientific reports 5, 13612	11	2015
Chemical antagonism between photodynamic agents and chemotherapeutics: mechanism and avoidance Q Meng, J Meng, W Ran, J Su, Y Yang, P Zhang, Y Li Chemical Communications 53 (92), 12438-12441	7	2017
Dynamic colloidal assembly pathways via low dimensional models Y Yang, R Thyagarajan, DM Ford, MA Bevan The Journal of chemical physics 144 (20), 204904	5	2016
Modeling depletion mediated colloidal assembly on topographical patterns Y Yang, TD Edwards, MA Bevan Journal of colloid and interface science 449, 270-278	4	2015
Interfacial and Confined Colloidal Rod Diffusion JL Bitter, Y Yang, G Duncan, H Fairbrother, MA Bevan Langmuir 33 (36), 9034-9042	2	2017
Interfacial colloidal rod dynamics: Coefficients, simulations, and analysis Y Yang, MA Bevan The Journal of chemical physics 147 (5), 054902	2	2017
An M-estimator for reduced-rank system identification S Chen, K Liu, Y Yang, Y Xu, S Lee, M Lindquist, BS Caffo, JT Vogelstein Pattern recognition letters 86, 76-81	2	2017

TITLE	CITED BY	YEAR
Grain boundary control in colloidal self-assembly with dynamic programming X Tang, Y Yang, MA Bevan, MA Grover 2014 American Control Conference, Portland, OR, 1120-1125	2	2014
Energy landscapes for ellipsoids in non-uniform AC electric fields I Torres-Díaz, B Rupp, Y Yang, MA Bevan Soft matter 14 (6), 934-944	1	2018
An m-estimator for reduced-rank high-dimensional linear dynamical system identification S Chen, K Liu, Y Yang, Y Xu, S Lee, M Lindquist, BS Caffo, JT Vogelstein arXiv preprint arXiv:1509.03927	1	2015
Optimal Navigation of Self-Propelled Colloids Y Yang, MA Bevan ACS nano 12 (11), 10712-10724		2018
Stochastic Modeling and Optimal Control for Colloidal Organization, Navigation, and Machines Y Yang Johns Hopkins University		2017
Hierarchical assembly of anisotropic particles in AC electric fields I Torres Diaz, B Rupp, X Hua, Y Yang, MA Bevan APS Meeting Abstracts		2016
Optimal Navigation of Self-Propelled Colloids in Microstructured Mazes Y Yang, M Bevan APS Meeting Abstracts		2016

Gmail Yuguang Yang <yangyutu123@gmail.com>

simulation method question

2 messages

Li Bo <libome@mail.tsinghua.edu.cn> Wed, Sep 19, 2018 at 9:01 PM
To: yangyutu123 <yangyutu123@gmail.com>

Dear Dr. Yuguang Yang,

I am Bo Li, an associate professor of School of Aerospace Engineering at Tsinghua University, China. Recently my group is developing a numerical simulation method for L shape microparticles system. It has come to my attention that you have published several papers in simulating different microparticle systems. Any chances you can take a look at our draft manuscript, particularly, the equation of motion and particle interactions? Could you help us check if they are correctly formulated?

Thank you for your time.

Best,

Bo Li

Associate Professor, Ph.D.
Institute of Biomechanics and Medical Engineering
Department of Engineering Mechanics
Tsinghua University
Beijing 100084, China

LiuYan-Collective_dynamics_of_active_rods_V2.docx
5360K

Yuguang YANG <yangyutu123@gmail.com> Sat, Sep 22, 2018 at 9:26 AM
To: Bo Li <libome@mail.tsinghua.edu.cn>

Hi Dear Professor Li,

I added some comments along with the equation of motion and simulation method. They are overall accurate, but more details are needed.
Let me know if you have other questions.

Best
Yuguang Yang

[Quoted text hidden]

Collective dynamics of active rods with chiral symmetry_LiuYan.docx
5364K

2010

Mathematical Contest In Modeling

Certificate of Achievement

Be It Known That The Team Of

Cong Zhao
Yuguang Yang
Zuogong Yue

With Faculty Advisor

Xinxin Xu

Of

Zhejiang University

Was Designated As

Outstanding Winner

Frank R. Giordano, Contest Director

Administered by The Consortium for Mathematics and Its Applications

Marvin Keener, Head Judge

Major funding provided by the National Security Agency

Mathematical Contest in Modeling background [1]

Mathematical Contest in Modeling (MCM) is a multi-day, international contest, specifically for mathematical modeling held annually in USA, since 1985 by COMAP (Consortium of Mathematics and its Applications) and sponsored by SIAM (Society for Industrial and Applied Mathematics), the NSA (National Security Agency), and INFORMS (Institute for Operations Research and the Management Sciences). MCM challenges teams of students to clarify, analyze, and propose solutions to open-ended problems. The contest attracts diverse students and faculty advisors from over 900 institutions around the world.

At the beginning of the contest, teams have a choice between two problems (Prior to 2016). Problem A involves a system that requires the use of continuous mathematics, and thus often involves concepts from geometry, physics, or engineering. Problem B involves a system that requires the use of discrete mathematics. Every year, thousands of international teams of three undergraduates compete to produce original mathematical papers in response to one of two modeling problems.

School of winning teams	Winning count from 2005-2015	Country
Harvard University	6	US
Tsinghua University	5	China
Rensselaer Polytechnic Institute	4	US
University of Colorado	4	US
University of Colorado Boulder	4	US
Duke University	3	US
Harvey Mudd College	3	US
Zhejiang University	3	China
Massachusetts Institute of Technology	3	US
Duke University	3	US
Bethel University	3	US

[1] https://en.wikipedia.org/wiki/Mathematical_Contest_in_Modeling

http://www.comap.com/undergraduate/contests/mcm/previous-contests.php

Gmail Yuguang Yang <yangyutu123@gmail.com>

Reviewer Invitation New Submission (Default)

1 message

Xuehai Yan (Colloids and Surfaces A: Physicochemical and Engineering Aspects) <EviseSupport@elsevier.com>
Reply-To: yanxh@ipe.ac.cn
To: yyang60@jhu.edu
Thu, Sep 13, 2018 at 8:43 AM

Ref: COLSUA_2018_163
Title: Filling gaps in the knowledge of melittin on lipid membranes
Journal: Colloids and Surfaces A: Physicochemical and Engineering Aspects
Corresponding Author: M. Florencia Martini
Co-authors: M. Jose Elías Tissera, anibal disalvo, Andrea C Cutró

Dear Dr. YANG,

I would like to invite you to review the above-referenced manuscript. To maintain our journal's high standards we need the best reviewers, and given your expertise in this area I would greatly appreciate your contribution.

Please note: Reviews are subject to a confidentiality policy.

Please find the abstract of the manuscript at the end of this email.

If you have any concerns about potential conflicts of interest, please consult the Editor.

If you are willing to review this manuscript, please click on the link below:
Accept Invitation

If you accept this invitation, I would appreciate your submitting your review within 14 days.

Please submit your review via EVISE® at: http://www.evise.com/evise/faces/pages/navigation/NavController.jspx?JRNL_ACR=COLSUA.

If you cannot review this manuscript, please click on the link below. I would also appreciate your suggestions for alternate reviewers.
Decline

Please also note that authors have been invited to convert their supplementary material into a Data in Brief article (a data description article). You may notice this change alongside the revised manuscript. You do not need to review this, but may need to look at the files in order to confirm that any supporting information you requested is present there.

Please also note that authors have been invited to convert their supplementary material into a MethodsX article (a method description article). You may notice this change alongside the revised manuscript. You do not need to review this, but may need to look at the files in order to confirm that any supporting information you requested is present there.

I look forward to receiving your response.

Kind regards,

Xuehai Yan
Editor
Colloids and Surfaces A: Physicochemical and Engineering Aspects

Abstract:

Melittin (ML) is a small peptide of 26 residues rich in arginine (Arg) and lysine (Lys). Several studies have been done to understand the mechanism of interaction with neutral and negatively charged lipids. However, it is not known with certainty how this interaction depends on the electrostatic or hydrophobic forces according to the composition of the

membrane, nor with the different organization of lipids on the membrane, such as the microdomains that could take place in it. Therefore, comparative studies of the interaction and the effect of ML with respect to cationic peptides (Arg-7 and Lys-5) were conducted to get a deeper insight of the ML interaction mechanism with membranes. In this regard, measurements of zeta potential of different model membranes (DOPC, DMPC and DMPE liposomes) in the presence of the peptides, and molecular dynamics simulations were performed. In the special case of DMPC, we worked in its gel like-ripple phase, in order to analyzed defects of packing that potentially expose hydrocarbon regions. In relation with experimental results, molecular analysis of ML interaction with zwiterionic lipid membrane in its ripple phase was performed by unbiased molecular dynamics simulations. The results allow us to remark that ML penetration is favored in the gel-liquid crystalline phase transition in zwitterionic lipids. The importance of this study lies in the understanding of the first stages of action of the ML in eukaryotic membranes, in model systems of its main lipid composition.

Free access to ScienceDirect and Scopus

To assist you with reviewing this manuscript it is our pleasure to offer you 30 days of free access to ScienceDirect and Scopus. Your complimentary access starts from the day you accept this review invitation and will ensure that you can access ScienceDirect and Scopus both from home and via your institute. Just click on 'Go to Review' and then on the 'Go to Scopus' link under the Useful links section on the My Review tab or click here for more information.

Have questions or need assistance?

For more information on the review process, please visit the Reviewer Support site.

For further assistance, please visit our Customer Support site. Here you can search for solutions on a range of topics, find answers to frequently asked questions, and learn more about EVISE® via interactive tutorials. You can also talk 24/5 to our customer support team by phone and 24/7 by live chat and email.

Gmail

Yuguang Yang <yangyutu123@gmail.com>

Thank you for reviewing manuscript Filling gaps in the knowledge of melittin on lipid membranes

1 message

Colloids and Surfaces A: Physicochemical and Engineering Aspects <EviseSupport@elsevier.com>
Reply-To: colsua@elsevier.com
To: yyang60@jhu.edu

Sun, Sep 16, 2018 at 9:50 PM

This message was sent automatically. Please do not reply.

Ref: COLSUA_2018_163
Title: Filling gaps in the knowledge of melittin on lipid membranes
Journal: Colloids and Surfaces A: Physicochemical and Engineering Aspects

Dear Dr. YANG,

Thank you for your review for the above-referenced manuscript. I greatly appreciate the commitment of your time and expertise. Without the dedication of reviewers like you, it would be impossible to manage an efficient peer review process and maintain the high standards necessary for a successful journal.

When a final decision has been reached regarding this manuscript you will be able to view this decision, as well as reviews submitted by any other reviewers, at: http://www.evise.com/evise/faces/pages/navigation/NavController.jspx?JRNL_ACR=COLSUA. You can also access your review comments here, at any time.

I hope that you will consider Colloids and Surfaces A: Physicochemical and Engineering Aspects as a potential journal for your own publications in the future.

Kind regards,

Xuehai Yan
Editor
Colloids and Surfaces A: Physicochemical and Engineering Aspects

Have questions or need assistance?
For further assistance, please visit our Customer Support site. Here you can search for solutions on a range of topics, find answers to frequently asked questions, and learn more about EVISE® via interactive tutorials. You can also talk 24/5 to our customer support team by phone and 24/7 by live chat and email.

Gmail Yuguang Yang <yangyutu123@gmail.com>

Reviewer Invitation New Submission (Default)

1 message

Xuehai Yan (Colloids and Surfaces A: Physicochemical and Engineering Aspects) <EviseSupport@elsevier.com>
Reply-To: yanxh@ipe.ac.cn
To: yyang60@jhu.edu
Tue, Aug 21, 2018 at 10:23 AM

Ref: COLSUA_2018_11
Title: A new insight into the mechanism of the scale inhibition: DLS study of gypsum nucleation in presence of phosphonates using nanosilver dispersion as an internal light scattering intensity reference
Journal: Colloids and Surfaces A: Physicochemical and Engineering Aspects
Corresponding Author: Konstantin Popov
Co-authors: Maxim Oshchepkov, Elena Afanas'eva, Elena Koltinova, Yulia Dikareva, Hannu Rönkkömäki

Dear Dr Yang,

I would like to invite you to review the above-referenced manuscript. To maintain our journal's high standards we need the best reviewers, and given your expertise in this area I would greatly appreciate your contribution.

Please note: Reviews are subject to a confidentiality policy.

Please find the abstract of the manuscript at the end of this email.

If you have any concerns about potential conflicts of interest, please consult the Editor.

If you are willing to review this manuscript, please click on the link below:
Register to accept

If you accept this invitation, I would appreciate your submitting your review within 14 days.

Please submit your review via EVISE® at: http://www.evise.com/evise/faces/pages/navigation/NavController.jspx?JRNL_ACR=COLSUA.

If you cannot review this manuscript, please click on the link below. I would also appreciate your suggestions for alternate reviewers.
Decline

Please also note that authors have been invited to convert their supplementary material into a Data in Brief article (a data description article). You may notice this change alongside the revised manuscript. You do not need to review this, but may need to look at the files in order to confirm that any supporting information you requested is present there.

Please also note that authors have been invited to convert their supplementary material into a MethodsX article (a method description article). You may notice this change alongside the revised manuscript. You do not need to review this, but may need to look at the files in order to confirm that any supporting information you requested is present there.

I look forward to receiving your response.

Kind regards,

Xuehai Yan
Editor
Colloids and Surfaces A: Physicochemical and Engineering Aspects

Abstract:

Scaling in RO facilities, boilers, heat exchangers, evaporation plants, and oilfield applications is a serious problem worldwide. A widely used solution for controlling scale deposition is an application of chemical inhibitors. However,

irrespective of the broad and a long-term antiscalant application, the mechanisms of scale inhibition are still the matter of discussions. In order to provide a new insight into the mechanism of the scale inhibition, a novel dynamic light scattering (DLS) special technique is used to study the bulk supersaturated gypsum aqueous solutions during the induction period. It is based on the standard Ag nanoparticles (ARGOVIT) injection into the supersaturated gypsum solution. These nanoparticles act as an internal indifferent light scattering intensity reference, and provide a semiquantitative measurement of a relative gypsum particles content in a blank solution and in the system treated with phosphonates: amino-tris(methylenephosphonic acid), ATMP; 1-hydroxyethane-1,1-bis(phosphonic acid), HEDP; 2-phosphonobutane-1,2,4-tricarboxylic acid, PBTC. It is found that ATMP sufficiently reduces the number of gypsum nuclei, spontaneously formed in the supersaturated solutions. The less effective inhibitors of Gypsum scaling HEDP and PBTC also reduce the gypsum nuclei number, but to a less extent. A tentative nonconventional mechanism of scale inhibition in the bulk supersaturated aqueous solutions of gypsum is proposed. It assumes that the active crystal formation centers already exist in any analytical grade aqueous solution in the form of solid nanoimpurities (solid suspended particles) with a size ranging from one to several hundred nm. Those nanoimpurities that become initially covered by Ca2+ and SO42- ions, then provide the fast formation of CaSO4•2H2O phase without significant antiscalant resistance. Meanwhile the antiscalant molecules compete with Ca2+ and SO42- ions for these solid suspended particles and blocks them. Therefore the number of primary gypsum nucleation centers diminishes significantly. Thus the concentration of corresponding CaSO4•2H2O particles during induction period in presence of ATMP gets reduced at least 5-fold. Therefore the collision rate of such particles decreases 25-fold. This explains both induction time prolongation by ATMP and sub-stoichiometry of its efficacy. HEDP and PBTC reveal less inhibition efficacy and corresponding solutions indicate more Gypsum nucleation centers relative to ATMP.

Gmail

Yuguang Yang <yangyutu123@gmail.com>

Thank you for reviewing manuscript A new insight into the mechanism of the scale inhibition: DLS study of gypsum nucleation in presence of phosphonates using nanosilver dispersion as an internal light scattering intensity reference

1 message

Colloids and Surfaces A: Physicochemical and Engineering Aspects <EviseSupport@elsevier.com>
Reply-To: colsua@elsevier.com
To: yyang60@jhu.edu

Mon, Aug 27, 2018 at 10:11 PM

This message was sent automatically. Please do not reply.

Ref: COLSUA_2018_11
Title: A new insight into the mechanism of the scale inhibition: DLS study of gypsum nucleation in presence of phosphonates using nanosilver dispersion as an internal light scattering intensity reference
Journal: Colloids and Surfaces A: Physicochemical and Engineering Aspects

Dear Dr. YANG,

Thank you for your review for the above-referenced manuscript. I greatly appreciate the commitment of your time and expertise. Without the dedication of reviewers like you, it would be impossible to manage an efficient peer review process and maintain the high standards necessary for a successful journal.

When a final decision has been reached regarding this manuscript you will be able to view this decision, as well as reviews submitted by any other reviewers, at: http://www.evise.com/evise/faces/pages/navigation/NavController.jspx?JRNL_ACR=COLSUA. You can also access your review comments here, at any time.

I hope that you will consider Colloids and Surfaces A: Physicochemical and Engineering Aspects as a potential journal for your own publications in the future.

Kind regards,

Xuehai Yan
Editor
Colloids and Surfaces A: Physicochemical and Engineering Aspects

Have questions or need assistance?
For further assistance, please visit our Customer Support site. Here you can search for solutions on a range of topics, find answers to frequently asked questions, and learn more about EVISE® via interactive tutorials. You can also talk 24/5 to our customer support team by phone and 24/7 by live chat and email.

Gmail

Yuguang Yang <yangyutu123@gmail.com>

Thank you for reviewing manuscript A new insight into the mechanism of the scale inhibition: DLS study of gypsum nucleation in presence of phosphonates using nanosilver dispersion as an internal light scattering intensity reference

1 message

Colloids and Surfaces A: Physicochemical and Engineering Aspects <EviseSupport@elsevier.com>
Reply-To: colsua@elsevier.com
To: yyang60@jhu.edu

Tue, Oct 2, 2018 at 8:15 PM

This message was sent automatically. Please do not reply.

Ref: COLSUA_2018_11_R1
Title: A new insight into the mechanism of the scale inhibition: DLS study of gypsum nucleation in presence of phosphonates using nanosilver dispersion as an internal light scattering intensity reference
Journal: Colloids and Surfaces A: Physicochemical and Engineering Aspects

Dear Dr. YANG,

Thank you for your review for the above-referenced manuscript. I greatly appreciate the commitment of your time and expertise. Without the dedication of reviewers like you, it would be impossible to manage an efficient peer review process and maintain the high standards necessary for a successful journal.

When a final decision has been reached regarding this manuscript you will be able to view this decision, as well as reviews submitted by any other reviewers, at: http://www.evise.com/evise/faces/pages/navigation/NavController.jspx?JRNL_ACR=COLSUA. You can also access your review comments here, at any time.

I hope that you will consider Colloids and Surfaces A: Physicochemical and Engineering Aspects as a potential journal for your own publications in the future.

Kind regards,

Xuehai Yan
Editor
Colloids and Surfaces A: Physicochemical and Engineering Aspects

Have questions or need assistance?
For further assistance, please visit our Customer Support site. Here you can search for solutions on a range of topics, find answers to frequently asked questions, and learn more about EVISE® via interactive tutorials. You can also talk 24/5 to our customer support team by phone and 24/7 by live chat and email.

Gmail

Yuguang Yang <yangyutu123@gmail.com>

Review invitation for revised manuscript COLSUA_2018_11_R1

1 message

Xuehai Yan (Colloids and Surfaces A: Physicochemical and Engineering Aspects) <EviseSupport@elsevier.com>
Reply-To: yanxh@ipe.ac.cn
To: yyang60@jhu.edu

Sun, Sep 30, 2018 at 10:29 AM

Ref: COLSUA_2018_11_R1
Title: A new insight into the mechanism of the scale inhibition: DLS study of gypsum nucleation in presence of phosphonates using nanosilver dispersion as an internal light scattering intensity reference
Journal: Colloids and Surfaces A: Physicochemical and Engineering Aspects
Corresponding Author: Konstantin Popov

Dear Dr. YANG,

The above-referenced manuscript is under consideration for publication. As you kindly reviewed the original version, I would be grateful if you could evaluate whether the authors have adequately addressed your concerns in this revision, and provide a recommendation on its suitability for publication. Our goal is to provide as rapid a response as possible to our authors, so please reply to this invitation as soon as possible.

If you have any concerns about potential conflicts of interest, please consult the Editor.

If you are willing to review this manuscript, please click on the link below:
Accept Invitation

If you accept this invitation, I would appreciate your submitting your review within 14 days.

Please submit your review via EVISE® at: http://www.evise.com/evise/faces/pages/navigation/NavController.jspx?JRNL_ACR=COLSUA.

If you cannot review this manuscript, please click on the link below. I would also appreciate your suggestions for alternate reviewers.
Decline

Please also note that authors have been invited to convert their supplementary material into a Data in Brief article (a data description article). You may notice this change alongside the revised manuscript. You do not need to review this, but may need to look at the files in order to confirm that any supporting information you requested is present there.

Please also note that authors have been invited to convert their supplementary material into a MethodsX article (a method description article). You may notice this change alongside the revised manuscript. You do not need to review this, but may need to look at the files in order to confirm that any supporting information you requested is present there.

I look forward to receiving your response.

Kind regards,

Xuehai Yan
Editor
Colloids and Surfaces A: Physicochemical and Engineering Aspects

ABSTRACT:

Scaling in reverse osmosis facilities, boilers, heat exchangers, evaporation plants, and oilfield applications is a serious problem worldwide. A widely used solution for controlling scale deposition is an application of chemical inhibitors. However, irrespective of the broad and a long-term antiscalant application, the mechanisms of scale inhibition are still the matter of discussions. In order to provide a new insight into the mechanism of the scale inhibition, a novel dynamic light

scattering (DLS) special technique is used to study the bulk supersaturated gypsum aqueous solutions during the induction period. It is based on the standard Ag nanoparticles (ARGOVIT) injection into the supersaturated gypsum solution. These nanoparticles act as an internal indifferent light scattering intensity reference, and provide a semiquantitative measurement of a relative gypsum particles content in a blank solution and in the system treated with phosphonates: amino-tris(methylenephosphonic acid), ATMP; 1-hydroxyethane-1,1-bis(phosphonic acid), HEDP; 2-phosphonobutane-1,2,4-tricarboxylic acid, PBTC. It is found that ATMP sufficiently reduces the number of gypsum nuclei, spontaneously formed in the supersaturated solutions. The less effective inhibitors of gypsum scaling HEDP and PBTC also reduce the gypsum nuclei number, but to a less extent. A tentative nonconventional mechanism of scale inhibition in the bulk supersaturated aqueous solutions of gypsum is proposed.

Free access to ScienceDirect and Scopus

To assist you with reviewing this manuscript it is our pleasure to offer you 30 days of free access to ScienceDirect and Scopus. Your complimentary access starts from the day you accept this review invitation and will ensure that you can access ScienceDirect and Scopus both from home and via your institute. Just click on 'Go to Review' and then on the 'Go to Scopus' link under the Useful links section on the My Review tab or click here for more information.

Have questions or need assistance?

For further assistance, please visit our Customer Support site. Here you can search for solutions on a range of topics, find answers to frequently asked questions, and learn more about EVISE® via interactive tutorials. You can also talk 24/5 to our customer support team by phone and 24/7 by live chat and email.

Reviewer Invitation New Submission (Default)

1 message

Xuehai Yan (Colloids and Surfaces A: Physicochemical and Engineering Aspects) <EviseSupport@elsevier.com>
Reply-To: yanxh@ipe.ac.cn
To: yyang60@jhu.edu

Wed, Aug 29, 2018 at 9:25 AM

Ref: COLSUA_2018_22
Title: A finite membrane element formulation for surfactants
Journal: Colloids and Surfaces A: Physicochemical and Engineering Aspects
Corresponding Author: Farshad Roohbakhshan
Co-authors: Roger Sauer

Dear Dr. YANG,

I would like to invite you to review the above-referenced manuscript. To maintain our journal's high standards we need the best reviewers, and given your expertise in this area I would greatly appreciate your contribution.

Please note: Reviews are subject to a confidentiality policy.

Please find the abstract of the manuscript at the end of this email.

If you have any concerns about potential conflicts of interest, please consult the Editor.

If you are willing to review this manuscript, please click on the link below:
Accept Invitation

If you accept this invitation, I would appreciate your submitting your review within 14 days.

Please submit your review via EVISE® at: http://www.evise.com/evise/faces/pages/navigation/NavController.jspx?JRNL_ACR=COLSUA.

If you cannot review this manuscript, please click on the link below. I would also appreciate your suggestions for alternate reviewers.
Decline

Please also note that authors have been invited to convert their supplementary material into a Data in Brief article (a data description article). You may notice this change alongside the revised manuscript. You do not need to review this, but may need to look at the files in order to confirm that any supporting information you requested is present there.

Please also note that authors have been invited to convert their supplementary material into a MethodsX article (a method description article). You may notice this change alongside the revised manuscript. You do not need to review this, but may need to look at the files in order to confirm that any supporting information you requested is present there.

I look forward to receiving your response.

Kind regards,

Xuehai Yan
Editor
Colloids and Surfaces A: Physicochemical and Engineering Aspects

Abstract:

Surfactants play an important role in various physiological and biomechanical applications. An example is the respiratory system, where pulmonary surfactants facilitate the breathing and reduce the possibility of airway blocking by lowering the surface tension when the lung volume is decreased during exhalation. This function is due to the dynamic surface tension

of pulmonary surfactants, which depends on the concentration of surfactants spread on the liquid layer lining the interior surface of the airways and alveoli. Here, a finite membrane element formulation for liquids is introduced that allows for the dynamics of concentration-dependent surface tension, as is the particular case for pulmonary surfactants. A straightforward approach is suggested to model the contact line between liquid drops/menisci and planar solid substrates, which allows the presented framework to be easily used for drop shape analysis. It is further shown how line tension can be taken into account. Following an isogeometric approach, NURBS-based finite elements are used for the discretization of the membrane surface. The capabilities of the presented computational model is demonstrated by different numerical examples - such as the simulation of liquid films, constrained and unconstrained sessile drops, pendant drops and liquid bridges - and the results are compared with experimental data.

Gmail

Yuguang Yang <yangyutu123@gmail.com>

Thank you for reviewing manuscript A finite membrane element formulation for surfactants

1 message

Colloids and Surfaces A: Physicochemical and Engineering Aspects <EviseSupport@elsevier.com>
Reply-To: colsua@elsevier.com
To: yyang60@jhu.edu

Tue, Sep 4, 2018 at 10:20 PM

This message was sent automatically. Please do not reply.

Ref: COLSUA_2018_22
Title: A finite membrane element formulation for surfactants
Journal: Colloids and Surfaces A: Physicochemical and Engineering Aspects

Dear Dr. YANG,

Thank you for your review for the above-referenced manuscript. I greatly appreciate the commitment of your time and expertise. Without the dedication of reviewers like you, it would be impossible to manage an efficient peer review process and maintain the high standards necessary for a successful journal.

When a final decision has been reached regarding this manuscript you will be able to view this decision, as well as reviews submitted by any other reviewers, at: http://www.evise.com/evise/faces/pages/navigation/NavController.jspx?JRNL_ACR=COLSUA. You can also access your review comments here, at any time.

I hope that you will consider Colloids and Surfaces A: Physicochemical and Engineering Aspects as a potential journal for your own publications in the future.

Kind regards,

Xuehai Yan
Editor
Colloids and Surfaces A: Physicochemical and Engineering Aspects

Have questions or need assistance?
For further assistance, please visit our Customer Support site. Here you can search for solutions on a range of topics, find answers to frequently asked questions, and learn more about EVISE® via interactive tutorials. You can also talk 24/5 to our customer support team by phone and 24/7 by live chat and email.

Gmail Yuguang Yang <yangyutu123@gmail.com>

Review invitation for revised manuscript COLSUA_2018_22_R1

1 message

Xuehai Yan (Colloids and Surfaces A: Physicochemical and Engineering Aspects) <EviseSupport@elsevier.com>
Reply-To: yanxh@ipe.ac.cn
To: yyang60@jhu.edu

Sun, Nov 4, 2018 at 9:12 PM

Ref: COLSUA_2018_22_R1
Title: A finite membrane element formulation for surfactants
Journal: Colloids and Surfaces A: Physicochemical and Engineering Aspects
Corresponding Author: Farshad Roohbakhshan

Dear Dr. YANG,

The above-referenced manuscript is under consideration for publication. As you kindly reviewed the original version, I would be grateful if you could evaluate whether the authors have adequately addressed your concerns in this revision, and provide a recommendation on its suitability for publication. Our goal is to provide as rapid a response as possible to our authors, so please reply to this invitation as soon as possible.

If you have any concerns about potential conflicts of interest, please consult the Editor.

If you are willing to review this manuscript, please click on the link below:
Accept Invitation

If you accept this invitation, I would appreciate your submitting your review within 7 days.

Please submit your review via EVISE® at: http://www.evise.com/evise/faces/pages/navigation/NavController.jspx?JRNL_ACR=COLSUA.

If you cannot review this manuscript, please click on the link below. I would also appreciate your suggestions for alternate reviewers.
Decline

Please also note that authors have been invited to convert their supplementary material into a Data in Brief article (a data description article). You may notice this change alongside the revised manuscript. You do not need to review this, but may need to look at the files in order to confirm that any supporting information you requested is present there.

Please also note that authors have been invited to convert their supplementary material into a MethodsX article (a method description article). You may notice this change alongside the revised manuscript. You do not need to review this, but may need to look at the files in order to confirm that any supporting information you requested is present there.

I look forward to receiving your response.

Kind regards,

Xuehai Yan
Editor
Colloids and Surfaces A: Physicochemical and Engineering Aspects

ABSTRACT:

Surfactants play an important role in various physiological and biomechanical applications. An example is the respiratory system, where pulmonary surfactants facilitate the breathing and reduce the possibility of airway blocking by lowering the surface tension when the lung volume decreases during exhalation. This function is due to the dynamic surface tension of pulmonary surfactants, which depends on the concentration of surfactants spread on the liquid layer lining the interior surface of the airways and alveoli. Here, a finite membrane element formulation for liquids is introduced that allows for the

dynamics of concentration-dependent surface tension, as is the particular case for pulmonary surfactants. A straightforward approach is suggested to model the contact line between liquid drops/menisci and planar solid substrates, which allows the presented framework to be easily used for drop shape analysis. It is further shown how line tension can be taken into account. Following an isogeometric approach, NURBS-based finite elements are used for the discretization of the membrane surface. The capabilities of the presented computational model is demonstrated by different numerical examples - such as the simulation of liquid films, constrained and unconstrained sessile drops, pendant drops and liquid bridges - and the results are compared with experimental data.

Free access to ScienceDirect and Scopus

To assist you with reviewing this manuscript it is our pleasure to offer you 30 days of free access to ScienceDirect and Scopus. Your complimentary access starts from the day you accept this review invitation and will ensure that you can access ScienceDirect and Scopus both from home and via your institute. Just click on 'Go to Review' and then on the 'Go to Scopus' link under the Useful links section on the My Review tab or click here for more information.

Have questions or need assistance?

For further assistance, please visit our Customer Support site. Here you can search for solutions on a range of topics, find answers to frequently asked questions, and learn more about EVISE® via interactive tutorials. You can also talk 24/5 to our customer support team by phone and 24/7 by live chat and email.

Gmail

Yuguang Yang <yangyutu123@gmail.com>

Thank you for reviewing manuscript A finite membrane element formulation for surfactants

1 message

Colloids and Surfaces A: Physicochemical and Engineering Aspects <EviseSupport@elsevier.com>
Reply-To: colsua@elsevier.com
To: yyang60@jhu.edu

Fri, Nov 9, 2018 at 7:57 AM

This message was sent automatically. Please do not reply.

Ref: COLSUA_2018_22_R1
Title: A finite membrane element formulation for surfactants
Journal: Colloids and Surfaces A: Physicochemical and Engineering Aspects

Dear Dr. YANG,

Thank you for your review for the above-referenced manuscript. I greatly appreciate the commitment of your time and expertise. Without the dedication of reviewers like you, it would be impossible to manage an efficient peer review process and maintain the high standards necessary for a successful journal.

When a final decision has been reached regarding this manuscript you will be able to view this decision, as well as reviews submitted by any other reviewers, at: http://www.evise.com/evise/faces/pages/navigation/NavController.jspx?JRNL_ACR=COLSUA. You can also access your review comments here, at any time.

I hope that you will consider Colloids and Surfaces A: Physicochemical and Engineering Aspects as a potential journal for your own publications in the future.

Kind regards,

Xuehai Yan
Editor
Colloids and Surfaces A: Physicochemical and Engineering Aspects

Have questions or need assistance?
For further assistance, please visit our Customer Support site. Here you can search for solutions on a range of topics, find answers to frequently asked questions, and learn more about EVISE® via interactive tutorials. You can also talk 24/5 to our customer support team by phone and 24/7 by live chat and email.

Gmail Yuguang Yang <yangyutu123@gmail.com>

Invitation to review a paper for PLOS ONE PONE-D-18-25745 - [EMID:fea82d9db9816f03]

1 message

PLOS ONE <em@editorialmanager.com> Tue, Sep 11, 2018 at 11:31 AM
Reply-To: PLOS ONE <plosone@plos.org>
To: Yuguang Yang <yyang60@jhu.edu>

Dear Dr. Yang,

I am writing to invite you to review a manuscript for PLOS ONE entitled "Molecular dynamics study on the combination of different microtubule targeting" (PONE-D-18-25745).

Please note that if an "R" appears towards the end of the manuscript number, this may be a revised version of a manuscript you'd previously reviewed.

The author list and abstract are appended below, plus more detailed information about PLOS ONE and its editorial criteria.

If you accept this assignment, you are confirming that you have no competing interests that may affect your ability to provide an objective evaluation. Our Competing Interests policy can be found here.

By agreeing to review, you are also committing to a confidential review process. Please do not share this manuscript with anyone who is not directly involved in the review process, including colleagues and other experts in the field. Reviewers may not share or act upon any confidential information gained in the review process. After publication, reviewers may only use publicly published data (i.e. the contents of the published article) and not information from any earlier drafts, unless they have obtained permission from the authors.

If you **ACCEPT** to review this paper, please click the following link: Agree to Review

I would appreciate receiving your review within 21 calendar days of your acceptance.

PLOS ONE employs a structured reviewer form to help reviewers focus on our publication criteria. We encourage you to read about the form. You can also visit the PLOS Reviewer Center for peer review guides, tips, and other resources.

If you **DECLINE** to review this paper, please click the following link: Decline to Review

If you have any questions or concerns, please contact us at plosone@plos.org.

With kind regards,
Dr. Jie Zheng
Academic Editor

Manuscript #: PONE-D-18-25745
Title: Molecular dynamics study on the combination of different microtubule targeting
Authors: Zhenhua Tian; Zhongping Li; Yanyan Chu; Wenbao Li

ABSTRACT:

Plinabulin is a synthetic analog of diketopiperazine phenylahistin, which was isolated from Aspergillus. The combination of plinabulin and docetaxel, is in a world-wide Phase 3 clinical trial for non-small cell lung cancer. Both plinabulin and docetaxel are microtubule targeting agents (MTA). Here, homology model, molecular dynamic simulations and binding free energy calculations were combined used to gain insight into the interaction mechanisms and to investigate the feasibility of combined application of other MTAs.

About PLOS ONE

PLOS ONE is one of the journals published by the Public Library of Science. Its editorial criteria are very straightforward; PLOS ONE objectively concentrates on the technical aspects of a study rather than the more subjective evaluations (of 'impact' or 'interest level') used by other journals. In essence, PLOS ONE wishes to publish ANY report of scientific research that will make a valid contribution to the scientific record. The journal encompasses the full breadth of scientific research by publishing, in an Open Access environment, contributions from all areas of science.

To be accepted for publication in PLOS ONE, research articles must satisfy the following criteria:

1. The study presents the results of primary scientific research.
2. Results reported have not been published elsewhere.
3. Experiments, statistics, and other analyses are performed to a high technical standard and are described in sufficient detail.
4. Conclusions are presented in an appropriate fashion and are supported by the data.
5. The article is presented in an intelligible fashion and is written in standard English.
6. The research meets all applicable standards for the ethics of experimentation and research integrity.
7. The article adheres to appropriate reporting guidelines and community standards for data availability.

Please visit http://www.plosone.org for more information about PLOS ONE.

Trouble with the links?

You may also go to the Editorial Manager website directly at https://www.editorialmanager.com/pone/ and log in to accept or decline the assignment. If you do not have your username and password, they can be retrieved by clicking the *Send Username/Password* link. Please be sure to enter the email address at which you received the reviewer invitation.

If you would like additional guidance, see this 2-minute video tutorial, which provides step-by-step instructions on how to accept or decline an assignment within the website.

If you would like your personal information to be removed from the database, please contact the publication office.

Gmail

Yuguang Yang <yangyutu123@gmail.com>

Thank you for the review of PONE-D-18-25745 - [EMID:bfde3c4b40f6dd7e]

1 message

PLOS ONE <em@editorialmanager.com> Sat, Sep 15, 2018 at 3:29 PM
Reply-To: PLOS ONE <plosone@plos.org>
To: Yuguang Yang <yyang60@jhu.edu>

PONE-D-18-25745
Molecular dynamics study on the combination of different microtubule targeting
Miss Zhenhua Tian

Dear Dr. Yang,

Thank you for taking the time to review PLOS ONE manuscript PONE-D-18-25745 'Molecular dynamics study on the combination of different microtubule targeting.' We greatly appreciate your assistance.

To access a copy of your submitted comments please navigate to the 'Completed Assignments' folder of the Reviewer Main Menu in your Editorial Manager account. Once the editor has proceeded to make a decision you can expect to receive a notification.

If PLOS were to publish reviewers' comments and all peer review content alongside articles, would you read this material?

Yes, that would be helpful
https://surveys.plos.org/s3/ONE-Rev-ReadPostedPeerReview?answer=YesHelpful

Maybe, it would depend on the article and comments
https://surveys.plos.org/s3/ONE-Rev-ReadPostedPeerReview?answer=MaybeHelpful

No, this would not be helpful
https://surveys.plos.org/s3/ONE-Rev-ReadPostedPeerReview?answer=NotHelpful

Thank you for your support of PLOS ONE.

Kind regards,
PLOS ONE
plosone@plos.org

If you would like your personal information to be removed from the database, please contact the publication office.

Gmail

Yuguang Yang <yangyutu123@gmail.com>

Thank you for submitting your review of Manuscript ID CPS-2018-0409 for the journal Colloid and Polymer Science

1 message

Colloid and Polymer Science <onbehalfof@manuscriptcentral.com> Thu, Sep 6, 2018 at 9:38 PM
Reply-To: yu.zhu@uakron.edu
To: yyang60@jhu.edu

06-Sep-2018

Dear Dr. Yuguang Yang,

thank you for reviewing manuscript CPS-2018-0409 entitled "Silver and Gold nanoparticles Functionalized with Naphthalene Diimide" for the journal Colloid and Polymer Science.

On behalf of the Editors of the journal Colloid and Polymer Science, we appreciate the voluntary contribution that each reviewer gives to the Journal. We thank you for your participation in the online review process and hope that we may call upon you again to review future manuscripts.

Sincerely,
Prof. Yu Zhu
Regional Editor, Colloid and Polymer Science
yu.zhu@uakron.edu, yu.zhu08@gmail.com

Gmail Yuguang Yang <yangyutu123@gmail.com>

Invitation to Review for the journal Colloid and Polymer Science

1 message

Colloid and Polymer Science <onbehalfof@manuscriptcentral.com> Mon, Sep 3, 2018 at 10:01 PM
Reply-To: yu.zhu@uakron.edu
To: yyang60@jhu.edu

Dear Mr. Yang,

Manuscript ID CPS-2018-0409 entitled "Silver and Gold nanoparticles Functionalized with Naphthalene Diimide" with Dr. Paul as contact author has been submitted to the journal Colloid and Polymer Science.

I invite you to review this manuscript. The abstract appears at the end of this letter.

Please let me know as soon as possible if you will be able to review by using these links:

*** PLEASE NOTE: This is a two-step process. After clicking on the link, you will be directed to a webpage to confirm. ***

Agreed: https://mc.manuscriptcentral.com/cps?URL_MASK=ba629310c9564553b39164aa6eb679d1

Declined: https://mc.manuscriptcentral.com/cps?URL_MASK=37d59b2f3b5349109cccc6a0c817e441

Unavailable: https://mc.manuscriptcentral.com/cps?URL_MASK=ac651a5344774f8eb1d8b05973c2e445

If you are unable to review at this time, I would appreciate you recommending another expert reviewer.

Of course you may also e-mail me your reply.

Once you accept my invitation to review this manuscript, you will be notified via e-mail about how to access Manuscript Central, our online manuscript submission and review system. You will then have access to the manuscript and reviewer instructions in your Reviewer Center.

I realize that our expert reviewers greatly contribute to the high standards of the Journal, and I thank you for your present and/or future participation.

Sincerely,
Prof. Yu Zhu
Associate Editor Colloid and Polymer Science
yu.zhu@uakron.edu, yu.zhu08@gmail.com

MANUSCRIPT DETAILS

TITLE: Silver and Gold nanoparticles Functionalized with Naphthalene Diimide

AUTHORS: Paul, Samir; Cammarata, Vince

ABSTRACT: Functionalization of metal nanoparticles with surface ligands effects their growth, shape and size as well as the optical and electronic properties. The change of optical property of the nanoparticles due to their surface ligand is an important field of nanoparticles application. Here we report synthesis and characterization of redox active naphthalene diimide (NDI) functionalized metal nanoparticles. Silver and gold nanoparticles were synthesized from silver neodecanoate and gold (I) sodium thiosulfate, respectively, in presence of DPA-NDI-SH (where DPA= diphenylamine) in a single reaction vessel. Dimethyl sulfoxide (DMSO) and dimethyl formamide (DMF) were used as both solvent and reducing agent for Ag and Au nanoparticles, respectively. Analyses by XRD, TEM and FT-IR indicated well dispersed naphthalene diimide coated nanoparticles. Also the optical properties of the nanoparticles showed a red shift of plasmon band due to charge transfer between surface molecule and core structure interface. On the basis of this optical property, these hybrid nanostructure could be useful to design nano optoelectronic devices.

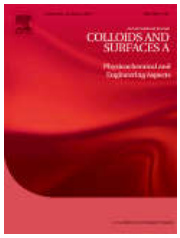

(https://www.sciencedirect.com/science/journal/09277757)
ISSN: 0927-7757

Colloids and Surfaces A: Physicochemical and Engineering Aspects

An International Journal Devoted to the Principles and Applications of Colloid and Interface Science

Editor-in-Chief: J.B. Li (https://www.journals.elsevier.com:443/colloids-and-surfaces-a-physicochemical-and-engineering-aspects/editorial-board/jb-li)

› View Editorial Board (https://www.journals.elsevier.com:443/colloids-and-surfaces-a-physicochemical-and-engineering-aspects/editorial-board)

Submit Your Paper (https://ees.elsevier.com/colsua)

Supports Open Access (http://www.elsevier.com/journals/colloids-and-surfaces-a-physicochemical-and-engineering-aspects/0927-7757/open-access-options)

View Articles (https://www.sciencedirect.com/science/journal/09277757)

Guide for Authors

Abstracting/ Indexing (http://www.elsevier.com/journals/colloids-and-surfaces-a-physicochemical-and-engineering-aspects/0927-7757/abstracting-indexing)

Track Your Paper

Order Journal (https://www.elsevier.com/journals/institutional/colloids-and-surfaces-a-physicochemical-and-engineering-aspects/0927-7757)

Sample Issue (https://www.sciencedirect.com/science/journal/sample/09277757)

Journal Metrics

› CiteScore: **2.84** ⓘ

Impact Factor: **2.829**
5-Year Impact Factor: **2.852**
Source Normalized Impact per Paper (SNIP): **1.016**
SCImago Journal Rank (SJR): **0.753**

> View More on Journal Insights

Your Research Data

> Share your research data (https://www.elsevier.com/authors/author-services/research-data)

> Visualize your data (http://www.elsevier.com/authors/author-services/data-visualization)

> Data in Brief co-submission (https://www.elsevier.com/authors/author-services/research-data/data-articles/DIB-co-submission)

> MethodsX co-submission (https://www.elsevier.com/authors/author-services/research-data/materials-and-methods/mex-co-submission)

Related Links

> Author Stats

> Researcher Academy

> Author Services (https://www.elsevier.com/authors/author-services)

> Try out personalized alert features

Related Publications

Advances in Colloid and Interface Science (https://www.elsevier.com/locate/inca/500842)

Colloid and Interface Science Communications (https://www.elsevier.com/locate/inca/731952)

Colloids and Surfaces B: Biointerfaces (https://www.elsevier.com/locate/inca/523888)

Current Opinion in Colloid & Interface Science (https://www.elsevier.com/locate/inca/620053)

Journal of Colloid and Interface Science (https://www.elsevier.com/locate/inca/622861)

Colloids and Surfaces A: Physicochemical and Engineering Aspects is an international journal devoted to the science underlying applications of **colloids** and **interfacial** phenomena.

The journal aims at publishing high quality research papers featuring new materials or new insights into the role of **colloid** and **interface science** in (for example) food, energy, minerals processing, pharmaceuticals or the environment.

Criteria for publication in *Colloids and Surfaces A* are novelty, quality and current interest. Manuscripts which only make routine use of or minor extensions to well established methodologies (e.g. fitting adsorption data to a Langmuir or Freundlich isotherm) are not appropriate for the journal.

For online article submission please go to: http://ees.elsevier.com/colsua

Benefits to authors

We also provide many author benefits, such as free PDFs, a liberal copyright policy, special discounts on Elsevier publications and much more. Please click here for more information on our author services (http://www.elsevier.com/authors/author-services).

Please see our Guide for Authors (http://www.elsevier.com/journals/colloids-and-surfaces-a-physicochemical-and-engineering-aspects/0927-7757/guide-for-authors) for information on article submission. If you require any further information or help, please visit our Support Center

Hide full Aims & Scope

Most Downloaded | Recent Articles | Most Cited | Open Access Articles

Emulsions stabilized with solid nanoparticles: Pickering emulsions
Yves Chevalier | Marie-Alexandrine Bolzinger

Foam stability in the presence and absence of hydrocarbons: From bubble- to bulk-scale
Kofi Osei-Bonsu | Nima Shokri | ...

Advanced fabrication and properties of hybrid polyethylene tetraphalate fiber–silica aerogels from plastic bottle waste
Steven Salomo | Thanh X. Nguyen | ...

> View All Most Downloaded Articles (https://www.journals.elsevier.com:443/colloids-and-surfaces-a-physicochemical-and-engineering-aspects/most-downloaded-articles)

Most Downloaded Articles

Recent Articles

Most Cited Articles

Recent Open Access Articles

(http://www.facebook.com/elsevierchemistry) (//twitter.com/ELSCHEMENG) (http://plus.google.com/+elsevierchemistry/posts) (/colloids-and-surfaces-a-physicochemical-and-engineering-aspects/rss) (http://www.elsevier.com/locate/colloidsandsurfaces)

Announcements (https://www.journals.elsevier.com:443/colloids-and-surfaces-a-physicochemical-and-engineering-aspects/announcements)

Heliyon Partner Journal

This journal has partnered with *Heliyon*, an open access journal from Elsevier publishing quality peer reviewed research across all disciplines. Heliyon's team of experts provides editorial excellence, fast publication, and high visibility for your paper. Authors can quickly and easily transfer their research from a Partner Journal to *Heliyon* without the need to edit, reformat or resubmit.
>Learn more at Heliyon.com

> View All (https://www.journals.elsevier.com:443/colloids-and-surfaces-a-physicochemical-and-engineering-aspects/announcements)

Mendeley Data (https://www.journals.elsevier.com:443/colloids-and-surfaces-a-physicochemical-and-engineering-aspects/mendeley)

The latest Mendeley datasets for Colloids and Surfaces A: Physicochemical and Engineering Aspects.

Data for: Silica Oxide Encapsulated Natural Zeolite for High Efficiency Removal of Low Concentration Heavy Metals in Water
Ming Hui Liang | Jingyi Cai | ...
11 files (2018)

Data for: Filling gaps in the knowledge of melittin on lipid membranes
M. Florencia Martini
80 files (2018)

View All (https://www.journals.elsevier.com:443/colloids-and-surfaces-a-physicochemical-and-engineering-aspects/mendeley)

Call for Papers (https://www.journals.elsevier.com:443/colloids-and-surfaces-a-physicochemical-and-engineering-aspects/call-for-papers)

Call for paper for Virtual Special Issue on Phenomena in complex wetting (https://www.journals.elsevier.com:443/colloids-and-surfaces-a-physicochemical-and-engineering-aspects/call-for-papers/virtual-special-issue-phenomena-in-complex-wetting)

View All (https://www.journals.elsevier.com:443/colloids-and-surfaces-a-physicochemical-and-engineering-aspects/call-for-papers)

Conferences (https://www.journals.elsevier.com:443/colloids-and-surfaces-a-physicochemical-and-engineering-aspects/conferences)

6th International Conference on Multifunctional, Hybrid and Nanom (HYMA2019) (https://www.journals.elsevier.com:443/colloids-and-surfaces-a-physicochemical-and-engineering-aspects/conferences/6th-international-conference-on-multifunctional-hybrid)

6th Nano Today Conference (https://www.journals.elsevier.com:443/colloids-and-surfaces-a-physicochemical-and-engineering-aspects/conferences/6th-nano-today-conference)

9th International Colloids Conference (https://www.journals.elsevier.com:443/colloids-and-surfaces-a-physicochemical-and-engineering-aspects/conferences/9th-international-colloids-conference)

View All (https://www.journals.elsevier.com:443/colloids-and-surfaces-a-physicochemical-and-engineering-aspects/conferences)

News (https://www.journals.elsevier.com:443/colloids-and-surfaces-a-physicochemical-and-engineering-aspects/news)

ECIS 2017, 31st Conference of the European Colloid and Interface Society, Madrid, Spain (https://www.journals.elsevier.com:443/colloids-and-surfaces-a-physicochemical-and-engineering-aspects/news/ecis-2017-31st-conference-of-the-european-colloid-and-interf)

Publisher's Note: Editorial Changes (https://www.journals.elsevier.com:443/colloids-and-surfaces-a-physicochemical-and-engineering-aspects/news/publishers-note-editorial-changes)

We're pleased to announce the launch of FlatChem! (https://www.journals.elsevier.com:443/colloids-and-surfaces-a-physicochemical-and-engineering-aspects/news/we-are-pleased-to-announce-the-launch-of-flatchem)
Elsevier's newest chemistry journal

View All (https://www.journals.elsevier.com:443/colloids-and-surfaces-a-physicochemical-and-engineering-aspects/news)

Special Issues (https://www.journals.elsevier.com:443/colloids-and-surfaces-a-physicochemical-and-engineering-aspects/special-issues)

Special issues published in Colloids and Surfaces A: Physicochemical and Engineering Aspects.

"A Collection of Papers Presented at the 31st ECIS Meeting, Madrid, Spain, 3-8 September, 2017"
Enrique Lopez-Cabarcos | Marco Laurenti | ...

Special issue:Food Colloids
Reinhard Miller | Anwesha Sarkar | ...

Phenomena in complex wetting
Reinhard Miller | Günter Auernhammer | ...

View All (https://www.journals.elsevier.com:443/colloids-and-surfaces-a-physicochemical-and-engineering-aspects/special-issues)

PlumX Metrics (https://www.journals.elsevier.com:443/colloids-and-surfaces-a-physicochemical-and-engineering-aspects/top-articles)

Below is a recent list of 2017/2018 articles that have had the most social media attention. The Plum Print next to each article shows the relative activity in each of these categories of metrics: Captures, Mentions, Social Media and Citations. Go here to learn more about PlumX Metrics.

Recombinant protein-based nanocarriers and their association with cationic liposomes: Characterization and in vitro evaluation

Hydrogels incorporated with silver nanocolloids prepared from antioxidant rich Aerva javanica as disruptive agents against burn wound infections

Effects of aging on the yielding behaviour of acid and salt induced Laponite gels

View All (https://www.journals.elsevier.com:443/colloids-and-surfaces-a-physicochemical-and-engineering-aspects/top-articles)

Colloids and Surfaces A: Physicochemical and Engineering Aspects

Readers
View Articles
Sample Issue
Volume/Issue Alert
Personalized Recommendations

Authors (http://www.elsevier.com/authors/home)
Author Information Pack (http://www.elsevier.com/journals/colloids-and-surfaces-a:-physicochemical-and-engineering-aspects/0927-7757?generatepdf=true)
Submit Your Paper
Track Your Paper
Early Career Resources (http://www.elsevier.com/early-career-researchers/training-and-workshops)
Rights and Permissions (https://www.elsevier.com/about/policies/copyright/permissions)
Webshop
Support Center

Librarians (https://www.elsevier.com/librarians)
Ordering Information and Dispatch Dates (http://www.elsevier.com/journals/colloids-and-surfaces-a-physicochemical-and-engineering-aspects/0927-7757/order-journal)
Abstracting/ Indexing (http://www.elsevier.com/journals/colloids-and-surfaces-a-physicochemical-and-engineering-aspects/0927-7757/abstracting-indexing)

Editors (http://www.elsevier.com/editors/home)
Publishing Ethics Resource Kit (http://www.elsevier.com/editors/perk)
Guest Editors (http://www.elsevier.com/editors/guest-editors)
Support Center

Reviewers (http://www.elsevier.com/reviewers/home)
Reviewer Guidelines (http://www.elsevier.com/reviewersguidelines)
Log in as Reviewer
Reviewer Recognition (https://www.elsevier.com/reviewers/becoming-a-reviewer-how-and-why#recognizing)
Support Center

Advertisers Media Information (https://www.elsevier.com/advertisers)

Societies (http://www.elsevier.com/societies/home)

(https://www.elsevier.com)

(https://www.elsevier.com) RELX Group™ (http://www.reedelsevier.com/)

(https://twitter.com/ElsevierConnect) (https://www.facebook.com/ElsevierConnect) (https://www.linkedin.com/company/reed-elsevier) (https://www.mendeley.com/groups/)

" "

Journal Information

The world's first multidisciplinary Open Access journal, *PLOS ONE* accepts scientifically rigorous research, regardless of novelty. *PLOS ONE*'s broad scope provides a platform to publish primary research, including interdisciplinary and replication studies as well as negative results. The journal's publication criteria are based on high ethical standards and the rigor of the methodology and conclusions reported.

Scope

PLOS ONE features reports of original research from the natural sciences, medical research, engineering, as well as the related social sciences and humanities that will contribute to the base of scientific knowledge. By not excluding research on the basis of subject area, *PLOS ONE* facilitates the discovery of connections between research whether within or between disciplines.

We will also consider the following article types:

- **Systematic reviews.** We consider publishing systematic reviews only if the methods ensure the comprehensive and unbiased sampling of existing literature.
- **Submissions describing methods, software, databases, or other tools.** We consider submissions describing methods, software, databases, or other tools if they follow the appropriate reporting guidelines.
- **Qualitative research.** We consider publishing qualitative research only if it adheres to appropriate study design and reporting guidelines.
- **Studies reporting negative results.**

For more information, see our criteria for publication and read our submission guidelines.

Criteria for Publication

1. The study presents the results of primary scientific research.
2. Results reported have not been published elsewhere.
3. Experiments, statistics, and other analyses are performed to a high technical standard and are described in sufficient detail.
4. Conclusions are presented in an appropriate fashion and are supported by the data.
5. The article is presented in an intelligible fashion and is written in standard English.
6. The research meets all applicable standards for the ethics of experimentation and research integrity.
7. The article adheres to appropriate reporting guidelines and community standards for data availability.

PLOS ONE encourages researchers to share early versions of their manuscripts via preprint server, either before or after submission; posting to a preprint server will not preclude consideration of your manuscript.

Rigorous Peer Review

Often a journal's decision not to publish a paper reflects an editor's opinion about what is likely to have substantial impact in a given field. These subjective judgments can delay the publication of work that later proves to be of major significance. *PLOS ONE* will thoroughly peer-review your submissions and publish all papers that are judged to be technically rigorous. Judgments about the importance of any particular paper are then made after publication by the readership, who are the most qualified to determine what is of interest to them.

Each submission to *PLOS ONE* passes through a rigorous quality control and peer-review evaluation process before receiving a decision. The initial in-house quality control check deals with issues such as competing interests; ethical requirements for studies involving human participants or animals; financial disclosures; full compliance with PLOS' data availability policy, etc. Submissions may be returned to authors for queries, and will not be seen by our Editorial Board or peer reviewers until they pass this quality control check.

Once each manuscript has passed quality control, it is assigned to a member of the Editorial Board, who takes responsibility as the Academic Editor for the submission. The Academic Editor is responsible for conducting the peer-review process and for making a decision to accept, invite revision of, or reject the article.

Read more about the editorial and peer review process.

Read the guidelines for reviewers.

Editorial Oversight

PLOS ONE is run as a partnership between in-house PLOS staff and an international Editorial Board, ensuring fast, fair, and professional peer review.

Editor-in-Chief

Joerg Heber

PLOS ONE Editors

View the biographies of the *PLOS ONE* Editors.

Editorial Board

View the *PLOS ONE* Editorial Board.

Resources for Editors. Board members can sign in to the private Editorial Board Knowledge Base to download the Academic Editor Handbook, watch courses on topics such as competing interests and finding reviewers, and communicate with fellow editors in discussion forums.

Submit Your Manuscript

For more information about submitting to *PLOS ONE*, read our checklist for getting started and our guidelines for preparing a submission.

Open Access

PLOS applies the Creative Commons Attribution (CC BY) license to works we publish. This license was developed to facilitate open access – namely, free immediate access to, and unrestricted reuse of, original works of all types.

Under this license, authors agree to make articles legally available for reuse, without permission or fees, for virtually any purpose. Anyone may copy, distribute, or reuse these articles, as long as the author and original source are properly cited. Read PLOS' licenses and copyright policy.

Journal Impact and Article Metrics

PLOS does not consider Impact Factor to be a reliable or useful metric to assess the performance of individual articles. PLOS supports DORA – the San Francisco Declaration on Research Assessment – and does not promote our journal Impact Factors. We will provide the metric to individuals when specifically requested.

Read more about our pledge with DORA and our concerns with journal-level research assessment.

PLOS promotes the use of Article-Level Metrics (ALMs), which enable scientists and the general public to engage more dynamically with published research. ALMs reflect the changing impact of research over time, incorporate academic as well as social impacts of research, and assess the impact of research before the accrual of academic citations. Read more about ALMs.

Publication Fees

PLOS ONE publication fees are US$1595 per manuscript and will be billed upon acceptance. Authors' ability to pay publication fees will never be a consideration in the decision whether to publish. Read more about publication fees and publication fee support.

Indexing and Archiving

See publishing details for all PLOS journal titles, including ISSN and indexing and archiving information.

About PLOS Journals

PLOS (Public Library of Science) publishes a suite of influential journals from all areas of science and medicine that contain rigorously reported, peer-reviewed Open Access research articles. The journals vary in their criteria for publication and, with the exception of *PLOS ONE*, also publish a variety of influential and educational non-research content. The journals are editorially independent. Read more about the PLOS suite of journals.

Contact

Visit the Contact page for details about whom to contact with different queries.

Give Feedback

How helpful was the information on this page?

Not at all helpful	Not very helpful	Helpful	Very helpful	Extremely helpful
○	○	○	○	○

Send feedback

Kolloid-Zeitschrift und Zeitschrift für Polymere

ISSN: 0303-402X (Print) 1435-1536 (Online)
This journal was previously published under other titles *(view Journal History)*

Description

Colloid and Polymer Science - a leading international journal of longstanding tradition - is devoted to colloid and polymer science and its interdisciplinary interactions. As such, it responds to a demand which has lost none of its actuality as revealed in the trends of contemporary materials science. To enable an effective and fast dissemination of scientific manuscripts, four categories of contributions are presented:

- Invited review articles
- Perspectives
- Original contributions
- Short communications

The latter will be published with high priority, at least within two weeks after acceptance of the manuscript. (The usual time between acceptance and publishing OnlineFirst is typically three weeks.) With this immediacy, Colloid and Polymer Science serves as a reliable partner for an effective distribution of scientific results.

Purely application-oriented manuscripts as well as routine work are not accepted.

hide

Latest Articles

1. Original Contribution

   Phase diagram of colloidal crystals of poly(methyl methacrylate) spheres in the exhaustively deionized dispersion

   Tsuneo Okubo, *Hiroshi Kimura*, *Akira Tsuchida* (January 2019)

2. Original Contribution

   Self-assembly and rheological behavior of oleic acid-based pseudo-tetrameric surfactants

   Chaowang Li, *Danhua Xie*, *Xiaomei Pei*, *Binglei Song*... (January 2019)

3. Invited Review

   Precision polymer network science with tetra-PEG gels—a decade history and future

   Mitsuhiro Shibayama, *Xiang Li*, *Takamasa Sakai* (January 2019)

See all articles

About this Journal

Journal Title
Colloid and Polymer Science
Coverage
Volume 1 / 1906 - Volume 297 / 2019
Print ISSN
0303-402X
Online ISSN
1435-1536
Publisher
Springer Berlin Heidelberg

Additional Links

- *Register for Journal Updates*
- *Editorial Board*
- *About This Journal*
- *Manuscript Submission*

Topics

- *Polymer Sciences*
- *Soft and Granular Matter, Complex Fluids and Microfluidics*
- *Characterization and Evaluation of Materials*
- *Physical Chemistry*
- *Food Science*
- *Nanotechnology and Microengineering*

Industry Sectors

- *Automotive*
- *Chemical Manufacturing*
- *Biotechnology*
- *Electronics*
- *IT & Software*
- *Consumer Packaged Goods*
- *Energy, Utilities & Environment*
- *Aerospace*
- *Oil, Gas & Geosciences*

Previous Title	Print ISSN	Online ISSN
Kolloid-Zeitschrift und Zeitschrift für Polymere	0023-2904	1435-1536
Kolloid-Zeitschrift	0368-6590	1435-1536
Zeitschrift für Chemie und Industrie der Kolloide	0368-6590	1435-1536

Support

For: **YUGUANG YANG**

U.S. Customs and Border Protection
Securing America's Borders

Most Recent I-94

Admission (I-94) Record Number : 06049654530
Most Recent Date of Entry: 2013 September 06
Class of Admission : F1
Admit Until Date : D/S
Details provided on the I-94 Information form:

Last/Surname :	**YANG**
First (Given) Name :	**YUGUANG**
Birth Date :	**1988 October 09**
Passport Number :	**G42226545**
Country of Issuance :	**China**

Get Travel History

Effective April 26, 2013, DHS began automating the admission process. An alien lawfully admitted or paroled into the U.S. is no longer required to be in possession of a preprinted Form I-94. A record of admission printed from the CBP website constitutes a lawful record of admission. See 8 CFR § 1.4(d).

If an employer, local, state or federal agency requests admission information, present your admission (I-94) number along with any additional required documents requested by that employer or agency.

Note: For security reasons, we recommend that you close your browser after you have finished retrieving your I-94 number.

OMB No. 1651-0111
Expiration Date: 03/31/2019

For inquiries or questions regarding your I-94, please click here

THE UNITED STATES OF AMERICA

I-797A | NOTICE OF ACTION | DEPARTMENT OF HOMELAND SECURITY U.S. CITIZENSHIP AND IMMIGRATION SERVICES

Receipt Number		Case Type
EAC1715050427		I129 - PETITION FOR A NONIMMIGRANT WORKER
Received Date	**Priority Date**	**Petitioner**
04/11/2017		WELLS FARGO BANK NA,
Notice Date	**Page**	**Beneficiary**
06/12/2017	2 of 2	YANG, YUGUANG

The Small Business Regulatory Enforcement and Fairness Act established the Office of the National Ombudsman (ONO) at the Small Business Administration. The ONO assists small businesses with issues related to federal regulations. If you are a small business with a comment or complaint about regulatory enforcement, you may contact the ONO at www.sba.gov/ombudsman or phone 202-205-2417 or fax 202-481-5719.

NOTICE: Although this application or petition has been approved, USCIS and the U.S. Department of Homeland Security reserve the right to verify this information before and/or after making a decision on your case so we can ensure that you have complied with applicable laws, rules, regulations, and other legal authorities. We may review public information and records, contact others by mail, the internet or phone, conduct site inspections of businesses and residences, or use other methods of verification. We will use the information obtained to determine whether you are eligible for the benefit you seek. If we find any derogatory information, we will follow the law in determining whether to provide you (and the legal representative listed on your Form G-28, if you submitted one) an opportunity to address that information before we make a formal decision on your case or start proceedings.

Please see the additional information on the back. You will be notified separately about any other cases you filed.

Vermont Service Center
U. S. CITIZENSHIP & IMMIGRATION SVC
75 Lower Welden Street
Saint Albans VT 05479-0001

Customer Service Telephone: 800-375-5283

PLEASE TEAR OFF FORM I-94 PRINTED BELOW AND STAPLE TO ORIGINAL I-94 IF AVAILABLE

Detach This Half for Personal Records

VOID VOID VOID

Receipt Number

I-94#

NAME

CLASS

VALID FROM UNTIL

PETITIONER

VOID VOID VOID

US Citizenship and Immigration Services

I94 Departure Record

14. Family Name

15. First (Given) Name

16. Date of Birth

17. Country of Citizenship

FORM I-797A [REV. 08/01/16]

ADDITIONAL INFORMATION FOR APPLICANT/PETITIONER

If this is an approval notice for Form I-102, Application For Initial/ Replacement I-94, save the upper portion of this I-797A, Notice of Action, for your records. If this is an approval notice for Form I-129, Petition for a Nonimmigrant Worker, the petitioner should keep the upper part of this I-797A.

Please note that simply filing an application, petition or request, or having an approved petition does not give the person it was filed for (also known as the beneficiary) permission to legally enter the United States. It also does not grant any legal immigration status.

Include a copy of this notice if you:

- Write to USCIS or a U.S. Consulate about your case or
- File another application or petition with USCIS based on this decision.

USCIS will notify you separately about any other application or petition you have filed.

Inquiries

If you have questions about your application or petition, you may:

- Go to https://egov.uscis.gov/casestatus to check your case status online.
- Call the National Customer Service Center at 1-800-375-5283.
- Telecommunications Device for the Deaf (TDD) 1-800-767-1833.
- Send us a letter and include a copy of this notice.
- Schedule an appointment at a local USCIS office using InfoPass at https://infopass.uscis.gov.

If you filed Form I-907, Request for Premium Processing Service, and you have any questions about the decision or status of your application or petition, please follow the instructions for contacting the Premium Processing Unit printed on the receipt notice we mailed you.

APPROVAL OF NONIMMIGRANT PETITION

If we approved a nonimmigrant petition, it means that the beneficiary is eligible for the requested nonimmigrant classification. If this notice says that we are notifying a U.S. Consulate about the approval for the purpose of issuing a visa, contact the appropriate U.S. Consulate directly if you or the beneficiary has questions about the process. For more information about USCIS processing after a petition is approved, see the instructions on the form you filed.

FORM I-94 ATTACHMENT

You can find your replacement Form I-94 (Arrival/Departure Record) in the lower portion on the front side of this notice. Keep the right half of your replacement Form I-94 with your passport, along with a copy of your original I-94 if you have it. Keep the left half of your replacement Form I-94 in a safe place with your personal records. Submit a copy of your replacement Form I-94 with any future application or petition.

When you leave the United States, you must turn in the right half of your I-94 (kept in your passport) to the officials at the airport, border or seaport. If you do not do so, it may delay your entry into the United States in the future. You may stay in the United States only until the date indicated on this form. If you want to remain in the United States past this date, you will need further authorization from USCIS.

If you are a student planning to reenter the United States within 30 days to return to the same school, review the "Instructions to Students" on Page 3 of Form I-20 before surrendering your replacement I-94.

If you lose the right half of your replacement Form I-94 (kept in your passport), submit a copy of the left half of the Form I-94 (that you keep with your personal records), along with a new Form I-102, to apply for a new replacement I-94.

Warning: If you accept employment without our authorization, you may be subject to removal or deportation.

THE UNITED STATES OF AMERICA

I-797A | NOTICE OF ACTION | DEPARTMENT OF HOMELAND SECURITY U.S. CITIZENSHIP AND IMMIGRATION SERVICES

Receipt Number		Case Type
EAC1715050427		I129 - PETITION FOR A NONIMMIGRANT WORKER
Received Date	**Priority Date**	**Petitioner**
04/11/2017		WELLS FARGO BANK NA,
Notice Date	**Page**	**Beneficiary**
06/12/2017	1 of 2	YANG, YUGUANG

WELLS FARGO BANK NA
c/o MEGHAN T HOUSTON
BAKER & MCKENZIE LLP
815 CONNECTICUT AVE NW
WASHINGTON DC 20006

Notice Type: Approval Notice
Class: H1B
Valid from 10/01/2017 to 09/04/2020

The above petition and change of status have been approved. The status of the named foreign worker(s) in this classification is valid as indicated above. The foreign worker(s) can work for the petitioner, but only as detailed in the petition and for the period authorized. Changes in employment or training may require you to file a new Form I-129 petition. Since this employment or training authorization stems from the filing of this petition, separate employment or training authorization documentation is not required. The I-94 attached below may contain a grace period of up to 10 days before, and up to 10 days after the petition validity period for the following classifications: CW-1, E-1, E-2, E-3, H-1B, H-2B, H-3, L-1A, L-1B, O-1, O-2, P-1, P-2, P-3, TN-1, and TN-2. H-2A nonimmigrants may contain a grace period of up to one week before and 30 days after the petition validity period. The grace period is a period of authorized stay but does not provide the beneficiary authorization to work beyond the petition validity period. The decision to grant a grace period and the length of the granted grace period is discretionary, final and cannot be contested on motion or appeal. Please contact the IRS with any questions about tax withholding.

The petitioner should keep the upper portion of this notice. The lower portion should be given to the worker. He or she should keep the right part with his or her Form I-94, *Arrival-Departure Record*. The I-94 portion should be given to the U.S. Customs and Border Protection when he or she leaves the United States. The left part is for his or her records. A person granted a change of status who leaves the U.S. must normally obtain a visa in the new classification before returning. The left part can be used in applying for the new visa. If a visa is not required, he or she should present it, along with any other required documentation, when applying for reentry in this new classification at a port of entry or pre-flight inspection station. The petitioner may also file Form I-824, *Application for Action on an Approved Application or Petition*, to request that we notify a consulate, port of entry, or pre-flight inspection office of this approval.

The approval of this visa petition does not in itself grant any immigration status and does not guarantee that the alien beneficiary will subsequently be found to be eligible for a visa, for admission to the United States, or for an extension, change, or adjustment of status.

THIS FORM IS NOT A VISA AND MAY NOT BE USED IN PLACE OF A VISA.

Please see the additional information on the back. You will be notified separately about any other cases you filed.

Vermont Service Center
U. S. CITIZENSHIP & IMMIGRATION SVC
75 Lower Welden Street
Saint Albans VT 05479-0001

Customer Service Telephone: 800-375-5283

PLEASE TEAR OFF FORM I-94 PRINTED BELOW AND STAPLE TO ORIGINAL I-94 IF AVAILABLE

Detach This Half for Personal Records

Receipt# EAC1715050427
I-94# 060496545 30
NAME YANG, YUGUANG
CLASS H1B
VALID FROM 10/01/2017 **UNTIL** 09/13/2020

PETITIONER
WELLS FARGO BANK NA,
550 S 4TH ST
MINNEAPOLIS MN 55415

060496545 30
Receipt Number EAC1715050427
US Citizenship and Immigration Services

I94 Departure Record
Petitioner: WELLS FARGO BANK NA

14. Family Name	
YANG	
15. First (Given) Name	**16. Date of Birth**
YUGUANG	10/09/1988
17. Country of Citizenship	
CHINA, PEOPLE'S REPUBLIC OF	

ADDITIONAL INFORMATION FOR APPLICANT/PETITIONER

If this is an approval notice for Form I-102, Application For Initial/ Replacement I-94, save the upper portion of this I-797A, Notice of Action, for your records. If this is an approval notice for Form I-129, Petition for a Nonimmigrant Worker, the petitioner should keep the upper part of this I-797A.

Please note that simply filing an application, petition or request, or having an approved petition does not give the person it was filed for (also known as the beneficiary) permission to legally enter the United States. It also does not grant any legal immigration status.

Include a copy of this notice if you:

- Write to USCIS or a U.S. Consulate about your case or
- File another application or petition with USCIS based on this decision.

USCIS will notify you separately about any other application or petition you have filed.

Inquiries

If you have questions about your application or petition, you may:

- Go to https://egov.uscis.gov/casestatus to check your case status online.
- Call the National Customer Service Center at 1-800-375-5283.
- Telecommunications Device for the Deaf (TDD) 1-800-767-1833.
- Send us a letter and include a copy of this notice.
- Schedule an appointment at a local USCIS office using InfoPass at https://infopass.uscis.gov.

If you filed Form I-907, Request for Premium Processing Service, and you have any questions about the decision or status of your application or petition, please follow the instructions for contacting the Premium Processing Unit printed on the receipt notice we mailed you.

APPROVAL OF NONIMMIGRANT PETITION

If we approved a nonimmigrant petition, it means that the beneficiary is eligible for the requested nonimmigrant classification. If this notice says that we are notifying a U.S. Consulate about the approval for the purpose of issuing a visa, contact the appropriate U.S. Consulate directly if you or the beneficiary has questions about the process. For more information about USCIS processing after a petition is approved, see the instructions on the form you filed.

FORM I-94 ATTACHMENT

You can find your replacement Form I-94 (Arrival/Departure Record) in the lower portion on the front side of this notice. Keep the right half of your replacement Form I-94 with your passport, along with a copy of your original I-94 if you have it. Keep the left half of your replacement Form I-94 in a safe place with your personal records. Submit a copy of your replacement Form I-94 with any future application or petition.

When you leave the United States, you must turn in the right half of your I-94 (kept in your passport) to the officials at the airport, border or seaport. If you do not do so, it may delay your entry into the United States in the future. You may stay in the United States only until the date indicated on this form. If you want to remain in the United States past this date, you will need further authorization from USCIS.

If you are a student planning to reenter the United States within 30 days to return to the same school, review the "Instructions to Students" on Page 3 of Form I-20 before surrendering your replacement I-94.

If you lose the right half of your replacement Form I-94 (kept in your passport), submit a copy of the left half of the Form I-94 (that you keep with your personal records), along with a new Form I-102, to apply for a new replacement I-94.

Warning: If you accept employment without our authorization, you may be subject to removal or deportation.

中华人民共和国外交部请各国军政机关对持照人予以通行的便利和必要的协助。

The Ministry of Foreign Affairs of the People's Republic of China requests all civil and military authorities of foreign countries to allow the bearer of this passport to pass freely and afford assistance in case of need.

护照
PASSPORT

类型 / Type
P

国家码 / Country Code
CHN

护照号 / Passport No.
G42226545

姓 / Surname
阳 / YANG

名 / Given names
宇光 / YUGUANG

性别 / Sex
男 / M

出生日期 / Date of birth
09 OCT 1988

签发日期 / Date of issue
22 APR 2010

签发机关 / Authority
公安部出入境管理局
Exit & Entry Administration
Ministry of Public Security

出生地点 / Place of birth
广西 / GUANGXI

签发地点 / Place of issue
浙江 / ZHEJIANG

有效期至 / Date of expiry
21 APR 2020

52621102

P<CHNYANG<<YUGUANG<<<<<<<<<<<<<<<<<<<<<<<<<<<<

G422265454CHN8810090M2004219192033O1<<<<<<18

29

签证 Visas

G42226545

VISA

UNITED STATES OF AMERICA

Issuing Post Name
SHANGHAI

Control Number
20111539740008

Surname
YANG

Given Name
YUGUANG

Visa Type /Class
R F1

Passport Number
G42226545

Sex
M

Birth Date
09OCT1988

Nationality
CHIN

Entries
M

Issue Date
30JUN2011

Expiration Date
28JUN2012

0101

Annotation
N0008209211
JOHNS HOPKINS UNIVERSITY-HOMEWOOD CAMPUS
CLEARANCE RECEIVED 29-JUN-2011

SB46237

* *

VNUSAYANG<<YUGUANG<<<<<<<<<<<<<<<<<<<<<<<<

G422265454CHN8810090M1206289F1SHGONEFK540138


25
G42226545
Visas
09 JUL 19
07 JUL 10
2010
JUL 10 2010
VISA
UNITED STATES OF AMERICA
Issuing Post Name
SHANGHAI
Control Number
20101521630001
Surname
YANG
Given Name
YUGUANG
Visa Type /Class
R F1
Passport Number
G42226545
Sex
M
Birth Date
09OCT1988
Nationality
CHIN
Entries
M
Issue Date
02JUN2010
Expiration Date
31MAY2011
0101
Annotation
N0007236792
UC DAVIS EXTENSION, INTERNATIONAL PROGRAMS002
* *
VNUSAYANG<<YUGUANG<<<<<<<<<<<<<<<<<<<<<<<<
G422265454CHN8810090M1105315F1SHGOH4E6540131

February 16, 2017

Yuguang Yang
2337 William Street
Palo Alto, CA 94306

yangyutu123@gmail.com

Dear Yuguang:

Congratulations! I am very pleased to confirm our offer of employment to you for the position of Quantitative Associate in Charlotte, NC. As discussed, your start date is June 12, 2017. Your position, group placement, and location are based upon business needs and are subject to change.

At Wells Fargo, you will have the opportunity to start developing your career and taking advantage of programs and resources that will help you begin realizing your full personal and professional potential as we work together to serve our customers and our communities.

COMPENSATION
As we discussed, your annual base salary rate will be $125,000.00. You will receive your base salary every two weeks, on the Friday following the end of each two-week pay period. Your base salary compensates you for all hours worked in any given week and your biweekly base salary will be calculated based on the exact number of business days within each calendar year.

INCENTIVE PAY
You will be eligible to participate in an incentive plan. The amount earned, if any, will be determined in accordance with plan terms, and is contingent upon accomplishment of performance objectives.

The determination and payment of compensation are subject to the conditions and restrictions imposed under applicable laws, rules and regulations. Your rights to, or receipt of, compensation pursuant to this offer may be limited, modified, cancelled or recovered to ensure compliance with all such applicable laws, rules, regulations and guidance that may be issued there under.

BENEFITS
Wells Fargo provides a comprehensive benefits package to help team members maintain their overall health and wellness and to achieve financial security. Your benefits coverage will take effect the first of the month following the completion of one full calendar month of employment. We'll provide you with more detailed information soon. If you haven't received your benefits materials by the end of your first work week, call the Wells Fargo's dedicated support center for team members, at 1-877-HRWELLS (1-877-479-3557) to order a benefits enrollment kit. If you don't enroll during your initial benefits enrollment period, your next annual enrollment opportunity will be for benefits effective the following year.

RELOCATION
Moving to a new home or a new city can be a challenging time, to help you with your relocation Wells Fargo will pay you a lump sum of $12,000, plus tax gross-up. You will also receive assistance with finding a home in the new location. Once management submits the authorization for your relocation to the Wells Fargo Global Relocation team, a Wells Fargo Relocation Consultant will contact you to discuss the program benefits and how best to help support you in your relocation and the tax implications of your relocation benefits. Wells Fargo's relocation repayment agreement will apply to these benefits.

VISA SPONSORSHIP
This offer is contingent on demonstrating that you will be authorized to work in the United States in this position upon the start of employment at Wells Fargo. Accordingly, Wells Fargo reserves the right to revoke this offer if you do not demonstrate that you are authorized to work as of your scheduled start date on June 12, 2017. It is Wells Fargo's intention to apply for sponsorship of an H-1B Visa should you require one when you commence employment on June 12, 2017 subject to the visa requirements and approval of the United States Immigration and Citizenship Service

(USCIS). The earliest such visas can be effective is in October of 2017 due to USCIS processing times and other factors. Consequently, you must possess current authorization to work in the United States from June 12, 2017 through at least October, 2017, and possibly longer depending the H-1B processing times. Wells Fargo will cover the fees and costs associated with the visa process. You should understand that Wells Fargo reserves the right to stop the visa petition process at any time for any reason. Please be advised that as an employee on visa sponsorship, you will not be able to post for any other jobs within Wells Fargo because the visa is linked to the specific position for which you were hired. Furthermore, there is no guarantee that the present visa sponsorship will lead to an extension of the current visa, transfer to another status, or sponsorship for permanent residency.

DEGREE REQUIREMENT
This offer is contingent on either possessing a Ph.D., or finishing all requirements for a Ph.D. before June 12, 2017 and actually being granted the degree before January 31, 2018. Failure to receive the degree by this time can be cause for dismissal.

The enclosed Offer Summary outlines the specifics of our offer. If you are in agreement with these terms, please sign and date the acknowledgement and verbally communicate your decision before faxing the signed document. We would like to receive your acceptance by 5 pm EST on Thursday, February 23rd.

You'll quickly discover that key values at Wells Fargo include accountability, integrity, customer focus, and diversity. As a financial services institution, we are entrusted with confidential information and the resources of our customers - a trust we take very seriously. We also have a responsibility as an employer to share with you some basic conditions of employment at Wells Fargo - you'll find those within this letter; please read them carefully.

When you start work, you'll receive access to the Handbook for Wells Fargo Team Members, tax forms, and additional paperwork that you will need to get started in your new career. On your first day, please be sure to bring acceptable documents for establishing your employment eligibility as outlined in the Conditions of Employment at the end of this letter. You will need these documents in order to complete your new hire paperwork.

If you have any questions, please contact me at (704) 715-7802. We look forward to having you join us!

We look forward to having you join us!

Shasta Cornelius
Senior Recruiter | Wells Fargo
Ph: 704-715-7802 | Cell: 704-749-4431 | Fax: 866-405-9752
shasta.cornelius@wellsfargo.com

Offer Acceptance for Yuguang Yang

Conditions of employment at Wells Fargo

The offer letter, including these Conditions of Employment, the Trade Secrets Agreement, and the Arbitration Agreement, constitutes the entire agreement between you and Wells Fargo. No other guarantees or promises of any kind have been made concerning the terms of your employment. Only an officer of Wells Fargo, at the level of executive vice president or higher, who is authorized by the senior Human Resources manager for your region or line of business, may change or modify these terms.

Both you and Wells Fargo have the right to terminate your employment at any time, with or without advance notice and with or without cause. This is called "employment at will."

This offer is contingent on your ability to provide, on or before the first day of employment, documentation that verifies your identification and eligibility to work in the United States, as outlined by the Immigration Reform and Control Act of 1986. As a result of federal legislation, and because Wells Fargo is a federal contractor, this offer is also contingent on your ability to successfully pass the federal E-Verify system check within the requisite period of time permitted by the E-Verify rules.

As part of the process to verify your identity and eligibility to work in the United States, you should take the following steps to be prepared on your first day of employment:

1. Access the electronic Form I-9, Employment Eligibility Verification, using the CARCO system. A link to the system will be emailed to your home email address before your hire date.

2. Follow the instructions for completing section 1 of Form I-9.

3. Determine which acceptable document(s) you will provide on your first day of employment to verify your identity and eligibility to work in the United States. The lists of acceptable documents are on Form I-9. Verify that the documents meet the unexpired date(s) requirement under Form I-9 rules.

4. Bring the original document(s) (including a picture ID for E-Verify identification purposes) on your first day and each day thereafter until your manager (or manager's designee) completes the review and verification process.

As a federally insured institution, Wells Fargo is unable to employ individuals who have been convicted of, or participated in a pre-trial diversion program with respect to, a crime of dishonesty or breach of trust, or any person who does not meet Wells Fargo's bond requirements. Wells Fargo also may elect not to employ individuals with certain convictions for crimes involving violence or harassment. Therefore, this offer is contingent on the results of your background investigation which includes fingerprinting, required regulatory reviews and any ongoing screening for continued employment.

To protect Wells Fargo's intellectual property and human capital, all new hires are required to complete a corporate Trade Secrets Agreement. The Trade Secrets Agreement contains an agreement not to disclose Wells Fargo trade secrets and confidential and proprietary information, an agreement for non-solicitation, and assignment of inventions to Wells Fargo if the inventions were made or conceived while you were employed by Wells Fargo.

In addition, when employment disputes cannot be resolved internally, it is helpful to do so through private arbitration instead of court. All new hires are required to complete an Arbitration Agreement in which you and Wells Fargo mutually agree to final and binding arbitration of your employment disputes when they cannot be resolved internally.

Team members support our focus on building strong customer relationships balanced with a strong risk mitigating and compliance-driven culture which firmly establishes those disciplines as critical to the success of our customers and company. They are accountable for execution of all applicable risk programs (Credit, Market, Financial Crimes, Operational, Regulatory Compliance), which includes effectively following and adhering to applicable Wells Fargo policies and procedures, appropriately fulfilling risk and compliance obligations, timely and effective escalation and remediation of issues, and making sound risk decisions. There is emphasis on proactive monitoring, governance, risk identification and escalation, as well as making sound risk decisions commensurate with the business unit's risk appetite and all risk and compliance program requirements.

By signing and returning a copy of this letter, you accept and agree to all terms and conditions of this offer of employment.

Accepted and agreed to:

Yuguang Yang — 2/20/2017

Signature for Yuguang Yang — Date

Employee ID Number: _____

Hiring Manager please send signed copies to:
Local Team Member File
New Hire Forms Processing, MAC S4101-163

Together we'll go far

LIU & ASSOCIATES, PLLC
ATTORNEYS AT LAW

5718 WESTHEIMER ROAD
SUITE 1100
HOUSTON, TX 77057

TEL: 800-878-1807
FAX: 866-608-2766
ZLIU@NIWUS.COM
www.niwus.com

DOCUMENTS LIST:
NATIONAL INTEREST WAIVER (NIW I-140) PETITION

1. Original, signed recommendation letters;

2. Your Curriculum Vitae;

3. Copy of your M.S. or Ph.D. degree certificate(s); if submitting foreign degree, please provide evaluation report that your educational background is at least equivalent to a Master's degree in the United States;

4. Copy of all available journal articles or conference publications, abstracts, programs/presentations (we do not need power point slides), in final published formats;

5. ISI Web of Knowledge ranking of journals in which you are published and/or journal information from the journal web site;

6. Citation report of your publications, if any:
   - Find your citations on ISI Web of Science, Google Scholar, or another major citation database. Use only ONE database that returns the most number of total citations.
   - The citation report should list the authors and titles of the cited article **and** each article citing to your work. Do not copy/paste the report. Print directly from the web site with URL and date stamp.

7. Evidence of your work being implemented by others. Evidences may include:
   - Contracts with companies using your products; or
   - Patents/licensed technology being used by others.

8. Copy of media or news reports about you and your work. Evidence may include:
   - The title, date, and author of the published material; and
   - Circulation information of the media or newspaper.

9. Documents of your participation, either individually or on a panel, as the judge of the work of others in your field, if any. Evidences may include:
   - Copy of e-mails, directly addressed to you, requesting your reviewer work **and** acknowledging your completion of reviewer work;
   - Copy of e-mails, directly addressed to you, requesting your service on conference program committees and documentary evidence acknowledging your service (e.g., e-mails or conference program listing your name as committee member); and
   - Copy of e-mails, directly addressed to you, inviting you to join the Editorial Board of scientific journal and documentary evidence acknowledging your service (e.g., e-mails and/or listing on journal web site).

- Print background information about each journal or conference from its web site.

10. Documents of membership in professional associations that require outstanding achievements. Evidences may include:
    - Copy of your membership card, letter, or e-mail indicating your membership;
    - The section of the association's constitution or bylaws that discuss the criteria for your level of membership;
    - Information establishing individuals who review prospective members' applications are recognized as national or international experts in the field; and
    - Information about the organization, its goals, mission, and target membership.

11. Copy of certificates for major national or international awards for outstanding achievement. Evidences may include:
    - Published announcement regarding the award issued by granting organization;
    - Documentary evidence of the selection criteria used to grant the awards; and
    - Documentary evidence demonstrating: the significance of the awards, including the national or international recognition that the awards share; the reputation of the organization granting the awards; the geographic scope for which candidates may apply; how many awards are given each year; previous winners who enjoy national or international acclaim; and media attention that the awards receive.

12. Copy of job offer letter and/or originally signed employment verification letter from current employer;

13. Copy of previously filed immigrant petition receipt/approval/denial notice if applicable;

14. Copy of your passport (biographic page and visa stamps), both sides of all Forms I-94, and evidence of your current nonimmigrant visa status (such as I-20s, OPT card, I-797As, DS-2019s);

15. Declaration of Authenticity of Documents signed and dated by you;

16. Completed Questionnaire (if not already emailed to attorney); and

17. USCIS Filing Fees:
    - $700.00 Form I-140 filing fee
    - *Make check payable to "U.S. Department of Homeland Security"*
    - *Per USCIS instructions, please be sure the account holder's name, address, and phone number are on the top left corner of each check.*
    - *If the petitioner is not the account holder, please write the petitioner's name on the memo line of each check.*

General Comments:

* All documents obtained from the Internet must be printed directly from the web site with web address/URL and date stamp.

** Attach a certified English translation to any foreign language document. The translation must be completed by a translator (other than yourself) who is fluent in both English and the foreign language. Please contact our office for a sample. (Scientific publications in a foreign language only require an English abstract).

*** Retain a copy of all documents for your records and **mail a hard copy of the supporting documents and signed letters of recommendation to our office** to be submitted to USCIS. The signed and dated "DECLARATION OF AUTHENTICITY OF DOCUMENTS" should be included with the physical documents.

**** If you are filing more than one type of petition (e.g., NIW and EB-1A), please provide a full set of documents for each petition.

***** Do not staple your documents together. We prefer that you use paper clips to separate and divide your documents.

****** Upon receipt of the physical supporting documents, our office will prepare the petition letter in approximately two (2) weeks. No additional documents will be considered or inserted once we have begun to work on the petition letter.

DECLARATION OF AUTHENTICITY OF DOCUMENTS

I hereby declare that the copies of the documents submitted are exact photocopies of unaltered original documents. I understand that I maybe be required to submit original documents to an Immigration or Consular Officer at a later date.

Yuguang Yang
_____
Name of Beneficiary

Yuguang YANG
_____
Signature of Beneficiary

12/31/2018
Date: _____

LIU & ASSOCIATES, PLLC
ATTORNEYS AT LAW

5718 WESTHEIMER ROAD
SUITE 1100
HOUSTON, TX 77057

TEL: 800-878-1807
FAX: 866-608-2766
ZLIU@NIWUS.COM
www.niwus.com

NIW I-140 Petition Questionnaire

(We will use the information to complete several immigration forms that will be filed with the USCIS. Please provide as much accurate information as possible. *)*

I. Information about You and Your Job

Your Name in English	
Last Name	Yang
First Name	Yuguang
Middle Name	

Your Name in Your Native Language (e.g., Chinese characters)	
Last Name	阳
First Name	宇光
Middle Name	

Current Physical Address in the U.S.	
Street Number and Name	232 Queens Road
Apt./Ste./Flr.	Apt 51
City, State, Zip code	28204

Current Mailing Address (if different)	
Street Number and Name	
Apt./Ste./Flr.	
City, State, Zip Code	

Information About You and Your Job	
Daytime Phone #	410-294-6268
Mobile Phone #	410-294-6268
Email	yangyutu123@gmail.com
Date of Birth	10/9/1988
Social Security #	276194312
City of Birth	Guiling
Province/State of Birth	Guangxi
Country of Birth	China
Country of Citizenship	China
Country of Nationality	China
USCIS A# (if any)	

Passport #	G42226545
Passport Country of Issuance	China
Date Passport Expires (mm/dd/yyyy)	4/21/2020
Date of Last Arrival in the U.S.	9/6/2013
I-94 #	06049654530
Current Nonimmigrant Status	H1B
Expiration Date	9/4/2020
Country of Last Permanent Residence Abroad	China
Job Title	Quantitative associate
Annual Income	$180,000.00
Name and Address of Employer	Wells Fargo Bank NA 815 connecticut Ave NW Washington Dc 20006

Your Foreign Address (in English)	
Street Number and Name	lingchaun xian lingbei road #54
Apt./Ste./Flr.	
City or Town	Guiling shi
Postal Code	541200
Province	Guangxi Province
Country	China

Your foreign address in your native language (such as Chinese characters)	
Street Number and Name	中国广西桂林灵川县灵北路 54 号
Apt./Ste./Flr.	
City or Town	桂林市
Postal Code	541200
Province	广西省
Country	中国

If you or anyone has filed an immigration petition before, please provide the following information (Please contact your attorney if you are unsure):	
Receipt # of previously filed petition(s)	
Date when the petition(s) was/were filed	
Service Center(s) where the petition(s) was/were filed	
Result of the previously filed petition(s)	
Approval/denial date(s) of the previously filed petition(s)	

II. Your Education

Name of College/University	Field of Study	From mm/yy	To mm/yy	Degree
Johns Hopkins University	Chemical Engineering	09/11	02/17	Ph.D
Johns Hopkins University	Computer Science	09/14	01/16	Master
Zhejiang University	Polymer Science and Engineering	09/08	07/11	BE

III. Information about Your Spouse and All Children

Spouse	
Last Name	
First Name	
Middle Name	
Date of Birth	
Country of Birth	
Present Address (if different)	
Applying for Adjustment of Status *	☐ Yes ☐ No
Applying for a Visa Abroad **	☐ Yes ☐ No
Gender	☐ Male ☐ Female

Child	
Last Name	
First Name	
Middle Name	
Date of Birth	
Country of Birth	
Present Address (if different)	
Applying for Adjustment of Status *	☐ Yes ☐ No
Applying for a Visa Abroad **	☐ Yes ☐ No
Gender	☐ Male ☐ Female

Child	
Last Name	
First Name	
Middle Name	
Date of Birth	
Country of Birth	
Present Address (if different)	

Applying for Adjustment of Status *	☐ Yes ☐ No
Applying for a Visa Abroad **	☐ Yes ☐ No
Gender	☐ Male ☐ Female

Child	
Last Name	
First Name	
Middle Name	
Date of Birth	
Country of Birth	
Present Address (if different)	
Applying for Adjustment of Status *	☐ Yes ☐ No
Applying for a Visa Abroad **	☐ Yes ☐ No
Gender	☐ Male ☐ Female

** If the person is in the U.S. and will remain in the U.S. for the foreseeable future to apply for green card, then filing Form I-485 application for adjustment of status is recommended. Check "Yes.".*

*** If the person is outside the U.S. or plans to leave the U.S. for an extended period in the future, then applying for immigrant visa/green card through Consular Processing at the U.S. embassy abroad is recommended. Check "Yes.").*

IV. Your work/research experience during the last three (3) years. Also, list any other jobs related to your occupation.

Current Employer	
Name	Wells Fargo Bank
Address	550 South Tryon Street Suit 400
Date Started (mm/yy)	07/17
Date Left (mm/yy)	Current
Type of Business	Financing
Job Title	Quantitative associate
No. of hours per week	40
Describe in detail the duties performed, including use of tools, machines, equipment	
Construct and calibrate pricing and risk analytics models for financial derivatives. Develop production computation code for pricing and risk analytics.	

Past Employer	
Name	
Address	
Date Started (mm/yy)	
Date Left (mm/yy)	

Type of Business	
Job Title	
No. of hours per week	
Describe in detail the duties performed, including use of tools, machines, equipment	

Past Employer	
Name	
Address	
Date Started (mm/yy)	
Date Left (mm/yy)	
Type of Business	
Job Title	
No. of hours per week	
Describe in detail the duties performed, including use of tools, machines, equipment	

Past Employer	
Name	
Address	
Date Started (mm/yy)	
Date Left (mm/yy)	
Type of Business	
Job Title	
No. of hours per week	
Describe in detail the duties performed, including use of tools, machines, equipment	

Past Employer	
Name	
Address	
Date Started (mm/yy)	
Date Left (mm/yy)	
Type of Business	
Job Title	
No. of hours per week	
Describe in detail the duties performed, including use of tools, machines, equipment	

Past Employer	
Name	
Address	
Date Started (mm/yy)	

Date Left (mm/yy)	
Type of Business	
Job Title	
No. of hours per week	
Describe in detail the duties performed, including use of tools, machines, equipment	

CERTIFICATION

I understand that the foregoing information provided in the Questionnaire and given to Liu & Associates, PLLC will be used to prepare related immigration form(s) that I will need to sign for the applications.

I understand that when I sign the immigration form(s), I am certifying under penalty of perjury under the laws of the United States of America that the information in the immigration form(s) as well as all evidence submitted with the petition is true and correct.

Yuguang Yang
Please type your name to electronically sign this certification

Yuguang Yang
Please re-type you name to confirm your electronic signature

12/31/2018

Date